Design and synthesis of blue thermally activated delayed fluorescence emitters for organic light emitting diodes

Dongyang Chen

A thesis submitted for the degree of PhD
at the
University of St Andrews

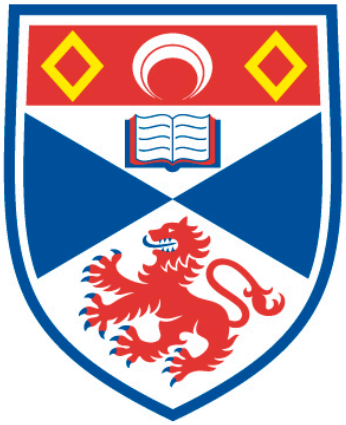

2022

Identifier to use to cite or link to this thesis:

DOI: https://doi.org/10.17630/sta/164

Candidate's declaration

I, Dongyang Chen, do hereby certify that this thesis, submitted for the degree of PhD, which is approximately 60,000 words in length, has been written by me, and that it is the record of work carried out by me, or principally by myself in collaboration with others as acknowledged, and that it has not been submitted in any previous application for any degree. I confirm that any appendices included in my thesis contain only material permitted by the 'Assessment of Postgraduate Research Students' policy.

I was admitted as a research student at the University of St Andrews in August 2016.

I received funding from an organization or institution and have acknowledged the funder(s) in the full text of my thesis.

Date 01/12/2021 Signature of candidate

Supervisor's declaration

I hereby certify that the candidate has fulfilled the conditions of the Resolution and Regulations appropriate for the degree of PhD in the University of St Andrews and that the candidate is qualified to submit this thesis in application for that degree. I confirm that any appendices included in the thesis contain only material permitted by the 'Assessment of Postgraduate Research Students' policy.

Date 01/12/2021 Signature of supervisor

Permission for publication

In submitting this thesis to the University of St Andrews we understand that we are giving permission for it to be made available for use in accordance with the regulations of the University Library for the time being in force, subject to any copyright vested in the work not being affected thereby. We also understand, unless exempt by an award of an embargo as requested below, that the title and the abstract will be published, and that a copy of the work may be made and supplied to any bona fide library or research worker, that this thesis will be electronically accessible for personal or research use and that the library has the right to migrate this thesis into new electronic forms as required to ensure continued access to the thesis.

I, Dongyang Chen, have obtained, or am in the process of obtaining, third-party copyright permissions that are required or have requested the appropriate embargo below.

The following is an agreed request by candidate and supervisor regarding the publication of this thesis:

Printed copy

Embargo on all of print copy for a period of 2 years on the following ground(s):

- Publication would preclude future publication

Supporting statement for printed embargo request

Two of the Chapters are still not published yet.

Electronic copy

Embargo on all of electronic copy for a period of 2 years on the following ground(s):

- Publication would preclude future publication

Supporting statement for electronic embargo request

Two of the Chapters are still not published yet.

Title and Abstract

- I agree to the title and abstract being published.

Date 01/12/2021 Signature of candidate

Date 01/12/2021 Signature of supervisor

Underpinning Research Data or Digital Outputs

Candidate's declaration

I, Dongyang Chen, understand that by declaring that I have original research data or digital outputs, I should make every effort in meeting the University's and research funders' requirements on the deposit and sharing of research data or research digital outputs.

Date 01/12/2021 Signature of candidate

Permission for publication of underpinning research data or digital outputs

We understand that for any original research data or digital outputs which are deposited, we are giving permission for them to be made available for use in accordance with the requirements of the University and research funders, for the time being in force.

We also understand that the title and the description will be published, and that the underpinning research data or digital outputs will be electronically accessible for use in accordance with the license specified at the point of deposit, unless exempt by award of an embargo as requested below.

The following is an agreed request by candidate and supervisor regarding the publication of underpinning research data or digital outputs:

Embargo on all of electronic files for a period of 2 years on the following ground(s):

- Publication would preclude future publication

Supporting statement for embargo request

Two of the Chapters are still not published yet.

Title and Description

- I require an embargo on the description only

Date 01/12/2021 Signature of candidate

Date 01/12/2021 Signature of supervisor

Abstract

Thermally activated delayed fluorescence (TADF) has emerged as one of the most promising and efficient approaches to realize highly efficient organic light-emitting diodes (OLEDs). It took only several years for OLEDs using organic TADF emitters to reach efficiencies comparable to phosphorescent OLEDs. Chapter 1 presents an overview of the TADF mechanism and focuses more specifically on blue TADF emitter design and their use in OLEDs. There is still room for improvement in terms of highly efficient deep-blue TADF emitters. These include improving exciton lifetime and reducing exciton annihilation in device, and optimizing the orientation of the transition dipole moment of the emitter to enhance light out-coupling. This thesis is focused on blue TADF emitter design and makes efforts to address these issues, and throughout the projects in this thesis, various design strategies are presented to optimize blue TADF materials for OLED applications.

In Chapter 2, three TADF emitters each with a multichromphore structure are presented. In Chapter 3, we explored the use of heteroaromatic bridges between donor and acceptor units for efficient blue TADF emitter design and synthesized four TADF emitters based on different heteroaromatic sulfones as acceptors. In Chapter 4, we synthesized two pyrazine-based emitters bearing a mono and dipyrazine acceptors and di-*tert*-butylcarbazole as the donor, and in Chapter 5, two pyridine-containing ambipolar hosts were designed and employed as the host for yellow TADF OLEDs. In Chapter 6, to improve and control the orientation of TADF emitters in solution-processed films we explored introducing mesogens onto to TADF emitter. The compound **DiKTaLC** exhibits both TADF and liquid crystal character. The transition dipole moment of the as-prepared spin-coated neat film of **DiKTaLC** shows preferential

horizontal orientation. In Chapter 7, we explored the possibility of using nanohoop structures in terms of cycloparaphenylenes (CPPs) for TADF emitter design. The photophysical properties of these materials are investigated, and state-of-the-art OLED performances are demonstrated.

Acknowledgement

First of all, I would like to thank Prof. Eli Zysman-Colman for the constant support, guidance and help provided to me throughout my PhD journey. I am also grateful for the financial support from China Scholarship Council.

Sincere thanks go to all the St Andrews chemistry staff, include but not limited to our kind and helpful secretary group, store, and service staff. A special gratitude goes to Dr. David B. Cordes and Prof. Alexandra M. Z. Slawin for the X-ray crystallography

I also wanted to thank all my collaborators.

I would like to thank Dr. Pachaiyappan Rajamalli, our collaboration is fruitful and reliable in the last four years, and I am totally grateful.

I would like to thank Prof. Ifor Samuel and his group for their help and guidance with photophysical measurements.

I would like to thank Prof. Hronori Kaji, Prof. Shigeru Yamago, Prof. Eiichi Kayahara, Prof. Katsuaki Suzuki, Dr. Yoshimasa Wada, Dr Liangsheng Sun, and the whole group members for their hospitality and guidance during my time in Kyoto. It was an amazing experience.

I would like to thank Prof. Malte Gather and Dr. Francisco Tenopala Carmona for the help of orientation study.

I would like to thank Prof. Lachat Sabine and Mr. Knöller Julius Agamemnon for your help with liquid crystal material's thermal property investigation.

Thank you to all the great colleagues I had the pleasure to work with during my time spent in EZ-C group. A special thank you to the colleagues I began this PhD with: Dr. Adam Henwood, Dr. Claus Hierlinger, Dr. Laura Abad Galan, Dr. Diego Martir, Dr. Nidhi Sharma,

Dr. Chenfei Li, Boyi Song and Dr. Michael Yin Wong. Thank you to the great people who joined the group at later stages: Dave Hall, Changfeng Si, Sen Wu, Dr John Marques Dos Santos, Dr Abhishek Kumar Gupta, Dr Shiv Kumar, Dr Campbell Mackenzie, Dr Tomas Matulaitis, Dr Ji Yeon Ryu, Dr Eduard Spuling, Dr Dianming Sun, Dr Subeesh Suresh, Dr Jiyu Tian, Hannah Bosch, Ana Neferu, Bryony Hockin, Dr. Graeme Copley, Peter Brown, Megan Bryden, Thomas Comerford, Ettore Crovini, Callum Prentice, Zhaoning Li. Thank you also to the rest of the EZ-C group, the countless colleagues and friends for our great time together.

I am grateful for my family in Hunan and UK.

Last but not least, thanks for all my friends in St Andrews, China, it was my honour to be their friend, and my achievement should be shared with all of you.

Abbreviations, Acronyms, and Terminology

ΔE_{ST}	Singlet-Triplet Energy Gap
γ	Charge carrier balance
η_{out}	Out-coupling efficiency
Q_{α}	Nuclear degree of freedom
$\hat{s}_i$	Spin operator of electron
ρ_{FCWD}	Franck-Condon-weighted density
λ	Marcus reorganization energy
λ_{PL}	Emission maximum of photoluminescence
λ_{EL}	Emission maximum of electroluminescence
μ_{10}	Transition dipole moment value
$\hat{l}_i$	Angular momentum
$\hbar$	Reduced Planck's constant
V_{SOC}^{eff}	Spin-orbital coupling operator
$\langle\tilde{\nu}\rangle_{av}$	Average wave number
c	Light speed
d	Distance
e	Charge of electron
E_S	Singlet energy
E_T	Triplet energy
f	Oscillator strength
J	Exchange energy

K	Coulombic energy
m_e	Electron mass
M_w	Weight-average molecular weight
M_n	Number-average molecular weight
k_B	Boltzmann's constant
k_{ISC}	Intersystem crossing rate
k_{nr}	nonradiative rate constant
k_r	Radiative rate constant
k_{RISC}	Reverse intersystem crossing rate
T	Temperature
T_g	Glass-Transition Temperature
T_d	Degradation temperature
Z_I^{eff}	Effective nuclear charge
AcOH	Acetic acid
ACQ	Aggregated Caused Quench
AFM	Atomic Force Microscopy
APS	Air Photoemission Spectroscopy
B3PYMPM	4,6-Bis(3,5-di(pyridin-3-yl)phenyl)-2-methylpyrimidine
BmPyPhB	1,3-Bis[3,5-di(pyridin-3-yl)phenyl]benzene
n-BuLi	*n*-butyllithium
CBP	4,4′-Bis(*N*-carbazolyl)-1,1′-biphenyl
CE	Current Efficiency

CIE	Commission internationale de l'éclairage
CPP	Cycloparaphenylene
DCM	Dichloromethane
DFT	Density Functional Theory
DMAC	9,9-Dimethyl-9,10-dihydroacridine
DMF	*N*,*N*-dimethylformamide
DPEPO	Bis[2-(diphenylphosphino)phenyl] ether oxide
DSC	Differential Scanning Calorimetry
EA	Ethyl Acetate
EL	Electroluminescent or Electroluminescence
EQE	External Quantum Efficiency
FMO	Frontier Molecular Orbital
FRET	Förster Resonance Energy Transfer
FWHM	Full Width at Half Maximum
GPC	Gel Permeation Chromatography
HFC	Hyperfine Coupling
HOMO	Highest Occupied Molecular Orbital
HONTO	Highest Occupied Natural Transition Orbital
HSOMO	Highest Singerly Occupied Molecular Orbital
ICT	Intramolecular Charge Transfer
IQE	Internal Quantum Efficiency
ISC	Intersystem Crossing

ITO	Indium Tin Oxide
LE	Locally-Excited
LEEC	Light-Emitting Electrochemical Cell
Liq	8-Quinolinolato lithium
LUMO	Lowest Unoccupied Molecular Orbital
LUNTO	Lowest Unoccupied Natural Transition Orbital
LSOMO	Lowest Singerly Occupied Molecular Orbital
*m*CP	1,3-Bis(*N*-carbazolyl)benzene
mCBP	3,3′-Di(9H-carbazol-9-yl)-1,1′-biphenyl
MR	Multi-Resonance
NBS	*N*-bromosuccinimide
NIR	Near-Infrared
NMP	*N*-Methyl-2-pyrrolidinone
NMR	Nuclear magnetic resonance
NPB	*N*,*N*′-Di(1-naphthyl)-*N*,*N*′-diphenyl-(1,1′-biphenyl)-4,4′-diamine
OLED	Organic Light-Emitting Diode
PDI	Polydispersity index
PE	Power Efficiency
PEDOT:PSS	Poly(3,4-ethylenedioxythiophene)-poly(styrenesulfonate)
PLQY	Photoluminescence Quantum Yield
PMMA	Poly(methyl methacrylate)
POM	Polarising Optical Microscopy

PPF	2,8-Bis(diphenylphosphineoxide)dibenzofuran
PPT	2,8-Bis(diphenylphosphoryl)dibenzo[b,d]thiophene
PVK	Poly(*N*-vinylcarbazole)
PyD2	2,6-Bis(9H-carbazol-9-yl)pyridine
RIC	Reverse Internal Conversion
RISC	Reverse Intersystem Crossing
SCE	Saturated Calomel Electrode
S_NAr	Nucleophilic Aromatic Substitution
SOC	Spin-Orbit Coupling
TADF	Thermally Activated Delayed Fluorescence
TAPC	4,4′-Cyclohexylidenebis[*N*,*N*-bis(4-methylphenyl)benzenamine]
TBAF	Tetrabutylammonium Fluoride
TBDMSCl	*Tert*-butyldimethylsilyl chloride
tBu-PBD	2-(4-*tert*-Butylphenyl)-5-(4-biphenylyl)-1,3,4-oxadiazole
TCTA	Tris(4-carbazoyl-9-ylphenyl)amine
TES	Triethylsilyl
TDM	Transition dipole moment
TD-DFT	Time-Dependent Density Functional Theory
THF	Tetrahydrofuran
TIPs	Triisopropylsilane
TIPSCl	Chlorotriisopropylsilane
TmPyPB	1,3,5-Tri(*m*-pyridin-3-ylphenyl)benzene

TPBI	2,2’,2’’-(1,3,5-Benzinetriyl)-tris(1-phenyl-1-*H*-benzimidazole)
TPA	Triplet-polaron annihilation
TTA	Triplet-triplet annihilation

Table of Contents

Chapter 2

Multichromophore Molecular Design for Efficient Thermally Activated Delayed Fluorescence Emitters with Near-Unity Photoluminescence Quantum Yields

Chapter 3

The use of Nitrogen-Heteroaromatic Bridges as a Design Strategy to Improve the Performance of Thermally Activated Delayed Fluorescence Organic Light Emitting Diodes

Chapter 4

Planar pyrazine based TADF emitter for deep blue bright organic light emitting diodes

Chapter 5

Bipyridine-containing Host Materials for High Performance Yellow Thermally Activated Delayed Fluorescence-based Organic Light Emitting Diodes with Very Low Efficiency Roll-Off

Chapter 6

Controlling the Emitter's Orientation in Solution-processed OLEDs using a Liquid Crystalline Multi-resonance TADF Emitter

Chapter 7

The Utilization of Cycloparaphenylene for Thermally Activated Delayed Fluorescence Emitters

Chapter 8

Experimental methods

Chapter 9

Appendix

Chapter 1

Background and Introduction

According to the latest energy consumption report in the UK (2020), the electricity consumption for lighting and displays in the UK has reached 27,000 GWh, which corresponds to 10% of the whole electricity consumption.[1] To achieve the government target of net-zero greenhouse gas emission, new lighting and display technology with high energy efficiency is essential. Organic light-emitting diodes (OLEDs) represent the most promising energy-efficient technology for future large-area, flexible displays, and solid lighting.[2–5] The high demand for cost-effective and energy-saving lighting and display drives the research of OLEDs to advance rapidly. During the last three decades of development, scientists have conducted extensive research for the working process of OLEDs and the luminescent mechanism of emitting molecules.[6–9] To date, OLED technology has matured, and products in the form of small and large displays have entered the consumer market. The research field around the OLED technology is still very active, where efforts have been directed towards materials development, light-outcoupling technology, and device lifetime, and further optimization and advancement continue apace.

1.1 Mechanism of light generation in OLEDs

1.1.1 Structure and operation

OLEDs are semiconductor light-emitting devices where the emissive electroluminescence layer is based on organic or organometallic materials. A typical OLEDs structure contains indium tin oxide (ITO) glass as a semitransparent anode, a hole transporting

layer (HTL), a light-emitting layer (EML), an electron transporting layer (ETL), and a layer of low work function metal as a cathode. When a voltage is applied to the electrodes, the light-emitting layer generates light. The light generation mechanism can be divided into four steps: carrier injection process, carrier transport process, excitons formation process, and excitons decay process. The four processes are shown in Figure **1.1a**.

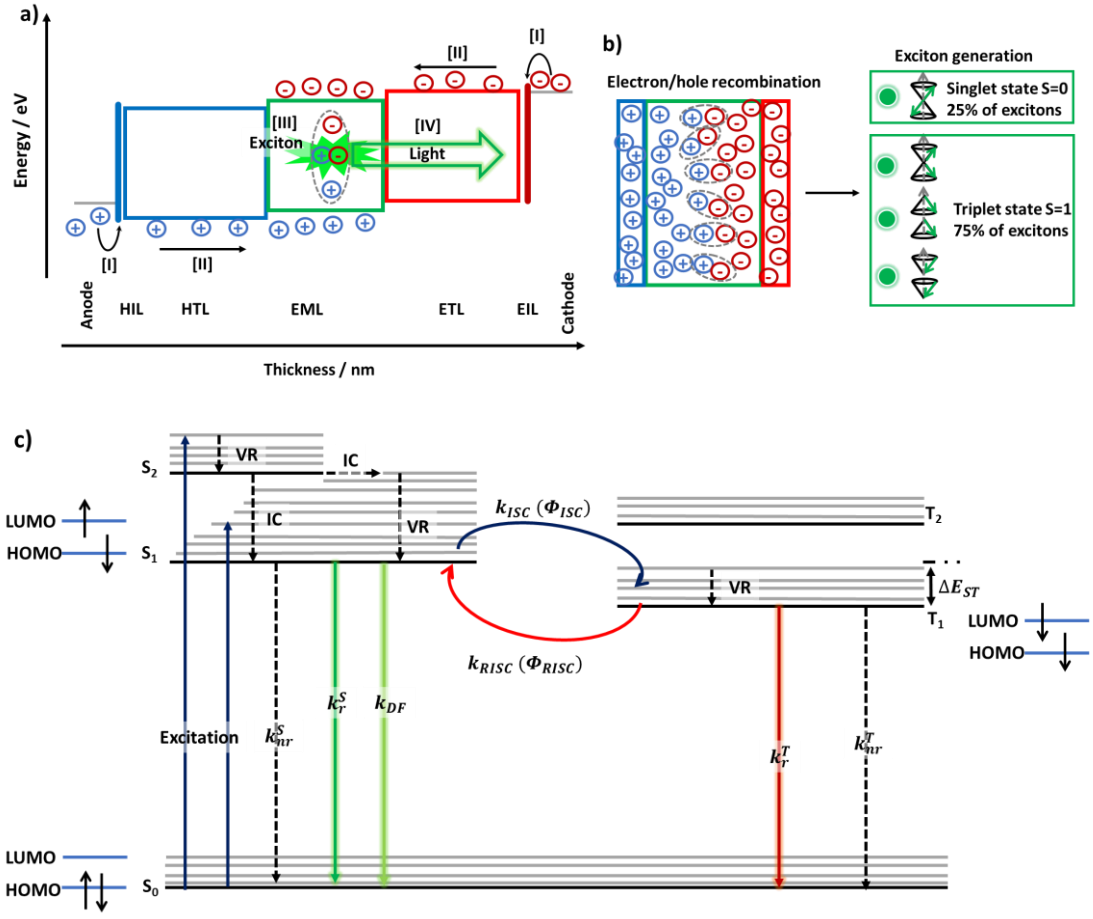

Figure **1.1**. a) Energy-level diagram of a multilayer OLED, b) exciton generation in EML and the four spin states, c) Perrin-Jablonski Diagram including possible transitions between the electronic states are represented including the spin configuration.

[I] Carrier injection process: The carrier injection process involves the injection of electrons and holes. The electrons are injected from the cathode to the lowest unoccupied molecular orbital (LUMO) of organic molecules in the electron transporting layer and form negative carriers. While holes are injected from the anode into the highest occupied molecular orbital (HOMO) of organic molecules in the hole transporting layer and form positive carriers. Increasing the interface recombination area between the organic layer and the electrode, could reduce the energy barrier between the interfaces and improve the injection efficiency of the carrier.[10]

[II] Carrier transportation process: Carriers that have been injected are transported in the organic layer along the direction of the electric field. In general, the carrier mobility of organic materials is low, typically ranging from 10^{-8} to 10^{-4} cm^2 V^{-1} s^{-1}.[10] The low carrier mobility of organic material is not conducive for effective carrier transport in the material. However, as OLEDs devices usually use ultra-thin (below 100 nm) film structure, it can generate high current density under low driving voltage, thus ensuring the device can produce desired luminous brightness under a low voltage.

[III] Exciton formation process: Injected electrons and holes, each with spin ½, form excitons upon recombination, driven by Coulombic forces, including 25% singlet excitons and 75% triplet excitons in the light-emitting layer (Figure **1.1b**).[11] The mechanism of singlet and triplet state formation is presented in section **1.1.2**. According to the early work of Adachi *et al.*, the width of the carrier recombination region in the OLEDs is only a few nanometers.[12] Therefore, the carrier mobility balance of organic layers, the thickness and the energy levels of organic layers should be considered when designing an OLEDs structure.

[IV] Exciton decay process: Excitons can decay to the S_0 via a variety of paths. The radiative decay of the exciton is the process of converting the potential energy of the exciton into the light.

The quantum efficiency of radiative decay is a crucial factor in determining the performance of the device. A good emitter for OLEDs should have a fast radiative rate constant (k_r) and a slow nonradiative rate constant (k_{nr}) to achieve high radiative decay efficiency. As the interaction between excitons can result in their quenching, the emitters are usually doped in a host material at a low concentration. The decay process is shown in Figure **1.1c**.

1.1.2 Formation of Electronic States – Singlet and Triplet States

In quantum mechanics, spin of an elementary particle, *s*, is restricted to either integer (for bosons) or half integer (for fermions) values. Electrons, protons, and neutrons are fermions and possess a spin of ½. The spin angular momentum $\vec{S}$ of an electron, which is a vector quantity, has a magnitude *S* of ½, and a direction of either + or -. Quantum mechanically, it is denoted by two eigenstates, $\boldsymbol{S}$ and S_z, where $\boldsymbol{S}$ is spin angular momentum operator and S_z is its projection on *z*-axis (Figure **1.2a**). The magnitudes (eigen values) of $\boldsymbol{S}$ and S_z are quantized and expressed as follows:

$|\boldsymbol{S}| = \sqrt{s(s+1)}\hbar$, and $S_z = m_s\hbar$, where *s* is electron spin (½) and $\hbar$ is the reduced Planck's constant, and m_s possess values from -s to +s and is the magnetic spin quantum number. Total possible values of m_s, i.e. spin multiplicity *m* is equal to 2*S*+1, where *S* is the total spin quantum number of a system. A two electrons system will have four possible spin eigenstates (see Figure **1.2b**). The first spin wavefunction has *S* = 0 and spin multiplicity *m* equal to 1. It has only a single

possible value of its *z*-component, i.e. eigenvalue $m_s = 0$, and is therefore called singlet. The next three spin wavefunctions have $S = 1$ and $m = 3$. They only differ in the z-component of the spin, which can take one of three eigenvalues ($m_s = 1, 0, -1$). This arrangement is therefore called triplet. A vectoral representation is given in the Figure **1.2b**. In OLEDs, before recombination, the respective electrons and holes are completely uncorrelated, so that the pairing of the two charge-carrier spins (fermions with spin-half) to one bosonic exciton is a truly statistical process. As the triplet states of organic molecules are threefold degenerate, there are three possibilities to form a triplet for each singlet state, as a result, 75% of the excitons are formed as triplets and the rest 25% as singlets.

The full wavefunction of a particle can be written as the product of a spatial wavefunction, which depends only on spatial coordinates, and a spin wavefunction, which is a function of the particle's spin. To preserve the Pauli exclusion principle, the symmetric spin wavefunctions of the triplet state are always combined with an antisymmetric spatial wavefunction, while the converse is the case for the singlet state. The S_0 of organic molecules is generally a singlet state, i.e., two electrons occupy a single orbital and have antiparallel paired spins. In the excited state, the two electrons are in different orbitals, i.e., one electron is in the HSOMO, and another one LSOMO, and they can either have electron spin antiparallel (↑↓) (singlet) or electron spin parallel (↑↑) (triplet), see Figure **1.2c**.

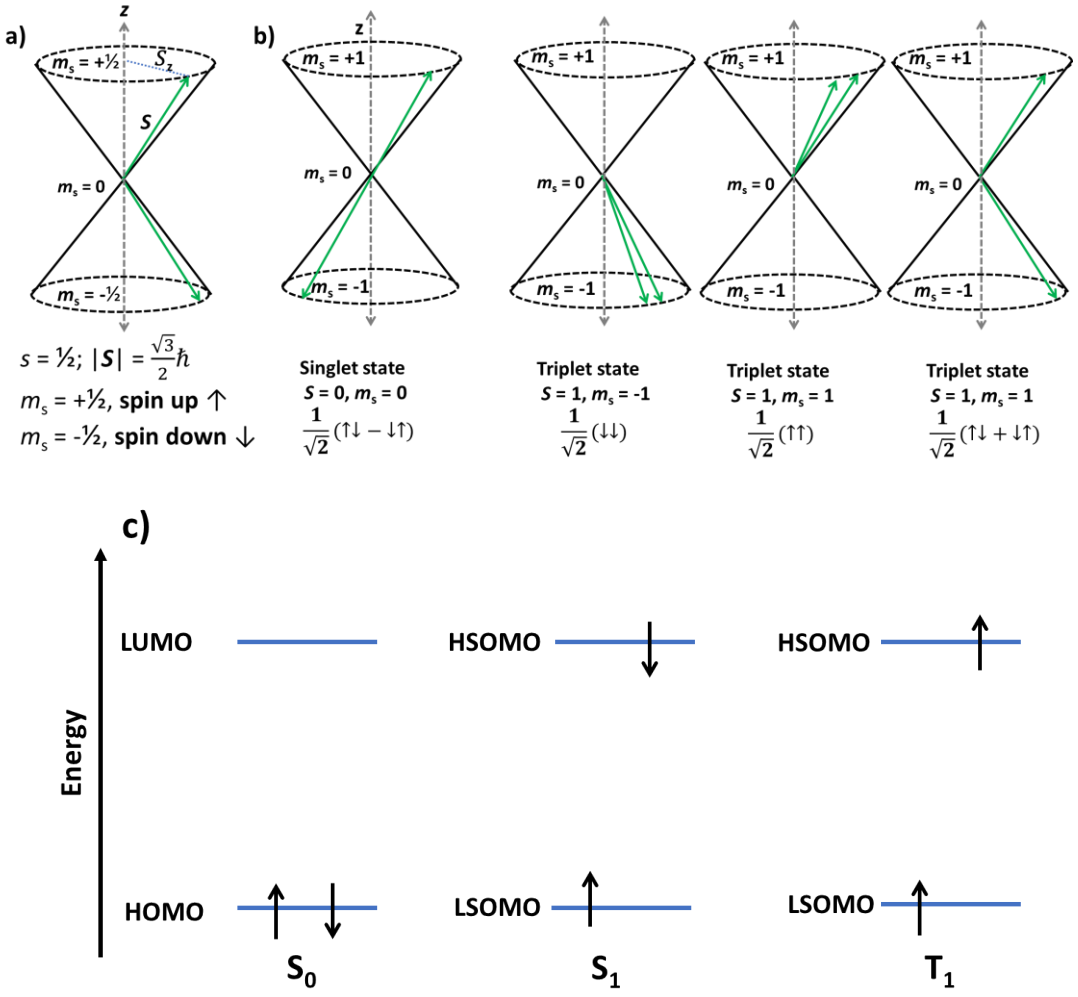

Figure **1.2**. a) Illustration of the formation of quantum states for a one electron system, b) Vectoral illustration of the relative orientation of the electron spins for singlet and triplet states for a two-electron system including the corresponding spin wavefunctions and eigen values of $\boldsymbol{S}$ and S_z, and c) Singlet and triplet states in an orbital configuration scheme.

According to the Spin selection rule, electronic transitions are spin-allowed only if the two states involved are of the same multiplicities.[13] Therefore, singlet-singlet and triplet-triplet transitions are spin-allowed but the singlet-triplet and triplet-singlet transitions are spin-forbidden. This rule, however, is broken in the presence of spin-orbital coupling (SOC), which is explained

in detail in section **1.3**.[14] Thus, if a conventional fluorescent material is used in OLEDs as the emitter, only 25% of the excitons can be harvested as fluorescence ($S_1 \rightarrow S_0$), as all triplets formed decay nonradiatively. Nowadays, with the innovative molecular designs, TTA emitters can harvest up to 62.5% of excitons, and organometallic complexes and TADF emitters can theoretically harvest 100% of the excitons as light. The triplet harvest mechanisms of these emitters are presented in section **1.2**.[15]

1.1.3 External Quantum Efficiency

The generated photons from then EML then interact with the layered thin-film architecture of the OLEDs through reflection, refraction, interference, and absorption. Eventually, some photons escape from the device to provide useful light (Figure **1.3**). The external quantum efficiency (EQE) is defined as the ratio of the number of photons emitted by the OLEDs to the number of electrons injected, which is the most representative performance indicator metric when comparing OLEDs.[16] The EQE can be expressed as the product of four parameters:

$$EQE = \gamma \cdot \eta_{eff} \cdot \eta_{S/T} \cdot \eta_{out} = IQE \cdot \eta_{out} \quad (1)$$

Where γ represents the charge carrier balance of the device, which relates the fraction of injected charges captured to form excitons in the emissive layer. In multilayer OLEDs, γ can be assumed to be unity as a careful selection of injection and transport layers are used to ensure this balance.[17] η_{eff} is the photoluminescence quantum efficiency of the emitter. It quantifies the competition between the radiative and nonradiative rates of the emissive excited state. $\eta_{S/T}$, accounts for the share of excitons that are able to decay radiatively due to the quantum-mechanics spin selection

rules. As discussed in section **1.1.2**, the fundamental efficiency of fluorescent materials is limited to 25% and 62.5% for the TTA emitters. Only phosphorescent and TADF materials can generate a tantalizing 100% efficiency from the charge capture.

These three factors together represent the internal quantum efficiency (IQE) of the OLED, which defines the fraction of photons generated per injected electrons, available for extraction out of the device.

The final factor, η_{out}, is the outcoupling efficiency. It depends on the optical environment and the orientation of the transition dipole momentum (TDM) of the emitter. On the molecular scale, photons are predominantly emitted perpendicular to the TDM of each emitter and the emission probability gradually falls off for angles. Thus, the direction of the photon generated during exciton relaxation depends on the orientation of the molecular TDM. Meanwhile, according to the *Snell*'s law, when light propagates through an interface of different layers (e.g., organic layer/glass substrate or glass substrate/air) at an angle greater than a critical angle defined by the refractive indices of the layers, total internal reflection will occur, trapping part of the light in so-called guided internal modes. Generally, as the emitter molecules are randomly oriented (isotropic) only about 20%–30% of the internally generated photons leave the device to be detected by the observer in standard device layouts (bottom emission),[18] indicating that there is much room for improvement. η_{out} can further be enhanced by achieving non-isotropic emitter orientation by preferred horizontal TDM alignment of the emitters. As shown in Figure **1.3.** the photons are emitted perpendicular to the TDM, and when the TDM of the emitter is preferentially horizontally oriented, total internal reflection is avoided. In such cases, the η_{out} can be enhanced

up to 45%.[19]

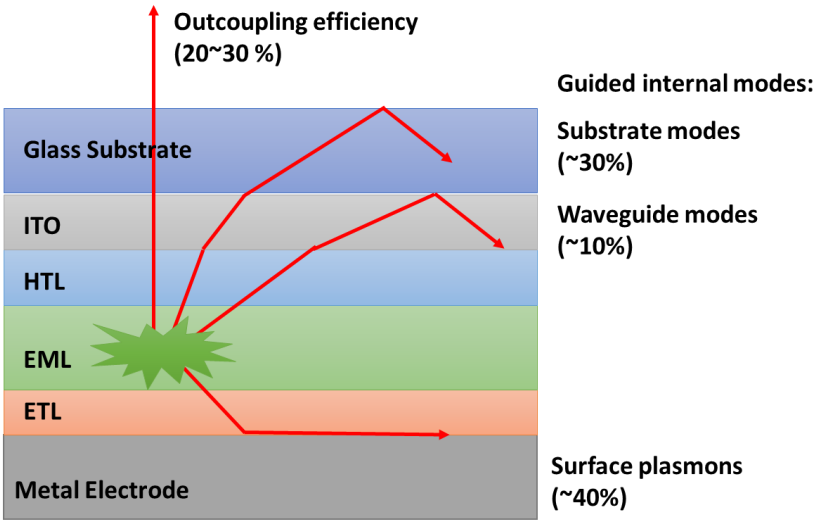

Figure **1.3.** Illustration of the light extraction from an OLEDs.

Taking into account a η_{out} of ca. 20% in a typical OLED, this results in EQE_{max} of 5% for emitters (fluorescence emitters) that can only harvest singlet excitons and 20% for emitters that can harvest both singlet and triplet excitons. OLEDs usually achieve the EQE_{max} at the turn on voltage with luminance below 10 cd m^{-2}, and due to the excitons quench and charge imbalance at higher current density, the EQE suffers roll-off at higher luminance. However, in application, typical brightness levels of mobile displays are between 100−400 cd m^{-2} while for general illuminations, higher values of 3000−5000 cd m^{-2} are required. Therefore, not only the EQE_{max} which has been cited only in many reports, but also the EQEs at practical luminance like 100 cd m^{-2} (EQE_{100}) or 1000 cd m^{-2} (EQE_{1000}) should be considered to properly evaluate the electroluminescence performance.

1.1.4 Emission color of OLEDs

To get full-color displays or white-light OLEDs, the combination of the three primary colors, red, green, and blue (RGB), is indispensable. The Commission Internationale de l'Éclairage (CIE) *x* and *y* coordinates are a useful tool to define the color detected by the human eye as shown in Figure **1.4**. The coordinates define each color with a combination of red, green and blue, all of which fall into a range between 0 to 1. Low *x* and low *y* stand for the blue color, low *x* and high *y* shows green color and high *x* and low *y* is for red color. The gamut of an RGB monitor can be displayed as a triangular region within the CIE diagram, and only the color inside the triangular region is accessible by combining the three primary colors with varying brightness. It is evident that the color region depends on the coordinates of the three primary colors, and what constitutes red, green, and blue depends on different standards adopted across the globe. For example, for blue, green, red, and white color, standard CIE coordinates defined by the National Television Standards Committee (NTSC), the television color standard in the USA are (0.14, 0.08), (0.20, 0.71), (0.67, 0.33), and (0.33, 0.33) respectively,[20] whereas the Phase Alternate Line (PAL) system, which is adopted in European and Asian define pure blue, green, red, and white color by CIE coordinates of (0.15, 0.06), (0.29, 0.60), (0.64, 0.33), and (0.33, 0.33), respectively.[21] Recently, BT.2020, a set of specifications covering various aspects of video broadcasting, has been recommended by the International Telecommunication Union as standards for Ultra HD projectors and televisions. According to BT.2020 the blue, green, red, and white color are defined by CIE coordinates of (0.13, 0.05), (0.17, 0.80), (0.71, 0.29), (0.71, 0.29) and (0.31, 0.33), respectively, which shows a larger color gamut than NTSC and PAL standard.[22]

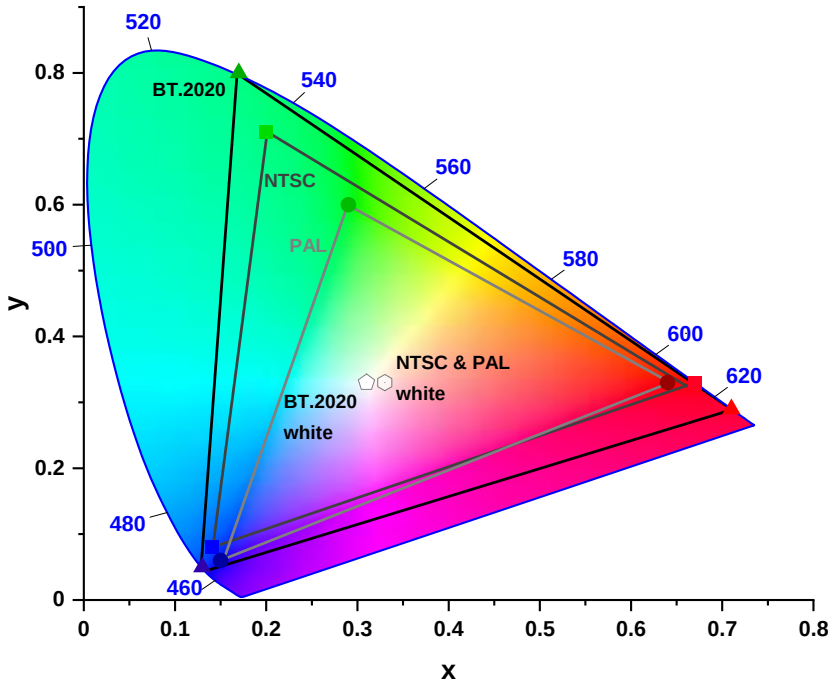

Figure **1.4.** A typical CIE 1931 color diagram. The x and y axes represent the fraction of red and green color in a given color respectively.

1.2 Development of OLEDs

The first generation of OLEDs utilized fluorophores as the emitter. In 1987, Tang and Van Slyke designed a multilayered structure electroluminance device where ITO glass was used as the anode; the tris(8-hydroxyquinolinato)aluminium (Alq_3) was used as the emitter in the light-emitting layer; 1,1-Bis[(di-4-tolylamino)phenyl]cyclohexane (TAPC) was used as the hole-transporting layer and magnesium alloy was used as the cathode.[2] The green emitting device reached a luminance of 1000 cd m^{-2} under 10 V drive voltage. Moreover, the lifetime of the device reached 100 h when the power efficiency was 1.5 lm W^{-1}. The high brightness, high efficiency, and long lifetime of this device attracted the attention of the world. Since then, research and development of OLED technology have continuously moved forward in academia as well as in

industry. Traditional fluorescent emitters were firstly used in OLEDs, as these emitters possess a wide chromatic range from deep-blue to red emission,[23] and good stability under electrochemical and photooxidation tests, which promote high stability of the devices as measured in terms of their device lifetimes.

However, in OLEDs charge carriers are injected and recombine to form singlet and triplet excitons in a ratio of 1:3, and only the transition from S_1 to S_0 is theoretically allowed for fluorescence, which indicates that 75% of the excitons cannot be harvested via radiation using traditional fluorescent emitters.[11] To utilize the triplet excitons, heavy metal complexes have been used as emitters in OLEDs, first demonstrated by Forrest *et al*.[8] The presence of the heavy metal atom enhances spin-orbit coupling leading to triplet excitons decaying from T_1 to S_0 as phosphorescence and facilitate ISC from S_1 to T_1.[8] This emission mechanism can use all the excitons generated in OLEDs theoretically and the invention of PhOLEDs brought organic electroluminescence into a whole new era. In the past 20 years, phosphorescent materials developed rapidly, and many highly efficient materials have been synthesized.[24–26] The EQE_{max} of green and blue PhOLEDs have exceeded 30% based on *fac*-$Ir(ppy)_3$ and $Ir(dfpysipy)_2(mpic)$,[27,28] respectively, and for red PhOLEDs based on PyThIr, the EQE_{max} reached 28%.[29] Moreover, the device operation lifetime (T_{50}) of green and red PhOLEDs have been optimized to 10^5 and 10^6 hours at a luminescence of 1000 cd m^{-2} which are comparable to the best fluorescence emitters based OLEDs.[30]

However, to date, the operation lifetime of blue PhOLEDs remains below 3 000 hours at 1000 cd m^{-2},[31] which is too short for practical applications and largely lags compared to green

and red PhOLEDs (~10^6 hours) and blue F-OLEDs (~10^4 hours).[30] The short operational lifetime of blue PhOLEDs can be ascribed to several factors. First, the intrinsically wide bandgap (E_g >3.0 eV) of blue emitter makes carrier injection and exciton confinement harder than for green and red emitter, requiring devices to be operated at high voltages, which leads to the increase density of polaron, and subsequent singlet-polaron and triplet-polaron quenching, which generate high-energy species that lead to photochemical degradation of the materials within the EML.[32] In addition, the scarcity of the transition metals on Earth renders these materials not sustainable. Therefore, finding new types of sustainable electroluminescent materials that can be produced at low cost, high luminous efficiency, and high exciton utilization is needed.

Another mechanism to use the triplet excitons is triplet-triplet annihilation (TTA), which occurs when two migrating non-radiative triplet excitons collide.[33,34] Upon collision they form an encounter complex that can further transform into a radiative singlet exciton of twice the energy of T_1 and another at the S_0 state.[33,34] The generated singlet exciton then decays to S_0 state as delayed fluorescence and contributes to the IQE boost. To have a TTA process, generally, the energy of the two triplet excitons should be higher than the energy of singlet exciton, which makes TTA especially useful for achieving highly efficient blue emission with similar lifetime performance to blue F-OLEDs.[35] Polycyclic aromatic hydrocarbon derivatives such as anthracene, pyrene, and triphenylene are typically used as blue TTA emitters for OLEDs.[36] An EQE_{max} of 11.9%, CIE coordinates of (0.14, 0.16), and long operation lifetime of 8 000 hours at 1000 cd m^{-2} were achieved for a pyrene based TTA-OLEDs where TTA mechanism was confirmed by time-resolved electroluminescence measurements.[37] However, only 37.5% of the initial excitons (or

half of the available triplet excitons 75%/2) can be upconverted into singlet excitons using TTA, restricting the theoretical maximum of exciton utilization in TTA to 62.5%.[38] And as TTA is a bi-molecular process, a sufficiently high triplet concentration is needed to have high TTA efficiency, which also leads to various loss mechanisms and contributes to a severe efficiency roll-off in the device.[38]

The hot exciton mechanism is a strategy to theoretically harvest 100% of the excitons by involving S_m ($m \geq 1$) state and a close-to-resonant high-level triplet excited state T_n ($n \geq 2$) . The involved excited states usually show mixed locally-excited (LE) and charge transfer (CT) character (so called HLCT). The LE component can increase the radiative transition rate, thereby resulting in high Φ_{PL}, and the CT component can reduce the singlet-triplet energy gap (ΔE_{ST}), facilitating reverse intersystem crossing (RISC) from triplets to singlets, resulting in a high ratio of radiative singlet excitons.[39] As shown in Figure **1.5**, excitons on T_n (i.e. ‘‘hot’’ excitons) can go directly to excited S_m states via RISC with suitable electronic and energy alignment under electrical pumping. The exciton on S_m then can relax to S_1 by IC, and in principle, a 100% IQE can be achieved. However, the transition from T_n to S_m is competing with the internal conversion (IC) transition from T_n to T_1, and according to *Kasha*’s rule as photon emission (fluorescence or phosphorescence) occurs in decent yield only from the lowest excited state of a given multiplicity, and IC is so rapid that the majority of excited state molecules tend to occupy the lowest excited state (S_1 and T_1) instead of the upper lying states.[40] Therefore, it is quite challenging to design efficient HLCT active systems, and at present only a small number of materials purporting to show such a hot exciton mechanism have been reported.[41]

Recently, thermally activated delayed fluorescence (TADF) has emerged as one of the most promising and efficient triplet exciton harvesting mechanisms in OLEDs.[3,5,42] TADF materials can effectively utilize triplet excitons owing to the small ΔE_{ST}, which permits triplet excitons to be converted to singlet exciton via RISC process and decay to S_0 as delayed fluorescence, leading to the achievement of 100% IQE under electrical operation. Theoretically, the RISC rate and efficiency can be evaluated within the framework of Fermi's golden rule which confines the transition rate from one energy eigenstate of a quantum system to another eigenstate as a result of a weak perturbation. Thus, various molecular factors that affect the perturbation between two states, such as the SOC matrix elements (SOCME), ΔE_{ST}, and external factors like temperature and host matrix are taken into consideration. The detailed mechanism of TADF is discussed in section **1.3**. TADF, referred to as E-type delayed fluorescence in the early literature, was identified in 1961 as a photophysical mechanism from eosin, which emitted delayed fluorescence in ethanol at 70 ^{o}C.[43] Soon after, molecules like benzophenone,[44] 9,10-anthraquinone,[45] fullerene,[46] have been reported to undergo this mechanism during emission. After initial reports of organometallic based on heavy metals (Au and Sn),[47,48] the field has experienced a paradigm shift towards lighter elements such as copper and purely organic structures.[49] Adachi *et al*. reported a TADF-active Sn (IV)-porphyrin complex, where they showed an increase of the delayed fluorescence component from 0.6% at 300 K to 2.4% at 400 K.[48] In 2010, Deaton *et al*. designed a highly emissive bis(phosphine) diarylamido copper complex exhibiting a record high EQE_{max} of 23%.[49] In the following year, the first purely organic TADF emitter, **PIC-TRZ**, was reported by Adachi *et al.*[42] Yet, the EQE_{max} of the OLED achieved was

5.3%, which is close to the theoretical limit of conventional fluorescent emitters and hence did not provide particularly solid proof that the triplet excitons had been utilized. In 2012, a series of benchmark organic TADF emitters based on carbazole and phthalonitrile were reported by the same group, where the best performing OLEDs based on **4CzIPN** exhibited an astonishing EQE_{max} of 19.3%.[50] Such a high efficiency was attributed to the 100% exciton harvesting within the device.[50] Ever since, this field has attracted tremendous attention and as a result, electroluminescent devices using metal-free TADF emitters have already achieved comparable efficiencies to state-of-the-art PhOLEDs.[3] However, fundamental scientific challenges concerning simultaneously achieving stable pure-blue and deep-blue emission, long device operation lifetime, fast RISC rates with short exciton lifetimes, and small ΔE_{ST} must still be met in order for blue TADF materials to supplant fluorescent compounds.[51]

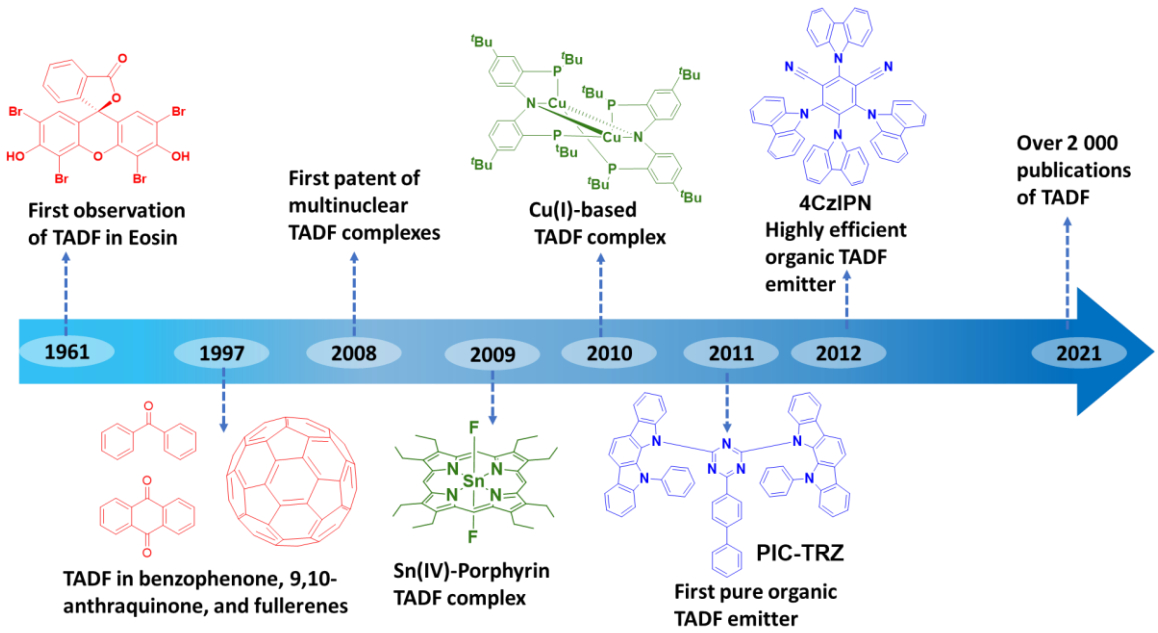

Figure 1.5. Timeline illustrating the evolution of TADF materials.

In the majority of molecular systems, the T_1 state lies energetically below the S_1 state due to exchange interactions, which stabilize triplets and destabilize singlets leading to a positive ΔE_{ST}. However, there is a recent growing interest in designing molecules with inverted S_1/T_1 states, which would allow replacing the up-conversion in TADF with a more efficient down-conversion. The potential for negative ΔE_{ST} in nitrogen-substituted phenalene analogues, such as heptazine has been discussed during the last two decades,[52] and theoretical studies have also suggested the possibility of negative ΔE_{ST} in these molecules by accounting for double-excitation configurations where two electrons of occupied orbitals have been promoted into virtual orbitals.[53] Although only a handful of reports about negative ΔE_{ST} in heptazine derivatives have been published, this new strategy may lead to a completely new class of emitters that can harvest both singlet and triplet excitons in OLEDs.

In summary, the blue emitter development remains a hurdle for high-performance OLEDs. For existing systems, the efficiency of blue F-OLEDs and TTA-OLEDs are lower than red and green PhOLEDs. In addition, the device lifetimes of blue PhOLEDs and TADF-OLEDs are still shorter than red and green devices. As green and red phosphorescent emitters have been commercially available, one of the most attractive features for TADF emitters lies in their potential to be used as efficient and stable blue alternatives to the state-of-the-art.

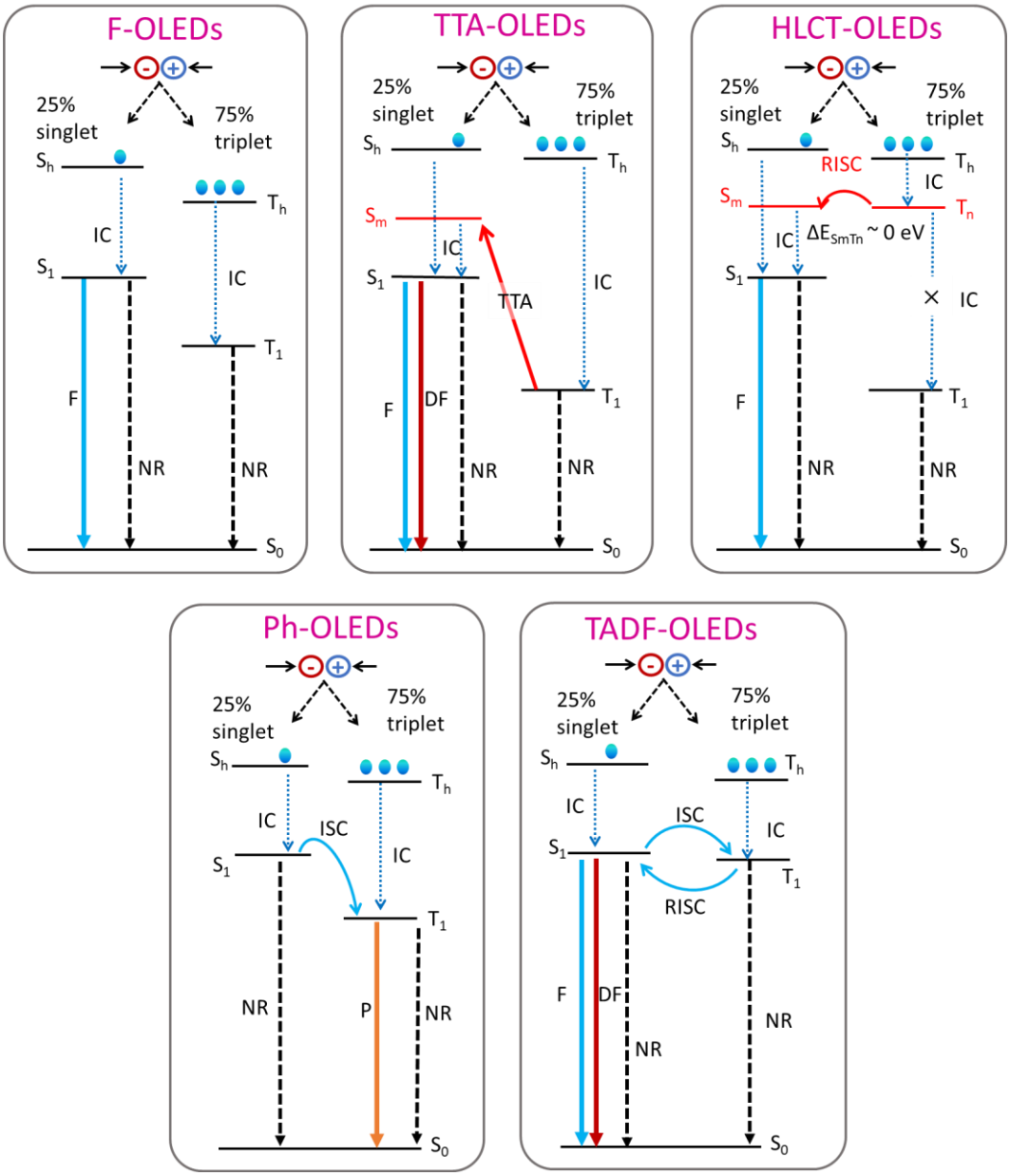

Figure 1.6. Mechanism of different types of OLEDs.

1.3 The mechanism of thermally activated delayed fluorescence

The electroluminescence and photoluminescence kinetics of thermally activated delayed fluorescent materials can be summarized in Figure **1.7**. The luminescence process consists of two components: the prompt fluorescent and the delayed fluorescent. In the prompt fluorescence

process, singlet excitons decay from the S_1 state to S_0 in the nanoseconds regime. For the delayed fluorescence process, triplet excitons from the T_1 state are first converted to singlet excitons that reside on the S_1 state by RISC. These then decay radiatively to the S_0. The lifetime of the delayed fluorescence process is much slower and usually in the range of microseconds or even milliseconds.[54]

In the OLED the electroluminescence process of TADF molecules has four steps: (1) electron and hole recombination generate singlet and triplet excitons at the ratio of 1:3. (2) Excitons in higher energy excited states transit to the lowest energy excited state (T_1 and S_1) through vibration relaxation (VR) and internal conversion (IC). (3) The triplet excitons accumulated in the triplet excited state T_1 are transferred to the single excited state S_1 through the thermally activated RISC process; (4) Singlet excitons, including those electrically excited and converted from triplet excitons, decay to S_0 by prompt and delayed fluorescence mechanism. Over the four steps, non-radiative processes in the triplet state are much slower than RISC, and the term k_{nr}^{T} can be ignored for simplicity, while for highly efficient emitters, as $k_r^S \gg k_{nr}^S$, the influence of k_{nr}^{S} can be omitted as well.[55]

For the remaining rate constants, k_r and k_{ISC} are larger than 10^6 s^{-1} while k_{RISC} is from 10^2 to 10^7 s^{-1},[56–59] as such, k_{RISC} becomes the rate-limited step in exciton dynamics processes. A fast k_{RISC} reduces the lifetime of triplet state, thus suppressing excited state quenching mechanisms such as triplet−triplet annihilation, and triplet−polaron annihilation, and reducing efficiency roll-off in OLEDs which is one of the major limitations in TADF OLEDs at present.[60] Thus, a deep understanding of the mechanism of RISC is required to push TADF materials design further.

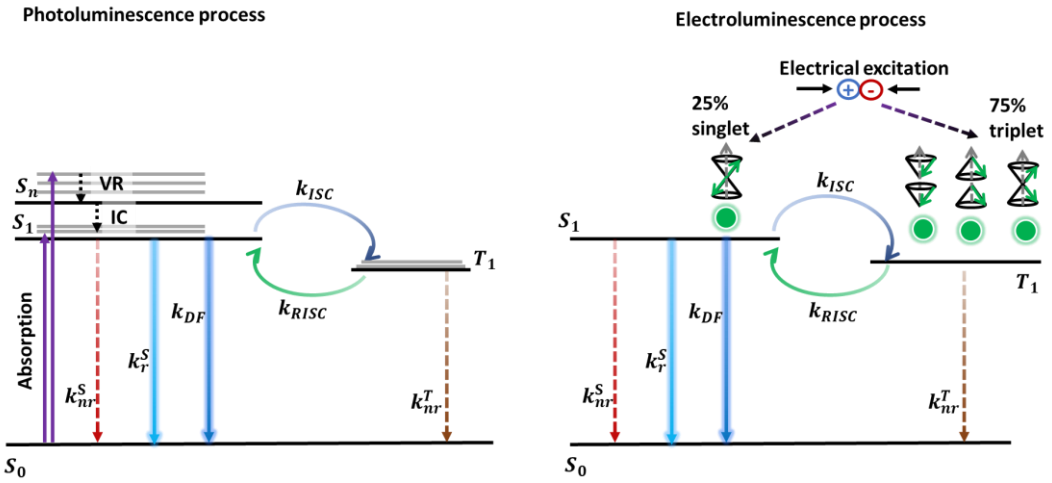

Figure 1.7. kinetics of thermally activated delayed fluorescence, k_r^S, k_{DF}, k_{ISC}, and k_{RISC} are rate constants for prompt fluorescence (PF) delayed fluorescence (DF), ISC, and RISC respectively. k_{nr}^S and k_{nr}^T are the non-radiative decay constants of S_1 and T_1 respectively.

1.3.1 Kinetics investigation of the RISC process

Albrecht outlined the four mechanisms for the mixing of the singlet and triplet states: (I) Direct spin−orbit coupling, driven by the differences in electronic character of the states. (II) Vibrational spin−orbit, in which the size of the SOCME depends on the motion along a particular nuclear degree of freedom, Q_α. (III) Spin−orbit coupling with vibronic coupling in the triplet manifold. (IV) Spin−orbit coupling with vibronic coupling in the singlet manifold.[61] Of these terms, only I and II can be present within first-order perturbation theory, while the latter two terms, involving a mixture of spin−orbit and nonadiabatic coupling, appear only within second-order perturbation theory.

Using the first-order perturbation theory (Fermi's golden rule formulation),[62,63] the reverse intersystem crossing rate (k_{RISC}) can be expressed as:

$$k_{RISC} = \frac{2\pi}{\hbar} |V_{SOC}|^2 \times \rho_{FCWD} \quad (2)$$

where $|V_{SOC}|^2$ is the spin-orbit coupling matrix element (SOCME) between S_1 and T_1 and ρ_{FCWD} is the Franck-Condon-weighted density of states,[64] which can be expressed as:

$$\rho_{FCWD} = \frac{1}{\sqrt{4\pi\lambda k_B T}} \exp\left(-\frac{(\Delta E_{ST}+\lambda)^2}{4\lambda k_B T}\right) \quad (3)$$

where λ is the Marcus reorganization energy associated with the intermolecular and intramolecular low-frequency vibrations; k_B is Boltzmann's constant; and T is temperature. Combing equations (2) and (3), it is evident that k_{RISC} is proportional to $|V_{SOC}|^2 \times \exp[-(\Delta E_{ST}^2)]$:

$$k_{RISC} \propto |V_{SOC}|^2 \times \exp[-(\Delta E_{ST}^2)] \quad (4)$$

As presented in equation (4), small ΔE_{ST} is critical to an efficient RISC process so long as SOC is non-zero. When an electron is excited from HOMO to LUMO, along with the electron orbital energy (E), the Coulombic (K) and the exchange (J) electrostatic interactions between the unpaired electrons determine the molecular energy of the lowest singlet (E_S) and triplet (E_T) excited states, which can be expressed mathematically as Equation (5) and Equation (6).[65]

$$E_S = E + K + J \quad (5)$$

$$E_T = E + K - J \quad (6)$$

Since both unpaired electrons (in the excited state) possess the same charge, K and J are defined as positive for the electron-electron electrostatic repulsions. Coulombic repulsions increase the energy of both singlet and triplet states. Exchange interactions, on the other hand, increase the energy of the singlet excited state but decrease the energy of the triplet state , and therefore, E_S is always higher than the E_T. Thus, ΔE_{ST} is the difference between E_S and E_T,

which is equal to twice that of J (Equation (7).[66]

$$\Delta E_{ST} = E_S - E_T = 2J \quad (7)$$

The exchange energy, *J* in turn depends upon the spatial overlap of the orbitals involved in the transition from the emissive excited state, which are almost always HOMO and LUMO wavefunctions, and can be described mathematically as equation (8).[67]

$$J = \iint \emptyset_L(1)\emptyset_H(2)\left(\frac{e^2}{r_1 - r_2}\right)\emptyset_L(2)\emptyset_H(2)dr_1 dr_2 \quad (8)$$

Where $\emptyset_{\mathrm{L}}$ and $\emptyset_{\mathrm{H}}$ are the wave functions of LUMO and HOMO, respectively, and e is the electron charge. Thus, the reduction of the electron exchange energy ΔE_{ST} can be achieved by reducing the HOMO / LUMO orbital overlap. The most common design is based on a twisted donor-acceptor architecture, as the HOMO will be located on the electron donor moiety while the LUMO will be confined to the electron acceptor moiety.[68,69]

The other important term relates to SOC, which is a relativistic effect that acts on both angular momentum and spin, leading to its defining characteristic of mixing orbital and spin degrees of freedom, thus allowing electronic states of different multiplicities to couple.[9,70]In a one-center approximation, the SOC operator V_{SOC}^{eff} can be expressed as:

$$V_{SOC}^{eff} = \frac{1}{2m_e^2c^2}\sum_l \sum_i \frac{Z_I^{eff}}{r_{il}^3}\hat{l}_i \cdot \hat{s}_i \quad (9)$$

Where m_e is the electron mass, c is the light speed, r is the radial distribution, Z_I^{eff} is the effective nuclear charge, $\hat{l}_i$ is the angular momentum, and $\hat{s}_i$ is the spin operator of electron *i*. For each nucleus, we can write a spin−orbit coupling constant $\zeta = \frac{Z_I^{eff}}{2m_e^2c^2r^3}$, which is proportional to the effective nuclear charge. This constant is therefore responsible for the heavy-atom effect, which governs the fast ISC rates observed in phosphorescent emitters, whereby

SOC is expected to increase with the atomic number. For pure organic material, this constant is small, and the integral over the two states involved must be considered. The integral of SOCME over the two states involved can be expressed as:

$$|V_{SOC}|_{ij} = \left\langle \psi_{S_i} \middle| |V_{SOC}| \middle| \psi_{T_j} \right\rangle \quad (10)$$

This integral depends principally on the character of the states involved, which has been outlined qualitatively by El-Sayed.[71] According to *EI-Sayed's* rule, there is no spin-orbit coupling between singlet and triplet states of the same configuration. To achieve effective spin-orbit coupling a change of molecular orbital type must be involved in this radiationless transition.[71] This original work was discussed in the context of organic chromophores considering the typical case of a transition from the lowest excited singlet state to the triplet manifold (i.e., ISC).[71] *El-Sayed's* rule predicts that $S_1(n, \pi^*) \rightsquigarrow T_1(\pi,\pi^*)$ or $S_l(\pi, \pi^*) \rightsquigarrow T_2(n, \pi^*) \rightsquigarrow T_1 (\pi, \pi^*)$ ISC should be much faster than $S_1(n, \pi^*) \rightsquigarrow T_1(n, \pi^*)$ ISC, as the same orbital configurations exist in the latter transition.[71]

For TADF emitters, as charge transfer strategy is commonly used to minimize the ΔE_{ST}, it was usually assumed that the lowest singlet and triplet states were of charge transfer (CT) character and the ISC is a spin-forbidden process according to *El-Sayed's* rule,[42,72] which indicates that the very small SOC between ^{1}CT and ^{3}CT is not enough to explain the fast experimental k_{RISC} up to 10^7 s^{-1} reported.[59,73,74]

Ogiwara *et al*. used time-resolved electron paramagnetic resonance (EPR) spectroscopy to propose that hyperfine coupling (HFC) could be involved in the RISC process when T_1 or a higher triplet (T_n) state is located extremely close to the ^{1}CT state.[75] In this mechanism, efficient RISC from T_n to S_1 can be achieved in two steps: first via RIC from T_1 to

T_n, a triplet state that is energetically proximal to S_1 and then, using hyperfine coupling, induced ISC to cross to the ^{1}CT (Figure **1.8a**). However, as the energy gap needs to be less than the *Zeeman* energy range of 0.21–0.40 cm^{-1} (i.e., $\Delta E_{S1Tn} < 10^{-4}$ meV) for efficient HFC-induced RISC, such a small energy gap could only be achieved in highly twisted donor-acceptor (D-A) molecules.[75]

Chen *et al*. used Fermi's Golden Rule to calculate the rate of RISC occurring via SOC only and the calculated results are significantly smaller than the experimental results, even for the allowed ^{1}CT to ^{3}LE transition.[76] Marian proposed that spin-orbit coupling between the singlet and triplet CT states can be mediated by an energetically close-lying triplet state with locally excited (LE) character,[77] and Gibson *et al.* used model quantum dynamics simulations to combine first-order and second-order perturbation theory to investigate the role of vibronic coupling between ^{3}LE and ^{3}CT on k_{RIC} and k_{RISC}.[78]

$$k_{RISC}^{i-f} = \frac{2\pi}{\hbar}\sum_{f}\left|\langle\Psi_f|V_{if}|\Psi_i\rangle + \sum_{n}\frac{\langle\Psi_f|V_{nf}|\Psi_n\rangle\langle\Psi_n|V_{in}|\Psi_i\rangle}{E_i - E_n}\right|^2 \delta(E_f - E_i) \qquad (11)$$

The first term of the equation is derived from Fermi's Golden rule describing the direct transition from initial state (Ψ_i) to the final state (Ψ_f) (first order perturbation theory), while the second term describes the coupling between the initial and final states mediated by an intermediate state (Ψ_n). If the emitter possesses more than one intermediate state, then all of these intermediate states should be integrated into the second term. For most TADF emitters the initial state (T_1) and final state (S_1) are of CT character and the coupling efficiency $|V_{if}|$ is close to zero according to *El-Sayed's* rule, unless hyperfine coupling is allowed.[71,75] If we consider the nature of an intermediate state (Ψ_n) is of LE character, the second term of equation (11) can be divided into equations (12) and (13):

$$k_{RIC} = \frac{2\pi}{\hbar} \left|\langle \Psi_{^3CT} | V_{vib} | \Psi_{^3LE} \rangle\right|^2 \delta\left(E_{^3CT} - E_{^3LE}\right) \quad (12)$$

$$k_{RISC} = \frac{2\pi}{\hbar} \left|\frac{\langle \Psi_{^1CT} | V_{SOC} | \Psi_{^3LE} \rangle \langle \Psi_{^3LE} | V_{vib} | \Psi_{^3CT} \rangle}{E_{^3CT} - E_{^3LE}}\right|^2 \delta\left(E_{^3CT} - E_{^3LE}\right) \quad (13)$$

Equations (12) and (13) indicate a two-step mechanism in the RISC process. Firstly, spin-vibronic coupling between ^{3}LE and ^{3}CT (IC and RIC) promotes an equilibrium between the two states, which depends on the efficiency of spin-vibronic coupling and the energy gap between these two states. Secondly, there is second order coupling between the ^{3}CT and the ^{1}CT, using the ^{3}LE as an intermediate state. The second order coupling is highly efficient because of the fast spin-vibronic coupling between ^{3}CT and ^{3}LE and efficient spin-orbital coupling between ^{3}LE and ^{1}CT.[71,79,80] Therefore, the dynamics of RISC are driven by two fast coupling processes (spin-vibronic coupling and spin-orbital coupling) (Figure **1.8b**).

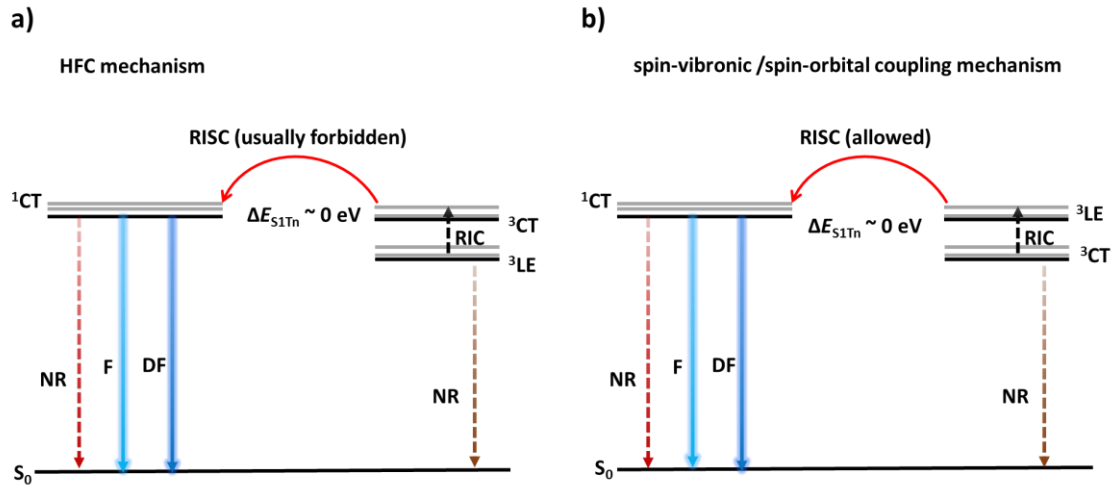

Figure **1.8**. Schematic energy level diagrams illustrating the effect of the environment of the relative splitting of the CT and LE states of TADF emitters.

However, both HFC and spin-vibronic/spin-orbital coupling mechanisms have been justified by just a handful of examples and hence cannot be generalized. In many TADF materials, singlet and triplet excited states are neither pure CT and/or LE character but possess a mixed CT-LE character with varying proportions and as a result, as long as ΔE_{ST} is sufficiently small, *El-Sayed*'s rule is not followed rigorously.[81,82]

1.3.2 Kinetics of radiative decay processes

The excitons at the excited singlet state will decay to the S_0 as fluorescence. For the ideal case of a negligible Stokes shift and a perfect mirror-image relationship of absorption and fluorescence spectrum, the radiative decay rate constant (k_r) can express as:[83]

$$k_r = 0.688 \times n^2 \langle \tilde{\nu} \rangle_{av}^2 f \quad (14)$$

Where the $\langle \tilde{\nu} \rangle_{av}$ is the average wave number corresponding to the transition, f is the oscillator strength, and n is the refractive index of the medium. The f is related to the transition dipole moment value (μ_{10}) by the relation:[84]

$$f = \frac{2 m_e \Delta E}{3\hbar^2 e^2} |\mu_{10}|^2 \quad (15)$$

Where m_e is the mass of the electron, ΔE is the energy of the transition, $\hbar$ is the reduced Planck's constant and e is the charge of the electron. μ_{10} can be expressed as the overlap density (ρ_{10}) between the electronic wave functions between S_0 and S_1 [Eq. (16)]:[85]

$$\mu_{10} = \int \rho_{10}(x)(-ex)dx \quad (16)$$

From Eq. (14–16), both μ_{10} and f are controlled by ρ_{10}. For most TADF emitters the orbitals

involved in the S_1−S_0 transition are the HOMO and LUMO, and ρ_{10} is positively strongly correlated to the HOMO−LUMO overlap density ($\rho_{HOMO-LUMO}$).[86] In such cases, k_r is significantly influenced by $\rho_{HOMO-LUMO}$. Evidently, it requires sufficient overlap to guarantee strong oscillator strength (*f*) between S_1 and the S_0, which affords an efficient radiative process. In this regard, a small yet sufficient overlap integral between the HOMO and LUMO wavefunctions is inevitable to accomplish a successful TADF molecule design that balances both k_{RISC} and k_r.[87]

1.4 Strategies for Designing Blue TADF Emitters

The design rules for blue highly efficient TADF emitters become clear once we understand the dynamics of TADF in OLEDs. For TADF emitter-based OLEDs, the harvesting of excitons includes: 1) radiative decay from the singlet excited state to the S_0; 2) RISC from triplets to singlet; 3) delayed radiative decay from the singlet excited state to the S_0. Processes 1) and 3) require a high quantum yield of the fluorescence and slow non-radiative decay from the triplet state so as not to compete with the dominant radiative decay mode, while for process 2) this requires a small ΔE_{ST} and strong SOC between S_1 and T_1 and/or spin-vibronic coupling assisted second order coupling between intermediate triplet states and S_1.[88] As illustrated in equations (8) and (16), small ΔE_{ST} can be achieved by reducing the overlap between HOMO and LUMO, while the fast decay from S_1 to S_0 requires sufficient overlap to guarantee strong *f* between S_1 and the S_0, which results in an efficient radiative process. Moreover, the character and relative energies of S_1, T_1, and intermediate triplet states should also be optimized to achieve pure blue (CIE_x+CIE_y < 0.20) or deep-blue ($CIE_x \leq 0.15$, $CIE_y \leq 0.10$) emission and efficient RISC.[88–90]

By far, molecules with D-A structures is the most widely used strategy for efficient TADF emitter design.[5,31,54] The CT state introduced by the D–A type TADF molecule plays a vital role in reducing the overlap integral of the frontier molecular orbitals (FMOs), which in turn leads to a reduced ΔE_{ST} and enhances the efficiency of the RISC process. During the past few years of rapid development of TADF materials, several distinct molecular designs have been explored. These include: intramolecular charge transfer (ICT) system, intermolecular charge transfer system (so called exciplex system), spiro-conjugation charge transfer system, through-space charge transfer (TSCT) system, and multi-resonance TADF (MR-TADF) system. Among these systems, examples of ICT, TSCT and MR-TADF have been the most successfully used for the development of efficient blue TADF emitters.

1.4.1 Intramolecular charge transfer blue TADF molecules

As the most adopted design strategy, the introduction of a twisted D–A framework can effectively reduce the overlap integral of the FMOs, thereby enabling an efficient RISC process. For blue TADF emitters, high energies of the singlet and triplet states are required, and the previous studies on traditional fluorescent materials have shown that limiting the conjugation length,[91] and adopting the appropriate donor/acceptor units are important to avoid an undesired red shift of the emission and maintain a high singlet and triplet energy level.[92,93] For blue TADF emitters, donors such as carbazole, 9,9-dimethyl-9,10-dihydroacridine (DMAC) and their derivatives are commonly used, owing to their moderately strong electron-donating ability and high-energy triplet states.[36,72,94–98] While a variety of weak acceptor units based on, for example,

triazine,[59,99] pyrimidine,[95,100] diphenylsulfone,[94,101] benzophenone,[102] triarylborane,[103,104] and heteraborins,[105,106] have been used for the design of blue and deep-blue TADF molecules. Figure **1.9** shows the commonly used donor and acceptor moieties that have been employed to obtain blue TADF emission. Through various combinations of these moieties and with careful structural modifications, a vast number of blue TADF emitters have been designed with emission color from sky-blue to deep-blue and EQE_{max} from 5% to above 30%.[94,101,103,104]

The design of efficient blue TADF materials is a complex and systematic project that requires delicate control in terms of high singlet energy level for emission, small ΔE_{ST} and strong SOC between excited states for efficient RISC, and adequate resonance strength to ensure rapid radiative decay and the suppression of non-radiative processes. Since the first reported TADF small molecule,[42] researchers have been exploring the optimal configuration for blue TADF design. Apart from adjusting the torsion angle or modulating the donor and acceptor selection, several strategies have proven to be successful in optimizing blue TADF emitter, which are presented in this section.

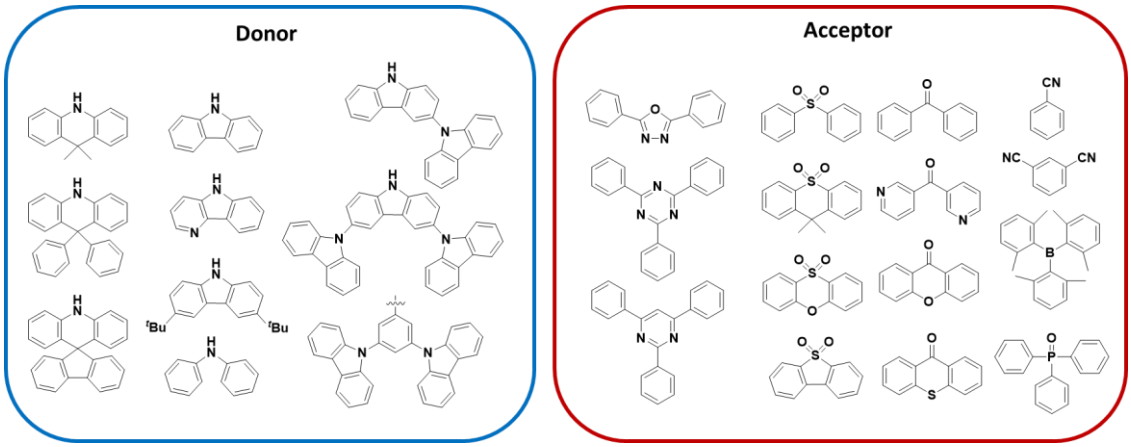

Figure 1.9. representative donors and acceptors for designing blue TADF emitters

Expansion of HOMO distribution

To address the contradiction between a large k_r and small ΔE_{ST}, Hirata *et al*. reported that a large delocalization of the HOMO and LUMO in CT materials can increase the TDM, and as oscillator strength is proportional to the square value of the TDM, a large k_r can be achieved, even when the overlap integral of the FMOs is relatively small.[56] A sky-blue TADF emitter **2a** based on 1,3,5-triazine and carbazole derivatives adopted such a design principle, showed both fast k_r ($>10^8$ s^{-1}) and small ΔE_{ST} (<0.1 eV), leading to nearly 100% Φ_{PL} in 6 wt% doped bis[2-(diphenylphosphino)phenyl] ether oxide (DPEPO) film.[56] The reference compound **1a** showed weaker HOMO delocalizing capability although the ΔE_{ST} is similar. This resulted in a k_r that was reduced to 2×10^7 s^{-1}, and as a result the Φ_{PL} reduced to 40%. The EQE_{max} of OLEDs using **1a** and **2a** as emitters were 7.7 % and 20.6%, respectively, with corresponding IQE values of 40%, and 100%, assuming a η_{out} of 20%, and exhibited sky-blue emission with CIE coordinates of (0.26, 0.43), and (0.19. 0.35), respectively.[56]

This work indicates that extending the molecular orbitals while limiting the overlap between FMOs can suppress a decrease in oscillator strength and k_r while minimizing ΔE_{ST}. Therefore, bearing this strategy of expanding the HOMO distribution, it is very promising to obtain TADF molecules with strong oscillating strength and efficient radiative decay. However, the extended donor moiety increases the molecular conjugation and causes the emission to red-shift, which makes the strategy less desirable for blue emitter design.

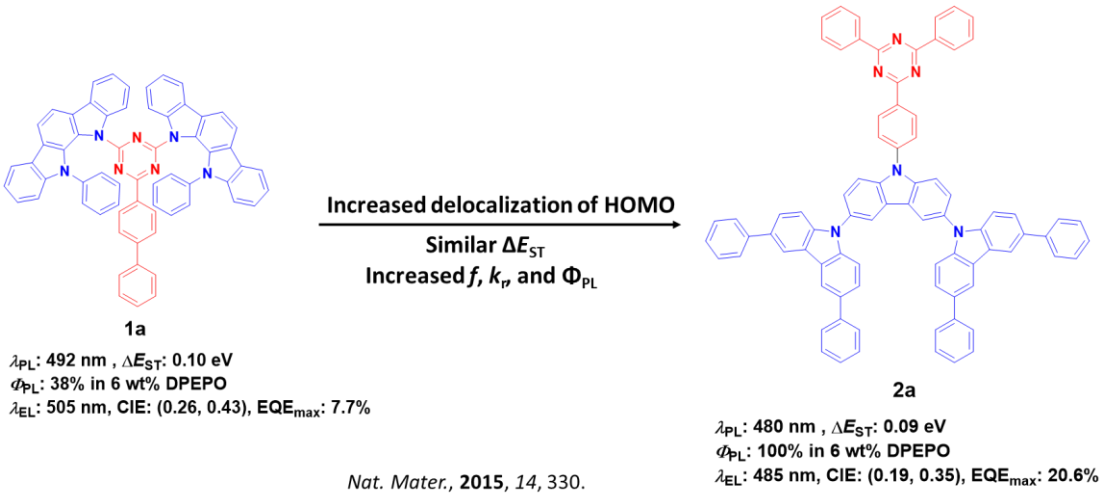

Figure **1.10**. Chemical structures and key photophysics and device information for **1a** and **2a**.

Expansion of emitting core within a single TADF molecule

Another method of enhancing the Φ_{PL} of TADF materials is through incorporation of two emitting TADF cores within one molecule. Multiple chromophores can be advantageous since the light absorption is intensified, and consequently boost the f and k_r^S, as the f is proportional to the integral of absorption coefficients (ε) over the entire the absorption band.[84] The dual-core TADF concept was originally proposed by Lee *et al*. and involved connecting two **DCzIPN** molecules on the acceptor side.[107] The resulted dual-core blue emitter (**DDCzIPN**) exhibited an intensified CT absorption with ε of 3.7×10^5 M^{-1} cm^{-1}, higher Φ_{PL} of 91% in toluene, and slightly increased ΔE_{ST} of 0.11 eV in 1 wt% doped polystyrene film, compared to corresponding respective values of 0.8×10^5 M^{-1} cm^{-1}, 61% and 0.05 eV, for **DCzIPN**.[107] However, the interconnection *via* the phenyl core increased the degree of conjugation and caused the red-shift of emission. In the device, the EQE_{max} of **DDCzIPN** improved from 16.4% for **DCzIPN** to 18.9% at the cost of λ_{EL} red-shifted from 450 nm to 495 nm.[107]

To reduce the conjugation between two TADF emitting units, Lee *et al.* further developed connecting two **DCzIPN** molecules through the donor side, as the dihedral angle between two carbazole units depends on the linking position of carbazole.[108] The resulting "twin-emitter" **34TCzPN** and **44TCzPN** possess improved photophysical properties compared to the single core emitter **DCzIPN**, without an significant red-shift of the emission. In the devices based on **34TCzPN** and **44TCzPN**, blue emission with λ_{EL} of 475 nm and 470 nm were achieved with improved EQE_{max} of 21.8 % and 19.5% respectively.[108]

Deep blue emission with narrowed full width at half maximum (FWHM) was also achieved in **CzBPCN**, which is a molecule that contains two connected TADF emitters within an interlocked molecular design.[109] The carbazoles from the dual cores form an interlocked structure to suppress the rotation of the central biphenyl ring. The molecule exhibited deep blue emission with λ_{PL} of 453 nm and Φ_{PL} of 76% in toluene. The OLEDs showed an EQE_{max} of 14.0% with a narrow FWHM of 48 nm and λ_{EL} of 460 nm leading to deep blue emission with CIE coordinates of (0.14, 0.12).[109]

This strategy is quite efficient as it boosts the absorptivity coefficient compared to the single TADF emitter without a large change in ΔE_{ST} value. Through careful adjustment of the connection of the two individual emitting cores, it is possible to obtain TADF emitters with improved optoelectronic properties.

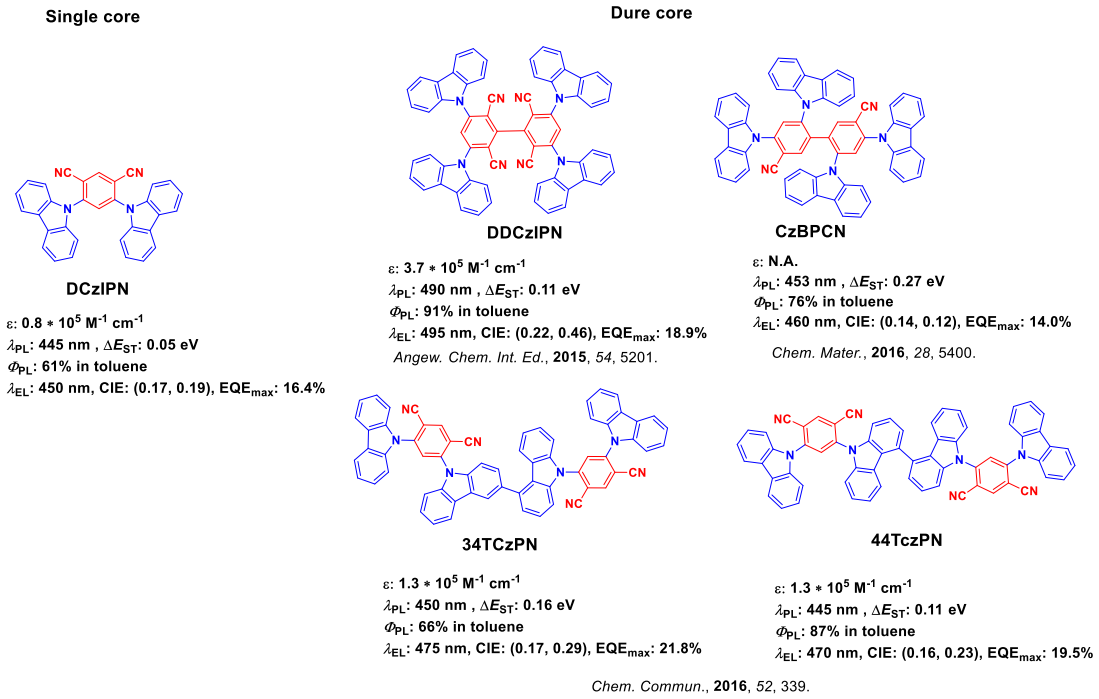

Figure **1.11**. Concept of dual core design for TADF blue emitters and the key photophysical and device data.

^{3}LE, ^{3}CT, and ^{1}CT degenerated TADF design

As shown in section **1.3.1**, the ^{3}LE state plays a vital role in both HFC and spin-vibronic coupling mechanisms for RISC, and its energetic relation between ^{3}CT and ^{1}CT can largely affect the RISC rate as strong SOC can be expected between the CT and energetically close-lying LE states of different spin multiplicities. Adachi *et al.* investigated the relation between the RISC process and the location of ^{3}CT, ^{1}CT, and ^{3}LE states.[93] Four blue ICT molecules (**Cz-TRZ1** to **Cz-TRz4**) with similar acceptor and donor moieties but different ^{3}CT, ^{1}CT, and ^{3}LE energies were studied.[93] The four compounds exhibited high Φ_{PL} (> 85%) in 6 wt% doped DPEPO films, and deep-blue to blue emission (λ_{PL} from 432 nm to 465 nm) in toluene. For **Cz-TRZ1**, a rather large ΔE_{ST} of 0.46 eV was observed in toluene, which resulted in almost negligible delayed emission in

6 wt% DPEPO film with τ_d of 28.9 μs and k_{RISC} of 0.3×10^3 s^{-1}.[93] The ΔE_{ST} for **Cz-TRZ3** and **Cz-TRZ4** are 0.17 and 0.15 eV, in 6 wt% DPEPO film, respectively, and the phosphorescence of both emitters showed vibrational structure, which indicates LE character for their T_1 states.[93] The transient decays of **Cz-TRZ3** and **Cz-TRZ4** exhibited significantly increased delayed components compared to **Cz-TRZ1**, k_{RISC} was improved to 1.5×10^4 s^{-1} and 2.8×10^4 s^{-1}, respectively. **Cz-TRZ2** possesses the smallest ΔE_{ST} of 0.07 eV, and both T_1 and S_1 states are of CT character and are energetically degenerate with the LE energy states of the donor and acceptor moieties.[93] As the ^{3}LE, ^{3}CT, and ^{1}CT states of **Cz-TRZ2** are degenerate, efficient RISC can occur via both HFC and spin-vibronic coupling mechanisms. Evidently, **Cz-TRZ2** exhibited the shortest τ_d of 3.5 μs and fastest k_{RISC} of 1.8×10^5 s^{-1}. The devices based on **Cz-TRZ1** to **Cz-TRZ4** exhibited EQE_{max} of 7.2%, 22.0%, 19.2% and 18.7% with CIE of (0.14, 0.12), (0.15, 0.25), (0.15, 0.10) and (0.15, 0.10), respectively.[93]

Another work from Adachi *et al.* used SOCME values between excited states to illustrate the impact of designing compounds with degenerate ^{3}LE, ^{3}CT, and ^{1}CT states on the efficiency of RISC and device performance.[98] Two emitters, **TMCz-BO** and **TMCz-3P**, with small ΔE_{ST} but different relative energies of their ^{1}CT, ^{3}CT, and ^{3}LE states were designed. **TMCz-BO**, whose ^{1}CT (2.95 eV), ^{3}CT (2.93 eV), and ^{3}LE (3.00 eV from the acceptor unit) states are close in energy, compared to **TMCz-3P** whose ^{3}LE (2.76 eV) was significantly more stabilized from its ^{1}CT (2.89 eV) in 30 wt% 2,8-bis(diphenylphosphineoxide)dibenzofuran (PPF) film.[98] They proposed that the efficient RISC for **TMCz-BO** was allowed via ^{3}CT → ^{3}LE → ^{1}CT as the energetically close-lying excited states can induce efficient thermally activated RIC from the ^{3}CT

to ^{3}LE states, and then RISC can be accelerated from ^{3}LE to ^{1}CT states mediated by a much larger SOCME value between ^{1}CT and ^{3}LE (0.124 cm^{-1}) than ^{1}CT and ^{3}CT (0.001 cm^{-1}).[98] Whereas for **TMCz-3P**, although large SOCME value (0.128 cm^{-1}) between ^{1}CT and ^{3}LE was predicted, as ΔE_{ST} (0.13 eV) is larger than the thermal energy ($k_BT \approx 0.03$ eV), the direct spin-flip process was suppressed.[98] The HFC between ^{1}CT and ^{3}CT is less efficient because of the negligible SOCME value (0.001 cm^{-1}). The proposed mechanism is supported by the photophysical data as **TMCz-BO** possesses a small ΔE_{ST} of 0.02 eV, fast τ_d of 0.75 μs, and fast k_{RISC} of 1.9×10^6 s^{-1} in PPF, while for **TMCz-3P**, the ΔE_{ST} is 0.13 eV, τ_d increased to 14.5 μs, and the k_{RISC} plummeted to 0.3×10^5 s^{-1}.[98] As a result, the device based on **TMCz-BO** achieved high EQE_{max} of 20.7% with CIE coordinates of (0.14, 0.18) and the efficiency remained high at 17.4% at 1000 cd m^{-2}, while the device based on **TMCz-3P** exhibited EQE_{max} of 20.4% but the efficiency dropped to 12.8% at 1000 cd m^{-2}; CIE coordinates in this device were (0.14, 0.26).[98]

Constructing molecules possessing degenerate ^{3}LE, ^{3}CT, and ^{1}CT states is one of the most popular and effective strategies to boost the RISC rate for TADF emitters. This strategy is compatible with other strategies to obtain efficient blue TADF emitters with short exciton lifetime and fast k_{RISC}, which are presented in the following sections.

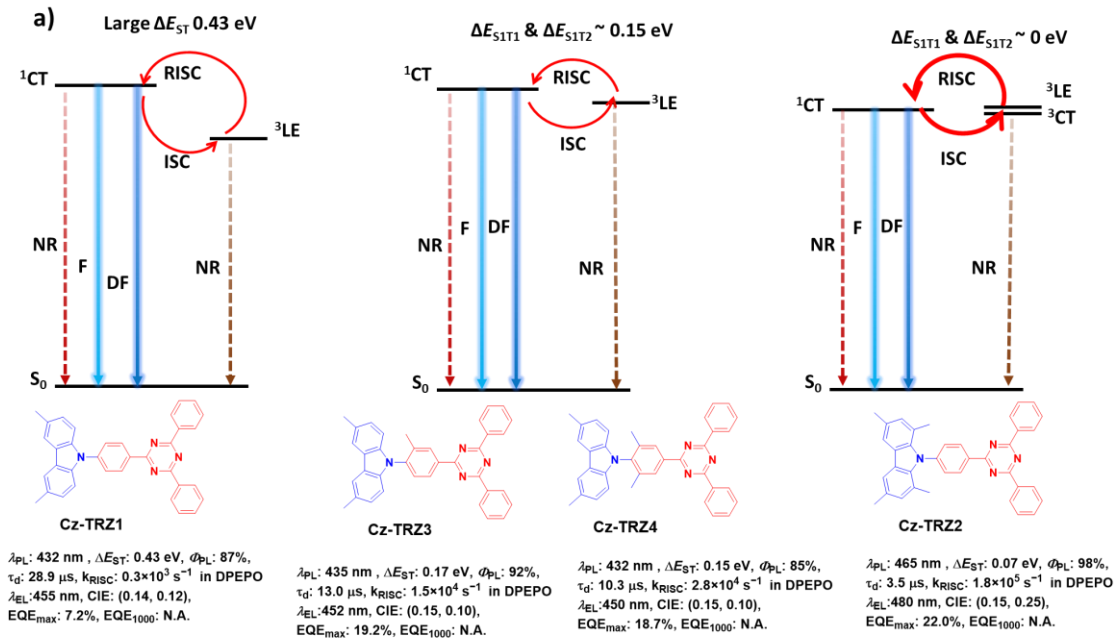

Angew. Chem. Int. Ed., **2017**, *56*, 1571.

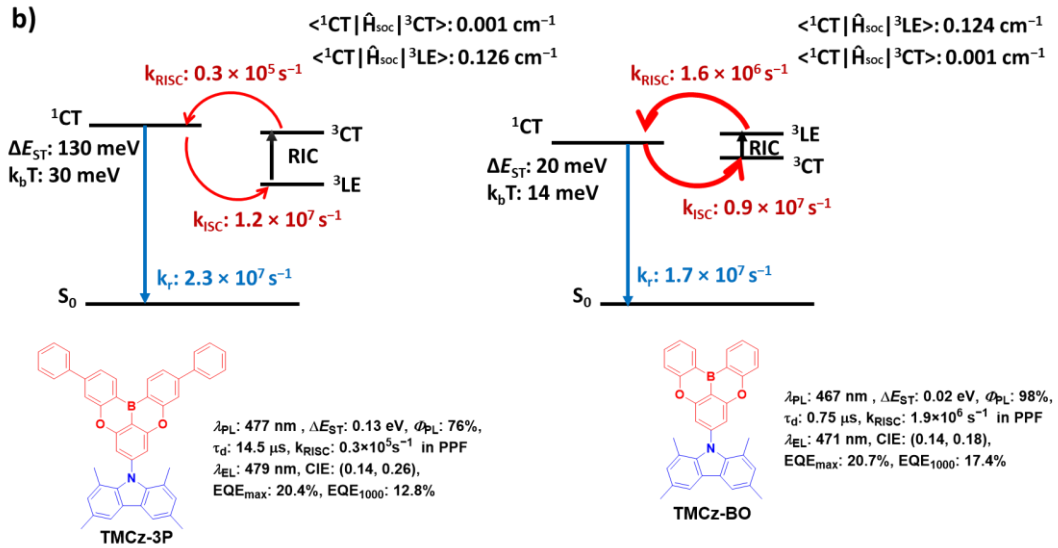

Nat. Commun., **2020**, *11*, 1765.

Figure **1.12**. Schematic illustration of TADF mechanisms, key photophysical and device data of a) **Cz-TRZ1-4**, and b) **TMCz-3P** and **TMCz-BO**.

Multiple donors TADF molecular design

The presence of intermediate triplet states lying above T_1 and below S_1 have been shown

to facilitate RISC and render TADF more efficient by opening up a RIC pathway that is mediated by spin-vibronic coupling between T_1 and one or more of the intermediate states, followed by RISC.[110] A dense number of intermediate excited states can be achieved by introducing multiple donors in the emitter, as the presence of multiple donors, each possessing slightly different conformations, and thereby presenting slightly different electronic coupling with the central acceptor guarantees a dense population of excited states.[110]

This design is exemplified in **DCzBN1** and **5CzBN** where either two carbazoles or five carbazoles were connected to the benzonitrile core. Both **DCzBN1** and **5CzBN** possess a highly twisted structure and corresponding ΔE_{ST} of 0.31 and 0.22 eV in toluene.[97,111] The time-dependent density functional theory (TD-DFT) calculations revealed the existence of three intermediate triplet states for **5CzBN**, while for **DCzBN3** only one intermediate state was predicted. The presence of the intermediate states in **5CzBN** helps to explain the shorter τ_d of 3.1 μs and faster k_{RISC} of 1.1×10^5 s^{-1} in toluene, compared to 18 μs of τ_d and 0.8×10^5 s^{-1} of k_{RISC} for **DCzBN1**. **5CzBN** also possesses a higher Φ_{PL} of 65% in doped 20 wt% 3,3′-Di(9H-carbazol-9-yl)-1,1′-biphenyl (mCBP) films compared to 28% for **DCzBN1** in 10 wt% DPEPO film.[97,111]

Adachi *et al*. optimized the structure of **5CzBN** by introducing a second type of donor. The optimized molecule **3Cz2DPhCzBN** contains three diphenyl-substituted carbazole units and two undecorated carbazoles coupled to benzonitrile.[97] As the diphenyl carbazole possesses a lower ^{3}LE than carbazole, the intermediate triplet states in **3Cz2DPhCzBN** are closer to ^{1}CT (S_1) and ^{3}CT (T_1) than **5CzBN**, thus improving the RISC via ^{3}CT and ^{3}LE mixing.[97] The molecule **3Cz2DPhCzBN** showed shorter τ_d of 5.6 μs than **5CzBN** (10.2 μs), two times faster k_{RISC} (9.9 ×

10^5 s^{-1}) than **5CzBN** (3.6×10^5 s^{-1}) in 20 wt% doped mCBP film and the Φ_{PL} also improved to 85% compared to 65% of **5CzBN** in 20 wt% doped mCBP film. The OLEDs based on **3Cz2DPhCzBN** exhibited a high EQE_{max} of 20.9% with CIE of (0.21, 0.44), compared to 18.0% with CIE of (0.22, 0.40) for **5CzBN**.[97] More importantly, **3Cz2DPhCzBN** exhibited minimum efficiency roll-off, as the EQE remained 20.7% at 1000 cd m^{-2} compared to 13.9% of **5CzBN**.[97]

The drawback of the multiple donor design is that the emission red-shifts due to the increased molecular conjugation. Duan *et al*. adopted benzonitrile as a weaker acceptor to replace the cyano group to construct blue emission with multiple donors design.[112] The additional phenyl bridge can significantly reduce the electronic coupling between acceptor and donor units, establishing both small ΔE_{ST} and a high CT energy to approach the ^{3}LE state for more efficient CT-LE mixing. The molecule **p4TCzPhBN** showed small ΔE_{ST} of 0.10 eV and high k_{RISC} of 2.4×10^6 s^{-1} in toluene, and the OLEDs based on **p4TCzPhBN** exhibited blue emission with of λ_{EL} of 468 nm and CIE of (0.15, 0.19) and an EQE_{max} of 22.8% and EQE_{1000} of 20.4% were achieved.[112]

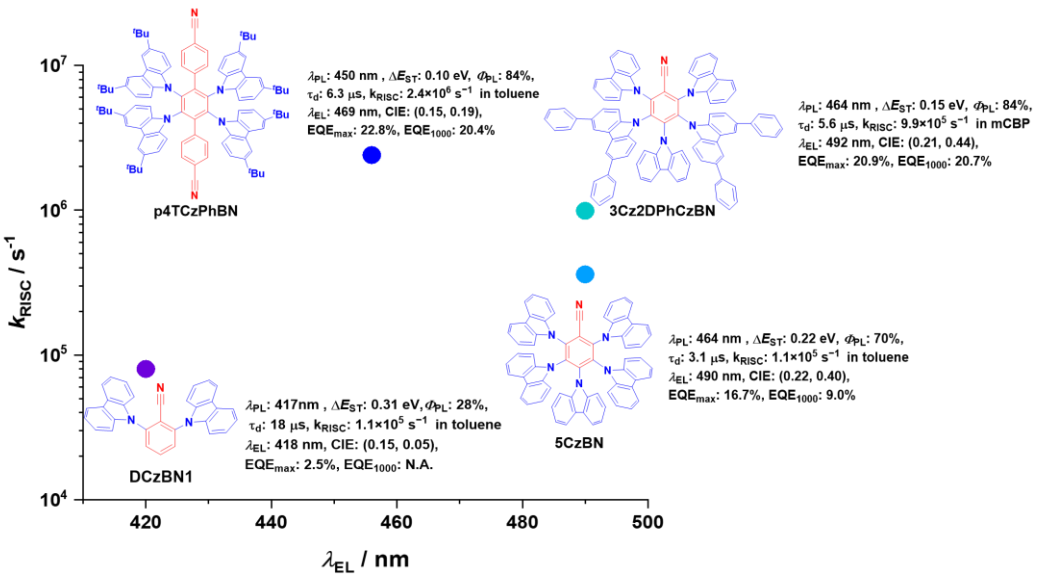

Figure **1.13**. Schematic illustration of Multiple donors TADF molecule design based on CzBN derivatives.

Heteroatom-incorporated TADF design

Heteroatoms, such as sulfur, oxygen, nitrogen, and halogen atoms have been shown to enhance the SOC of TADF material due to the heavy atom effect.[113,114] Yasuda *et al*. discovered that incorporating a sulfur atom with a TADF emitter can enhance SOC due to the heavy atom effect associated with the sulfur atom.[115] The three compounds **MPAc-BS**, **MPAc-BO**, and **MPAc-BN**, which fused either a sulfur, oxygen, or nitrogen atom into the boron-based acceptor, exhibited similar small ΔE_{ST} (< 0.05 eV) and almost unity Φ_{PL} except **MPAc-BN** (63%) in doped 50 wt% PPF film.[115] The TD-DFT calculations revealed that all three emitters possessed degenerate ^{1}CT (S_1), ^{3}CT (T_1), and ^{3}LE (T_2). Moreover, the T_2 state of **MPAc-BS** exhibited a significantly large SOCME value (4.67 cm^{-1}) with its S_1 state, which was more than 10 times larger than those of **MPAc-BO** and **MPAc-BN** (SOCME = 0.41 and 0.38 cm^{-1}, respectively).[115]

Therefore, the thia-bridged **MPAc-BS** was expected to undergo RISC more efficiently than **MPAc-BO** and **MPAc-BN**. Evidently, **MPAc-BS** exhibited very short τ_d of 1.3 μs and fast k_{RISC} of 3.5×10^6 s^{-1} in 50 wt% PPF film, compared to 1.8 μs and 1.0×10^6 s^{-1} for **MPAc-BO**, and 18 μs and 1.8×10^5 s^{-1} for **MPAc-BN**, respectively.[115] The OLEDs based on **MPAc-BS** achieved excellent EL performance, with a EQE_{max} of 22.8% and small efficiency roll-off with EQE_{1000} of 19.0 % with λ_{EL} of 487 nm, while for **MPAc-BO**, the EQE_{max} was 21.3% with λ_{EL} of 474 nm, and EQE_{1000} plummeted to 8.0% due to the longer exciton lifetime and less efficient RISC.[115]

Yasuda *et al*. further introduced a silicon atom within the donor unit of **MPAc-BS** to improve the SOC efficiency, and designed two blue emitters **MPASi-BS** and **MFASi-BS**.[116] The closely lying ^{1}CT, ^{3}CT, and ^{3}LE states and heavy atom effect improved the SOC between the singlet and triplet states and thus enhanced further the RISC process.[116] Compared to k_{RISC} of 3.5×10^6 s^{-1} in doped PPF for the prototype material **MPAc-BS**, the silicon involved **MPASi-BS** and **MFASi-BS** exhibited k_{RISC} above 1×10^7 s^{-1} in 50 wt% doped PPF.[116] In addition to fast k_{RISC}, the high Φ_{PL} (close to 100%), and small ΔE_{ST} (<0.11 eV) of **MPASi-BS** and **MFASi-BS** make them highly efficient TADF emitters.[116] The devices based on **MPASi-BS** and **MFASi-BS** exhibited sky-blue emission with λ_{EL} of 478 nm 484 nm, respectively, and EQE_{max} of 27.6% and 23.9% with small efficiency roll-off (EQE_{1000} of 26.1% and 21.9%, respectively).[116]

These two works provided an interesting strategy of introducing non-metallic “heavy atoms” and enhanced SOC. The utilization of the heavy-atom effect could help in designing more efficient blue TADF emitters with relatively short decay lifetimes and lower efficiency roll-offs.

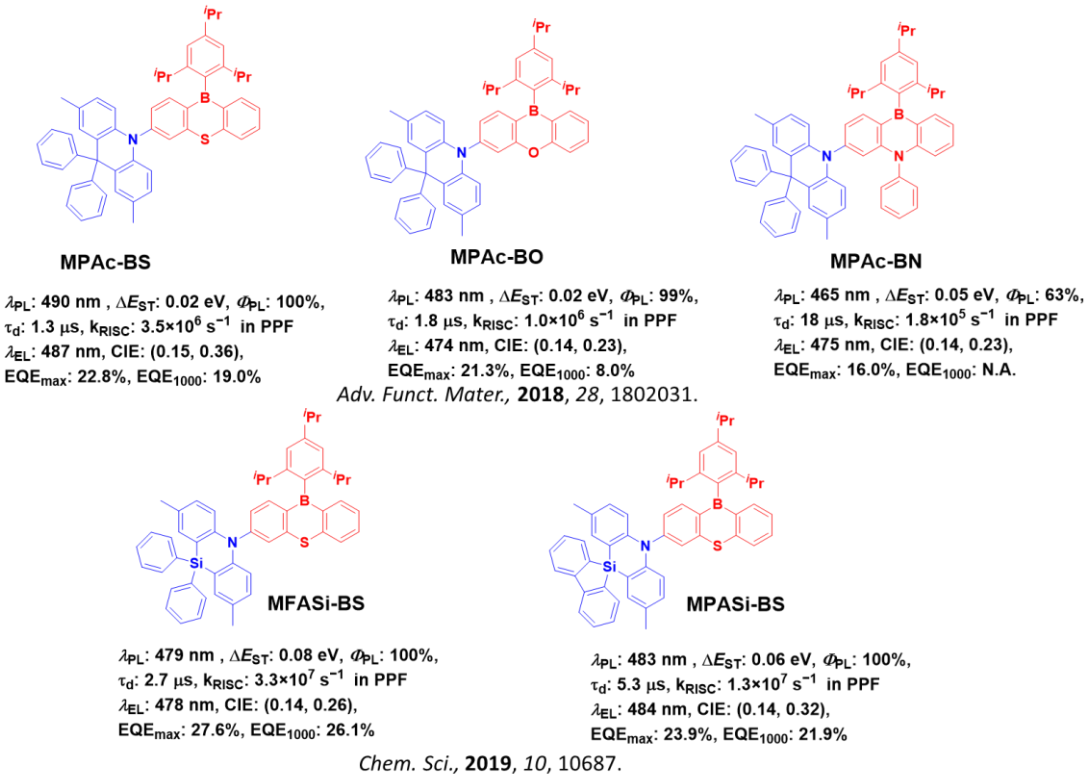

Figure **1.14**. Molecular structures and key photophysical parameters of some heteroatom-containing TADF materials

TADF molecules with highly horizontally oriented transition dipoles

As shown in **1.1.2**, the η_{out} for typical multilayred OLEDs is limited to be 20~30% due to the isotropic orientation of the emitters within the EML. In order to enhance the η_{out} to exceed this theoretical limit, emitters TDMs that are highly horizontally oriented are highly desired to reduce the surface plasmon mode, which constitutes almost 40% of photon loss.[117] For molecules with a donor-acceptor structure, the TDM typically points in the direction that connects these two moieties, which means if the TADF emitter adopted linear D-A structure, the TDM generally coincides with molecule's long axis. Through a horizontally aligned emitting layer, the surface plasmon can be reduced according to the ratio of isotropic/horizontal orientation of TDM.

Recently, a review work from Zysman-Colman, Gather *et al*. concluded that higher degrees of TDM horizontal orientation are achieved for TADF emitters with longer molecular backbone, and heavier molecular weight.[118] Several representative blue emitters with horizontal oriented TDM are presented in this section.

Wu *et al*. reported three triazine-based TADF molecules, **DMAC-TRZ**, **DPAC-TRZ** and **spiroAC-TRZ** with acridine derivatives as donors.[119] Compared to **DMAC-TRZ** or **DPAC-TRZ**, which exhibited a flexible structure along the C9-N10 axis of the acridine, the more rigid and longer **spiroAC-TRZ** backbone resulted in the highest horizontal oriented ratio ($\Theta_{//}$) of 83% among all three molecules when doped 12 wt% in mCPCN.[119] Combined with almost 100% of Φ_{PL}, the OLEDs based on **spiroAC-TRZ** exhibited sky-blue emission (CIE=(0.18, 0.43)), and achieved EQE_{max} of 36.7% and EQE_{1000} of 30.5% without any internal or external optical out-coupling improvement methods such as periodic gratings, low refractive index grids, or scattering particles between substrate and electrode.[119]

Liu *et al*. further pushed the horizontal orientation ratio to an even higher level (>90%) by employing spiro-biacridine (SBA) as a central donor for the A-π-D-π-A long molecular backbone design.[120] The three blue emitters **PM-SBA**, **IPN-SBA**, and **PX-SBA** possessed Φ_{PL} of 73–63% and high $\Theta_{//}$ values of 87%, 93%, and 91% in 20 wt% doped DPEPO films, respectively, were recorded.[120] The corresponding TADF-OLEDs achieved EQE_{max} of 29.6%, 24.7%, and 20.8% and CIE coordinates of (0.17, 0.28), (0.19, 0.33), and (0.16, 0.15) with evaluated η_{out} of 30–40%, respectively.[120] Therefore, the efficiency of the OLEDs can be boosted to even beyond the theoretical upper limit via adopting emitters with horizontally oriented TDM, which requires fully

consideration of molecular weights, backbone length, and molecular thickness.

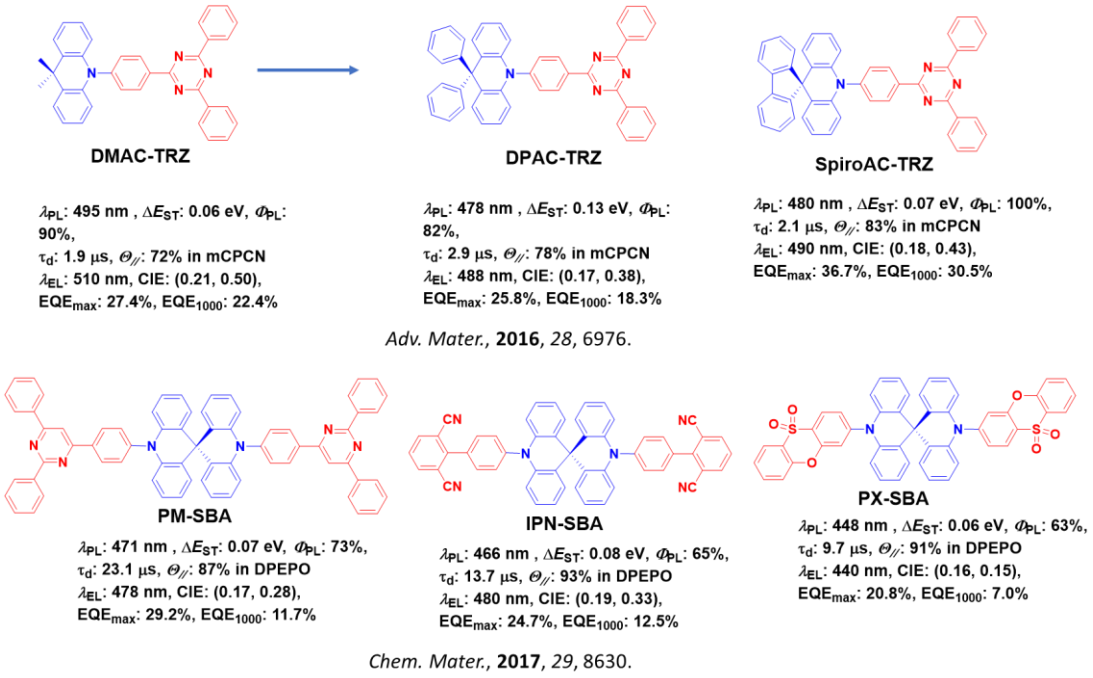

Figure **1.15**. Typical examples of blue TADF materials that are highly horizontally oriented in doped films and key photophysics and device factors.

The strategy of introducing a twisted donor-acceptor structure to cause HOMO/LUMO separation to enhance the CT character and PL efficiency has been is by far the most successful and effective method to realize highly efficient blue TADF molecule construction and could help to guide a lot of researchers in engineering the optimal blue TADF molecule structure.

1.4.2 Through-space charge transfer (TSCT) blue TADF molecules

As presented in the section above, the majority of the reported blue TADF emitters utilize twisted donor-acceptor systems to reduce the π-conjugation and minimize the exchange

integral. The through-space charge transfer (TSCT) molecular design on the other hand, offers an alternative and effective approach for HOMO/LUMO separation where the acceptor and donor are spatially separated about a rigid molecular framework. The CT state is induced through aromatic π-stacking interactions between the donor and acceptor. In a typical TSCT system, the donor and acceptor moieties are disposed co-facially with each other, where the interplanar distance is usually in the order of the van der Waals distances of 3-3.5 Å for efficient ICT.[87]

Swager *et al*. firstly adopted this strategy to construct a blue emitter that employed a 9,9-dimethylxanthene to mediate a through-space charge transfer between donor and acceptor moieties (**XtBuCT**).[121] Crystal structures revealed an ''U'' shaped and co-facial intramolecular alignment of donor (*tert*-butyl carbazole) and acceptor (2,4-diphenyl-1,3,5-triazine) with a distance (*d*) of 3.3 Å, which mediates the TSCT.[121] The TD-DFT calculations of **XtBuCT** showed that this structure can lead to sufficient HOMO/LUMO separation with a minuscule ΔE_{ST} of 0.007 eV. [121] However, the low overlap led to small oscillator strength of 0.0004, which was responsible for the low Φ_{PL} of 35% in 10 wt% doped DPEPO film.[121]

Lu *et al*. explored this strategy and combined through space and through bond charge transfer mechanisms together in emitters **B-oCz** and **B-oTC**.[122] The donor groups in both emitters were *ortho*-substituted and the ΔE_{ST} and oscillator length (*f*) values of **B-oCz** and **B-oTC** from TD-DFT were estimated to be 0.068 eV (f = 0.0019) and 0.046 eV (f = 0.0014), respectively.[122] The crystal structure revealed that the carbazole moiety was disposed co-facially on one of the aryl rings of the triarylboron group with close intramolecular distance in the range of 2.70-3.55 Å, enabling a strong through space interactions.[122] The charge transfer therefore can

occur through the aryl linker and through space simultaneously in these emitters. Considering the strong intramolecular interactions, which could efficiently suppress the non-radiative decay, the small ΔE_{ST} as well as appropriately strong oscillator lengths make these materials desirable candidates for efficient TADF. As a matter of fact, both emitters exhibited blue emission with λ_{PL} of 465 nm and 476 nm and Φ_{PL} of 61% and 94% in neat films, and they possessed ΔE_{ST} of 0.06 eV and 0.05 eV and τ_d of 15 μs and 12 μs for **B-oCz** and **B-oTC**, respectively.[122] The solution-processed non-doped OLEDs exhibited EQE_{max} values of 8% and 19.1% for **B-oCz** and **B-oTC**-based devices, respectively.[122]

Recent work from Kaji *et al.* showed that a degenerate set of ^{1}CT, ^{3}CT and ^{3}LE states can be obtained by controlling the distance and the relative disposition between the donor and acceptor segments.[123] The optimized blue emitter **TPaT-tFFO**, where triptycene (Tp) was used as the scaffold to realize the "tilted face-to-face" donor–acceptor alignment with an optimized distance 4.72 Å, which according to TD-DFT calculations the ^{1}CT and ^{3}CT states of the emitter are degenerate with both the ^{3}LE states of the donor and acceptor moieties.[123] The molecule exhibited weak CT absorption ($\varepsilon \approx 2 \times 10^2$ cm^{-1} M^{-1} at 380 nm) in toluene, and a degenerate alignment of ^{1}CT-^{3}LE-^{3}CT states with very small ΔE_{ST} (^{1}CT-^{3}CT) of 0.036 eV and ΔE_{ST} (^{3}LE-^{1}CT) of 0.007 eV in 25 wt% doped mCBP film.[123] Moreover, the TD-DFT calculations predicted a rather high SOCME value of 0.61 cm^{-1} between ^{1}CT and ^{3}LE, which indicate an efficient RISC.[123] The emitter exhibited a sky-blue emission with λ_{PL} of 487 nm, Φ_{PL} of 84%, τ_d of 4.4 μs and fast k_{RISC} of 1.2×10^7 s^{-1} in toluene. Devices based on **TPaT-tFFO** also displayed excellent performance, and an EQE_{max} of 19.2% was realized which, upon using an outcoupling

sheet, was increased up to 29%.[123]

From the examples discussed above, it is evident that a through-space charge transfer design provides an interesting alternative mechanism towards realizing TADF. However, simultaneously maintaining a high Φ_{PL} and fast k_{RISC} is still a challenge for the community working towards blue TADF emitters.

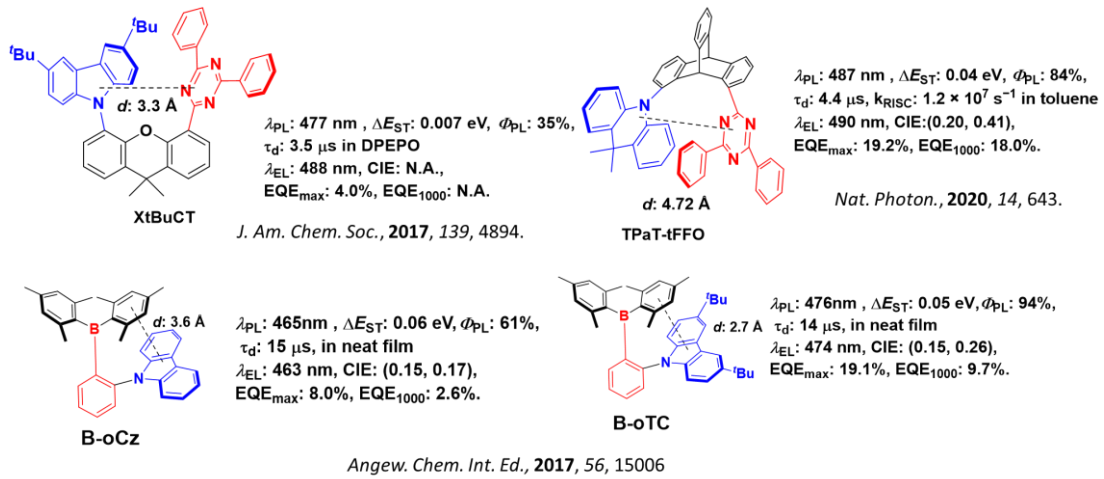

Figure **1.16**. Molecular structures and key photophysics and device factors of representative blue through-space charge transfer TADF emitters.

1.4.3 Multi-resonance effect induced TADF (MR-TADF) molecules

Notably, emission from ICT type TADF emitters suffers from a broad full width at half maximum (FWHM) owing to the strong ICT and inevitable geometric relaxation that occurs between the excited and ground states, resulting in energy band broadening from the diverse molecular conformations that exists within organic semiconductor films. The typical FWHM in OLEDs for these emitters are in the range of 70–100 nm, which is detrimental for the display

color purity and makes it difficult to achieve deep-blue emission with CIE_y value below 0.1 as it requires that most of the emission must fall within the deep-blue region.[36,72,94–98]

To address this issue Hatakeyama *et al*. synthesized two novel boron-based TADF materials with ultrapure blue emission and very narrow FWHM, in significant contrast to the features of the previously reported typical ICT-type TADF molecules.[124] In particular, instead of introducing a long-range ICT effect for FMOs separation, the HOMOs and LUMOs of **DABNA-1** and **DABNA-2** were limited within localized rigid structures.[124] As the boron and nitrogen atoms could induce an opposite resonance effect to the benzene ring, the effective separation of the FMOs distribution was achieved in the case of *para*-substitution, which guaranteed a small ΔE_{ST} for TADF to be present in these rigid polycyclic aromatic compounds.[124] The rigid conformation can also suppress geometric relaxation in the excited state, thus restricting the FWHM of these compounds to extremely small values. The benefit of MR-TADF molecules **DABNA-1** and **DABNA-2** consisted not only of strong oscillator strength (f = 0.21 and 0.41), small ΔE_{ST} (0.18 and 0.14 eV), and high Φ_{PL} (88% and 90%), but also a significantly improved color purity, with narrowed FWHM (~30 nm) in 1 wt% doped mCBP film.[124] OLEDs using **DABNA-1** or **DABNA-2** as the emitter showed λ_{EL} at 459 nm and 467 nm, CIE coordinates (0.13, 0.09) and (0.12, 0.13), respectively.[124] The device with **DABNA-2** showed a higher EQE_{max} of 20.2% compared to 13.5% for that with **DABNA-1**, which represented a record-setting performance for blue OLEDs at the time of publication.[124] Unfortunately, the maximum luminance (Lum_{max}) for both devices cannot reach 1000 cd m^{-2} owing to the serious efficiency roll-off caused by long exciton lifetime (~ 100 μs) and slow k_{RISC} (~1.0×10^4 s^{-1}).[124] Still, MR-TADF material possess huge potential as ultrapure

blue emitters and has progressed significantly ever since. Representative works on blue MR-TADF emitters are presented in this section.

Hatakeyama *et al*. further designed a related pentacene system substituted with peripheral diphenylamines (**ν-DABNA**), the FWHM is further narrowed to 14 nm in toluene and 18 nm in OLED, respectively.[106] The narrow FWHM originates from minimizing the vibronic coupling between the S_0 and S_1 states and the vibrational relaxation at the S_1 state, which was well supported by TD-DFT calculations.[106] Moreover, **ν-DABNA** showed blue emission with λ_{PL} of 467 nm (FWHM = 18), minimal ΔE_{ST} of 0.02 eV, short τ_d of 4.1 μs and Φ_{PL} of 90% in the bespoke MR-TADF host DOBNA-OAr.[106] Deep blue devices exhibited outstanding EQE_{max} of 34.4% and low efficiency roll-off (EQE_{1000} = 26.0%) and CIE of (0.12,0.11) were achieved for **ν-DABNA**.[106] Although the reason for the improved photophysics of **ν-DABNA** remains elusive, in terms of both EQE_{max} and color purity ***ν*-DABNA** is one of the best blue TADF emitter at the moment.

The MR-TADF category was further enriched by using carbonyl and the nitrogen atoms for the opposite resonance effect.[125] Lee *et al*. identified the MR-TADF character of quinolino[3,2,1-*de*]acridine-5,9-dione (**QAO** also known as **DiKTa**) which has two carbonyls and one nitrogen atom fused as a rigid planar structure.[125] The DFT calculation revealed that the HOMO electron clouds of **DiKTa** are mainly located on the nitrogen atom and *ortho*- and *para*-carbons relative to it, whereas the LUMOs are concentrated on the carbonyl groups as well as the *meta*-carbons relative to the nitrogen atom.[125] This similar HOMO and LUMO separation pattern of **DABNA-1** indicates that **DiKTa** has the potential to be a MR-TADF emitter.[125] **DiKTa** exhibited Φ_{PL} of 72% in mCP film and associated with small ΔE_{ST} 0.18 eV in toluene.[125] The

OLEDs based on **DiKTa** showed a narrow emission (FWHM = 39 nm) band at λ_{EL} = 468 nm, which is the character of MR-TADF emitters, and exhibited a high EQE_{max} of 19.4%.[125] However, the OLEDs also suffered from severe efficiency roll-off (EQE reduced to 1.0% at 1000 cd m^{-2}), which may be due to the long-lived τ_d (93 μs in mCP) and intermolecular interaction caused quench from its close packing.[125]

To mitigate the ACQ and aggregate emission from planar MR-TADF molecules, our group reported a mesitylated derivative of **DiKTa**, **Mes_3DiKTa** as the mesityl groups would adopt an orthogonal conformation and thus not affect the multi-resonance mechanism and their twisted structure will inhibit ACQ.[126] The modified emitter presented a small ΔE_{ST} of 0.20 eV and Φ_{PL} of 80%, which is close to **DiKTa** of 0.21 eV, and 72%, respectively, in 3.5 wt% mCP film.[126] The aggregate emission was completed suppressed in **Mes_3DiKTa**, as its neat film retained narrow spectral shape, in contrast to **DiKTa**, which exhibited a distinct second, broad peak at 540 nm.[126] The ACQ was significantly suppressed in the solid-state of **Mes_3DiKTa** as the Φ_{PL} remained 42% at 10 wt% mCP, while for **DiKTa** the Φ_{PL} was dropped to 15%.[126] The OLED based on **Mes_3DiKTa** showed an EQE_{max} of 21.2% with CIE (0.12,0.32) compared **DiKTa** with EQE_{max} of 14.7% and CIE (0.14,0.18). Improved efficiency roll-off was observed for the device with **Mes_3DiKTa** where there was only 31% roll-off at 100 cd m^{-2} compared to 44% for the OLED with **DiKTa**.[126]

The introduction of MR-TADF emitters provides a family of compounds that show significantly improved efficiency and color purity of blue and deep-blue TADF emitters. More theoretical and experimental investigations are highly desired for a clearer understanding of the

excited-state behavior of this class of compound, including how to modulate the nature of the excited states, ΔE_{ST} and k_{RISC}, and to determine the role that intermediate states play in RISC in these compounds. Meanwhile, the molecular structures and types of MR-TADF materials are still very limited, and efficiency roll-off and device stability must be optimized for MR-TADF based OLEDs. However, despite the small number of structurally related examples reported, it is already evident that MR-TADF emitters are an incredibly promising class of compounds.

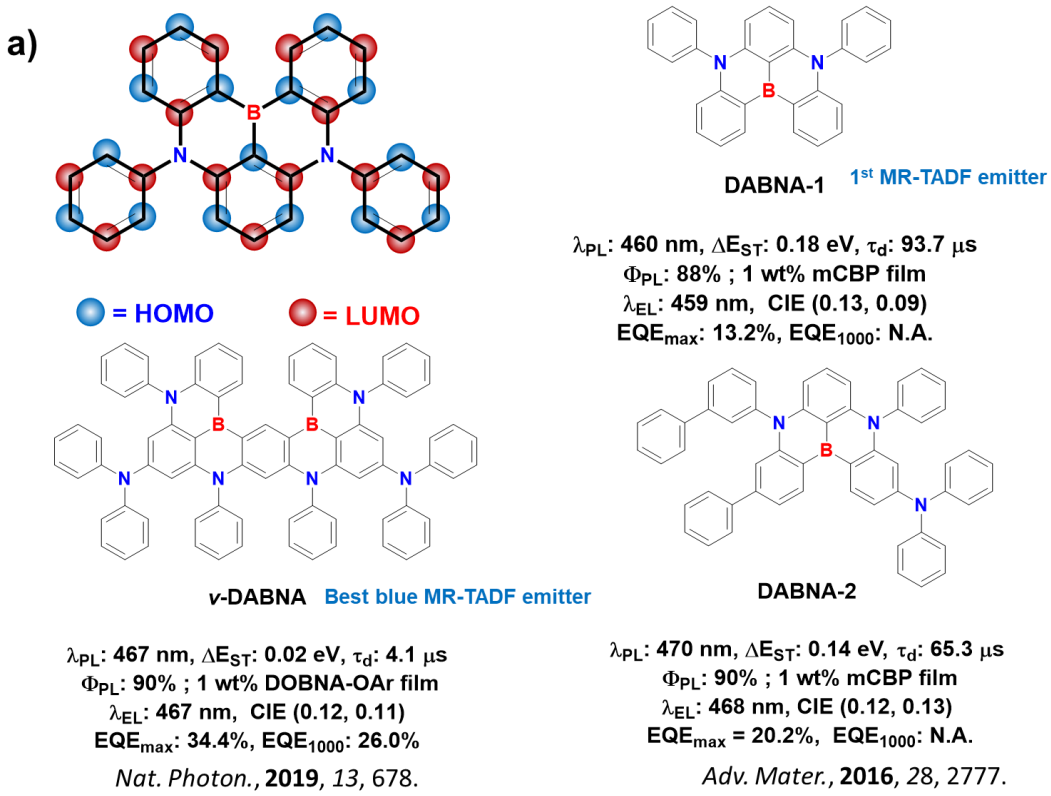

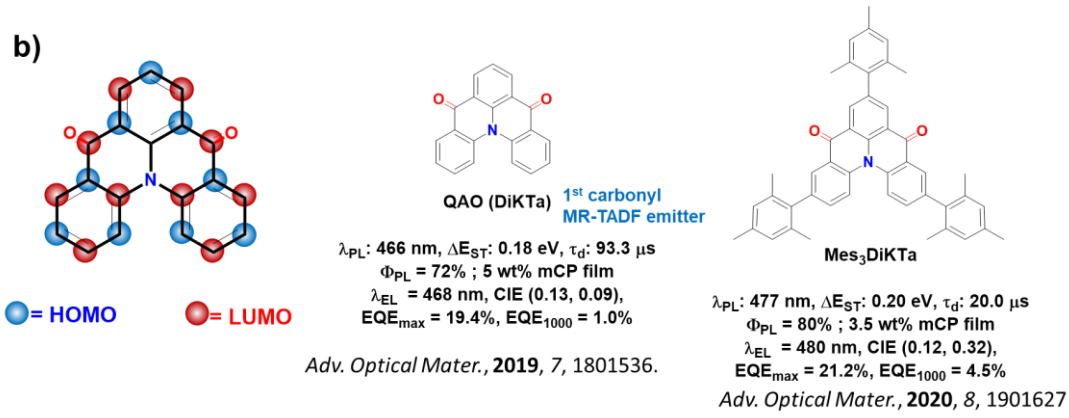

Figure **1.17**. Illustration of the distribution of HOMO and LUMO in (a **DABNA-1** and b) **QAO** (**DiKTa**), and representative examples of blue MR-TADF emitters.

An exciplex is generated by charge transfer between electron donor and electron acceptor molecules in the excited state, and as there is no strong bonding between the donor and acceptor moieties, the ΔE_{ST} for exciplex system is close to 0 eV. Exciplex systems usually are used as host materials, rather as emitter due to the relatively low Φ_{PL} compared to other systems.[127] For spiro-conjugation system, most examples show green to yellow emission in OLEDs,[128–132] and there exists only a few blue emitters with spiro-conjugation system that have been reported to date.[133]

1.5 Aims for Projects

The development of TADF emitters is rapid and thriving. It took only several years for organic small molecules to reach efficiencies comparable to phosphorescent materials. The breakthrough of blue TADF-OLEDs also demonstrates the significance of developing TADF materials as the next generation OLED emitters. There is still a lot to be done in terms of highly efficient deep-blue TADF emitters, triplet lifetime and annihilation inhibition in device, horizontal

dipole moment modulation for high η_{out}, and most importantly, operating stability of the TADF-OLEDs. These challenges still require researchers to comprehensively explore more TADF systems before these materials possess the right combination of properties to be adopted within OLEDs. This thesis is focused on TADF emitter design and makes efforts to address these issues.

Firstly, in **Chapter 2**, to improve the Φ_{PL} of TADF emitters, we designed and synthesized three TADF emitters (***p*-di2CzPN**, ***m*-di2CzPN**, and **1,3,5-tri2CzPN**) with multichromphores structure. Photophysical measurements show three emitters have ultra-high PLQY in toluene solution and in doped poly(methyl methacrylate) (PMMA) film. The **1,3,5-tri2CzPN** exhibited high EQE_{max} in the solution-processed OLEDs devices.

Secondly, we explored using of heteroaromatic bridges between donor and acceptor units for efficient blue TADF emitter design. In **Chapter 3**, we synthesized four TADF emitters based on different heteroaromatic sulfones as acceptors and di(tert-butyl)carbazole as the donor: **pDTCz-2DPyS**, **pDTCz-3DPyS**, **pDTCz-DPzS**, and **pDTCz-DPmS**. The molecular conformations and photophysics of these four molecules were studied and we obtained pure blue emission, and high EQE_{max} in OLEDs based on **pDTCz-2DPyS**, **pDTCz-3DPyS**, and **pDTCz-DPmS**, which were more than three times higher than the reference device with **pDTCz-DPS** using the same device configuration. OLEDs based on **pDTCz-DPzS** exhibited green emission and high EQE_{max} above 20%.

In **Chapter 4**, we synthesized two pyrazine-based emitters **DTCz-Pz** and **DTCz-DPz** bearing a mono and dipyrazine acceptors and di-*tert*-butylcarbazole as the donor. These two materials show reasonably high Φ_{PL}, ranging from 76 to 96%, in both toluene solution and doped

2,8-bis(diphenylphosphoryl)dibenzo[b,d]thiophene (PPT) thin films. Blue-emitting OLEDs were fabricated using these emitting materials. The devices showed EQE_{max} of 11.6% for the **DTCz-Pz** device with CIE (0.15, 0.16) and 7.2% for the **DTCz-DPz** device with CIE (0.15, 0.30).

In **Chapter 5**, two pyridine containing ambipolar host materials **3-CBPy** and **4-mCBPy** were designed and employed as the host for yellow TADF emitter **tri-PXZ-TRZ**. The OLEDs devices based on **3-CBPy** and **4-mCBPy** show markedly improved EQE and decreased roll-off compared to devices with commercial host materials.

To improve and control the orientation of TADF emitters, in **Chapter 6**, we explored introducing mesogens onto TADF emitter. Multi-resonant TADF emitter 5H-Quino[3,2,1-de] acridine-5,9-dione (**DiKTa**) was chosen as the pseudo-planar emitting core and attached three 1,6-dioxyhexyl-[1,1'-biphenyl]-4-carbonitrile mesogenic groups. The compound **DiKTaLC** exhibits TADF character in the solid state with a Φ_{PL} of 41% in neat film. The liquid crystal character of **DiKTaLC** was confirmed by polarising optical microscopy (POM) and differential scanning calorimetry (DSC), as the material displays nematic liquid crystalline phase under 108 ^{o}C. The as prepared pristine neat film of **DiKTaLC** shows preferential horizontal orientation.

In **Chapter 7**, we explored the possibility of using nanohoop structures in terms of cycloparaphenylenes (CPPs) for TADF emitter design. DFT and TDA-DFT calculations were applied to design CPP based TADF emitter. The results revealed that the macrocycles **4PXZPh-[10]CPP**, where four bulky electron-donating moieties 10-phenyl-10H-phenoxazine are connected to [10]CPP, showed sufficient HOMO/LUMO separation and small ΔE_{ST} of 0.08 eV. **4PXZPh-[10]CPP** exhibited biexponential decay in polar solvents (DCM and THF) with τ_d in

the range 0.4 -0.5 μs. In bipolar host 2,6-bis(9H-carbazol-9-yl)pyridine (PyD2), **4PXZPh-[10]CPP** showed sky-blue emission with λ_{PL} = 480 nm and Φ_{PL} = 25% in the 15 wt% doped film. We fabricated solution-processed OLEDs based on **4PXZPh-[10]CPP**, however, the device performance was unsatisfying and device optimization is expected to carry on.

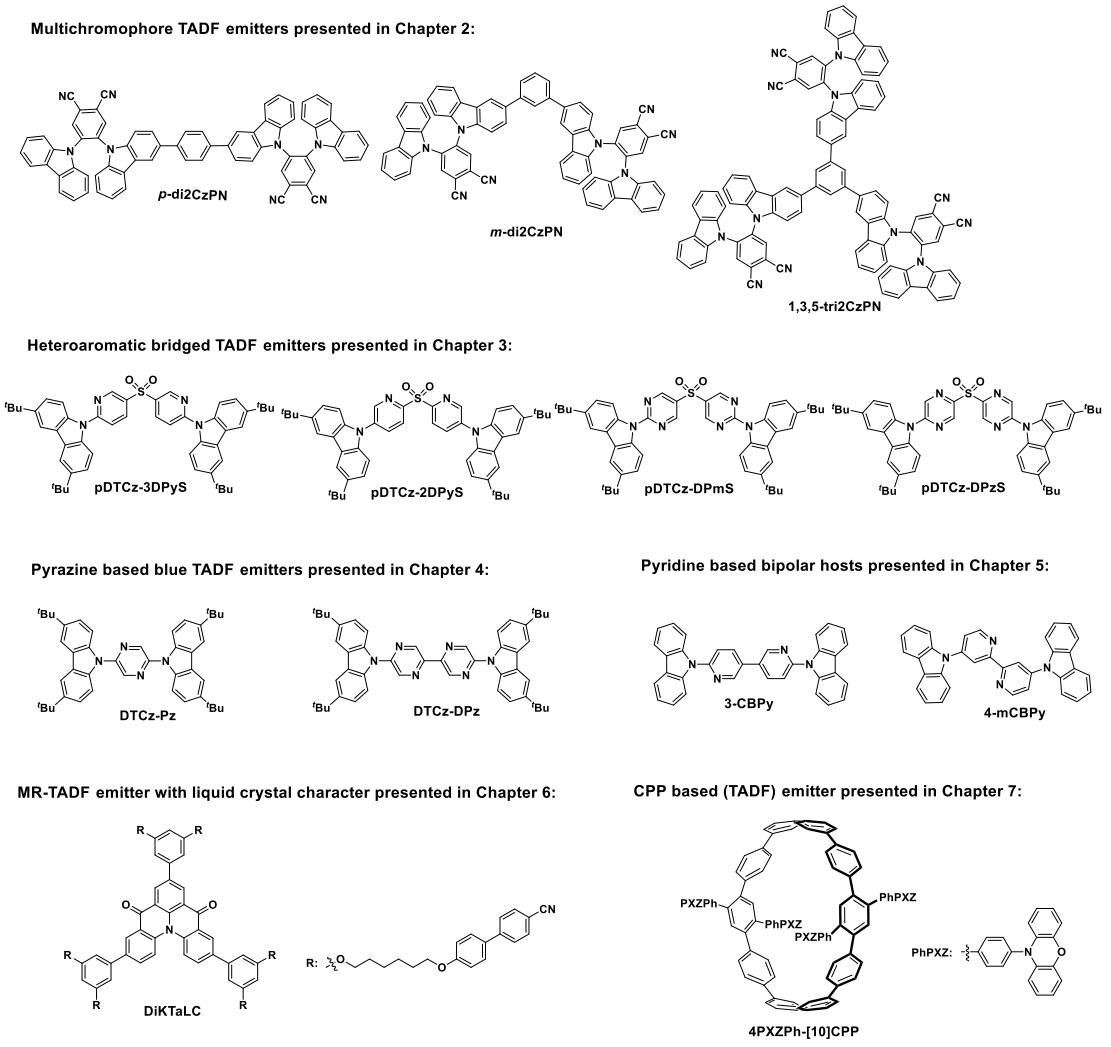

Figure **1.18**. Molecular structures of all the materials investigated in this work.

References

(1) https://doi.org/https://www.gov.uk/government/statistics/energy-consumption-in-the-uk.

(2) Tang, C. W.; Vanslyke, S. A. Organic Electroluminescent Diodes. *Appl. Phys. Lett.* **1987**, *51*, 913–915. https://doi.org/10.1063/1.98799.

(3) Hong, G.; Gan, X.; Leonhardt, C.; Zhang, Z.; Seibert, J.; Busch, J. M.; Bräse, S. A Brief History of OLEDs—Emitter Development and Industry Milestones. *Adv. Mater.* **2021**, *33*, 2005630. https://doi.org/10.1002/adma.202005630.

(4) Song, J.; Lee, H.; Jeong, E. G.; Choi, K. C.; Yoo, S. Organic Light-Emitting Diodes: Pushing Toward the Limits and Beyond. *Adv. Mater.* **2020**, *32*, 1907539. https://doi.org/10.1002/adma.201907539.

(5) Wong, M. Y.; Zysman-Colman, E. Purely Organic Thermally Activated Delayed Fluorescence Materials for Organic Light-Emitting Diodes. *Adv. Mater.* **2017**, *29*, 1605444. https://doi.org/10.1002/adma.201605444.

(6) Kido, J.; Kimura, M.; Nagai, K. Multilayer White Light-Emitting Organic Electroluminescent Device. *Science* **1995**, *267*, 1332–1334. https://doi.org/10.1126/science.267.5202.1332.

(7) Segal, M.; Baldo, A.; Holmes, J.; Forrest, R.; Soos, G. Excitonic Singlet-Triplet Ratios in Molecular and Polymeric Organic Materials. *Phys. Rev. B - Condens. Matter Mater. Phys.* **2003**, *68*, 075211. https://doi.org/10.1103/PhysRevB.68.075211.

(8) Baldo, M. A.; O'Brien, DF; You, Y. E. Al. Highly Efficient Phosphorescent Emission from Organic Electroluminescent Devices. *Nature* **1998**, *395*, 151–154. https://doi.org/10.1038/25954.

(9) Penfold, T. J.; Gindensperger, E.; Daniel, C.; Marian, C. M. Spin-Vibronic Mechanism for Intersystem Crossing. *Chem. Rev.* **2018**, *118*, 6975−7025.

(10) Davids, P. S.; Campbell, I. H.; Smith, D. L. Device Model for Single Carrier Organic Diodes. *J. Appl. Phys.* **1997**, *82*, 6319–6325. https://doi.org/10.1063/1.366522.

(11) Forrest, S. R.; O'Brien, D. F. Excitonic Singlet-Triplet Ratio in a Semiconducting Organic Thin Film. *Phys. Rev. B - Condens. Matter Mater. Phys.* **1999**, *60*, 14422–14428. https://doi.org/10.1103/PhysRevB.60.14422.

(12) Oyamada, T.; Sasabe, H.; Oku, Y.; Shimoji, N.; Adachi, C. Estimation of Carrier Recombination and Electroluminescence Emission Regions in Organic Light-Emitting Field-Effect Transistors Using Local Doping Method. *Appl. Phys. Lett.* **2006**, *88*, 093514. https://doi.org/10.1063/1.2181629.

(13) Ellis, A. M.; Feher, M.; Wright, T. G. *Electronic and Photoelectron Spectroscopy: Fundamentals and Case Studies*; Cambridge University Press: Cambridge, 2005.

(14) Harris, D. C.; Bertolucci, M. D. *Symmetry and Spectroscopy: An Introduction to Vibrational and Electronic Spectroscopy.*; DOVER PUBLICATIONS, INC.: New York, 1978.

(15) Will, P.; Reineke, S. *21 - Organic Light-Emitting Diodes*, 2nd ed.; Elsevier Ltd., 2019. https://doi.org/10.1016/B978-0-08-102284-9.00021-8.

(16) Reineke, S.; Thomschke, M.; Lüssem, B.; Leo, K. White Organic Light-Emitting Diodes: Status and Perspective. *Rev. Mod. Phys.* **2013**, *85*, 1245–1293. https://doi.org/10.1103/RevModPhys.85.1245.

(17) Adachi, C.; Baldo, M. A.; Thompson, M. E.; Forrest, S. R. Nearly 100% Internal Phosphorescence Efficiency in an Organic Light Emitting Device. *J. Appl. Phys.* **2001**, *90*, 5048–5051. https://doi.org/10.1063/1.1409582.

(18) Greenham, N. C.; Friend, R. H.; Bradley, D. D. C. Angular Dependence of the Emission from a Conjugated Polymer Light-Emitting Diode : Implications for Efficiency Calculations. *Adv. Mater.* **1994**, *6*, 491–494. https://doi.org/10.1201/b10862-5.

(19) Furno, M.; Meerheim, R.; Hofmann, S.; Lüssem, B.; Leo, K. Efficiency and Rate of Spontaneous Emission in Organic Electroluminescent Devices. *Phys. Rev. B* **2012**, *85*, 115205. https://doi.org/10.1103/PhysRevB.85.115205.

(20) https://en.wikipedia.org/wiki/NTSC.

(21) https://en.wikipedia.org/wiki/PAL.

(22) https://en.wikipedia.org/wiki/Rec._2020.

(23) Zhu, M.; Yang, C. Blue Fluorescent Emitters: Design Tactics and Applications in Organic Light-Emitting Diodes. *Chem. Soc. Rev.* **2013**, *42*, 4963–4976. https://doi.org/10.1039/c3cs35440g.

(24) Liu, H.; Cheng, G.; Hu, D.; Shen, F.; Lv, Y.; Sun, G.; Yang, B.; Lu, P.; Ma, Y. A Highly Efficient, Blue-Phosphorescent Device Based on a Wide-Bandgap Host/FIrpic: Rational Design of the Carbazole and Phosphine Oxide Moieties on Tetraphenylsilane. *Adv. Funct. Mater.* **2012**, *22*, 2830–2836. https://doi.org/10.1002/adfm.201103126.

(25) Ulbricht, C.; Beyer, B.; Friebe, C.; Winter, A.; Schubert, U. S. Recent Developments in the Application of Phosphorescent Iridium(III) Complex Systems. *Adv. Mater.* **2009**, *21*, 4418–4441. https://doi.org/10.1002/adma.200803537.

(26) Lee, J.; Chen, H. F.; Batagoda, T.; Coburn, C.; Djurovich, P. I.; Thompson, M. E.; Forrest, S. R. Deep Blue Phosphorescent Organic Light-Emitting Diodes with Very High Brightness and Efficiency. *Nat. Mater.* **2016**, *15*, 92–98. https://doi.org/10.1038/nmat4446.

(27) Kim, K. H.; Moon, C. K.; Lee, J. H.; Kim, S. Y.; Kim, J. J. Highly Efficient Organic Light-Emitting Diodes with Phosphorescent Emitters Having High Quantum Yield and Horizontal Orientation of Transition Dipole Moments. *Adv. Mater.* **2014**, *26*, 3844–3847. https://doi.org/10.1002/adma.201305733.

(28) Shin, H.; Ha, Y. H.; Kim, H. G.; Kim, R.; Kwon, S. K.; Kim, Y. H.; Kim, J. J. Controlling Horizontal Dipole Orientation and Emission Spectrum of Ir Complexes by Chemical Design of Ancillary Ligands for Efficient Deep-Blue Organic Light-Emitting Diodes. *Adv. Mater.* **2019**, *31*, 1–6. https://doi.org/10.1002/adma.201808102.

(29) Yang, X.; Guo, H.; Liu, B.; Zhao, J.; Zhou, G.; Wu, Z.; Wong, W. Y. Diarylboron-Based Asymmetric Red-Emitting Ir(III) Complex for Solution-Processed Phosphorescent

Organic Light-Emitting Diode with External Quantum Efficiency above 28%. *Adv. Sci.* **2018**, *5*, 1701067. https://doi.org/10.1002/advs.201701067.

(30) Scholz, S.; Kondakov, D.; Lüssem, B.; Leo, K. Degradation Mechanisms and Reactions in Organic Light-Emitting Devices. *Chem. Rev.* **2015**, *115*, 8449–8503. https://doi.org/10.1021/cr400704v.

(31) Sudheendran Swayamprabha, S.; Dubey, D. K.; Shahnawaz; Yadav, R. A. K.; Nagar, M. R.; Sharma, A.; Tung, F. C.; Jou, J. H. Approaches for Long Lifetime Organic Light Emitting Diodes. *Adv. Sci.* **2021**, *8*, 2002254. https://doi.org/10.1002/advs.202002254.

(32) Giebink, N. C.; D'Andrade, B. W.; Weaver, M. S.; MacKenzie, P. B.; Brown, J. J.; Thompson, M. E.; Forrest, S. R. Intrinsic Luminance Loss in Phosphorescent Small-Molecule Organic Light Emitting Devices Due to Bimolecular Annihilation Reactions. *J. Appl. Phys.* **2008**, *103*, 044509. https://doi.org/10.1063/1.2884530.

(33) Kondakov, D. Y. Triplet-Triplet Annihilation in Highly Efficient Fluorescent Organic Light-Emitting Diodes: Current State and Future Outlook. *Philos. Trans. R. Soc. A Math. Phys. Eng. Sci.* **2015**, *373*, 20140321. https://doi.org/10.1098/rsta.2014.0321.

(34) Manna, M. K.; Shokri, S.; Wiederrecht, G. P.; Gosztola, D. J.; Ayitou, A. J. L. New Perspectives for Triplet-Triplet Annihilation Based Photon Upconversion Using All-Organic Energy Donor & Acceptor Chromophores. *Chem. Commun.* **2018**, *54*, 5809–5818. https://doi.org/10.1039/c8cc01553h.

(35) Kondakov, D. Y. Characterization of Triplet-Triplet Annihilation in Organic Light-Emitting Diodes Based on Anthracene Derivatives. *J. Appl. Phys.* **2007**, *102*, 114504. https://doi.org/10.1063/1.2818362.

(36) Cao, C.; Yang, G. X.; Tan, J. H.; Shen, D.; Chen, W. C.; Chen, J. X.; Liang, J. L.; Zhu, Z. L.; Liu, S. H.; Tong, Q. X.; Lee, C. S. Deep-Blue High-Efficiency Triplet-Triplet Annihilation Organic Light-Emitting Diodes Using Donor- and Acceptor-Modified Anthracene Fluorescent Emitters. *Mater. Today Energy* **2021**, *21*, 100727. https://doi.org/10.1016/j.mtener.2021.100727.

(37) Suzuki, T.; Nonaka, Y.; Watabe, T.; Nakashima, H.; Seo, S.; Shitagaki, S.; Yamazaki, S. Highly Efficient Long-Life Blue Fluorescent Organic Light-Emitting Diode Exhibiting Triplet-Triplet Annihilation Effects Enhanced by a Novel Hole-Transporting Material. *Jpn. J. Appl. Phys.* **2014**, *53*, 052102. https://doi.org/10.7567/JJAP.53.052102.

(38) Ieuji, R.; Goushi, K.; Adachi, C. Triplet–Triplet Upconversion Enhanced by Spin–Orbit Coupling in Organic Light-Emitting Diodes. *Nat. Commun.* **2019**, *10*, 13044. https://doi.org/10.1038/s41467-019-13044-1.

(39) Hu, D.; Yao, L.; Yang, B.; Ma, Y. Reverse Intersystem Crossing from Upper Triplet Levels to Excited Singlet: A “hot Excition” Path for Organic Light-Emitting Diodes. *Philos. Trans. R. Soc. A Math. Phys. Eng. Sci.* **2015**, *373*, 20140318. https://doi.org/10.1098/rsta.2014.0318.

(40) Kasha, M. Characterization of Electronic Transitions in Complex Molecules. *Discuss. Faraday Soc.* **1950**, *9*, 14–19.

(41) Xu, Y.; Xu, P.; Hu, D.; Ma, Y. Recent Progress in Hot Exciton Materials for Organic Light-Emitting Diodes. *Chem. Soc. Rev.* **2021**, *50*, 1030–1069. https://doi.org/10.1039/d0cs00391c.

(42) Endo, A.; Sato, K.; Yoshimura, K.; Kai, T.; Kawada, A.; Miyazaki, H.; Adachi, C. Efficient Up-Conversion of Triplet Excitons into a Singlet State and Its Application for Organic Light Emitting Diodes. *Appl. Phys. Lett.* **2011**, *98*, 083302. https://doi.org/10.1063/1.3558906.

(43) Parker, C. A.; Hatchard, C. G. Triplet-Singlet Emission in Fluid Solutions. Phosphorescence of Eosin. *Trans. Faraday Soc.* **1961**, *57*, 1894–1904. https://doi.org/10.1039/TF9615701894.

(44) Wolf, M. W.; Legg, K. D.; Brown, R. E.; Singer, L. A.; Parks, J. H. Photophysical Studies on the Benzophenones. Prompt and Delayed Fluorescences and Self-Quenching. *J. Am. Chem. Soc.* **1975**, *97*, 4490–4497. https://doi.org/10.1021/ja00849a008.

(45) Itoh, T. Emission Spectrum of 9,10-Anthraquinone Vapor. *Spectrochim. Acta Part A Mol. Spectrosc.* **1986**, *42*, 1083–1084. https://doi.org/https://doi.org/10.1016/0584-8539(86)80023-X.

(46) Berberan-Santos, M. N.; Garcia, J. M. M. Unusually Strong Delayed Fluorescence of C70. *J. Am. Chem. Soc.* **1996**, *118*, 9391–9394. https://doi.org/10.1021/ja961782s.

(47) Yersin, H.; and Monkowius, U., DE 10 2008 033 563 A1. 2008.

(48) Endo, A.; Ogasawara, M.; Takahashi, A.; Yokoyama, D.; Kato, Y.; Adachi, C. Thermally Activated Delayed Fluorescence from Sn4+-Porphyrin Complexes and Their Application to Organic Light Emitting Diodes - A Novel Mechanism for Electroluminescence. *Adv. Mater.* **2009**, *21*, 4802–4806. https://doi.org/10.1002/adma.200900983.

(49) Deaton, J. C.; Switalski, S. C.; Kondakov, D. Y.; Young, R. H.; Pawlik, T. D.; Giesen, D. J.; Harkins, S. B.; Miller, A. J. M.; Mickenberg, S. F.; Peters, J. C. E-Type Delayed Fluorescence of a Phosphine-Supported Cu 2(μ-NAr_2)$_2$ Diamond Core: Harvesting Singlet and Triplet Excitons in OLEDs. *J. Am. Chem. Soc.* **2010**, *132*, 9499–9508. https://doi.org/10.1021/ja1004575.

(50) Uoyama, H.; Goushi, K.; Shizu, K.; Nomura, H.; Adachi, C. Highly Efficient Organic Light-Emitting Diodes from Delayed Fluorescence. *Nature* **2012**, *492*, 234–238.

(51) Cai, X.; Su, S. Marching Toward Highly Efficient, Pure-Blue, and Stable Thermally Activated Delayed Fluorescent Organic Light-Emitting Diodes. *Adv. Funct. Mater.* **2018**, *28*, 1802558. https://doi.org/10.1002/adfm.201802558.

(52) Ehrmaier, J.; Rabe, E. J.; Pristash, S. R.; Corp, K. L.; Schlenker, C. W.; Sobolewski, A. L.; Domcke, W. Singlet-Triplet Inversion in Heptazine and in Polymeric Carbon Nitrides. *J. Phys. Chem. A* **2019**, *123*, 8099–8108. https://doi.org/10.1021/acs.jpca.9b06215.

(53) De Silva, P. Inverted Singlet-Triplet Gaps and Their Relevance to Thermally Activated Delayed Fluorescence. *J. Phys. Chem. Lett.* **2019**, *10*, 5674–5679. https://doi.org/10.1021/acs.jpclett.9b02333.

(54) Tao, Y.; Yuan, K.; Chen, T.; Xu, P.; Li, H.; Chen, R.; Zheng, C.; Zhang, L.; Huang, W. Thermally Activated Delayed Fluorescence Materials towards the Breakthrough of Organoelectronics. *Adv. Mater.* **2014**, *26*, 7931–7958. https://doi.org/10.1002/adma.201402532.

(55) Cai, X.; Li, X.; Xie, G.; He, Z.; Gao, K.; Liu, K.; Chen, D.; Cao, Y.; Su, S. J. "rate-Limited Effect" of Reverse Intersystem Crossing Process: The Key for Tuning Thermally Activated Delayed Fluorescence Lifetime and Efficiency Roll-off of Organic Light Emitting Diodes. *Chem. Sci.* **2016**, *7*, 4264–4275. https://doi.org/10.1039/c6sc00542j.

(56) Hirata, S.; Sakai, Y.; Masui, K.; Tanaka, H.; Lee, S. Y.; Nomura, H.; Nakamura, N.; Yasumatsu, M.; Nakanotani, H.; Zhang, Q.; Shizu, K.; Miyazaki, H.; Adachi, C. Highly Efficient Blue Electroluminescence Based on Thermally Activated Delayed Fluorescence. *Nat. Mater.* **2015**, *14*, 330–336. https://doi.org/10.1038/nmat4154.

(57) Zhang, Q.; Li, B.; Huang, S.; Nomura, H.; Tanaka, H.; Adachi, C. Efficient Blue Organic Light-Emitting Diodes Employing Thermally Activated Delayed Fluorescence. *Nat. Photonics* **2014**, *8*, 326–332. https://doi.org/10.1038/nphoton.2014.12.

(58) Furue, R.; Matsuo, K.; Ashikari, Y.; Ooka, H.; Amanokura, N.; Yasuda, T. Highly Efficient Red–Orange Delayed Fluorescence Emitters Based on Strong π-Accepting Dibenzophenazine and Dibenzoquinoxaline Cores: Toward a Rational Pure-Red OLED Design. *Adv. Opt. Mater.* **2018**, *6*, 1701147. https://doi.org/10.1002/adom.201701147.

(59) Cui, L.; Gillett, A. J.; Zhang, S.; Ye, H.; Liu, Y.; Chen, X.; Lin, Z.; Evans, E. W.; Myers, W. K.; Ronson, T. K.; Nakanotani, H.; Reineke, S.; Bredas, J.; Adachi, C.; Friend, R. H.

Fast Spin-Flip Enables Efficient and Stable Organic Electroluminescence from Charge-Transfer States. *Nat. Photon.* **2020**, *14*, 636–642.

(60) Lee, J. H.; Chen, C. H.; Lee, P. H.; Lin, H. Y.; Leung, M. K.; Chiu, T. L.; Lin, C. F. Blue Organic Light-Emitting Diodes: Current Status, Challenges, and Future Outlook. *J. Mater. Chem. C* **2019**, *7*, 5874–5888. https://doi.org/10.1039/c9tc00204a.

(61) Albrecht, A. C. Vibronic-Spin-Orbit Perturbations and the Assignment of the Lowest Triplet State of Benzene. *J. Chem. Phys.* **1963**, *38*, 354–365. https://doi.org/10.1063/1.1733665.

(62) Robinson, G. W.; Frosch, R. P. Electronic Excitation Transfer and Relaxation. *J. Chem. Phys.* **1963**, *38*, 1187–1203. https://doi.org/10.1063/1.1733823.

(63) Lawetz, V.; Orlandi, G.; Siebrand, W. Theory of Intersystem Crossing in Aromatic Hydrocarbons. *J. Chem. Phys.* **1972**, *56*, 4058–4072. https://doi.org/10.1063/1.1677816.

(64) Schmidt, K.; Brovelli, S.; Coropceanu, V.; Beljonne, D.; Cornil, J.; Bazzini, C.; Caronna, T.; Tubino, R.; Meinardi, F.; Shuai, Z.; Brédas, J. L. Intersystem Crossing Processes in Nonplanar Aromatic Heterocyclic Molecules. *J. Phys. Chem. A* **2007**, *111*, 10490–10499. https://doi.org/10.1021/jp075248q.

(65) Zhao, Q.; Morrison, R. C.; Parr, R. G. From Electron Densities to Kohn-Sham Kinetic Energies, Orbital Energies, Exchange-Correlation Potentials, and Exchange-Correlation Energies. *Phys. Rev. A* **1994**, *50*, 2138–2142. https://doi.org/10.1103/PhysRevA.50.2138.

(66) Köhler, A.; Beljonne, D. The Singlet-Triplet Exchange Energy in Conjugated Polymers. *Adv. Funct. Mater.* **2004**, *14*, 11–18. https://doi.org/10.1002/adfm.200305032.

(67) Kresse, G.; Furthmüller, J. Efficient Iterative Schemes for Ab Initio Total-Energy Calculations Using a Plane-Wave Basis Set. *Phys. Rev. B* **1996**, *54*, 11169–11186. https://doi.org/10.1103/PhysRevB.54.11169.

(68) Tanaka, H.; Shizu, K.; Miyazaki, H.; Adachi, C. Efficient Green Thermally Activated Delayed Fluorescence (TADF) from a Phenoxazine–Triphenyltriazine (PXZ–TRZ) Derivative. *Chem. Commun.* **2012**, *48*, 11392–11394. https://doi.org/10.1039/c2cc36237f.

(69) Chen, D. Y.; Liu, W.; Zheng, C. J.; Wang, K.; Li, F.; Tao, S. L.; Ou, X. M.; Zhang, X. H. Isomeric Thermally Activated Delayed Fluorescence Emitters for Color Purity-Improved Emission in Organic Light-Emitting Devices. *ACS Appl. Mater. Interfaces* **2016**, *8*, 16791–16798. https://doi.org/10.1021/acsami.6b03954.

(70) Gibson, J.; Monkman, A.; Penfold, T. The Importance of Vibronic Coupling for Efficient Reverse Intersystem Crossing. *ChemPhysChem* **2016**, *17*, 2956–2961.

(71) M. A. El-Sayed. Spin–Orbit Coupling and the Radiationless Processes in Nitrogen. *J. Chem. Phys.* **1963**, *38*, 2834–2838.

(72) Tsai, W. L.; Huang, M. H.; Lee, W. K.; Hsu, Y. J.; Pan, K. C.; Huang, Y. H.; Ting, H. C.; Sarma, M.; Ho, Y. Y.; Hu, H. C.; Chen, C. C.; Lee, M. T.; Wong, K. T.; Wu, C. C. A Versatile Thermally Activated Delayed Fluorescence Emitter for Both Highly Efficient Doped and Non-Doped Organic Light Emitting Devices. *Chem. Commun.* **2015**, *51*, 13662–13665. https://doi.org/10.1039/c5cc05022g.

(73) Zhang, Q.; Li, J.; Shizu, K.; Huang, S.; Hirata, S.; Miyazaki, H.; Adachi, C. Design of E Ffi Cient Thermally Activated Delayed Fluorescence Materials for Pure Blue Organic Light Emitting Diodes. *J. Am. Chem. Soc.* **2012**, *134*, 14706–14709.

(74) Dias, F. B.; Bourdakos, K. N.; Jankus, V.; Moss, K. C.; Kamtekar, K. T.; Bhalla, V.; Santos, J.; Bryce, M. R.; Monkman, A. P. Triplet Harvesting with 100% Efficiency by Way of Thermally Activated Delayed Fluorescence in Charge Transfer OLED Emitters. *Adv. Mater.* **2013**, *25*, 3707–3714. https://doi.org/10.1002/adma.201300753.

(75) Ogiwara, T.; Wakikawa, Y.; Ikoma, T. Mechanism of Intersystem Crossing of Thermally Activated Delayed Fluorescence Molecules. *J. Phys. Chem. A* **2015**, *119*, 3415–3418. https://doi.org/10.1021/acs.jpca.5b02253.

(76) Chen, X. K.; Zhang, S. F.; Fan, J. X.; Ren, A. M. Nature of Highly Efficient Thermally Activated Delayed Fluorescence in Organic Light-Emitting Diode Emitters: Nonadiabatic Effect between Excited States. *J. Phys. Chem. C* **2015**, *119*, 9728–9733. https://doi.org/10.1021/acs.jpcc.5b00276.

(77) Marian, C. M. Mechanism of the Triplet-to-Singlet Upconversion in the Assistant Dopant ACRXTN. *J. Phys. Chem. C* **2016**, *120*, 3715–3721. https://doi.org/10.1021/acs.jpcc.6b00060.

(78) Gibson, J.; Monkman, A. P.; Penfold, T. J. The Importance of Vibronic Coupling for Efficient Reverse Intersystem Crossing in Thermally Activated Delayed Fluorescence Molecules. *ChemPhysChem* **2016**, *17*, 2956–2961. https://doi.org/10.1002/cphc.201600662.

(79) Tatchen, J.; Gilka, N.; Marian, C. M. Intersystem Crossing Driven by Vibronic Spin-Orbit Coupling: A Case Study on Psoralen. *Phys. Chem. Chem. Phys.* **2007**, *9*, 5209–5221. https://doi.org/10.1039/b706410a.

(80) Etinski, M.; Rai-Constapel, V.; Marian, C. M. Time-Dependent Approach to Spin-Vibronic Coupling: Implementation and Assessment. *J. Chem. Phys.* **2014**, *140*, 114104. https://doi.org/10.1063/1.4868484.

(81) Lobsiger, S.; Etinski, M.; Blaser, S.; Frey, H. M.; Marian, C.; Leutwyler, S. Intersystem Crossing Rates of S 1 State Keto-Amino Cytosine at Low Excess Energy. *J. Chem. Phys.* **2015**, *143*, 234301. https://doi.org/10.1063/1.4937375.

(82) Lee, D. R.; Kim, M.; Jeon, S. K.; Hwang, S. H.; Lee, C. W.; Lee, J. Y. Design Strategy for 25% External Quantum Efficiency in Green and Blue Thermally Activated Delayed Fluorescent Devices. *Adv. Mater.* **2015**, *27*, 5861–5867. https://doi.org/10.1002/adma.201502053.

(83) Mohanty, J.; Nau, W. M. Refractive index effects on the oscillator strength and radiative decay rate of 2,3-diazabicyclo[2.2.2]oct-2-ene. *Photochem. Photobiol. Sci.* **2004**, *3*, 1026–1031. https://doi.org/10.1039/B412936A.

(84) Hilborn, R. C. Einstein Coefficients, Cross Sections, f Values, Dipole Moments, and All That . *Am. J. Phys.* **1982**, *50*, 982–986. https://doi.org/10.1119/1.12937.

(85) Shizu, K.; Tanaka, H.; Uejima, M.; Sato, T.; Tanaka, K.; Kaji, H.; Adachi, C. Strategy for Designing Electron Donors for Thermally Activated Delayed Fluorescence Emitters. *J. Phys. Chem. C* **2015**, *119*, 1291–1297. https://doi.org/10.1021/jp511061t.

(86) Manzhos, S.; Segawa, H.; Yamashita, K. Derivative Coupling Constants of NK1, NK7 Dyes and Their Relation to Excited State Dynamics in Solar Cell Applications. *Chem. Phys. Lett.* **2011**, *501*, 580–586. https://doi.org/10.1016/j.cplett.2010.11.049.

(87) Liang, X.; Tu, Z. L.; Zheng, Y. X. Thermally Activated Delayed Fluorescence Materials: Towards Realization of High Efficiency through Strategic Small Molecular Design. *Chem. - A Eur. J.* **2019**, *25*, 5623–5642. https://doi.org/10.1002/chem.201805952.

(88) Etherington, M. K.; Gibson, J.; Higginbotham, H. F.; Penfold, T. J.; Monkman, A. P. Revealing the Spin-Vibronic Coupling Mechanism of Thermally Activated Delayed Fluorescence. *Nat. Commun.* **2016**, *7*, 13680.

(89) Zhang, D.; Cai, M.; Zhang, Y.; Zhang, D.; Duan, L. Sterically Shielded Blue Thermally Activated Delayed Fluorescence Emitters with Improved Efficiency and Stability. *Mater. Horizons* **2016**, *3*, 145–151. https://doi.org/10.1039/c5mh00258c.

(90) Hosokai, T.; Matsuzaki, H.; Nakanotani, H.; Tokumaru, K.; Tsutsui, T.; Furube, A.; Nasu, K.; Nomura, H.; Yahiro, M.; Adachi, C. Evidence and Mechanism of Efficient Thermally Activated Delayed Fluorescence Promoted By Delocalized Excited States. *Sci. Adv.* **2017**, *3*, 1603282.

(91) Ritchie, J.; Crayston, J. A.; Markham, J. P. J.; Samuel, I. D. W. Effect of Meta-Linkages on the Photoluminescence and Electroluminescence Properties of Light-Emitting Polyfluorene Alternating Copolymers. *J. Mater. Chem.* **2006**, *16*, 1651. https://doi.org/10.1039/b517672g.

(92) Ahn, T.; Min, S. J.; Shim, H. K.; Hwang, D. H.; Zyung, T. Blue Electroluminescent Polymers: Control of Conjugation Length by Kink Linkages and Substituents in the Poly(p-Phenylenevinylene)-Related Copolymers. *Macromolecules* **1999**, *32*, 3279–3285. https://doi.org/10.1021/ma981864w.

(93) Cui, L. S.; Nomura, H.; Geng, Y.; Kim, J. U. k.; Nakanotani, H.; Adachi, C. Controlling Singlet–Triplet Energy Splitting for Deep-Blue Thermally Activated Delayed Fluorescence Emitters. *Angew. Chemie - Int. Ed.* **2017**, *56*, 1571–1575. https://doi.org/10.1002/anie.201609459.

(94) Zhang, Q.; Li, B.; Huang, S.; Nomura, H.; Tanaka, H.; Adachi, C. Efficient Blue Organic Light-Emitting Diodes Employing Thermally Activated Delayed Fluorescence. *Nat. Photonics* **2014**, *8*, 326–332. https://doi.org/10.1038/nphoton.2014.12.

(95) Park, I. S.; Lee, J.; Yasuda, T. High-Performance Blue Organic Light-Emitting Diodes with 20% External Electroluminescence Quantum Efficiency Based on Pyrimidine-Containing Thermally Activated Delayed Fluorescence Emitters. *J. Mater. Chem. C* **2016**, *4*, 7911–7916. https://doi.org/10.1039/c6tc02027e.

(96) Wu, S.; Aonuma, M.; Zhang, Q.; Huang, S.; Nakagawa, T.; Kuwabara, K.; Adachi, C. High-Efficiency Deep-Blue Organic Light-Emitting Diodes Based on a Thermally Activated Delayed Fluorescence Emitter. *J. Mater. Chem. C* **2014**, *2*, 421–424. https://doi.org/10.1039/c3tc31936a.

(97) Noda, H.; Nakanotani, H.; Adachi, C. Excited State Engineering for Efficient Reverse Intersystem Crossing. *Sci. Adv.* **2018**, *4*, eaao6910.

(98) Kim, J. U.; Park, I. S.; Chan, C.; Tanaka, M.; Nakanotani, H.; Adachi, C. Nanosecond-Time-Scale Delayed Fluorescence Molecule for Deep-Blue OLEDs with Small Efficiency Rolloff. *Nat. Commun.* **2020**, *11*, 1765. https://doi.org/10.1038/s41467-020-15558-5.

(99) Sun, J. W.; Baek, J. Y.; Kim, K. H.; Moon, C. K.; Lee, J. H.; Kwon, S. K.; Kim, Y. H.; Kim, J. J. Thermally Activated Delayed Fluorescence from Azasiline Based Intramolecular Charge-Transfer Emitter (DTPDDA) and a Highly Efficient Blue Light Emitting Diode. *Chem. Mater.* **2015**, *27*, 6675–6681. https://doi.org/10.1021/acs.chemmater.5b02515.

(100) Li, B.; Li, Z.; Hu, T.; Zhang, Y.; Wang, Y.; Yi, Y.; Guo, F.; Zhao, L. Highly Efficient Blue Organic Light-Emitting Diodes from Pyrimidine-Based Thermally Activated Delayed Fluorescence Emitters. *J. Mater. Chem. C* **2018**, *6*, 2351–2359. https://doi.org/10.1039/C7TC05746F.

(101) Zhang, Q.; Li, J.; Shizu, K.; Huang, S.; Hirata, S.; Miyazaki, H.; Adachi, C. Design of E Ffi Cient Thermally Activated Delayed Fluorescence Materials for Pure Blue Organic Light Emitting Diodes. *J. Am. Chem. Soc.* **2012**, *134*, 14706–14716.

(102) Rajamalli, P.; Senthilkumar, N.; Huang, P. Y.; Ren-Wu, C. C.; Lin, H. W.; Cheng, C. H. New Molecular Design Concurrently Providing Superior Pure Blue, Thermally Activated Delayed Fluorescence and Optical Out-Coupling Efficiencies. *J. Am. Chem. Soc.* **2017**, *139*, 10948–10951. https://doi.org/10.1021/jacs.7b03848.

(103) Lee, Y. H.; Park, S.; Oh, J.; Shin, J. W.; Jung, J.; Yoo, S.; Lee, M. H. Rigidity-Induced Delayed Fluorescence by Ortho Donor-Appended Triarylboron Compounds: Record-High Efficiency in Pure Blue Fluorescent Organic Light-Emitting Diodes. *ACS Appl. Mater. Interfaces* **2017**, *9*, 24035–24042. https://doi.org/10.1021/acsami.7b05615.

(104) Lee, Y. H.; Park, S.; Oh, J.; Woo, S. J.; Kumar, A.; Kim, J. J.; Jung, J.; Yoo, S.; Lee, M. H. High-Efficiency Sky Blue to Ultradeep Blue Thermally Activated Delayed Fluorescent Diodes Based on Ortho-Carbazole-Appended Triarylboron Emitters: Above 32% External Quantum Efficiency in Blue Devices. *Adv. Opt. Mater.* **2018**, *6*, 1800385. https://doi.org/10.1002/adom.201800385.

(105) Liang, X.; Yan, Z. P.; Han, H. B.; Wu, Z. G.; Zheng, Y. X.; Meng, H.; Zuo, J. L.; Huang, W. Peripheral Amplification of Multi-Resonance Induced Thermally Activated Delayed Fluorescence for Highly Efficient OLEDs. *Angew. Chemie - Int. Ed.* **2018**, *57*, 11316–11320. https://doi.org/10.1002/anie.201806323.

(106) Kondo, Y.; Yoshiura, K.; Kitera, S.; Nishi, H.; Oda, S.; Gotoh, H.; Sasada, Y.; Yanai, M.; Hatakeyama, T. Narrowband Deep-Blue Organic Light-Emitting Diode Featuring an

Organoboron-Based Emitter. *Nat. Photonics* **2019**, *13*, 678–682. https://doi.org/10.1038/s41566-019-0476-5.

(107) Cho, Y. J.; Jeon, S. K.; Chin, B. D.; Yu, E.; Lee, J. Y. The Design of Dual Emitting Cores for Green Thermally Activated Delayed Fluorescent Materials. *Angew. Chemie - Int. Ed.* **2015**, *54*, 5201–5204. https://doi.org/10.1002/anie.201412107.

(108) Kim, M.; Jeon, S. K.; Hwang, S.-H.; Lee, S.; Yu, E.; Lee, J. Y. Highly Efficient and Color Tunable Thermally Activated Delayed Fluorescent Emitters Using a "Twin Emitter" Molecular Design. *Chem. Commun.* **2016**, *52*, 339–342. https://doi.org/10.1039/C5CC07999C.

(109) Cho, Y. J.; Jeon, S. K.; Lee, S. S.; Yu, E.; Lee, J. Y. Donor Interlocked Molecular Design for Fluorescence-like Narrow Emission in Deep Blue Thermally Activated Delayed Fluorescent Emitters. *Chem. Mater.* **2016**, *28*, 5400–5405. https://doi.org/10.1021/acs.chemmater.6b01484.

(110) Noda, H.; Chen, X. K.; Nakanotani, H.; Hosokai, T.; Miyajima, M.; Notsuka, N.; Kashima, Y.; Brédas, J. L.; Adachi, C. Critical Role of Intermediate Electronic States for Spin-Flip Processes in Charge-Transfer-Type Organic Molecules with Multiple Donors and Acceptors. *Nat. Mater.* **2019**, *18*, 1084–1090. https://doi.org/10.1038/s41563-019-0465-6.

(111) Chan, C.; Cui, L.; Kim, J. U.; Nakanotani, H.; Adachi, C. Rational Molecular Design for Deep-Blue Thermally Activated Delayed Fluorescence Emitters. *Adv. Funct. Mater.* **2018**, *28*, 1706023. https://doi.org/10.1002/adfm.201706023.

(112) Zhang, D.; Song, X.; Gillett, A. J.; Drummond, B. H.; Jones, S. T. E.; Li, G.; He, H.; Cai, M.; Credgington, D.; Duan, L. Efficient and Stable Deep-Blue Fluorescent Organic Light-Emitting Diodes Employing a Sensitizer with Fast Triplet Upconversion. *Adv. Mater.* **2020**, *32*, 1908355. https://doi.org/10.1002/adma.201908355.

(113) Chen, X. K.; Bakr, B. W.; Auffray, M.; Tsuchiya, Y.; Sherrill, C. D.; Adachi, C.; Bredas, J. L. Intramolecular Noncovalent Interactions Facilitate Thermally Activated Delayed Fluorescence (TADF). *J. Phys. Chem. Lett.* **2019**, *10*, 3260–3268. https://doi.org/10.1021/acs.jpclett.9b01220.

(114) Chen, Z.; Ni, F.; Wu, Z.; Hou, Y.; Zhong, C.; Huang, M.; Xie, G.; Ma, D.; Yang, C. Enhancing Spin-Orbit Coupling by Introducing a Lone Pair Electron with p Orbital Character in a Thermally Activated Delayed Fluorescence Emitter: Photophysics and Devices. *J. Phys. Chem. Lett.* **2019**, *10*, 2669–2675. https://doi.org/10.1021/acs.jpclett.9b00937.

(115) Park, I. S.; Matsuo, K.; Aizawa, N.; Yasuda, T. High-Performance Dibenzoheteraborin-Based Thermally Activated Delayed Fluorescence Emitters: Molecular Architectonics for Concurrently Achieving Narrowband Emission and Efficient Triplet–Singlet Spin Conversion. *Adv. Funct. Mater.* **2018**, *28*, 1802031. https://doi.org/10.1002/adfm.201802031.

(116) Matsuo, K.; Yasuda, T. Blue Thermally Activated Delayed Fluorescence Emitters Incorporating Acridan Analogues with Heavy Group 14 Elements for High-Efficiency Doped

and Non-Doped OLEDs. *Chem. Sci.* **2019**, *10*, 10687–10697. https://doi.org/10.1039/c9sc04492b.

(117) Hong, K.; Lee, J. L. Review Paper: Recent Developments in Light Extraction Technologies of Organic Light Emitting Diodes. *Electron. Mater. Lett.* **2011**, *7*, 77–91. https://doi.org/10.1007/s13391-011-0601-1.

(118) Tenopala-Carmona, F.; Lee, O. S.; Crovini, E.; Neferu, A. M.; Murawski, C.; Olivier, Y.; Zysman-colman, E.; Gather, M. C. Identification of the Key Parameters for Horizontal Transition Dipole Orientation in Fluorescent and TADF Organic Light-Emitting Diodes. *Adv. Mater.* **2021**, *33*, 2100677. https://doi.org/10.1002/adma.202100677.

(119) Lin, T. A.; Chatterjee, T.; Tsai, W. L.; Lee, W. K.; Wu, M. J.; Jiao, M.; Pan, K. C.; Yi, C. L.; Chung, C. L.; Wong, K. T.; Wu, C. C. Sky-Blue Organic Light Emitting Diode with 37% External Quantum Efficiency Using Thermally Activated Delayed Fluorescence from Spiroacridine-Triazine Hybrid. *Adv. Mater.* **2016**, *28*, 6976–6983. https://doi.org/10.1002/adma.201601675.

(120) Liu, M.; Komatsu, R.; Cai, X.; Hotta, K.; Sato, S.; Liu, K.; Chen, D.; Kato, Y.; Sasabe, H.; Ohisa, S.; Suzuri, Y.; Yokoyama, D.; Su, S. J.; Kido, J. Horizontally Orientated Sticklike Emitters: Enhancement of Intrinsic Out-Coupling Factor and Electroluminescence Performance. *Chem. Mater.* **2017**, *29*, 8630–8636. https://doi.org/10.1021/acs.chemmater.7b02403.

(121) Tsujimoto, H.; Ha, D. G.; Markopoulos, G.; Chae, H. S.; Baldo, M. A.; Swager, T. M. Thermally Activated Delayed Fluorescence and Aggregation Induced Emission with Through-

Space Charge Transfer. *J. Am. Chem. Soc.* **2017**, *139*, 4894–4900. https://doi.org/10.1021/jacs.7b00873.

(122) Chen, X. L.; Jia, J. H.; Yu, R.; Liao, J. Z.; Yang, M. X.; Lu, C. Z. Combining Charge-Transfer Pathways to Achieve Unique Thermally Activated Delayed Fluorescence Emitters for High-Performance Solution-Processed, Non-Doped Blue OLEDs. *Angew. Chemie - Int. Ed.* **2017**, *56*, 15006–15009. https://doi.org/10.1002/anie.201709125.

(123) Wada, Y.; Nakagawa, H.; Matsumoto, S.; Wakisaka, Y.; Kaji, H. Organic Light Emitters Exhibiting Very Fast Reverse Intersystem Crossing. *Nat. Photonics* **2020**, *14*, 643–649. https://doi.org/10.1038/s41566-020-0667-0.

(124) Hatakeyama, T.; Shiren, K.; Nakajima, K.; Nomura, S.; Nakatsuka, S.; Kinoshita, K.; Ni, J.; Ono, Y.; Ikuta, T. Ultrapure Blue Thermally Activated Delayed Fluorescence Molecules: Efficient HOMO-LUMO Separation by the Multiple Resonance Effect. *Adv. Mater.* **2016**, *28*, 2777–2781. https://doi.org/10.1002/adma.201505491.

(125) Yuan, Y.; Tang, X.; Du, X. Y.; Hu, Y.; Yu, Y. J.; Jiang, Z. Q.; Liao, L. S.; Lee, S. T. The Design of Fused Amine/Carbonyl System for Efficient Thermally Activated Delayed Fluorescence: Novel Multiple Resonance Core and Electron Acceptor. *Adv. Opt. Mater.* **2019**, *7*, 1801536. https://doi.org/10.1002/adom.201801536.

(126) Hall, D.; Suresh, S. M.; dos Santos, P. L.; Duda, E.; Bagnich, S.; Pershin, A.; Rajamalli, P.; Cordes, D. B.; Slawin, A. M. Z.; Beljonne, D.; Köhler, A.; Samuel, I. D. W.; Olivier, Y.; Zysman-Colman, E. Improving Processability and Efficiency of Resonant TADF

Emitters: A Design Strategy. *Adv. Opt. Mater.* **2020**, *8*, 1901627. https://doi.org/10.1002/adom.201901627.

(127) Sarma, M.; Wong, K.-T. Exciplex: An Intermolecular Charge-Transfer Approach for TADF. *ACS Appl. Mater. Interfaces* **2018**, *10*, 19279–19304. https://doi.org/10.1021/acsami.7b18318.

(128) Nakagawa, T.; Ku, S. Y.; Wong, K. T.; Adachi, C. Electroluminescence Based on Thermally Activated Delayed Fluorescence Generated by a Spirobifluorene Donor–Acceptor Structure. *Chem. Commun.* **2012**, *48*, 9580–9582. https://doi.org/10.1039/c2cc31468a.

(129) Méhes, G.; Nomura, H.; Zhang, Q.; Nakagawa, T.; Adachi, C. Enhanced Electroluminescence Efficiency in a Spiro-Acridine Derivative through Thermally Activated Delayed Fluorescence. *Angew. Chemie - Int. Ed.* **2012**, *51*, 11311–11315. https://doi.org/10.1002/anie.201206289.

(130) Nasu, K.; Nakagawa, T.; Nomura, H.; Lin, C.-J.; Cheng, C.-H.; Tseng, M.-R.; Yasuda, T.; Adachi, C. A Highly Luminescent Spiro-Anthracenone-Based Organic Light-Emitting Diode Exhibiting Thermally Activated Delayed Fluorescence. *Chem. Commun.* **2013**, *49*, 10385. https://doi.org/10.1039/c3cc44179b.

(131) Ohkuma, H.; Nakagawa, T.; Shizu, K.; Yasuda, T.; Adachi, C. Thermally Activated Delayed Fluorescence from a Spiro-Diazafluorene Derivative. *Chem. Lett.* **2014**, *43*, 1017–1019. https://doi.org/10.1246/cl.140360.

(132) Wang, Y. K.; Wu, S. F.; Yuan, Y.; Li, S. H.; Fung, M. K.; Liao, L. S.; Jiang, Z. Q. Donor-σ-Acceptor Molecules for Green Thermally Activated Delayed Fluorescence by Spatially Approaching Spiro Conformation. *Org. Lett.* **2017**, *19*, 3155–3158. https://doi.org/10.1021/acs.orglett.7b01281.

(133) Rao, J.; Zhao, C.; Wang, Y.; Bai, K.; Wang, S.; Ding, J.; Wang, L. Achieving Deep-Blue Thermally Activated Delayed Fluorescence in Nondoped Organic Light-Emitting Diodes through a Spiro-Blocking Strategy. *ACS Omega* **2019**, *4*, 1861–1867. https://doi.org/10.1021/acsomega.8b03296.

Chapter 2

Multichromophore Molecular Design for Efficient Thermally Activated Delayed Fluorescence Emitters with Near-Unity Photoluminescence Quantum Yields

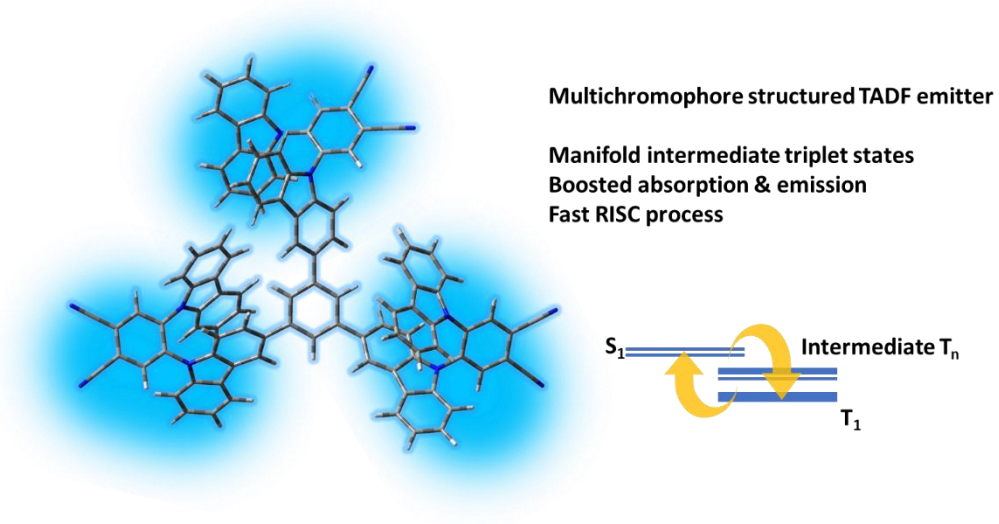

The work presented in this Chapter has been published in the Journal of Organic Chemistry,

Dongyang Chen,[a] Yu Kusakabe,[b] Yongxia Ren,[b] Dianming Sun,[a] Pachaiyappan Rajamalli,[a] Yoshimasa Wada,[b] Katsuaki Suzuki,[b] Hironori Kaji,[b]* and Eli Zysman-Colman[a]* Multichromophore Molecular Design for Efficient Thermally Activated Delayed Fluorescence Emitters with Near-Unity Photoluminescence Quantum Yields. *J. Org. Chem.*, **2021**, *86*, 11531–11544. DOI: doi.org/10.1021/acs.joc.1c01101.

Collaborators in this Chapter are from:

[a] Organic Semiconductor Centre, EaStCHEM School of Chemistry, University of St Andrews, St Andrews, Fife KY16 9ST, UK

[b] Institute for Chemical Research, Kyoto University, Uji, Kyoto 611-0011, Japan

Yu Kusakabe, Yongxia Ren, and Yoshimasa Wada from Kyoto University carried out the kinetics study of the emitters in host materials and the device fabrication. Dr. Dianming Sun, and Dr. Pachaiyappan Rajamalli also contributed to the preliminary device fabrication.

I completed all the synthesis and characterization, DFT and TD-DFT calculations, electrochemistry, photophysics in solutions and PMMA films, and I am the principal author of the manuscript.

2.1 Introduction

As discussed in **Chapter 1**, a small exchange integral between FMOs is required for TADF mechanism, which is frequently obtained by separating and/or electronically decoupling the donor and acceptor fragments.[1–4] However, the limited overlap between the HOMO and LUMO also leads to a low *f*, resulting in an inefficient radiative decay from S_1 to S_0, which is detrimental for TADF emitters to achieve high Φ_{PL}.[5,6] Tremendous efforts have been devoted to designing molecules that can achieve simultaneously small ΔE_{ST} and high Φ_{PL}.[7–10]

The Φ_{PL} of TADF molecules can be increased by intensifying light absorption, which can occur by incorporating two luminophores into one emitter molecule.[11,12] Lee *et al.* firstly explored a dual emitting core design where two TADF luminophores were directly connected via a single bond.[11–13] The blue TADF emitter, 4,6-di(carbazol-9-yl)isophthalonitrile (**DCzIPN**) was utilized as the luminophore and dual cores emitters, named **DDCzIPN**, **33TCzPN**, **34TCzPN**, and **44TCzPN** were obtained by connecting two **DCzIPN** molecules at different positions (Figure **2.1**).[11,12] The common feature of these emitters is that ΔE_{ST} remains largely unaffected but the Φ_{PL} increases.[11,12] As a result, the EQE_{max} of the OLEDs improved from 16.4% for **DCzIPN** to 18.9% (**DDCzIPN**), 17.4% (**33TCzPN**), 20.5% (**34TCzPN**), and 19.5% (**44TCzPN**).[11,12] Deep blue emission with narrowed FWHM was also achieved in **CzBPCN**, which contains dual TADF cores.[13] The carbazoles from the dual cores form an interlocked structure to suppress the rotation of the central biphenyl ring. The molecule exhibited deep blue emission with λ_{PL} at 453 nm and Φ_{PL} of 76% in toluene.[13] The OLED showed an EQE_{max} of 14.0% with a narrow FWHM of 48 nm leading to deep blue emission with CIE coordinates of (0.14, 0.12).[13] This dual emitting strategy was adopted

by other groups towards high-efficiency TADF emitter design. Yang *et al*. reported two TADF emitters bearing dual emitting cores **2,2′-DPXZ-PN** and **3,3′-DPXZ-PN**.[14] Compared to the mono emitter **PXZ-PN**, **2,2′-DPXZ-PN** and **3,3′-DPXZ-PN** showed increased molar absorptivity coefficients in toluene for the charge transfer (CT) state and the Φ_{PL} values also increased from 49% of **PXZ-CN** to 67% and 82%, respectively, for **2,2′-DPXZ-PN** and **3,3′-DPXZ-PN** in 10 wt% doped 4,4′-bis(N-carbazolyl)-1,1′-biphenyl (CBP) films.[14] As a result, the devices with **2,2′-DPXZ-PN** and **3,3′-DPXZ-PN** showed respective EQE_{max} of 13% and 15%, together with small efficiency roll-off (12% and 14% at 1000 cd m^{-2}, respectively).[14] These examples demonstrate that the multiple emitting cores design is an effective approach to improve molecular photophysics and electroluminescence properties.[13–17]

Recently, the presence of intermediate triplet states lying between T_1 and S_1 have been shown to facilitate RISC and render TADF more efficient by opening a reverse internal conversion (RIC) pathway that is mediated by spin-vibronic coupling between T_1 and one or more of the intermediate states, followed by RISC.[10,18,19] This situation typically occurs when there are multiple donors about a single acceptor as exists in the molecules **5CzBN** and **5CzTRZ**. The presence of multiple donors, each possessing slightly different conformations, and thereby presenting slightly different electronic coupling with the central acceptor guarantees a dense population of excited states.[10,18] We expect molecule with more than one emitting core can also possess dense intermediate triplet states as the conformational variation of each of the emitting cores can result in different degrees of electronic coupling, thus improve the RISC process.

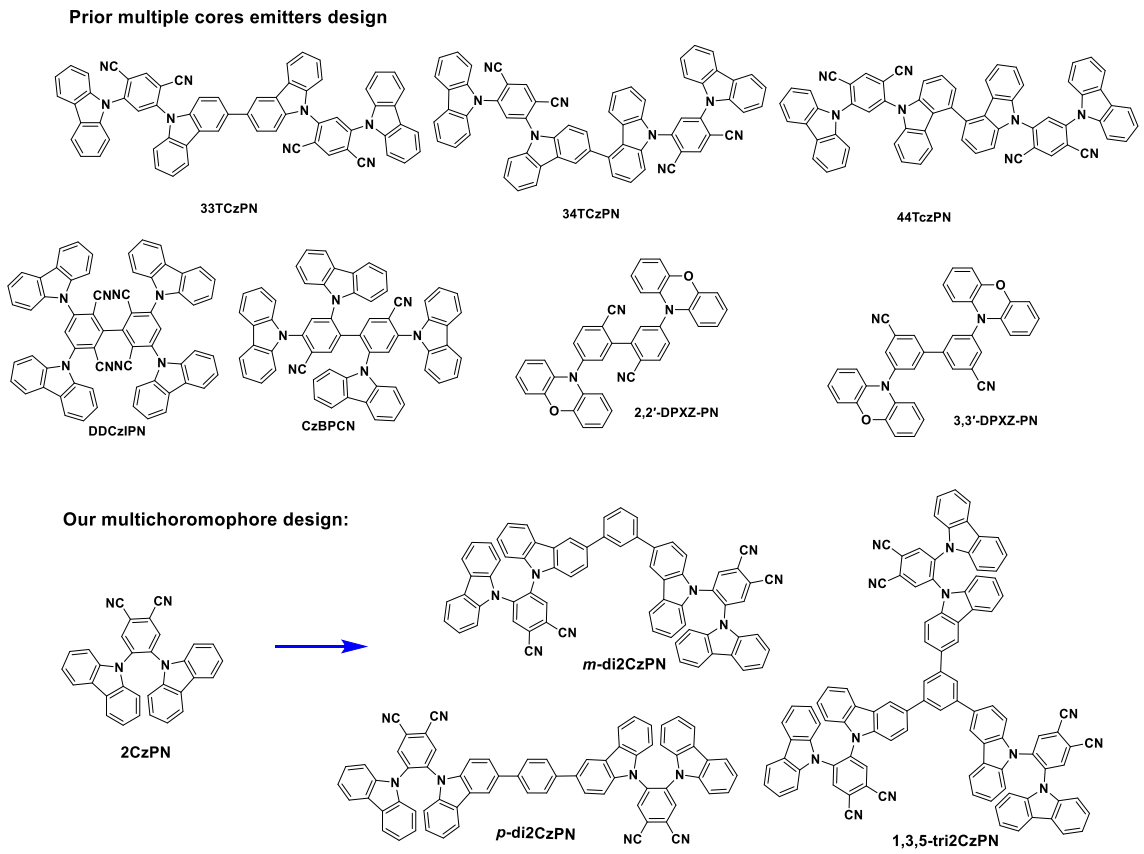

Figure **2.1.** Multichoromophore molecular structures discussed in this Chapter.

In this Chapter, we connect **2CzPN** (Figure **2.1**) to a central benzene ring to construct dual and treble core TADF emitters and these emitters achieved both high Φ_{PL} and small ΔE_{ST}. The different connecting positions to a central benzene ring, namely 1,4 positions, 1,3 positions and 1,3,5 positions, offering three multichoromphore emitters: ***p*-di2CzPN**, ***m*-di2CzPN** and **1,3,5-tri2CzPN**, respectively. The TDA-DFT calculations show that the three emitters possess smaller ΔE_{ST}, higher *f*, and an increased density of intermediate triplet states between S_1 and T_1 than for **2CzPN**. Three highly soluble emitters all exhibited near quantitative Φ_{PL} in toluene. High Φ_{PL}s were also achieved in doped films, 59% and 70% for ***p*-di2CzPN** and ***m*-di2CzPN** in 10 wt%

DPEPO doped films, respectively, and 54% for **1,3,5-tri2CzPN** in 20 wt% doped CBP film. The k_{RISC} for ***p*-di2CzPN** and ***m*-di2CzPN** in DPEPO films reached 1.1×10^5 s^{-1} and 0.7×10^5 s^{-1}, respectively, and k_{RISC} for **1,3,5-tri2CzPN** in CBP film reached 1.7×10^5 s^{-1}. A solution-processed organic light-emitting diode based on **1,3,5-tri2CzPN** exhibited a sky-blue emission with CIE coordinate of (0.22, 0.44), and achieved an EQE_{max} of 7.1%.

2.2 Synthesis

Three multi-donor structures were synthesized first. Carbazole was regioselectively brominated using NBS in acetonitrile (MeCN),[20] and then the carbazole reacted with chlorotriisopropylsilane (TIPSCl) assisted by sodium hydride in THF to obtain its *N*-tri*iso*propylsilyl ether, **3-BrTIPSCz**.[21] **3-BrTIPSCz** was converted to **3-BpinTIPSCz** under palladium-catalysed Miyaura borylation conditions.[22,23] This intermediate was then reacted with 1,4-dibromobenzene, 1,3-dibromobenzene or 1,3,5-tribromobenzene under Suzuki-Miyaura coupling conditions.[23] The crude products reacted with tetrabutylammonium fluoride (TBAF) in THF solution via nucleophilic substitution mechanism to afford, respectively, **para-2Cz**, **meta-2Cz** and **tri-3Cz** in moderate yield (~ 55%).

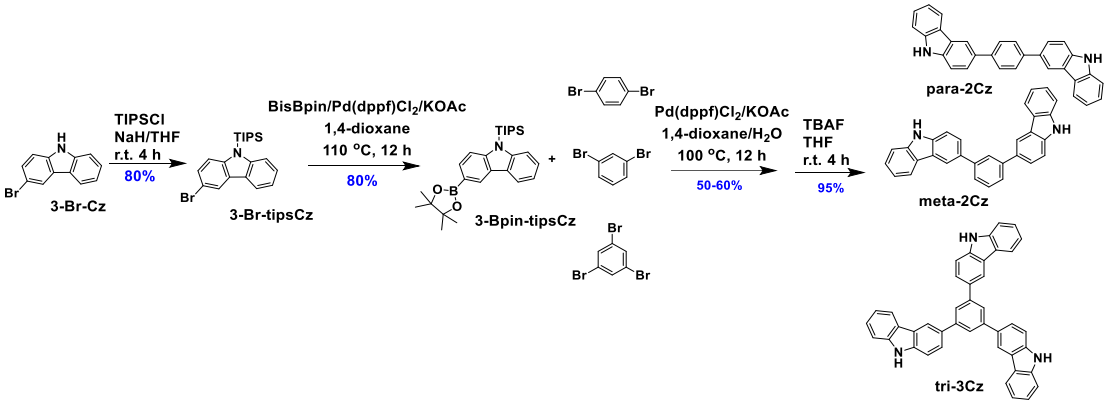

Scheme 2.1. synthesis of multi-carbazole precursors.

CzFPN was synthesized by an S_NAr reaction between carbazole and 4,5-difluorophthalonitrile assisted by NaH in THF in good yield (80%). The three multichromophore emitters ***p*-di2CzPN, *m*-di2CzPN** and **1,3,5-tri2CzPN** were obtained in good yield (~55%) from the S_NAr reaction of **CzFPN** with **para-2Cz, meta-2Cz** or **tri-3Cz**. The identity and purity of the three emitters were verified by a combination of melting point, determination ^1H NMR, ^{13}C NMR, HRMS, elemental analysis and HPLC analysis. Detailed synthesis and compounds characterization are listed in **2.8 Experimental section**.

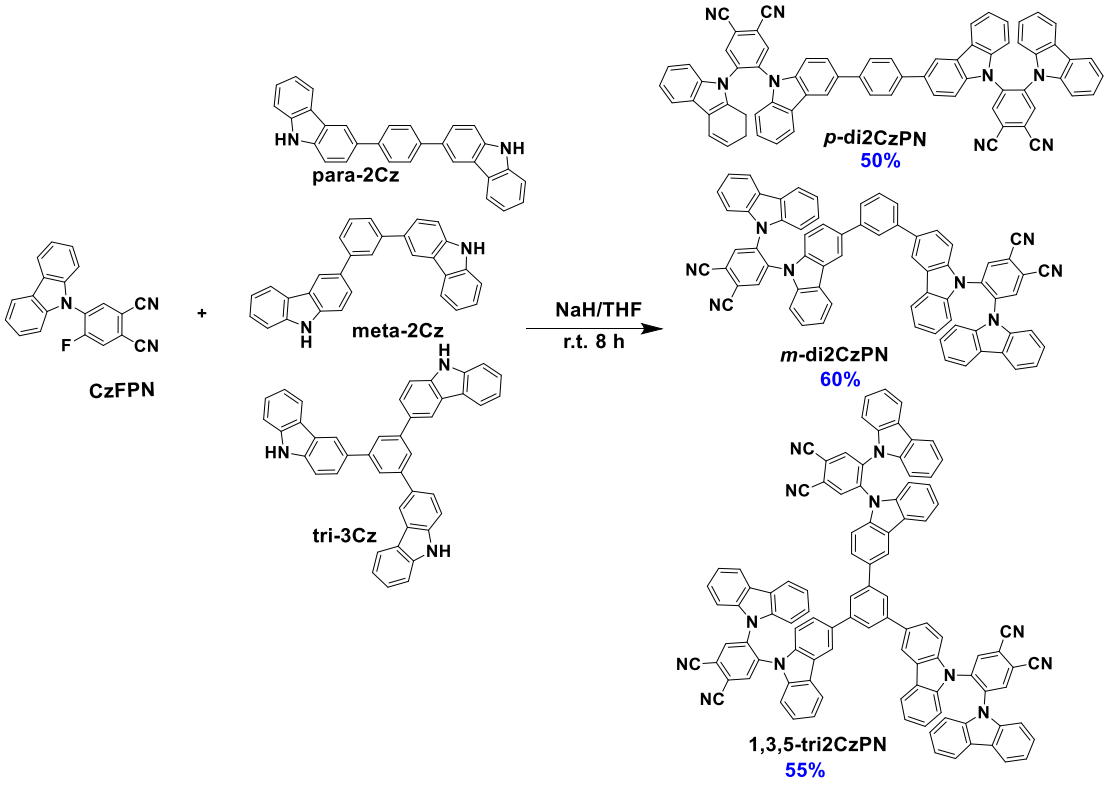

Scheme **2.2**. Synthesis of multichromophore emitters.

2.3 Theoretical calculations

To gain insight into their optoelectronic properties, we performed DFT calculations and TD- DFT calculations using the Tamm-Dancoff approximation (TDA-DFT) calculations on ***p*-di2CzPN, *m*-di2CzPN, 1,3,5-tri2CzPN** and the reference compound, **2CzPN**.[24] The ground state, singlet and triplet excited state geometries were calculated in the gas phase using PBE0/6-31g(d, p).[25,26] As shown in Figure **2.2**, the HOMO of **2CzPN** is localized on the two carbazoles and the central benzene while the LUMO is localized on the phthalonitrile moiety. For the multichoromophore emitters, due to the extended conjugation, the HOMOs are delocalized across

the carbazole-phenyl-carbazole motif and the LUMOs are located on the phthalonitrile moieties. The small overlap between HOMO and LUMO ensures that the three emitters possess small ΔE_{ST} values. Due to the extended conjugation of the linked carbazole moieties, the HOMOs of ***p*-di2CzPN, *m*-di2CzPN,** and **1,3,5-tri2CzPN** are destabilized by 0.24 eV, 0.07 eV, and 0.02 eV, respectively, compared to **2CzPN**, and the LUMOs are stabilized by 0.09 eV, 0.14 eV, and 0.21 eV, respectively, compared to **2CzPN**. As a result, the HOMO-LUMO gap (ΔE_g) of ***p*-di2CzPN, *m*-di2CzPN,** and **1,3,5-tri2CzPN** are reduced to 3.38 eV, 3.50 eV, and 3.49 eV, respectively, compared to 3.71 eV of **2CzPN**. TDA-DFT calculations indicate that the energies of the S_1 state of the three emitters are stabilized by 0.18 eV, 0.15 eV, and 0.10 eV compared to **2CzPN** while there is only a modest change in the energies of the T_1 state, thereby leading to smaller ΔE_{ST} values.

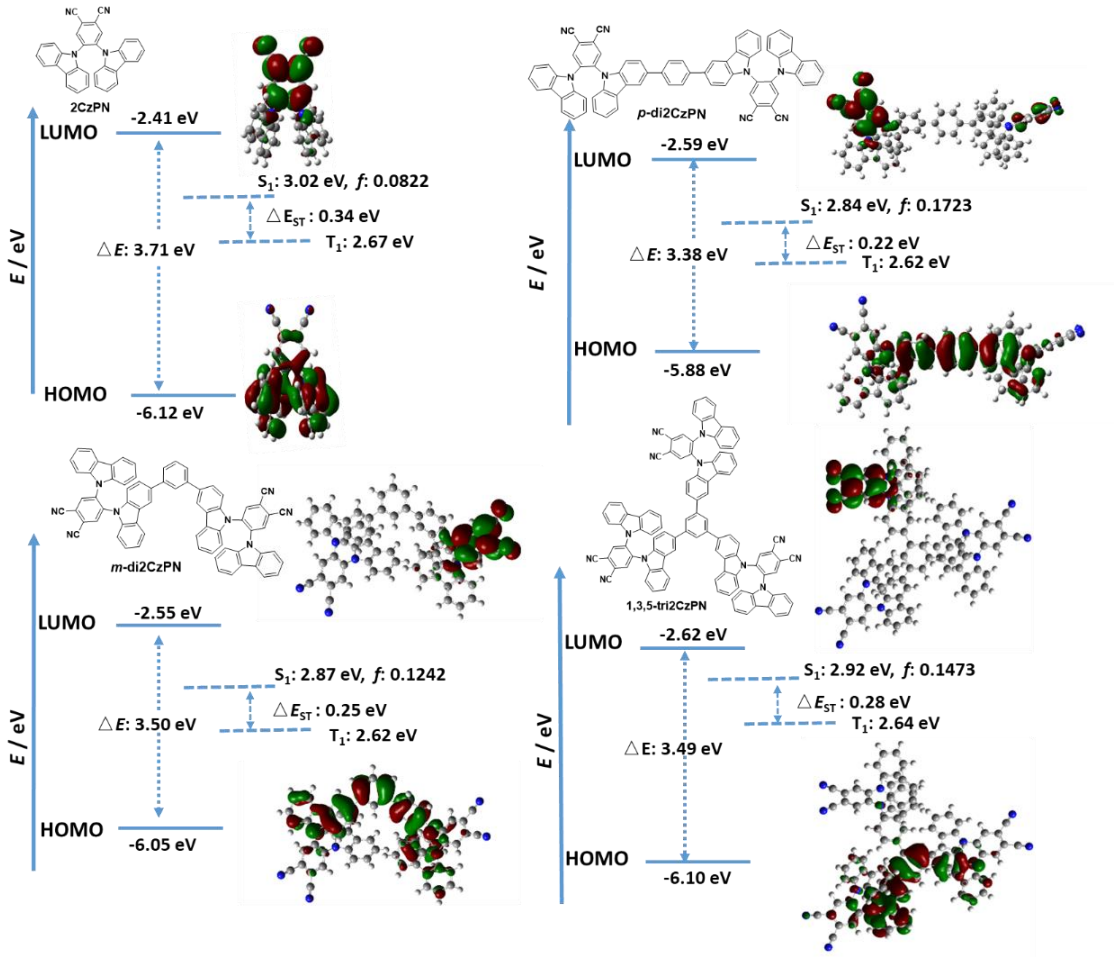

Figure **2.2**. Theoretical modelling of the energies of the HOMO/LUMO and the S_1 and T_1 states of ***p*-di2CzPN**, ***m*-di2CzPN**, **1,3,5-tri2CzPN**, and reference compound **2CzPN** in the gas phase and the electron density distribution of the frontier molecular orbitals (isovalue = 0.02).

Table **2.1**. Calculated HOMO/LUMO and singlet/triplet state energy levels for three emitters

Compounds	**HOMO**[a] **/ eV**	**LUMO**[a] **/ eV**	**ΔE**[b] **/ eV**	**S_1**[a] **/ eV**	**T_1**[a] **/ eV**	**ΔE_{ST}**[c] **/ eV**	***f***
***p*-di2CzPN**	−5.88	−2.50	3.38	2.84	2.62	0.22	0.1723
***m*-di2CzPN**	−6.05	−2.55	3.50	2.87	2.62	0.25	0.1242
1,3,5-tri2CzPN	−6.10	−2.62	3.49	2.92	2.64	0.28	0.1473
2CzPN	−6.12	−2.41	3.71	3.02	2.67	0.34	0.0822

[a] Calculated at the PBE0/6-31g(d,p) level in the gas phase; [b] ΔE = |HOMO-LUMO|; [c] ΔE_{ST} = $E(S_1)$-$E(T_1)$.

Table **2.2**. Exited states involved in the main UV-vis transitions of three emitters

Compounds	**Excited State**	**Energy/ eV; nm**	***f***	**Nature**	**Character of the transition**
***p*-di2CzPN**	S_1	2.84; 437	0.1723	H→L (81%)	CT
	S_4	3.14; 395	0.1044	H→(L+2) (49%) (H−4)→L (14%) (H−2)→(L+3) (7%)	HLCT
	S_9	3.43; 361	0.1495	H→(L+3) (66%) (H−1)→(L+2) (5%)	LE
***m*-di2CzPN**	S_1	2.87; 432	0.1242	H→L (59%) (H−1) →L (34%)	CT
	S_2	2.90; 427	0.0715	(H−2)→(L+1) (48%) (H−1)→(L+1) (42%)	HLCT
	S_3	3.06; 406	0.0820	(H−3)→(L+1) (80%) (H−2)→(L+3) (15%)	HLCT
	S_{10}	3.43; 361	0.1495	(H−2)→(L+3) (55%) (H−1)→(L+4) (32%)	HLCT
1,3,5-tri2CzPN	S_1	2.92; 425	0.1473	H→L (59%) (H−1) →L (34%)	CT
	S_2	2.90; 427	0.0715	(H−2)→(L+1) (48%) (H−1)→(L+1) (42%)	HLCT
	S_3	3.06; 406	0.0820	(H−3)→(L+1) (80%) (H−2)→(L+3) (15%)	HLCT
	S_{10}	3.43; 361	0.1495	(H−2)→(L+3) (55%) (H−1)→(L+4) (32%)	HLCT

The natural transition orbital (NTO) analysis of the three multichoromophore emitters (Figure **2.3–2.6**), show that T_1 is localized to one emitting core and this state possesses similar

symmetry to that of the T_1 state of **2CzPN**; the highest occupied NTO (HONTO) is distributed over whole molecule while the lowest unoccupied NTO (LUNTO) is located on the phthalonitrile moiety. The S_1 states of the three multichoromophore emitters also only involve one emitting core, where the HONTOs are located on the two carbazoles moieties and the central phenyl ring, and the LUNTOs are localized on the phthalonitrile moiety. The magnitude of the stabilization of the S_1 state is proportional to the degree of conjugation present about the central benzene scaffold as shown in Figure **2.2**. The ΔE_{ST} values for three emitters are 0.22 eV (***p*-di2CzPN**), 0.25 eV (***m*-di2CzPN**), and 0.28 eV (**1,3,5-tri2CzPN**), compare to 0.34 eV of **2CzPN**. According to the TDA-DFT calculations, the multichoromophore structures possess manifold intermediate triplets between S_1 and T_1 due in part to the slightly differing CT states in each of the cores. Take **1,3,5-tri2CzPN** for example (Figure **2.6**), TDA-DFT calculations predict five intermediate triplet states below S_1, while for **2CzPN** (Figure **2.3**) only one intermediate triplet state below S_1 exists. The smaller ΔE_{ST} values and the greater density of intermediate triplet states for the three multichoromophore emitters can lead to multiple RISC transition channels via intermediate triplets to S_1, leading to a more efficient RISC process than is present in the reference emitter **2CzPN**. Importantly, TDA-DFT calculation also showed that the transitions involved in the S_1 state of the three multichoromophore emitters have much stronger *f*, compared to **2CzPN** (Table **2.1**), which is predictive of a higher radiative rate constant that would be evidenced by a higher Φ_{PL}.

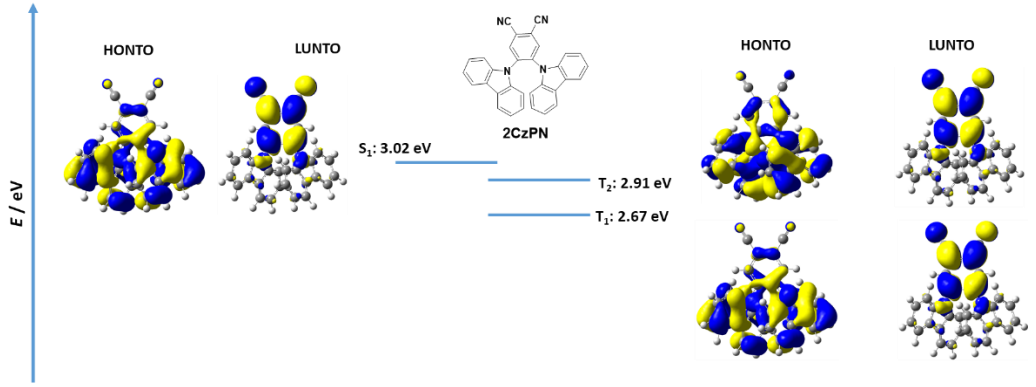

Figure **2.3**. Natural transition orbitals analysis of **2CzPN**.

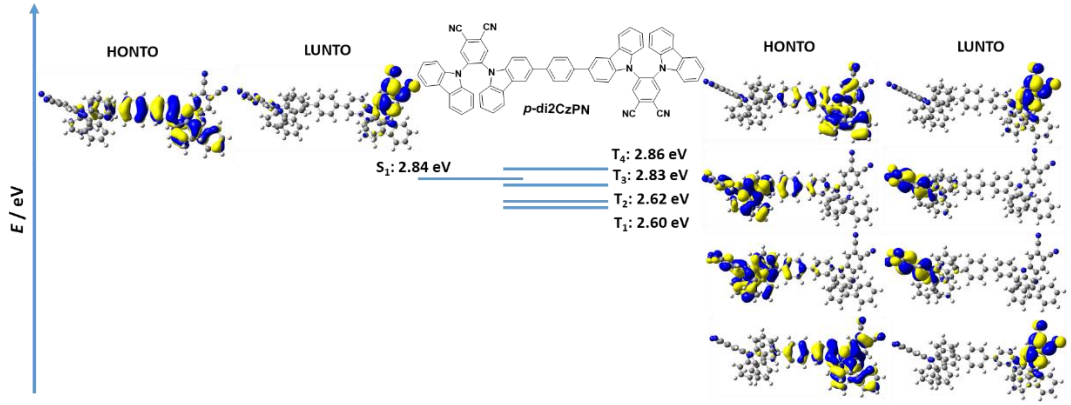

Figure **2.4** Natural transition orbitals analysis of ***p*-di2CzPN**.

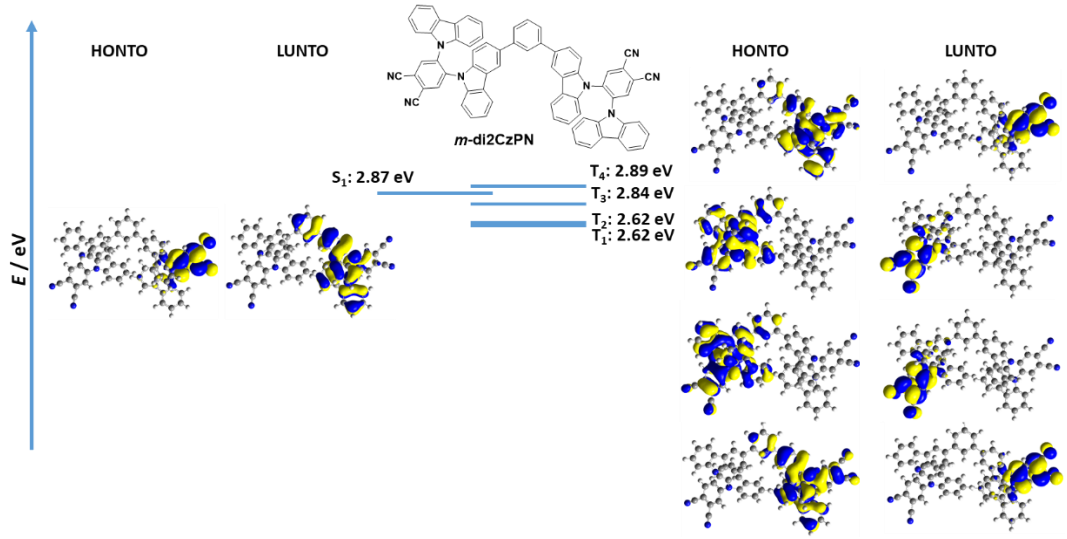

Figure **2.5**. Natural transition orbitals analysis of ***m*-di2CzPN**.

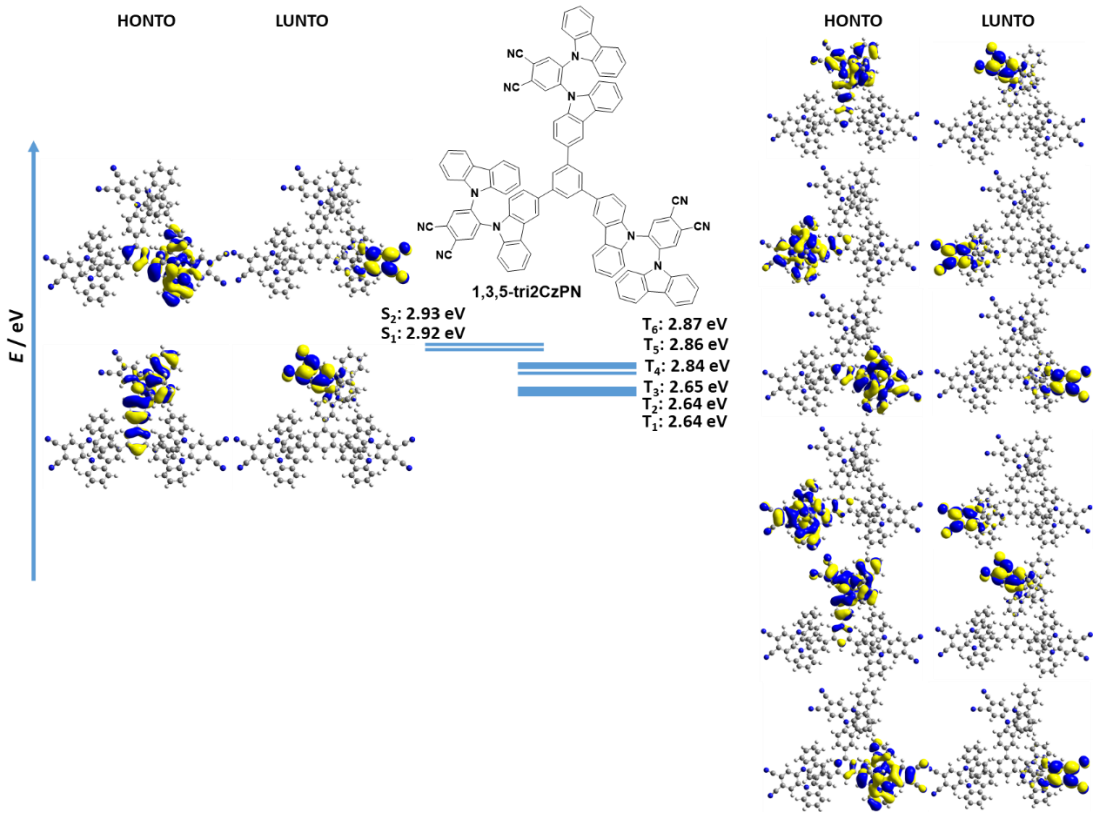

Figure **2.6**. Natural transition orbitals analysis of **1,3,5-tri2CzPN**.

2.4. Electrochemistry

Cyclic voltammetry (CV) and differential pulse voltammograms (DPV) were measured in MeCN with tetra(n-butyl)ammonium hexafluorophosphate (*n*-Bu_4NPF_6) as the supporting electrolyte in order to experimentally ascertain HOMO and LUMO energy levels, of the three emitters and **2CzPN** (Figure **2.7**). The ***p*-di2CzPN** exhibited an irreversible reduction wave while ***m*-di2CzPN**, **1,3,5-tri2CzPN**, and **2CzPN** exhibited pseudo-reversible reduction waves. The three emitters and **2CzPN** exhibited broad, irreversible oxidation waves. The DPV results indicated the three emitters have single electron reduction processes and no further reduction waves were observed scanning from −2 V, which are ascribed to reduction of one of the

phthalonitriles while there are a series of closely related carbazole-based oxidation waves. The HOMO and LUMO values were inferred from the peaks of the oxidation and reduction waves in the DPVs, respectively. The HOMO energies for **2CzPN**, ***p*-di2CzPN**, ***m*-di2CzPN**, and **1,3,5-tri2CzPN** were determined to be −5.64 eV, −5.65 eV, −5.80 eV, and −5.82 eV, respectively. The HOMO energies of the emitters are slightly stabilized (~ 0.2 eV) than those predicted by the DFT calculations yet reproduce the trends observed, while the HOMO energy of **2CzPN** is much more stabilized (0.48 eV) than DFT-predicted calculation. The LUMO energies for **2CzPN**, ***p*-di2CzPN**, ***m*-di2CzPN**, and **1,3,5-tri2CzPN** were determined to be −2.71 eV, −3.00 eV, −3.03 eV, and −2.98 eV, respectively, which are moderately stabilized (~ 0.4 eV) than those predicted by the DFT calculations. The more stabilized LUMOs of the three multichoromophores than **2CzPN** matched the trend predicted by the DFT calculation.

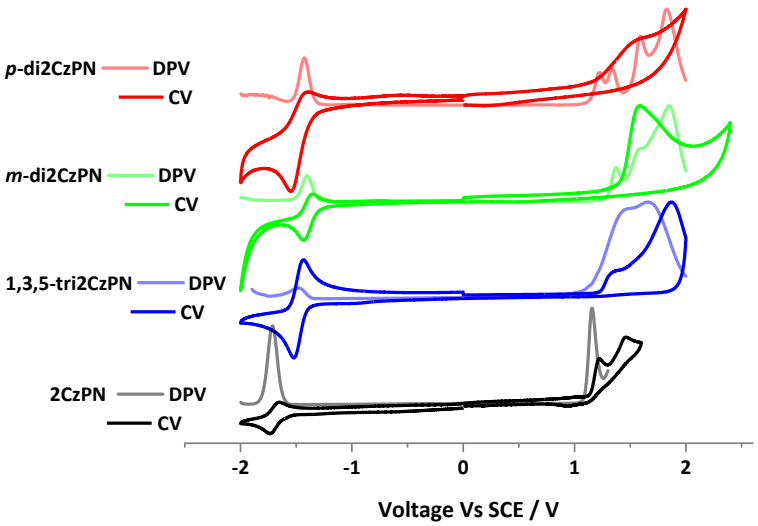

Figure **2.7.** CV and DPV of **2CzPN**, ***p*-di2CzPN**, ***m*-di2CzPN**, and **1,3,5-tri2CzPN** in MeCN with 0.1 M n-Bu_4NPF_6 as the supporting electrolyte. Measured condition: scan rate 100 mV/s, calibrated against a Fc/Fc^+ redox couple and referenced versus SCE.[27]

2.5 Photophysical Properties

The photophysical properties of ***p*-di2CzPN**, ***m*-di2CzPN**, and **1,3,5-tri2CzPN** were next investigated both in solution and in thin films. The photophysical properties of the three emitters are summarized in Table **2.3**. Room-temperature ultraviolet-visible (UV-*vis*) absorption and photoluminescence (PL) spectra of ***p*-di2CzPN**, ***m*-di2CzPN**, and **1,3,5-tri2CzPN** and the reference compound **2CzPN** in dilute toluene solution are shown in Figure **2.8**. According to the TDA-DFT calculations (Table **2.2**), all four compounds exhibited high intensity locally excited transitions between 280 to 340 nm and intramolecular charge-transfer (ICT) transition absorption bands in the range from 360 to 440 nm. The ICT absorption bands of ***p*-di2CzPN**, ***m*-di2CzPN**, and **1,3,5-tri2CzPN** are much stronger compared to that of **2CzPN**. The molar absorptivity coefficient (ε) for the ICT band of **2CzPN** at 380 nm is 1.2×10^4 M^{-1} cm^{-1} while for ***p*-di2CzPN**, ***m*-di2CzPN**, and **1,3,5-tri2CzPN**, ε increases to 2.5×10^4 M^{-1} cm^{-1}, 2.5×10^4 M^{-1} cm^{-1}, and 3.82×10^4 M^{-1} cm^{-1}, respectively, which is proportial to the number of emitter units. The optical bandgaps (E_{opt}), determined from the intersection point of the normalized absorption and emission spectra, of **2CzPN**, ***p*-di2CzPN**, ***m*-di2CzPN**, and **1,3,5-tri2CzPN** are 2.99 eV, 2.85 eV, 2.89 eV, and 2.92 eV, respectively (Figure **2.9d**). The λ_{PL}s for **2CzPN**, ***p*-di2CzPN**, ***m*-di2CzPN**, and **1,3,5-tri2CzPN** are 475 nm, 494 nm, 485 nm, and 484 nm in toluene. The nearly identical emission profiles for ***m*-di2CzPN**, and **1,3,5-tri2CzPN** demonstrate that there is essentially no conjugation from the weak conjugated meta-connection impacting the energy of the emissive excited state while the enhanced conjugation is responsible for the red-shifted emission in ***p*-di2CzPN**. To corroborate the ICT nature of the emission, we measured the PL spectra in solvents of varying

polarity. In each case, as the polarity of the solvent increased the PL spectrum red-shifted and broadened, thereby showing a strong positive solvatochromism (Figure **2.9**).

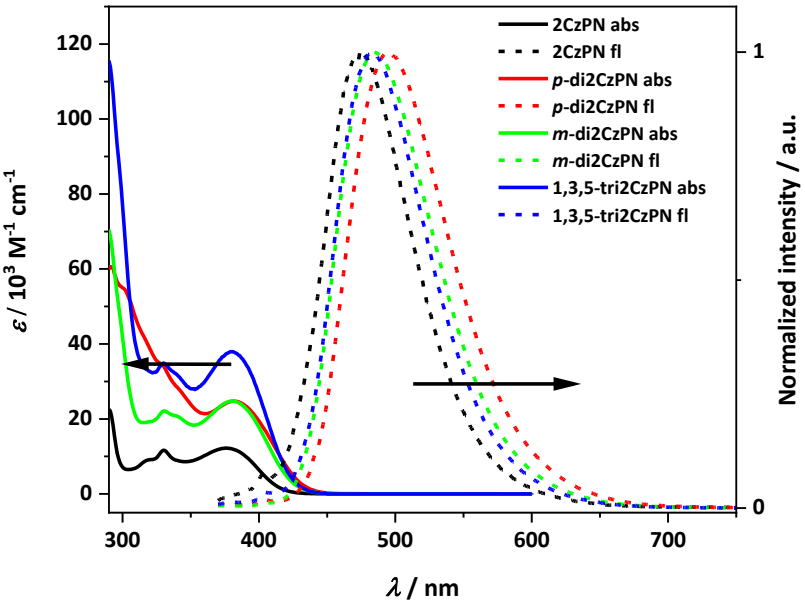

Figure **2.8**. Absorption and normalized emission spectra of **2CzPN**, ***p*-di2CzPN**, ***m*-di2CzPN**, and **1,3,5-tri2CzPN** in toluene solution (10^{-5} M). λ_{exc} = 355 nm.

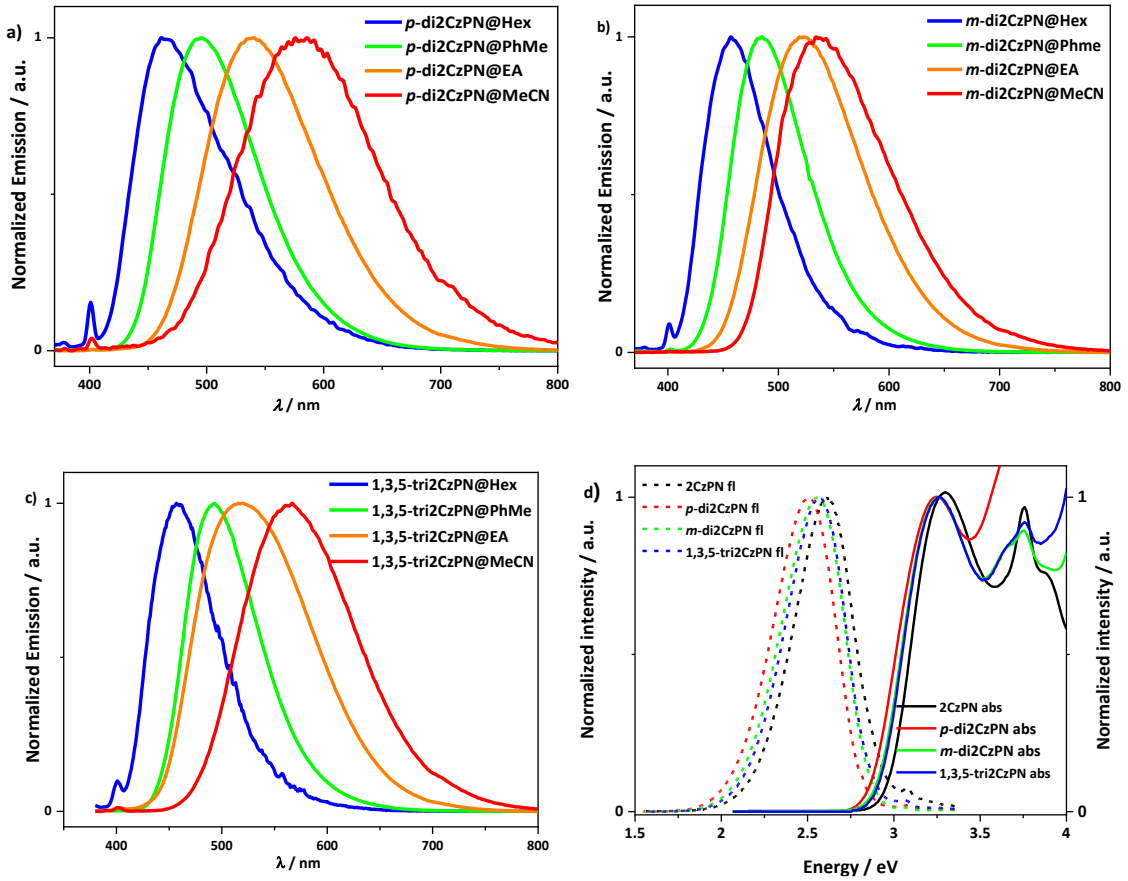

Figure 2.9. Solvatochromic emission studies of a) ***p*-di2CzPN**, b) ***m*-di2CzPN**, and c) **1,3,5-tri2CzPN** (λ_{exc} = 378 nm), and d) normalized UV-vis and fluorescence spectra in toluene for **2CzPN**, ***p*-di2CzPN**, ***m*-di2CzPN**, and **1,3,5-tri2CzPN** (λ_{exc} = 360 nm).

The three emitters exhibited near quantitative Φ_{PL} in toluene, values that were strongly quenched under aerated conditions. For ***p*-di2CzPN**, ***m*-di2CzPN**, and **1,3,5-tri2CzPN** in aerated toluene, the Φ_{PL} values were 39%, 27% and 34%, respectively, while under oxygen-free conditions the Φ_{PL} values reached, respectively, 98%, 96% and 99%. These compounds are thus significantly more emissive than **2CzPN,** with Φ_{PL} of 26% in aerated and 28% in oxygen-free toluene.[28] The oxygen sensitivity is an indication of accessible triplet excited states, and is a

frequent characteristic of TADF emitters. We next measured the time-resolved emission decays in toluene. Each of the three emitters exhibit a prompt decay component with the lifetime in the nanosecond region and bi-exponential delayed decay kinetics with the lifetimes in the microsecond region (Figure **2.10**). The prompt decay lifetimes (τ_p) for ***p*-di2CzPN**, ***m*-di2CzPN**, and **1,3,5-tri2CzPN** are 13.4 ns, 15.0 ns, and 14.9 ns, respectively, while the average delayed decay lifetimes ($\tau_{d,avg}$) are 2.4 μs for ***p*-di2CzPN**, 22.2 μs for ***m*-di2CzPN**, and 58.2 μs for **1,3,5-tri2CzPN**. Compared to the emission decay of **2CzPN** (24.4 ns (99.5%) and 1.1 μs (0.5%)),[28] the three multichoromophore emitters exhibited longer delayed lifetime and a significantly increased delayed component in toluene.

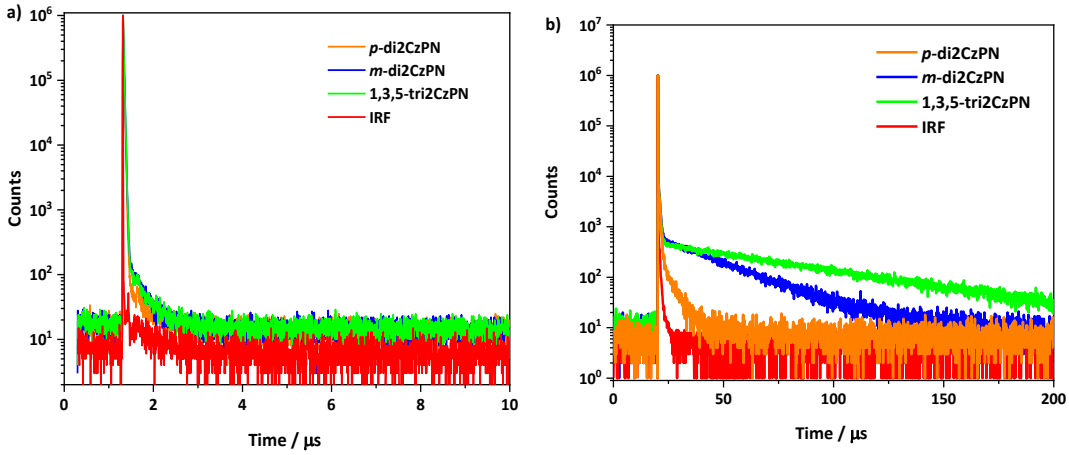

Figure 2.10. Transient PL decay spectra of ***p*-di2CzPN**, ***m*-di2CzPN**, and **1,3,5-tri-2CzPN** in a) aerated toluene and b) degassed toluene (concentration 10^{-5} M, λ_{exc} = 378 nm).

We next investigated the photophysical properties of the three emitters in 10 wt% doped poly(methyl methacrylate) (PMMA) films as the polarity of PMMA closely mimics that of

toluene.[29] The ***m*-di2CzPN** and **1,3,5-tri2CzPN** compounds showed slightly red-shifted emission maxima compared to those in toluene at 498 nm and 494 nm, respectively while the peak for ***p*-di2CzPN** was red-shifted to 516 nm (Figure **2.11a**). The Φ_{PL} values under N_2 for **2CzPN**, ***p*-di2CzPN**, ***m*-di2CzPN** and **1,3,5-tri2CzPN** are 76%,[28] 64%, 77% and 78%, respectively. The time-resolved emission decays were obtained under oxygen-free conditions (Figure **2.12**). Similar to the profiles in toluene, the τ_p values for ***p*-di2CzPN**, ***m*-di2CzPN**, **and 1,3,5-tri2CzPN** are 29 ns, 38 ns, and 26 ns, respectively, which are slightly longer than that of **2CzPN** (18 ns). The $\tau_{d,avg}$ values are 286.3 μs for ***p*-di2CzPN**, 311.0 μs for ***m*-di2CzPN**, 262.4 μs for **1,3,5-tri2CzPN**, respectively, which are much shorter than the $\tau_{d,avg}$ of **2CzPN** in PMMA film (1.5 ms).[28]

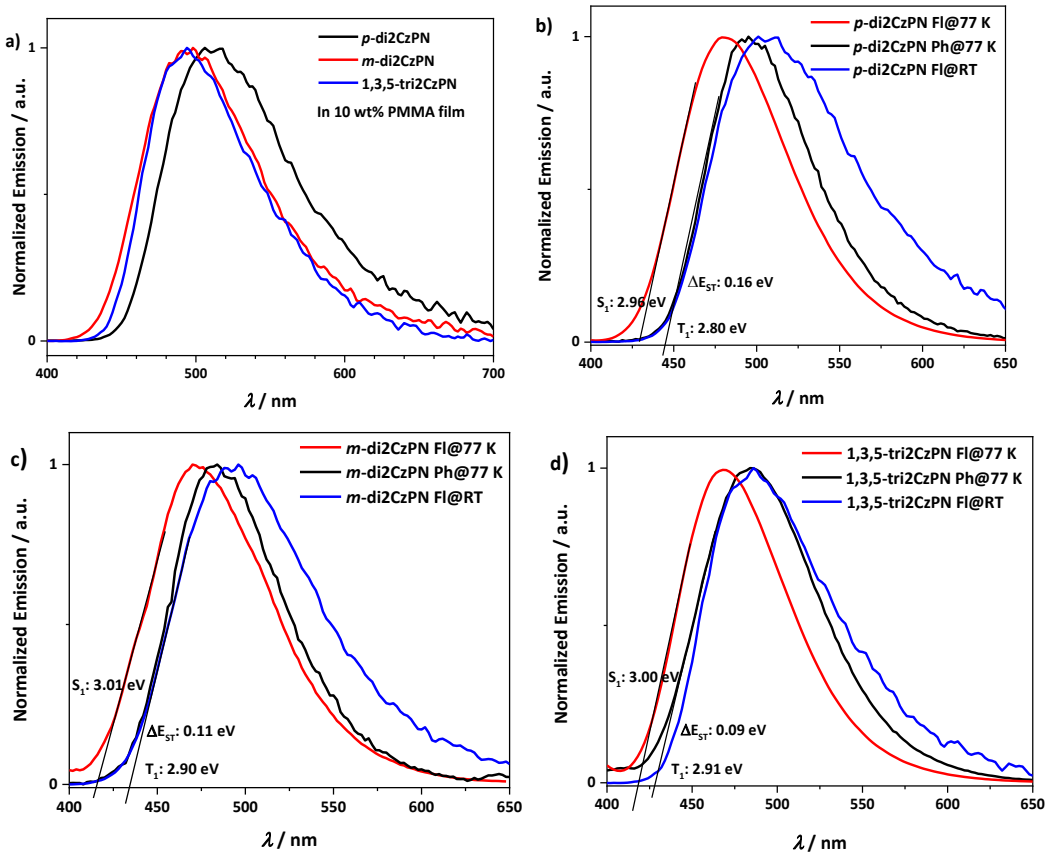

Figure **2.11**. a) Fluorescence (Fl) 10 wt% PMMA films of ***p*-di2CzPN**, ***m*-di2CzPN**, and **1,3,5-tri2CzPN** at room temperature; Fluorescence and phosphorescence (Ph) spectra of 10 wt% PMMA films of (a) ***p*-di2CzPN**, (b) ***m*-di2CzPN**, and (c) **1,3,5-tri2CzPN** at 77 K. The fluorescence spectra were sliced from 1 ns to 100 ns while the phosphorescence spectra were sliced from 2 ms to 10 ms (λ_{exc} = 378 nm).

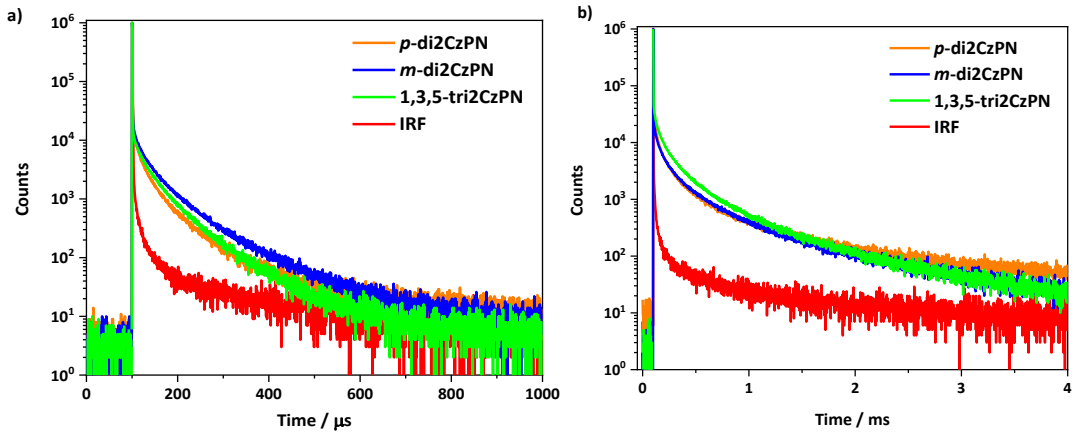

Figure **2.12**. Transient PL decays of ***p*-di2CzPN**, ***m*-di2CzPN**, and **1,3,5-tri-2CzPN** in 10 wt% doped PMMA films under a) aerate and b) vacuum conditions (λ_{exc} = 378 nm, time region: (a) 1 ms and (b) 4 ms).

Prompt fluorescence and phosphorescence spectra were obtained by time-resolved emission spectroscopy (TRES) measurement in 10 wt% doped PMMA at 77 K. The prompt emission spectrum of each emitter exhibited continuous red-shifting from 1 ns to 100 ns, which could be ascribed to the energetic relaxation of molecular vibration and rotation (Figure **2.13**).[30] The phosphorescence spectra were obtained from integration of the TRES spectrum from 2 ms to 9 ms (Figure **2.13**). The room temperature emission spectra of ***p*-di2CzPN**, ***m*-di2CzPN**, and **1,3,5-tri2CzPN** are ca. 20 nm red-shifted and are slightly broader compared to their corresponding prompt fluorescence spectra measured at 77 K. We calculated the energy of the singlet state from the onset of the fluorescence spectra from 1 ns and the energy of the triplet state from the onset of the phosphorescence spectra from 2 ms (Figure **2.11**). The S_1 energies for ***p*-di2CzPN**, ***m*-di2CzPN**, and **1,3,5-tri2CzPN** were calculated to be 2.96 eV, 3.01 eV, and 3.00 eV, respectively, which closely match those of the TDA-DFT calculation, while the T_1 state was found

at 2.80 eV, 2.90 eV, and 2.91 eV, respectively, which are slightly destabilized compared to those calculated by TDA-DFT. The ΔE_{ST} values for ***p*-di2CzPN**, ***m*-di2CzPN**, and **1,3,5-tri2CzPN** are 0.16 eV, 0.11 eV, and 0.09 eV, which are reduced compared to 0.20 eV for **2CzPN** in PMMA film.[28] These small ΔE_{ST} values are consistent with an efficient TADF process, which are consistent with the shorter delayed lifetimes of the three multichoromophore emitters in the doped PMMA films.

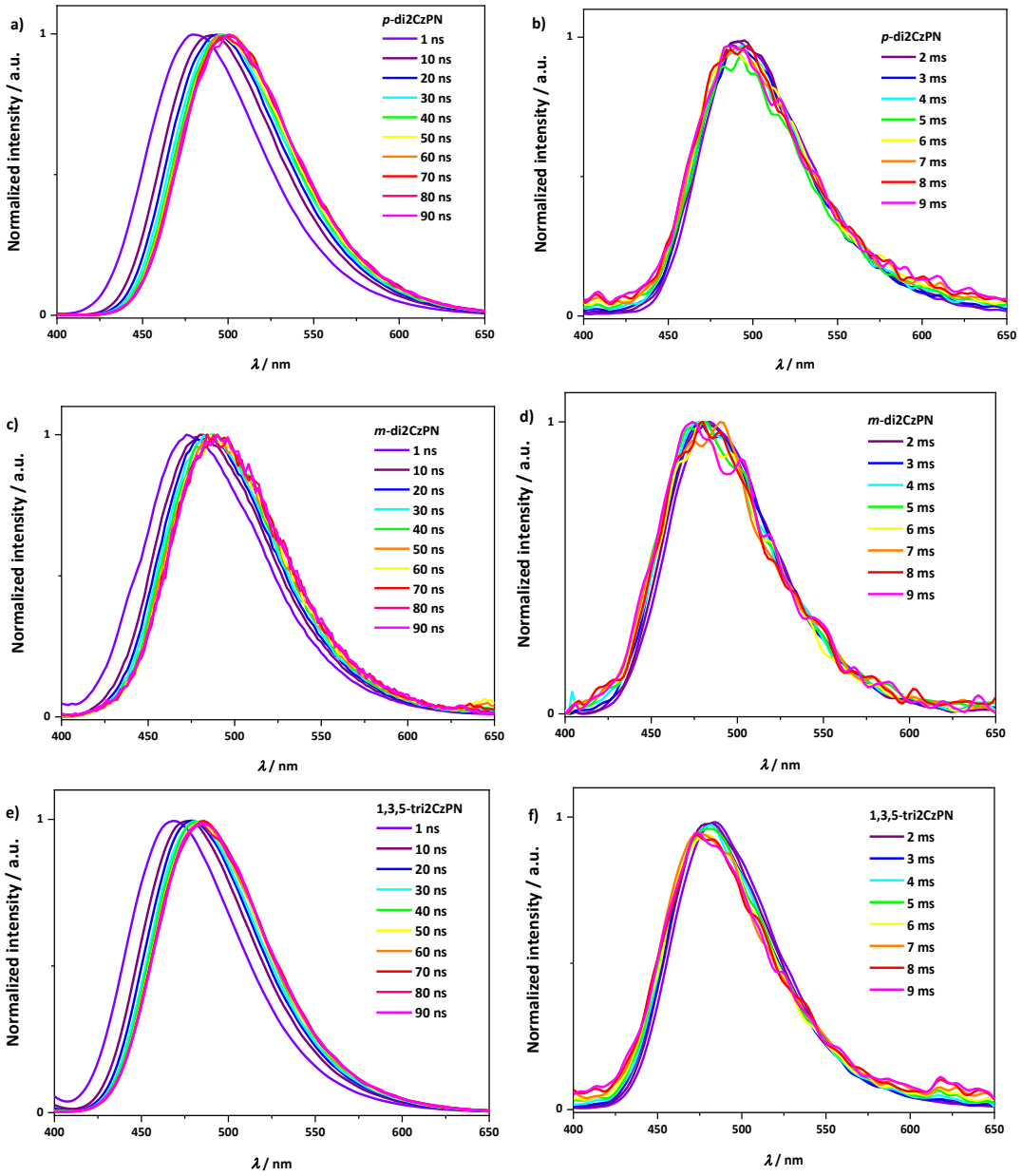

Figure **2.13**. Time resolved emission spectra of 10 wt% (a and b) ***p*-di2CzPN**, (c and d) ***m*-di2CzPN**, and (e and f) **1,3,5-tri-2CzPN** doped PMMA film at 77 K in time region of 100 ns and 10 ms (λ_{exc} = 378 nm).

Prompt fluorescence and phosphorescence spectra were obtained by time-resolved emission spectroscopy (TRES) measurement in 10 wt% doped PMMA at 77 K. The prompt emission spectrum of each emitter exhibited continuous red-shifting from 1 ns to 100 ns, which could be ascribed to the energetic relaxation of molecular vibration and rotation (Figure **2.13**).[30] The phosphorescence spectra were obtained from integration of the TRES spectrum from 2 ms to 9 ms (Figure **2.13**). The room temperature emission spectra of ***p*-di2CzPN**, ***m*-di2CzPN**, and **1,3,5-tri2CzPN** are ca. 20 nm red-shifted and are slightly broader compared to their corresponding prompt fluorescence spectra measured at 77 K. We calculated the energy of the singlet state from the onset of the fluorescence spectra from 1 ns and the energy of the triplet state from the onset of the phosphorescence spectra from 2 ms (Figure **2.11**). The S_1 energies for ***p*-di2CzPN**, ***m*-di2CzPN**, and **1,3,5-tri2CzPN** were calculated to be 2.96 eV, 3.01 eV, and 3.00 eV, respectively, which closely match those of the TDA-DFT calculation, while the T_1 state was found at 2.80 eV, 2.90 eV, and 2.91 eV, respectively, which are slightly destabilized compared to those calculated by TDA-DFT. The ΔE_{ST} values for ***p*-di2CzPN**, ***m*-di2CzPN**, and **1,3,5-tri2CzPN** are 0.16 eV, 0.11 eV, and 0.09 eV, which are reduced compared to 0.20 eV for **2CzPN** in PMMA film.[28] These small ΔE_{ST} values are consistent with an efficient TADF process, which are consistent with the shorter delayed lifetimes of the three multichoromophore emitters in the doped PMMA films.

To corroborate the TADF character of the three emitters in doped PMMA films, we measured the temperature-dependent time-resolved decay spectra (Figure **2.14**). In each case, the

delayed fluorescence increased with increasing temperature, which is a hallmark of TADF as the RISC process becomes suppressed at low temperatures.

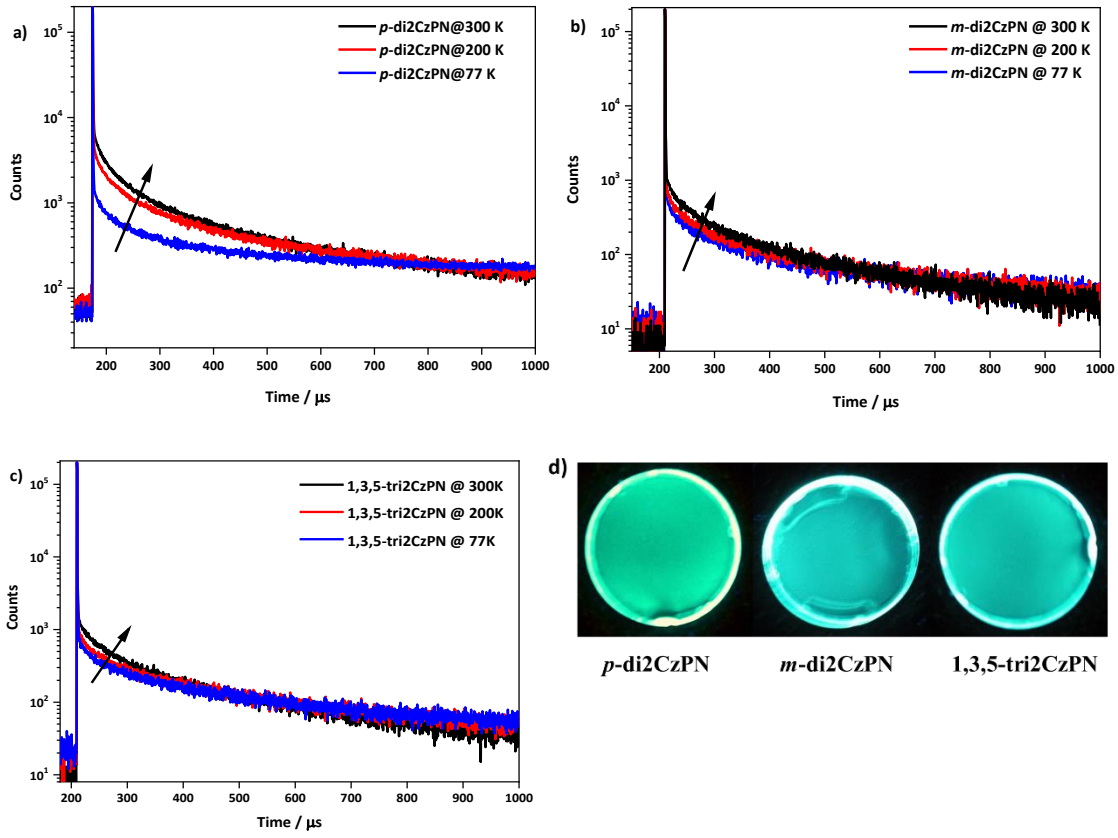

Figure **2.14.** Temperature-dependent time-resolved PL decay spectra of 10 wt% doped PMMA films of (a) ***p*-di2CzPN**, (b) ***m*-di2CzPN**, and (c) **1,3,5-tri2CzPN** (d) Photos of 10 wt% PMMA films of ***p*-di2CzPN**, ***m*-di2CzPN**, and **1,3,5-tri2CzPN**. (λ_{exc} = 378 nm, time region: 1 ms)

Table **2.3.** Key Photophysical data of ***p*-di2CzPN**, ***m*-di2CzPN** and **1,3,5-tri2CzPN**.

Compound	λ_{abs} **(ε)[a] / nm (10^{-3} m^{-1} cm^{-1})**	λ_{PL} **/ nm**	Φ_{PL}[c] **/ %**	$S_1/T_1/\Delta E_{ST}$[d] **/ eV**	τ_p[e] **/ ns**	$\tau_{d,avg}$[e] **/ µs**	**HOMO/LUMO /**ΔE_g[f] **/ eV**
***p*-di2CzPN**	326 (35), 382 (25)	494[a]/ 516[b]	52/64	2.96/2.80/ 0.16	29	286.3	−5.65/−3.00/ 2.65
***m*-di2CzPN**	332 (22), 381 (25)	485[a]/ 498[b]	59/77	3.01/2.90/ 0.11	38	311.0	−5.80/−3.03/ 2.77
1,3,5-tri2CzPN	330 (35), 381 (38)	483[a]/ 494[b]	58/78	3.00/2.91/ 0.09	26	262.4	−5.82/−2.98/ 2.84

[a] Measured in toluene solution (λ_{exc} = 378 nm), [b] Measured in 10 wt% doped PMMA films (λ_{exc} = 378 nm), [c] Measured by integrating sphere of 10 wt% doped PMMA film under air/N_2 ((λ_{exc} = 360 nm), [d] S_1 is obtained from the onset of the prompt emission measured at 77 K, T_1 is obtained from the onset of the phosphorescence spectrum measured at 77 K, $\Delta E_{ST} = S_1 - T_1$, [e] τ_p (prompt lifetime) and $\tau_{d,avg}$ (average delayed lifetime) were obtained from the transient PL decay of doped film under vacuum, λ_{exc} = 378 nm, measure region: 50 µs and 4 ms, [f] HOMO and LUMO values were obtained from the redox potentials from the DPV, $E_{HOMO/LUMO} = -(E_{ox/red} + 4.8)$ where $E_{ox/red}$ were taken from DPV scan corrected vs. Fc/Fc^+, $\Delta E_g = E_{LUMO} - E_{HOMO}$.[27]

The kinetics of the three multichoromophore emitters and the reference emitter **2CzPN** were investigated in 10 wt% doped DPEPO films for ***p*-di2CzPN**, ***m*-di2CzPN**, and **2CzPN**, and 20 wt% doped CBP film for **1,3,5-tri2CzPN** (Figure **2.15**, Table **2.4**). The three emitters all exhibit high Φ_{PL} values in host matrices suitable for OLEDs. In 10 wt% DPEPO doped films ***p*-di2CzPN** has a Φ_{PL} of 59%, of which 21% is the prompt fluorescence quantum yield (Φ_p) and

38% is the delayed fluorescence quantum yield (Φ_d). For ***m*-di2CzPN**, the Φ_{PL} is higher at 70%, which distributes as 22% of Φ_p and 48% of Φ_d. The Φ_{PL} for **1,3,5-tri2CzPN** is 54% with 32% of Φ_p and 22% of Φ_d in the 20 wt% CBP doped film. The Φ_{PL} for **2CzPN** reached 98% with 21% of Φ_p and 77% of Φ_d in the 10 wt% DPEPO film. The prompt lifetimes for ***p*-di2CzPN**, ***m*-di2CzPN**, and **1,3,5-tri2CzPN** are 18 ns, 17 ns, and 21 ns compared to 20 ns of **2CzPN**, and τ_d values are 25.7 μs, 44.2 μs, and 9.8 μs, respectively, which are much shorter than the 137 μs of **2CzPN**. The k_{RISC} values for ***p*-di2CzPN**, ***m*-di2CzPN**, and **1,3,5-tri2CzPN** are calculated to be 1.1×10^5 s^{-1}, 0.7×10^5 s^{-1}, and 1.7×10^5 s^{-1}, respectively, which are faster than **2CzPN** (0.3×10^5 s^{-1}). **1,3,5-tri2CzPN** exhibits the fastest k_{RISC} value, which is ascribed to the small ΔE_{ST} and the greater density of intermediate triplet states predicted by TDA-DFT calculation.

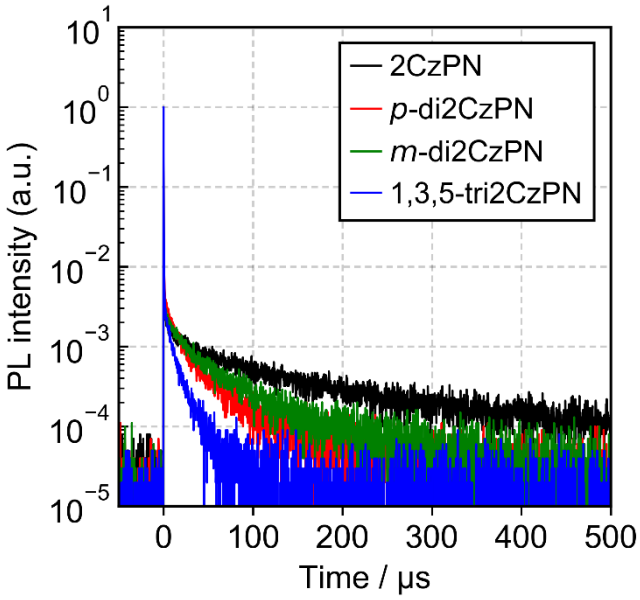

Figure **2.15**. PL decay spectra of 10 wt% doped DPEPO films of **2CzPN**, ***p*-di2CzPN**, ***m*-di2CzPN**, and a 20 wt% doped CBP film of **1,3,5-tri2CzPN** (λ_{exc} = 280 nm).

Table **2.4**: Exciton lifetime and the kinetic constants of three multichoromophore emitters and **2CzPN** in host materials. Φ_{PL}, τ_p, and $\tau_{d,avg}$ are measured under inert atmosphere.

Compound	**matrix**	λ_{PL} **/ nm**	Φ_{PL} **/ %**	Φ_p **/ %**	Φ_d **/ %**	τ_p **/ ns**	$\tau_{d,avg}$ **/ µs**	k_r^s **/10^7 s^{-1}**	k_{ISC} **/ 10^7 s^{-1}**	k_{RISC} **/ 10^5 s^{-1}**
***p*-di2CzPN**	10 wt% in DPEPO	531	59	21	39	18	25.7	1.2	3.7	1.1
***m*-di2CzPN**	10 wt% in DPEPO	510	70	22	48	17	44.2	1.3	4.0	0.7
1,3,5-tri2CzPN	20 wt% in CBP	505	54	32	22	21	9.8	1.5	2.0	1.7
2CzPN	10 wt% in DPEPO	496	98	21	77	20	137	1.1	4.0	0.3

2.6 Electroluminescence Properties

A solution-processed OLED based on **1,3,5-tri2CzPN** was fabricated using the architecture: ITO (50 nm)/Poly(3,4-ethylenedioxythiophene)-poly(styrenesulfonate) (PEDOT:PSS) (35 nm)/20 wt% **1,3,5-tri2CzPN**:CBP/1,3-Bis[3,5-di(pyridin-3-yl)phenyl] benzene (BmPyPhB) (30 nm)/8-Quinolinolato lithium (Liq) (1 nm)/Al (80 nm). PEDOT:PSS layer and the emitting layer were deposited by spin-coating process and the other layers were thermally vacuum-deposited. In the device, PEDOT:PSS was used as a hole injection and transporting layer, while BmPyPhB was used as an electron-transporting and LiQ was used as injection layer. The turn-on voltage for the device is 5.6 V and the device exhibits sky-blue emission with the λ_{EL} at 500 nm with CIE of (0.22, 0.44) and EQE_{max} of 7.1 % at 0.1 mA cm^{-2}, while the Lum_{max} reaches 1,000 cd m^{-2}. Considering the Φ_{PL} of **1,3,5-tri2CzPN** in CBP (54%), the EQE_{max} of 7.1% from device is close to the theoretical EQE_{max} of 10.8% under the assumption that (1) the charge balance is unity; (2) the efficiency of radiative exciton production is unity, and

(3) the light out-coupling efficiency is 0.2. The device suffers severe efficiency roll-off as the EQE decreases to 1% at 10 mA cm^{-2}.

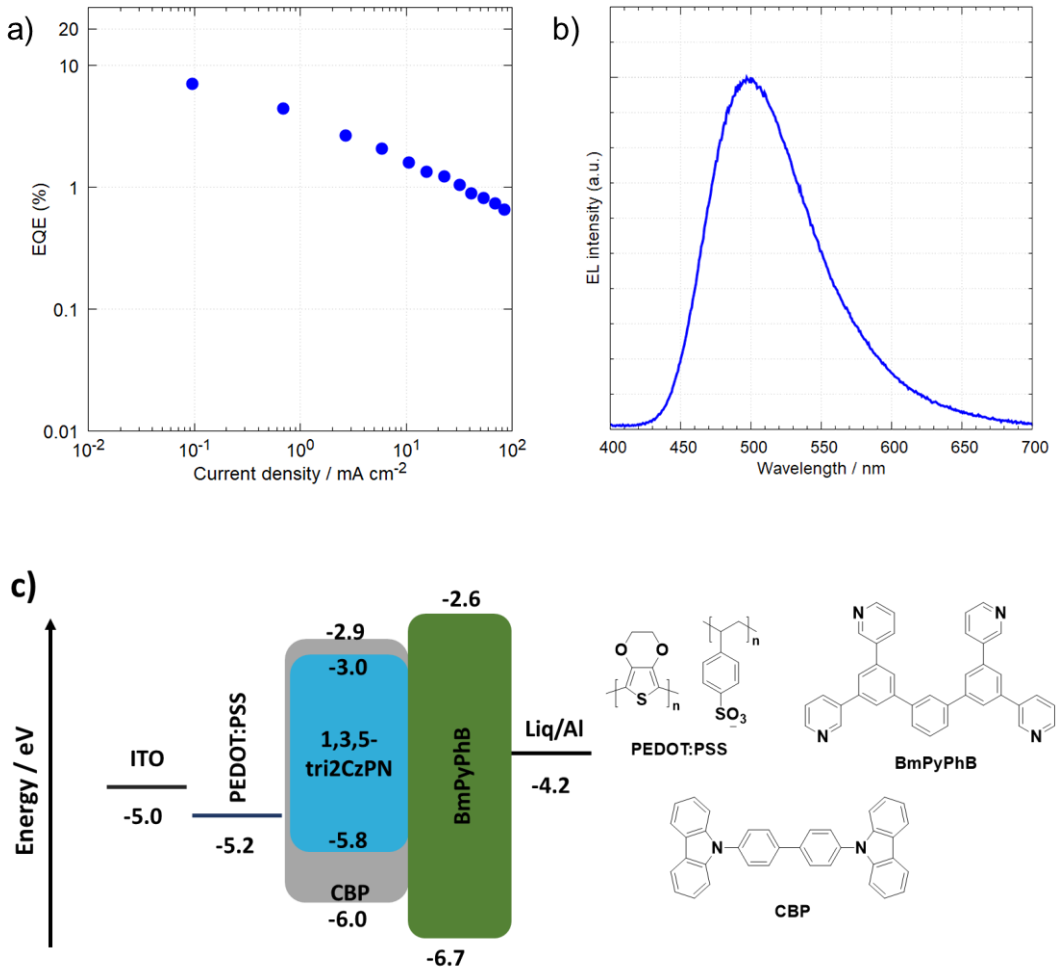

Figure **2.16**. (a) EQE-current-density characteristics, (b) EL spectra of OLEDs, and (c) Device architecture and molecular structures of materials used for **1,3,5-tri2CzPN** based OLEDs.

2.7 Conclusions

By connecting TADF emitting core **2CzPN** to a central benzene ring, three multichromophore emitters, ***p*-di2CzPN**, ***m*-di2CzPN** and **1,3,5-tri2CzPN**, were synthesized and

characterized. The multichromophore molecular structure results in an improved molar extinction coefficient for the low-energy charge transfer states and near unity photoluminescence quantum yield values in solution. TDA-DFT calculations showed that density intermediate triplet states between S_1 and T_1 could contribute to an improved TADF efficiency. The three emitters exhibit smaller ΔE_{ST} values leading to fast delayed lifetimes in doped films. The k_{RISC} for **1,3,5-tri2CzPN** reaches 1.7×10^5 s^{-1}, which is more than five times faster than **2CzPN** (0.3×10^5 s^{-1}), while the k_{RISC} for ***p*-di2CzPN** and ***m*-di2CzPN** are more than three and two times faster than **2CzPN**, respectively. A solution-processed OLED based on **1,3,5-tri2CzPN** shows a sky-blue emission with CIE coordinates of (0.22, 0.44) and achieves an EQE_{max} of 7.4%. This work demonstrates that the multichromophore molecular design is a practical route to improve simultaneously the Φ_{PL} and RISC efficiency.

2.8 Experimental section

General consideration

All experiments were carried out with commercial solvents from Fisher Scientific Ltd, except where specifically mentioned. Commercially obtained chemicals were used as received. All manipulations were carried out under an inert atmosphere using standard Schlenk line techniques.

^{1}H NMR, and ^{13}C NMR were recorded at room temperature on a Bruker Avance spectrometer at 400 MHz and 100 MHz, respectively. ^{1}H NMR and ^{13}C NMR spectra were referenced to the residual solvent peaks ($CDCl_3$ = 7.26 ppm for ^{1}H NMR and 77.16 ppm for ^{13}C NMR). The

following abbreviations have been used for multiplicity assignments: “s” for singlet, “d” for doublet, “t” for triplet, “m” for multiplet and “br” for broad. Elemental analysis was measured by London Metropolitan University. Samples for high resolution mass spectrum (HRMS) were sent to the National Mass Spectrometry Facility in Swansea (EPSRC) for analysis by nano-electrospray on an Orbitrap instrument.

Materials and synthesis

Synthesis of 3-bromide-Carbazole (3-BrCz)

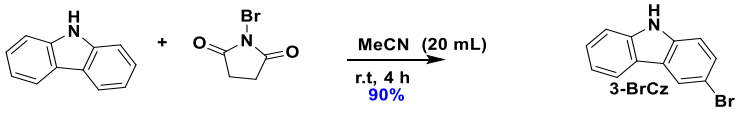

3-BrCz was synthesized according to the literature.[21] To a 250 mL flask, carbazole (1.7 g, 10 mmol, 1 equiv.) was dissolved in 10 mL of acetonitrile and cooled down in ice-water bath. The acetonitrile solution of *N*-bromosuccinimide (1.7 g, 11 mmol, 1.1 equiv.) was added into the carbazole solution dropwise. The mixture was stirred for 4 h at room temperature and washed with water and extracted with dichloromethane (DCM) three times (30 mL×3). The organic solvent was removed under reduced pressure. The crude product was recrystallized in DCM and hexane (1/20) to obtain **3-BrCz** as white solid powder.

Yield: 90%. $\mathbf{R_f}$ = 0.46 (20% DCM/Hexane). **Mp**: 195-197 °C (Lit. Mp.[21] 197-198 °C). **^{1}H NMR (400 MHz, $CDCl_3$) δ (ppm):** 11.43 (s, 1H), 8.36 (d, J=1.9 Hz, 1H), 8.16 (d, J=7.8 Hz, 1H), 7.56-7.37 (m, 4H), 7.24-7.09 (m, 1H). **^{13}C NMR (100 MHz, $CDCl_3$) δ (ppm):** 140.5, 138.7, 128.2, 126. 7, 124.7, 123.1, 121.8, 121.0, 119.3, 113.2, 111.5, 110.9. **LRMS** (ESI-MS) **[M-H]$^-$**

Calculated: ($C_{12}H_7{}^{79}BrN$) 245.98; **Found**: 246.08. The characterization matches that previously reported.[21]

Synthesis of 3-bromo-9-(triisopropylsilyl)-9*H*-carbazole (3-Br-tipsCz)

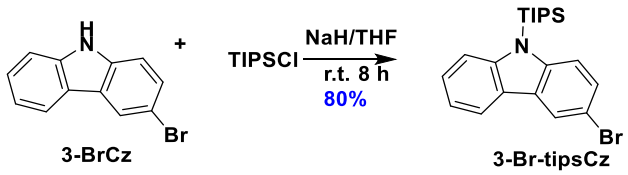

To a 250 mL flask, sodium hydride (500 mg, 12 mmol, 1.2 equiv.) was added and the flask was degassed by three cycles of vacuum-nitrogen purging. Then **3-BrCz** (2.5 g, 10 mmol, 1 equiv.) was dissolved in 20 mL of THF and added into the flask dropwise. After the mixture was stirred for 30 min in ice-water bath, chlorotriisopropylsilane (TIPSCl) (2.9 g, 15 mmol, 1.5 equiv.) dissolved in 20 mL of THF was added dropwise into the solution. The mixture was warmed up to room temperature and stirred for 8 h. A trace of water was injected to the mixture to quench the reaction. The mixture was washed with water and extracted with DCM three times (50 mL×3). The organic solvent was removed under reduced pressure and the crude product was purified by column chromatography. DCM/Hexane=1/10 was used as eluent to obtain **3-Br-tipsCz** as a white wax solid.

Yield: 80%. **R_f**: 0.66 (10% DCM/Hexane) **Mp:** 37-40 °C. **^{1}H NMR (400 MHz, $CDCl_3$) δ (ppm):** 8.19 (d, *J* = 2.2 Hz, 1H), 8.04 (d, *J* = 7.7 Hz, 1H), 7.71 (d, *J* = 8.5 Hz, 1H), 7.58 (dd, *J* = 9.0 Hz, 2.4Hz, 1H), 7.49 -7.40 (m, 2H), 7.28 -7.22 (m, 1H), 2.25 - 1.77 (m, 3H), 1.21 (d, *J* = 7.5 Hz, 18H). **^{13}C NMR (100 MHz, $CDCl_3$) δ (ppm):** 145.4, 143.7, 128.5, 127.8, 126.0, 125.4, 122.4, 119.9,

115.5, 114.2, 112.4, 18.6, 13.8. **HRMS** (LTQ Orbitrap XL) **[M+H]$^+$ Calculated: ($C_{21}H_{28}{}^{79}BrNSi$)** 402.1249; **Found**: 402.1247.

Synthesis of 3-(4,4,5,5-tetramethyl-1,3,2-dioxaborolan-2-yl)-9-(triisopropylsilyl)-9H-carbazole (3-Bpin-tipsCz)

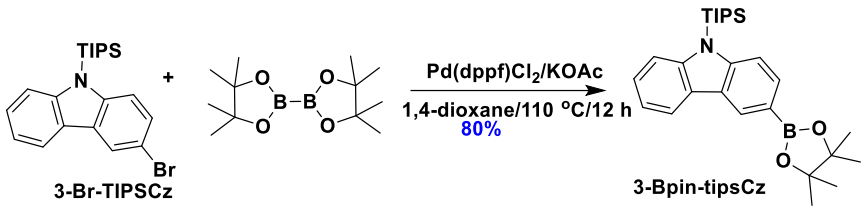

To a 100 mL flask were added **3-Br-tipsCz** (400 mg, 1 mmol, 1 equiv.), bis(pinacolato)diboron (300 mg, 1.2 mmol, 1.2 equiv.), 1,1′-bis(diphenyl-phosphino)ferrocene]dichloro palladium (II) (100 mg, 0.1 mmol, 0.1 equiv.), potassium acetate (990 mg, 10 mmol, 10 equiv.), and 20 mL of 1,4-dioxane. The mixture was degassed via three times of freeze-pump-thaw cycles and stirred at 110 °C for 12 h under nitrogen. The mixture was washed with water and extracted with DCM three times (50 mL ×3). The organic solvent was removed under reduced pressure and the crude product was purified by column chromatography. DCM/Hexane=1/3 was used as eluent to obtain **3-Bin-tipsCz** as a white solid.

Yield: 80%. **R_f**: 0.44 (25% DCM/Hexane) **Mp:** 51-53 °C. **^{1}H NMR (400 MHz, $CDCl_3$) δ (ppm):** 8.58 (s, 1H), 8.15 (d, J=2.2 Hz, 1H), 7.85 (dd, *J* = 8.4 Hz, 1.3 Hz, 1H), 7.71 (dd, *J* = 8.5 Hz, 4.1 Hz, 2H), 7.38 (dd, *J* = 8.5 Hz, 7.1 Hz, 1H), 7.28-7.23 (m, 1H), 2.02 (m, 3H), 1.21 (d, *J* = 7.5 Hz, 18H). **^{13}C NMR (100 MHz, $CDCl_3$) δ (ppm):** 147.4, 145.1, 132.3, 131.7, 127.8, 127.0, 125.3,

120.0, 114.0, 113.5, 110.6, 110.0, 24.9, 18.5, 13.8, 12.3. **HRMS** (LTQ Orbitrap XL) **[M+H]$^+$ Calculated: ($C_{27}H_{41}BNO_2Si$)** 450.2995; **Found**: 450.2995.

Synthesis of 1,4-bis(9-(triisopropylsilyl)-9*H*-carbazol-3-yl)benzene (para-2tipsCz)

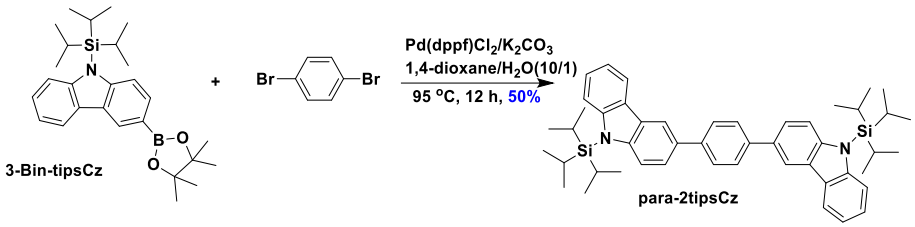

General procedure A

To a 100 mL flask were added **3-Bpin-tipsCz** (1.1 g, 2.5 mmol, 2.5 equiv.), 1,4-dibromonbenzene (235 mg, 1 mmol, 1 equiv.), 1,1′-bis(diphenyl-phosphino)ferrocene]dichloro palladium (II) (100 mg, 0.1 mmol, 0.1 equiv.), potassium carbonate (1.4 g, 10 mmol, 10 equiv.), 20 mL of 1,4-dioxane, and 2 mL of distilled water. The mixture was degassed via three freeze-pump-thaw cycles and stirred at 95 °C for 12 h under nitrogen. The mixture was washed with water and extracted with dichloromethane (DCM) three times (50 mL×3). The organic solvent was removed under reduced pressure and purified by column chromatography. DCM/Hexane=1:5 was used as eluent to obtain **para-2tipsCz** as a white solid.

Yield: 50%. **R_f**: 0.62 (20% DCM/Hexane). **Mp:** 78 °C-81 °C. **^{1}H NMR (400 MHz, *d*-DMSO) δ (ppm):** 8.54 (d, *J* = 1.8 Hz, 2H), 8.24 (dt, *J* = 7.8 Hz, 1.0 Hz, 2H), 7.90 (s, 4H), 7.79 (dd, *J* = 8.4 Hz, 1.8 Hz, 2H), 7.60 (d, *J* = 8.5 Hz, 2H), 7.56 - 7.49 (m, 2H), 7.42 (dd, *J* = 8.2 Hz, 1.2 Hz, 2H), 7.20 (dd, *J* = 8.0 Hz, 1.0 Hz, 2H), 2.72 (m, 6H), 1.55 (d, *J* = 7.5 Hz, 36H). **^{13}C NMR (100 MHz, *d*-DMSO) δ (ppm):** 140.7, 139.7, 131.0, 127.5, 126.2, 124.9, 123.6, 123.1, 121.0, 119.1, 118.5,

111.8, 111.6, 18.6, 13.8. **HRMS** (LTQ Orbitrap XL) **[M+H]$^+$ Calculated: ($C_{48}H_{61}N_2Si_2$)** 721.4361; **Found**: 721.4368.

Synthesis of 1,3-bis(9-(triisopropylsilyl)-9H-carbazol-3-yl)benzene (meta-2tipsCz)

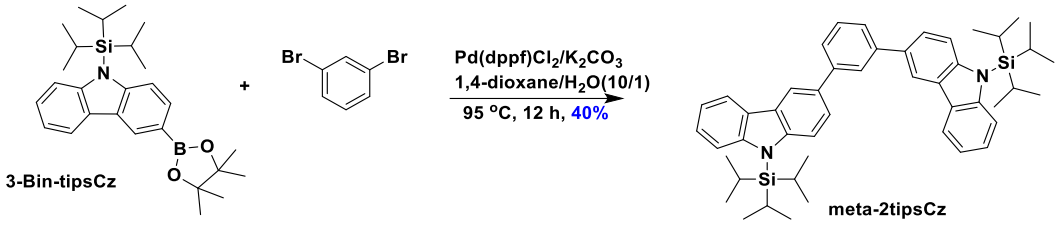

Synthesized as **General procedure A** to afford **meta-2tipsCz** as a white solid.

Yield: 40%. **R_f**: 0.62 (20% DCM/Hexane). **Mp:** 70 °C-73 °C. **^{1}H NMR (400 MHz, *d*-DMSO) δ (ppm):** 8.61 (d, *J* = 1.8 Hz, 2H), 8.29 (d, *J* = 7.8 Hz, 2H), 8.15 (t, *J* = 1.8 Hz, 1H), 7.86 (dd, *J* = 8.4 Hz, 1.8 Hz, 2H), 7.73 (dd, *J* = 7.7 Hz, 1.8 Hz, 2H), 7.66 - 7.56 (m, 3H), 7.55 - 7.48 (m, 2H), 7.42 (dd, *J* = 8.2 Hz, 1.2 Hz, 2H), 7.20 (dd, *J* = 7.9 Hz, 1.0 Hz, 2H), 2.72 (m, 6H), 1.55 (d, *J* = 7.5 Hz, 36H). **^{13}C NMR (100 MHz, d-DMSO) δ (ppm):** 143.3, 141.7, 139.9, 131.6, 129.9, 126.2, 125.6, 125.3, 123.6, 123.1, 121.1, 119.1, 118.6, 111.7, 111.5, 18.6, 13.8. **HRMS** (LTQ Orbitrap XL) **[M+H]$^+$ Calculated: ($C_{48}H_{61}N_2Si_2$)** 721.4361; **Found**: 721.4368.

Synthesis of 1,3,5-tris(9-(triisopropylsilyl)-9H-carbazol-3-yl)benzene (tri-3tipsCz)

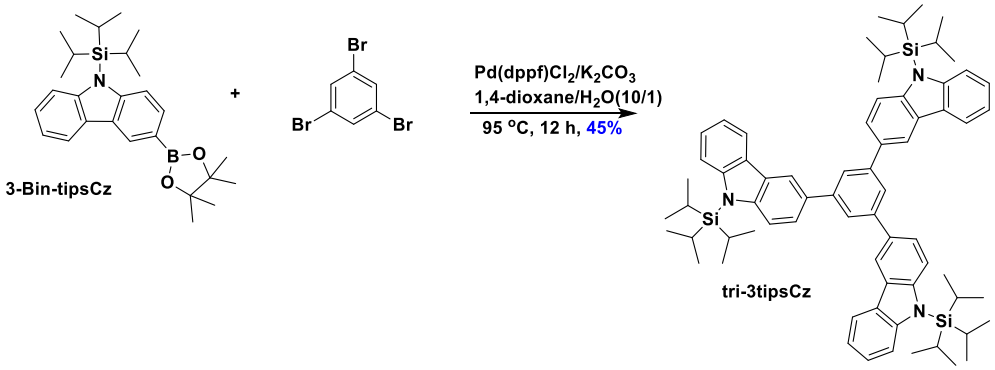

Synthesized as **General procedure A** to obtain **tri-3tipsCz** as a white solid.

Yield: 45%. $\mathbf{R_f}$: 0.60 (15 % DCM/Hexane). **Mp:** 86 ºC-88 ºC. **^{1}H NMR (400 MHz, *d*-DMSO) δ (ppm):** 8.75 (s, 3H), 8.35 (d, *J* = 7.8 Hz, 3H), 8.09 (s, 3H), 8.05 - 7.86 (m, 3H), 7.65 (d, *J* = 8.4 Hz, 3H), 7.54 (d, *J* = 8.1 Hz, 3H), 7.42 (t, *J* = 7.7 Hz, 3H), 7.21 (t, *J* = 7.5 Hz, 3H), 2.72 (m, 9H), 1.55 (d, *J* = 7.5 Hz, 54H). **^{13}C NMR (100 MHz, d-DMSO) δ (ppm):** 143.0, 140.7, 140.1, 131.9, 125.9, 123.6, 122.8, 121.2, 120.6, 119.4, 118.9, 111.7, 111.4, 18.6, 13.8. **HRMS** (LTQ Orbitrap XL) **[M+H]$^+$ Calculated: ($\mathbf{C_{69}H_{88}N_3Si_3}$)** 1042.6288; **Found**: 1042.6281.

Synthesis of 1,4-di(9H-carbazol-3-yl)benzene (para-2Cz)

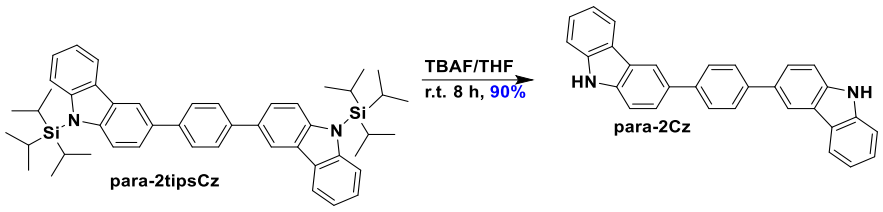

General procedure B

To a 100 mL flask was added tetrabutylammonium fluoride (TBAF) (600 mg, 2.5 mmol, 2,5 equiv.), and **para-2tipsCz** (720 mg, 1 mmol, 1 equiv.) in 10 mL of THF was slowly added and the mixture stirred at room temperature for 8 h. The reaction mixture was filtered, and the solvent removed under reduced pressure and purified by column chromatography. DCM/Hexane=1/1 was used as eluent to obtained **para-2Cz** as white solid.

Yield: 90%. $\mathbf{R_f}$: 0.55 (50% DCM/Hexane) **Mp:** 184 ºC-186 ºC. **^{1}H NMR (400 MHz, *d*-DMSO) δ (ppm):** 11.42 (s, 2H), 8.53 (d, *J* = 1.8 Hz, 2H), 8.25 (dt, *J* = 7.8 Hz, 1.0 Hz, 2H), 7.90 (s, 4H), 7.79 (dd, *J* = 8.4 Hz, 1.8 Hz, 2H), 7.60 (d, *J* = 8.5 Hz, 2H), 7.56 - 7.49 (m, 2H), 7.42 (dd, *J* = 8.2 Hz, 1.2 Hz, 2H), 7.20 (dd, *J* = 8.0 Hz, 1.0 Hz, 2H). **^{13}C NMR (100 MHz, *d*-DMSO) δ (ppm):**

140.7, 139.7, 131.0, 127.5, 126.2, 124.9, 123.6, 123.1, 121.0, 119.1, 118.5, 111.8, 111.6. **HRMS** (LTQ Orbitrap XL) **[M+H]$^+$ Calculated: ($C_{30}H_{21}N_2$)** 409.1699; **Found**: 409.1700.

Synthesis of 1,3-di(9H-carbazol-3-yl)benzene (meta-2Cz)

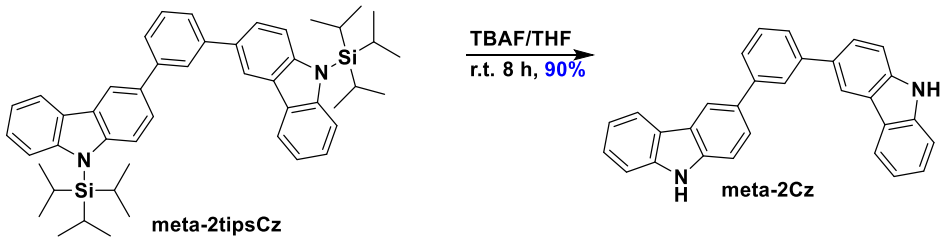

Synthesized as **General procedure B**. DCM/Hexane=1/1 was used as eluent to obtained meta-2Cz as white solid.

Yield: 90%. **R_f**: 0.61 (50% DCM/Hexane). **Mp:** 160 ºC-165 ºC. **^{1}H NMR (400 MHz, *d*-DMSO) δ (ppm):** 11.36 (s, 2H), 8.61 (d, *J* = 1.8 Hz, 2H), 8.29 (d, *J* = 7.8 Hz, 2H), 8.15 (t, *J* = 1.8 Hz, 1H), 7.86 (dd, *J* = 8.4 Hz, 1.8 Hz, 2H), 7.73 (dd, *J* = 7.7 Hz, 1.8 Hz, 2H), 7.66 - 7.56 (m, 3H), 7.55 - 7.48 (m, 2H), 7.42 (dd, *J* = 8.2 Hz, 1.2 Hz, 2H), 7.20 (dd, *J* = 7.9 Hz, 1.0 Hz, 2H). **^{13}C NMR (100 MHz, *d*-DMSO) δ (ppm):** 142.4, 140.7, 139.8, 131.6, 129.9, 126.2, 125.6, 125.3, 125.3, 123.6, 123.1, 121.1, 119.1, 118.6, 111.7, 111.5. **HRMS** (LTQ Orbitrap XL) **[M+H]$^+$ Calculated: ($C_{30}H_{21}N_2$)** 409.1699; **Found**: 409.1700.

Synthesis of 1,3,5-tri(9*H*-carbazol-3-yl)benzene (tri-3Cz)

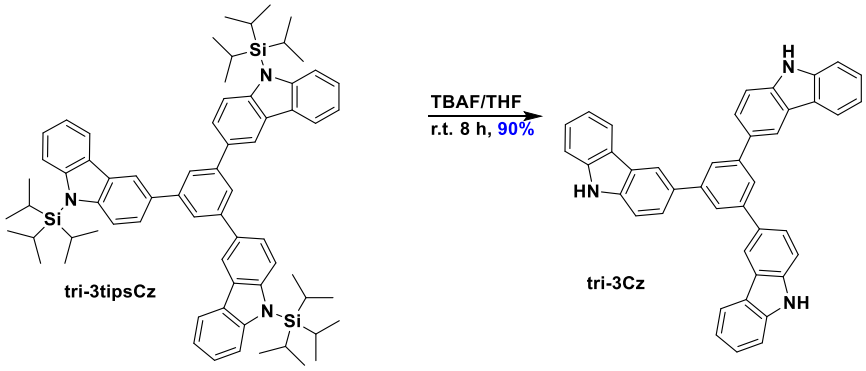

Synthesized as **General procedure B**. DCM/Hexane=1/1 was used as eluent to obtained **tri-3Cz** as white solid.

Yield: 90%. **R_f**: 0.46 (50% DCM/Hexane). **Mp:** 173 ºC-176 ºC. **^{1}H NMR (400 MHz, *d*-DMSO) δ (ppm):** 11.41 (s, 3H), 8.74 (s, 3H), 8.33 (d, *J* = 7.8 Hz, 3H), 8.09 (s, 3H), 8.05 - 7.86 (m, 3H), 7.65 (d, *J* = 8.4 Hz, 3H), 7.54 (d, *J* = 8.1 Hz, 3H), 7.42 (t, *J* = 7.7 Hz, 3H), 7.21 (t, *J* = 7.5 Hz, 3H). **^{13}C NMR (100 MHz, *d*-DMSO) δ (ppm):** 143.0, 140.7, 140.1, 131.9, 125.9, 123.6, 122.8, 121.2, 120.6, 119.4, 118.9, 111.7, 111.4. **HRMS** (LTQ Orbitrap XL) **$[M+H]^+$ Calculated: ($C_{30}H_{21}N_2$)** 574.2278; **Found**: 574.2271.

Synthesis of 4-(9H-carbazol-9-yl)-5-fluorophthalonitrile (CzFPN)

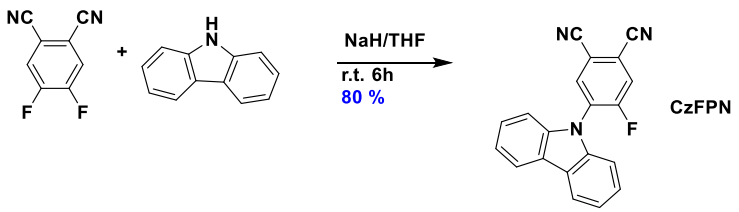

General procedure C

CzFPN was synthesized based on a modified literature protocol.[31] To a 100 mL of flask were added 4,5-difluorophthalonitrile (820 mg, 5.5 mmol, 1.1 equiv.) and sodium hydride (300 mg, 6 mmol, 1.2 equiv.), and the flask was degassed by three cycles of vacuum-nitrogen purging.

Carbazole (800 mg, 5 mmol, 1 equiv.) was dissolved in 20 mL of THF and added dropwise into the flask under ice-water bath. After bubbling ceased, the mixture was warmed to room temperature and stirred for 6 h. Afterwards, 1 mL of water was injected to quench the reaction. The mixture was washed with water and extracted with DCM three times (50 mL×3). The organic solvent was removed under reduced pressure and the crude product was purified by column chromatography. DCM/Hexane=1/3 was used as eluent to obtain **CzFPN** as light green solid.

Yield: 80%. **R_f**: 0.55 (50% DCM/Hexane). **Mp:** 221 °C-225 °C. **^{1}H NMR (400 MHz, $CDCl_3$) δ (ppm):** 8.23 - 8.08 (m, 3H), 7.87 (d, *J* = 9.0 Hz, 1H), 7.51 (dd, *J* = 8.3 Hz, 1.3 Hz, 2H), 7.41 (dd, *J* = 7.5, 1.0 Hz, 2H), 7.28 - 7.18 (m, 2H). **^{13}C NMR (100 MHz, $CDCl_3$) δ (ppm):** 160.7, 158.0, 139.4, 134.5, 131.5, 126.8, 124.5, 123.5, 123.3, 122.0, 120.8, 115.8, 114.0, 113.6. **HRMS** (LTQ Orbitrap XL) **$[M+H]^+$ Calculated: ($C_{20}H_{11}FN_3$)** 329.1197; **Found**: 329.1201.

Synthesis of 5,5'-(1,4-phenylenebis(9H-carbazole-3,9-diyl))bis(4-(9H-carbazol-9-yl) phthalonitrile) (*p*-di2CzPN)

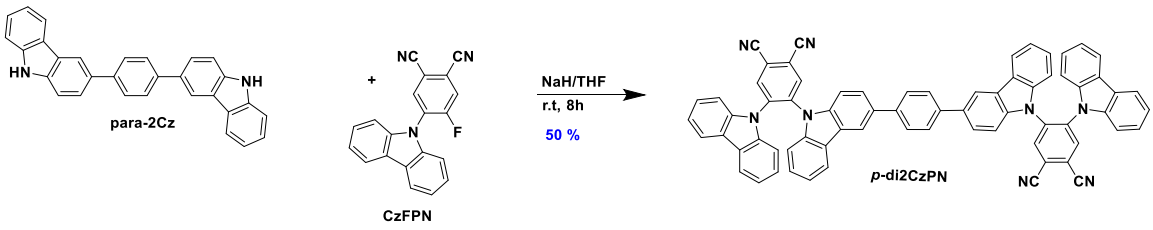

***p*-di2CzPN** was synthesized as **General procedure C**, DCM/Hexane=1/1 was used as eluent and recrystallized in DCM/methanol (1/10) to obtained ***p*-di2CzPN** as yellow solid.

Yield: 50%. **R_f** = 0.40 (60% DCM/Hexane). **Mp:** 278-283 °C. **^{1}H NMR (400 MHz, $CDCl_3$) δ (ppm):** 8.35 (d, *J* = 2.1 Hz, 4H), 8.05 (d, *J* = 1.7 Hz, 2H), 7.92 - 7.79 (m, 6H), 7.60 (s,4H), 7.35

(dd, *J* = 8.6, 1.8 Hz, 2H), 7.23 - 7.07 (m, 20H). **^{13}C NMR (100 MHz, $CDCl_3$) δ (ppm):** 139.6, 138.8, 138.4, 138.3, 137.8, 135.5, 135.4, 134.4, 127.4, 127.3, 126.5, 126.3, 125.4, 124.9, 124.4, 121.9, 121.7, 120.5, 118.6, 114.8, 114.5, 109.4, 109.2, 109.0. **HRMS** (LTQ Orbitrap XL) **$[M+NH_4]^+$ Calculated: ($C_{70}H_{42}N_9$)** 1008.3558; **Found**: 1008.3558. **Elemental analysis: Calced for $C_{70}H_{38}N_8$**: C, 84.83; H, 3.86; N, 11.31. Found: C, 84.95; H, 3.92; N, 11.20. **HPLC:** 15% H_2O/MeCN, 1.0 mL min^{-1}, 300 nm; tr (99.6 %) = 8.6 min.

Synthesis of 5,5'-(1,3-phenylenebis(9H-carbazole-3,9-diyl))bis(4-(9H-carbazol-9-yl) phthalonitrile) (*m*-di2CzPN)

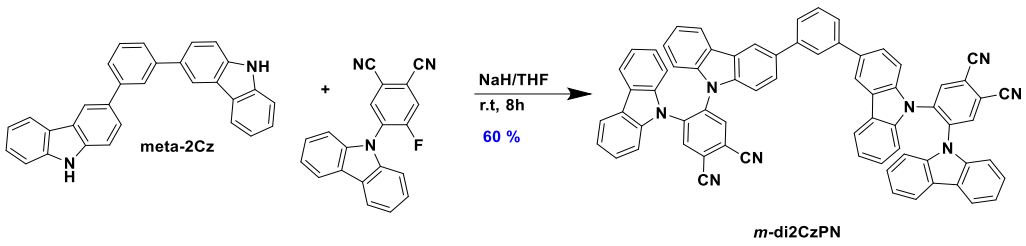

***m*-di2CzPN** was synthesized as **General procedure C** and obtained as yellow solid.

Yield: 60%. **R_f**: 0.41 (50% DCM/Hexane). **Mp:** 270-276 °C. **^{1}H NMR (400 MHz, $CDCl_3$) δ (ppm):** 8.37 (d, *J* = 3.6 Hz, 4H), 8.08 (s, 2H), 7.90 (d, *J* = 7.3 Hz, 2H), 7.84 (dd, *J* = 7.4 Hz, 3.5 Hz, 4H), 7.74 (s, 1H), 7.52 (d, *J* = 1.8 Hz, 3H), 7.37 (dd, *J* = 8.5 Hz, 1.7 Hz, 2H), 7.24 - 7.07 (m, 20H). **^{13}C NMR (100 MHz, $CDCl_3$) δ (ppm):** 141.7, 138.8, 138.5, 138.4, 138.3, 138.3, 137.8, 135.5, 135.4, 134.9, 129.3, 126.5, 126.3, 126.3, 125.8, 125.6, 124.9, 124.4, 124.2, 121.9, 121.7, 120.5, 119.0, 114.8, 114.8, 114.5, 109.4, 109.2, 109.0, 108.9. **HRMS** (LTQ Orbitrap XL) **$[M+H]^+$ Calculated: ($C_{70}H_{39}N_8$)** 991.3292; Found: 991.3296. **Elemental analysis: Calced for $C_{70}H_{38}N_8$**: C, 84.83; H, 3.86; N, 11.31. Found: C, 84.72; H, 3.92; N, 11.19. **HPLC:** 15% H_2O/MeCN, 1.0 mL min^{-1}, 300 nm; tr (99.2 %) = 7.9 min.

Synthesis of 5,5',5''-(benzene-1,3,5-triyltris(9H-carbazole-3,9-diyl))tris(4-(9H-carbazol-9-yl) phthalonitrile) (1,3,5-tri2CzPN)

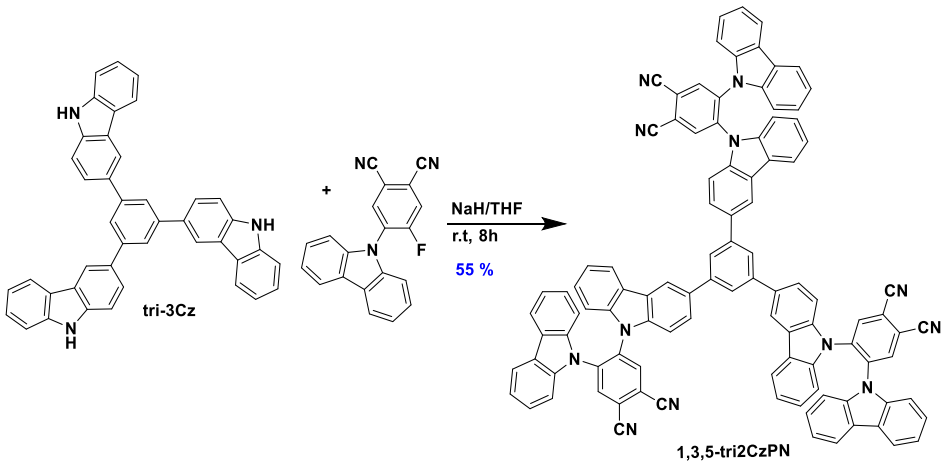

1,3,5-tri2CzPN was synthesized as **General procedure C** and obtained as yellow solid.

Yield: 55%. **R_f**: 0.38 (50% DCM/Hexane). **Mp:** 310-315 °C. **^{1}H NMR (400 MHz, $CDCl_3$) δ (ppm):** 8.38 (d, *J* = 4.0 Hz, 6H), 8.13 (d, *J* = 1.7 Hz, 3H), 7.97 - 7.90 (m, 3H), 7.87 - 7.82 (m, 6H), 7.69 (s, 3H), 7.43 (dd, *J* = 8.5 Hz, 1.5 Hz, 3H), 7.21 - 7.08 (m, 30H). **^{13}C NMR (100 MHz, $CDCl_3$) δ (ppm):** 142.3, 138.9, 138.4, 137.9, 135.5, 135.4, 134.8, 126.6, 126.4, 125.7, 124.9, 124.8, 124.4, 124.3, 121.9, 121.7, 120.6, 119.0, 114.9, 114.5, 109.5, 109.3, 109.1. **HRMS** (LTQ Orbitrap XL) **$[M+H]^+$ Calculated: ($C_{102}H_{55}N_{12}$)** 1447.4667; **Found**: 1447.4677. **Elemental analysis: Calced for $C_{102}H_{54}N_{12}$**: C, 84.63; H, 3.76; N, 11.61. Found: C, 84.59; H, 3.65; N, 11.72. **HPLC:** 10% H_2O/MeCN, 1.0 mL min^{-1}, 300 nm; tr (99.6 %) = 5.6 min.

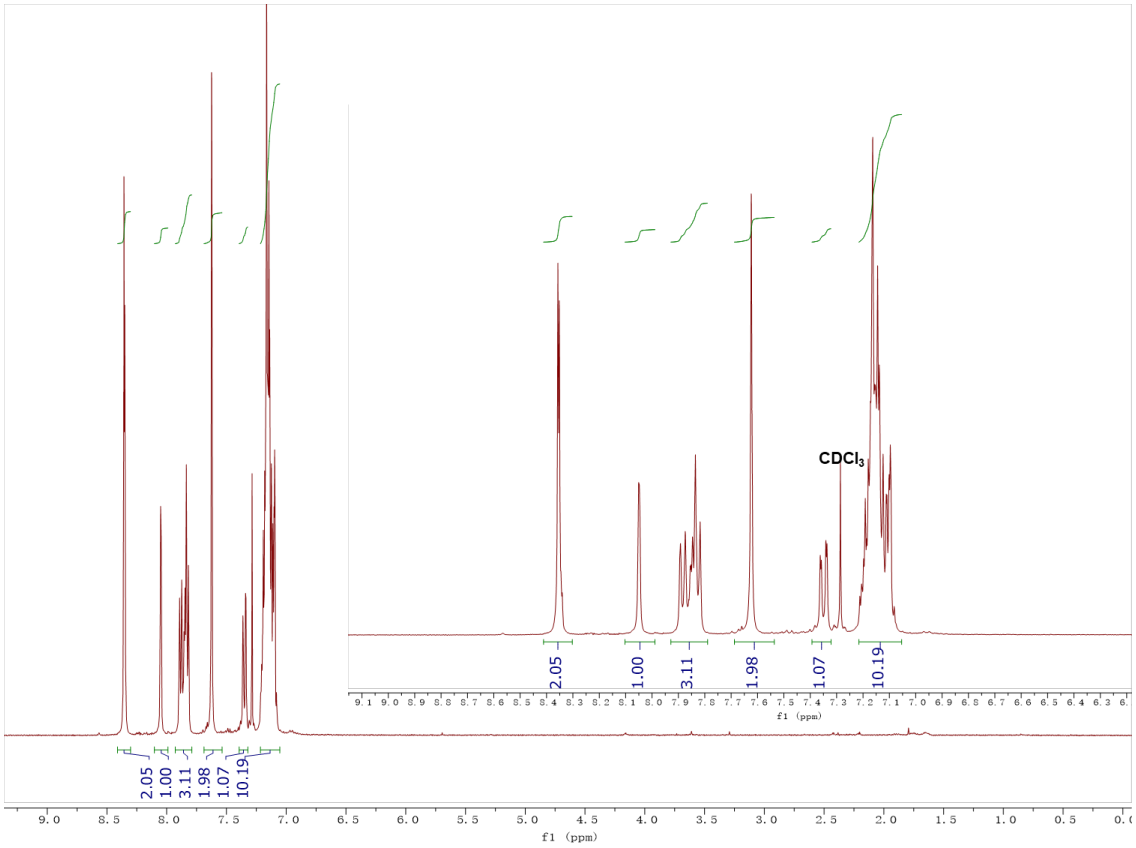

Figure **2.17**. ^{1}H NMR of ***p*-di2CzPN** in $CDCl_3$

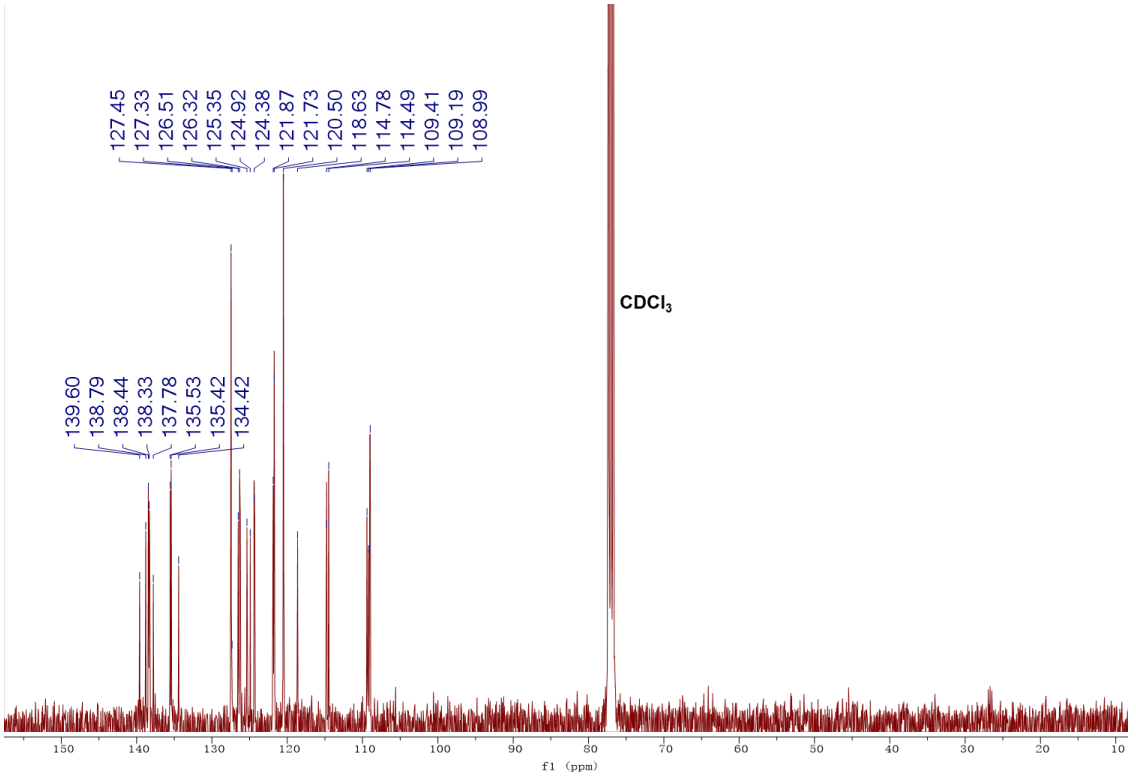

Figure **2.18**. ^{13}C NMR of ***p*-di2CzPN** in $CDCl_3$

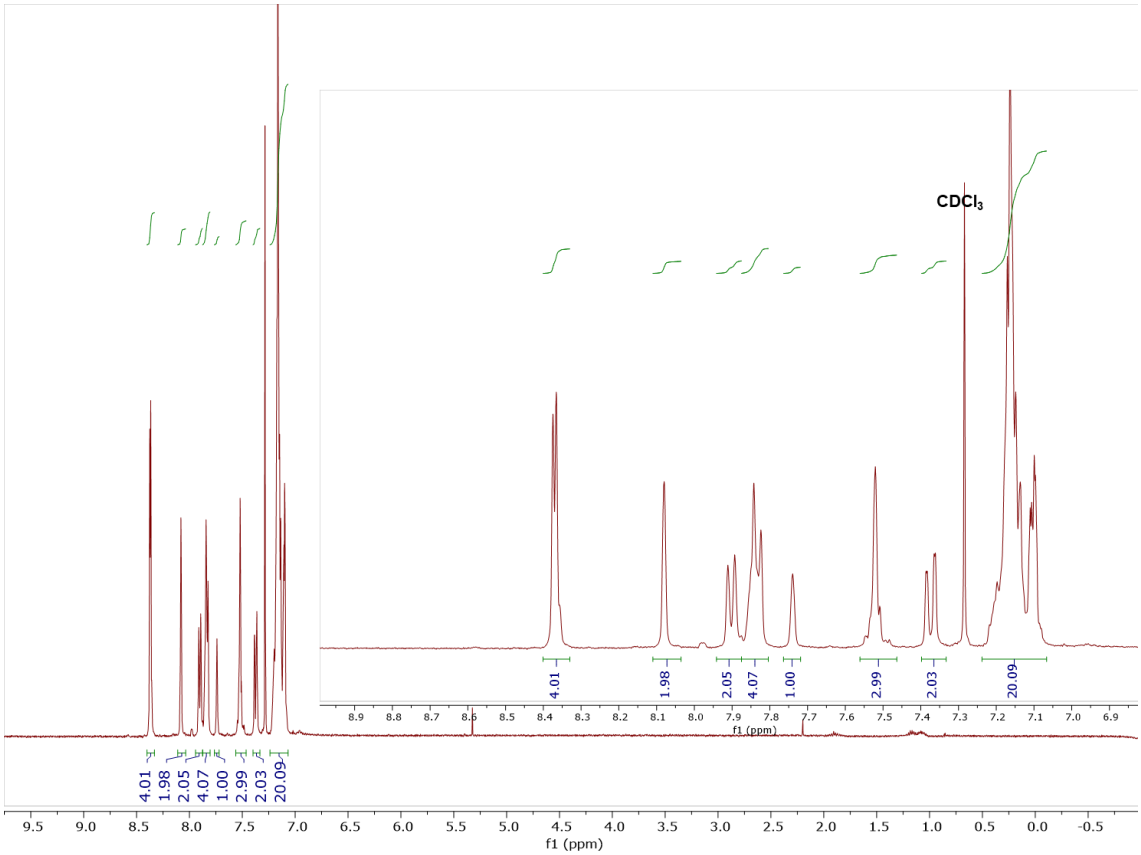

Figure **2.19**. ^{1}H NMR of ***m*-di2CzPN** in $CDCl_3$

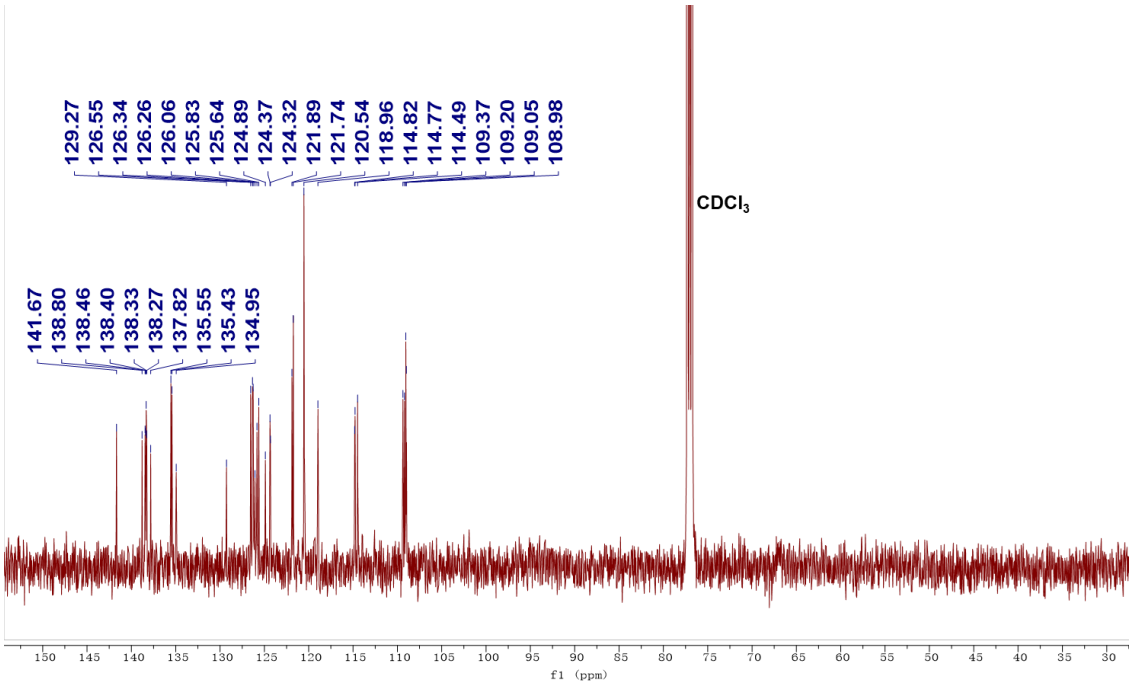

Figure **2.20**. ^{13}C NMR of ***m*-di2CzPN** in $CDCl_3$

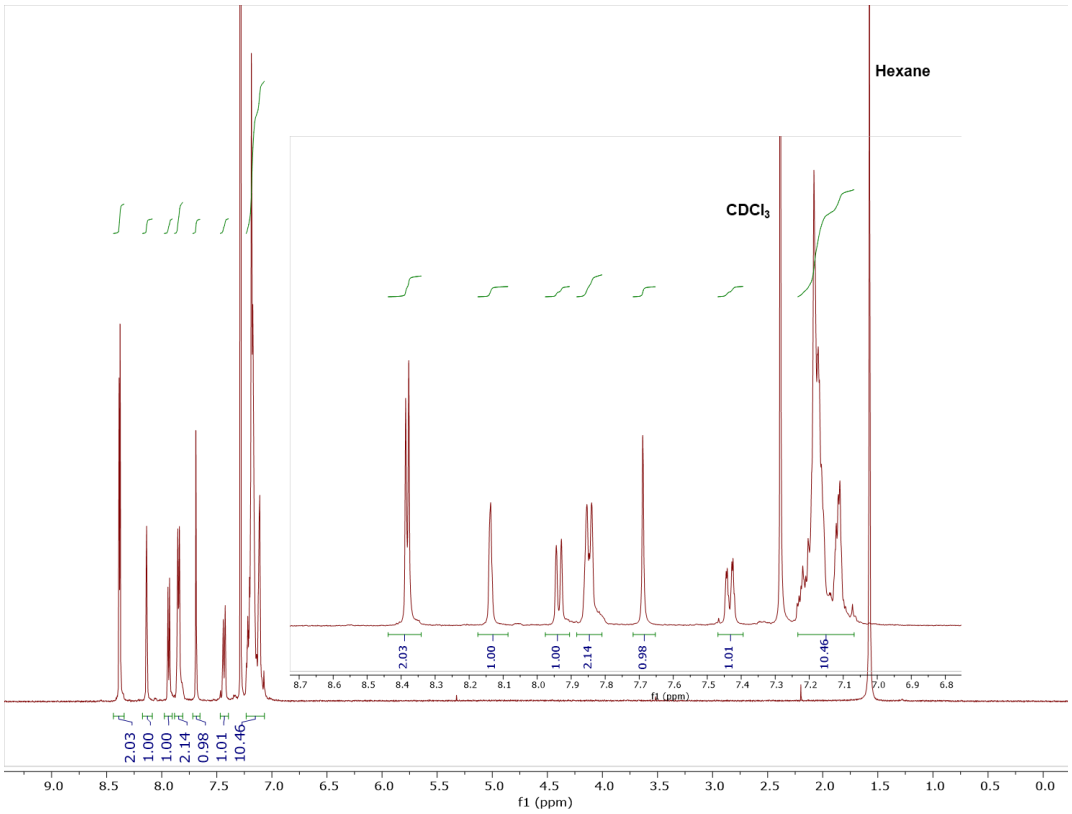

Figure **2.21**. ^{1}H NMR of **1,3,5-tri2CzPN** in $CDCl_3$

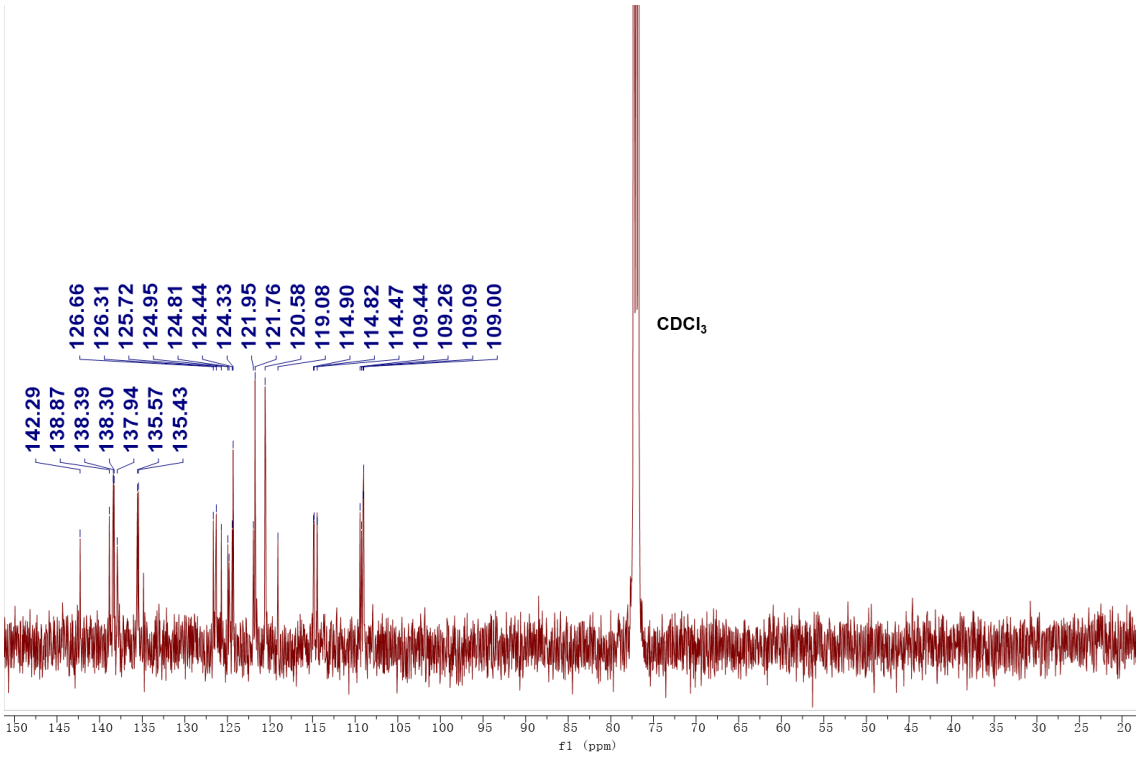

Figure **2.22**. ^{13}C NMR of **1,3,5-tri2CzPN** in $CDCl_3$

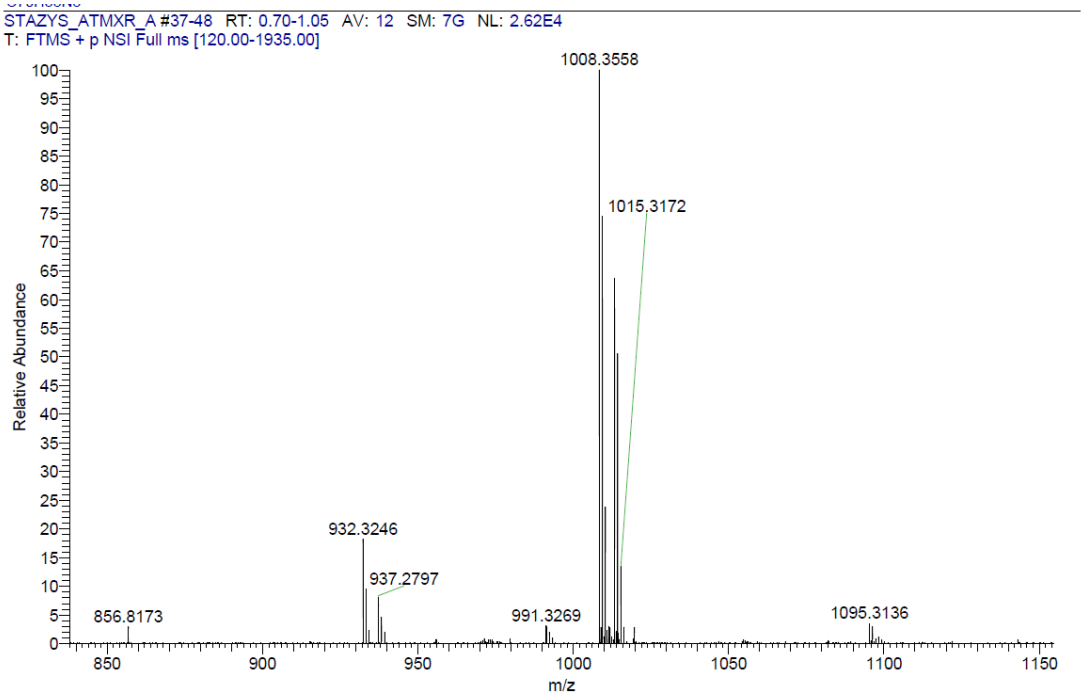

Figure **2.23**. HRMS of ***p*-di2CzPN**.

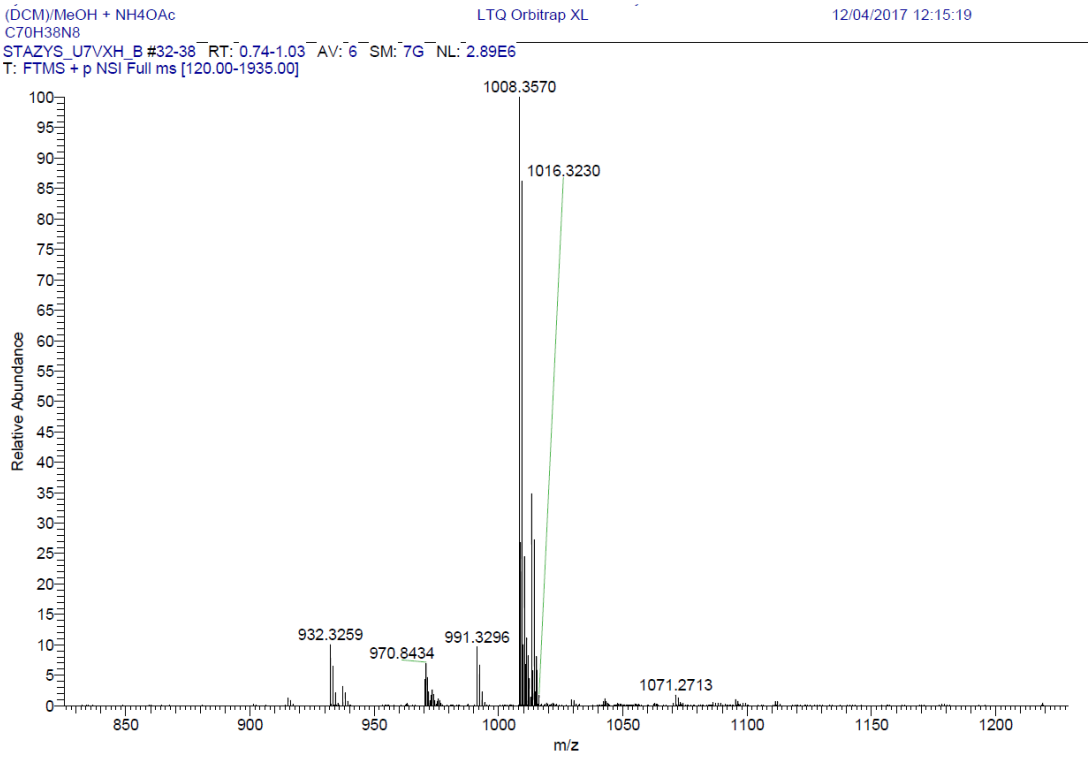

Figure **2.24**. HRMS of ***m*-di2CzPN**.

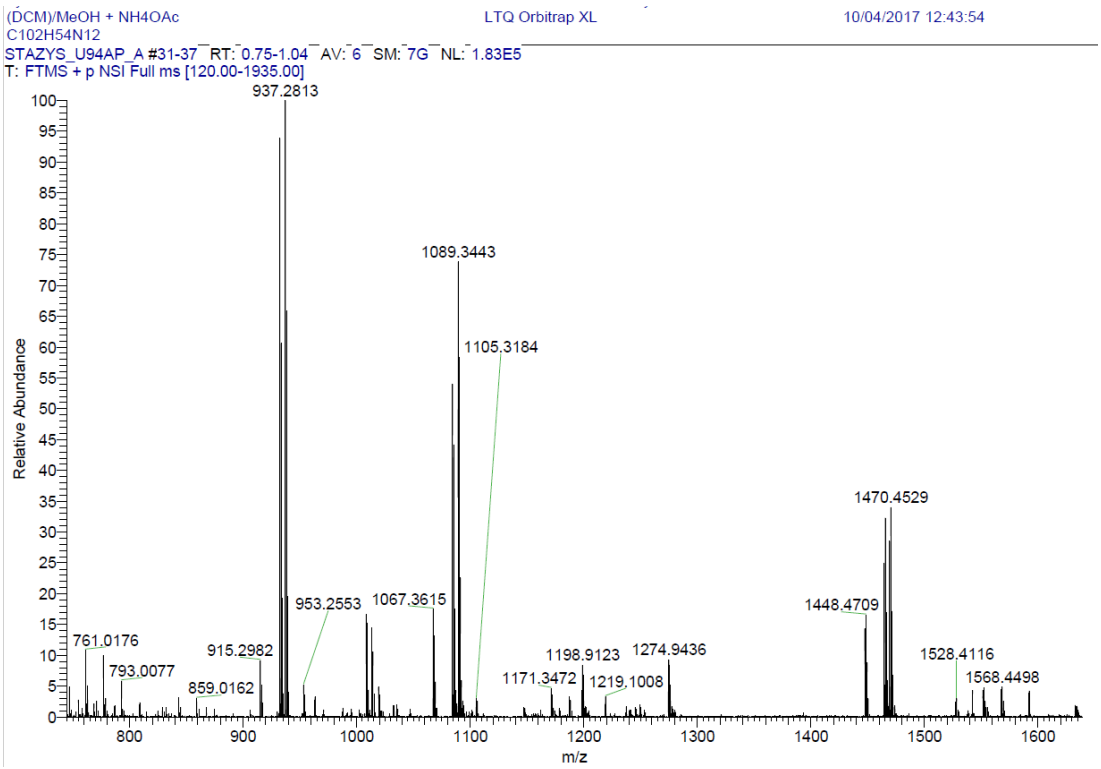

Figure **2.25**. HRMS of **1,3,5-tri2CzPN**.

LONDON metropolitan university

Elemental Analysis Service

Please send completed form and samples to:

Stephen Boyer
School of Human Sciences
Science Centre
London Metropolitan University
29 Hornsey Road
London N7 7DD

Telephone: 020 7133 3605
Fax: 020 7133 2577
Email: s.boyer@londonmet.ac.uk

Sample submitted by: Dongyang Chen
Address: **EZC group, School of Chemistry, University of St Andrews, North Haugh,St Andrews, Fife, KY16 9ST**
Telephone: 07743430420 Email: dc217@st-andrews.ac.uk
Date Submitted:09/05/2018

Please submit ca. 5 mg of sample.

Sample Reference No.: dc-para-2CzPN
Name of Compound: para-2CzPN
Molecular Formula: C70H38N8
Stability: Air stable
Hazards: none
Other Remarks:

Element	Expected %	Found (1)	Found (2)	
Carbon	84.83	84.01	84.95	
Hydrogen	3.86	4.00	4.00	
Nitrogen	11.31	11.11	11.18	

Authorising Signature:

Date Completed: 23/5/18	Signature:
Comments:	

Figure **2.26**. Elemental analysis of ***p*-di2CzPN**.

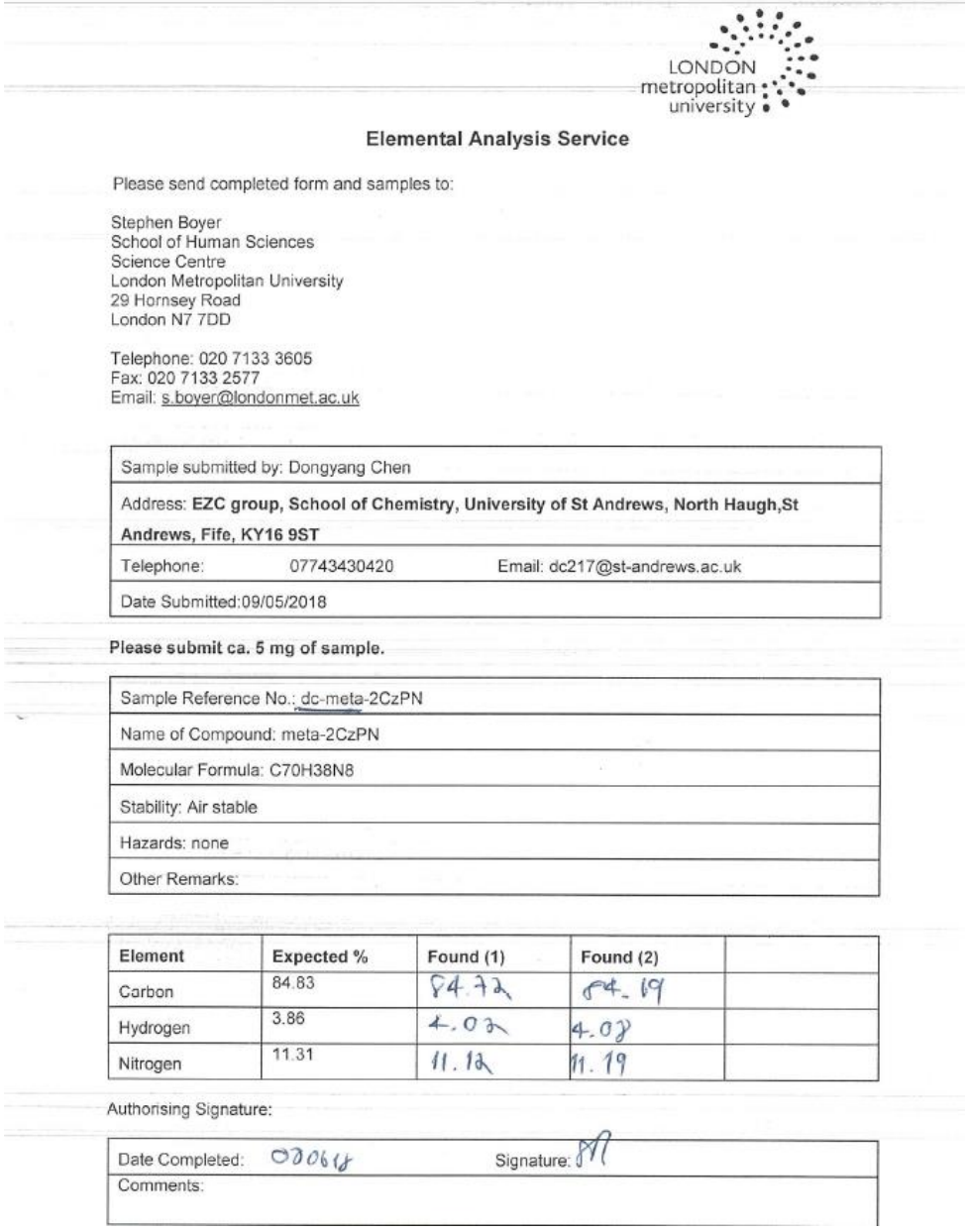

LONDON metropolitan university

Elemental Analysis Service

Please send completed form and samples to:

Stephen Boyer
School of Human Sciences
Science Centre
London Metropolitan University
29 Hornsey Road
London N7 7DD

Telephone: 020 7133 3605
Fax: 020 7133 2577
Email: s.boyer@londonmet.ac.uk

Sample submitted by: Dongyang Chen
Address: **EZC group, School of Chemistry, University of St Andrews, North Haugh,St Andrews, Fife, KY16 9ST**
Telephone: 07743430420 Email: dc217@st-andrews.ac.uk
Date Submitted:09/05/2018

Please submit ca. 5 mg of sample.

Sample Reference No.: dc-meta-2CzPN
Name of Compound: meta-2CzPN
Molecular Formula: C70H38N8
Stability: Air stable
Hazards: none
Other Remarks:

Element	Expected %	Found (1)	Found (2)	
Carbon	84.83	84.72	84.69	
Hydrogen	3.86	4.02	4.03	
Nitrogen	11.31	11.12	11.19	

Authorising Signature:

Date Completed: 030618	Signature:
Comments:	

Figure **2.27**. Elemental analysis of ***m*-di2CzPN**.

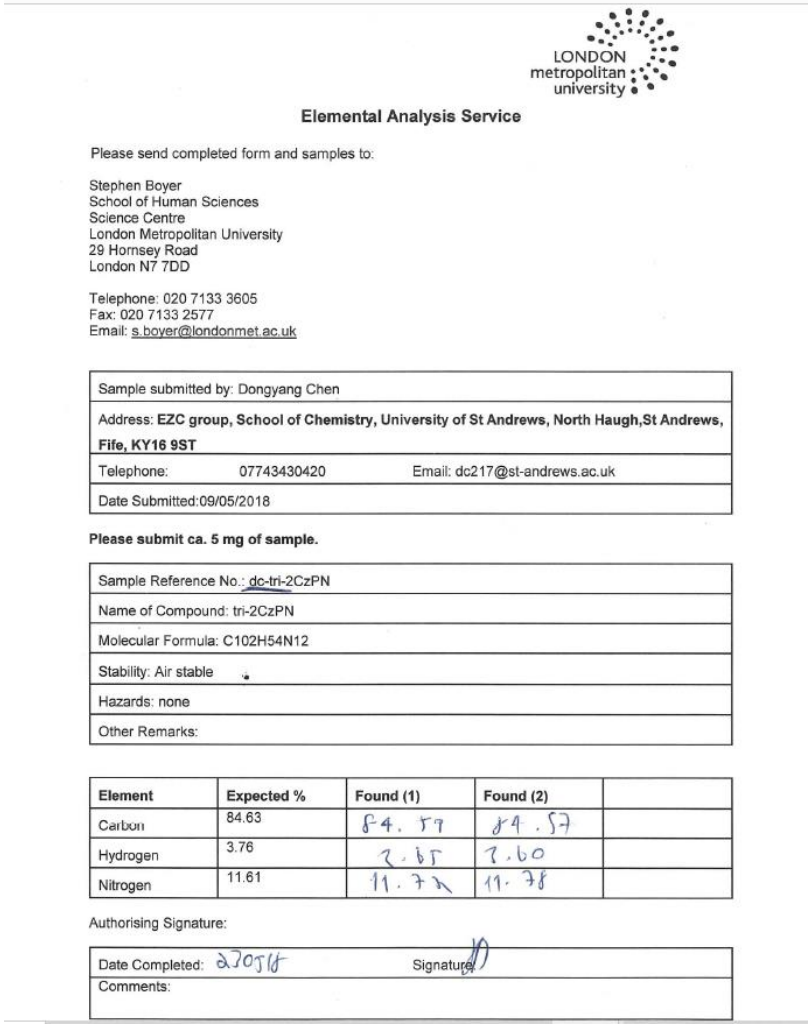

LONDON metropolitan university

Elemental Analysis Service

Please send completed form and samples to:

Stephen Boyer
School of Human Sciences
Science Centre
London Metropolitan University
29 Hornsey Road
London N7 7DD

Telephone: 020 7133 3605
Fax: 020 7133 2577
Email: s.boyer@londonmet.ac.uk

Sample submitted by: Dongyang Chen
Address: **EZC group, School of Chemistry, University of St Andrews, North Haugh,St Andrews, Fife, KY16 9ST**
Telephone: 07743430420 Email: dc217@st-andrews.ac.uk
Date Submitted:09/05/2018

Please submit ca. 5 mg of sample.

Sample Reference No.: dc-tri-2CzPN
Name of Compound: tri-2CzPN
Molecular Formula: C102H54N12
Stability: Air stable
Hazards: none
Other Remarks:

Element	Expected %	Found (1)	Found (2)	
Carbon	84.63	84.59	84.57	
Hydrogen	3.76	3.65	3.60	
Nitrogen	11.61	11.72	11.78	

Authorising Signature:

Date Completed: 21/05/18	Signature:
Comments:	

Figure **2.28**. Elemental analysis of **1,3,5-tri2CzPN**.

SHIMADZU LabSolutions **Analysis Report**

<Sample Information>

Sample Name	: dc-para-2CzPN		
Sample ID	: MeCN(85)		
Data Filename	: 25082018_MeCN(85)_dc-para-2CzPN.lcd		
Method Filename	: AcN(85).lcm		
Batch Filename	: dc-para-2CzPN MeCN(85).lcd		
Vial #	: 1-100	Sample Type	: Unknown
Injection Volume	: 5 uL		
Date Acquired	: 25/08/2018 18:32:55	Acquired by	: ezc-7
Date Processed	: 25/08/2018 19:02:56	Processed by	: ezc-7

<Chromatogram>

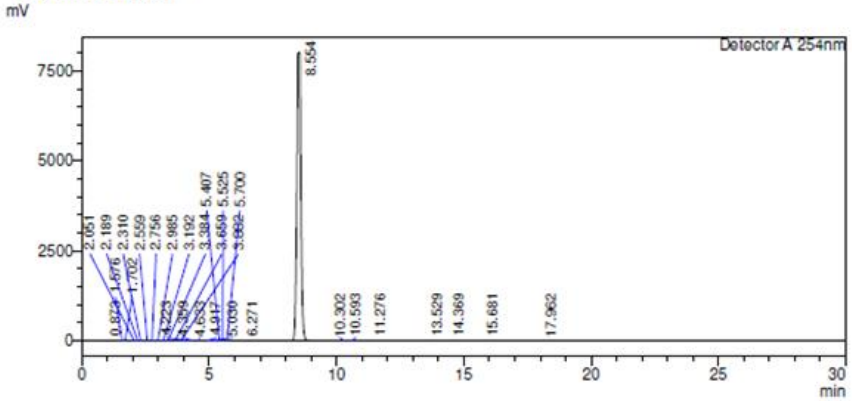

<Peak Table>

Detector A 254nm

Peak#	Ret. Time	Area	Height	Conc.	Unit	Area%
1	0.873	1008	154	0.000		0.001
2	1.576	31744	2832	0.000		0.035
3	1.702	23912	1980	0.000		0.027
4	2.051	22572	3362	0.000		0.025
5	2.189	8122	1375	0.000		0.009
6	2.310	7976	1083	0.000		0.009
7	2.559	25407	1820	0.000		0.028
8	2.756	11260	1409	0.000		0.013
9	2.985	19920	1401	0.000		0.022
10	3.192	20004	2073	0.000		0.022
11	3.384	19721	1900	0.000		0.022
12	3.659	13111	1203	0.000		0.015
13	3.882	14492	812	0.000		0.016
14	4.223	3439	504	0.000		0.004
15	4.359	5317	513	0.000		0.006
16	4.633	43495	5507	0.000		0.048
17	4.917	1432	208	0.000		0.002
18	5.030	2301	215	0.000		0.003
19	5.407	3625	310	0.000		0.004
20	5.525	2134	294	0.000		0.002
21	5.700	3411	332	0.000		0.004
22	6.271	26879	3088	0.000		0.030
23	8.554	89640784	8000043	0.000		99.587
24	10.302	7299	544	0.000		0.008
25	10.593	6280	484	0.000		0.007
26	11.276	2378	153	0.000		0.003
27	13.529	35630	2246	0.000		0.040
28	14.369	2736	159	0.000		0.003
29	15.681	1252	82	0.000		0.001
30	17.962	4950	273	0.000		0.005
Total		90012589	8036361			100.000

Figure **2.29**. HPLC report of ***p*-di2CzPN**.

SHIMADZU
LabSolutions **Analysis Report**

<Sample Information>

Sample Name	: Meta-2CzPN		
Sample ID	: Meta-2CzPN		
Data Filename	: 27042018__dc-meta-2CzPN		
Method Filename	: AcN (90).lcm		
Batch Filename	: meta-2CzPN 2		
Vial #	: 82	Sample Type	: Unknown
Injection Volume	: 10 uL		
Date Acquired	: 27/04/2018 20:34:45	Acquired by	: ezc-7
Date Processed	: 27/04/2018 21:04:48	Processed by	: ezc-7

<Chromatogram>

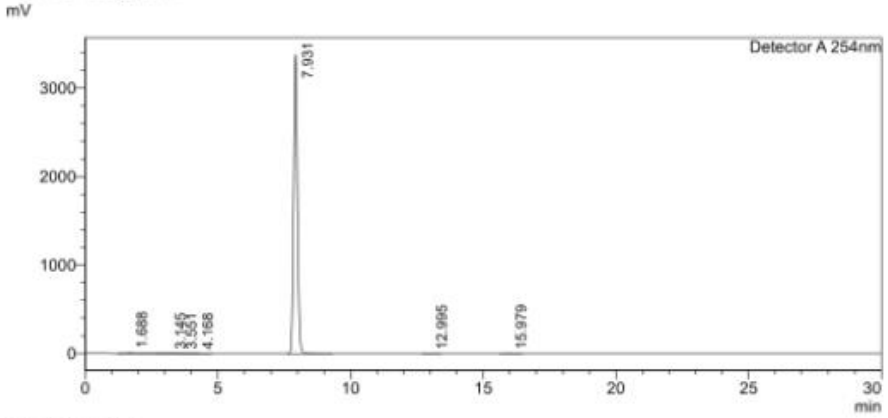

<Peak Table>

Detector A 254nm

Peak#	Ret. Time	Area	Height	Conc.	Unit	Mark	Area%
1	1.688	216630	17252	0.000		S	0.631
2	3.145	21343	715	0.000		TV	0.062
3	3.551	14944	532	0.000		TV	0.044
4	4.168	3361	391	0.000		TV	0.010
5	7.931	34069548	3381698	0.000			99.206
6	12.995	5712	399	0.000			0.017
7	15.979	10837	614	0.000			0.032
Total		34342375	3401602				100.000

Figure **2.30**. HPLC report of ***m*-di2CzPN**.

SHIMADZU LabSolutions **Analysis Report**

<Sample Information>

Sample Name	: dc-tri-2CzPN		
Sample ID	: MeCN(90)		
Data Filename	: 24082018_MeCN(90)_tri-2CzPN-S_003.lcd		
Method Filename	: AcN(90).lcm		
Batch Filename	: tri-2CzPN-MeCN(90).lcb		
Vial #	: 1-100	Sample Type	: Unknown
Injection Volume	: 5 uL		
Date Acquired	: 24/08/2018 20:21:10	Acquired by	: ezc-7
Date Processed	: 24/08/2018 20:52:23	Processed by	: ezc-7

<Chromatogram>

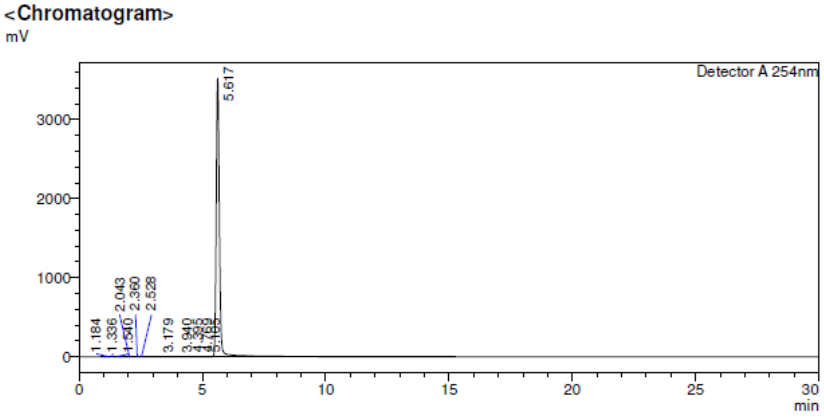

<Peak Table>

Detector A 254nm

Peak#	Ret. Time	Area	Height	Conc.	Unit	Area%
1	1.184	3608	346	0.000		0.011
2	1.336	3225	322	0.000		0.010
3	1.540	2329	349	0.000		0.007
4	2.043	12116	518	0.000		0.036
5	2.360	9047	630	0.000		0.027
6	2.528	21253	995	0.000		0.064
7	3.179	7566	541	0.000		0.023
8	3.940	33509	1326	0.000		0.101
9	4.395	19876	976	0.000		0.060
10	4.769	6875	566	0.000		0.021
11	5.105	10391	577	0.000		0.031
12	5.617	33170086	3523208	0.000		99.610
Total		33299881	3530354			100.000

Figure **2.31**. HPLC report of **1,3,5-tri2CzPN**.

Reference

(1) Zhang, Z.; Crovini, E.; dos Santos, P. L.; Naqvi, B. A.; Cordes, D. B.; Slawin, A. M. Z.; Sahay, P.; Brütting, W.; Samuel, I. D. W.; Bräse, S.; Zysman-Colman, E. Efficient Sky-Blue Organic Light-Emitting Diodes Using a Highly Horizontally Oriented Thermally Activated Delayed Fluorescence Emitter. *Adv. Opt. Mater.* **2020**, *8*, 2001354. https://doi.org/10.1002/adom.202001354.

(2) Chen, D. Y.; Liu, W.; Zheng, C. J.; Wang, K.; Li, F.; Tao, S. L.; Ou, X. M.; Zhang, X. H. Isomeric Thermally Activated Delayed Fluorescence Emitters for Color Purity-Improved Emission in Organic Light-Emitting Devices. *ACS Appl. Mater. Interfaces* **2016**, *8*, 16791–16798. https://doi.org/10.1021/acsami.6b03954.

(3) Dos Santos, P. L.; Chen, D.; Rajamalli, P.; Matulaitis, T.; Cordes, D. B.; Slawin, A. M. Z.; Jacquemin, D.; Zysman-Colman, E.; Samuel, I. D. W. Use of Pyrimidine and Pyrazine Bridges as a Design Strategy to Improve the Performance of Thermally Activated Delayed Fluorescence Organic Light Emitting Diodes. *ACS Appl. Mater. Interfaces* **2019**, *11*, 45171–45179. https://doi.org/10.1021/acsami.9b16952.

(4) Kaji, H.; Suzuki, H.; Fukushima, T.; Shizu, K.; Suzuki, K.; Kubo, S.; Komino, T.; Oiwa, H.; Suzuki, F.; Wakamiya, A.; Murata, Y.; Adachi, C. Purely Organic Electroluminescent Material Realizing 100% Conversion from Electricity to Light. *Nat. Commun.* **2015**, *6*, 9476. https://doi.org/10.1038/ncomms9476.

(5) Samanta, P. K.; Kim, D.; Coropceanu, V.; Brédas, J. L. Up-Conversion Intersystem Crossing Rates in Organic Emitters for Thermally Activated Delayed Fluorescence: Impact of the Nature of Singlet vs Triplet Excited States. *J. Am. Chem. Soc.* **2017**, *139*, 4042–4051. https://doi.org/10.1021/jacs.6b12124.

(6) Tsujimoto, H.; Ha, D.-G.; Markopoulos, G.; Chae, H. S.; Baldo, M. A.; Swager, T. M. Thermally Activated Delayed Fluorescence and Aggregation Induced Emission with Through-Space Charge Transfer. *J. Am. Chem. Soc.* **2017**, *139*, 4894–4900. https://doi.org/10.1021/jacs.7b00873.

(7) Wang, K.; Zheng, C. J.; Liu, W.; Liang, K.; Shi, Y. Z.; Tao, S. L.; Lee, C. S.; Ou, X. M.; Zhang, X. H. Avoiding Energy Loss on TADF Emitters: Controlling the Dual Conformations of D–A Structure Molecules Based on the Pseudoplanar Segments. *Adv. Mater.* **2017**, *29*, 1701476. https://doi.org/10.1002/adma.201701476.

(8) Rajamalli, P.; Senthilkumar, N.; Huang, P. Y.; Ren-Wu, C. C.; Lin, H. W.; Cheng, C. H. New Molecular Design Concurrently Providing Superior Pure Blue, Thermally Activated Delayed Fluorescence and Optical Out-Coupling Efficiencies. *J. Am. Chem. Soc.* **2017**, *139*, 10948–10951. https://doi.org/10.1021/jacs.7b03848.

(9) Hall, D.; Suresh, S. M.; dos Santos, P. L.; Duda, E.; Bagnich, S.; Pershin, A.; Rajamalli, P.; Cordes, D. B.; Slawin, A. M. Z.; Beljonne, D.; Köhler, A.; Samuel, I. D. W.; Olivier, Y.; Zysman-Colman, E. Improving Processability and Efficiency of Resonant TADF Emitters: A Design Strategy. *Adv. Opt. Mater.* **2020**, *8*, 1901627. https://doi.org/10.1002/adom.201901627.

(10) Cui, L.; Gillett, A. J.; Zhang, S.; Ye, H.; Liu, Y.; Chen, X.; Lin, Z.; Evans, E. W.; Myers, W. K.; Ronson, T. K.; Nakanotani, H.; Reineke, S.; Bredas, J.; Adachi, C.; Friend, R. H. Fast Spin-Flip Enables Efficient and Stable Organic Electroluminescence from Charge-Transfer States. *Nat. Photon.* **2020**, *14*, 636–642.

(11) Cho, Y. J.; Jeon, S. K.; Chin, B. D.; Yu, E.; Lee, J. Y. The Design of Dual Emitting Cores for Green Thermally Activated Delayed Fluorescent Materials. *Angew. Chemie Int. Ed.* **2015**, *54*, 5201–5204. https://doi.org/10.1002/anie.201412107.

(12) Kim, M.; Jeon, S. K.; Hwang, S. H.; Lee, S. S.; Yu, E.; Lee, J. Y. Highly Efficient and Color Tunable Thermally Activated Delayed Fluorescent Emitters Using a "Twin Emitter" Molecular Design. *Chem. Commun.* **2016**, *52*, 339–342. https://doi.org/10.1039/c5cc07999c.

(13) Cho, Y. J.; Jeon, S. K.; Lee, S. S.; Yu, E.; Lee, J. Y. Donor Interlocked Molecular Design for Fluorescence-like Narrow Emission in Deep Blue Thermally Activated Delayed Fluorescent Emitters. *Chem. Mater.* **2016**, *28*, 5400–5405. https://doi.org/10.1021/acs.chemmater.6b01484.

(14) Wei, D.; Ni, F.; Wu, Z.; Zhu, Z.; Zou, Y.; Zheng, K.; Chen, Z.; Ma, D.; Yang, C. Designing Dual Emitting Cores for Highly Efficient Thermally Activated Delayed Fluorescent Emitters. *J. Mater. Chem. C* **2018**, *6*, 11615–11621. https://doi.org/10.1039/c8tc02849d.

(15) Park, H.-J.; Han, S. H.; Lee, J. Y. A Directly Coupled Dual Emitting Core Based Molecular Design of Thermally Activated Delayed Fluorescent Emitters. *J. Mater. Chem. C* **2017**, *5*, 12143–12150. https://doi.org/10.1039/C7TC03133E.

(16) Cha, J. R.; Lee, C. W.; Lee, J. Y.; Gong, M. S. Design of Ortho-Linkage Carbazole-Triazine Structure for High-Efficiency Blue Thermally Activated Delayed Fluorescent Emitters. *Dye. Pigment.* **2016**, *134*, 562–568. https://doi.org/10.1016/j.dyepig.2016.08.023.

(17) Park, S. Y.; Choi, S.; Park, G. E.; Kim, H. J.; Lee, C.; Moon, J. S.; Kim, S. W.; Park, S.; Kwon, J. H.; Cho, M. J.; Choi, D. H. Unconventional Three-Armed Luminogens Exhibiting Both Aggregation-Induced Emission and Thermally Activated Delayed Fluorescence Resulting in High-Performing Solution-Processed OLEDs. *ACS Appl. Mater. Interfaces* **2018**, *10*, 14966–14977. https://doi.org/10.1021/acsami.7b19681.

(18) Noda, H.; Chen, X.; Nakanotani, H.; Hosokai, T.; Miyajima, M.; Notsuka, N.; Kashima, Y.; Brédas, J.; Adachi, C. Critical Role of Intermediate Electronic States for Spin-Flip Processes in Charge-Transfer-Type Organic Molecules with Multiple Donors and Acceptors. *Nat. Mater.* **2019**, *18*, 1084–1090. https://doi.org/10.1038/s41563-019-0465-6.

(19) Zhang, D.; Cai, M.; Zhang, Y.; Zhang, D.; Duan, L. Materials Horizons Sterically Shielded Blue Thermally Activated Delayed Fluorescence Emitters with Improved Efficiency and Stability. *Mater. Horiz.* **2016**, *3*, 145–151. https://doi.org/10.1039/c5mh00258c.

(20) Zysman-Colman, E.; Arias, K.; Siegel, J. S. Synthesis of Arylbromides from Arenes and Nbromosuccinimide Bromosuccinimide (NBS) in Acetonitrile - A Convenient Method for Aromatic Bromination. *Can. J. Chem.* **2009**, *87*, 440–447. https://doi.org/10.1139/V08-176.

(21) Wong, M. Y.; La-Placa, M.-G.; Pertegas, A.; Bolink, H. J.; Zysman-Colman, E. Deep-Blue Thermally Activated Delayed Fluorescence (TADF) Emitters for Light-Emitting

Electrochemical Cells (LEECs). *J. Mater. Chem. C* **2017**, *5*, 1699–1705. https://doi.org/10.1039/C6TC04821H.

(22) Chen, B.; Ding, J.; Wang, L.; Jing, X.; Wang, F. A Solution-Processable Phosphonate Functionalized Deep-Blue Fluorescent Emitter for Efficient Single-Layer Small Molecule Organic Light-Emitting Diodes. *Chem. Commun.* **2012**, *48*, 8970–8972. https://doi.org/10.1039/c2cc34712a.

(23) Ishiyama, T.; Murata, M.; Miyaura, N. Palladium(0)-Catalyzed Cross-Coupling Reaction of Alkoxydiboron with Haloarenes: A Direct Procedure for Arylboronic Esters. *J. Org. Chem.* **1995**, *60*, 7508–7510. https://doi.org/10.1021/jo00128a024.

(24) Pople, J. A.; Binkley, J. S.; Seeger, R. Theoretical Models Incorporating Electron Correlation. *Int. J. Quantum Chem.* **1976**, *10*, 1–19. https://doi.org/10.1002/qua.560100802.

(25) Adamo, C.; Barone, V. Toward Reliable Density Functional Methods without Adjustable Parameters: The PBE0 Model. *J. Chem. Phys.* **1999**, *110*, 6158–6170. https://doi.org/10.1063/1.478522.

(26) Moral, M.; Muccioli, L.; Son, W. J.; Olivier, Y.; Sancho-Garcia, J. C. Theoretical Rationalization of the Singlet-Triplet Gap in Oleds Materials: Impact of Charge-Transfer Character. *J. Chem. Theory Comput.* **2015**, *11*, 168–177. https://doi.org/10.1021/ct500957s.

(27) Pavlishchuk, V. V.; Addison, A. W. Conversion Constants for Redox Potentials Measured versus Different Reference Electrodes in Acetonitrile Solutions at 25°C. *Inorganica Chim. Acta* **2000**, *298*, 97–102. https://doi.org/10.1016/S0020-1693(99)00407-7.

(28) Wong, M. Y.; Krotkus, S.; Copley, G.; Li, W.; Murawski, C.; Hall, D.; Hedley, G. J.; Jaricot, M.; Cordes, D. B.; Slawin, A. M. Z.; Olivier, Y.; Beljonne, D.; Muccioli, L.; Moral, M.; Sancho-Garcia, J.-C.; Gather, M. C.; Samuel, I. D. W.; Zysman-Colman, E. Deep-Blue Oxadiazole-Containing Thermally Activated Delayed Fluorescence Emitters for Organic Light-Emitting Diodes. *ACS Appl. Mater. Interfaces* **2018**, *10*, 33360–33372. https://doi.org/10.1021/acsami.8b11136.

(29) Wang, X.; Yan, Q.; Chu, P.; Luo, Y.; Zhang, Z.; Wu, S.; Wang, L.; Zhang, Q. Analysis on Fluorescence of Dual Excitable Eu(TTA)3DPBT in Toluene Solution and PMMA. *J. Lumin.* **2011**, *131*, 1719–1723. https://doi.org/10.1016/j.jlumin.2011.03.061.

(30) dos Santos, P. L.; Ward, J. S.; Congrave, D. G.; Batsanov, A. S.; Stacey, J. E.; Penfold, T. J.; Monkman, A. P.; Bryce, M. R. Triazatruxene: A Rigid Central Donor Unit for a D-A3 Thermally Activated Delayed Fluorescence Material Exhibiting Sub-Microsecond Reverse Intersystem Crossing and Unity Quantum Yield via Multiple Singlet-Triplet State Pairs. *Adv. Sci.* **2018**, *5*, 1700989. https://doi.org/10.1002/advs.201700989.

(31) Uoyama, H.; Goushi, K.; Shizu, K.; Nomura, H.; Adachi, C. Highly Efficient Organic Light-Emitting Diodes from Delayed Fluorescence. *Nature* **2012**, *492*, 234–238.

Chapter 3

The use of Nitrogen-Heteroaromatic Bridges as a Design Strategy to Improve the Performance of Thermally Activated Delayed Fluorescence Organic Light Emitting Diodes

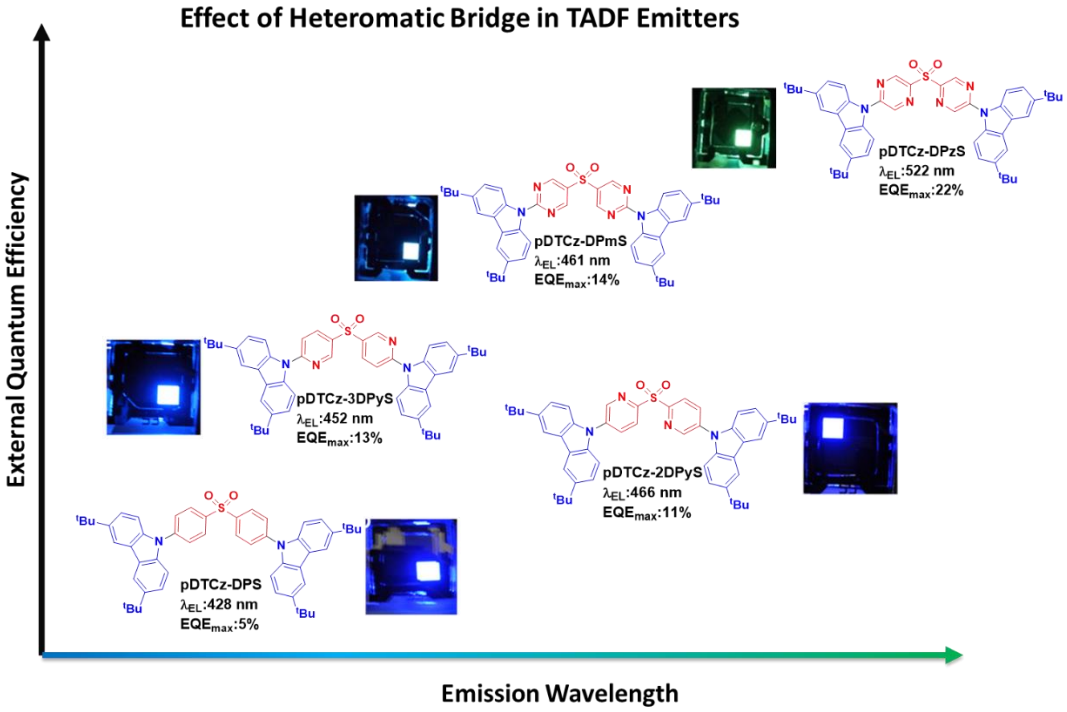

The work presented in this Chapter has been published as:

Pachaiyappan Rajamalli,[a]* Dongyang Chen,[a] Wenbo Li,[b] Ifor D.W. Samuel,[b] and Eli Zysman-Colman[a]* *J. Mater. Chem. C*, **2019**, *7*, 6664-6671. **DOI:** 10.1039/C9TC01498E

Paloma L. dos Santos,[b] Dongyang Chen,[a] Pachaiyappan Rajamalli,[a] Tomas Matulaitis,[a] David B. Cordes,[a] Alexandra M. Z. Slawin,[a] Denis Jacquemin,[c] Eli Zysman-Colman,[a]* and Ifor D. W. Samuel[b]* *ACS Appl. Mater. Interfaces*, **2019**, *11*, 45171-45179. **DOI:** 10.1021/acsami.9b16952

Collaborators in this Chapter are from:

[a] Organic Semiconductor Centre, EaStCHEM School of Chemistry, University of St Andrews, St Andrews, Fife KY16 9ST, UK

[b] Organic Semiconductor Centre, SUPA, School of Physics and Astronomy, University of St Andrews, St Andrews, Fife KY16 9SS, UK

[c] CEISAM, UMR-CNRS 6230, University of Nantes, 2 rue de la Houssinière, 44322 Nantes, France

The molecular design of the four emitters in this Chapter is the result of discussions with Dr. Pachaiyappan Rajamalli.

Dr. Pachaiyappan Rajamalli carried out the solid-state photophysics measurements and device fabrication of **pDTCz-2DPyS** and **pDTCz-3DPyS**.

Dr. Paloma L. dos Santos and Dr. Tomas Matulaitis carried out the solid-state photophysics measurements of **pDTCz-DPmS** and **pDTCz-DPzS**, and the devices were fabricated by Dr. Paloma L. dos Santos.

I completed all of the synthesis and characterization, DFT and TD-DFT calculations presented in this chapter, electrochemistry, photophysics in solutions and contributed to the paper writing.

3.1 Introduction

A major challenge in OLEDs is the development of bright and stable blue devices that satisfy the color purity requirements that the industry imposes for high-definition displays. For example, the NTSC states blue devices should CIE coordinates of (0.14, 0.08). It is particularly challenging to generate highly emissive and stable blue OLEDs for several reasons, including the difficulty to inject charges into the emitter due to its wide electrochemical gap, and emitter degradation resulting from bond dissociation energies of the emitter that are on the same order as its emissive state energy.[1,2] Presently, a huge focus on TADF research has been devoted towards designing blue emitters, and there exist several reports of devices showing an EQE_{max} exceeding 20% and suppressed efficiency roll-off.[3–5] However, further optimization of their molecular design and the corresponding device performance is required to improve the efficiency roll-off to make them attractive to industry, allowing them to replace the presently used fluorescent blue emitters in commercialized OLEDs. A design strategy that employs rigid donor-acceptor structures with intramolecular hydrogen-bonding is an attractive way to achieve efficient, deep blue-emitting TADF-based OLEDs. Previous work by Su *et al.*[6] and Cheng *et al.*[7] have shown that the incorporation of intramolecular hydrogen bonding within TADF emitters significantly enhances the intramolecular charge transfer strength while reducing the donor–acceptor (D-A) dihedral angle, resulting in accelerated radiative and suppressed nonradiative decay processes.[6,7]

To address the challenge of deep blue TADF emitters, we modified a benchmark blue TADF emitter **pDTCz-DPS** (originally reported as **tCz-DPS**) and using heteroaromatic rings as bridging units to construct rigid donor-acceptor structures. The choice of DTCz as the donor

resulted from a recognition that the *tert*-butyl groups protected the reactive 3- and 6-positions of the carbazole, thereby improving both the chemical and electrochemical stability as well as enhancing the Φ_{PL}.[8] Two emitters based on pyridinyl sulfone, 9,9'-(sulfonylbis(pyridine-6,3-diyl))bis(3,6-di-*tert*-butyl-9H-carbazole) (**pDTCz-2DPyS**) and 9,9'-(sulfonylbis(pyridine-5,2-diyl))bis(3,6-di-tert-butyl-9H-carbazole) (**pDTCz-3DPyS**) (Figure **3.1**), differ only in the regiochemistry of the substitution about the pyridine ring. In **pDTCz-3DPyS** the DTCz is attached to the 2-position of the pyridine ring thereby permitting intramolecular hydrogen-bonding between the donor and pyridine unit. On the other hand, in **pDTCz-2DPyS** the DTCz is connected to the 3- position of the pyridine ring and thus no hydrogen-bonding between the donor and acceptor is possible. We further extend this concept by exploring the impact of pyrimidine and pyrazine bridges in DTCz-sulfone containing D-A-D emitters. Two isomeric emitters, 9,9'-(sulfonylbis(pyrimidine-5,2-diyl))bis(3,6-di-*tert*-butyl-9H-carbazole) (**pDTCz-DPmS**) and 9,9'-(sulfonylbis(pyrazine-5,2-diyl))bis(3,6-di-*tert*-butyl-9H-carbazole) (**pDTCz-DPzS**) (Figure **3.1**) are synthesized and investigated.

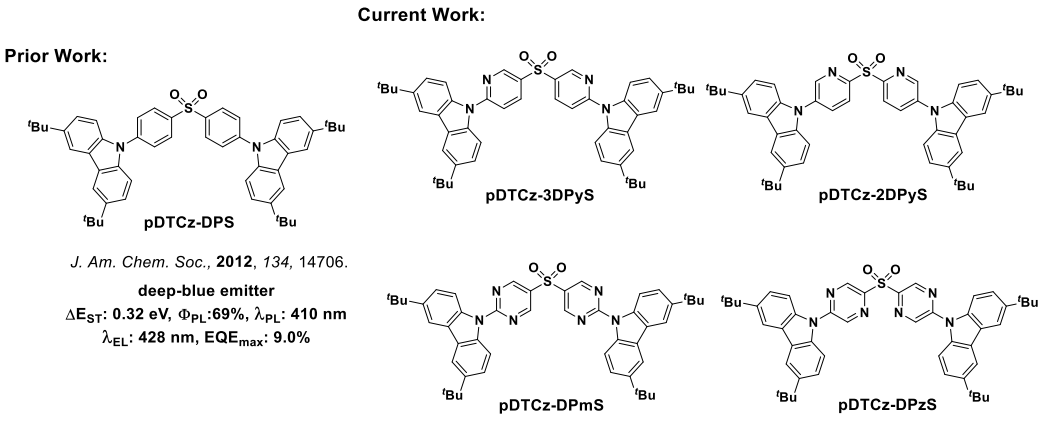

Figure **3.1**. Chemical structures of **pDTCz-3DPyS**, **pDTCz-2DPyS**, **pDTCz-DPmS**, **pDTCz-DPzS**, and reference emitter **pDTCz-DPS**.

Our systematic work showed that the presence/absence of H-bonding directly influences the performance of these four emitters and is contrasted to the previously reported state-of-the-art deep blue TADF emitter **pDTCz-DPS**. The pyridine bridged emitters show blue emission with λ_{PL} = 443 nm in toluene. Both emitters exhibited decreased ΔE_{ST} gaps (ΔE_{ST} = 0.21 eV and 0.22 eV for **pDTCz-3DPyS** and **pDTCz-2DPyS**, respectively) and improved Φ_{PL} values (81% and 72% for **pDTCz-3DPyS** and **pDTCz-2DPyS**, respectively) in 10 wt% doped DPEPO compared to reference emitter **pDTCz-DPS** (ΔE_{ST} = 0.27 eV and Φ_{PL}= 66%) under the same conditions. Pleasantly, OLEDs with both pyridinyl sulfone-based compounds show good performance, with EQE_{max} of 13.4% and 11.4% for the devices with **pDTCz-3DPyS** and **pDTCz-2DPyS**, respectively, compared to 4.6% for **pDTCz-DPS**, using the same device configuration. In addition, **pDTCz-3DPyS** shows pure blue electroluminescence with CIE coordinates of (0.15, 0.12) compared to **pDTCz-2DPyS** with coordinates of (0.15, 0.19). For **pDTCz-DPmS** and **pDTCz-DPzS**, both emitters contain more planar donor-bridge conformations that are stabilized by intramolecular hydrogen bonding. The photophysical analysis reveals that both emitters possess even smaller ΔE_{ST} (~0.15 eV) while maintaining high Φ_{PL} (~70%), and more importantly, much faster τ_d of 127 μs and 108 μs for **pDTCz-DPmS** and **pDTCz-DPzS**, compared to 288 μs and 809 μs for **pDTCz-3DPyS** and **pDTCz-2DPyS**, respectively, which indicates more efficient RISC for **pDTCz-DPmS** and **pDTCz-DPzS**. With the pyrimidine bridge, blue-emitting OLEDs using **pDTCz-DPmS** are obtained with EQE_{max}= 14%, and EQE_{100} = 7% (at 100 cd/m^2), with CIE coordinates (0.19, 0.26), representing a modest improvement in the EQE_{max} and a substantial improvement in the efficiency roll-off compared to **pDTCz-3DPyS** and **pDTCz-2DPyS**. With

the pyrazine bridge in **pDTCz-DPzS**, a much larger enhancement in the EQE_{max} and much-reduced efficiency roll-off is obtained (EQE_{max}=22%, EQE_{100}=14%). However, due to the use of the stronger ICT between **DPzS** acceptor and carbazole donor, green OLEDs are obtained. Thus, with this work, a more profound understanding about the subtle relationship between molecular structure and the TADF mechanism is achieved, advancing the design strategies of TADF materials.

3.2 Synthesis

The synthesis of four emitters is outlined in Scheme **3.1**. For the synthesis of **pDTCz-2DPyS**, the **DPBr-S** was synthesized following Duan's work where Na_2S was used as chalcogen source and reacted with aryl iodide to get diaryl chalcogenides catalysed by copper (I) iodine in DMF.[9] The **DPBr-S** was further oxide by hydrogen peroxide in acetic acid to obtain the acceptor moiety **DPBr-SO2**. Then the donor, di-*tert*-butyl-9H-carbazole (tCz) were reacted with **BrPy-SO2** via Ullman C-N coupling mechanism to obtain **pDTCz-2DPyS**.[10] While **pDTCz-3DPyS**, **pDTCz-DPmS**, and **pDTCz-DPzS**, were accessed in three steps consisting of one step of copper Ullmann C-N coupling between the tCz and the respective iodine aryl rings[10] and one step of the diaryl chalcogenides synthesis followed Duan's method,[9] and finally, the diaryl chalcogenides were oxide by hydrogen peroxide to obtain the sulfone derivatives. The four emitters were characterized by a combination of ^{1}H and ^{13}C NMR spectroscopy, HRMS, melting point determination, and elemental analysis. The four emitters were purified by silica gel

chromatography and temperature gradient vacuum sublimation, and the purity was established by high HPLC analysis. The detailed synthesis and compounds characterization are shown in section

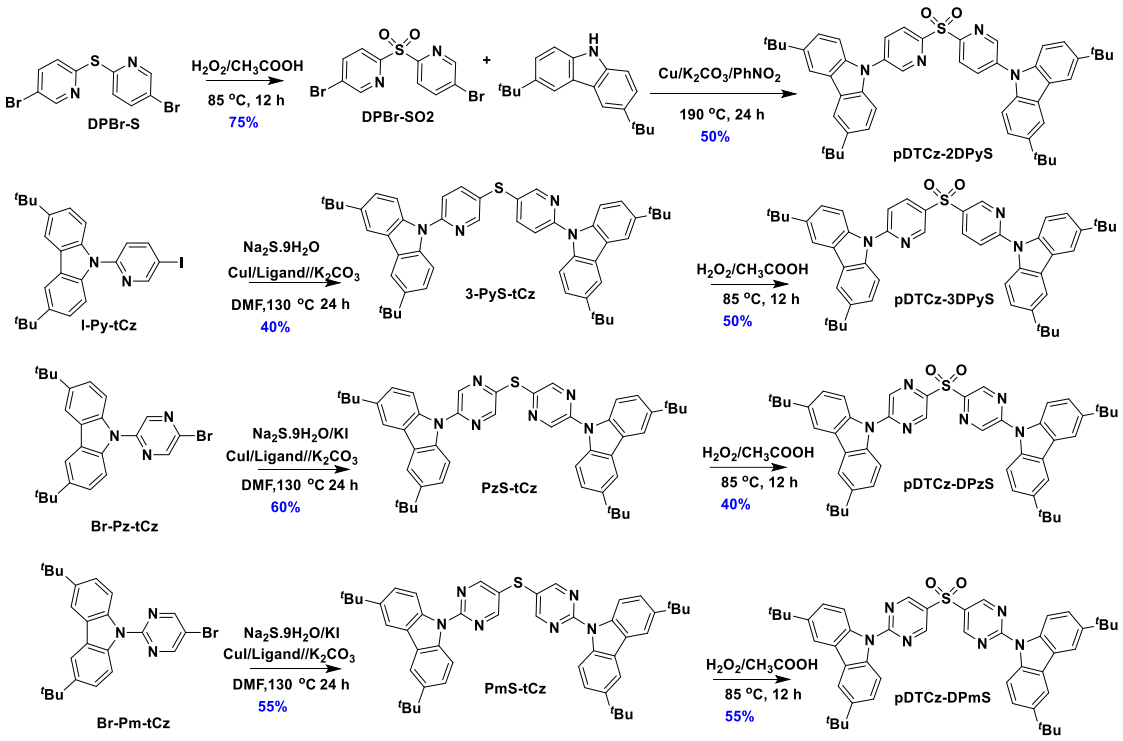

Scheme **3.1.** Synthesis of **pDTCz-2DPyS**, **pDTCz-3DPyS**, **pDTCz-DPzS** and **pDTCz-DPmS**.

Single crystal of **pDTCz-2DPyS**, **pDTCz-3DPyS**, **pDTCz-DPmS**, and **pDTCz-DPzS**, were grown by the slow evaporation of mixed solutions of chlorobenzene/methanol (**pDTCz-DPzS** and **pDTCz-DPmS**) or toluene/methanol (**pDTCz-3DPyS** and **pDTCz-2DPyS**). The structures of the four emitters were confirmed by single crystal X-ray diffraction analysis (Figure **3.2**). The conformation of **pDTCz-DPmS** in the crystal reveals a very small dihedral angle between the donor DTCz and adjoining pyrimidine [12.2(3)°] bridge that is coupled with

an N···H distances of 2.30 and 2.35 Å between the pyrimidine nitrogen and the proximal hydrogen atoms of the *tert*-butyl carbazole, indicative of a moderate hydrogen bond. For **pDTCz-DPzS**, and **pDTCz-3DPyS** only the *gauche* conformer was found in the crystal structure where the two pyrazine or two pyridine rings are symmetrically disposed. The dihedral angle between the donor DTCz and adjoining pyrazine is larger at 38.20(8)° in the single crystal than that of **pDTCz-DPmS** and is slightly smaller than that found in **pDTCz-2DPyS** (42.77 and 51.66°) and **pDTCz-3DPyS** [41.54(6)°]. The distance between one of the two pyrazine nitrogen atoms and one of the proximal hydrogen atoms of the *tert*-butyl carbazole in **pDTCz-DPzS** (2.56 Å) is almost identical to that seen in **pDTCz-3DPyS** (2.57 Å), again indicative of a weak hydrogen bond. While for **pDTCz-2DPyS**, as the nitrogen atoms in pyridine rings are not close to any hydrogen atom, no equivalent hydrogen bond is presented.

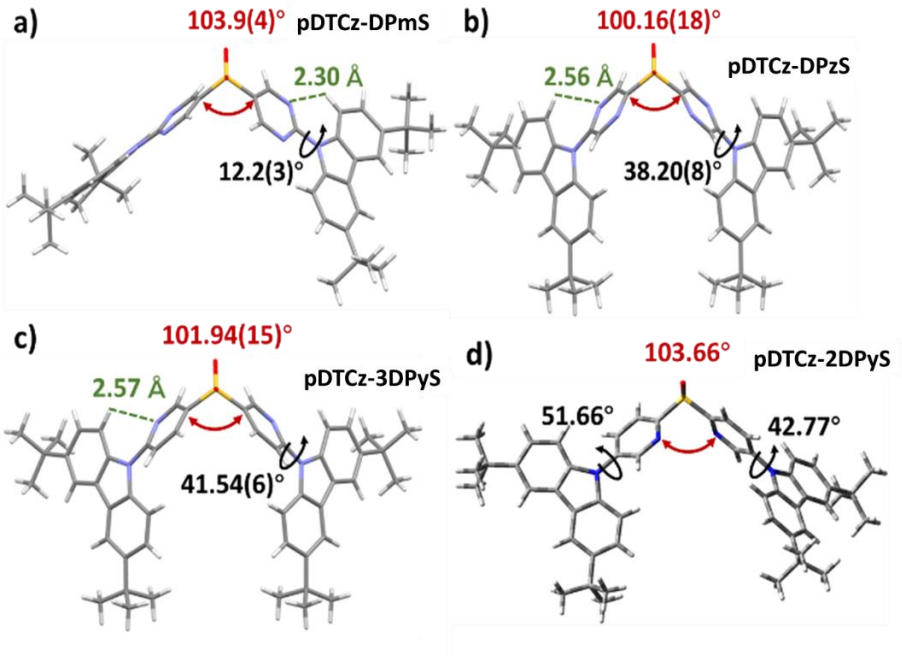

Figure **3.2**. Crystal structure of (a) **pDTCz-DPmS**, (b) **pDTCz-DPzS** and (c) **pDTCz-3DPyS** and (d) **pDTCz-2DPyS**. Solvent molecules and minor components of disorder omitted.

3.3 Theoretical Calculations

DFT calculations based on PBE0/6-31G(d,p) calculations,[11,12] were performed for **pDTCz-2DPyS**, **pDTCz-3DPyS**, **pDTCz-DPzS**, **pDTCz-DPmS**, and reference emitter **pDTCz-DPS** to gain insights into the lowest energy conformation in the ground state, the associated energies, and the nature of the frontier molecular orbitals. Optimization of the ground state geometries started from the X-ray single crystal structures. The Tamm-Dancoff approximation (TDA)[13,14] of TD-DFTwas applied to determine the nature of both the excited singlet and triplet states as well as to estimate ΔE_{ST}.

The DFT-optimized structure of **pDTCz-DPmS** reveals an almost completely planar donor and bridge conformation with dihedral angle between the DTCz and pyrimidine bridge as small as [0.66(7)°]. The N···H distances between the pyrimidine nitrogen and the proximal hydrogen atoms of DTCz were found to be 2.24 Å, which are shorter than those found in the single crystal. Turning to the **pDTCz-DPzS** and **pDTCz-3DPyS**, the DFT-optimized structure predicts a smaller dihedral angle between the DTCz and heteromatic rings of 32.9° and 32.5°, which are ca. 6° and 9° smaller than that found in their crystal structure, respectively. While for **pDTCz-2DPyS**, the DFT-optimized structure predicts a 5° larger dihedral angle (47.5°) than its crystal structure. Analogously, for **pDTCz-DPmS**, **pDTCz-DPzS** and **pDTCz-3DPyS** the N···H distances between the nitrogen atoms of the heteroaromatic rings and the proximal hydrogen atoms were found to be shorter than those found in the single crystal (calculated 2.24 Å, 2.38 Å, and 2.37 Å compared to 2.30 Å, 2.56 Å and 2.57 Å in single crystals, respectively). Despite these small deviations in geometry, the DFT-optimized structures generally match closely those found

in the single crystal. Figure **3.3** shows the relative orbital energies and electron density distribution of the HOMOs and LUMOs of **pDTCz-DPS**, **pDTCz-3DPyS**, **pDTCz-2DPyS**, **pDTCz-DPmS** and **pDTCz-DPzS**. In each case, the HOMO is localized on the DTCz donors and slightly extending to the phenyl or heterocyclic bridges while the LUMO is localized on both the sulfone and phenyl or heterocyclic rings, with the exception of **pDTCz-DPmS**, where there is a delocalization of the LUMO over the entire molecule. The LUMO energies of **pDTCz-3DPyS**, **pDTCz-2DPyS**, are stabilized to -1.71 eV, -1.56 eV, respectively, compared to -1.50 eV of of **pDTCz-DPS**. While for **pDTCz-DPmS** and **pDTCz-DPzS**, The LUMOs are further stabilized to -1.86 eV and -2.11 eV, respectively. Conversely, the HOMO energies of **pDTCz-3DPyS**, **pDTCz-2DPyS**, are destabilized to -5.77 eV, -5.74 eV, respectively, compared to -5.65 eV of of **pDTCz-DPS**. While for **pDTCz-DPmS** and **pDTCz-DPzS**, The HOMOs are further destabilized to -5.98 eV and -5.95 eV, respectively. Both **pDTCz-2DPyS** and **pDTCz-3DPyS** show comparable calculated ΔE_{ST} (~0.39 eV) and S_1 (~3.48 eV) and T_1 energies (~3.10 eV) (Table **3.1**) to the reference emitter **pDTCz-DPS**. For **pDTCz-DPmS** and **pDTCz-DPzS** the ΔE_{ST} values are slightly increased to ~0.49 eV due to the increased HOMO/LUMO overlap. The S_1 of **pDTCz-DPmS** is destabilized to 3.56 eV, while the S_1 of **pDTCz-DPzS** is stabilized to 3.23 eV. The high S_1 energies of **pDTCz-DPmS**, **pDTCz-2DPyS** and **pDTCz-3DPyS** indicate that these materials are likely to be deep blue emitters. The calculated *f*, for the transition to the S_1 state are 0.51, and 0.35 for **pDTCz-DPzS**, and **pDTCz-2DPyS**, respectively, which are comparable to 0.48 for the same transition in **pDTCz-DPS**. By contrast, *f* improved to 0.78 and

0.94 for **pDTCz-DPmS** and **pDTCz-3DPyS**, reflecting the much efficient radiative transition between S_1 to S_0.

Table **3.1.** Calculated HOMO/LUMO and $S_1/T_1/\Delta E_{ST}$ energies for **pDTCz-DPS**, **pDTCz-3DPyS**, **pDTCz-2DPyS**, **pDTCz-DPmS**, and **pDTCz-DPzS**.

Compound	**HOMO / eV**	**LUMO / eV**	**ΔE_g / eV**	**S_1 / eV**	**T_1 / eV**	**ΔE_{ST} / eV**	***f***
pDTCz-DPS	-5.63	-1.50	4.02	3.48	3.13	0.35	0.48
pDTCz-3DPyS	-5.77	-1.71	4.06	3.45	3.02	0.43	0.78
pDTCz-2DPyS	-5.74	-1.56	4.23	3.51	3.12	0.39	0.35
pDTCz-DPmS	-5.98	-1.86	4.12	3.56	3.05	0.51	0.95
pDTCz-DPzS	-5.95	-2.11	3.84	3.23	2.76	0.47	0.51

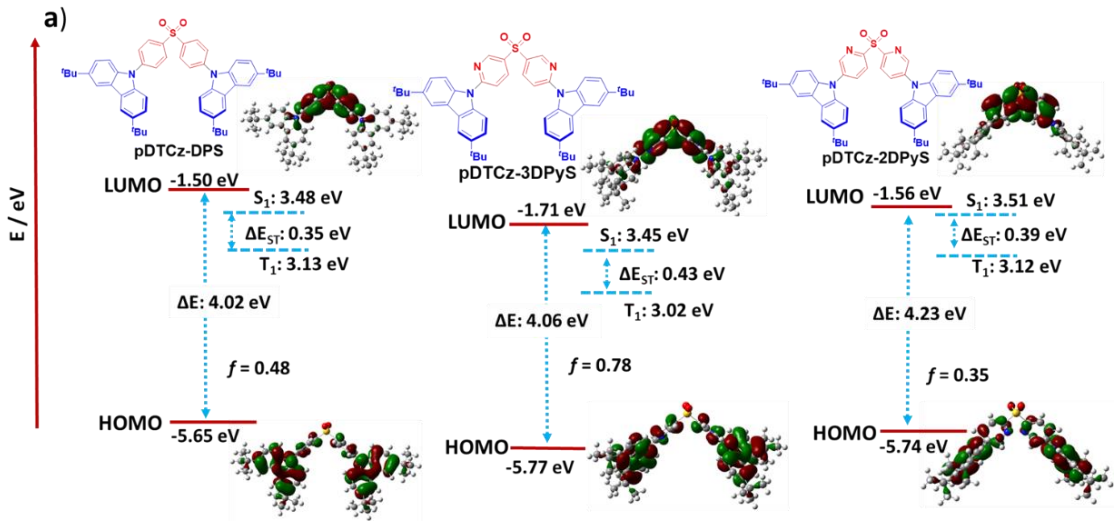

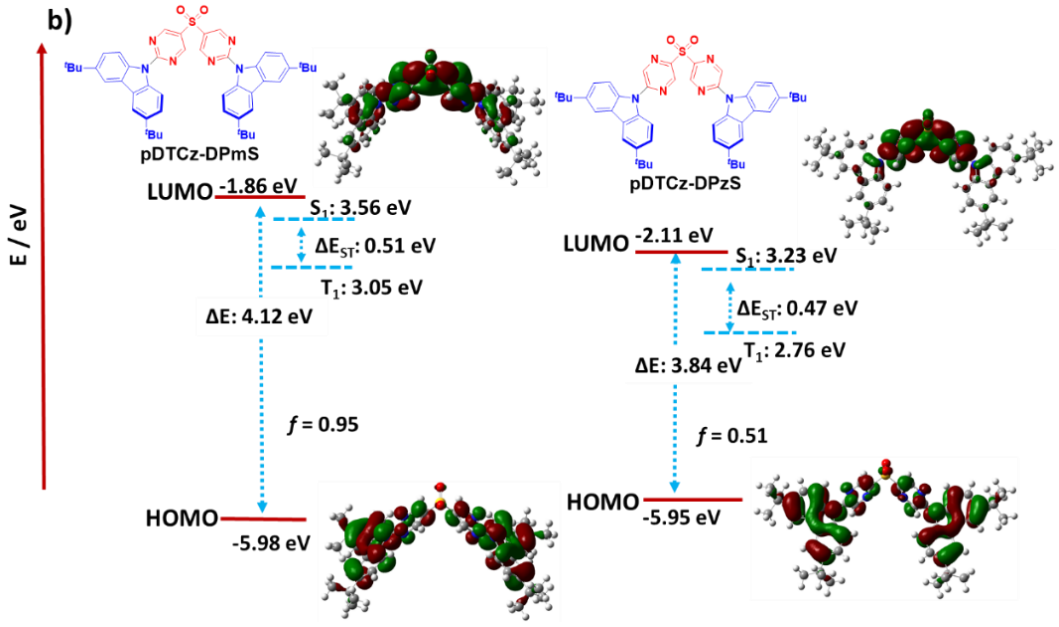

Figure **3.3**. Calculated HOMO, LUMO, S_1 and T_1 energies, as well as HOMO and LUMO topologies (isovalue = 0.02) of a) **pDTCz-DPs**, **pDTCz-3DPyS**, and **pDTCz-2DPyS**, and b) **pDTCz-DPmS** and **pDTCz-DPzS**.

3.4 Thermal analysis

The thermal stability of these materials was investigated using thermogravimetric analysis (TGA) and differential thermal analysis (DTA) (Figure **3.4**). Our four emitters showed very high thermal stability with very high melting (T_m) and degradation temperatures (T_d). The T_m for **pDTCz-DPmS** and **pDTCz-DPzS** are 399 °C and 392 °C, which are much higher than those of **pDTCz-2DPyS** (353 °C) and **pDTCz-3DPyS** (361 °C) while the T_d (weight loss of 5%) are 416 °C and 446 °C, which are similar to **pDTCz-2DPyS** (391 °C) and **pDTCz-3DPyS** (448 °C). Considering almost the same molecular weight of all four compounds, the observed

substantially higher T_m for **pDTCz-DPmS** and **pDTCz-DPzS** can be ascribed in part to the existence of the greater intramolecular hydrogen bonding in these compounds as compared to the pyridine analogues.

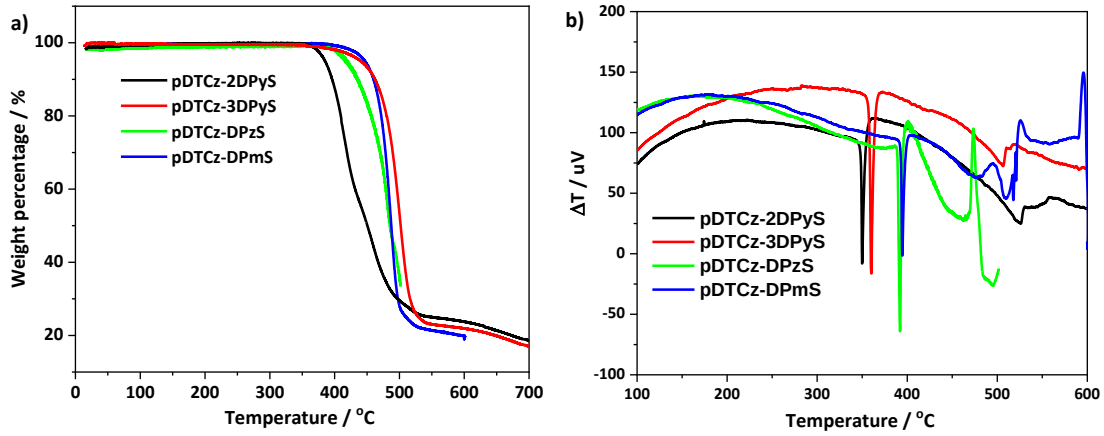

Figure **3.4**. The a) TGA and b) DTA traces of **pDTCz-3DPyS**, **pDTCz-2DPyS**, **pDTCz-DPmS** and **pDTCz-DPzS**.

3.5 Electrochemistry

Electrochemical measurements for of **pDTCz-3DPyS**, **pDTCz-2DPyS**, **pDTCz-DPmS** and **pDTCz-DPzS** were carried out in DCM in order to determine the energies of the frontier energy levels (Figure **3.5**). The CV traces of **pDTCz-3DPyS**, **pDTCz-2DPyS**, **pDTCz-DPmS**, and **pDTCz-DPzS** show irreversible reduction waves at E_{pc} = -2.07 V, -1.99 V, and -1.83 V, respectively, while the CV trace of **pDTCz-DPzS** shows a pseudo-reversible reduction wave with E_{pc} = -1.42 V. The DPV traces of **pDTCz-2DPyS**, **pDTCz-3DPyS**, **pDTCz-DPmS** and

pDTCz-DPzS show reduction peaks at -1.88 V, -1.90 V, -1.82 V and -1.46 V, respectively. From this, the LUMO levels of **pDTCz-2DPyS**, **pDTCz-3DPyS**, **pDTCz-DPmS** and **pDTCz-DPzS** can be estimated at -2.46 eV, -2.44, -2.52 eV and -2.88 eV, respectively, from the DPVs. Compared to the corresponding values in **pDTCz-2DPyS** and **pDTCz-3DPyS**, a stronger LUMO stabilization in **pDTCz-DPzS** was observed, whereas **pDTCz-DPmS** shows a slight stabilization in the LUMO energy; these results are in line with the LUMO energies calculated by DFT. The oxidation wave for **pDTCz-DPmS** is irreversible and E_{pa}^{ox} =1.58 V, while the oxidation wave for **pDTCz-2DPyS**, **pDTCz-3DPyS**, and **pDTCz-DPzS** are pseudo-reversible with E_{pa}^{ox} = 1.33, 1.31, and 1.48 V, respectively. The DPV traces of **pDTCz-2DPyS**, **pDTCz-3DPyS**, **pDTCz-DPmS** and **pDTCz-DPzS** show oxidation peaks at 1.26, 1.27, 1.48 and 1.50 V, respectively. The corresponding HOMO levels of **pDTCz-DPmS** and **pDTCz-DPzS** are calculated to be -5.60, -5.61, -5.82 and -5.84 eV, respectively. In line with the DFT calculation, the HOMO values of **pDTCz-DPmS** and **pDTCz-DPzS** are deeper than those of **pDTCz-2DPyS** and **pDTCz-3DPyS**.

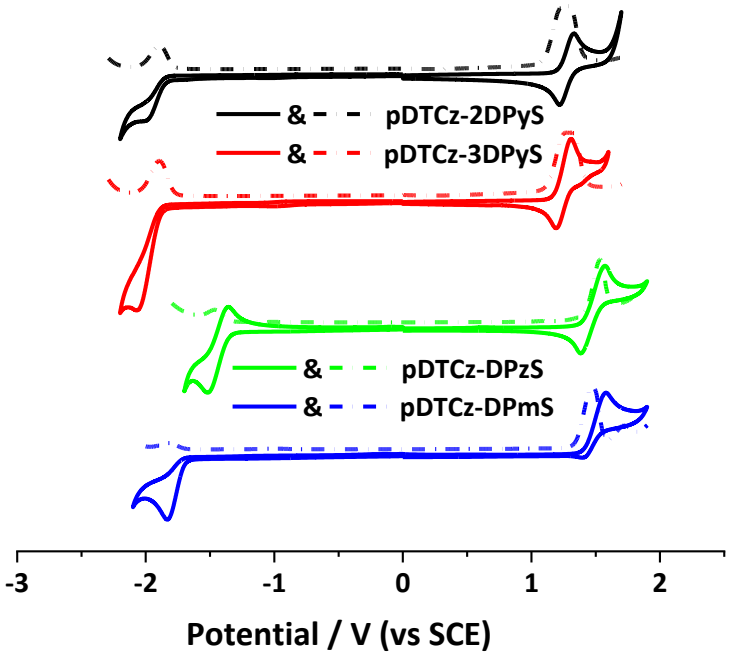

Figure **3.5**. CVs and DPVs of **pDTCz-2DPyS**, **pDTCz-3DPyS**, **pDTCz-DPmS**, and **pDTCz-DPzS** in DCM, reported versus SCE (Fc/Fc^+ = 0.46 V in DCM[15], scan rate = 50 mV s^{-1}).

3.6 Photophysical Characterization

The UV-*vis* absorption and steady-state photoluminescence (PL) spectra of **pDTCz-2DPyS**, **pDTCz-3DPyS**, **pDTCz-DPmS**, and **pDTCz-DPzS** in toluene are shown in Figure **3.6**. Low energy bands absorption around 354 – 360 nm are observed for **pDTCz-3DPyS**, **pDTCz-2DPyS**, and **pDTCz-DPmS**, while for **pDTCz-DPzS** the absorption is red-shifted to 389 nm. In line with TD-DFT calculations, these transitions have both π–π* character and significant CT character. **pDTCz-DPmS**, and **pDTCz-DPzS** show more pronounced low energy absorption bands as ε are above 5.0×10^4 M^{-1} cm^{-1} compared to 4.0×10^4 and 2.6×10^4 M^{-1} cm^{-1} for **pDTCz-3DPyS** and **pDTCz-2DPyS**, respectively, values that match the predicted oscillator strength

trends determined by TDA-DFT calculations. The higher energy bands are at similar energies (280-330 nm) to the four emitters, indicating the donor-localized π-π* transitions. **pDTCz-2DPyS** and **pDTCz-3DPyS** exhibit almost identical PL spectra in toluene with λ_{PL} = 443 nm and FWHM of 75 nm, while for **pDTCz-DPmS**, and **pDTCz-DPzS** the λ_{PL} are red-shifted to 484 and 530 nm and show broader emission with FWHM of 111 and 117 nm, respectively. The Φ_{PL} measured in toluene under an N_2 atmosphere are 47%, 50%, 55%, and 49% for **pDTCz-2DPyS**, **pDTCz-3DPyS**, **pDTCz-DPmS**, and **pDTCz-DPzS**, respectively, and are reduced to below 40% under aerated conditions (Table **3.2**).

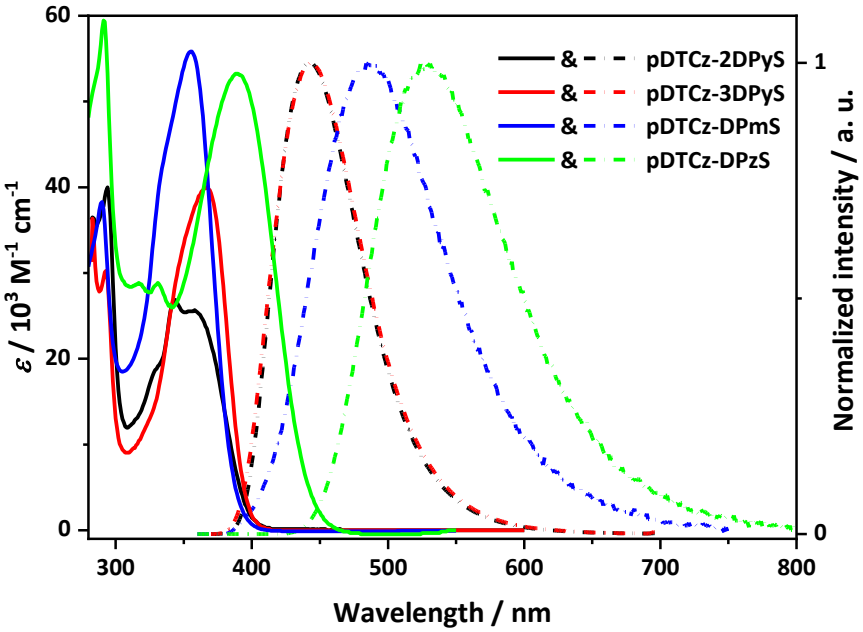

Figure **3.6**. Absorption (solid) and emission (dashed) spectra of **pDTCz-2DPyS**, **pDTCz-3DPyS**, **pDTCz-DPmS**, and **pDTCz-DPzS** in toluene solution (λ_{exc} = 360 nm).

Figures **3.7** show the normalized steady-state photoluminescence (PL) spectra of the four emitters, in different solvents. In all solvents, the PL spectra show emission with a CT character, evidenced by their Gaussian band shape and positive solvatochromism. As expected, **pDTCz-DPzS** shows a red-shifted emission compared to that of **pDTCz-2DPyS**, **pDTCz-3DPyS**, and **pDTCz-DPmS**. Moreover, the magnitude of the positive solvatochromism is larger in **pDTCz-DPzS** than other three emitters, indicating stronger ICT occurring in this compound, in line with the frontier orbitals.

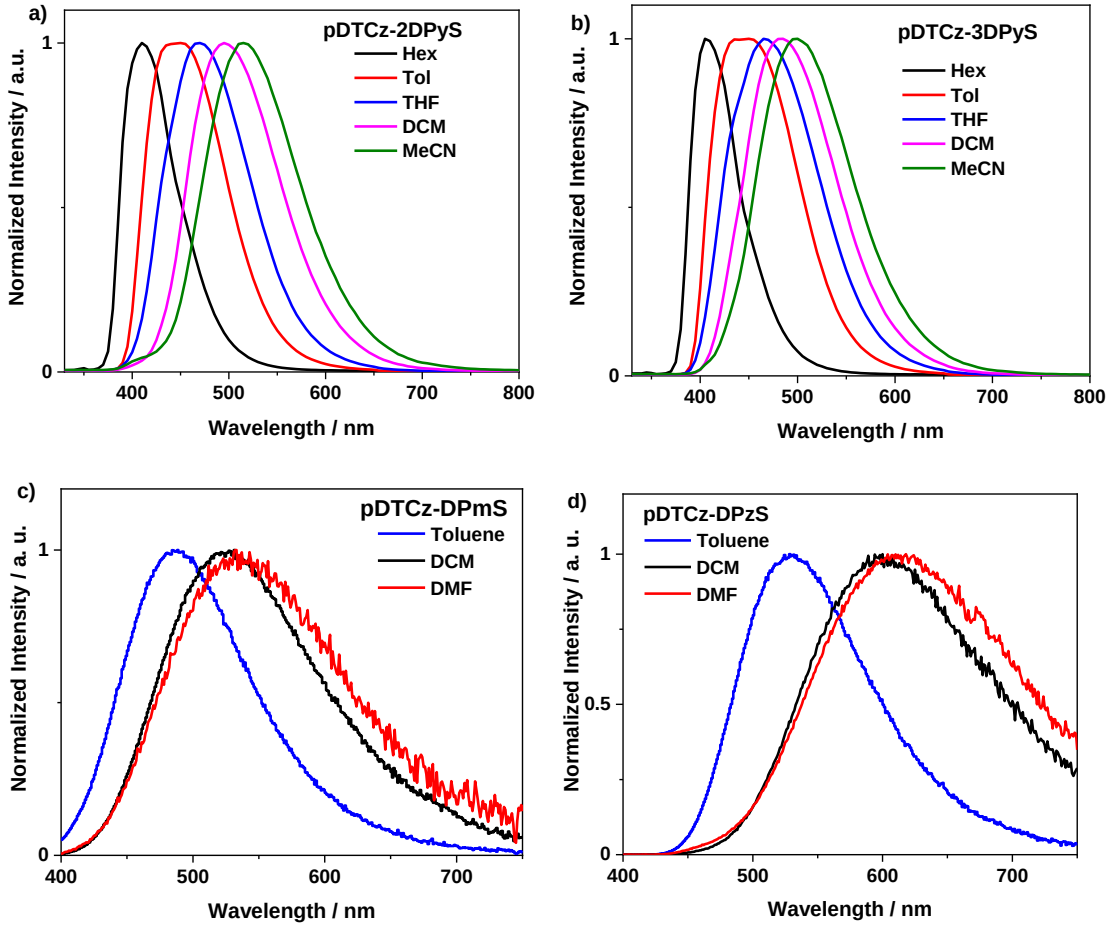

Figure **3.7**. Photoluminescence solvatochromic study for a) **pDTCz-2DPyS**, b) **pDTCz-3DPyS**, c) **pDTCz-DPmS**, and d) **pDTCz-DPzS**. λ_{exc} = 360 nm.

To assess the emission properties of these emitters in the solid state, their photophysical properties were first investigated in PMMA film. Thin films were prepared by spin-coating a 10 wt% chlorobenzene solution of emitter in PMMA (Fig. **3.8a**). The emission peak is slightly red-shifted by 5 nm for **pDTCz-3DPyS** and 10 nm for **pDTCz-2DPyS**, while for **pDTCz-DPmS**, and **pDTCz-DPzS** the peaks are 38 and 16 nm blue-shifted compared to their respective emission in toluene. The Φ_{PL} in 10 wt% doped PMMA films under an N_2 atmosphere are 51% and 52%, 48%, and 55% for **pDTCz-2DPyS**, **pDTCz-3DPyS**, **pDTCz-DPmS**, and **pDTCz-DPzS**, respectively, and are reduced to 44%, 47%, 33%, and 44% respectively, under air, indicating the presence of an accessible triplet state in both solution and thin film state. DPEPO was chosen to be the appropriate host for the four emitters due to its high triplet energy, suitable HOMO-LUMO levels and the high measured Φ_{PL} values for all four emitters observed in this host. The Φ_{PL} in doped DPEPO films under nitrogen were measured to be 81%, 72%, 73%, and 68% for **pDTCz-2DPyS**, **pDTCz-3DPyS**, **pDTCz-DPmS**, and **pDTCz-DPzS**, respectively, and these values decreased, respectively, to 62%, 61%, 63% and 59% under air. Our four emitters show higher Φ_{PL} values than the reference emitter **pDTCz-DPS** (66%/59% N_2/air) and reflect the supressed non-radiative decay in these emitters.

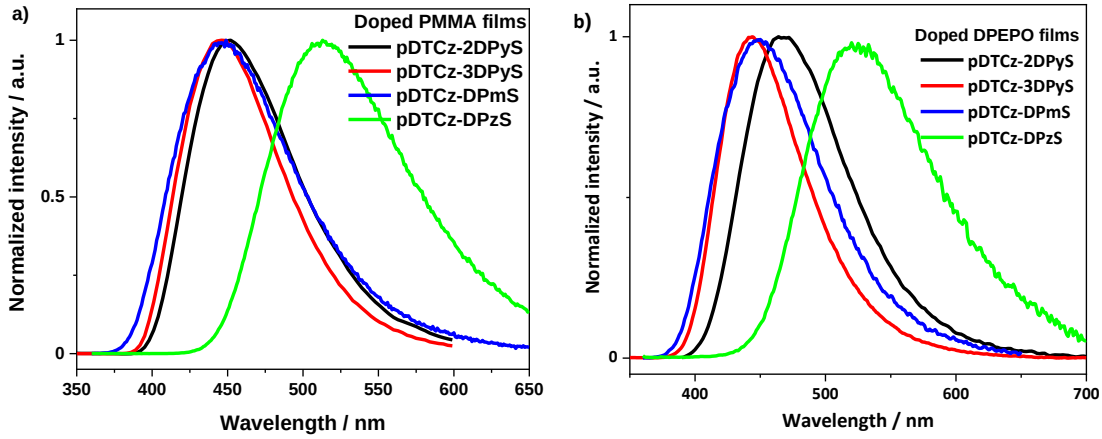

Figure **3.8**. Normalized PL spectra of 10 wt% four emitters in a) PMMA and b) DPEPO films (λ_{exc} = 360 nm).

The S_1 energies of the four emitters estimated from the onset of PL spectra at room temperature in DPEPO host, are 3.06, 3.17, 3.07 and 2.72 eV for the **pDTCz-2DPyS**, **pDTCz-3DPyS**, **pDTCz-DPmS** and **pDTCz-DPzS**, respectively. The T_1 energies of four emitters are determined from the onset of the phosphorescence spectra in DPEPO host and are 2.84, 2.95, 2.92, and 2.56 eV for **pDTCz-2DPyS**, **pDTCz-3DPyS**, **pDTCz-DPmS** and **pDTCz-DPzS**, respectively (Figure **3.9**). Compared to the TDA-DFT calculations, the T_1 energies of the four emitters in DPEPO are slightly destabilized (~ 0.15 eV), while the S_1 energies are significantly stabilized (~ 0.45 eV), which results much reduced ΔE_{ST} values in DPEPO than the values predicted by TDA-DFT calculations. The ΔE_{ST} values for **pDTCz-2DPyS** and **pDTCz-3DPyS** are 0.22 and 0.21 eV, while for **pDTCz-DPmS** and **pDTCz-DPzS**, the ΔE_{ST} are further reduced to 0.15 and 0.16 eV, respectively, indicating a relatively low energy barrier for RISC to occur in

the four emitters and the enhancement of TADF by use of pyrimidine and pyrazine over pyridine-based analogues.

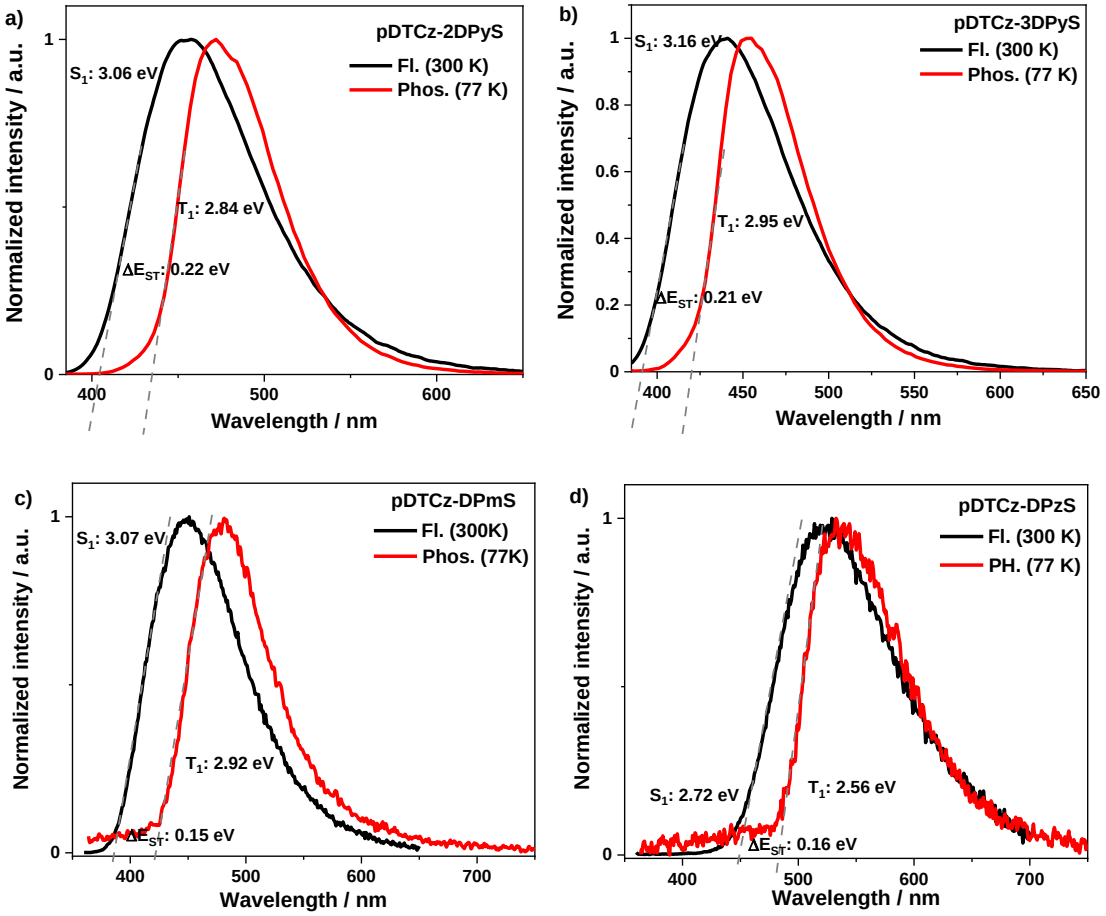

Figure **3.9**. Phosphorescence (PH) spectra and fluorescence (Fl) spectra of a) **pDTCz-2DPyS**, b) **pDTCz-3DPyS**, c) **pDTCz-DPmS**, and d) **pDTCz-DPzS** in doped DPEPO films. PH measurements were performed at 77 K with time delay of 1 ms and integration time of 9 ms (λ_{exc} = 343 nm).

Table **3.2.** Key Photophysical data of **pDTCz-2DPyS**, **pDTCz-3DPyS**, **pDTCz-DPmS**, and **pDTCz-DPzS**.

Compound	λ_{abs} (ε)[a] / nm (/ 10^3 m^{-1} cm^{-1})	λ_{PL} / nm	Φ_{PL} (Air/N_2) / %	HOMO/LUMO/ ΔE_g[d] / eV
pDTCz-2DPyS	310 (20),	443[a]/448[b]	37/47[a]	−5.60/−2.46/3.14
	362 (26)		51/44[c]	
pDTCz-3DPyS	312 (16),	443[a]/448[b]	40/50[a]	−5.61/−2.44/3.17
	361 (40)		47/52[c]	
pDTCz-DPmS	310 (40),	484[a]/446[b]	35/55[a]	−5.82/−2.52/3.30
	350 (56)		33/48[c]	
pDTCz-DPzS	320 (31),	530[a]/514[b]	30/49[a]	−5.84/−2.88/2.96
	400 (54)		44/55[c]	

[a] Measured in toluene solution (λ_{exc} = 378 nm), Φ_{PL} measured in aerated or degassed solution at room temperature. (Standard: quinine sulfate in 0.1 M H_2SO_4, Φ_{PL} = 0.54). [b] Measured in 10 wt% doped PMMA films (λ_{exc} = 378 nm), [c] Measured using an integrating sphere of 10 wt% doped PMMA films under air/N_2 (λ_{exc} = 360 nm), [d] HOMO and LUMO values were obtained from the redox potentials from the DPV, $E_{HOMO/LUMO} = -(E_{ox/red} + 4.8)$ where $E_{ox/red}$ are from DPV scan corrected vs Fc/Fc^+, $\Delta E_g = E_{LUMO} - E_{HOMO}$.[15]

The kinetics of the four emitters were investigated in 10 wt% doped DPEPO films. The prompt fluorescence, τ_p, lifetimes of the four emitters were measured at room temperature using a short time window (100 ns) and found to have average lifetime of 13, 7, 6 and 10 ns for **pDTCz-2DPyS**, **pDTCz-3DPyS**, **pDTCz-DPmS** and **pDTCz-DPzS**, respectively. Figure **3.10** shows the emission decays of the four emitters in DPEPO films measured under vacuum at room

temperature. The four films show delayed fluorescence with average lifetimes, $\tau_{d,avg}$ of 809, 288, 127, and 108 μs, for **pDTCz-2DPyS**, **pDTCz-3DPyS**, **pDTCz-DPmS** and **pDTCz-DPzS**, respectively. The k_{RISC} values for **pDTCz-DPmS** and **pDTCz-DPzS** are calculated to be 3.5 × 10^3 s^{-1} and 3.8 × 10^3 s^{-1}, respectively, which are faster than **pDTCz-2DPyS** (1.0 × 10^3 s^{-1}), and **pDTCz-3DPyS** (1.6 × 10^3 s^{-1}). The faster k_{RISC} values for **pDTCz-DPmS** and **pDTCz-DPzS** were ascribed to the smaller ΔE_{ST} values, which led to an accelerated RISC process and improved efficiency roll-off as discussed in the device (see Section **3.7**).

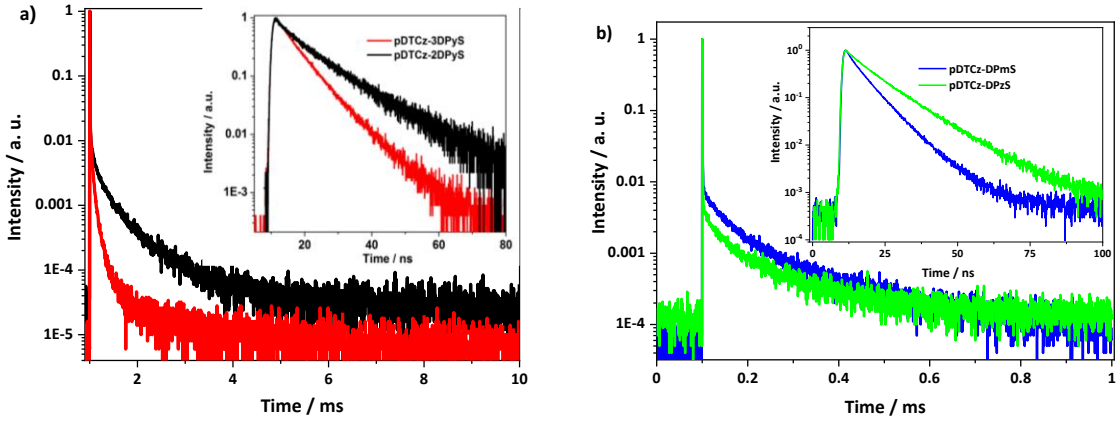

Figure **3.10**. Time-resolved decay of a) **pDTCz-2DPyS** and **pDTCz-3DPyS** and b) **pDTCz-DPmS** and **pDTCz-DPzS** in 10 wt% DPEPO film (λ_{exc} = 379 nm).

TADF was identified to be the main mechanism responsible to generate the delayed fluorescence (DF) in the emitters as the magnitude of DF was found to be temperature dependent (Figure **3.11**), which further corroborate the TADF characters of the four emitters. The photophysical properties in the solid state of four emitters are summarized in Table **3.3**.

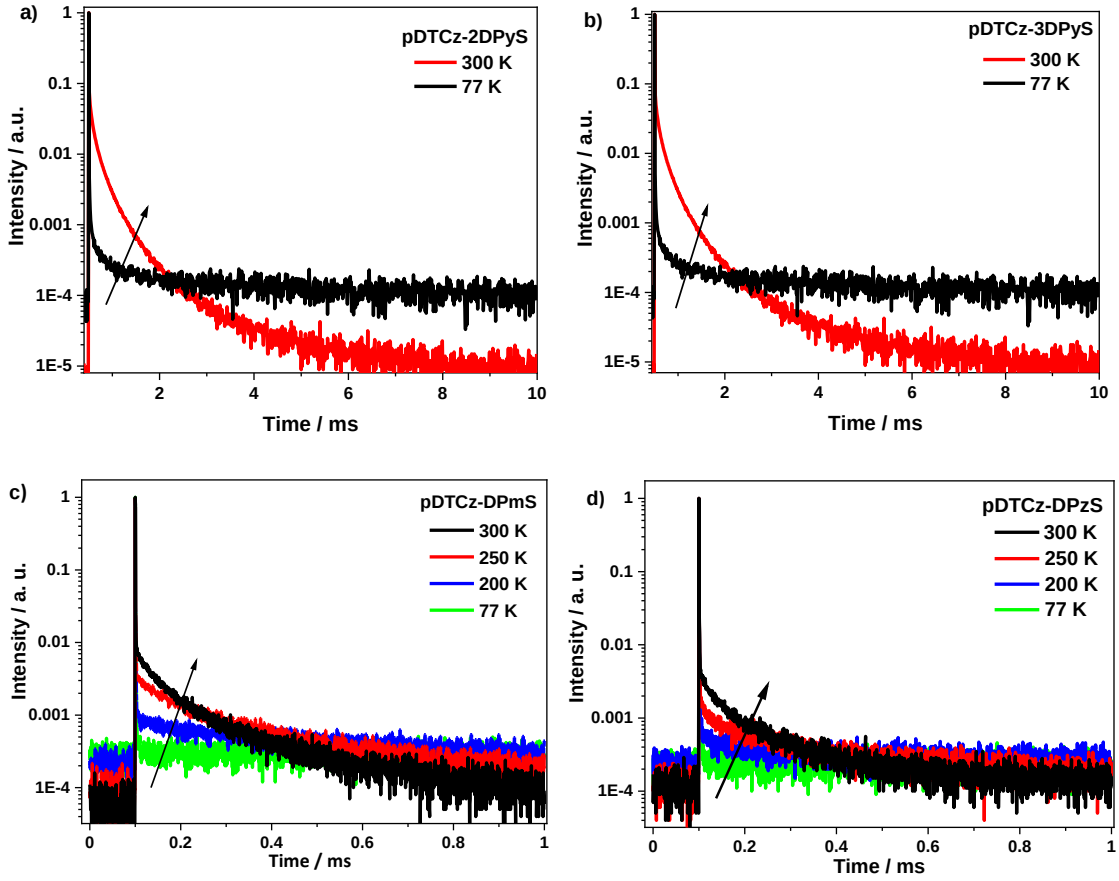

Figure **3.11**. Temperature-dependent time-resolved decay of a) **pDTCz-2DPyS**, b) **pDTCz-3DPyS**, c) **pDTCz-DPmS** and d) **pDTCz-DPzS** in 10 wt% DPEPO film, the arrows in figures show the delayed component increase with the temperature (λ_{exc} = 379 nm).

Table **3.3.** Exciton lifetime and the kinetic constants of **pDTCz-2DPyS**, **pDTCz-3DPyS**, **pDTCz-DPmS**, and **pDTCz-DPzS**, in DPEPO host.

Compound	S_1 / eV	T_1 / eV	ΔE_{ST} / eV	Φ_{PL} / %	$\tau_{p,avg}$ / ns	$\tau_{d,avg}$ / µs	k_r^s /10^7 s^{-1}	k_{ISC} / 10^7 s^{-1}	k_{RISC} / 10^3 s^{-1}
pDTCz-2DPyS	3.06	2.84	0.22	62/81	13	809	4.7	2.9	1.0
pDTCz-3DPyS	3.16	2.95	0.21	61/72	7	288	8.7	5.6	1.6
pDTCz-DPmS	3.07	2.92	0.15	63/73	6	127	10.5	6.2	3.5
pDTCz-DPzS	2.72	2.56	0.16	59/68	10	108	5.9	4.1	3.8

S_1= singlet state energy obtained from the onset of the photoluminescence spectra measured at room temperature with excitation wavelength at 340 nm; T_1 = triplet state energy obtained from the onset of the phosphorescence spectra measured at 77 K with excitation wavelength at 343 nm; $\Delta E_{ST} = E(S_1) - E(T_1)$; Φ_{PL} = photoluminescence quantum yield measured using an integrating sphere under air / nitrogen flow with excitation wavelength at 300 nm; $\tau_{p,avg}$ = average prompt fluorescence lifetime measured at room temperature with time window of 100 ns. $\tau_{d,avg}$ = average delayed fluorescence lifetime measured at room temperature with time window of 1 ms; All measurements were performed in co-doped DPEPO film (10 wt%).

3.7 Device performance

Given the promising photophysical properties of the four emitters, we next fabricated multilayer devices using these emitters as dopants. The schematic representation of the device architecture and molecular structures of the materials used in the devices are shown in Figure **3.12**

and Figure **3.13**. For OLEDs based **pDTCz-3DPyS** (device A), **pDTCz-2DPyS** (device B), and **pDTCz-DPS** (device C), the device stacks are fabricated as ITO/N,N′-Di(1-naphthyl)-N,N′-diphenyl-(1,1′-biphenyl)-4,4′-diamine (NPB) (30 nm)/TAPC (20 nm)/*m*CP (10 nm)/ DPEPO:Dopant (7 wt%) (30 nm)/DPEPO (5 nm)/1,3,5-tri(m-pyridin-3-ylphenyl)benzene (TmPyPb) (30 nm)/LiF (1 nm)/Al (100 nm). In these devices, NPB acts as the hole injection material, TAPC is the hole transporting material, *m*CP is the exciton blocking layer, DPEPO is the host material, and TmPyPb is the electron-transporting material. The electroluminescence properties of the devices are shown in Figure **3.12**. and summarized in Table **3.4**. Devices A, B and C show EQE_{max} of 13.4%, 11.4%, and 4.7%, respectively. The CIE coordinates of devices A, B, and C are (0.15, 0.13), (0.15, 0.18), and (0.15, 0.08), respectively. Both devices A and B are show blue emission with an improved performance compared to device C with the reference emitter **pDTCz-DPS**. The maximum current and power efficiencies (CE and PE) are 13.2, 15.1, 2.5 cd A^{-1}, and 10.9, 11.6, 2.2 lm W^{-1}, respectively, for devices A, B and C. However, both devices A and B suffer from a severe efficiency roll-off, and low maximum luminance due to the long delayed lifetimes and slow k_{RISC} rates.

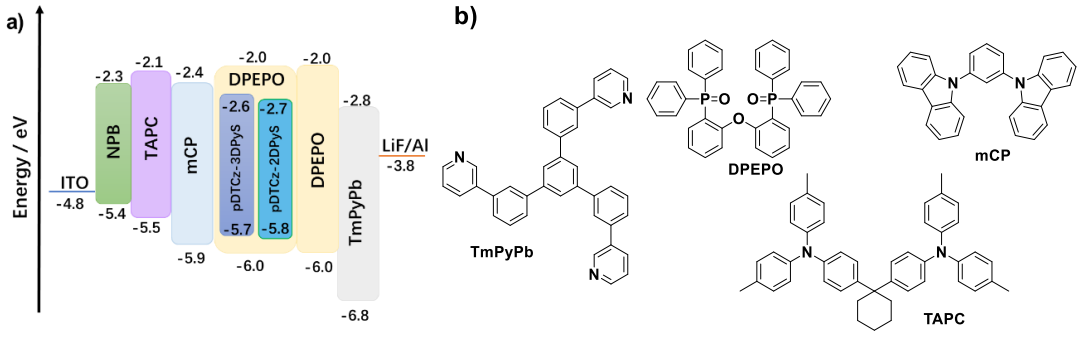

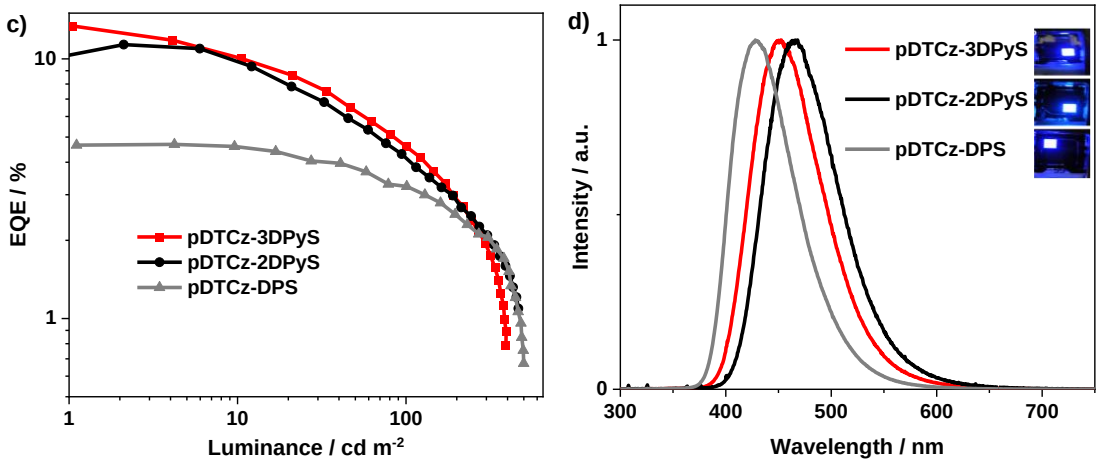

Figure **3.12**. a) Device architecture and b) molecular structures of materials used in **pDTCz-2DPyS** (device A), **pDTCz-3DPyS** (device B), and **pDTCz-DPS** (device C) devices. c) external quantum efficiencies versus brightness curves of device A, B and C. d) Electroluminescence (EL) spectrum of device A, B and C.

For the OLEDs with **pDTCz-DPmS** and **pDTCz-DPzS**, the device stacks are ITO/TAPC (40nm)/mCP (10nm)/ DPEPO:Dopant (7 wt%)/DPEPO (10nm)/TmPyPB (40nm)/LiF (1nm)/Al (100nm). In these devices only TAPC was used as a hole injection and transporting layer. Figure **3.13** shows the electroluminescence (EL) spectra of **pDTCz-DPmS** (device D) and **pDTCz-DPzS** (device E) based devices. The CIE chromaticity coordinates are (0.19, 0.26) and (0.31, 0.53) for device D and E. The device based on **pDTCz-DPzS** shows green emission, which is consistent with the stronger acceptor in **pDTCz-DPzS**.

Figure **3.13c** shows a representative EQE versus brightness curve for both devices. Device D shows an EQE_{max} of 14% at 6 cd/m^2. The EQE values of device D1 decrease considerably at 100 cd/m^2 (EQE_{100} = 7%), which is likely due to poor charge balance in the device

owing to the *n*-type nature of the DPEPO host. The device shows a low turn-on voltage (~ 3.5 eV) and brightness levels reaching 240 cd/m^2 (EQE = 2.9%). Device E shows an EQE_{max} of 12% at 10 cd/m^2. At 100 cd/m^2, the EQE value is still high at EQE_{100} of 14%. Device D2 also shows a low turn-on voltage (~ 4.3 eV) and brightness levels reaching higher levels, 961 cd/m^2 (EQE = 4.1%).

Compared to **pDTCz-3DPyS** and **pDTCz-2DPyS** as the emitters dispersed in DPEPO, the **pDTCz-DPmS** and **pDTCz-DPzS** devices show improvements in both EQE_{max} and EQE_{100} values. The EQE_{max} increased from 13% **pDTCz-3DPyS**:DPEPO and 11% **pDTCz-2DPyS:DPEPO** to 14% in **pDTCz-DPmS**:DPEPO and 22% in **pDTCz-DPzS**:DPEPO. However, the greatest improvement in device performance is related to the efficiency roll-off. The **pDTCz-3DPyS**:DPEPO OLEDs showed a efficiency drop of 67% from its EQE_{max} value at 100 cd/m^2 while for the **pDTCz-2DPyS**:DPEPO OLEDs the efficiency roll-off is 63%. The **pDTCz-DPmS** and **pDTCz-DPzS** devices, however, show smaller efficiency roll-offs of 51% and 36% for devices D and E, respectively, which is contributed by the smaller ΔE_{ST} values and faster delayed lifetimes of **pDTCz-DPmS** and **pDTCz-DPzS** in DPEPO. On the other hand, the **pDTCz-3DPyS**:DPEPO and **pDTCz-2DPyS**:DPEPO devices show sharp blue EL spectra. While device D shows a slightly red-shifted λ_{EL} of 461 nm compared to **pDTCz-3DPyS**:DPEPO (λ_{EL} = 452 nm) and a similar EL maximum to **pDTCz-2DPyS**:DPEPO (λ_{EL} = 466 nm), its spectra is broader, reflected by the larger FWHM. For device E the λ_{EL} of 521 nm is strongly red-shifted. Therefore, with the addition of a second nitrogen atom in the bridge of the emitters there is significant improvement in device performance, but at the cost of lower color purity.

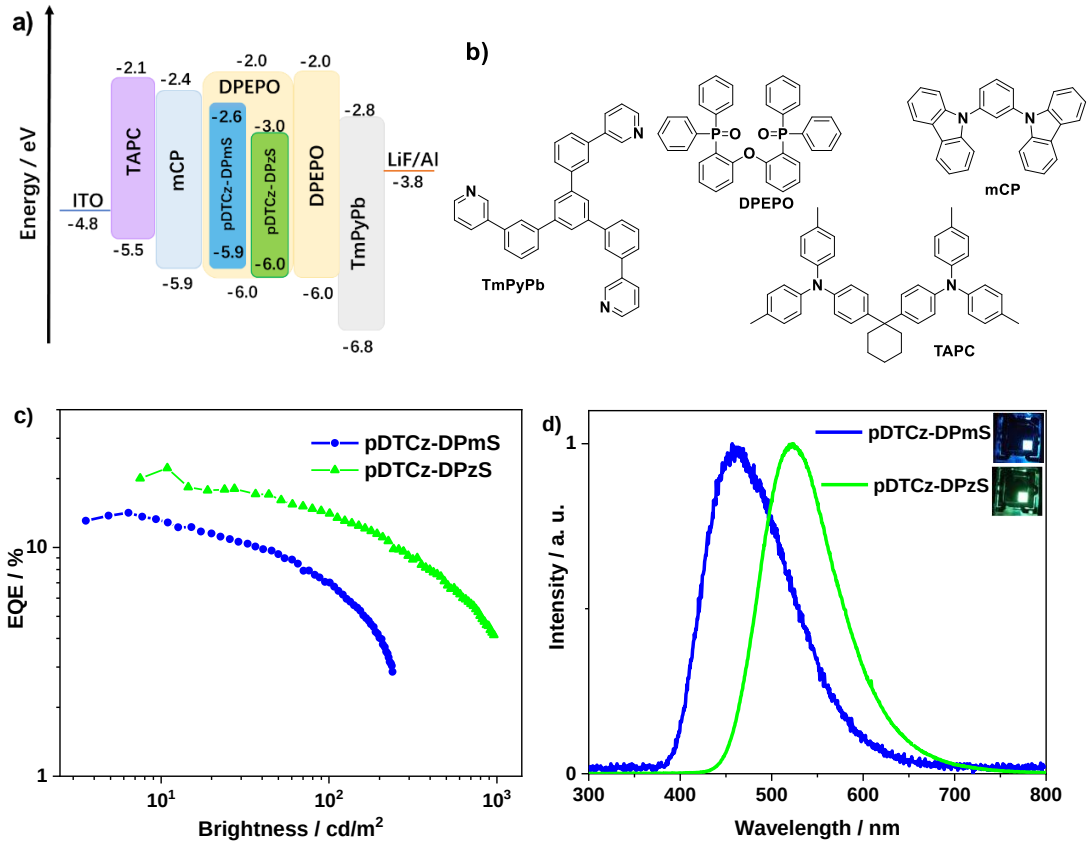

Figure **3.13**. a) Device architecture and b) molecular structures of materials used in **pDTCz-DPmS** (device D), and **pDTCz-DPzS** (device E) devices. c) external quantum efficiencies versus brightness curves of device D and E. d) Electroluminescence (EL) spectrum of device D and E.

Table **3.4.** OLEDs performance of our four emitters and reference emitter **pDTCz-DPS**

Device	**V_{on} / V**	**EQE_{max} / %**	**EQE_{100} / %**	**Lum_{max} / cd m^{-2}**	**CIE (x,y)**	**λ_{EL} / nm**
pDTCz-DPS	4.0	4.6	3.2	499	(0.15, 0.08)	428
pDTCz-2DPyS	3.6	11.4	4.2	462	(0.15, 0.18)	462
pDTCz-3DPyS	3.5	13.4	4.5	392	(0.15, 0.13)	452
pDTCz-DPmS	3.6	14.3	7.1	240	(0.19, 0.26)	461
pDTCz-DPzS	4.4	22.2	14.2	961	(0.31, 0.53)	522

3.8 Conclusions

We have designed four D-A-D TADF emitters, **pDTCz-2DPyS**, **pDTCz-3DPyS**, **pDTCz-DPmS**, and **pDTCz-DPzS**, that include acceptor moieties containing pyridine, pyrimidine, and pyrazine groups. The excited states of the four emitters possess strong charge transfer character and $\Delta E_{ST} < 0.22$ eV, and so these compounds emit via a TADF mechanism. High photoluminescence quantum yields of between 68-81% were achieved when dispersed in DPEPO as a host matrix. Vacuum-deposited OLEDs were fabricated and showed deep-blue to green electroluminescence, with EQE_{max} of 11.4% (at 4.5 cd/m^2), 13.4% (1.4 cd/m^2), 14.3% (at 6.4 cd/m^2), and 22.2% (at 10.9 cd/m^2) using **pDTCz-2DPyS**, **pDTCz-3DPyS**, **pDTCz-DPmS**, and **pDTCz-DPzS** as emitters, respectively. These OLEDs showed improved EQE_{max} values and efficiency roll-off when compared to the device using the reference emitter **pDTCz-DPS** (EQE_{max} = 4.6% at 0.9 cd/m^2). Further, the OLEDs with **pDTCz-DPmS**, and **pDTCz-DPzS** showed further improved EQE_{max} and efficiency roll-off compared to the devices with **pDTCz-2DPyS** and **pDTCz-3DPyS**. These improvements result from the more planar donor-bridge conformations that are stabilized by intramolecular hydrogen bonding adopted by **pDTCz-3DPyS**, **pDTCz-DPmS** and **pDTCz-DPzS**. These results show that small changes in the structure of the bridge unit play a crucial role in achieving highly efficient TADF OLEDs.

3.9 Experimental section

General consideration

All experiments were carried out with commercial solvents from Fisher Scientific Ltd, except where specifically mentioned. Commercially obtained chemicals were used as received. All manipulations were carried out under an inert atmosphere using standard Schlenk line techniques.

^{1}H NMR, and ^{13}C NMR were recorded at room temperature on a Bruker Avance spectrometer at 400 MHz and 100 MHz, respectively. ^{1}H NMR and ^{13}C NMR spectra were referenced to the residual solvent peaks ($CDCl_3$ = 7.26 ppm for ^{1}H NMR and 77.16 ppm for ^{13}C NMR). The following abbreviations have been used for multiplicity assignments: “s” for singlet, “d” for doublet, “t” for triplet, “m” for multiplet and “br” for broad. Elemental analysis was measured by London Metropolitan University. Samples for high resolution mass spectrum (HRMS) were sent to the National Mass Spectrometry Facility in Swansea (EPSRC) for analysis by nano-electrospray on an Orbitrap instrument.

Materials and synthesis

Synthesis of bis(5-bromopyridin-2-yl)sulfone (DPBr-S)

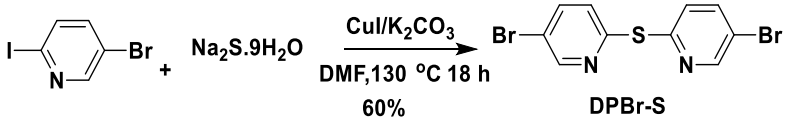

DPBr-S was synthesized based on modified literature.[9] To a 150 mL three neck flask were added 2-iodo-5-bromopyridine (280 mg, 1 mmol, 1 equiv.), sodium sulfide (140 mg, 0.6 mmol, 0.6

equiv.), copper (I) iodide (30 mg, 0.1 mmol, 0.1 equiv.) and potassium carbonate (140 mg, 1 mmol, 1 equiv.). The flask was by three cycles of vacuum-nitrogen purging and 10 mL of DMF was injected. The mixture was stirred at 130 °C for 18 h under nitrogen atmosphere. The mixture was washed with water and extracted with ethyl acetate (3×50 mL). The combined organic layers were dried with anhydrous magnesium sulfate and organic solvent was removed under reduced pressure. The crude product was purified by silica gel column chromatography. DCM/Hexane=1/1 was used as eluent to obtain **DPBr-S** as a white solid.

DPBr-S: R_f = 0.5 (50% DCM/Hexane). **Yield:** 80%. **Mp:** 75-77°C. **^{1}H NMR (400 MHz, $CDCl_3$) δ (ppm):** 8.61 (s, 2H), 7.77 (dd, *J* = 8.4, 2.4 Hz, 2H), 7.39 (d, *J* = 8.4 Hz, 2H). **^{13}C NMR (101 MHz, $CDCl_3$) δ (ppm):** 154.7, 151.2, 139.7, 127.1, 125.3. **HR ESI-MS: $[M+H]^+$:** calcd for $[C_{10}H_7{}^{79}Br_2N_2S]^+$: 346.8670; found: 346.8673.

Synthesis of 6,6'-sulfonylbis(3-bromopyridine) (DPBr-SO_2)

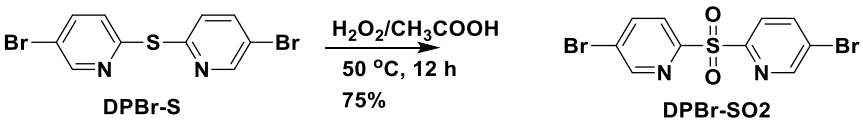

To a 50 mL flask was dissolved DPBr-S (60 mg, 0.2 mmol, 1 equiv.) in 2 mL of glacial acetic acid. 2 mL of hydrogen peroxide solution (30 wt%, 100 equiv.) was added and the mixture was stirred at 50 °C for 12 h. The mixture was poured into 20 mL of ice water and extracted with DCM (3×20 mL). The combined organic layers were dried with anhydrous magnesium sulfate and organic solvent was removed under reduced pressure. The crude product was purified by silica gel column chromatography. DCM/Hexane=1/1 was used as eluent to obtain DPBr-SO_2 as a white

solid. **DPBr-SO_2: R_f** = 0.3 (50% DCM/Hexane). **Yield:** 75%. **Mp:** 98-100˚C. **^{1}H NMR (400 MHz, $CDCl_3$) δ (ppm):** 8.72 - 8.65 (m, 2H), 8.02 (dd, *J* = 8.4 Hz, 2.3 Hz, 2H), 7.93 (dd, *J* = 8.4 Hz, 0.7 Hz, 2H). **^{13}C NMR (101 MHz, $CDCl_3$) δ (ppm):** 162.0, 151.3, 140.7, 123.0, 120.9. **HR ESI-MS: $[M+H]^+$:** calcd for $[C_{10}H_7{}^{79}Br_2N_2O_2S]^+$: 378.8569; found: 378.8567.

Synthesis of 9,9'-(sulfonylbis(pyridine-6,3-diyl))bis(3,6-di-*tert*-butyl-9H-carbazole) (pDTCz-2DPyS)

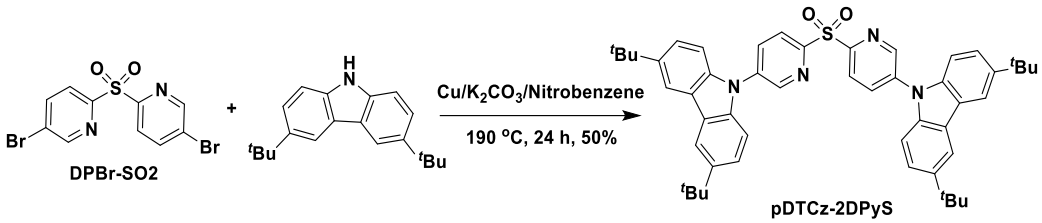

To a 50 mL flask were added DPBr-SO_2 (50 mg, 0.13 mmol, 1 equiv.), di-*tert*-butyl-9H-carbazole (100 mg, 0.3 mmol, 2.3 equiv.), copper powder (10 mg, 0.14 mmol, 1.1 equiv.) and potassium carbonate (50 mg, 0.4 mmol, 3 equiv.). The flask was degassed by three cycles of vacuum-nitrogen purging and 5 mL of nitrobenzene was added. The mixture was stirred at 190 °C for 24 h under a nitrogen atmosphere. After completion of reaction, water was added to the reaction mixture and extracted with DCM (3×50 mL). The combined organic layers were dried with anhydrous magnesium sulfate and organic solvent was removed under reduced pressure. The crude product was purified by silica gel column chromatography. DCM/Hexane=1/2 was used as eluent to afford **pDTCz-2DPyS** as a white solid.

pDTCz-2DPyS: R_f = 0.7 (90% DCM/Hexane). **Yield:** 50%. **Mp:** 220-225˚C. **^{1}H NMR (400 MHz, $CDCl_3$) δ (ppm):** 9.08 (dd, *J* = 2.5, 0.7 Hz, 2H), 8.67 (dd, J = 8.4, 0.7 Hz, 2H), 8.29 (dd, J

= 8.4, 2.5 Hz, 2H), 8.16 (dd, *J* = 1.9, 0.7 Hz, 4H), 7.53 (dd, *J* = 8.7, 1.9 Hz, 4H), 7.48 (dd, *J* = 8.6, 0.7 Hz, 4H), 1.49 (s, 36H). **^{13}C NMR (101 MHz, $CDCl_3$) δ (ppm):** 153.3, 147.7, 144.8, 138.9, 137.9, 134.8, 125.4, 124.5, 124.2, 116.8, 108.8, 34.9, 31.9. **HR ESI-MS: $[M+H]^+$:** calcd for $[C_{50}H_{54}N_4O_2SH]^+$: 775.4040, found 775.4033. **Elemental analysis:** Calcd for $C_{50}H_{54}N_4O_2S$: C, 77.48; H, 7.02; N, 7.23. Found: C, 77.37; H, 6.91; N, 7.29. **HPLC:** H_2O (5%) /MeCN, 1.0 mL min^{-1}, 300 nm; tr (99.4 %) = 1.6 min.

Synthesis of 9-(5-bromopyridin-2-yl)-3,6-di-*tert*-butyl-9H-carbazole (PBr-TC)

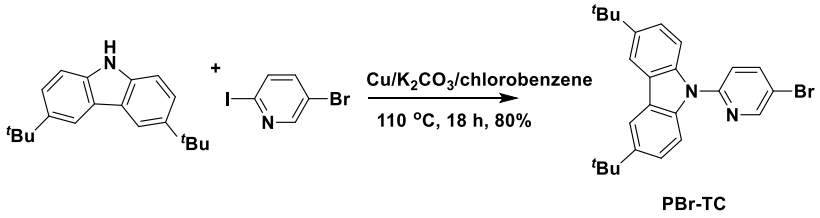

PBr-TC

To a 250 mL flask were added 2-iodo-5-bromopyridine (1.4 g, 5 mmol, 1 equiv.), di-*tert*-butyl-9H-carbazole (1.4 g, 5 mmol, 1 equiv.), copper powder (320 mg, 5 mmol, 1 equiv.) and potassium carbonate (2.2 g, 15 mmol, 3 equiv.). The flask was degassed by three cycles of vacuum-nitrogen purging and 20 mL of chlorobenzene was injected. The mixture was stirred at 110 °C for 18 h under nitrogen atmosphere. After completion of reaction, water was added to the reaction mixture and extracted with DCM (3 x 50 mL). The combined organic layers were dried with anhydrous magnesium sulfate. The organic solvent was removed under reduced pressure and the crude product was purified by silica gel column chromatography. DCM/Hexane=1/3 was used as eluent to afford **PBr-TC** as a white solid.

PBr-TC: R_f = 0.4 (20% DCM/Hexane). **Yield: 80%**. **Mp:** 185-188˚C. **^{1}H NMR (400 MHz, $CDCl_3$) δ (ppm):** 8.75 (dd, *J* = 2.6 Hz, 0.7 Hz, 1H), 8.12 (d, *J* = 1.9 Hz, 2H), 8.01 (dd, *J* = 8.6 Hz, 2.5 Hz, 1H), 7.80 (dd, *J* = 8.7 Hz, 0.6 Hz, 2H), 7.58 (dd, *J* = 8.6 Hz, 0.7 Hz, 1H), 7.52 (dd, *J* = 8.7 Hz, 2.0 Hz, 2H), 1.49 (s, 18H). **^{13}C NMR (101 MHz, $CDCl_3$) δ (ppm):** 150.9, 150.4, 144.3, 140.8, 137.5, 124.6, 124.1, 119.2, 116.2, 110.7, 34.8, 31.9. **HR TOF-MS: $[M+H]^+$:** calcd for $[C_{25}H_{28}{}^{79}BrN_2]^+$: 435.1436; found: 435.1433.

Synthesis of 9-(5-iodopyridin-2-yl)-3,6-di-*tert*-butyl-9H-carbazole (PI-TC)

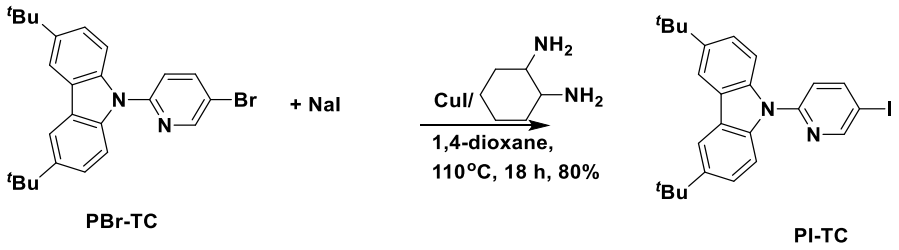

To a 100 mL flask were added **PBr-TC** (250 mg, 0.6 mmol, 0.6 equiv.), sodium iodide (150 mg, 1 mmol, 1 equiv.), and copper(I) iodide (20 mg, 0.1 mmol, 0.1 equiv.). The flask was degassed by three cycles of vacuum-nitrogen purging and 20 mL of chlorobenzene was injected. The reaction mixture was stirred at 110 ºC for 18 h under a nitrogen atmosphere. After completion of reaction, water was slowly added to the reaction mixture and extracted with DCM (3 x 50 mL). The combined organic layers were dried with anhydrous magnesium sulfate and organic solvent was removed under reduced pressure. The crude product was purified by silica gel column chromatography. DCM/Hexane=1/3 was used as eluent to obtain **PI-TC** as a white solid.

PI-TC: R_f = 0.5 (25% DCM/Hexane). **Yield: 80%**. **Mp:** 200-203˚C. **^{1}H NMR (400 MHz, $CDCl_3$) δ (ppm):** 8.89 (dd, *J* = 2.3 Hz, 0.7 Hz, 1H), 8.18 (dd, *J* = 8.5 Hz, 2.4 Hz, 1H), 8.12 (dd,

J = 2.0 Hz, 0.6 Hz, 2H), 7.81 (dd, *J* = 8.7 Hz, 0.6 Hz, 2H), 7.55 - 7.47 (m, 3H), 1.48 (s, 18H). **^{13}C NMR (101 MHz, $CDCl_3$) δ (ppm):** 155.4, 150.4, 146.3, 144.3, 140.8, 137.5, 124.5, 124.1, 119.2, 116.2, 110.7, 34.8, 31.9. **HR ESI-MS: $[M+H]^+$:** calcd for $[C_{25}H_{28}IN_2]^+$: 483.1285; found: 483.1292.

Synthesis of bis(6-(3,6-di-*tert*-butyl-9H-carbazol-9-yl)pyridin-3-yl)sulfone (3DPS-pDTC)

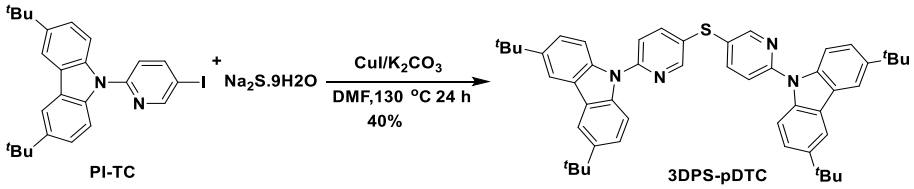

To a 100 mL three necks flask were added PI-TC (300 mg, 0.6 mmol, 2 equiv.), sodium sulfide (70 mg, 0.3 mmol, 1 equiv.), copper(I) iodide (15 mg, 0.05 mmol, 0.3 equiv.) and potassium carbonate (80 mg, 0.7 mmol, 2.3 equiv.). The flask was degassed by three cycles of vacuum-nitrogen purging and 10 mL of DMF was injected. The mixture was stirred at 130 °C for 24 h under a nitrogen atmosphere. The reaction mixture poured into water and extracted with ethyl acetate (3×20 mL). The combined organic layers were dried with magnesium sulfate and organic solvent was removed under reduced pressure. The crude product was purified by silica gel column chromatography. DCM/Hexane=1/1 was used as eluent to afford **3DPS-pDTC** as white solid.

3DPS-pDTC: R_f = 0.6 (60% DCM/Hexane). **Yield: 40%**. **Mp:** 165-168˚C. **^{1}H NMR (400 MHz, $CDCl_3$) δ (ppm):** 8.78 (dd, *J* = 2.5 Hz, 0.7 Hz, 2H), 8.12 (dd, *J* = 2.0 Hz, 0.6 Hz, 4H), 7.96 (dd, *J* = 8.5 Hz, 2.5 Hz, 2H), 7.87 (dd, *J* = 8.7 Hz, 0.6 Hz, 4H), 7.69 (dd, *J* = 8.5 Hz, 0.8 Hz, 2H), 7.55 - 7.49 (m, 4H), 1.49 (s, 36H). **^{13}C NMR (101 MHz, $CDCl_3$) δ (ppm):** 151.7, 151.4, 144.4, 141.24,

137.6, 127.6, 124.7, 124.0, 118.3, 116.2, 111.0, 34.8, 31.9. **HR ESI-MS: $[M+H]^+$:** calcd for $[C_{50}H_{55}N_2S]^+$: 742.4040, found 742.4034.

Synthesis of 9,9'-(sulfonylbis(pyridine-5,2-diyl))bis(3,6-di-tert-butyl-9H-carbazole) (pDTCz-3DPyS)

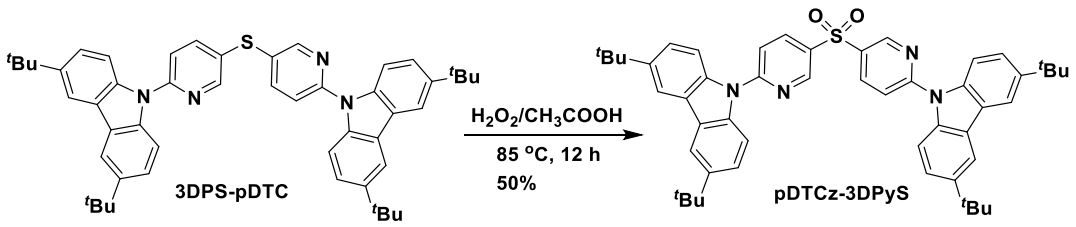

To **3DPS-pDTC** (70 mg, 0.1 mmol, 1 equiv.) in 2 mL of glacial acetic acid was added 2 mL of hydrogen peroxide solution (30 wt%, 200 equiv.). The reaction mixture was stirred at 50 °C for 12 h. The mixture was poured into 20 mL of ice water and extracted with dichloromethane (3×20 mL). The combined organic layer was dried with magnesium sulfate and dried with anhydrous magnesium sulfate and organic solvent was removed under reduced pressure and the crude product was purified by silica gel column chromatography. DCM/Hexane=1/1 was used as eluent to obtain **pDTCz-3DPyS** as a white solid.

pDTCz-3DPyS: R_f = 0.3 (50% DCM/Hexane). **Yield: 50%**. **Mp:** 268-270 ˚C. **^{1}H NMR (400 MHz, $CDCl_3$) δ (ppm):** 9.30 (d, *J* = 2.5 Hz, 2H), 8.43 (dd, *J* = 8.7, 2.6 Hz, 2H), 8.10 (d, *J* = 2.0 Hz, 4H), 7.99 (d, *J* = 8.8 Hz, 4H), 7.87 (d, *J* = 8.7 Hz, 2H), 7.53 (dd, *J* = 8.8, 2.0 Hz, 4H), 1.48 (s, 36H). **^{13}C NMR (101 MHz, $CDCl_3$) δ (ppm):** 56.0, 149.1, 137.2, 131.1, 132.8, 125., 124.4, 116.8, 116.4, 111.8, 34.8, 31.8. **HR ESI-MS: $[M+H]^+$:** calcd for $[C_{50}H_{55}N_2O_2S]^+$: 775.4040, found 775.4034. **Elemental analysis:** Calcd for $C_{50}H_{54}N_4O_2S$: C, 77.48; H, 7.02; N,

7.23. Found: C, 77.31; H, 7.05; N, 7.30. **HPLC:** 5% H_2O/MeCN, 1.0 mL min^{-1}, 300 nm; tr (98.2 %) = 6.1 min.

Synthesis of 9-(5-bromopyrazin-2-yl)-3,6-di-*tert*-butyl-9H-carbazole (**tCz-BrPz**)

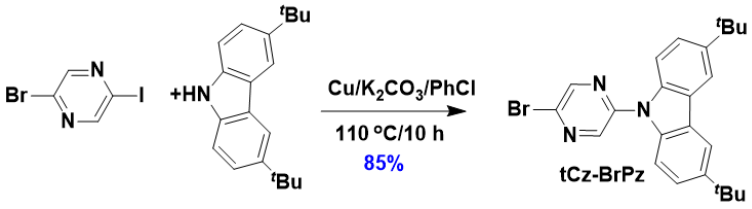

To a 250 mL flask were added 2-bromo-5-iodopyrazine (2.9 g, 10 mmol, 1 equiv.), di-*tert*-butyl-9H-carbazole (3.0 g, 11 mmol, 1.1 equiv.), copper powder (640 mg, 10 mmol, 1 equiv.) and potassium carbonate (4.5 g, 30 mmol, 3 equiv.). The flask was degassed by three cycles of vacuum-nitrogen purging and 50 mL of chlorobenzene was injected. The mixture was stirred at 110 °C for 10 h under a nitrogen atmosphere. After cooling, water was added to the reaction mixture followed by extraction with DCM (3 × 50 mL). The combined organic layers were dried with anhydrous magnesium sulfate. The organic solvent was removed under reduced pressure and the crude product was purified by silica gel column chromatography. DCM/Hexane=1/3 was used as eluent to afford **tCz-BrPz** as a faint yellow solid.

Yield: 85%. **R_f:** 0.65 (33% DCM/Hexanes). **Mp:** 180-182 °C. **^{1}H NMR (400 MHz, $CDCl_3$) δ (ppm):** 8.84 (d, J = 1.4 Hz, 1H), 8.74 (d, J = 1.4 Hz, 1H), 8.13 (dd, J = 2.0, 0.6 Hz, 2H), 7.84 (dd, J = 8.8, 0.7 Hz, 2H), 7.54 (dd, J = 8.7, 2.0 Hz, 2H), 1.49 (s, 18H). **^{13}C NMR (101 MHz, $CDCl_3$) δ (ppm):** 148.0, 145.9, 145.3, 139.3, 137.1, 134.6, 125.1, 124.4, 116.5, 110.7, 34.8, 31.9. **HRMS** (LTQ Orbitrap XL) **$[M+H]^+$ Calculated: ($C_{24}H_{27}N_3{}^{79}Br$)** 436.1383; **Found:** 436.1380.

Synthesis of bis(5-(3,6-di-*tert*-butyl-9H-carbazol-9-yl)pyrazin-2-yl)sulfane (**tCz-PzS**)

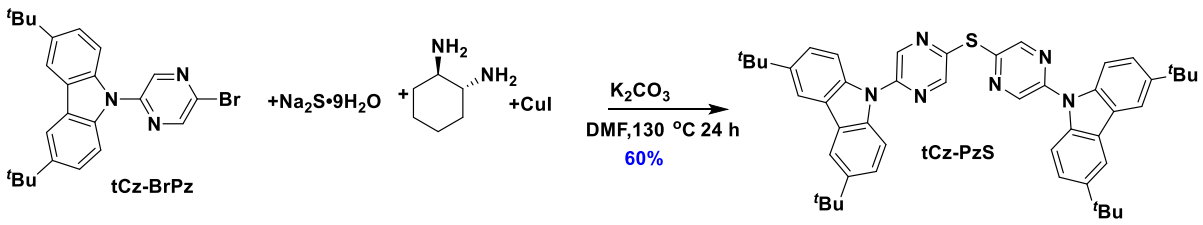

To a 100 mL three neck flask were added **tCz-BrPz** (960 mg, 2.2 mmol, 2.2 equiv.), sodium sulfide hydrate (100 mg, 1 mmol, 1 equiv.), copper(I) iodide (40 mg, 0.2 mmol, 0.2 equiv.), *trans*-1,2-cyclohexanediamine (45 mg, 0.4 mmol, 0.4 equiv.), and potassium carbonate (700 mg, 5 mmol, 5 equiv.). The flask was degassed by three cycles of vacuum-nitrogen purging and 20 mL of DMF was injected. The mixture was stirred at 130 °C for 24 h under a nitrogen atmosphere. The reaction mixture poured into 100 mL of icy water and extracted by ethyl acetate (3×20 mL). The combined organic layers were dried with magnesium sulfate and organic solvent was removed under reduced pressure. The crude product was purified by silica gel column chromatography. DCM/Hexane=1/1 was used as eluent to afford **tCz-PzS** as a white solid.

Yield: 60%. **R_f:** 0.52 (33% DCM/Hexanes). **Mp:** 211-212 °C. **^{1}H NMR (500 MHz, $CDCl_3$) δ (ppm):** 9.02 (s, 2H), 8.85 (s, 2H), 8.13 (d, *J* = 1.9 Hz, 4H), 7.91 (d, *J* = 8.7 Hz, 4H), 7.55 (dd, *J* = 8.7, 1.9 Hz, 4H), 1.49 (s, 36H). **^{13}C NMR (126 MHz, $CDCl_3$) δ (ppm):** 151.3, 148.3, 145.3, 144.8, 140.6, 137.5, 137.0, 125.2, 124.4, 116.5, 110.8, 34.8, 31.9. **HRMS** (LTQ Orbitrap XL) **$[M+H]^+$ Calculated: ($C_{48}H_{53}N_6S$)** 745.4047; **Found:** 745.4043.

Synthesis of 9,9'-(sulfonylbis(pyrazine-5,2-diyl))bis(3,6-di-*tert*-butyl-9H-carbazole) (**pDTCz-DPzS**)

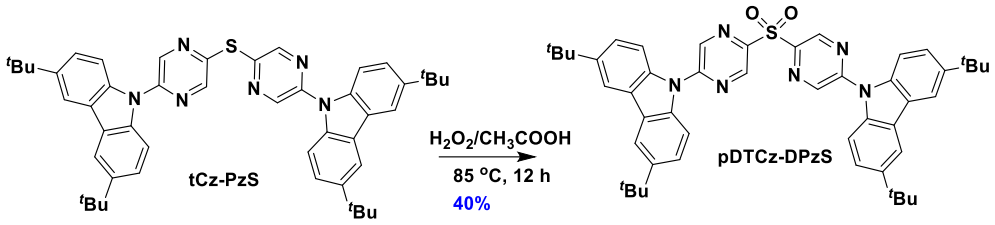

To a 100 mL two neck flask were added **tCz-PzS** (1.5 g, 2 mmol, 1 equiv.) and 20 mL of acetic acid. After tCz-PzS was dissolved in acetic acid, 30 mL of 30 wt% hydrogen peroxide was injected. The mixture was heated to 85 °C for 12 h. The mixture was then poured into 100 mL of icy water and extracted by DCM (3×50 mL). The combined organic layers were dried with magnesium sulfate and the organic solvent was removed under reduced pressure. The crude product was purified by silica gel column chromatography. DCM/ Hexanes = 4/1 was used as eluent to afford **pDTCz-DPzS** as a light-green solid. **Yield:** 40%. **R_f:** 0.68 (75% DCM/Hexanes). **Mp:** 292-294 °C. **^{1}H NMR (500 MHz, $CDCl_3$) δ (ppm):** 9.54 (d, *J* = 1.3 Hz, 2H), 9.18 (d, *J* = 1.3 Hz, 2H), 8.10 (d, *J* = 1.9 Hz, 4H), 8.06 (d, *J* = 8.7 Hz, 4H), 7.55 (dd, *J* = 8.8, 2.0 Hz, 4H), 1.49 (s, 36H). **^{13}C NMR (126 MHz, $CDCl_3$) δ (ppm):** 151.5, 146.7, 145.7, 144.1, 138.3, 136.6, 126.1, 124.7, 116.6, 112.1, 34.9, 31.8. **HRMS** (LTQ Orbitrap XL) **$[M+H]^+$ Calculated: ($C_{48}H_{53}N_6O_2S$)** 777.3945; **Found:** 777.3939. **Elemental analysis: Calcd for $C_{48}H_{52}N_6O_2S$**: C, 74.20; H, 6.75; N, 10.82. Found: C, 74.38; H, 6.81; N, 10.95. **HPLC:** 10% H_2O/MeCN, 1.0 mL min^{-1}, 300 nm; tr (98.5 %) = 17.7 min.

Synthesis of 9-(5-bromopyrimidin-2-yl)-3,6-di-*tert*-butyl-9H-carbazole (tCz-BrPm)

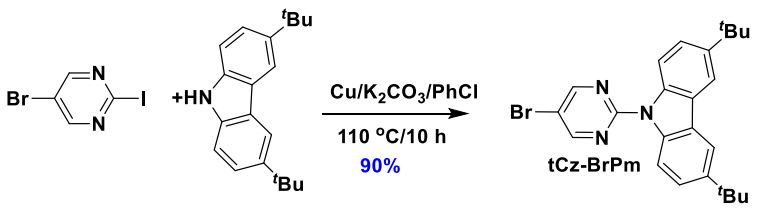

To a 250 mL flask were added 5-bromo-2-iodopyrimidine (2.9 g, 10 mmol, 1 equiv.), di-*tert*-butyl-9H-carbazole (3 g, 11 mmol, 1.1 equiv.), copper powder (640 mg, 10 mmol, 1 equiv.) and potassium carbonate (4.5 g, 30 mmol, 3 equiv.). The flask was degassed by three cycles of vacuum-nitrogen purging and 50 mL of chlorobenzene was injected. The mixture was stirred at 110 °C for 10 h under nitrogen atmosphere. The reaction mixture was then poured into water and extracted with DCM (3 × 50 mL). The combined organic layers were dried with anhydrous magnesium sulfate, filtered and the solvent removed under reduced pressure. The crude product was purified by silica gel column chromatography. DCM/Hexane=1/3 was used as eluent to afford **tCz-BrPm** as a white solid.

Yield: 90%. **R_f:** 0.65 (33% DCM/Hexanes). **Mp:** 197-199 °C. **^{1}H NMR (400 MHz, $CDCl_3$) δ (ppm):** 8.81 (s, 2H), 8.72 (d, *J* = 8.9 Hz, 2H), 8.08 (dd, *J* = 2.0, 1.0 Hz, 2H), 7.57 (dd, *J* = 8.8, 2.1 Hz, 2H), 1.50 (s, 18H). **^{13}C NMR (101 MHz, $CDCl_3$) δ (ppm):** 158.1, 157.3, 145.7, 137.2, 126.1, 124.3, 116.0, 115.6, 112.2, 34.8, 31.8. **HRMS** (LTQ Orbitrap XL) **$[M+H]^+$ Calculated: ($C_{24}H_{27}N_3{}^{79}Br$)** 436.1383; **Found:** 436.1380.

Synthesis of bis(2-(3,6-di-*tert*-butyl-9H-carbazol-9-yl) pyrimidin-5-yl) sulfane (**tCz-PmS**)

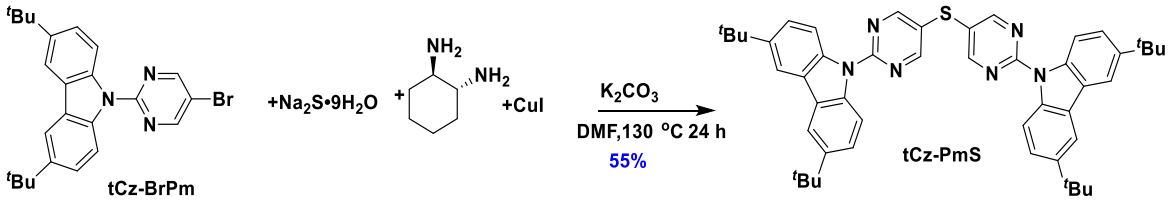

To a 100 mL three neck flask were added **tCz-BrPm** (960 mg, 2.2 mmol, 2.2 equiv.), sodium sulfide hydrate (100 mg, 1 mmol, 1 equiv.), copper(I) iodide (40 mg, 0.2 mmol, 0.2 equiv.), *trans*-

1,2-cyclohexanediamine (45 mg, 0.4 mmol, 0.4 equiv.), and potassium carbonate (700 mg, 5 mmol, 5 equiv.). The flask was degassed by three cycles of vacuum-nitrogen purging and 20 mL of DMF was injected. The mixture was stirred at 130 °C for 24 h under a nitrogen atmosphere. The reaction mixture was poured into 100 mL of icy water and extracted with ethyl acetate (3×20 mL). The combined organic layers were dried with magnesium sulfate and the organic solvent was removed under reduced pressure. The crude product was purified by silica gel column chromatography. DCM/Hexane=1/1 was used as eluent to afford **tCz-PmS** as a white solid.

Yield: 60%. **R_f:** 0.52 (33% DCM/Hexanes). **Mp:** 284-285 °C. **^{1}H NMR (400 MHz, $CDCl_3$) δ (ppm):** 8.92 (dd, *J* = 7.8, 2.9 Hz, 2H), 8.72 (dd, *J* = 8.9, 1.8 Hz, 2H), 8.08 (d, *J* = 2.0 Hz, 2H), 7.57 (dd, *J* = 8.9, 1.8 Hz, 2H), 1.50 (s, 18H). **^{13}C NMR (101 MHz, $CDCl_3$) δ (ppm):** 162.8, 158.0, 157.3, 145.7, 137.2, 126.1, 124.3, 116.2, 115.6, 34.8, 31.8. **HRMS** (LTQ Orbitrap XL) **$[M+H]^+$ Calculated: ($C_{48}H_{53}N_6S$)** 745.4047; **Found:** 745.4043.

Synthesis of 9,9'-(sulfonylbis(pyrimidine-5,2-diyl))bis(3,6-di-*tert*-butyl-9H-carbazole) (pDTCz-DPmS)

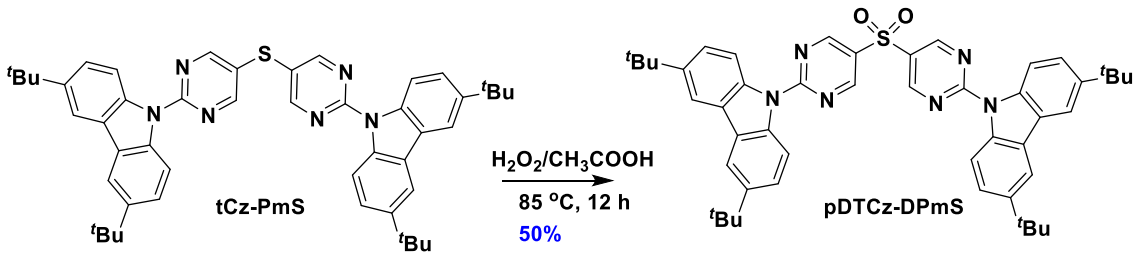

To a 100 mL of two neck flask were added tCz-PmS (1.5 g, 2 mmol, 1 equiv.) and 20 mL of acetic acid. After tCz-PmS was dissolved in acetic acid, 30 mL of 30 wt% hydrogen peroxide were injected. The mixture was heated to 85 °C for 12 h. The mixture was then poured into 100 mL of

icy water and extracted with DCM (3×50 mL). The combined organic layers were dried with magnesium sulfate, filtered and the organic solvent was removed under reduced pressure. The crude product was purified by silica gel column chromatography. DCM/ Hexanes = 4/1 was used as eluent to afford **pDTCz-DPmS** as a white solid.

Yield: 50%. **R_f:** 0.68 (75% DCM/Hexanes). **Mp:** 292-294 °C. **^{1}H NMR (500 MHz, $CDCl_3$) δ (ppm):** 9.31 (s, 4H), 8.84 (d, *J* = 8.9 Hz, 4H), 8.04 (d, *J* = 2.0 Hz, 4H), 7.57 (dd, *J* = 8.9, 2.0 Hz, 4H), 1.48 (s, 36H). **^{13}C NMR (126 MHz, $CDCl_3$) δ (ppm):** 160.2, 157.4, 147.2, 137.1, 128.6, 127.0, 124.7, 117.6, 115.8, 34.8, 31.7. **HRMS** (LTQ Orbitrap XL) **$[M+H]^+$ Calculated: ($C_{48}H_{53}N_6O_2S$)** 777.3945; **Found:** 777.3942. **Elemental analysis: Calcd for $C_{48}H_{52}N_6O_2S$**: C, 74.20; H, 6.75; N, 10.82. Found: C, 74.10; H, 6.82; N, 10.82. **HPLC:** 10% H_2O/MeCN, 1.0 mL min^{-1}, 300 nm; tr (97.5 %) = 29.2 min.

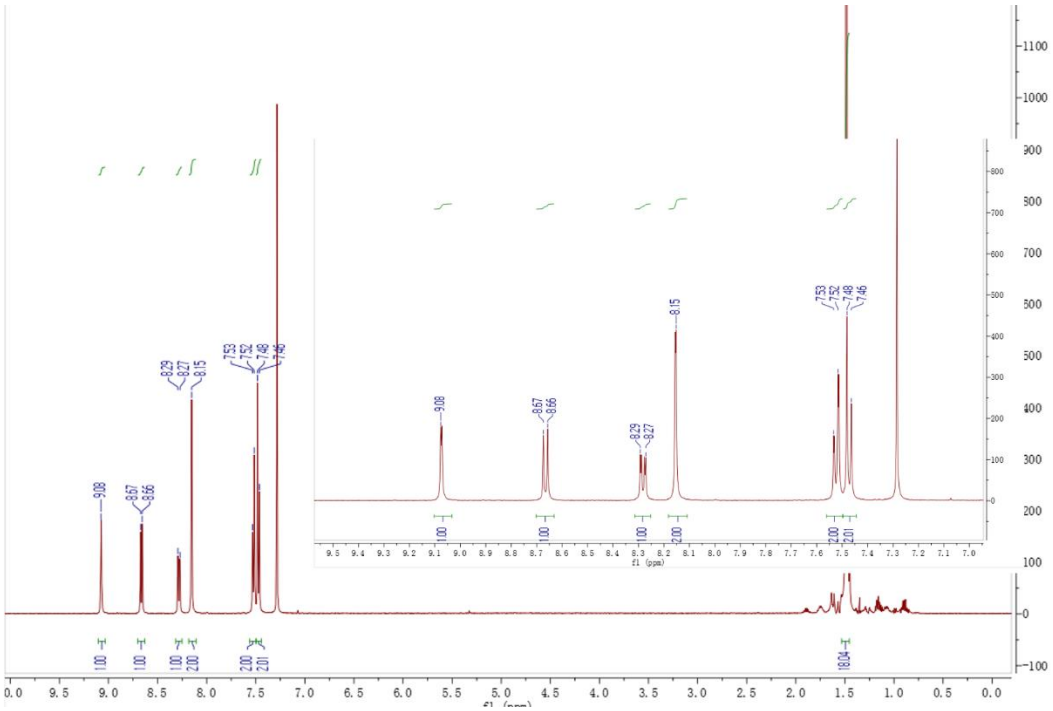

Figure **3.14.** ^{1}H NMR of **pDTCz-2DPyS** in $CDCl_3$

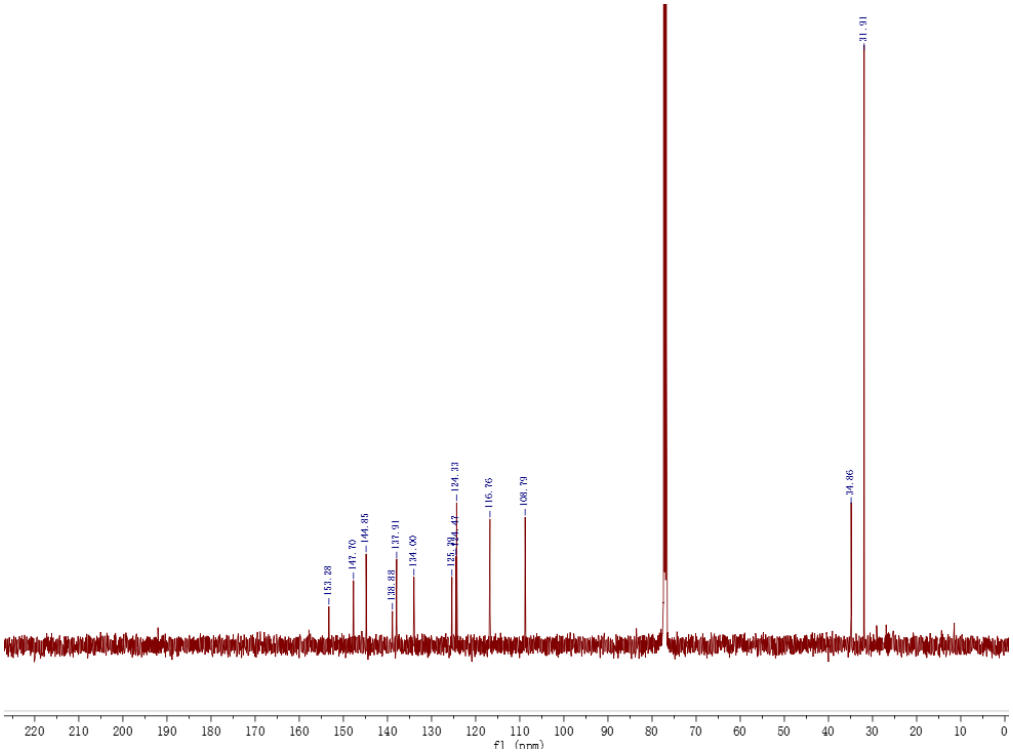

Figure **3.15.** ^{13}C NMR of **pDTCz-2DPyS** in $CDCl_3$

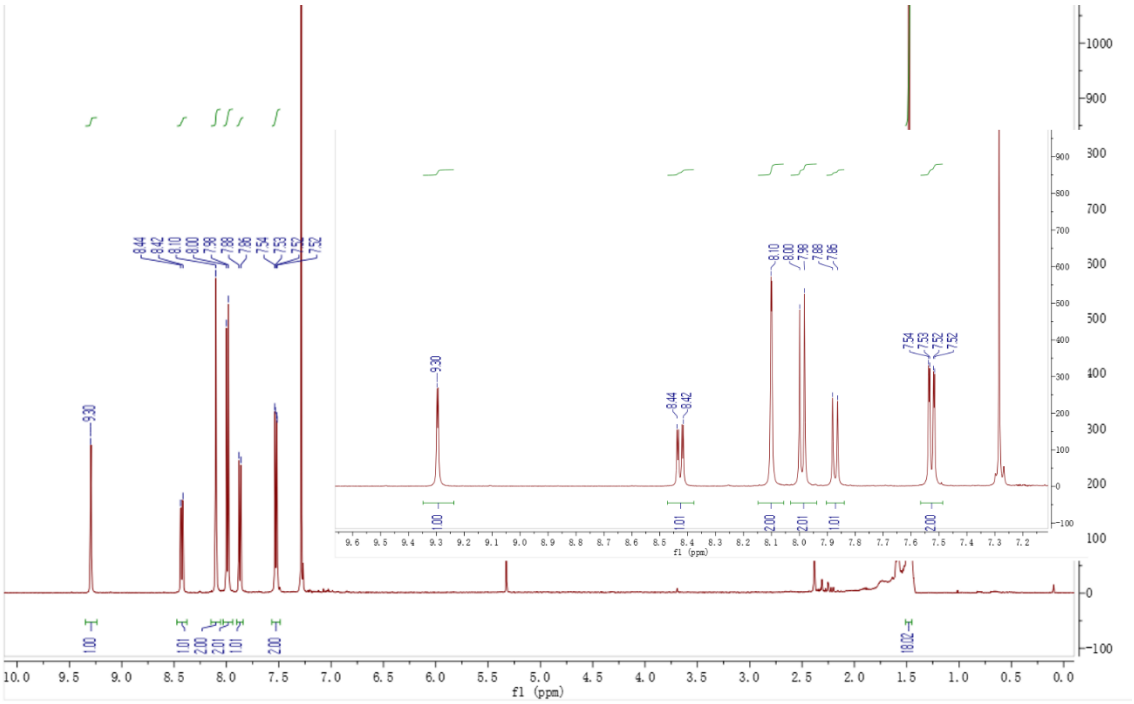

Figure **3.16.** ^{1}H NMR of **pDTCz-3DPyS** in $CDCl_3$

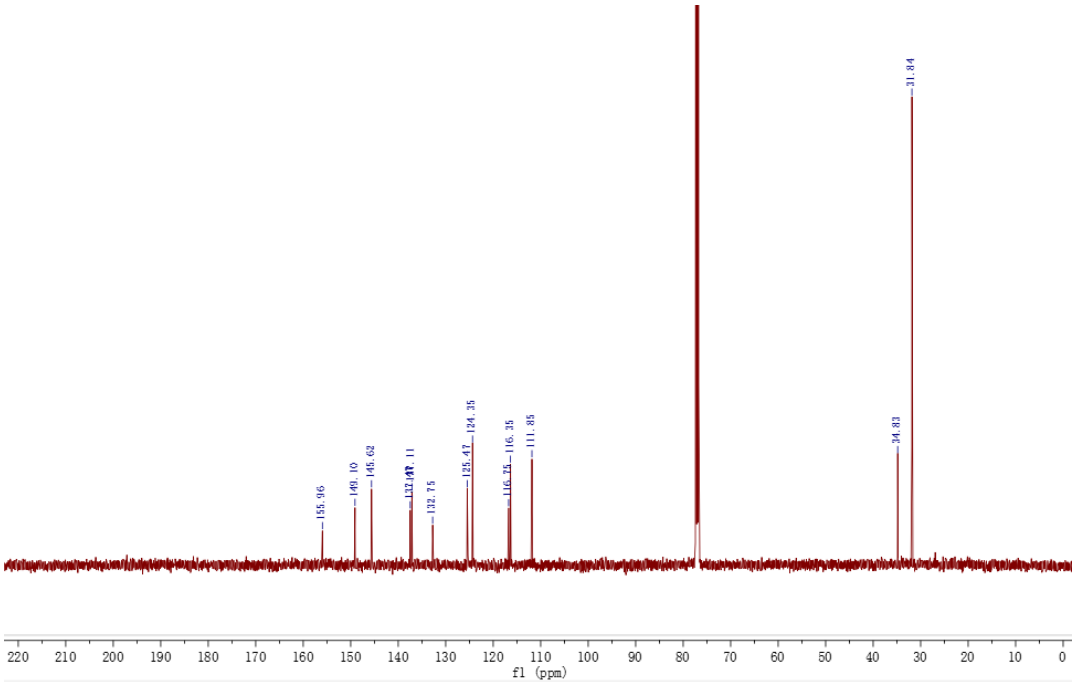

Figure **3.17.** ^{13}C NMR of **pDTCz-3DPyS** in $CDCl_3$

HPLC Trace Report30May2018

<Sample Information>

Sample Name	: 2PyS		
Sample ID	:		
Method Filename	: AcN (95).lcm		
Batch Filename	: ACN-95-350.lcb		
Vial #	: 1-73	Sample Type	: Unknown
Injection Volume	: 5 uL		
Date Acquired	: 23/05/2018 20:57:40	Acquired by	: ezc-7
Date Processed	: 23/05/2018 21:27:43	Processed by	: ezc-7

<Chromatogram>

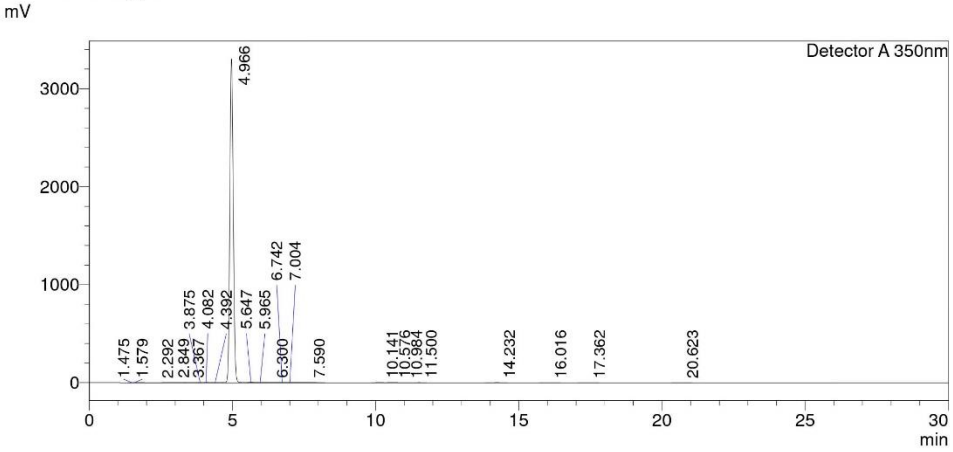

<Peak Table>

Detector A 350nm

Peak#	Ret. Time	Area	Height	Area%	Area/Height	Width at 5% Height
1	1.475	1771	658	0.006	2.693	0.132
2	1.579	17481	1370	0.063	12.761	--
3	2.292	1633	110	0.006	14.886	--
4	2.849	27078	771	0.098	35.107	--
5	3.367	10741	470	0.039	22.850	--
6	3.875	1638	300	0.006	5.470	--
7	4.082	41109	4902	0.148	8.387	--
8	4.392	11258	958	0.041	11.756	--
9	4.966	27478535	3301817	99.022	8.322	0.271
10	5.647	48734	5154	0.176	9.455	--
11	5.965	17151	1931	0.062	8.882	--
12	6.300	7738	846	0.028	9.142	0.290
13	6.742	2749	330	0.010	8.326	--
14	7.004	22471	2199	0.081	10.217	--
15	7.590	25297	1167	0.091	21.669	0.740
16	10.141	4248	251	0.015	16.918	--
17	10.576	13087	912	0.047	14.349	--
18	10.984	1417	97	0.005	14.572	--
19	11.500	3161	186	0.011	16.984	--
20	14.232	5646	295	0.020	19.147	0.717
21	16.016	1529	70	0.006	21.838	0.640
22	17.362	3054	163	0.011	18.692	0.612

Figure **3.18.** HPLC trace report of **pDTCz-2DPyS**

HPLC Trace Report30May2018

<Sample Information>

Sample Name	: 3PyS		
Sample ID	:		
Method Filename	: AcN (95).lcm		
Batch Filename	: ACN-95-350.lcb		
Vial #	: 1-72	Sample Type	: Unknown
Injection Volume	: 10 uL		
Date Acquired	: 23/05/2018 20:06:43	Acquired by	: ezc-7
Date Processed	: 23/05/2018 20:36:47	Processed by	: ezc-7

<Chromatogram>

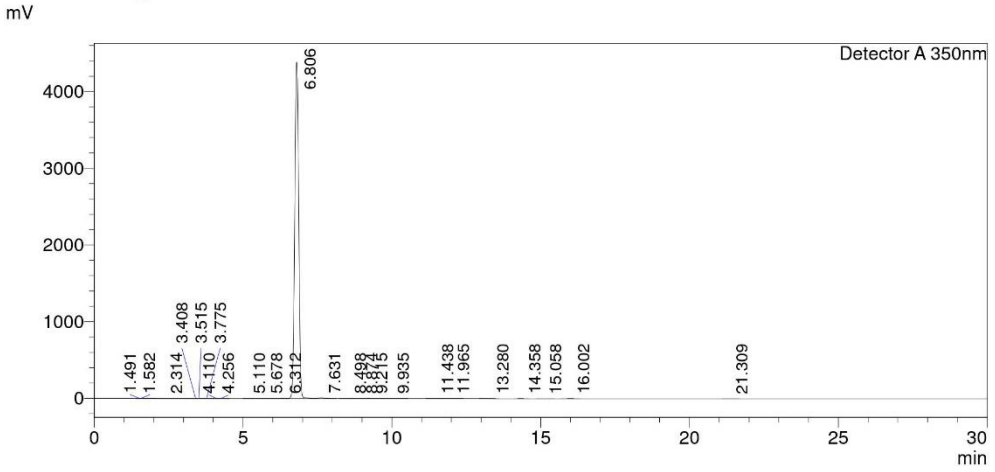

<Peak Table>

Detector A 350nm

Peak#	Ret. Time	Area	Height	Area%	Area/Height	Width at 5% Height
1	1.491	11408	5579	0.029	2.045	0.074
2	1.582	65401	3956	0.166	16.530	--
3	2.314	26912	761	0.068	35.377	--
4	3.408	2239	201	0.006	11.116	--
5	3.515	3528	250	0.009	14.093	--
6	3.775	3502	220	0.009	15.917	--
7	4.110	1570	194	0.004	8.101	--
8	4.256	4244	347	0.011	12.218	--
9	5.110	3777	514	0.010	7.346	0.311
10	5.678	14387	1512	0.036	9.513	0.391
11	6.312	31922	2883	0.081	11.072	--
12	6.806	38946211	4384056	98.806	8.884	0.286
13	7.631	162559	9513	0.412	17.088	--
14	8.498	12420	1108	0.032	11.208	--
15	8.874	13087	860	0.033	15.224	--
16	9.215	51141	3124	0.130	16.372	--
17	9.935	18667	922	0.047	20.253	0.716
18	11.438	6550	488	0.017	13.430	0.418
19	11.965	24207	1645	0.061	14.718	0.498
20	13.280	3803	221	0.010	17.171	0.562
21	14.358	1472	104	0.004	14.164	0.450
22	15.058	1197	57	0.003	21.154	0.569

Figure **3.19.** HPLC trace report of **pDTCz-3DPyS**

LONDON metropolitan university

Elemental Analysis Service

Please send completed form and samples to:

Stephen Boyer
School of Human Sciences
Science Centre
London Metropolitan University
29 Hornsey Road
London N7 7DD

Telephone: 020 7133 3605
Fax: 020 7133 2577
Email: s.boyer@londonmet.ac.uk

Sample submitted by: Dongyang
Address: **EZC group, School of Chemistry, University of St Andrews, North Haugh,St Andrews, Fife, KY16 9ST**
Telephone: 07743430420 Email: dc217@st-andrews.ac.uk
Date Submitted:12/09/2018

Please submit ca. 5 mg of sample.

Sample Reference No.: dc-2DPyS-tCz
Name of Compound:2DPyS-tCz
Molecular Formula: C48H54N4O2S
Stability: Air stable
Hazards: none
Other Remarks:

Element	Expected %	Found (1)	Found (2)	
Carbon	77.48	77.34	77.37	
Hydrogen	7.02	6.83	6.91	
Nitrogen	7.23	7.16	7.29	

Authorising Signature:

Date Completed: 19/09/18	Signature:
Comments:	

Figure **3.20.** Elemental analysis report of **pDTCz-2DPyS**

LONDON metropolitan university

Elemental Analysis Service

Please send completed form and samples to:

Stephen Boyer
School of Human Sciences
Science Centre
London Metropolitan University
29 Hornsey Road
London N7 7DD

Telephone: 020 7133 3605
Fax: 020 7133 2577
Email: s.boyer@londonmet.ac.uk

Sample submitted by: Dongyang
Address: **EZC group, School of Chemistry, University of St Andrews, North Haugh,St Andrews, Fife, KY16 9ST**
Telephone: 07743430420 Email: dc217@st-andrews.ac.uk
Date Submitted:12/09/2018

Please submit ca. 5 mg of sample.

Sample Reference No.: dc-3DPyS-tCz
Name of Compound:3DPyS-tCz
Molecular Formula: C48H54N4O2S
Stability: Air stable
Hazards: none
Other Remarks:

Element	Expected %	Found (1)	Found (2)	
Carbon	77.48	77.31	77.26	
Hydrogen	7.02	6.97	7.05	
Nitrogen	7.23	7.10	7.16	

Authorising Signature:

Date Completed: 17091j	Signature:
Comments:	

Figure **3.21.** Elemental analysis report of **pDTCz-3DPyS**

Reference

(1) Bui, T. T.; Goubard, F.; Ibrahim-Ouali, M.; Gigmes, D.; Dumur, F. Recent Advances on Organic Blue Thermally Activated Delayed Fluorescence (TADF) Emitters for Organic Light-Emitting Diodes (OLEDs). *Beilstein J. Org. Chem.* **2018**, *14*, 282–308. https://doi.org/10.3762/bjoc.14.18.

(2) Wong, M. Y.; Krotkus, S.; Copley, G.; Li, W.; Murawski, C.; Hall, D.; Hedley, G. J.; Jaricot, M.; Cordes, D. B.; Slawin, A. M. Z.; Olivier, Y.; Beljonne, D.; Muccioli, L.; Moral, M.; Sancho-Garcia, J.-C.; Gather, M. C.; Samuel, I. D. W.; Zysman-Colman, E. Deep-Blue Oxadiazole-Containing Thermally Activated Delayed Fluorescence Emitters for Organic Light-Emitting Diodes. *ACS Appl. Mater. Interfaces* **2018**, *10*, 33360–33372. https://doi.org/10.1021/acsami.8b11136.

(3) Ahn, D. H.; Kim, S. W.; Lee, H.; Ko, I. J.; Karthik, D.; Lee, J. Y.; Kwon, J. H. Highly Efficient Blue Thermally Activated Delayed Fluorescence Emitters Based on Symmetrical and Rigid Oxygen-Bridged Boron Acceptors. *Nat. Photonics* **2019**, *13*, 540–546. https://doi.org/10.1038/s41566-019-0415-5.

(4) Stachelek, P.; Ward, J. S.; dos Santos, P. L.; Danos, A.; Colella, M.; Haase, N.; Raynes, S. J.; Batsanov, A. S.; Bryce, M. R.; Monkman, A. P. Molecular Design Strategies for Color Tuning of Blue TADF Emitters. *ACS Appl. Mater. Interfaces* **2019**, *11*, 27125–27133. https://doi.org/10.1021/acsami.9b06364.

(5) Zhang, X.; Fuentes-Hernandez, C.; Zhang, Y.; Cooper, M. W.; Barlow, S.; Marder, S. R.; Kippelen, B. High Performance Blue-Emitting Organic Light-Emitting Diodes from Thermally Activated Delayed Fluorescence: A Guest/Host Ratio Study. *J. Appl. Phys.* **2018**, *124*, 055501. https://doi.org/10.1063/1.5041447.

(6) Rajamalli, P.; Senthilkumar, N.; Huang, P. Y.; Ren-Wu, C. C.; Lin, H. W.; Cheng, C. H. New Molecular Design Concurrently Providing Superior Pure Blue, Thermally Activated Delayed Fluorescence and Optical Out-Coupling Efficiencies. *J. Am. Chem. Soc.* **2017**, *139*, 10948–10951. https://doi.org/10.1021/jacs.7b03848.

(7) Wang, L.; Cai, X.; Li, B.; Li, M.; Wang, Z.; Gan, L.; Qiao, Z.; Xie, W.; Liang, Q.; Zheng, N.; Liu, K.; Su, S. Achieving Enhanced Thermally Activated Delayed Fluorescence Rates and Shortened Exciton Lifetimes by Constructing Intramolecular Hydrogen Bonding Channels. *ACS Appl. Mater. Interfaces* **2019**, *11*, 45999–46007. https://doi.org/10.1021/acsami.9b16073.

(8) Rajamalli, P.; Senthilkumar, N.; Gandeepan, P.; Huang, P. Y.; Huang, M. J.; Ren-Wu, C. Z.; Yang, C. Y.; Chiu, M. J.; Chu, L. K.; Lin, H. W.; Cheng, C. H. A New Molecular Design Based on Thermally Activated Delayed Fluorescence for Highly Efficient Organic Light Emitting Diodes. *J. Am. Chem. Soc.* **2016**, *138*, 628–634. https://doi.org/10.1021/jacs.5b10950.

(9) Li, Y.; Nie, C.; Wang, H.; Li, X.; Verpoort, F.; Duan, C. A Highly Efficient Method for the Copper-Catalyzed Selective Synthesis of Diaryl Chalcogenides from Easily Available Chalcogen Sources. *European J. Org. Chem.* **2011**, *2011* , 7331–7338. https://doi.org/10.1002/ejoc.201101121.

(10) Monnier, F.; Taillefer, M. Minireviews Catalytic C À C , C À N , and C À O Ullmann-Type Coupling Reactions. **2009**, *48*, 6954–6971. https://doi.org/10.1002/anie.200804497.

(11) Pople, J. A.; Binkley, J. S.; Seeger, R. Theoretical Models Incorporating Electron Correlation. *Int. J. Quantum Chem.* **2009**, *10*, 1–19. https://doi.org/10.1002/qua.560100802.

(12) Perdew, J. P.; Ernzerhof, M.; Burke, K. Rationale for Mixing Exact Exchange with Density Functional Approximations. *J. Chem. Phys.* **1996**, *105*, 9982–9985. https://doi.org/10.1063/1.472933.

(13) Grimme, S. Density Functional Calculations with Configuration Interaction for the Excited States of Molecules. *Chem. Phys. Lett.* **1996**, *259*, 128–137. https://doi.org/10.1016/0009-2614(96)00722-1.

(14) Hirata, S.; Head-Gordon, M. Time-Dependent Density Functional Theory within the Tamm–Dancoff Approximation. *Chem. Phys. Lett.* **1999**, *314*, 291–299. https://doi.org/10.1016/S0009-2614(99)01149-5.

(15) Gritzner, G.; Kuta, J. Recommendations on Reporting Electrode Potentials in Nonaqueous Solvents (Recommendations 1983). *Pure Appl. Chem.* **1984**, *56*, 461–466. https://doi.org/10.1351/pac198456040461.

Chapter 4

Planar pyrazine based TADF emitter for deep blue bright organic light emitting diodes

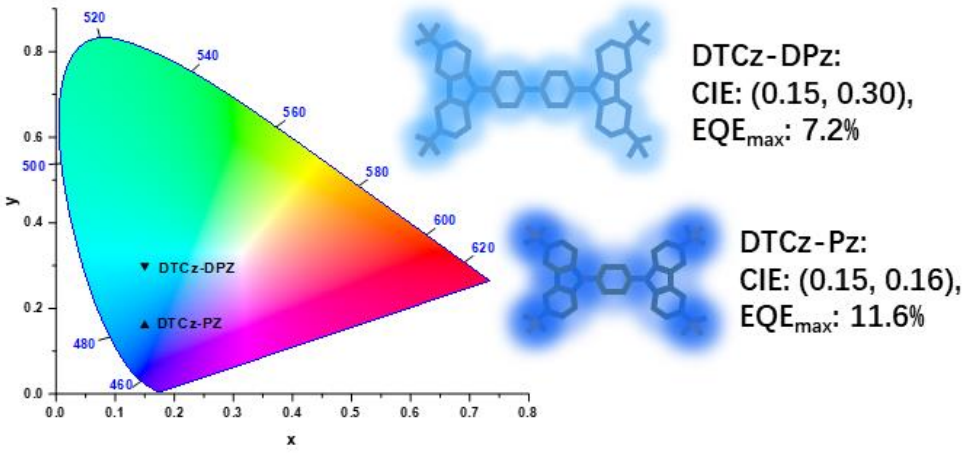

Part of the work presented in this Chapter has been published as:

Pachaiyappan Rajamalli,[a] Dongyang Chen,[a] Subeesh Madayanad Suresh,[a] Youichi Tsuchiya,[b] Chihaya Adachi,[b]* and Eli Zysman-Colman[a]* *Eur. J. Org. Chem.*, **2021**, *2021*, 2285-2293. **DOI:** 10.1002/ejoc.202100086

Collaborators in this Chapter are from

[a] Organic Semiconductor Centre, EaStCHEM School of Chemistry, University of St Andrews, St Andrews, Fife, KY16 9ST, UK

[b] Center for Organic Photonics and Electronics Research (OPERA),Kyushu University,744 Motooka, Nishi-ku, Fukuoka 819-0395, Japan

The molecular design of the **DTC-Pz** and **DTC-DPz** emitters in this Chapter is the result of discussions with Dr. Pachaiyappan Rajamalli.

Dr. Pachaiyappan Rajamalli carried out the solid-state photophysics measurements and device fabrication of **DTC-Pz** and **DTC-DPz**.

I completed all the synthesis and characterization, DFT and TD-DFT calculations, electrochemistry, photophysics in solutions, and I am the principal author of the manuscript.

4.1 Introduction

In **Chapter 3**, we used heteroaromatic rings (pyridine, pyrimidine, and pyrazine) as the bridging unit within the D-A molecular design to achieve highly efficient blue TADF emitters. Among the four emitters, pyrazine based **pDTCz-DPzS** shows stronger ICT and significantly stabilized S_1 and red-shifted emission compared to its analogues, which inspired us to explore the electron-withdrawing ability of pyrazine ring and the possibility of using pyrazine ring as acceptor for blue TADF emitter design.

In previous research, the nitrogen-containing heterocyclic acceptor triazine has been used widely in blue TADF emitters due to its high triplet energy (3.27 eV in 3-methylpentane[1]) and relatively weak electron-accepting properties ($E_{red}^{1/2}$ = -2.1 V vs SCE in MeCN[2]).[3–5] A prototypical example, **DMAC-Trz**, contains a TRZ as the electron-acceptor and DMAC as the electron donor. This compound is a sky-blue emitter where the OLEDs showed λ_{EL}= 504 nm and CIE coordinates of (0.22, 0.50) in 9-(3-(9H-carbazol-9-yl)phenyl)-9H-carbazole-3-carbonitrile (mCPCN) and, along with a high EQE_{max} of 26.5%. Researchers have tried to tune the emission color further towards the blue through structure optimization (Figure **4.1**).[6] Kaji *et al.* aimed decreasing the electron affinity of the electron acceptor by replacing the non-bridging phenyl rings in TRZ with adamantyl groups. The molecule **MA-TA** exhibited a destabilized LUMO of -2.96 eV compared to -3.12 eV for **DMAC-TRZ**, and a correspondingly destabilized S_1 level of 2.90 eV (in toluene) compared to 2.74 eV (in toluene) for **DMAC-TRZ**.[4,6] As a result, the OLEDs using **MA-TA** exhibited deep-blue emission with λ_{EL}= 465 nm and CIE coordinates of (0.15, 0.16), along with a high EQE_{max} of 22.1%.[4] Adachi *et al.* further pushed the color towards the

deep-blue region by using a weaker electron donor in 3,6-dimethylcarbazole coupled with a methylphenylene bridge that, due to the presence of the methyl group, increasing the torsion angle of the donor, leading to reduced conjugation, smaller ΔE_{ST} and a higher S_1 energy.[3] The molecule **Cz-TRZ3** possesses a shallow LUMO of -2.71 eV (in DCM) and a high S_1 energy of 3.10 eV (in toluene).[3] The OLEDs based on **Cz-TRZ3** exhibited deep-blue emission with CIE coordinates (0.15, 0.10) and EQE_{max} of 19.2%.[3] On the other hand, Chou *et al.* found that by simply replacing the triazine with pyrimidine can push the emission to higher energy as well.[7] The molecule **T3** possesses a much destabilized LUMO energy of -2.37 eV (in MeCN) and an S_1 energy of 2.95 eV (in toluene), while the device based on **T3** exhibited blue emission with λ_{EL}= 465 nm and CIE coordinates of (0.17, 0.21) and an EQE_{max} of 11.8%.[7] Wang *et al.* further blue-shifted the emission by using bespoke acridine–carbazole fused donor, and the bulky donor makes the molecule **12AcCz-PM** adopt a quasi-orthogonal conformation.[8] The S_1 of **12AcCz-PM** is 3.06 eV while the LUMO value is similar to **T3** at -2.31 eV (in MeCN).[8] The OLEDs based on **12AcCz-PM** exhibited deep blue emission with λ_{EL}= 438 nm and CIE coordinates (0.15, 0.06); however, the EQE_{max} was only 5.7% due in part to the large ΔE_{ST} (0.39 eV in DPEPO).[8]

These examples in the literature have shown that triazine and pyrimidine acceptors are compatible with obtaining blue and deep blue TADF emitters and reasonably high efficiencies in OLEDs. The related N-heterocycle, pyrazine, has thus far not been explored for blue TADF emitter design, though the pyrazine has been used within an electron-acceptor design to tune its electron affinity and the corresponding energies of the emitters.[9–11] Recently, Duan *et al.* reported a series of blue TADF emitters bearing pyrazine as an acceptor and benzofuro-carbazoles or

benzothieno-carbazoles as donor moieties.[12] Amongst the molecules in the study, **BFCZPZ2** possessed a moderately small ΔE_{ST} (0.31 eV in PPT) and Φ_{PL} of 91% in PPT).[12] The device based on **BFCZPZ2** exhibited deep blue emission with λ_{EL}= 464 nm and CIE coordinates of (0.15,0.16), and the EQE_{max} reached 21.3%, but reduced to 5.1% at 10 mA/cm^2.[12] This work showed the potential of pyrazine in the design of blue TADF materials.

In this Chapter, we present two TADF emitters, 2,5-bis(3,6-di-*tert*-butyl-9H-carbazol-9-yl)pyrazine (**DTCz-Pz**) and 5,5'-bis(3,6-di-*tert*-butyl-9H-carbazol-9-yl)-2,2'-bipyrazine (**DTCz-DPz**). Both **DTCz-Pz** and **DTCz-DPz** possess planar geometry with high Φ_{PL}, in toluene (69% and 96%, respectively) and doped thin films (70% and 65% in PPT, respectively). Although the ΔE_{ST}s of **DTCz-Pz** and **DTCz-DPz** are relatively large (0.27 eV and 0.38 eV in PPT, respectively), the presence of an intermediate triplet state provides a viable route for TADF. The OLEDs based on **DTCz-Pz** and **DTCz-DPz** exhibit deep blue and sky-blue emission with CIE coordinates of (0.15, 0.16) and (0.15, 0.30), and EQE_{max} of 11.6% and 7.2%, and Lum_{max} up to 6892 and 8802 cd m^{-2}, respectively.

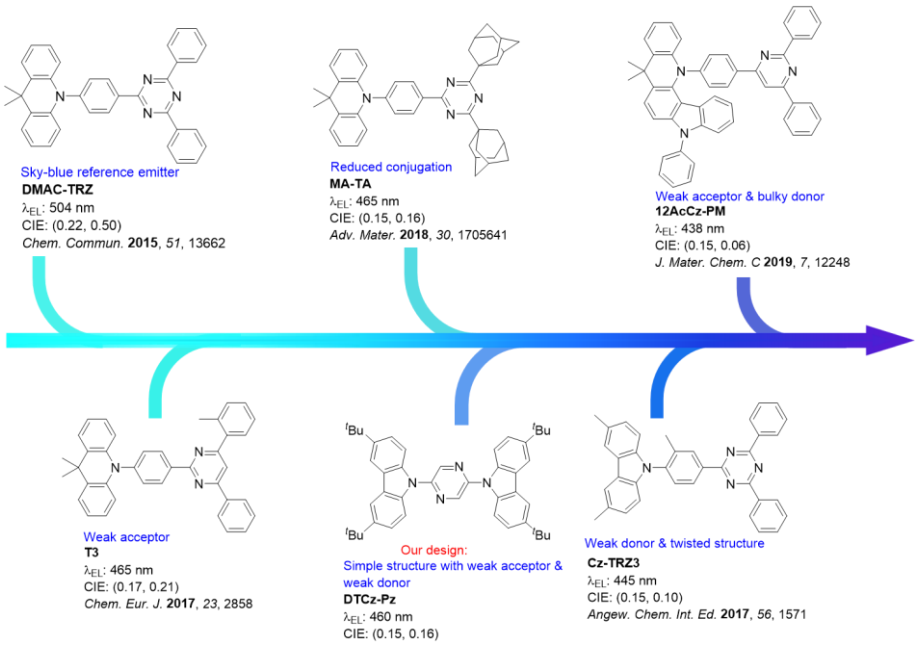

Figure **4.1**. Chemical structures of heteroaromatic acceptor in blue TADF emitters design.

4.2 Synthesis

DTCz-Pz was obtained in 77% yield via an Ullmann C-N coupling reaction between two equivalents of 3,6-di-*tert*-butyl-9*H*-carbazole (DTCz) and 2,5-dibromopyrazine in 1,3-dichlorobenzne where copper powder and 18-crown-6 were used as catalyst and ligand, respectively.[22] **DTCz-DPz** was obtained in moderate yield in a two-step protocol involving an Ullmann C-N coupling between DTCz and 2-bromo-5-iodopyrazine in chlorobenzene[22] followed by homocoupling of intermediate **DTCzPzBr** catalyzed by $Pd(PPh_3)_4$ in DMF. (Scheme **4.1**). Both emitters were characterized by combination of ^{1}H and ^{13}C NMR spectroscopy, high-resolution mass spectrometry, melting point determination, and elemental analysis. The two emitters were purified by silica gel chromatography followed by temperature gradient vacuum

sublimation, and the purity was verified by high performance liquid chromatography (HPLC) analysis. The detailed synthesis and compounds characterization are in **4.8**.

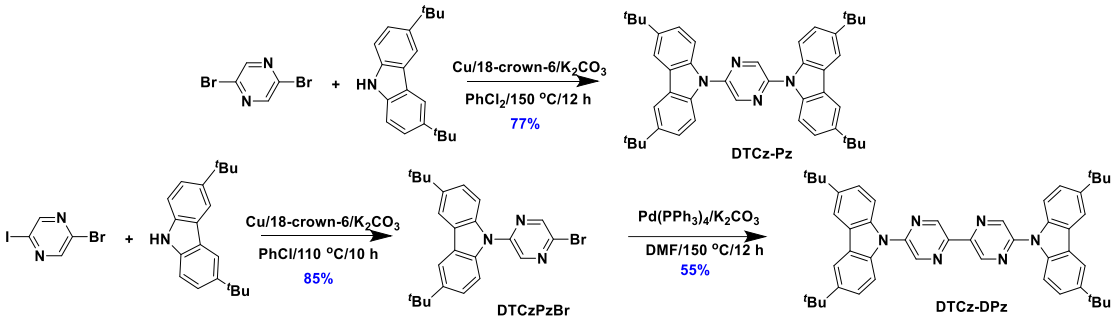

Scheme **4.1**. Synthesis route of **DTCz-Pz** and **DTCz-DPz**.

4.3 Theoretical Calculations

The S_0 geometries of **DTCz-Pz** and **DTCz-DPz** were optimized by DFT calculation and the excited states and their electronic configuration were predicted by time-dependent DFT calculations using the TDA-DFT at the PBE0/6-31G(d,p) level of theory in the gas phase.[13,14] The results are summarized in Figure **4.2**. The DFT modeling predicts a rather flat conformation with average dihedral angles between the DTCz moieties and the pyrazine ring(s) of [36.53(14)°]and [32.70(4)°], for **DTCz-Pz** and **DTCz-DPz**, respectively. The relatively small dihedral angles align with those observed in the single crystal for **pDTCz-DPzS** [38.20(8)°] presented in Chapter **3**, where the pyrazine ring was similarly connected to carbazole, indicating a likely intramolecular hydrogen bonding, analogously to that observed in **pDTCz-DPzS**. In both emitters, the HOMOs are distributed across the entire molecule while the LUMOs are mainly localized on the acceptor

cores. The more strongly electron-accepting DPz in **DTCz-DPz** results in more stabilized HOMO and LUMO levels compared to those in **DTC-Pz**. Analogously, the S_1 and T_1 levels are predicted to be slightly stabilized in **DTCz-DPz** compared to **DTCz-Pz**. Both emitters show high oscillator strength (0.24 and 1.39 for **DTCz-Pz** and **DTCz-DPz**, respectively) and large ΔE_{ST} values (0.52 eV for **DTCz-Pz** and 0.56 eV for **DTCz-DPz**). The higher energy intermediate triplet states of **DTCz-Pz** and **DTCz-DPz** were also studied (Figure **4.3**). For **DTCz-Pz**, the T_2 state (3.18 eV) is nearly degenerate with the S_1 state (3.19 eV). For **DTCz-DPz**, the T_2 state at 2.85 eV results in a ΔE_{S1T2} of 0.23 eV. The nature of the T_2 states for **DTCz-Pz** and **DTCz-DPz** is of locally excited (LE) character [HOMO to LUMO+1 (85%) for **DTCz-Pz**, HOMO-1 to LUMO+1 (40%) for **DTCz-DPz**] distributed over the whole molecule. This is different from the S_1 and T_1 states, which are dominated by a hybrid CT and LE transition from HOMO to LUMO. The presence of an intermediate T_2 state that is of different symmetry to S_1 in both **DTCz-Pz** and **DTCz-DPz** will contribute to a more efficient TADF as RISC will be faster, facilitated by spin-vibronic coupling between T_1 and T_2 and enhanced SOC between T_2 and S_1.[15,16] We calculated the $|V_{SOC}|^2$ values as the average spin-orbital coupling matrix elements (SOCME) between their S_1/T_1 states and S_1/T_2 states based on their optimized excited-state structures,[17] which are shown in Table **4.1**. The $|V_{SOC}|^2$ value between S_1/T_1 for **DTCz-Pz** is 0.017 cm^{-2} and this increases to 0.517 cm^{-2} for S_1/T_2 due to the different orbital character of T_2 compared to S_1. Analogously, the $|V_{SOC}|^2$ values for **DTCz-DPz** also increases from 0.003 cm^{-2} (between S_1/T_1) to 0.170 cm^{-2} (between S_1/T_2). The closely layered intermediate T_2 state and high SOCME values between the S_1/T_2 states provide an indirect route for RISC to occur despite the relatively large ΔE_{ST} for **DTCz-Pz** and **DTCz-DPz**.

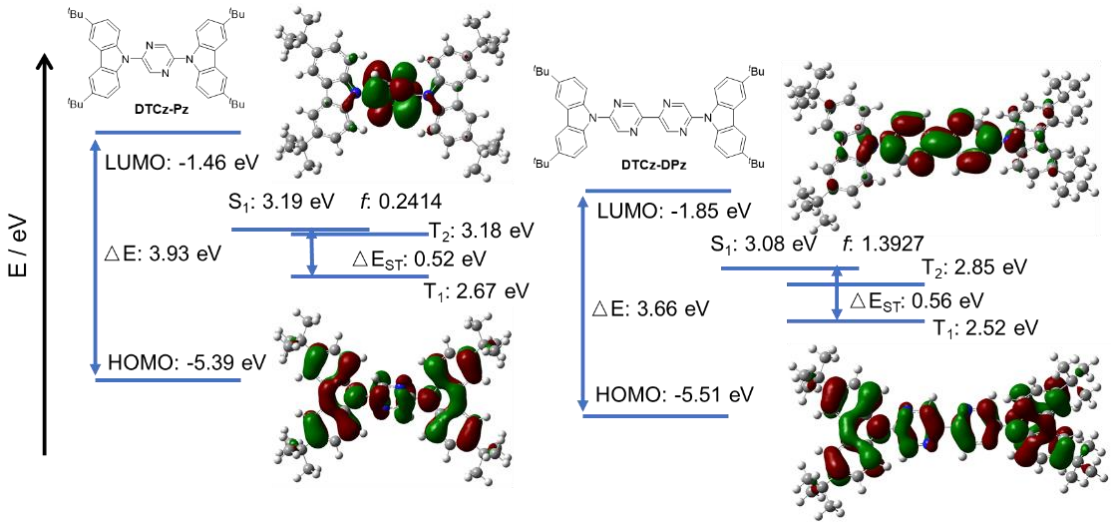

Figure **4.2**. Theoretical modelling of the energies of the HOMO/LUMO orbitals and the S_1 and T_1 states of **DTCz-Pz** and **DTCz-DPz** in the gas phase and the electron density distribution of the frontier molecular orbitals (isovalue = 0.02).

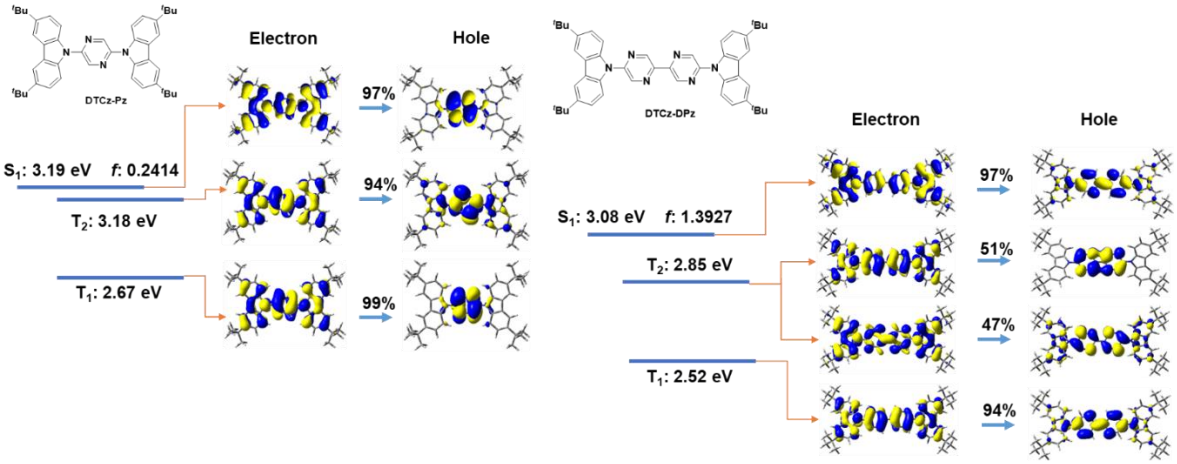

Figure **4.3.** Natural transition orbitals analysis of **DTCz-Pz** and **DTCz-DPz** (isovalue = 0.02).

Table **4.1**. Excited states energies, ΔE_{ST}s, and average $|V_{SOC}|^2$ values of **DTCz-Pz** and **DTCz-DPz**

Compound	**S_1 / eV**	**T_1 / eV**	**ΔE_{ST} / eV**	**$\lvert V_{SOC}^{S_1/T_1} \rvert^2$ / cm^{-2}**	**T_2 / eV**	**ΔE_{S1T2} / eV**	**$\lvert V_{SOC}^{S_1/T_2} \rvert^2$ / cm^{-2}**
DTCz-Pz	3.19	2.67	0.52	0.017	3.18	0.01	0.517
DTCz-DPz	3.08	2.52	0.56	0.003	2.85	0.23	0.170

S_1= singlet state energy; T_1 = triplet state; $\Delta E_{ST} = E(S_1) - E(T_1)$; $|V_{SOC}^{S_1/T_1}|^2$: SOCME between S_1 and T_1; $|V_{SOC}^{S_1/T_2}|^2$: SOCME between S_1 and T_2.

4.4 Thermal property and electrochemistry

The thermal properties of these emitters were determined by TGA (Figure **4.4a**). The results show that these compounds possess very high T_d (5% weight loss) of 411 °C and 459 °C, respectively for **DTCz-Pz** and **DTzC-DPz**.

CV and DPV measurements of **DTCz-Pz** and **DTCz-DPz** were carried out in DCM to estimate the HOMO and LUMO energies (Figure **4.4b**). The CV trace of **DTCz-Pz** shows a pseudo-reversible oxidation wave with E_{ox} = 1.22 V (obtained from DPV) while **DTCz-DPz** exhibited an irreversible oxidation with E_{ox} = 1.23 V (obtained from DPV). No reduction wave was observed for either compound within the DCM solvent window. The corresponding HOMO levels of **DTCz-Pz** and **DTCz-DPz** are -5.56 eV and -5.57 eV, which are slightly destabilized than the DFT calculation. The LUMO levels for **DTCz-Pz** (-2.58 eV), and **DTCz-DPz** (-2.73 eV) were inferred from the HOMO energies and the optical gap (E_g), which itself was determined

from the intersection of the normalized absorption and fluorescence spectra in toluene (2.98 and 2.84 eV, respectively, for **DTCz-Pz** and **DTCz-DPz**, Figure **4.5**).

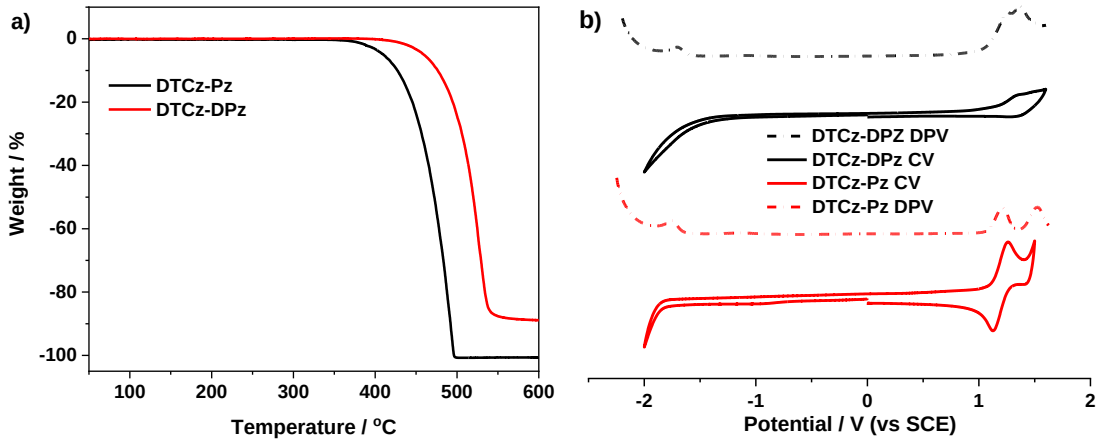

Figure **4.4**. a) Thermogravimetric analysis of **DTCz-Pz** and **DTCz-DPz**, b) CV (solid lines) and DPV (dashed lines) for **DTCz-Pz** and **DTCz-DPz** in degassed DCM solution containing [*n*Bu_4N]PF_6 as the supporting electrolyte and using Fc/Fc^+ as an external standard (Fc/Fc^+ = 0.46 eV versus SCE[18], scan rate = 100 mVs^{-1}).

4.5 Photophysical properties

The UV-*vis* absorption spectra of both emitters in toluene are shown in Figure **4.5a**. The profiles match closely to the calculated absorption spectra by TDA-DFT (Figure **4.5b** and **c**). The TDA-DFT calculations predict that both emitters should exhibit hybridized local and charge-transfer (HLCT) transitions from HOMO to LUMO at 380 nm for **DTCz-Pz** and 400 nm for **DTCz-DPz**. For **DTCz-DPz**, the molar absorptivity of this band is much higher than that of **DTCz-Pz** due to the larger HOMO/LUMO overlap, which aligns with the predicted high oscillator strength. The absorption bands at 330 nm and 300 nm for **DTCz-Pz** are assigned to

locally excited (LE) $\pi \rightarrow \pi^*$ transitions on the whole molecule and carbazole moiety, respectively, by TDA-DFT calculation (Figure **4.6a**). For **DTCz-DPz**, TDA-DFT predicted a higher energy HLCT transition on 340 nm and a LE transition on the carbazole moiety at 300 nm (Figure **4.6b**). The oscillator strengths (*f*) for **DTCz-Pz** and **DTCz-DPz** are calculated to be 0.2514 and 0.5255, respectively, from the spectra,[19] which are consistent with the trend observed from the TDA-DFT calculations (0.2414 and 1.3927, respectively). The steady-state PL spectra for **DTCz-Pz** and **DTC-DPz** are shown in Figures **4b** and **4c**, respectively. In toluene, **DTCz-Pz** shows structureless emission with λ_{PL} of 441 nm, suggesting emission from a CT state, while the profile for **DTCz-DPz** in toluene has a slightly red-shifted λ_{PL} of 455 nm. In *n*-hexane, both compounds show structured emission, though this is more pronounced in **DTCz-DPz**, indicating emission from an LE state. There is a modest positive solvatochromism observed for **DTCz-Pz** while the positive solvatochromism is more significant in **DTCz-DPz**, suggesting a more pronounced CT emissive state in this compound.

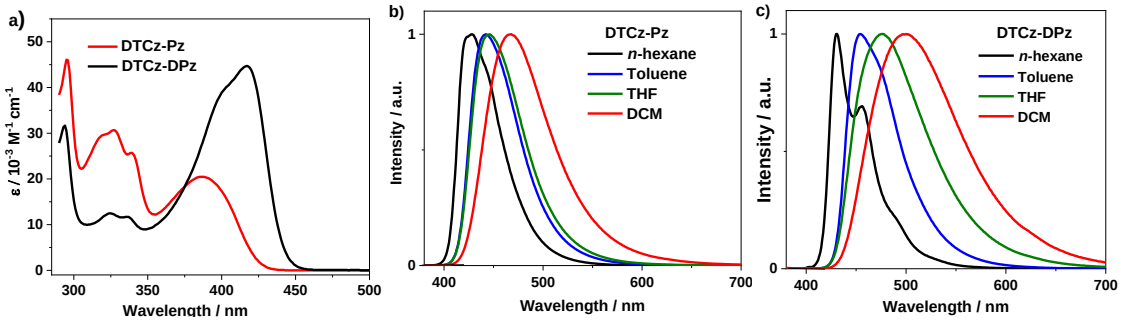

Figure **4.5**. a) Absorption spectra of **DTCz-Pz** and **DTCz-DPz** in toluene; b) Solvatochromic PL study of **DTCz-Pz**; c) Solvatochromic PL study of **DTCz-DPz** (λ_{exc} = 360 nm).

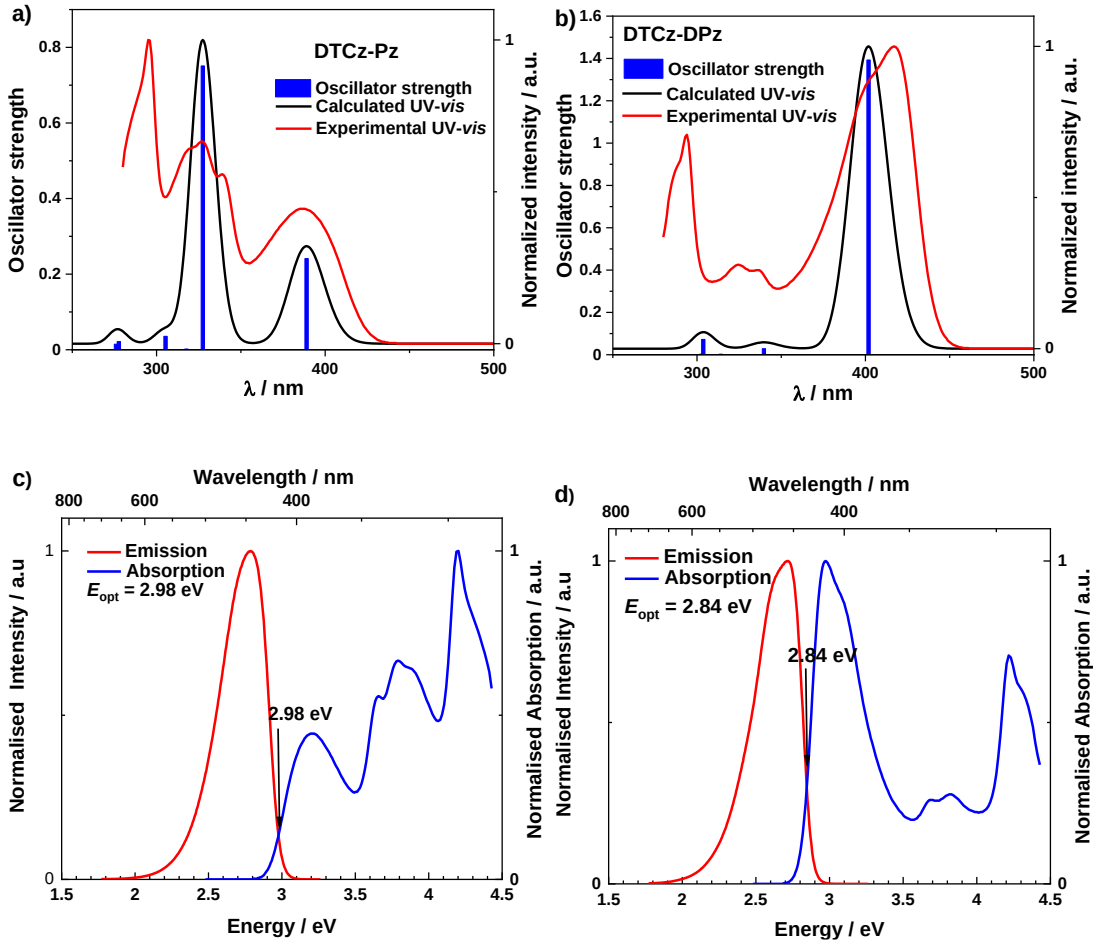

Figure **4.6**: Calculated and experimental (in toluene) UV-*vis* spectra and oscillator strength for a) **DTCz-Pz** and b) **DTCz-DPz**, and normalized UV-*vis* and fluorescence spectra in toluene for c) **DTCz-Pz** and d) **DTCz-DPz** (λ_{exc} = 360 nm).

The time-resolved PL decays of these materials were measured in 10^{-5} M toluene solution under nitrogen (Figure **4.7)**. In both compounds, the emission decays with bi-exponential kinetics. There is a nanosecond prompt emission, which occurs from direct radiative depopulation of the S_1 state with τ_1 of 6.0 ns (63.4%) and 2.9 ns (85.7%) for **DTCz-Pz** and **DTCz-DPz,** respectively. There is a second component with a lifetime (τ_2) of 93 ns (36.6%) and 121 ns (14.3%)

for **DTCz-Pz** and **DTCz-DPz**, respectively. Delayed compoent is not observed for these compounds in solution.

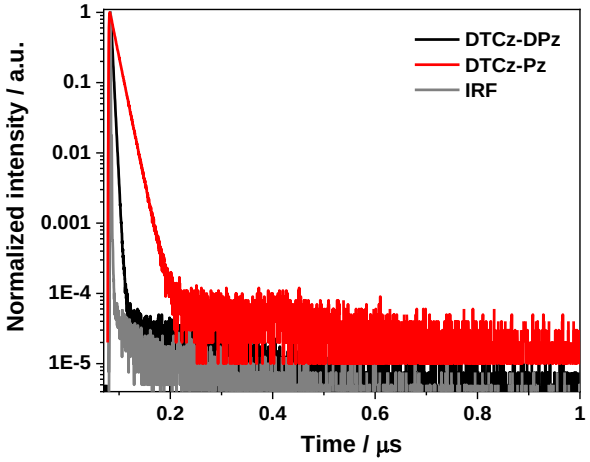

Figure **4.7.** Transient PL decay of a) **DTCz-Pz** and b) **DTCz-DPz** in toluene (λ_{exc} = 379 nm).

We next investigated the photophysical properties of the two emitters in a high triplet energy host matrix, PPT (E_T = 2.95 eV) and the photophysical properties are summarized in Table **4.2**.[20] Thin films of each emitter doped at 7 wt% in PPT were prepared by vacuum deposition. **DTCz-Pz** shows structureless, broad emission for both prompt fluorescence and phosphorescence at 77 K, pointing to ^{1}CT and ^{3}CT states (Figure **4.8**). By contrast, **DTCz-DPz** shows broad emission for the prompt fluorescence spectrum and structured emission for the phosphorescence spectrum, indicating that for the latter, emission originates from a LE state on the DPz moiety. The calculated ΔE_{ST} values determined from the onsets of the prompt fluorescence and phosphorescence spectra are 0.27 eV and 0.38 eV for **DTCz-Pz** and **DTCz-DPz**, respectively.

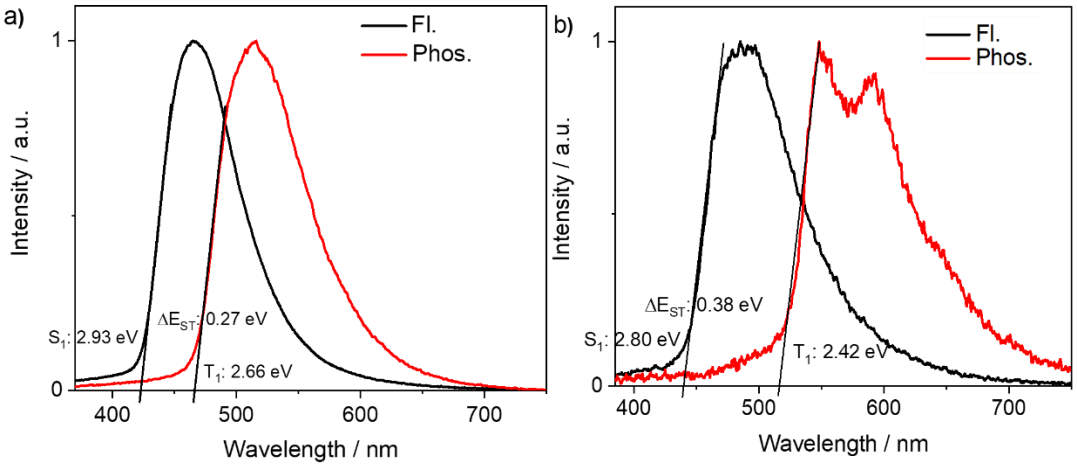

Figure **4.8** Prompt fluorescence (Fl.) (1-100 ns) and phosphorescence (Phos.) (1-10 ms) spectra of a) **DTCz-Pz** and b) **DTCz-DPz** at 77 K as 7 wt% doped PPT films (λ_{exc} = 343 nm).

The temperature-dependent time-resolved PL decays in doped PPT films are shown in Figure **4.9**. The relative intensities of the delayed PL of both **DTCz-Pz** and **DTCz-DPz** decreased with decreasing temperature, which is the typical behavior for TADF emitters. Both compounds show a dominant prompt nanosecond fluorescence component and only a very small delayed microsecond fluorescence component. For **DTCz-Pz**, the prompt fluorescence decays with bi-exponential kinetics with $\tau_{p,avg}$ of 8.0 ns. while the delayed fluorescence decays according to triexponential kinetics with $\tau_{d,avg}$ of 5.5 ms. For **DTCz-DPz**, $\tau_{p,avg}$ is 3.5 ns and the $\tau_{d,avg}$ is 8.0 ms. The significantly longer delayed lifetimes in **DTCz-DPz** are consistent with the larger ΔE_{ST} value. The delayed lifetimes are significantly reduced under air with τ_d of 4.2 μs (99.1%) for **DTCz-Pz** and 4.0 μs (99.5%) for **DTCz-DPz** (Figure **4.10**). The sensitivity to oxygen and temperature, corroborate the TADF characteristics of **DTCz-Pz** and **DTCz-DPz** in PPT film.

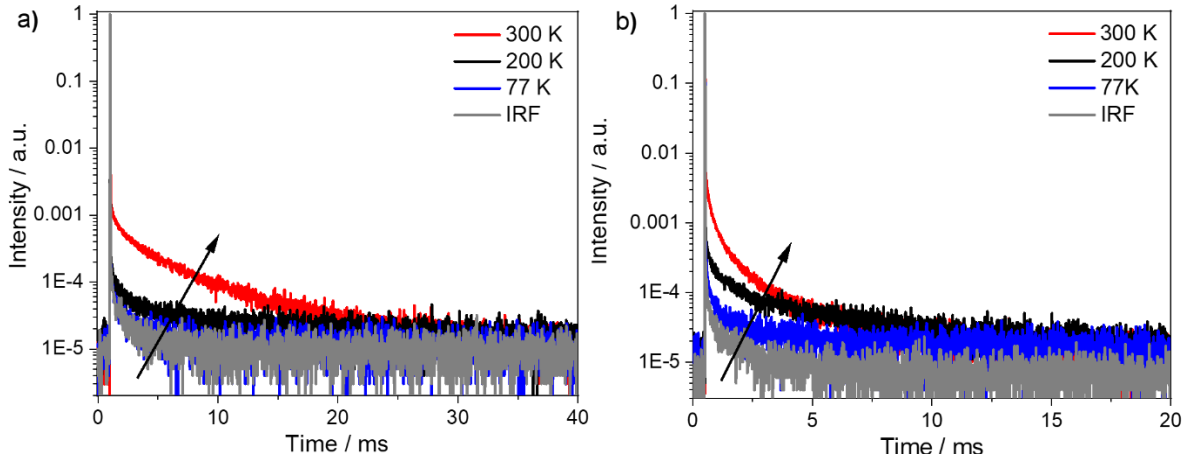

Figure **4.9.** Normalized temperature-dependent transient PL decays of a) **DTCz-Pz** and b) **DTCz-DPz** in 7 wt% doped PPT films (λ_{exc} = 379 nm).

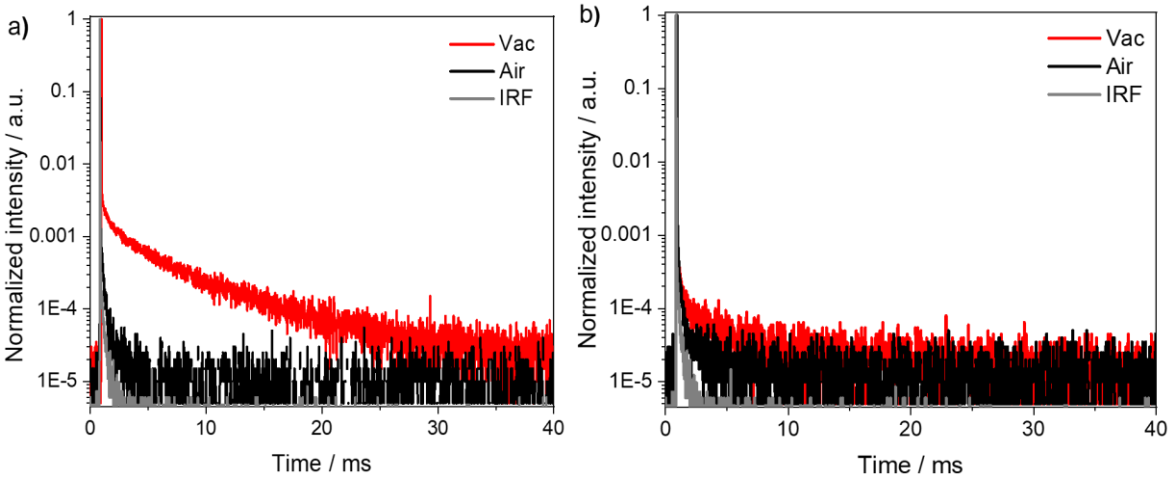

Figure **4.10.** Transient PL decays of a) **DTCz-Pz** and b) **DTCz-DPz** co-doped at 7 wt% in PPT film, measured under vacuum and air (λ_{exc} = 379 nm).

The absolute Φ_{PL} values measured using an integrating sphere under argon and air for the toluene solutions, and co-doped films are summarized in Table **4.2**. **DTCz-DPz** shows

significantly higher Φ_{PL} of 96% in degassed toluene than **DTCz-Pz** (69%), while the 7 wt% PPT doped films are similarly bright with Φ_{PL} of 70% and 65% for **DTCz-Pz** and **DTCz-DPz**, respectively.

Table **4.2**. Photophysical properties of **DTCz-Pz** and **DTCz-DPz** in PPT.[a]

Compound	**S_1 / eV**	**T_1 / eV**	**ΔE_{ST} / eV**	**Φ_{PL} / %**	**$\tau_{p,avg}$ / ns**	**$\tau_{d,avg}$ / ms**
DTCz-Pz	2.93	2.66	0.27	58 (air), 70 (N_2)	8.0	5.5
DTCz-DPz	2.80	2.42	0.38	60 (air), 65 (N_2)	3.5	8.0

[a.] S_1= singlet state energy obtained from the onset of the prompt fluorescence spectra (1-100 ns) measured at 77 K with λ_{exc} = 343 nm; T_1 = triplet state energy obtained from the onset of the phosphorescence spectra (1-10 ms) measured at 77 K with λ_{exc} = 343 nm; $\Delta E_{ST} = E(S_1) - E(T_1)$; Φ_{PL} measured using an integrating sphere under nitrogen flow with λ_{exc} = 340 nm; $\tau_{p,avg}$ = average prompt fluorescence lifetime measured at room temperature with time window of 100 ns (λ_{exc} = 379 nm). $\tau_{d,avg}$ = average delayed fluorescence lifetime measured at room temperature with time window of 1-40 ms (λ_{exc} = 379 nm). All measurements were performed in co-doped PPT film (7 wt%).

4.6 Electroluminescence properties

Next, we investigated the electroluminescence properties of these two emitters. Multilayer devices were fabricated using these materials as dopants with the following structures: ITO/ TAPC (40 nm)/ *m*CP (10 nm)/ PPT: **DTCz-Pz** or **DTCz-DPz** (7 wt%) (30 nm)/ PPT (10 nm)/TmPyPB (30 nm)/ LiF (0.7 nm)/ Al (100 nm). Where TAPC acts as the hole injection and

transporting layer, *m*CP is the exciton blocking layer, PPT is the host material, and TmPyPb is the electron-transporting material. The performance of the devices is summarized in Figure **4.11** and Table **4.3**. EQE-luminance curves reveal an EQE_{max} of 11.6% for the **DTCz-Pz** device and 7.2% for the **DTCz-DPz** device (Figure **4.11a**). These devices show significant efficiency roll-off at high luminance. **DTCz-Pz** and **DTCz-DPz**-based devices show EQE_{100} of 4.5% and 3.8% at 100 cd/m^2 and EQE_{1000} is further reduced to 2.5%, 2.8% at 1000 cd/m^2, respectively. The EL spectra show the deep blue (for the **DTCz-Pz** device) and sky blue (for the **DTCz-DPz** device) emission with CIE coordinates of (0.14, 0.16) and (0.15, 0.30), respectively. High Lum_{max} values of 6892 cd/m^2 and 8802 cd/m^2 were obtained for **DTCz-Pz** and **DTCz-DPz** devices, respectively, which are much higher than the Lum_{max} (< 1000 cd/m^2) of the heteromatic sulfone based blue emitter presented in Chapter **3**. The improved performance of **DTCz-Pz** and **DTCz-DPz** are attributed to the high Φ_{PL}, good thermal stability, and appropriate host PPT which possess better charge transport ability than DPEPO.[21]

Table **4.3**. Electroluminescence performances of **DTCz-Pz** and **DTCz-DPz**.

Device	EQE / %	Lum_{max} / cd m^{-2}	CE_{max} / cd A^{-1}	PE_{max} / lm W^{-1}	CIE	λ_{EL} / nm
DTCz-Pz	11.6[a]/4.5[b]/2.5[c]	6892	13	11	0.15, 0.16	460
DTCz-DPz	7.2[a]/3.8[b]/2.8[c]	8802	14	11	0.15, 0.30	484

[a] EQE_{max}; [b] EQE at 100 cd/m^2; [c] EQE at 1000 cd/m^2; Lum_{max}, maximum luminance; CE, current efficiency; PE, power efficiency; λ_{EL}, the wavelength where the EL spectrum has the highest intensity.

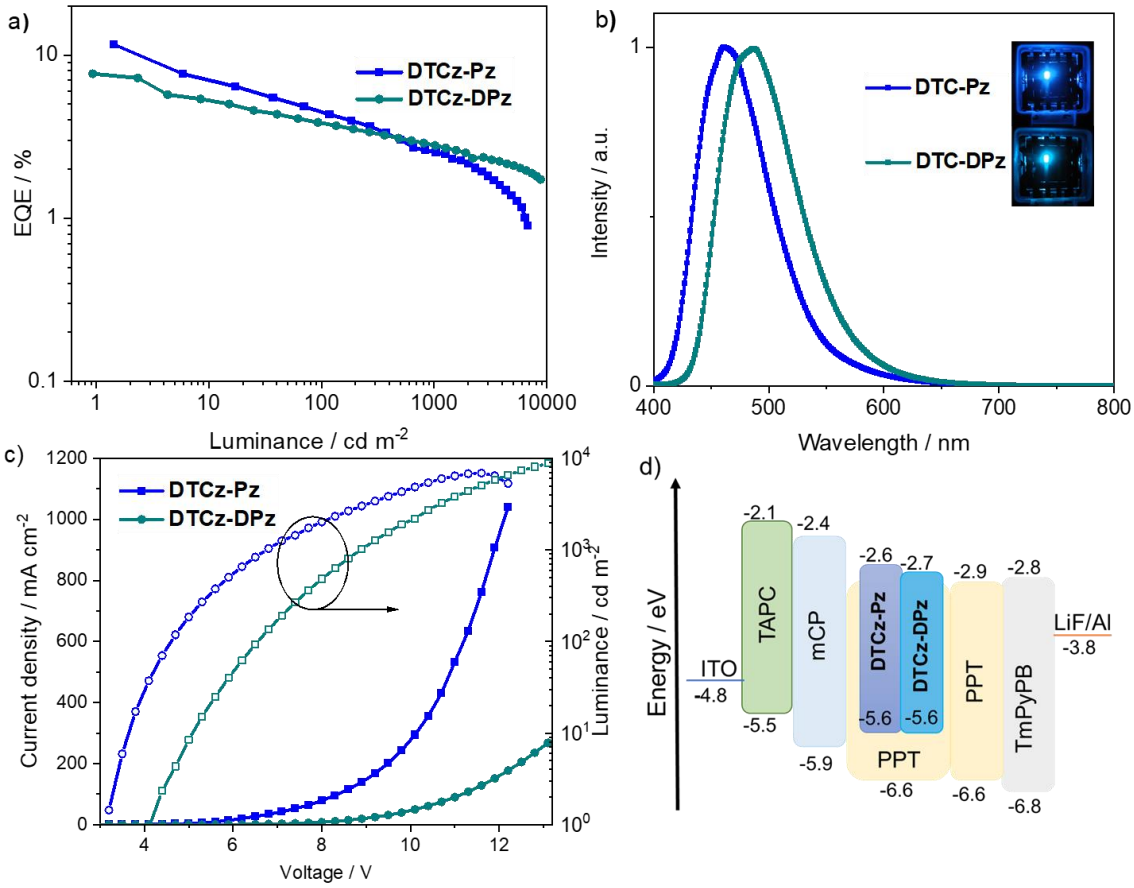

Figure **4.11.** a) Luminance vs EQE, b) EL spectra of device (Inset: Photograph of device **DTCz-Pz** and **DTCz-DPz**, c) Current density-voltage-luminance characteristics, and d) Device structure.

4.7 Conclusions and outlook

We have synthesized two pyrazine-based emitters **DTCz-Pz** and **DTCz-DPz** bearing a mono and dipyrazine acceptors and di-*tert*-butyl carbazole as the donor group. These two materials show reasonably high Φ_{PL}s, ranging from 76 to 96%, in both toluene solution and doped PPT thin films. The transient PL decay results in the doped thin film confirm that these compounds are TADF emitters. Blue-emitting OLEDs were fabricated using these emitting

materials. The devices showed EQE_{max} of 11.6% for the **DTCz-Pz** device with CIE (0.15, 0.16) and 7.2% for the **DTCz-DPz** device with CIE (0.15, 0.30).

However, the planar geometries of **DTCz-Pz** and **DTCz-DPz** lead to insufficient HOMO/LUMO separation and relative larger ΔE_{ST} (~0.30 eV), and long delayed lifetime (>5 ms) in the solid state. To reduce the ΔE_{ST} and boost the RISC efficiency, we further designed and synthesized a series of emitters with a tetra-substituted pyrazine structure (Figure **4.12**).

For **4CzPz** (recently reported by Monkam *et al*),[24] **4CbPz**, and **4tCzPz**, either four carbazoles, four carbolines, or four di-*tert*-butylcarbazoles are connected to pyrazine, while for **3CzBPz**, three carbazoles and one biphenyl unit are connected to pyrazine, and for **2CzBPz**, two carbazoles and two biphenyl units are connected to pyrazine. Tetrachloropyrazine (**4ClPz**) was synthesized firstly from dioxopiperazine reacted with phosphorus pentachloride in $POCl_3$ as the solvent.[23] **4ClPz** then reacted with either carbazole, 3,6-di-*tert*-butyl-9*H*-carbazole (tCz), or 5H-pyrido[3,2-b]indole (Cb) via S_NAr mechanism to obtain **4CzPz**, **4tCzPz** and **4CbPz** at moderate yields (~55%, Scheme **4.1**). For the synthesis of **3CzBPz**, **4ClPz** was converted to mono biphenyl substituted intermediate (**3ClBPz**) via Suzuki-Miyaura reaction first then reacted with carbazole via S_NAr mechanism to obtain **3CzBPz** at 70% yield.[25] While for the synthesis of **2CzBPz**, **4ClPz** was reacted with carbazole via S_NAr mechanism to obtain bis-carbazole substituted intermediate (**2Cz2ClPz**), then reacted with 2-Biphenylboronic acid via Suzuki-Miyaura reaction to obtain **2Cz2BPz** at yield of 65%.[25] The five emitters were characterized by combination of ^{1}H and ^{13}C NMR spectroscopy, high-resolution mass spectrometry, melting point determination, and elemental analysis. The five emitters were purified by silica gel chromatography followed by

temperature gradient vacuum sublimation, and the purity was verified by high performance liquid chromatography (HPLC), which are presented in **4.8 Experimental section**.

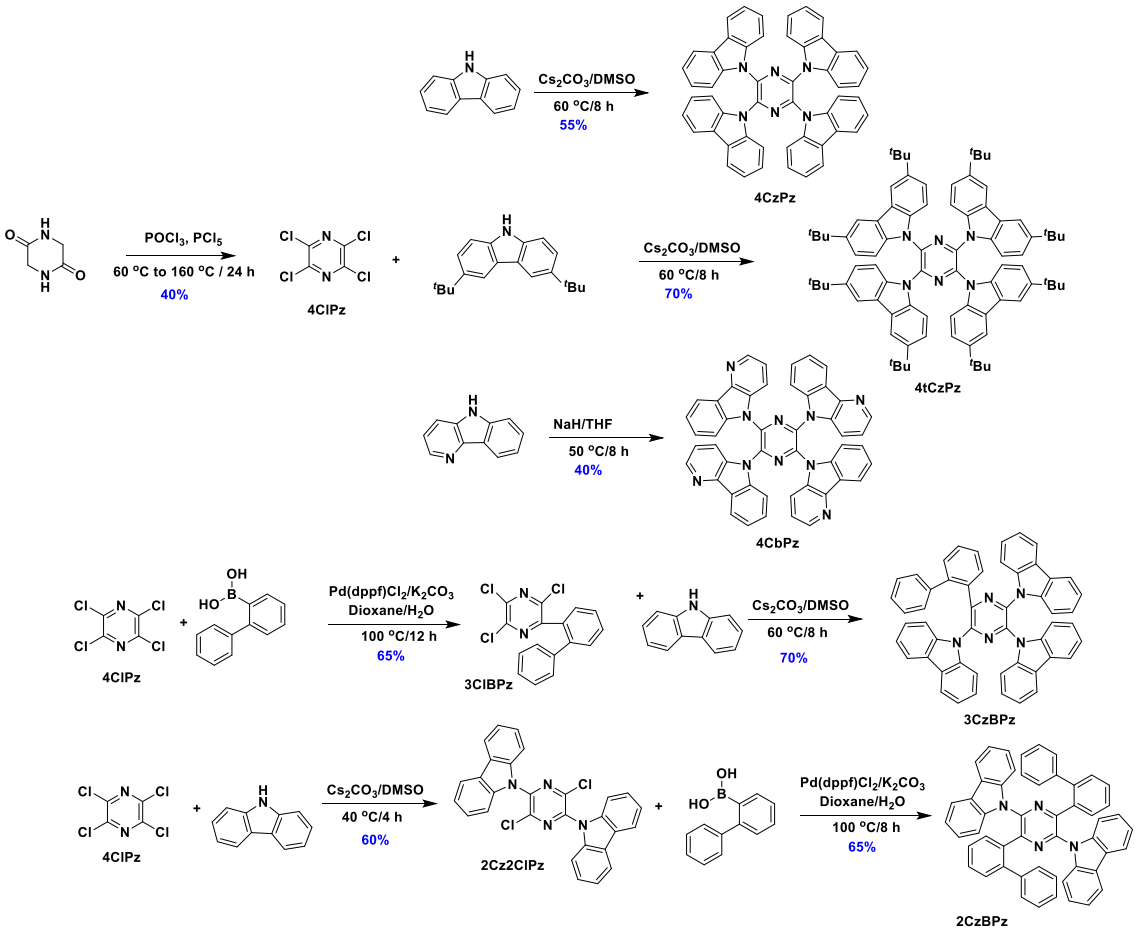

Scheme **4.2**. Synthesis route of **4CzPz**, **4CbPz**, **4tCzPz**, **3CzBPz**, and **2CzBPz**.

The DFT calculations predict the dihedral angles **4CzPz**, **4CbPz**, and **4tCzPz** between the donor moieties and pyrazine to be above 50°, compared to [36.53(14)°] for **DTCz-Pz**, while for **3CzBPz** and **2CzBPz**, the dihedral angles are slightly increased to [41.30(22)°] and [39.55(11)°], respectively. The HOMOs of **4CzPz**, **4CbPz**, and **4tCzPz** are distributed across the

whole molecule while the LUMOs are mainly localized on the acceptor cores, whereas for **3CzBPz** and **2CzBPz**, the HOMOs are located on the carbazole moieties and the pyrazine, and LUMOs are located on pyrazine and the phenyl rings connected to pyrazine. As using the ‘‘weaker’’ donor The HOMO values of **4CzPz**, **4CbPz**, **3CzBPz**, and **2CzBPz** are stabilized from -5.39 eV of **DTCz-Pz** to -5.52, -5.89, -5.50, and -5.52 eV, respectively, while for **4tCzPz**, the HOMO value is slightly destabilized to -5.25 eV. The LUMO values of **4CzPz**, **4CbPz**, **4tCzPz**, **3CzBPz**, and **2CzBPz** are stabilized from -1.46 eV of **DTCz-Pz** to -1.72, -2.02, -1.54, -1.62, and -1.66 eV, respectively. **4CzPz**, **4CbPz**, **4tCzPz**, and **3CzBPz** exhibited high oscillator strength above 0.2 and ΔE_{ST} around 0.50 eV, while for **2CzBPz** the oscillator strength is reduced to 0.02 and ΔE_{ST} narrowed to 0.39 eV. Intermediate triplets are predicted for these five molecules, which would render the RISC process despite the relatively large ΔE_{ST}. More TD-DFT calculations like NTO analysis and SOCME calculations, and photophysics and electrochemistry measurements will be carried out in the future to complete the characterization of these emitters and provide a more complete structure-property relationship, and finally we will try to apply these emitters for electroluminescence device.

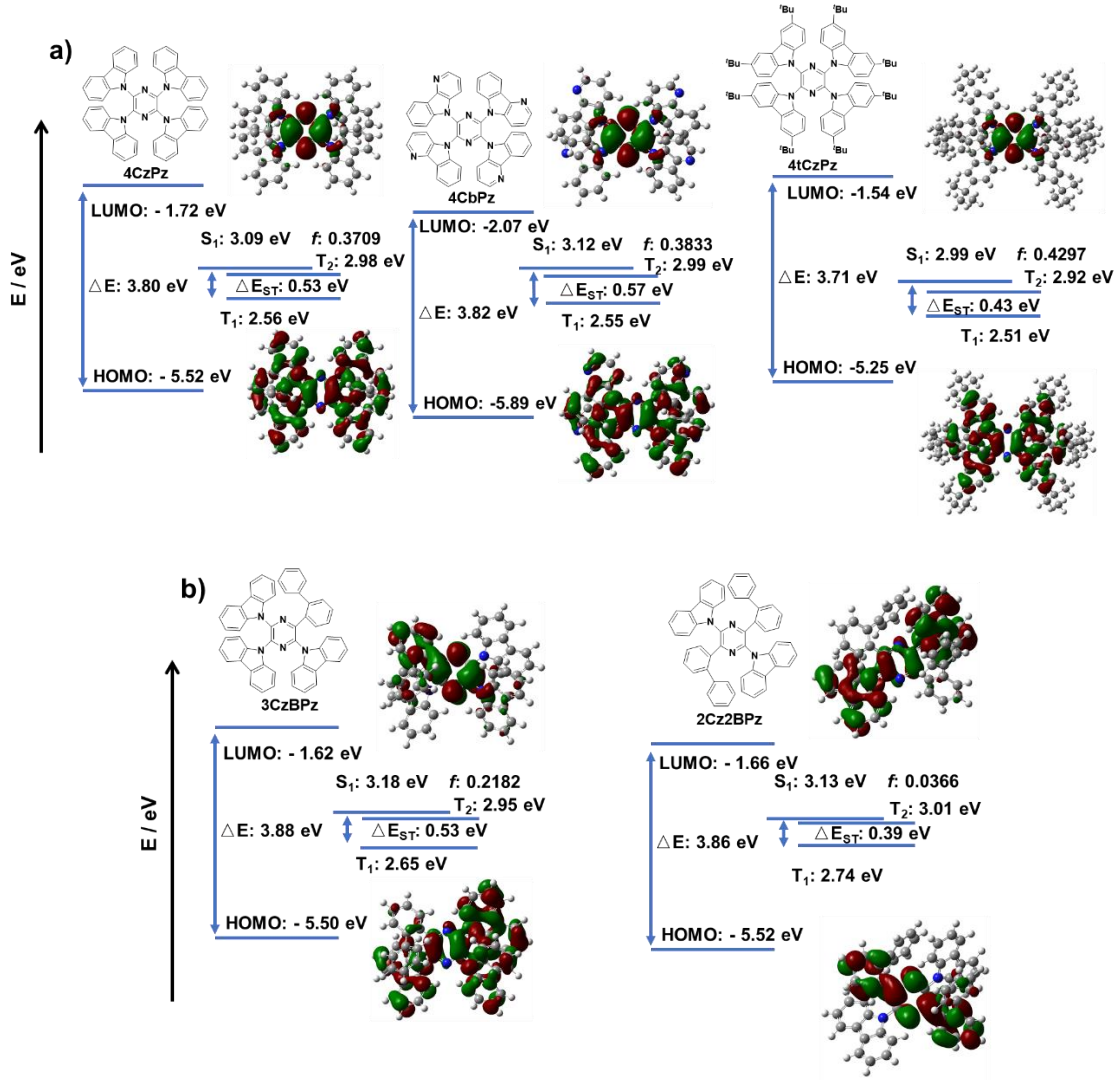

Figure **4.12**. Theoretical modelling of the energies of the HOMO/LUMO orbitals and the S_1 and T_1 states of a) **4CzPz**, **4CbPz**, and **4tCzPz**, and b) **3CzBPz** and **2CzBPz** in the gas phase and the electron density distribution of the frontier molecular orbitals (isovalue = 0.02).

4.8 Experimental section

General consideration

All experiments were carried out with commercial solvents from Fisher Scientific Ltd, except where specifically mentioned. Commercially obtained chemicals were used as received. All manipulations were carried out under an inert atmosphere using standard Schlenk line techniques.

^{1}H NMR, and ^{13}C NMR were recorded at room temperature on a Bruker Avance spectrometer at 400 MHz and 100 MHz, respectively. ^{1}H NMR and ^{13}C NMR spectra were referenced to the residual solvent peaks ($CDCl_3$ = 7.26 ppm for ^{1}H NMR and 77.16 ppm for ^{13}C NMR). The following abbreviations have been used for multiplicity assignments: “s” for singlet, “d” for doublet, “t” for triplet, “m” for multiplet and “br” for broad. Elemental analysis was measured by London Metropolitan University. Samples for high resolution mass spectrum (HRMS) were sent to the National Mass Spectrometry Facility in Swansea (EPSRC) for analysis by nano-electrospray on an Orbitrap instrument.

Materials and synthesis

2,5-bis(3,6-di-tert-butyl-9H-carbazol-9-yl)pyrazine (DTC-Pz)

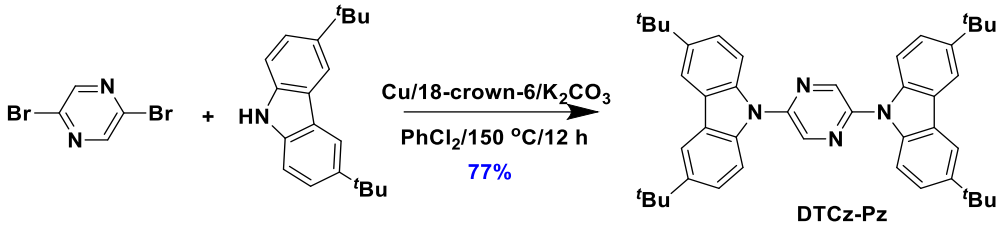

Synthesis of **DTCz-Pz** is based on a modified literature protocol.[22] To a 250 mL flask were added 2,5-dibromopyrazine (1.2 g, 5 mmol, 1 equiv.), di-*tert*-butyl-9H-carbazole (3.4 g, 12 mmol, 2.4 equiv.), copper powder (640 mg, 5 mmol, 1 equiv.), 18-crown-6 (150 mg, 1 mmol, 0.2 equiv.),

and potassium carbonate (4.5 g, 30 mmol, 6 equiv.). The flask was degassed by three cycles of vacuum-nitrogen purging and 50 mL of dichlorobenzene was injected. The mixture was stirred at 150 °C for 12 h under a nitrogen atmosphere. After cooling, water was added to the reaction mixture followed by extraction with DCM (3 × 50 mL). The combined organic layers were dried with anhydrous magnesium sulfate. The organic solvent was removed under reduced pressure and the crude product was purified by silica gel column chromatography. DCM/Hexane=1/3 was used as eluent to afford **DTC-Pz** as yellow solid.

Yield: 77%. **R_f**: 0.47 (50% DCM/Hexanes). **Mp**: 242-243 °C. **^{1}H NMR (400 MHz, $CDCl_3$) δ (ppm)**: 9.09 (s, 2H), 8.18 (d, *J* = 1.9 Hz, 4H), 7.94 (d, *J* = 8.7 Hz, 4H), 7.59 (dd, *J* = 8.7, 2.0 Hz, 4H), 1.52 (s, 36H). **^{13}C NMR (101 MHz, $CDCl_3$) δ (ppm)**: 145.3, 144.8, 138.1, 137.5, 124.8, 124.3, 116.4, 110.7, 34.8, 31.9. **HRMS** (LTQ Orbitrap XL) **$[M+H]^+$ Calculated: ($C_{44}H_{51}N_4$)** 635.4108; **Found**: 635.4104. **Elemental analysis: Calcd for $C_{44}H_{50}N_4$**: C, 83.24; H, 7.94; N, 8.82. **Found**: C, 84.10; H, 8.03; N, 8.83. **HPLC**: 5% H_2O/MeOH, 1.0 mL min^{-1}, 254 nm; tr (99.4 %) = 10.4 min.

9-(5-bromopyrazin-2-yl)-3,6-di-*tert*-butyl-9H-carbazole(DTCzPzBr)

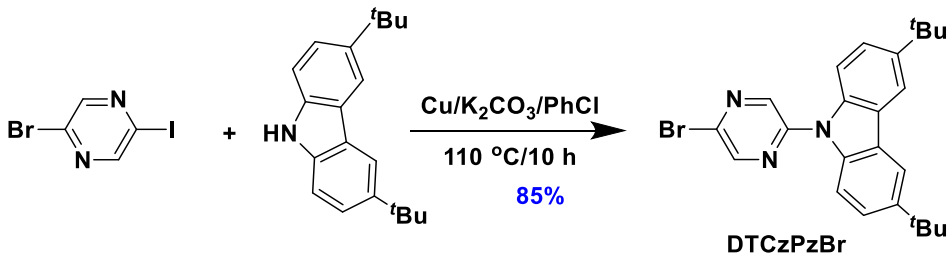

DTCzPzBr was synthesized according to the literature.[22] To a 250 mL flask were added 2-bromo-5-iodopyrazine (2.9 g, 10 mmol, 1 equiv.), di-*tert*-butyl-9H-carbazole (3.0 g, 11 mmol, 1.1 equiv.), copper powder (640 mg, 10 mmol, 1 equiv.) and potassium carbonate (4.5 g, 30 mmol, 3 equiv.). The flask was degassed by three cycles of vacuum-nitrogen purging and 50 mL of chlorobenzene was injected. The mixture was stirred at 110 °C for 10 h under a nitrogen atmosphere. After cooling, water was added to the reaction mixture followed by extraction with DCM (3 × 50 mL). The combined organic layers were dried with anhydrous magnesium sulfate. The organic solvent was removed under reduced pressure and the crude product was purified by silica gel column chromatography. DCM/Hexane=1/3 was used as eluent to afford **tCz-BrPz** as a faint yellow solid.

Yield: 85%. **R_f**: 0.65 (33% DCM/Hexanes). **Mp**: 180-182 °C (Lit.:[1] 180-182 °C). **^{1}H NMR (400 MHz, $CDCl_3$) δ (ppm)**: 8.84 (d, *J* = 1.4 Hz, 1H), 8.74 (d, *J* = 1.4 Hz, 1H), 8.13 (dd, *J* = 2.0, 0.6 Hz, 2H), 7.84 (dd, *J* = 8.8, 0.7 Hz, 2H), 7.54 (dd, *J* = 8.7, 2.0 Hz, 2H), 1.49 (s, 18H). **^{13}C NMR (101 MHz, $CDCl_3$) δ (ppm)**: 148.0, 145.9, 145.3, 139.3, 137.1, 134.6, 125.1, 124.4, 116.5, 110.7, 34.8, 31.9. **HRMS** (LTQ Orbitrap XL) **$[M+H]^+$ Calculated: ($C_{24}H_{27}N_3{}^{79}Br$)** 436.1383; **Found**: 436.1380. The characterization results matched literature results.[22]

5,5'-bis(3,6-di-tert-butyl-9H-carbazol-9-yl)-2,2'-bipyrazine(DTC-DPz)

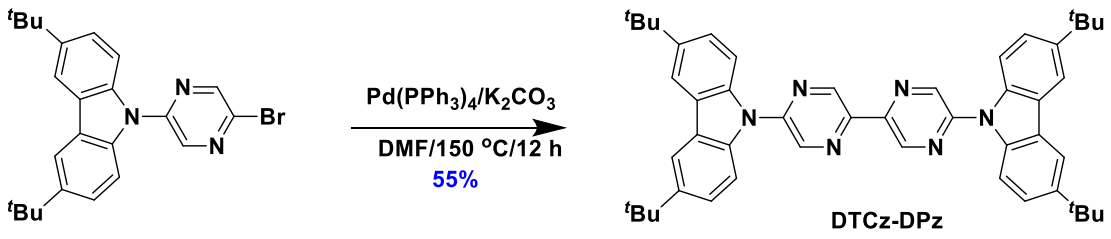

To a 250 mL flask were added 9-(5-bromopyrazin-2-yl)-3,6-di-tert-butyl-9H-carbazole(**tCz-BrPz**) (850 mg, 2 mmol, 1 equiv.), tetrakis(triphenylphosphine)palladium(0) (250 mg, 0.2 mmol, 0.1 equiv), potassium carbonate (900 mg, 6 mmol, 3 equiv.). The flask was degassed by three cycles of vacuum-nitrogen purging and 20 mL of DMF was injected. The mixture was stirred at 150 °C for 12 h under a nitrogen atmosphere. After cooling, the reaction mixture was poured into icy water followed by extraction with ether acetate (3 × 50 mL). The combined organic layers were dried with anhydrous magnesium sulfate. The organic solvent was removed under reduced pressure and the crude product was purified by silica gel column chromatography. DCM/Hexane=1/3 was used as eluent to afford **DTC-DPz** as a faint yellow solid.

Yield: 55%. **R_f**: 0.35 (33% DCM/Hexanes). **Mp**: 301-302 °C. **^{1}H NMR (500 MHz, $CDCl_3$) δ (ppm)**: 9.67 (s, 2H), 9.17 (s, 2H), 8.16 (d, *J* = 1.9 Hz, 4H), 8.01 (d, *J* = 8.7 Hz, 4H), 7.59 (dd, *J* = 8.8, 1.9 Hz, 4H), 1.51 (s, 36H). **^{13}C NMR (126 MHz, $CDCl_3$) δ (ppm)**: 149.0, 145.2, 141.6, 138.3, 137.2, 125.2, 124.4, 116.4, 111.2, 34.9, 31.9. **HRMS** (LTQ Orbitrap XL) **$[M+Na]^+$ Calculated: ($C_{48}H_{52}N_6Na$)** 735.4146; **Found**: 735.4142. **Elemental analysis**: **Calcd for $C_{44}H_{52}N_4$**: C, 80.86; H, 7.35; N, 11.79. **Found**: C, 80.93; H, 7.44; N, 11.79. **HPLC**: 10% H_2O/MeOH, 1.0 mL min^{-1}, 300 nm; tr (99.6 %) = 13.7 min.

Tetrachloropyrazine (4ClPz)

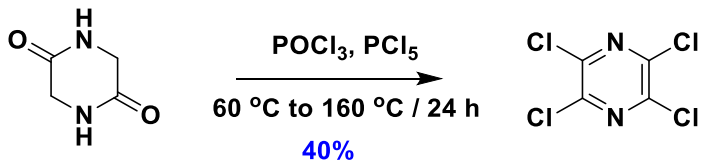

Synthesis of **4ClPz** was achieved by using a modified the literature procedure.[23] A mixture of 2,5-dioxopiperazine (1.1 g, 10 mmol, 1 equiv.) and phosphorus pentachloride (10.4 g, 50 mmol) were added to 30 mL (50 mmol, 5 equiv) of phosphorusoxychloride. The mixture was slowly heated up to 60°C whereby a vigorous reaction has occurred. After removing the solvent by distillation over vigreux condenser, the mixture was heated at 160-180 °C for 24h. The residue was dissolved in n-heptane and carefully added to icy water followed by extraction with DCM (3 × 50 mL). The combined organic layers were dried with anhydrous magnesium sulfate. The organic solvent was removed under reduced pressure and the crude product was purified by silica gel column chromatography. DCM/Hexane=1/10 was used as eluent to afford **4ClPz** as colorless solid.

Yield: 40%. **R_f**: 0.45 (10% DCM/Hexanes). **Mp**: 99-101 °C (Lit. Mp: 100 °C).[23] **^{13}C NMR (101MHz, $CDCl_3$) δ (ppm)**: 144.0; **LRMS** (GC-MS) **$[M]^+$ Calculated ($C_4Cl_4N_2$)**: 217.88; **Found**: 218.11. The characterization matches that previously reported.[23]

2,3,5,6-tetra(9*H*-carbazol-9-yl)pyrazine (4CzPz)

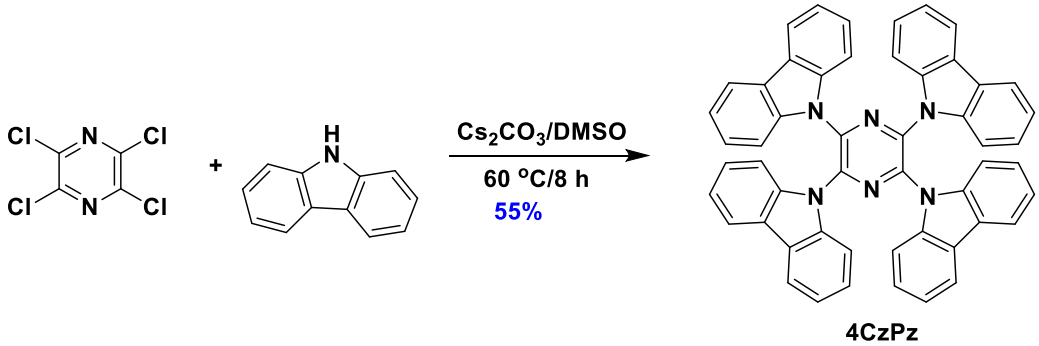

To a 250 mL flask were added **4ClPz** (210 mg, 1 mmol, 1 equiv.), carbazole (830 mg, 5 mmol, 5 equiv.), and cesium carbonate (1.6 g, 5 mmol, 5 quiv.). The flask was degassed by three cycles of

vacuum-nitrogen purging and 20 mL of DMSO was injected. The mixture was stirred at 60 °C for 8 h under a nitrogen atmosphere. After cooling, the reaction mixture was poured into icy water followed by extraction with ether acetate (3 × 50 mL). The combined organic layers were dried with anhydrous magnesium sulfate. The organic solvent was removed under reduced pressure and the crude product was purified by silica gel column chromatography. DCM/Hexane=1/3 was used as eluent to afford **4CzPz** as a light green solid.

Yield: 40%. **R_f**: 0.52 (40% DCM/Hexanes). **Mp**: over 410 °C. **^{1}H NMR (400 MHz, $CDCl_3$) δ (ppm)**: 7.89 – 7.85 (m, 8H), 7.55 (d, *J* = 8.2 Hz, 8H), 7.15 (ddd, *J* = 7.8, 7.2, 0.9 Hz, 8H), 7.02 (ddd, *J* = 8.4, 7.2, 1.3 Hz, 8H). **^{13}C NMR (101 MHz, $CDCl_3$) δ (ppm)**: 138.0, 135.3, 126.1, 124.5, 121.6, 119.8, 111.1. **HRMS** (ESI-MS) **$[M]^+$ Calculated: ($C_{52}H_{32}N_6$)** 741.2761; **Found**: 741.2736. **Elemental analysis**: **Calcd for $C_{52}H_{32}N_6$**: C, 84.30; H, 4.35; N, 11.34. **Found**: C, 84.60; H, 4.27; N, 11.11. **HPLC**: 5% H_2O/MeOH, 1.0 mL min^{-1}, 300 nm; tr (97.9 %) = 11.9 min. The characterization matches that previously reported.[24]

2,3,5,6-tetrakis(3,6-di-*tert*-butyl-9H-carbazol-9-yl)pyrazine (4tCzPz)

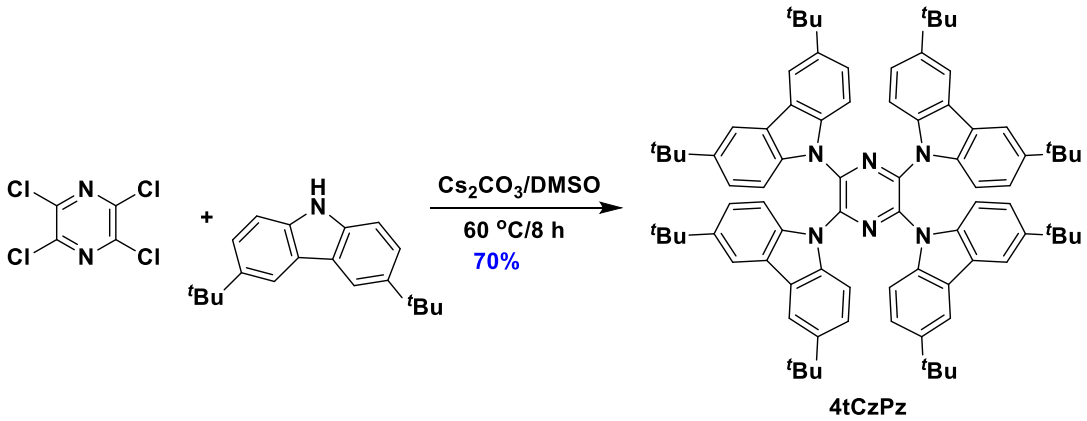

To a 250 mL flask were added **4ClPz** (210 mg, 1 mmol, 1 equiv.), di-*tert*-butyl-carbazole (1.4 g, 5 mmol, 5 equiv.), and cesium carbonate (1.6 g, 5 mmol, 5 quiv.). The flask was degassed by three cycles of vacuum-nitrogen purging and 20 mL of DMSO was injected. The mixture was stirred at 60 °C for 8 h under a nitrogen atmosphere. After cooling, the reaction mixture was poured into icy water followed by extraction with ether acetate (3 × 50 mL). The combined organic layers were dried with anhydrous magnesium sulfate. The organic solvent was removed under reduced pressure and the crude product was purified by silica gel column chromatography. DCM/Hexane=1/3 was used as eluent to afford **4tCzPz** as a yellow solid.

Yield: 70%. **R_f**: 0.72 (20% DCM/Hexanes). **Mp**: 400 °C. **^{1}H NMR (400 MHz, $CDCl_3$) δ (ppm)**: 7.89 – 7.85 (m, 8H), 7.55 (d, *J* = 8.2 Hz, 8H), 7.15 (ddd, *J* = 7.8, 7.2, 0.9 Hz, 8H), 7.02 (ddd, *J* = 8.4, 7.2, 1.3 Hz, 8H). **^{13}C NMR (101 MHz, $CDCl_3$) δ (ppm)**: 138.0, 135.3, 126.1, 124.5, 121.6, 119.8, 111.1, 34.5, 31.8. **HRMS** (ESI-MS) **$[M+H]^+$ Calculated: ($C_{84}H_{97}N_6$)** 1189.7696; **Found**: 1189.7678. **Elemental analysis**: **Calcd for $C_{84}H_{96}N_6$**: C, 84.80; H, 8.13; N, 7.06. **Found**: C, 84.84; H, 8.00; N, 7.08. **HPLC**: 20% THF/MeOH, 1.0 mL min^{-1}, 300 nm; tr (99.0 %) = 7.2 min.

2,3,5,6-tetrakis(5H-pyrido[3,2-b]indol-5-yl)pyrazine (4CbPz)

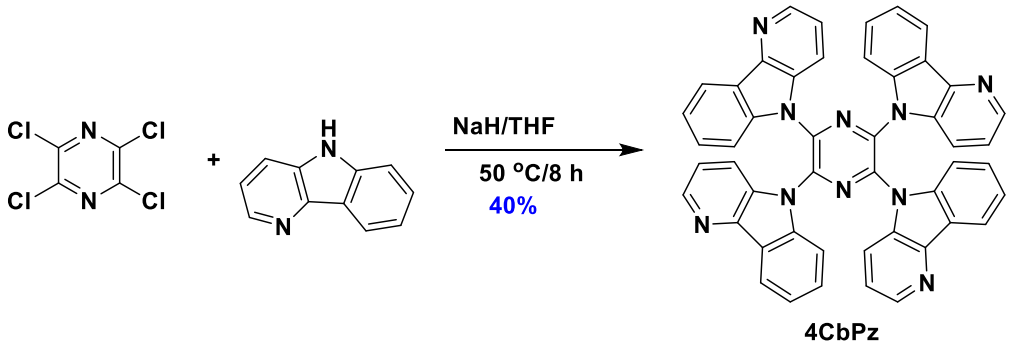

To a 250 mL flask were added **4ClPz** (210 mg, 1 mmol, 1 equiv.), 5H-pyrido[3,2-b]indole (840 mg, 5 mmol, 5 equiv.), and sodium hydride (240 mg, 5 mmol, 5 quiv.). The flask was degassed by three cycles of vacuum-nitrogen purging and 20 mL of THF was injected. The mixture was stirred at 50 °C for 8 h under a nitrogen atmosphere. After cooling, the reaction mixture was poured into icy water followed by extraction with DCM (3 × 50 mL). The combined organic layers were dried with anhydrous magnesium sulfate. The organic solvent was removed under reduced pressure and the crude product was purified by silica gel column chromatography. DCM was used as eluent to afford **4CbPz** as a light yellow solid.

Yield: 40%. **R_f**: 0.32 (DCM). **Mp**: over 410 °C. **^{1}H NMR (400 MHz, $CDCl_3$) δ (ppm)**: 8.51 (d, *J* = 4.6 Hz, 4H), 8.21 (d, *J* = 7.8 Hz, 4H), 7.89 – 7.70 (m, 4H), 7.65 – 7.47 (m, 4H), 7.29 (s, 4H), 7.17 (s, 4H), 7.00 (s, 4H). **^{13}C NMR (101 MHz, $CDCl_3$) δ (ppm)**: 153.0, 152.2, 146.3, 136.4, 132.3, 129.9, 128.9, 128.2, 122.5. **HRMS** (ESI-MS) **$[M+H]^+$ Calculated: ($C_{48}H_{29}N_{10}$)** 745.2498; **Found**: 745.2553. **Elemental analysis**: **Calcd for $C_{48}H_{28}N_{10}$**: C, 77.40; H, 3.79; N, 18.81. **Found**: C, 77.49; H, 3.66; N, 18.27. **HPLC**: 10% H_2O/MeOH, 1.0 mL min^{-1}, 300 nm; tr (97.5 %) = 11.8 min.

2-([1,1'-biphenyl]-2-yl)-3,5,6-trichloropyrazine (3ClBPz)

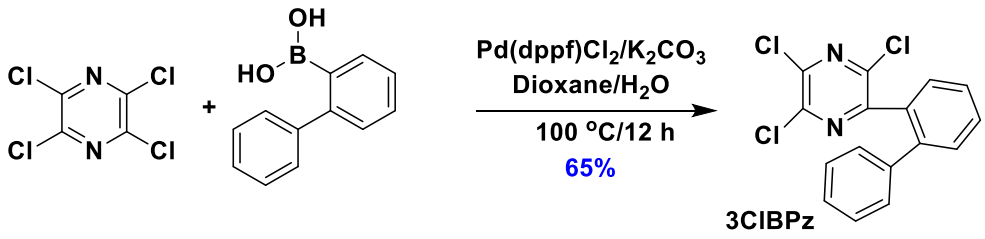

To a 250 mL flask were added **4ClPz** (210 mg, 1 mmol, 1 equiv.), [1,1'-biphenyl]-2-ylboronic acid (200 mg, 1 mmol, 1 equiv.), (1,1'-Bis(diphenylphosphino)ferrocene)palladium(II) dichloride (75 mg, 0.1 mmol, 0.1 equiv), potassium carbonate (450 mg, 3 mmol, 3 equiv.). The flask was degassed by three cycles of vacuum-nitrogen purging and 2 mL of deionized water and 8 mL of dioxane were injected. The mixture was stirred at 100 °C for 12 h under a nitrogen atmosphere. After cooling, the reaction mixture was poured into icy water followed by extraction with dcm (3 × 50 mL). The combined organic layers were dried with anhydrous magnesium sulfate. The organic solvent was removed under reduced pressure and the crude product was purified by silica gel column chromatography. DCM/Hexane=1/4 was used as eluent to afford **3ClBPz** as a white solid.

Yield: 65%. **R_f**: 0.62 (20% DCM/Hex). **Mp**: 150 °C. **^{1}H NMR (500 MHz, $CDCl_3$) δ (ppm)**: 7.64 – 7.57 (m, 1H), 7.55 – 7.46 (m, 3H), 7.29 (d, *J* = 2.4 Hz, 3H), 7.18 – 7.10 (m, 2H). **^{13}C NMR (126 MHz, $CDCl_3$) δ (ppm)**: 152.6, 144.4, 144.3, 143.8, 141.8, 140.0, 133.1, 130.3, 130.3, 130.0, 129.2, 128.4, 127.5, 127.5. **LRMS** (GC-MS) **$[M+H]^+$ Calculated: ($C_{16}H_9Cl_3N_2$)** 333.98; **Found**: 334.10.

9,9',9''-(6-([1,1'-biphenyl]-2-yl)pyrazine-2,3,5-triyl)tris(9H-carbazole) (3CzBPz)

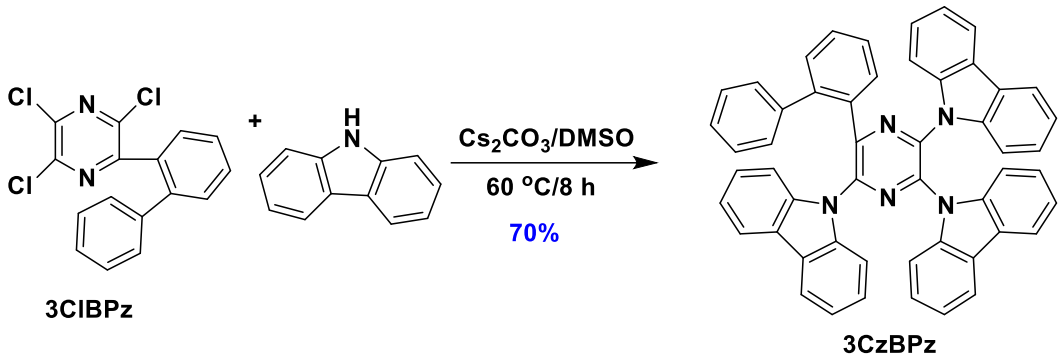

To a 250 mL flask were added **3ClBPz** (330 mg, 1 mmol, 1 equiv.), carbazole (660 mg, 4 mmol, 4 equiv.), and cesium carbonate (1.3 g, 4 mmol, 4 quiv.). The flask was degassed by three cycles of vacuum-nitrogen purging and 20 mL of DMSO was injected. The mixture was stirred at 60 °C for 8 h under a nitrogen atmosphere. After cooling, the reaction mixture was poured into icy water followed by extraction with ether acetate (3 × 50 mL). The combined organic layers were dried with anhydrous magnesium sulfate. The organic solvent was removed under reduced pressure and the crude product was purified by silica gel column chromatography. DCM/Hexane=1/3 was used as eluent to afford **3CzBPz** as a light yellow solid.

Yield: 70%. **R_f**: 0.42 (30% DCM/Hexanes). **Mp**: 400 °C. **^{1}H NMR (400 MHz, Acetone-*d*6) δ (ppm)**: 8.29 – 8.20 (m, 1H), 8.05 (d, J = 7.7 Hz, 2H), 8.01 – 7.87 (m, 4H), 7.55 (td, *J* = 7.6, 1.3 Hz, 5H), 7.37 (td, *J* = 7.6, 1.4 Hz, 1H), 7.25 – 6.99 (m, 15H), 6.94 – 6.78 (m, 3H), 6.72 – 6.56 (m, 2H). **^{13}C NMR (101 MHz, Acetone-*d*6) δ (ppm)**: 148.6, 142.6, 140.4, 139.4, 139.3, 138.7, 138.4, 134.7, 132.4, 130.2, 128.5, 128.1, 128.0, 126.5, 125.8, 124.0, 121.8, 121.3, 120.7, 120.1, 111.4. **HRMS** (ESI-MS) **$[M+H]^+$ Calculated: ($C_{52}H_{34}N_5$)** 728.2809; **Found**: 728.2804. **Elemental analysis**: **Calcd for $C_{52}H_{32}N_6$**: C, 85.81; H, 4.57; N, 9.62. **Found**: C, 85.60; H, 4.66; N, 9.46. **HPLC**: 2% H_2O/MeOH, 1.0 mL min^{-1}, 300 nm; tr (97.9 %) = 4.0 min.

9,9'-(3,6-dichloropyrazine-2,5-diyl)bis(9H-carbazole) (2Cz2ClPz)

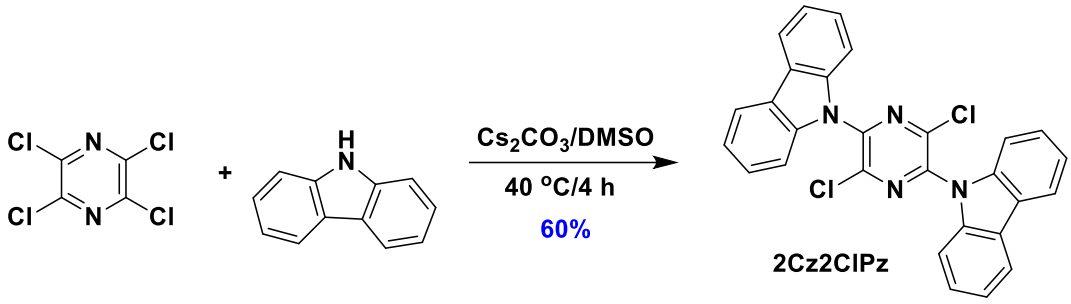

To a 250 mL flask were added **4ClPz** (210 mg, 1 mmol, 1 equiv.), carbazole (130 mg, 2 mmol, 2 equiv.), and cesium carbonate (640 g, 2 mmol, 2 quiv.). The flask was degassed by three cycles of vacuum-nitrogen purging and 20 mL of DMSO was injected. The mixture was stirred at 40 °C for 8 h under a nitrogen atmosphere. After cooling, the reaction mixture was poured into icy water followed by extraction with ether acetate (3 × 50 mL). The combined organic layers were dried with anhydrous magnesium sulfate. The organic solvent was removed under reduced pressure and the crude product was purified by silica gel column chromatography. DCM/Hexane=1/3 was used as eluent to afford **2Cz2ClPz** as a light green solid.

Yield: 60%. **R_f**: 0.42 (40% DCM/Hex). **Mp**: 250 °C. **^{1}H NMR (400 MHz, $CDCl_3$) δ (ppm)**: 8.22 – 8.17 (m, 1H), 7.58 – 7.50 (m, 3H), 7.48 – 7.39 (m, 1H). **^{13}C NMR (101 MHz, $CDCl_3$) δ (ppm)**: 142.6, 138.0, 135.1, 125.9, 124.5, 121.6, 119.8, 111.1. **LRMS** (GC-MS) **$[M+H]^+$ Calculated: ($C_{28}H_{17}Cl_2N_4$)** 479.08; **Found**: 479.19.

9,9'-(3,6-di([1,1'-biphenyl]-2-yl)pyrazine-2,5-diyl)bis(9H-carbazole) (2CzBPz)

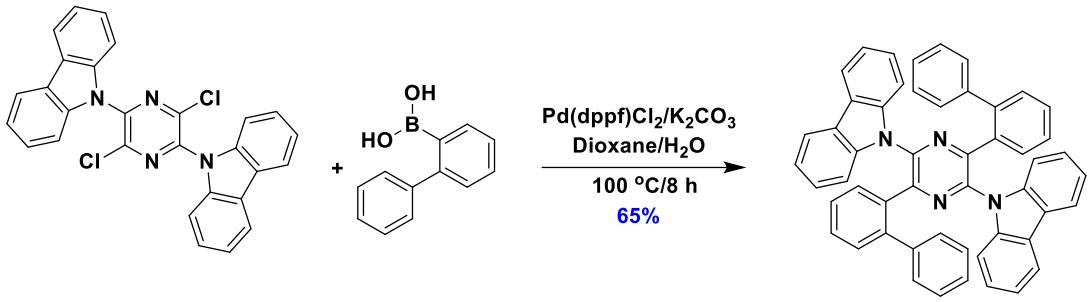

To a 250 mL flask were added **2Cz2ClPz** (480 mg, 1 mmol, 1 equiv.), [1,1'-biphenyl]-2-ylboronic acid (600 mg, 3 mmol, 3 equiv.), (1,1'-Bis(diphenylphosphino)ferrocene)palladium(II) dichloride (75 mg, 0.1 mmol, 0.1 equiv), potassium carbonate (1.3 g, 9 mmol, 9 equiv.). The flask was degassed by three cycles of vacuum-nitrogen purging and 2 mL of deionized water and 8 mL of dioxane were injected. The mixture was stirred at 100 °C for 12 h under a nitrogen atmosphere. After cooling, the reaction mixture was poured into icy water followed by extraction with dcm (3 × 50 mL). The combined organic layers were dried with anhydrous magnesium sulfate. The organic solvent was removed under reduced pressure and the crude product was purified by silica gel column chromatography. DCM/Hexane=1/4 was used as eluent to afford **2CzBPz** as a white solid.

Yield: 65%. **R_f**: 0.44 (20% DCM/Hexanes). **Mp**: 395 °C. **^{1}H NMR (400 MHz, *d*-DMSO) δ (ppm)**: 8.08 (d, *J* = 7.6 Hz, 4H), 8.04 – 7.93 (m, 2H), 7.46 (td, *J* = 7.6, 1.2 Hz, 2H), 7.31 (td, *J* = 7.6, 1.4 Hz, 2H), 7.16 (t, *J* = 7.5 Hz, 4H), 7.03 (t, *J* = 7.7 Hz, 4H), 7.00 – 6.86 (m, 12H), 6.48 (d, *J* = 7.0 Hz, 4H). **^{13}C NMR (101 MHz, *d*-DMSO) δ (ppm)**: 148.6, 142.6, 140.4, 139.3, 138.7, 134.7, 132.4, 130.3, 128.5, 128.1, 125.8, 121.8, 121.3, 120.7, 111.4. **HRMS** (ESI-MS) **$[M+H]^+$ Calculated: ($C_{52}H_{35}N_4$)** 715.2844; **Found**: 715.2856. **Elemental analysis**: **Calcd for $C_{52}H_{32}N_6$**:

C, 87.37; H, 4.79; N, 7.84. **Found**: C, 87.54; H, 4.89; N, 7.78. **HPLC**: 2% H_2O/MeOH, 1.0 mL min^{-1}, 300 nm; tr (98.5 %) = 4.8 min.

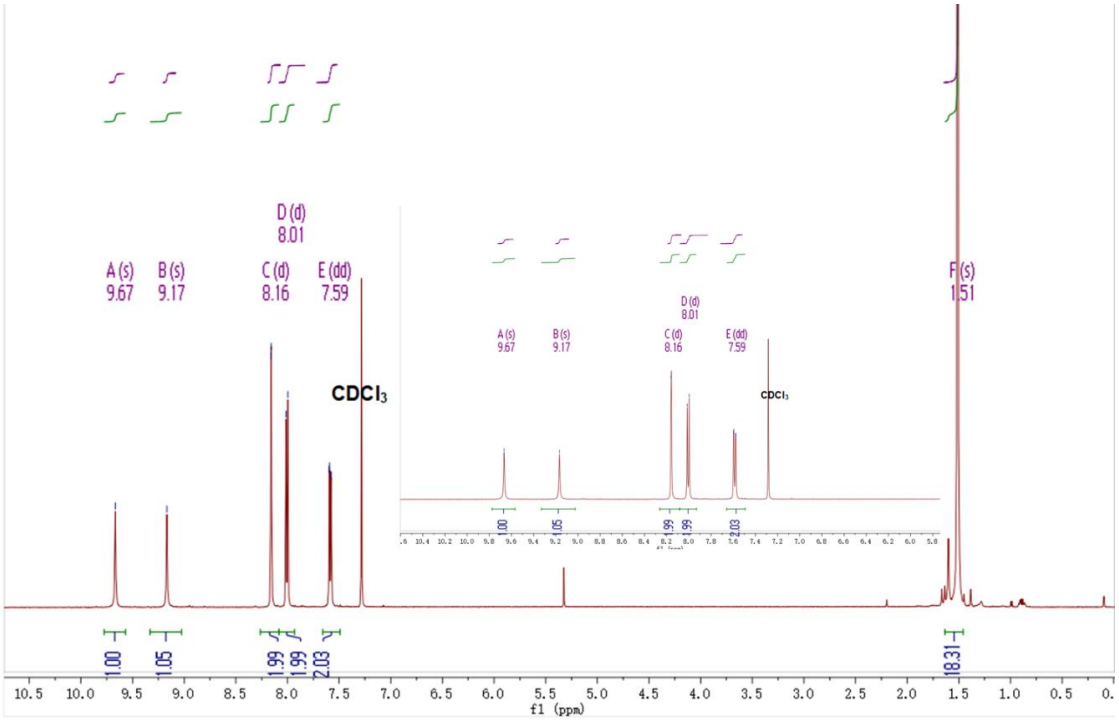

Figure **4.13**. ^1H NMR of **DTCz-Pz** in $CDCl_3$

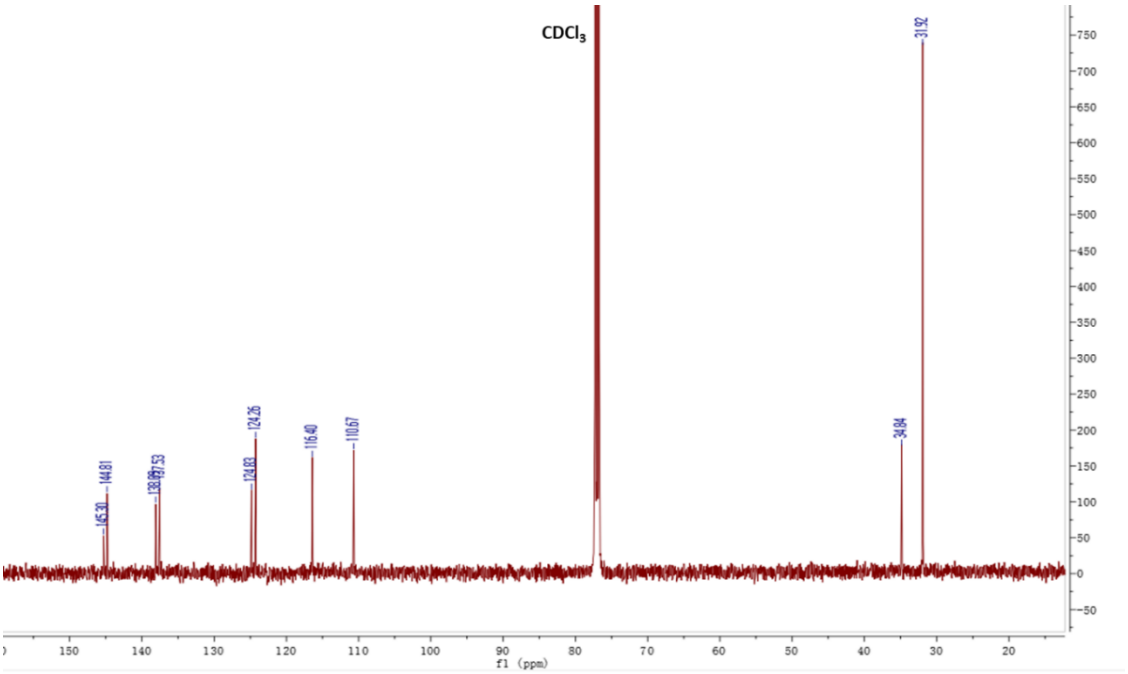

Figure **4.14**. ^{13}C NMR of **DTCz-Pz** in $CDCl_3$

LONDON metropolitan university

Elemental Analysis Service

Please send completed form and samples to:

Stephen Boyer
School of Human Sciences
Science Centre
London Metropolitan University
29 Hornsey Road
London N7 7DD

Telephone: 020 7133 3605
Fax: 020 7133 2577
Email: s.boyer@londonmet.ac.uk

Sample submitted by: Dongyang Chen
Address: **EZC group, School of Chemistry, University of St Andrews, Purdie Building, St Andrews, Fife, KY16 9ST**
Telephone: 07743430420 Email: dc217@st-amdrews.ac.uk
Date Submitted:02/12/2019

Please submit ca. 5 mg of sample.

Sample Reference No.: dc-tCzPz
Name of Compound: tCzPz
Molecular Formula: C44H50N4
Stability: Air stable
Hazards: none
Other Remarks:

Element	Expected %	Found (1)	Found (2)	
Carbon	83.24	84.15	84.05	
Hydrogen	7.94	8.03	8.03	
Nitrogen	8.82	8.83	8.83	

Authorising Signature:

Date Completed: 11/12/19	Signature:
Comments:	

Figure **4.15**. Elemental analysis of **DTCz-Pz**

SHIMADZU LabSolutions **Analysis Report**

<Sample Information>

Sample Name	: tCzPz		
Sample ID	:		
Data Filename	: tCzPz-1		
Method Filename	: 95% Methanol 5 Water 20 mins.lcm		
Batch Filename	: 090220202.lcb		
Vial #	: 1-38		
Injection Volume	: 5 uL		
Date Acquired	: 10/03/2020 14:07:37	Acquired by	: System Administrator
Date Processed	: 10/03/2020 14:22:48	Processed by	: System Administrator

<Chromatogram>

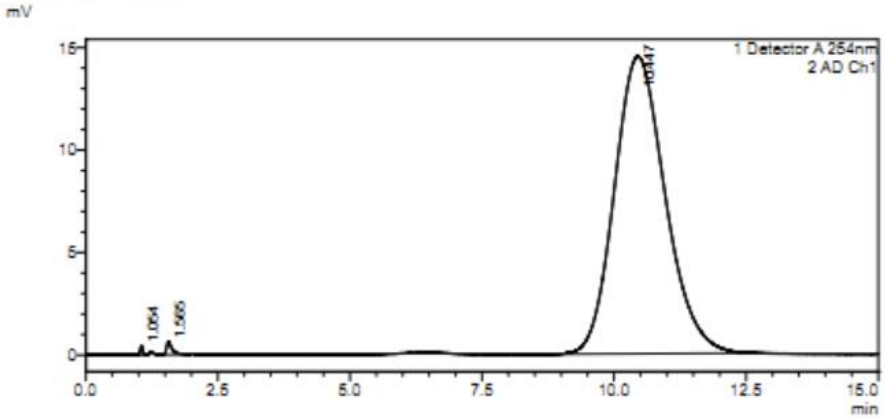

<Peak Table>

Detector A 254nm

Peak#	Ret. Time	Area	Height	Conc.	Unit	Mark	Area%
Total							

AD Ch1

Peak#	Ret. Time	Area	Height	Conc.	Unit	Mark	Area%
1	1.054	1474	443	0.000		V	0.151
2	1.565	4634	640	0.000		V	0.475
3	10.447	969310	14489	0.000		S	99.374
Total		975418	15572				100.000

Figure **4.16**. HPLC report of **DTCz-Pz**

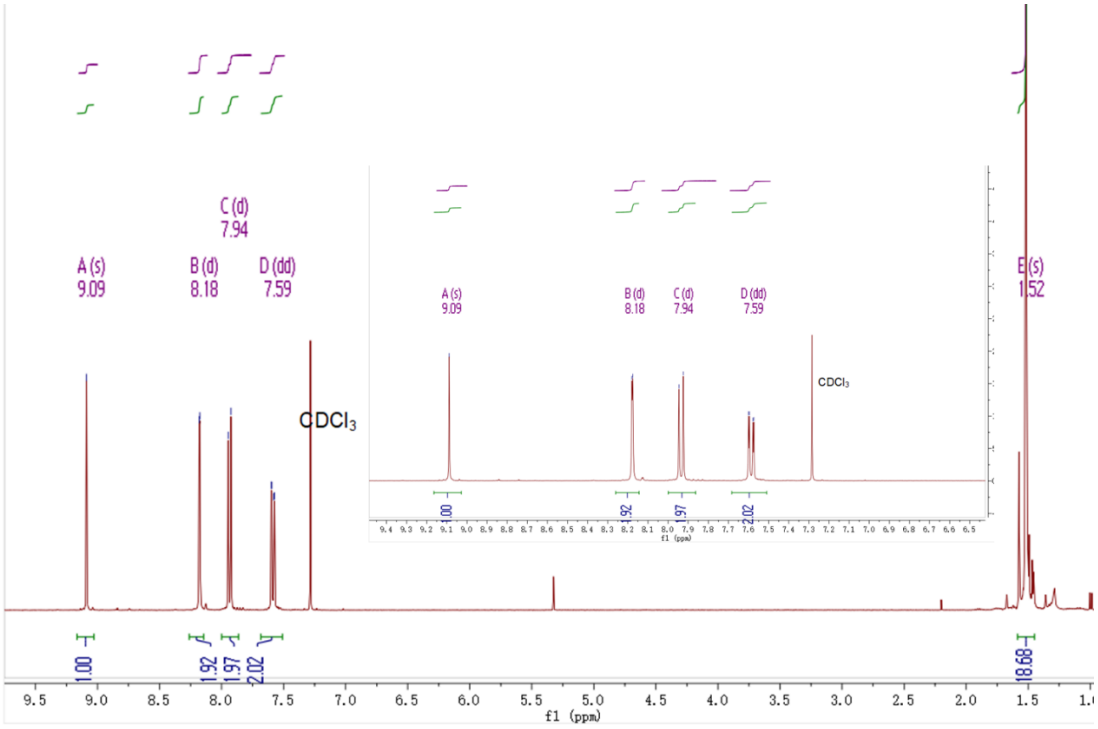

Figure **4.17**. [1]HNMR of **DTCz-DPz** in $CDCl_3$

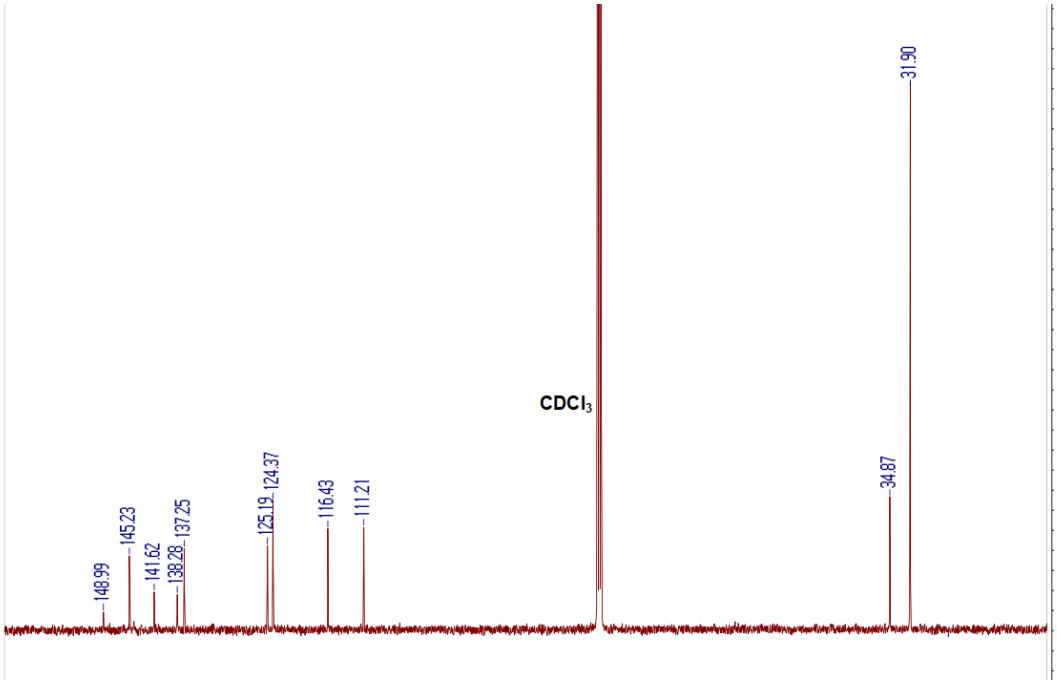

Figure **4.18**. [13]CNMR of **DTCz-DPz** in $CDCl_3$

LONDON metropolitan university

Elemental Analysis Service

Please send completed form and samples to:

Stephen Boyer
School of Human Sciences
Science Centre
London Metropolitan University
29 Hornsey Road
London N7 7DD

Telephone: 020 7133 3605
Fax: 020 7133 2577
Email: s.boyer@londonmet.ac.uk

Sample submitted by: Dongyang Chen
Address: **EZC group, School of Chemistry, University of St Andrews, North Haugh,St Andrews, Fife, KY16 9ST**
Telephone: 07743430420 Email: dc217@st-amdrews.ac.uk
Date Submitted:25/04/2018

Please submit ca. 5 mg of sample.

Sample Reference No.: dc-DiPztCz
Name of Compound: DiPztCz
Molecular Formula: C48H52N6
Stability: Air stable
Hazards: none
Other Remarks:

Element	Expected %	Found (1)	Found (2)	
Carbon	80.86	80.89	80.97	
Hydrogen	7.35	7.42	7.47	
Nitrogen	11.79	11.89	11.74	

Authorising Signature:

Date Completed: 27/07/18	Signature:
Comments:	

Figure **4.19**. Elemental analysis of **DTCz-DPz**

SHIMADZU LabSolutions **Analysis Report**

<Sample Information>

Sample Name	: tCzDPz		
Sample ID	: tCzDPz		
Data Filename	: 15032020_tCzDPz_001_15032020_tCzDPz_002.lcd		
Method Filename	: MeOH (90).lcm		
Batch Filename	: 15032020_tCzDPz_002.lcd		
Vial #	: 1-4	Sample Type	: Unknown
Injection Volume	: 2 uL		
Date Acquired	:15/03/2020 13:20:17	Acquired by	: ezc-7
Date Processed	:15/03/2020 13:20:17	Processed by	: ezc-7

<Chromatogram>

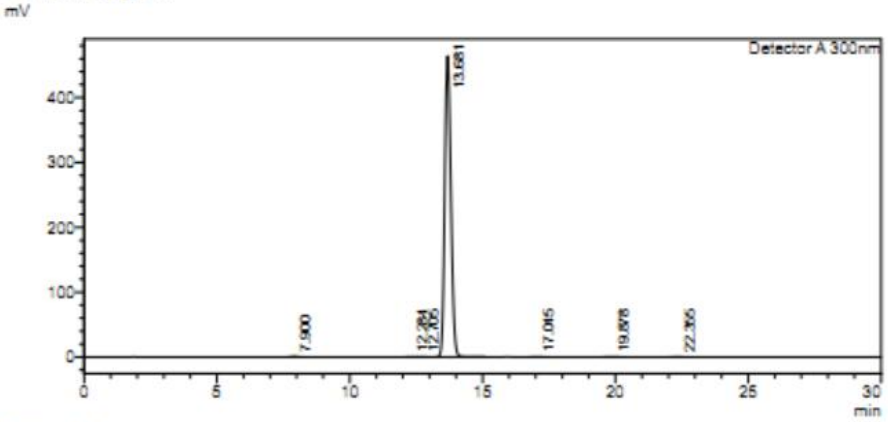

<Peak Table>

Detector A 300nm

Peak#	Ret. Time	Area	Height	Conc.	Unit	Mark	Area%
1	7.900	11888	1034	0.000	mg/L		0.162
2	12.284	1470	105	0.000			0.020
3	12.705	4480	309	0.000		V	0.061
4	13.681	7328316	464257	0.000	mg/L		99.609
5	17.045	2073	110	0.000			0.028
6	19.878	6718	345	0.000	mg/L		0.091
7	22.355	2113	102	0.000			0.029
Total		7357058	466263				100.000

Figure **4.20**. HPLC report of **DTCz-DPz**

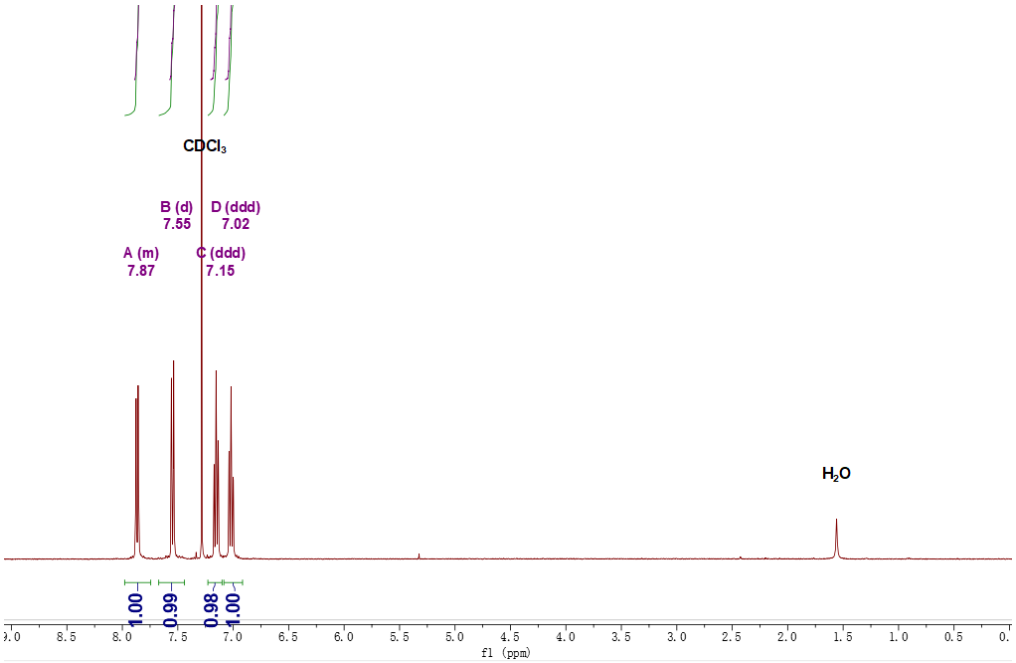

Figure **4.21**. ^{1}H NMR of **4CzPz** in $CDCl_3$

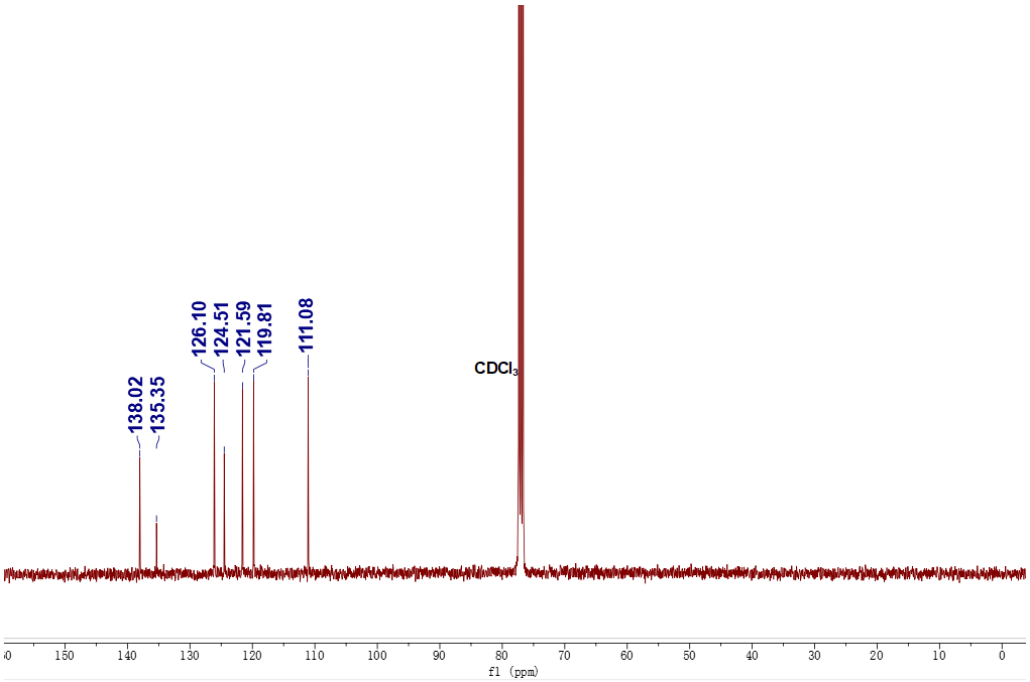

Figure **4.22**. ^{13}C NMR of **4CzPz** in $CDCl_3$

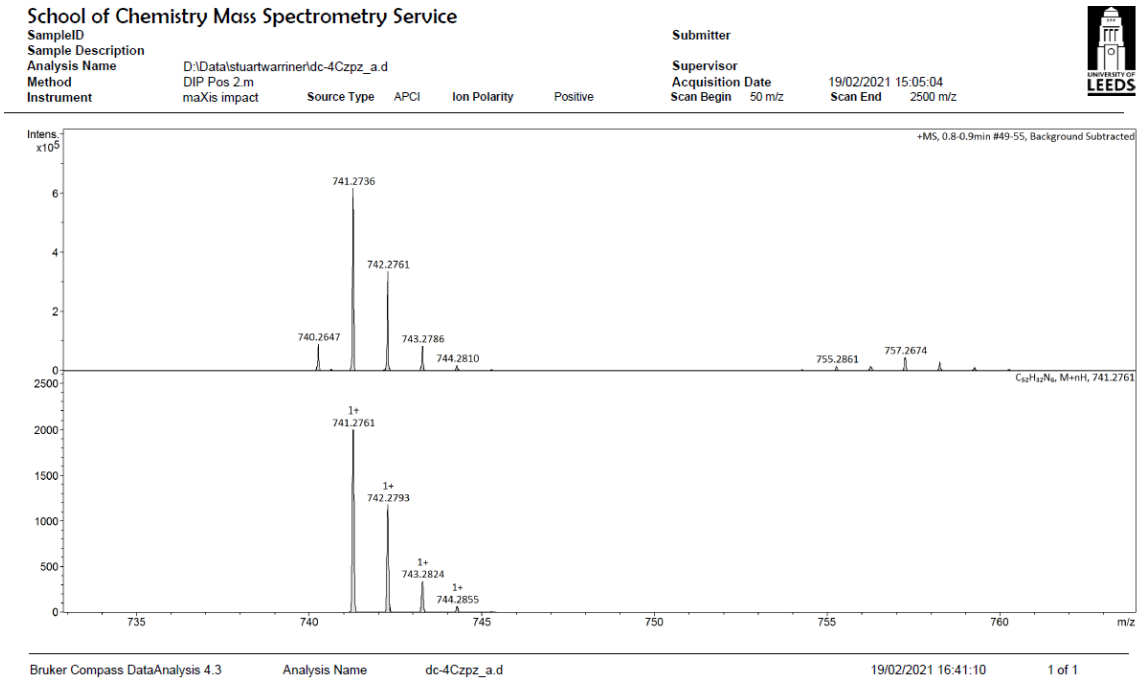

Figure **4.23**. HRMS of **4CzPz**

Elemental Analysis Service Request Form

Researcher name Dongyang Chen

Researcher email dc217@st-andrews.ac.uk

NOTE: Please submit ca. 10 mg of sample

Sample reference number	dc-II212
Name of Compound	4CzPz
Molecular formula	C52H32N6
Stability	stable
Hazards	low hazard
Other Remarks	

Analysis type:

Single ☐ **Duplicate**√☐ **Triplicate**☐

Analysis Result:

Element	Expected %	Found (1)	Found (2)	Found (3)
Carbon	84.30	84.89	84.30	
Hydrogen	4.35	4.24	4.28	
Nitrogen	11.34	11.11	11.02	
Oxygen				

Authorising Signature:

Date completed	26.02.21
Signature	J_Pc
comments	

Figure **4.24**. Elemental analysis of **4CzPz**

SHIMADZU LabSolutions **Analysis Report**

<Sample Information>

Sample Name	: 4CzPz 95 methanol		
Sample ID	:		
Data Filename	: 4CzPz4tCzPz2_28092020_4CzPz 95 methanol_003.lcd		
Method Filename	: 95% Methanol 5 Water 20 mins.lcm		
Batch Filename	: 4CzPz4tCzPz2.lcb		
Vial #	: 1-11	Sample Type	: Unknown
Injection Volume	: 10 uL		
Date Acquired	: 28/09/2020 12:25:52	Acquired by	: System Administrator
Date Processed	: 28/09/2020 12:50:55	Processed by	: System Administrator

<Chromatogram>

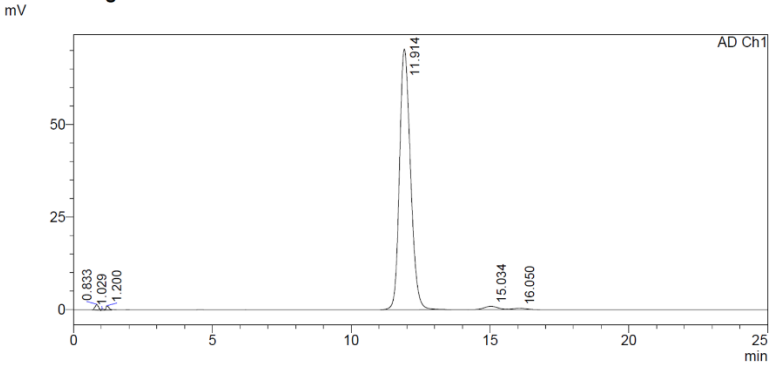

<Peak Table>

Peak#	Ret. Time	Area	Height	Conc.	Unit	Area%
1	0.837	11668	1472	0.000		0.592
2	1.203	8161	1039	0.000	mg/L	0.414
3	11.915	1930492	70276	0.000	mg/L	97.884
4	15.036	21908	763	0.000		1.111
Total		1972230	73551			100.000

Figure **4.25**. HPLC report of **4CzPz**

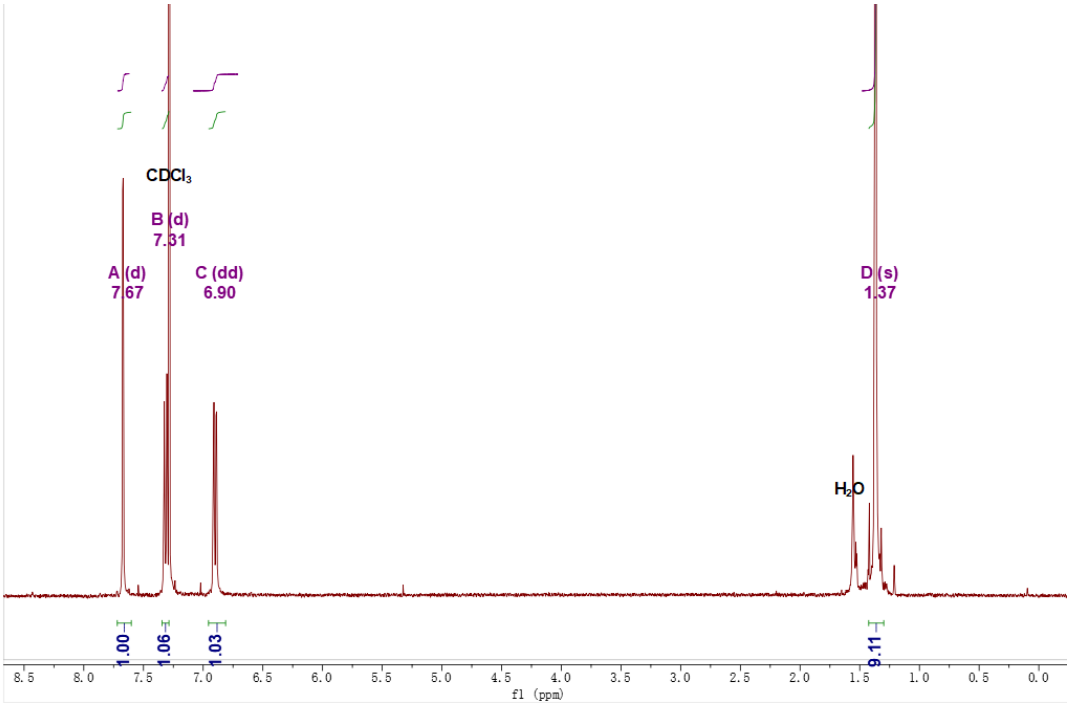

Figure **4.26**. ^{1}H NMR of **4tCzPz** in $CDCl_3$

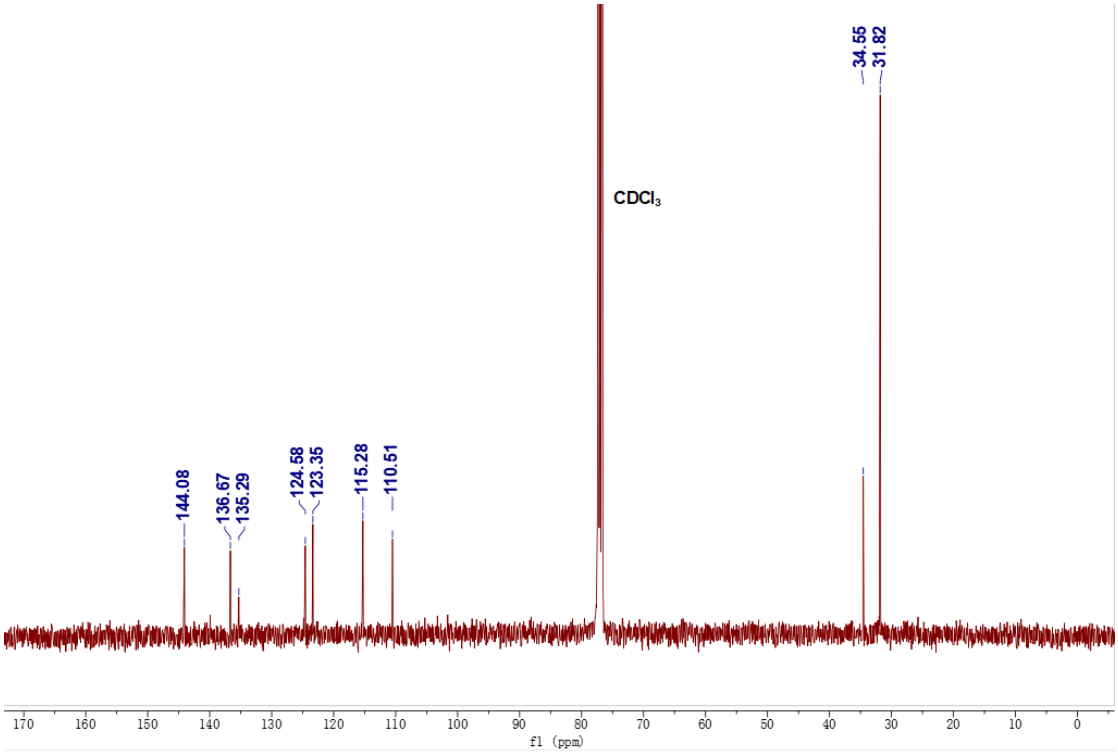

Figure **4.27**. ^{13}C NMR of **4tCzPz** in $CDCl_3$

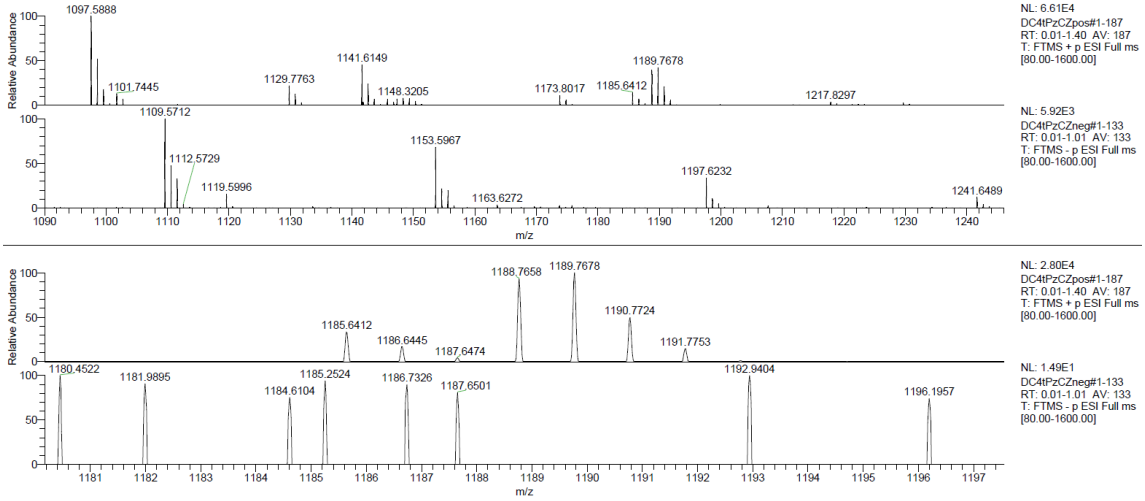

Figure **4.28**. HRMS of **4tCzPz**

Elemental Analysis Service Request Form

Researcher name Dongyang Chen

Researcher email dc217@st-andrews.ac.uk

NOTE: Please submit ca. 10 mg of sample

Sample reference number	dc-II213
Name of Compound	4tCzPz
Molecular formula	C84H96N6
Stability	stable
Hazards	low hazard
Other Remarks	

Analysis type:

Single ☐ **Duplicate**√☐ **Triplicate**☐

Analysis Result:

Element	Expected %	Found (1)	Found (2)	Found (3)
Carbon	84.80	85.65	84.02	
Hydrogen	8.13	7.96	8.00	
Nitrogen	7.06	7.15	7.01	
Oxygen				

Authorising Signature:

Date completed	26-02-21
Signature	J-P C.
comments	

Figure **4.29**. Elemental analysis of **4tCzPz**

HPLC Trace Report16Oct2020

<Sample Information>

Sample Name	: dc4tczpz 20THF		
Sample ID	:		
Method Filename	: 80% Methanol 20% THF 20 mins.lcm		
Batch Filename	: 4tczpz.lcb		
Vial #	: 1-13	Sample Type	: Unknown
Injection Volume	: 5 uL		
Date Acquired	: 16/10/2020 12:57:27	Acquired by	: System Administrator
Date Processed	: 16/10/2020 13:56:24	Processed by	: System Administrator

<Chromatogram>

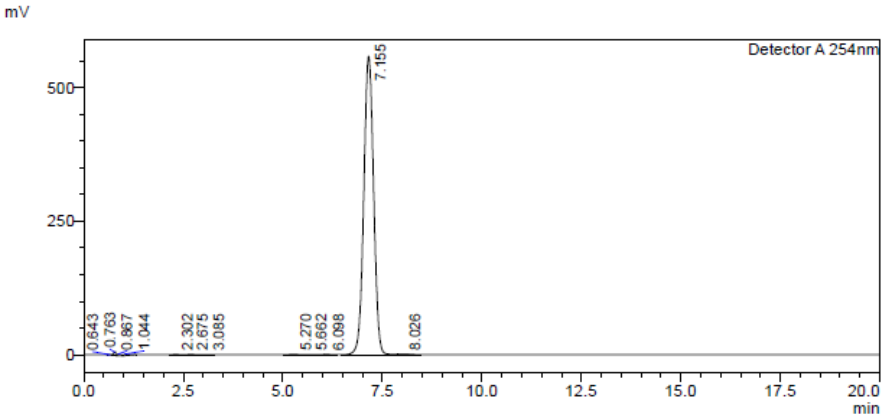

<Peak Table>

Detector A 254nm

Peak#	Ret. Time	Area	Height	Area%	Area/Height	Width at 5% Height
1	0.643	2858	490	0.029	5.831	–
2	0.763	25670	6389	0.264	4.018	–
3	0.867	16511	2934	0.170	5.627	–
4	1.044	22258	2542	0.229	8.756	0.298
5	2.302	5015	614	0.052	8.168	0.238
6	2.675	5955	610	0.061	9.762	0.284
7	3.085	2573	257	0.027	10.008	0.280
8	5.270	9070	701	0.093	12.943	0.405
9	5.662	1917	148	0.020	12.980	–
10	6.098	6179	440	0.064	14.039	–
11	7.155	9606364	558550	98.956	17.199	0.565
12	8.026	3368	250	0.035	13.472	0.371
Total		9707738	573925	100.000		

Figure **4.30**. HPLC report of **4tCzPz**

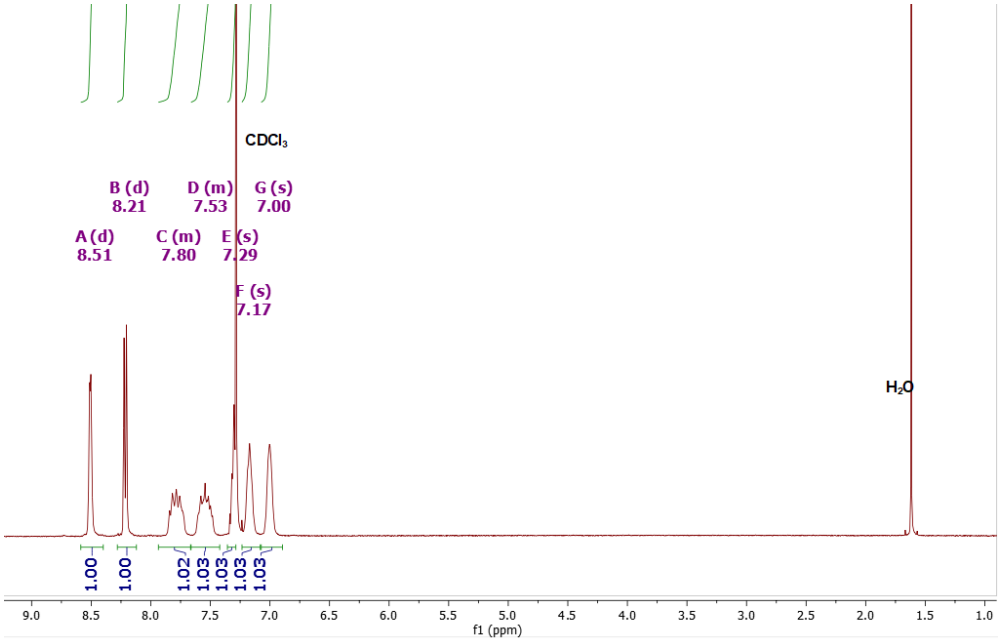

Figure **4.31**. ^{1}H NMR of **4CbPz** in $CDCl_3$

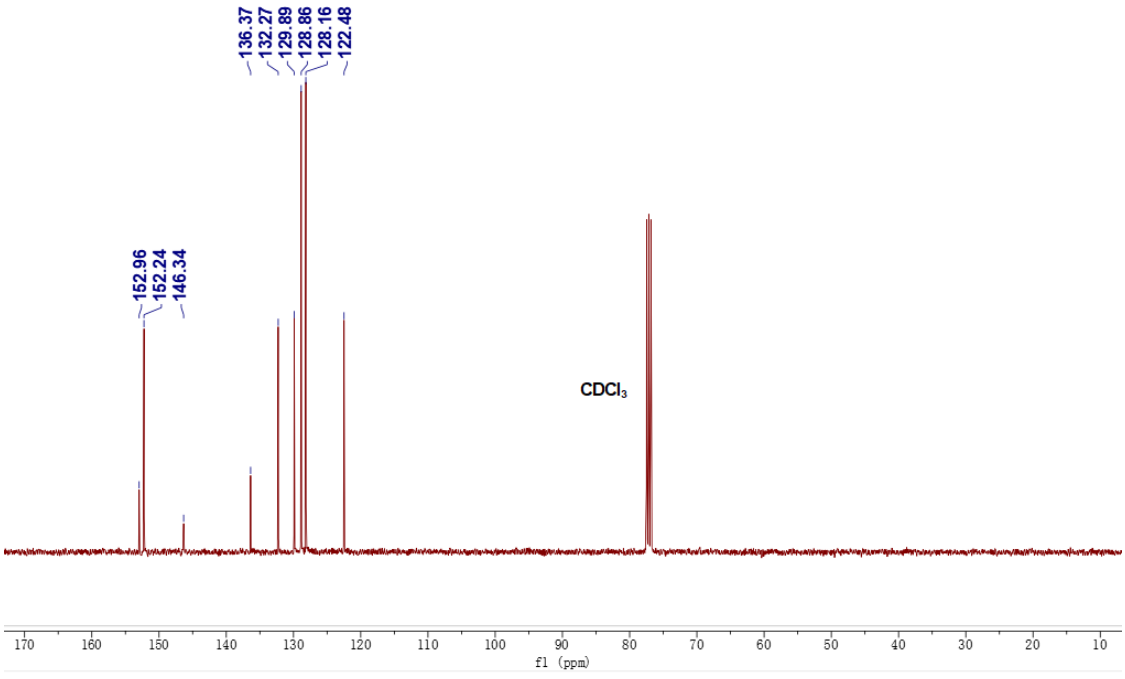

Figure **4.32**. ^{13}C NMR of **4CbPz** in $CDCl_3$

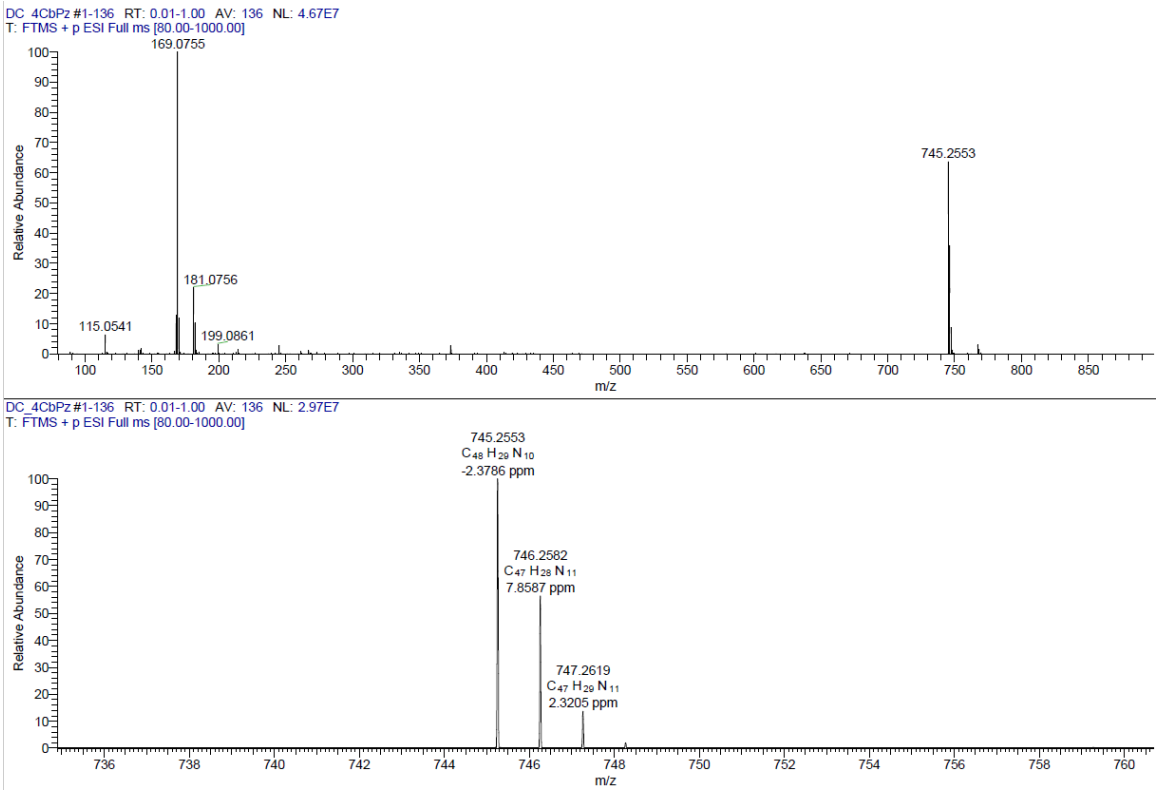

Figure **4.33**. HRMS of **4CbPz**

Elemental Analysis Service Request Form

Researcher name Dongyang Chen

Researcher email dc217@st-andrews.ac.uk

NOTE: Please submit ca. 10 mg of sample

Sample reference number	dc-II218
Name of Compound	4CbPz
Molecular formula	C48H28N10
Stability	stable
Hazards	low hazard
Other Remarks	

Analysis type:

Single ☐ **Duplicate**√☐ **Triplicate**☐

Analysis Result:

Element	Expected %	Found (1)	Found (2)	Found (3)
Carbon	77.40	77.43	77.56	
Hydrogen	3.79	3.58	3.66	
Nitrogen	18.81	18.27	18.20	
Oxygen				

Authorising Signature:

Date completed	26-02-21
Signature	J-PC
comments	

Figure **4.34**. Elemental analysis of **4CbPz**

HPLC Trace Report05Jan2021

<Sample Information>

Sample Name	: 4CbPz2		
Sample ID	:		
Method Filename	: 90% methanol 10 water 20 mins.lcm		
Batch Filename	: 4CbPz		
Vial #	: 1-11	Sample Type	: Unknown
Injection Volume	: 10 uL		
Date Acquired	: 12/12/2020 13:21:28	Acquired by	: System Administrator
Date Processed	: 12/12/2020 13:46:30	Processed by	: System Administrator

<Chromatogram>

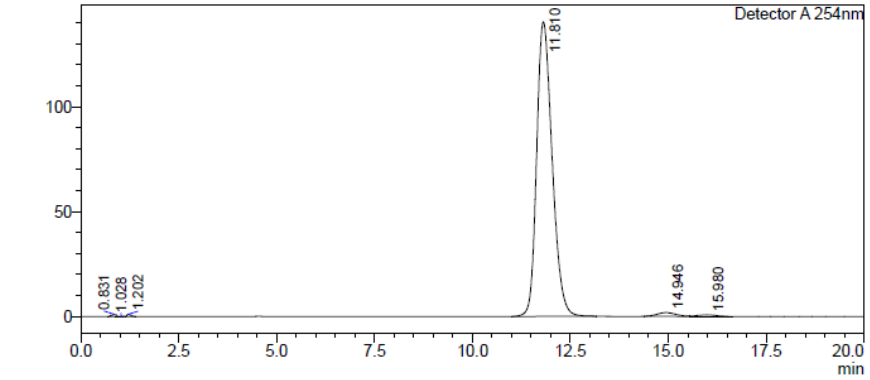

<Peak Table>

Detector A 254nm

Peak#	Ret. Time	Area	Height	Area%	Area/Height	Width at 5% Height
1	0.831	9378	1161	0.236	8.075	0.242
2	1.028	1695	286	0.043	5.920	--
3	1.202	7395	1122	0.186	6.592	--
4	11.810	3869579	140423	97.417	27.557	0.923
5	14.946	58749	1771	1.479	33.165	--
6	15.980	25385	743	0.639	34.171	--
Total		3972180	145507	100.000		

Figure **4.35**. HPLC report of **4CbPz**

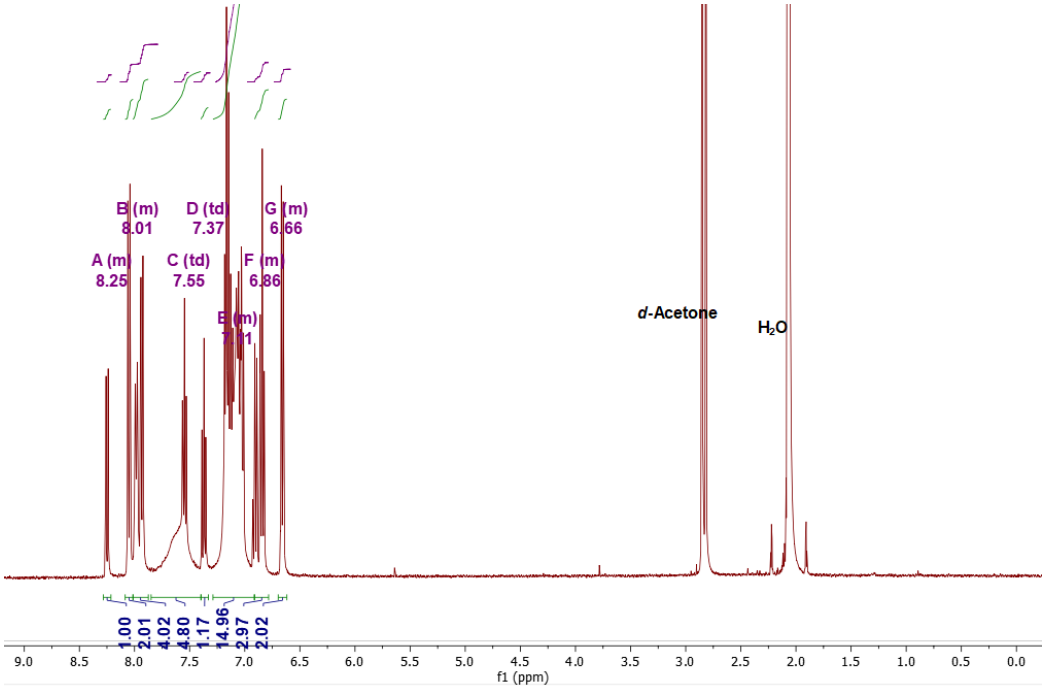

Figure **4.36**. [1]H NMR of **3CzBPz** in *d*-Acetone

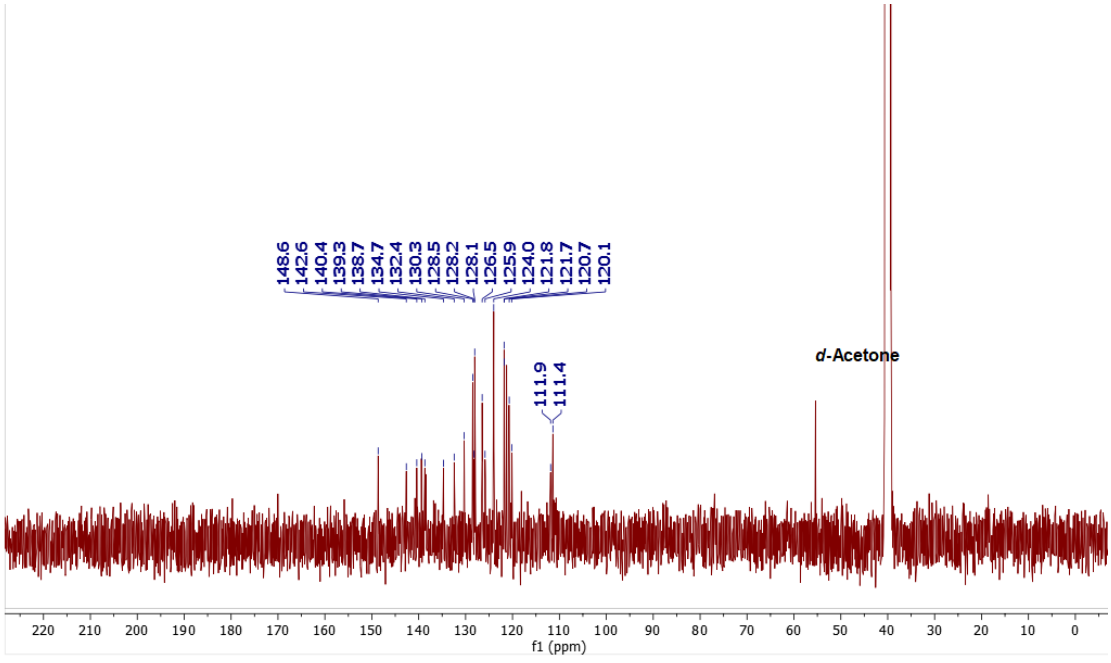

Figure **4.37**. [13]C NMR of **3CzBPz** in *d*-Acetone

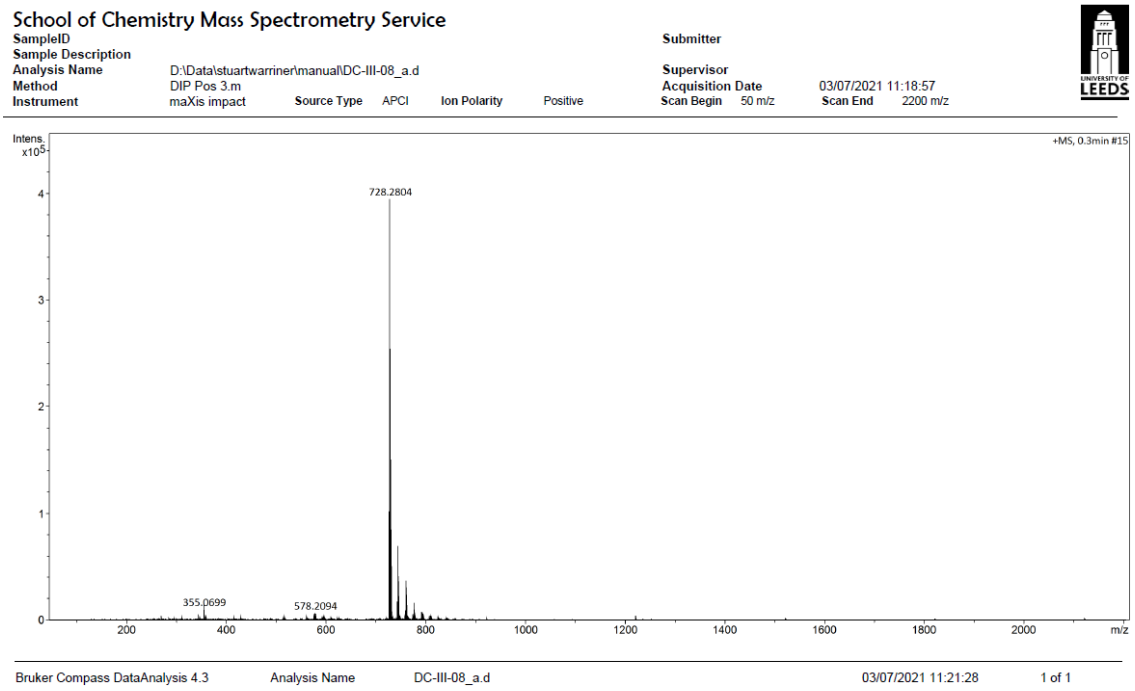

Figure **4.38**. HRMS of **3CzBPz**

Elemental Analysis Service Request Form

Researcher name Dongyang Chen

Researcher email dc217@st-andrews.ac.uk

NOTE: Please submit ca. 10 mg of sample

Sample reference number	dc-III07
Name of Compound	3CzBPz
Molecular formula	C52H33N5
Stability	stable
Hazards	low hazard
Other Remarks	

Analysis type:

Single ☐ **Duplicate**√☐ **Triplicate**☐

Analysis Result:

Element	Expected %	Found (1)	Found (2)	Found (3)
Carbon	85.81	85.53	85.60	
Hydrogen	4.57	4.66	4.66	
Nitrogen	9.62	9.46	9.47	
Oxygen				

Authorising Signature:

Date completed	21.05.21
Signature	J-PC
comments	

Figure **4.39**. Elemental analysis of **3CzBPz**

HPLC Trace Report17Apr2021

<Sample Information>

Sample Name	: 3CzBPz		
Sample ID	:		
Method Filename	: 98% Methanol 2 Water 20 mins.lcm		
Batch Filename	: 3CzBPz 2CzBPz 98 MeOH.lcb		
Vial #	: 1-37	Sample Type	: Unknown
Injection Volume	: 50 uL		
Date Acquired	: 12/04/2021 14:21:28	Acquired by	: System Administrator
Date Processed	: 12/04/2021 14:46:31	Processed by	: System Administrator

<Chromatogram>

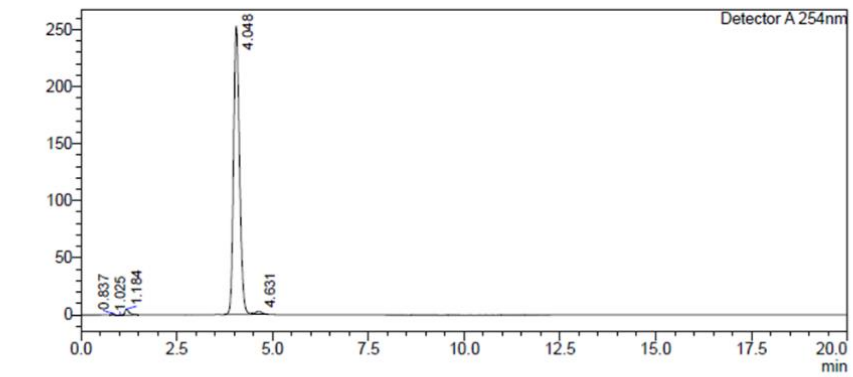

<Peak Table>

Detector A 254nm

Peak#	Ret. Time	Area	Height	Area%	Area/Height	Width at 5% Height
1	0.837	5330	1436	0.189	3.711	0.127
2	1.025	3572	443	0.127	8.072	--
3	1.184	38627	5250	1.372	7.358	--
4	4.048	2734332	252217	97.897	10.841	0.366
5	4.631	33933	2697	1.205	12.582	--
Total		2815793	262042	100.000		

Figure **4.40**. HPLC of **3CzBPz**

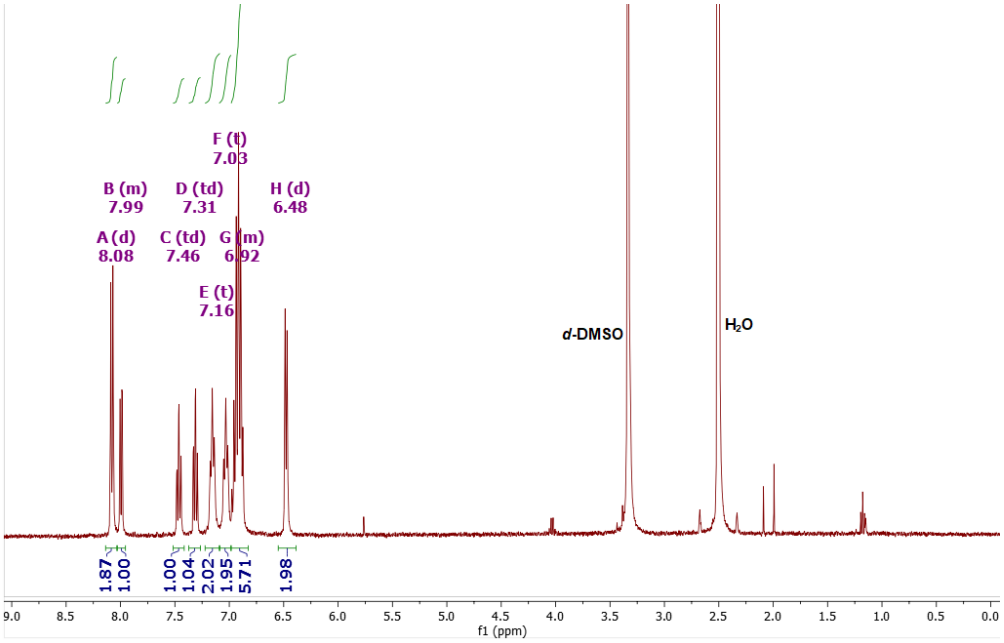

Figure **4.41**. [1]H NMR of **2CzBPz** in *d*-DMSO

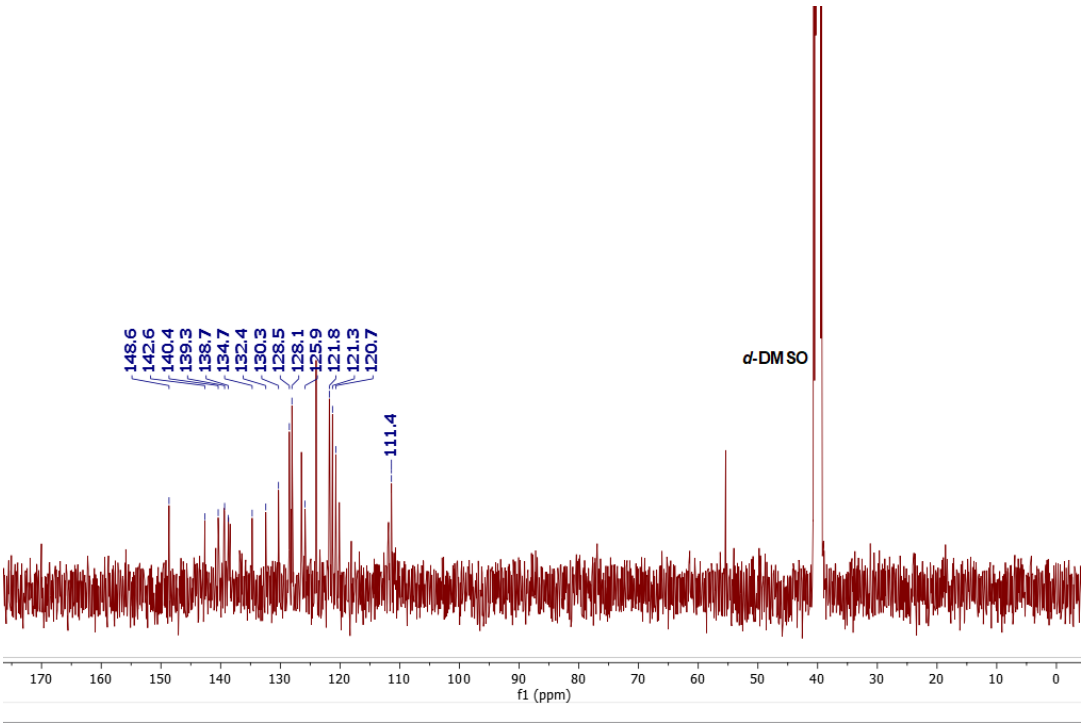

Figure **4.42**. [13]C NMR of **2CzBPz** in *d*-DMSO

Elemental Analysis Service Request Form

Researcher name Dongyang Chen

Researcher email dc217@st-andrews.ac.uk

NOTE: Please submit ca. 10 mg of sample

Sample reference number	dc-III12
Name of Compound	2CzBPz
Molecular formula	C52H34N4
Stability	stable
Hazards	low hazard
Other Remarks	

Analysis type:

Single ☐ **Duplicate**√☐ **Triplicate**☐

Analysis Result:

Element	Expected %	Found (1)	Found (2)	Found (3)
Carbon	87.37	87.54	89.44	
Hydrogen	4.79	4.89	4.97	
Nitrogen	7.84	7.78	7.93	
Oxygen				

Authorising Signature:

Date completed	21.05.21
Signature	J-Pc
comments	

Figure **4.43**. Elemental analysis of **2CzBPz**

HPLC Trace Report17Apr2021

<Sample Information>

Sample Name	: 3CzBPz		
Sample ID	:		
Method Filename	: 98% Methanol 2 Water 20 mins.lcm		
Batch Filename	: 3CzBPz 2CzBPz 98 MeOH.lcb		
Vial #	: 1-37	Sample Type	: Unknown
Injection Volume	: 50 uL		
Date Acquired	: 12/04/2021 14:21:28	Acquired by	: System Administrator
Date Processed	: 12/04/2021 14:46:31	Processed by	: System Administrator

<Chromatogram>

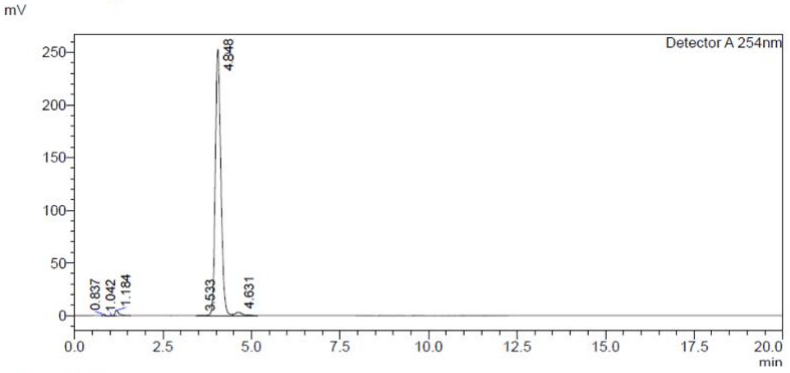

<Peak Table>

Detector A 254nm

Peak#	Ret. Time	Area	Height	Area%	Area/Height	Width at 5% Height
1	0.837	5342	1437	0.188	3.718	0.127
2	1.042	3488	485	0.123	7.191	--
3	1.184	40717	5299	1.432	7.684	--
4	3.533	2504	208	0.088	12.016	--
5	4.048	2744564	252439	98.523	10.872	0.367
6	4.631	46830	3059	1.647	15.311	--
Total		2843444	262927	100.000		

Figure **4.44**. HPLC report of **2CzBPz**

References

(1) Beinen, J. S.; Koben, J. G.; Hodgson, W. G. ESR and Phosphorescence Spectra of the Triplet States of Phenyl S-Triazines and Phenyl Benzenes. *J. Chem. Phys.* **1966**, *44* (8), 3095–3099.

(2) O'Reilly, J. E.; Elving, P. J. Electrochemical Reduction of Azabenzenes in Acetonitrile. Reactivity of the Diazine Radical Anion. *J. Am. Chem. Soc.* **1972**, *94* (23), 7941–7949. https://doi.org/10.1021/ja00778a001.

(3) Cui, L. S.; Nomura, H.; Geng, Y.; Kim, J. U. k.; Nakanotani, H.; Adachi, C. Controlling Singlet–Triplet Energy Splitting for Deep-Blue Thermally Activated Delayed Fluorescence Emitters. *Angew. Chemie - Int. Ed.* **2017**, *56* (6), 1571–1575.

(4) Wada, Y.; Kubo, S.; Kaji, H. Adamantyl Substitution Strategy for Realizing Solution-Processable Thermally Stable Deep-Blue Thermally Activated Delayed Fluorescence Materials. *Adv. Mater.* **2018**, *30* (8), 1–8.

(5) Woo, S. J.; Kim, Y.; Kwon, S. K.; Kim, Y. H.; Kim, J. J. Phenazasiline/Spiroacridine Donor Combined with Methyl-Substituted Linkers for Efficient Deep Blue Thermally Activated Delayed Fluorescence Emitters. *ACS Appl. Mater. Interfaces* **2019**, *11* (7), 7199–7207.

(6) Tsai, W.-L.; Huang, M.-H.; Lee, W.-K.; Hsu, Y.-J.; Pan, K.-C.; Huang, Y.-H.; Ting, H.-C.; Sarma, M.; Ho, Y.-Y.; Hu, H.-C.; Chen, C.-C.; Lee, M.-T.; Wong, K.-T.; Wu, C.-C. A Versatile Thermally Activated Delayed Fluorescence Emitter for Both Highly Efficient Doped and Non-Doped Organic Light Emitting Devices. *Chem. Commun.* **2015**, *51* (71), 13662–13665.

(7) Ganesan, P.; Ranganathan, R.; Chi, Y.; Liu, X. K.; Lee, C. S.; Liu, S. H.; Lee, G. H.; Lin, T. C.; Chen, Y. T.; Chou, P. T. Functional Pyrimidine-Based Thermally Activated Delay Fluorescence Emitters: Photophysics, Mechanochromism, and Fabrication of Organic Light-Emitting Diodes. *Chem. - A Eur. J.* **2017**, *23* (12), 2858–2866.

(8) Zhang, Q.; Sun, S.; Chung, W. J.; Yoon, S. J.; Wang, Y.; Guo, R.; Ye, S.; Lee, J. Y.; Wang, L. Highly Efficient TADF OLEDs with Low Efficiency Roll-off Based on Novel Acridine-Carbazole Hybrid Donor-Substituted Pyrimidine Derivatives. *J. Mater. Chem. C* **2019**, *7* (39), 12248–12255.

(9) Dos Santos, P. L.; Chen, D.; Rajamalli, P.; Matulaitis, T.; Cordes, D. B.; Slawin, A. M. Z.; Jacquemin, D.; Zysman-Colman, E.; Samuel, I. D. W. Use of Pyrimidine and Pyrazine Bridges as a Design Strategy to Improve the Performance of Thermally Activated Delayed Fluorescence Organic Light Emitting Diodes. *ACS Appl. Mater. Interfaces* **2019**, *11* (48), 45171–45179.

(10) Wang, S.; Cheng, Z.; Song, X.; Yan, X.; Ye, K.; Liu, Y.; Yang, G.; Wang, Y. Highly Efficient Long-Wavelength Thermally Activated Delayed Fluorescence OLEDs Based on Dicyanopyrazino Phenanthrene Derivatives. *ACS Appl. Mater. Interfaces* **2017**, *9* (11), 9892–9901.

(11) Liu, J.; Zhou, K.; Wang, D.; Deng, C.; Duan, K.; Ai, Q.; Zhang, Q. Pyrazine-Based Blue Thermally Activated Delayed Fluorescence Materials: Combine Small Singlet-Triplet Splitting with Large Fluorescence Rate. *Front. Chem.* **2019**, *7*, 1–9.

(12) Cai, M.; Auffray, M.; Zhang, D.; Zhang, Y.; Nagata, R.; Lin, Z.; Tang, X.; Chan, C.;

Lee, Y.; Huang, T.; Song, X.; Tsuchiya, Y.; Adachi, C.; Duan, L. Enhancing Spin-Orbital Coupling in Deep-Blue / Blue TADF Emitters by Minimizing the Distance from the Heteroatoms in Donors to Acceptors. *Chem. Eng. J.* **2020**, 127591, doi.org/10.1016/j.cej.2020.127591.

(13) Pople, J. A.; Binkley, J. S.; Seeger, R. Theoretical Models Incorporating Electron Correlation. *Int. J. Quantum Chem.* **1976**, *10*, 1–19.

(14) Adamo, C. Toward Reliable Density Functional Methods without Adjustable Parameters : The PBE0 Model. *J. Chem. Phys.* **1999**, *110*, 6158–6170.

(15) Etherington, M. K.; Gibson, J.; Higginbotham, H. F.; Penfold, T. J.; Monkman, A. P. Revealing the Spin-Vibronic Coupling Mechanism of Thermally Activated Delayed Fluorescence. *Nat. Commun.* **2016**, *7*, 13680.

(16) Cui, L.; Gillett, A. J.; Zhang, S.; Ye, H.; Liu, Y.; Chen, X.; Lin, Z.; Evans, E. W.; Myers, W. K.; Ronson, T. K.; Nakanotani, H.; Reineke, S.; Bredas, J.; Adachi, C.; Friend, R. H. Fast Spin-Flip Enables Efficient and Stable Organic Electroluminescence from Charge-Transfer States. *Nat. Photon.* **2020**, *14*, 636–642.

(17) Gao, X.; Bai, S.; Fazzi, D.; Niehaus, T.; Barbatti, M.; Thiel, W. Evaluation of Spin-Orbit Couplings with Linear-Response Time-Dependent Density Functional Methods. *J. Chem. Theory Comput.* **2017**, *13* (2), 515–524. https://doi.org/10.1021/acs.jctc.6b00915.

(18) Connelly, N. G.; Geiger, W. E. Chemical Redox Agents for Organometallic Chemistry. *Chem. Rev.* **1996**, *96* (2), 877–910.

(19) Tsuchiya, Y.; Tsuji, K.; Inada, K.; Bencheikh, F.; Geng, Y.; Kwak, H. S.; Mustard, T. J. L.; Halls, M. D.; Nakanotani, H.; Adachi, C. Molecular Design Based on Donor-Weak Donor Scaffold for Blue Thermally-Activated Delayed Fluorescence Designed by Combinatorial DFT Calculations. *Front. Chem.* **2020**, *8* (May), 2–11. https://doi.org/10.3389/fchem.2020.00403.

(20) Cai, X.; Padmaperuma, A. B.; Sapochak, L. S.; Vecchi, P. A.; Burrows, P. E. Electron and Hole Transport in a Wide Bandgap Organic Phosphine Oxide for Blue Electrophosphorescence. *Appl. Phys. Lett.* **2008**, *92*, 083308.

(21) Li, C.; Wang, Y.; Sun, D.; Li, H.; Sun, X.; Ma, D.; Ren, Z.; Yan, S. Thermally Activated Delayed Fluorescence Pendant Copolymers with Electron- and Hole-Transporting Spacers. *ACS Appl. Mater. Interfaces* **2018**, *10* (6), 5731–5739. https://doi.org/10.1021/acsami.8b00136.

(22) Dos Santos, P. L.; Chen, D.; Rajamalli, P.; Matulaitis, T.; Cordes, D. B.; Slawin, A. M. Z.; Jacquemin, D.; Zysman-Colman, E.; Samuel, I. D. W. Use of Pyrimidine and Pyrazine Bridges as a Design Strategy to Improve the Performance of Thermally Activated Delayed Fluorescence Organic Light Emitting Diodes. *ACS Appl. Mater. Interfaces* **2019**, *11* (48), 45171–45179. https://doi.org/10.1021/acsami.9b16952.

(23) Fleischhauer, J.; Zahn, S.; Beckert, R.; Grummt, U. W.; Birckner, E.; Görls, H. A Way to Stable, Highly Emissive Fluorubine Dyes: Tuning the Electronic Properties of Azaderivatives of Pentacene by Introducing Substituted Pyrazines. *Chem. - A Eur. J.* **2012**, *18* (15), 4549–4557. https://doi.org/10.1002/chem.201103350.

(24) Salah, L.; Etherington, M. K.; Shuaib, A.; Danos, A.; Nazeer, A. A.; Ghazal, B.; Prlj, A.; Turley, A. T.; Mallick, A.; McGonigal, P. R.; Curchod, B. F. E.; Monkman, A. P.; Makhseed, S. Suppressing Dimer Formation by Increasing Conformational Freedom in Multi-Carbazole Thermally Activated Delayed Fluorescence Emitters. *J. Mater. Chem. C* **2021**, *9* (1), 189–198. https://doi.org/10.1039/d0tc04222f.

(25) Ishiyama, T.; Murata, M.; Miyaura, N. Palladium(0)-Catalyzed Cross-Coupling Reaction of Alkoxydiboron with Haloarenes: A Direct Procedure for Arylboronic Esters. *J. Org. Chem.* **1995**, *60*, 7508–7510. https://doi.org/10.1021/jo00128a024.

Chapter 5

Bipyridine-containing Host Materials for High Performance Yellow Thermally Activated Delayed Fluorescence-based Organic Light Emitting Diodes with Very Low Efficiency Roll-Off

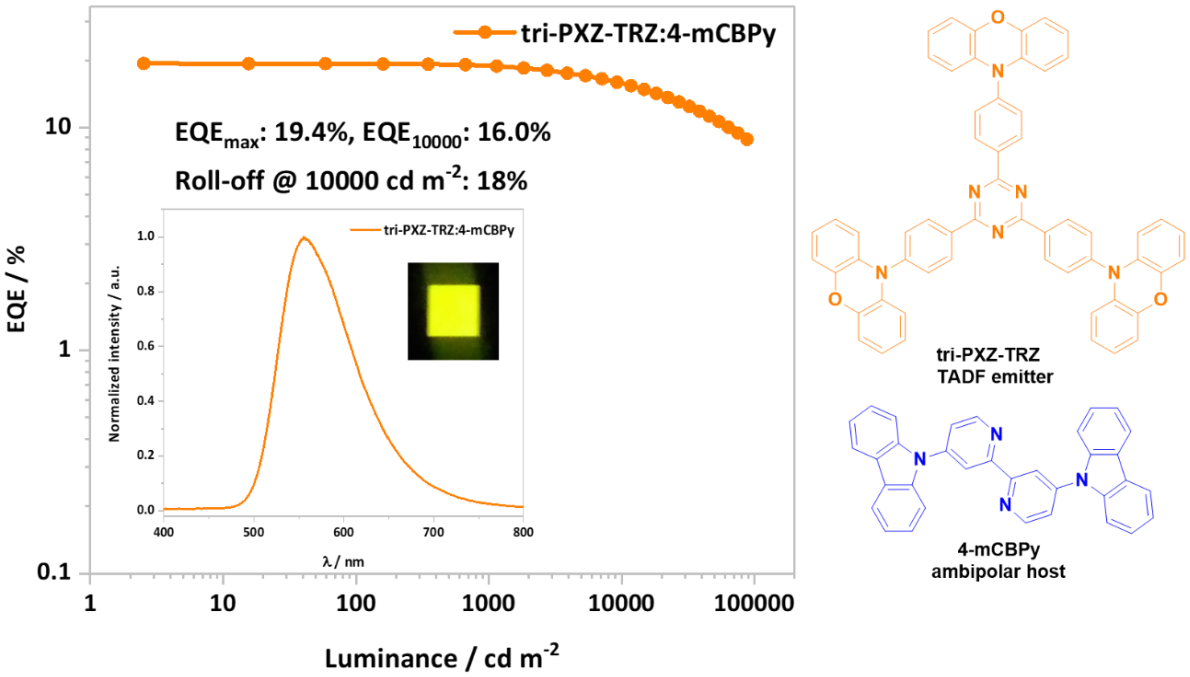

The Work presented in this Chapter has been published as:

Dongyang Chen,[a] Pachaiyappan Rajamalli,[a] Francisco Tenopala-Carmona,[b] Cameron L. Carpenter-Warren,[a] David B. Cordes,[a] Changmin Keum,[b] Alexandra M. Z. Slawin,[a] Malte Gather,[b] and Eli Zysman-Colman[a]* *Adv. Optical Mater.*, **2020**, *8*, 1901283. **DOI:** 10.1002/adom.201901283

Collaborators in this Chapter are from

[a] Organic Semiconductor Centre, EaStCHEM School of Chemistry, University of St Andrews, St Andrews, Fife, KY16 9ST, UK

[b] Organic Semiconductor Centre, SUPA School of Physics and Astronomy, University of St Andrews, St Andrews, Fife, KY16 9SS, UK

Dr. Pachaiyappan Rajamalli carried out the device fabrication and helped with the solid state Φ_{PL} measurements.

I completed all the syntheses and characterization, DFT and TD-DFT calculations, electrochemistry, thermal property measurements, photophysics measurements, and I am the principal author of the text.

5.1 Introduction

As shown in **Chapter 1**, TADF emitters usually have long emission lifetimes originating from the spin-forbidden up-conversion of triplet excitons into singlets. The long exciton lifetime can lead to a range of deactivation mechanisms in device including: triplet-triplet annihilation (TTA), and singlet-polaron annihilation (STA), which adversely affect OLED efficiency, stability, and efficiency roll-off.[1,2] To avoid concentration quenching the most common solution is to dope the emitter into an appropriate host. For TADF emitters that are themselves ambipolar, an ambipolar host can both tune the emission wavelength and improve the device performance by narrowing ΔE_{ST} and thereby boosting k_{RISC}.[3,4] However, currently most host materials used for TADF emitters are inherited from those used for phosphorescent OLEDs, which favor injection/diffusion of one type of charge carrier over the other, which can result in unbalanced charge injection into the emission layer.[5,6] The TADF OLEDs based on these traditional hosts usually exhibit higher turn-on voltages and quite severe efficiency roll-off.[7,8] To address these issues, several ambipolar host materials have been designed and employed in TADF based OLEDs.[4,9–12]

Efficient ambipolar hosts have been recently reported to improve the device performance for TADF-OLEDs.[9–12] The first sky-blue TADF OLEDs, reported in 2012, used PPT as host and **2CzPN** as emitter. The EQE_{max} for this OLEDs was only 8% at a current density of 5×10^{-4} mA cm^{-2}, with λ_{EL} of 470 nm.[13] Zhang *et al.* designed an ambipolar host, ***m*-CzCN**, possessing a cyano-substituted phenyl as the *n*-type unit and an *N*-phenyl-substituted carbazole as the *p*-type unit.[9] This host shows deep blue emission in the neat thin film with λ_{PL} at 403 nm and high energy

singlet (S_1) (3.48 eV) and triplet (T_1) (2.81 eV) states that match well the absorption of **2CzPN**, which permits efficient Förster resonance energy transfer (FRET) to confine the exciton on the emitter.[9] The host also exhibited preferable hole and electron mobilities (1.35×10^{-6} cm^2 V^{-1} s^{-1} and 2.40×10^{-7} cm^2 V^{-1} s^{-1}, respectively).[9] As a result, the OLEDs based on **2CzPN/*m*-CzCN** exhibited a much higher EQE_{max} = 15% (at a luminance of 100 cd m^{-2}) with CIE (0.17, 0.26).[9] This efficiency record was soon surpassed as Choi *et al.* who reported another ambipolar host **ZDN** for **2CzPN** that contains a carbazole p-type unit and a pyridoindole *n*-type unit, both attached to a dibenzothiophene.[10] The polar host stabilizes the S_1 state of **2CzPN** resulting in an increased k_{RISC}. The device based on **2CzPN/ZDN** exhibited an outstanding EQE_{max} of 25.7% (at a luminance of 45 cd m^{-2}).[10] However, the electroluminescence was red-shifted from (0.16, 0.30) in **mCP** to (0.19, 0.39) in **ZDN** and showed strong efficiency roll-off, with EQE_{1000} drops to 6%.[10] To address the issue of efficiency roll-off, Cheng *et al*. designed an ambipolar TADF host **BT-01**, which contains carbazole as the *n*-type unit and diphenylsulfone as the p-type unit.[4] The host has a ΔE_{ST} of 0.35 eV that is sufficiently small to allow the triplet excitons to upconvert to singlet excitons via RISC.[4] These singlet excitons are then transferred to the TADF emitter via FRET process. The high polarity of this host contributes to an increased TADF quantum efficiency (Φ_{TADF} = 53%) and faster k_{RISC} of 1.6×10^4 s^{-1} for **2CzPN**, both of which are higher than those in mCP host (Φ_{TADF} = 38%, k_{RISC} = 6.7×10^3 s^{-1}).[4] As a result of these attributes, the OLED based on **2CzPN/BT-01** shows an excellent EQE_{max} of 25.2% (at a luminance of 8 cd cm^{-2}) with CIE of (0.16, 0.31), and further shows improved efficiency roll-off with EQE_{1000} = 10%.[4] These metrics place this device amongst the best for **2CzPN**-based OLEDs and demonstrate that with a suitable

host, the efficiency of TADF-based OLEDs can be boosted significantly while maintaining very low efficiency roll-off. Despite the potential of suitably designed hosts, there is a dearth of reports for appropriate hosts for yellow to red TADF emitters.[11,12]

An ideal host material for yellow-to-red TADF emitters should have: (1) sufficiently high singlet and triplet state energies to avoid guest-to-host back energy transfer and guarantee that the excitons are confined in emitter; (2) appropriate HOMO and LUMO levels to avoid charge trapping on the host and to facilitate charge transport through the device; (3) broad spectral overlap with the emitters for efficient Förster resonance energy transfer; and (4) ambipolar character to facilitate charge transport and carrier injection.[14,15] To satisfy these requirements, the choice of electron and hole transporting moieties within the host structure should be carefully considered. In **Chapter 3**, we showed how the inclusion of pyridine rings has the ability to tune the electron acceptor strength. Further, pyridine and bipyridine moieties have been previously used within electron-transporting materials,[16,17] and there are a few reports of their use as ambipolar hosts due to their electron-transporting ability, while carbazole is commonly employed as a hole-transporting unit in the design of high-energy hosts like commercially available hosts CzSi and mCP.[18–20] The combination of bipyridine with carbazole should produce an ambipolar host with desirable charge transporting properties.

In this Chapter, we present bipyridine analogs of the two commonly used commercial hosts **mCBP** and **CBP**. The two new hosts are 4,4'-di(9H-carbazol-9-yl)-2,2'-bipyridine (**4-mCBPy**) and 6,6'-di(9H-carbazol-9-yl)-3,3'-bipyridine (**3-CBPy**), both of which were readily synthesized in one or two steps. Both materials possess high S_1 energies around 3.3 eV and T_1

energies around 2.7 eV and have deep HOMO (-5.75/-5.80 eV for **3-CBPy**/**4-mCBPy**) and shallow LUMO levels (-2.59/-2.70 eV for **3-CBPy**/**4-mCBPy**). All four materials were assessed as hosts in yellow TADF OLEDs using the previously reported **tri-PXZ-TRZ** as the emitter.[21] In the original report on **tri-PXZ-TRZ** in 2013, **mCBP** was used as host material and the device exhibited an EQE_{max} of 13.4%.[21] In the present work the devices employing **4-mCBPy** and **3-CBPy** as hosts showed much improved external quantum efficiencies, very low efficiency roll-off and turn-on voltages compared to analogous devices using **mCBP** and **CBP** as host materials.

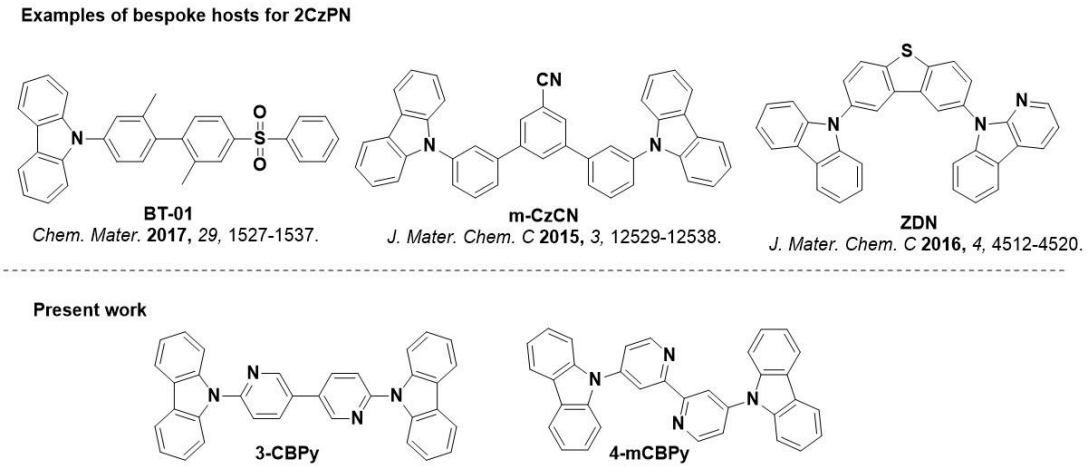

Figure **5.1**. The structures of bespoke hosts examples and hosts presented in this Chapter.

5.2 Synthesis

The two bipyridine-based hosts were easily obtained in high yields (Scheme **5.1**). For **3-CBPy**, 5-bromo-2-iodopyridine was first reacted with carbazole in a copper-promoted Ullman reaction to afford 9-(5-bromopyridin-2-yl)-9H-carbazole in excellent yield.[22] This intermediate was homocoupled, catalyzed by an *in situ*-formed nickel(0) species to obtain **3-CBPy** in 72%

over the two steps. The host **4-mCBPy** was prepared by copper-promoted Ullman reaction between 4,4'-dibromo-2,2'-bipyridine and excess carbazole.[22] Both syntheses of **3-CBPy** and **4-mCBPy** have been conducted on gram scale without loss of yield. The identity and purity of both compounds were ascertained using a combination of ^{1}HNMR and ^{13}CNMR spectroscopy, HRMS, HPLC, and elemental analysis. The detailed synthesis and compounds characterization are presented in **5.9 Experimental section**.

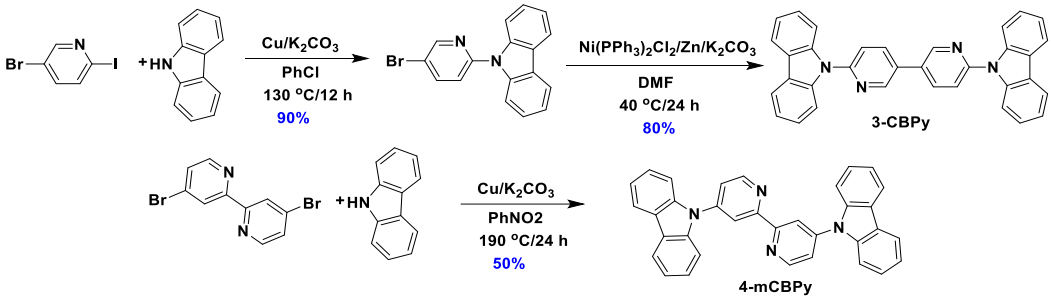

Scheme **5.1**. Synthesis of **3-CBPy** and **4-mCBPy**

Crystals of **3-CBPy** suitable for single crystal X-ray diffraction were obtained from a mixed solution of toluene and hexane while crystals of **4-mCBPy** were obtained by thermal sublimation. The bipyridine moiety in both **3-CBPy** and **4-mCBPy** exhibited a planar *trans* conformation (torsion angles of 1.44(11)° and 0°, respectively) while the torsion angles between the bipyridine and carbazoles were 36.54(12)° and 39.84(11)° (**3-CBPy**), and 39.55(11)°, respectively. The angles between pyridyl rings and those adjacent are maintained by CH···N hydrogen bonds with H···N distances of 2.58 – 2.65 Å and 2.46 Å for **3-CBPy** and **4-CBPy**,

respectively [C···N separations for **3-CBPy** of 3.0312(16) – 3.0998(17) Å and for **4-CBPy** of 2.7876(15) Å]. Only **3-CBPy** shows significant intermolecular interactions, with both π···π interactions between adjacent carbazoles at a centroid···centroid distance of 3.4949(8) Å, and CH···π interactions between pyridyl hydrogens and both carbazole and pyridyl π-systems at H···centroid separations of 2.63-2.93 Å and corresponding C···centroid separations of 3.1417(12)–3.6066(12) Å. These distances are close to the conventional van der Waals limit, but CH···π interactions have been suggested to be effective at distances beyond this limit. [23,24] No equivalent interactions are seen in **4-mCBPy**, the shortest centroid···centroid distance being 3.9506(10) Å and shortest CH···centroid separation being 3.53 Å. The interactions in **3-CBPy** give rise to sheets lying in the crystallographic *bc*-plane.

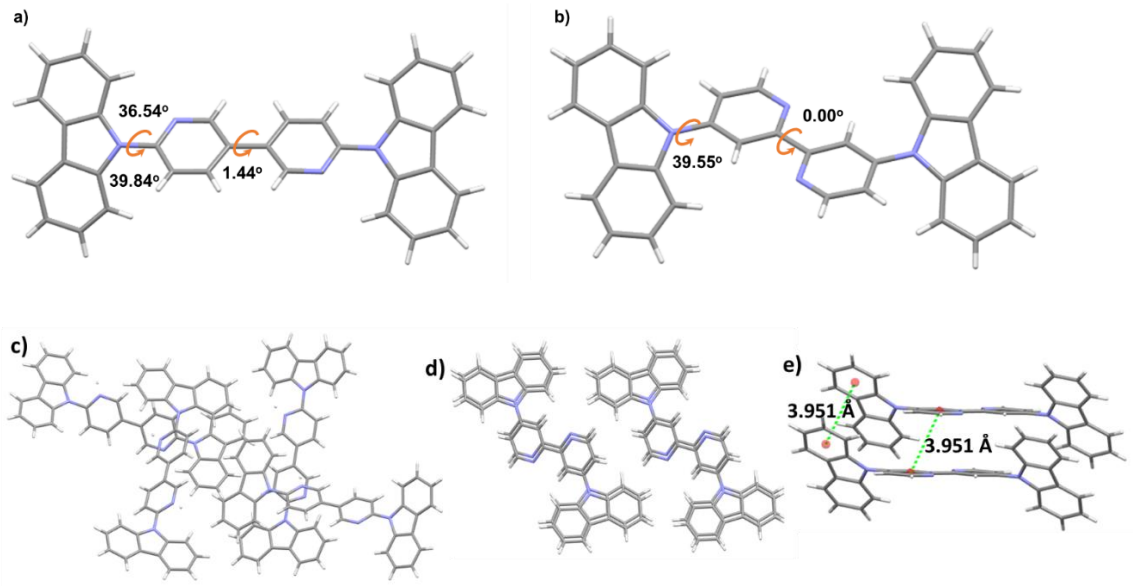

Figure **5.2**. Single crystal structure of (a) **3-CBPy** and (b) **4-mCBPy** (c) packing mode of **3-CBPy**, (d) packing mode of **4-mCBPy**, and (e) packing distance of **4-mCBPy**. Minor components of disorder are omitted for clarity.

5.3 Thermal property

The two hosts exhibited high melting (T_m) and thermal degradation temperatures (T_d) (defined as temperature at 5% weight loss) as assessed by TGA and DTA analysis, showing in Figure **5.3**. The T_m for **3-CBPy** and **4-mCBPy** were 310 °C and 320 °C, which are higher than the reported T_m of **CBP** (283 °C) and **mCBP** (271 °C).[25] The two hosts also exhibited superior thermal stability with no weight loss observed up to 350°C and a T_d for **3-CBPy** and **4-mCBPy** of 388 °C and 382 °C, respectively. The T_d values of the two new hosts are thus higher than both **CBP** (365 °C) and **mCBP** (315 °C).[25] The superior thermal stabilities of **3-CBPy** and **4-mCBPy** would (1) guarantee that these materials can be thermally sublimed and (2) support device stability at high driving voltage and high brightness.

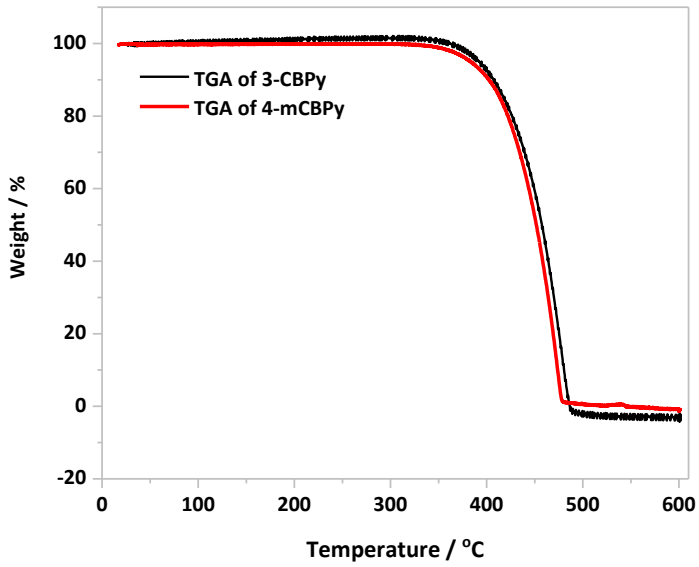

Figure **5.3**. Thermal gravimetric analysis plot of **3-CBPy** and **4-mCBPy**

5.4 Theoretical Calculations

DFT and time-dependent DFT calculations of **3-CBPy** and **4-mCBPy** using PBE0/6-31G(d, p) in the gas phase were undertaken to evaluate *in silico* their HOMO/LUMO and singlet/triplet state energies.[26,27] The results are summarized in Figure **5.4**. The modelling indicates that **4-mCBPy** possesses a slightly larger HOMO-LUMO gap than **3-CBPy** but that the frontier orbitals in the former are much more spatially separated, leading to a reduced exchange integral and a significantly smaller singlet-triplet energy gap compared to **mCBP** and **CBP**. In both hosts, the HOMO is mainly distributed on the carbazole moieties while the LUMO is localized on the bipyridine core. The HOMO of **3-CBPy**, however, is distributed across the entire molecule due to its more planar conformation in the gas phase. The increased conjugation present in **3-CBPy** leads to an increased HOMO energy of -5.66 eV compared to that in **4-mCBPy** at -5.83 eV. The trend in LUMO energies of **3-CBPy** and **4-mCBPy** are similar with values of -1.41 eV and -1.56 eV, respectively. TDDFT calculations reveal that the S_1 energies are essentially identical at ca. 3.60 eV for the two hosts, but that the T_1 energy of **3-CBPy** is more stabilized at 3.06 eV compared to that of **4-mCBPy** (3.28 eV). The HOMO and LUMO levels of **3-CBPy** are slightly stabilized with respect to **CBP**, owing to the presence of the electron-withdrawing bipyridine core in the former. Both the S_1 and T_1 energies of **3-CBPy** are stabilized compared to **CBP** while ΔE_{ST} is only slightly reduced. The comparison, however, is starker when comparing **4-mCBPy** to **mCBP**. The HOMO of **4-mCBPy** is stabilized by 0.17 eV while the LUMO is stabilized by 0.47 eV compared to **mCBP**, which leads to a markedly reduced HOMO-LUMO

gap of 4.27 eV for **4-mCBPy** compared to 4.57 eV for **mCBP**. The S_1 and T_1 states are likewise significantly stabilized in **4-mCBPy** compared to **mCBP**.

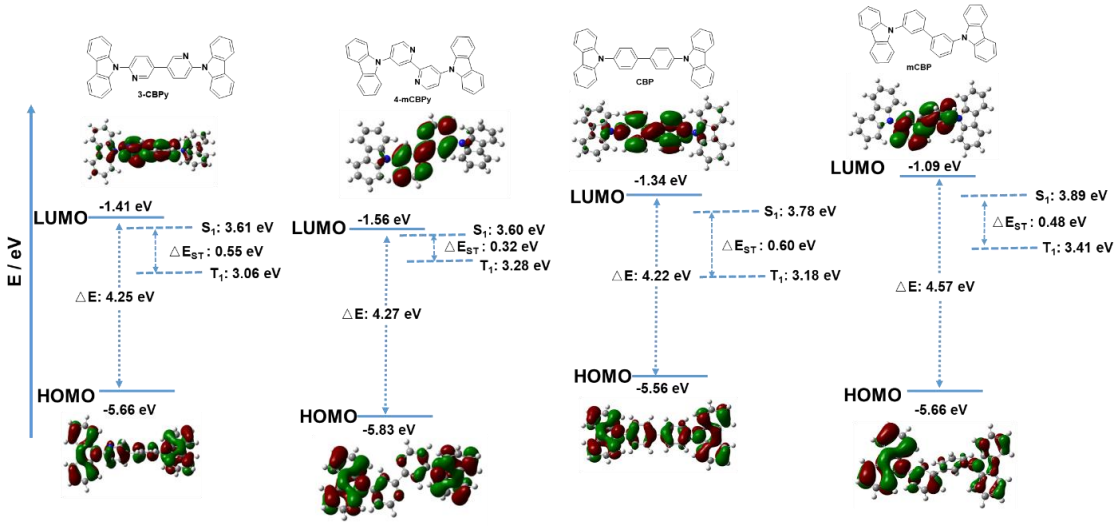

Figure **5.4**. Theoretical modelling of the energies of the HOMO/LUMO orbitals and the S_1 and T_1 states of **3-CBPy** and **4-mCBPy** and the electron density distribution of the frontier molecular orbitals.

5.5 Electrochemistry

The electrochemical properties of the two new hosts were analyzed by CV and differential DPV measurements using 0.1 M tetra(*n*-butyl)ammonium hexafluorophosphate (*n*-Bu_4NPF_6) as the supporting electrolyte in degassed DMF. Voltammograms are referenced versus Fc/Fc^+ and the data reported versus a saturated calomel electrode (SCE). As shown in Figure **5.5**, **3-CBPy** and **4-mCPy** have distinct irreversible oxidation and reduction waves, which are assigned to the oxidation of carbazole and reduction of the bipyridine moieties, respectively,

based on the DFT analysis. **3-CBPy** exhibited a slightly more negative reduction potential (E_{pc}^{red} = -1.66 V) than **4-mCBPy** (E_{pc}^{red} = -1.51 V), which indicates that 3,3'-bipyridyl possesses slightly weaker electron-withdrawing character than 4,4'-bipyridyl, conclusions in line with the DFT calculations. **4-mCBPy** shows a more stabilized oxidation (E_{pa}^{ox} = 1.55 V) than **3-CBPy** (E_{pa}^{ox} = 1.50 V), which is a function of the increased conjugation in the latter. The DPV scans show that both oxidation and reduction processes are mono-electronic in nature. The corresponding HOMO levels of **3-CBPy** and **4-mCBPy** were calculated to be -5.75 eV and -5.80 eV while the LUMO levels of **3-CBPy** and **4-mCBPy** were calculated to be -2.59 eV and -2.70 eV, respectively. The corresponding HOMO-LUMO gaps for **3-CBPy** and **4-mCBPy** are 3.16 eV and 3.10 eV, respectively. The HOMO/LUMO values of **3-CBPy** and **4-mCBPy** are comparable to the HOMO/LUMO values of **CBP** (-2.60 eV/-5.91 eV) and **mCBP** (-2.44 eV/-5.95 eV), and the trend in HOMO/LUMO values also broadly matched the DFT calculation.[27]

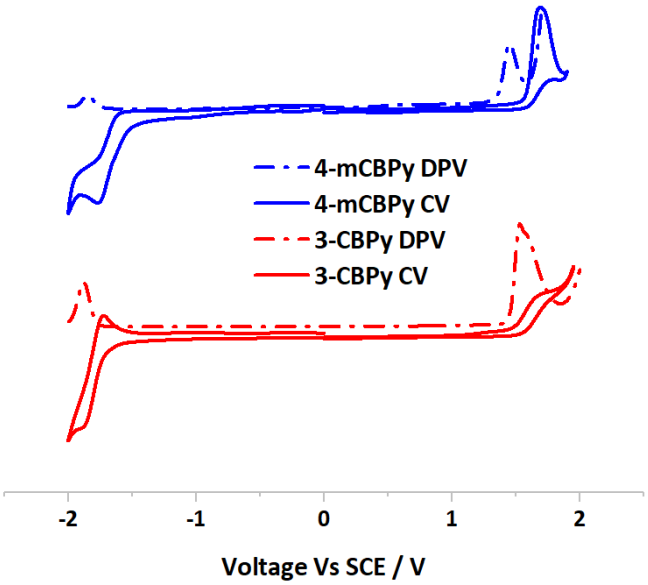

Figure **5.5**. Cyclic Voltammograms (CV, solid lines) and Differential Pulse Voltammograms (DPV, dashed lines) for **3-CBPy** and **4-mCBPy** in degassed DMF solution containing *n*-NBu_4PF_6 as the supporting electrolyte and using Fc/Fc^+ as an internal standard (Fc/Fc^+ = 0.55 eV versus SCE).[28]

5.6 Photophysical properties

The absorption and emission spectra of the two hosts in PhMe are shown in Figure **5.6**. Both hosts exhibited strong absorption bands at around 290 nm, which are assigned to π-π* transitions, and absorption bands in the range 330-350 nm. These low energy bands are assigned based on TDDFT calculations as hybrid charge-transfer and π-π* transitions (Figure **5.6b** and **c**). The optical gap energies (E_{opt}), determined from the intersection point of the normalized absorption and emission spectra, are 3.35 eV for **3-CBPy**, and 3.49 eV for **4-mCBPy**, respectively. The photoluminescence spectrum of **3-CBPy** shows a narrow and sharp profile with a maximum

of 384 nm while that of **4-mCBPy** is slightly red-shifted at 392 nm and broader. The unstructured character of both spectra is an indication of emission from a charge-transfer state. The emission spectra of both hosts were found to perfectly overlap with the absorption spectrum of the yellow TADF emitter **tri-PXZ-TRZ**, indicating that efficient FRET is feasible.

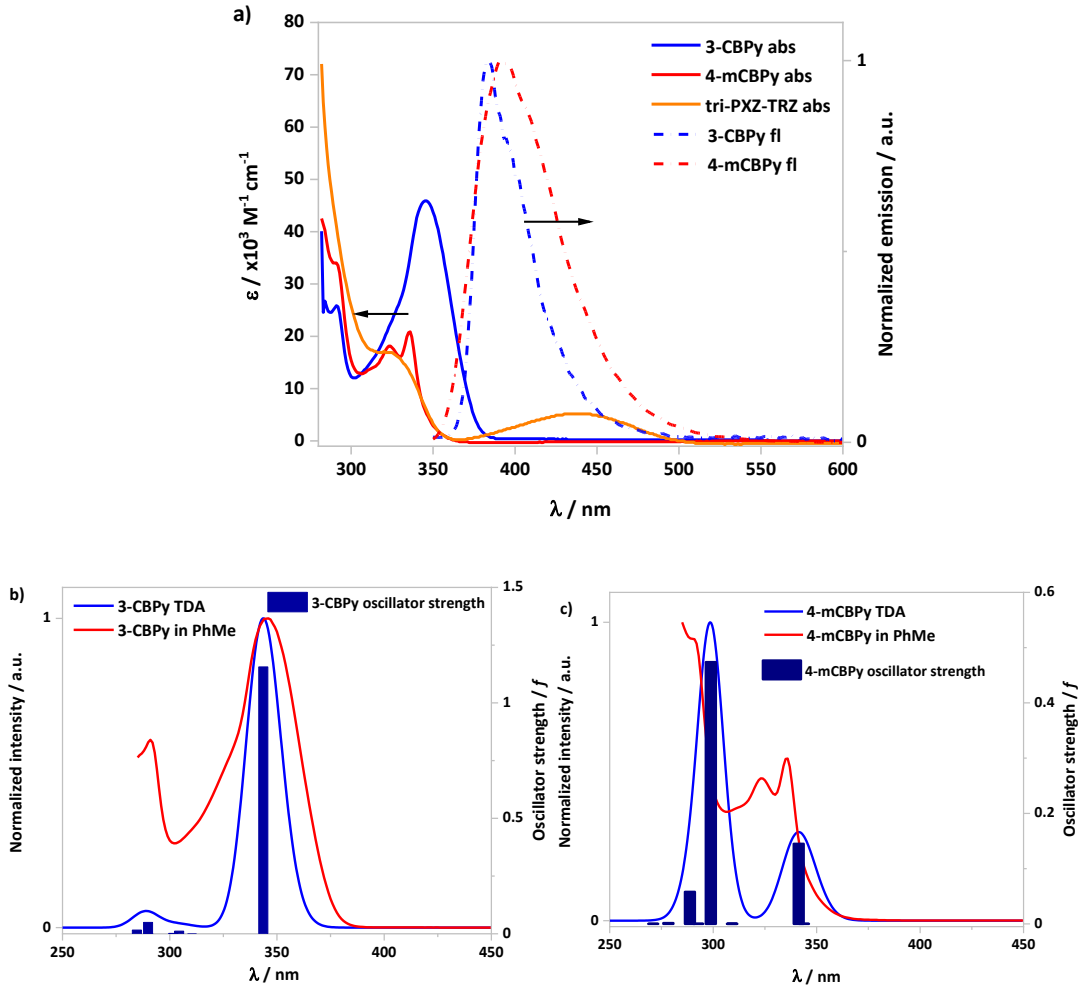

Figure **5.6**. (a) UV-vis absorption spectra of **3-CBPy**, **4-mCBPy** and **tri-PXZ-TRZ** and normalized photoluminescence spectra of **3-CBPy** and **4-mCBPy** in toluene (λ_{exc} = 340 nm), and TDA simulation and experimental UV-Vis spectra of (b) **3-CBPy** and (c) **4-mCBPy**.

The Φ_{PL} of **3-CBPy** and **4-mCBPy** were measured to be 23% and 17%, respectively, in degassed toluene solution and the emission lifetimes, (τ_{PL}) were 1.9 ns and 3.9 ns, respectively (Figure **5.7**), indicating that both compounds are fluorescent in nature. The Φ_{PL} of spin-coated neat films of **3-CBPy** and **4-mCBPy** under a nitrogen atmosphere are 9% and 6%, respectively. The 77 K prompt fluorescence and phosphorescence spectra of neat films of the two hosts were measured to determine the S_1 and T_1 energies (Figure **5.8**). The S_1 energies of **3-CBPy** and **4-mCBPy** were measured to be 3.26 eV and 3.32 eV while the T_1 energies were measured to be 2.67 eV and 2.72 eV, respectively. The experimental S_1 and T_1 energies of **3-CBPy** and **4-mCBPy** are more stabilized than the DFT results (S_1 = 3.61; T_1 = 3.06 eV for **3-CBPy** and S_1 = 3.60; T_1 = 3.28 eV for **4-mCBPy**) calculated in the gas phase. **3-CBPy** exhibited slightly lower energy S_1 and T_1 states due to the extended conjugation. The ΔE_{ST} of **3-CBPy** and 4-**mCBPy** were calculated to be 0.59 eV and 0.60 eV. The S_1 energy of **3-CBPy** and **4-mCBPy** are slightly lower than the reported S_1 energies of **CBP** (3.45 eV) and **mCBP** (3.58 eV) as the donor-acceptor structure contributes to the stabilization of the S_1 state. The T_1 energy of **3-CBPy** and **4-mCBPy** are similar to the reported T_1 energies of **CBP** (2.65 eV) and **mCBP** (2.75 eV).[29] The high triplet energies of **3-CBPy** and **4-mCBPy** should help to contain the triplet excitons within the emission layer.

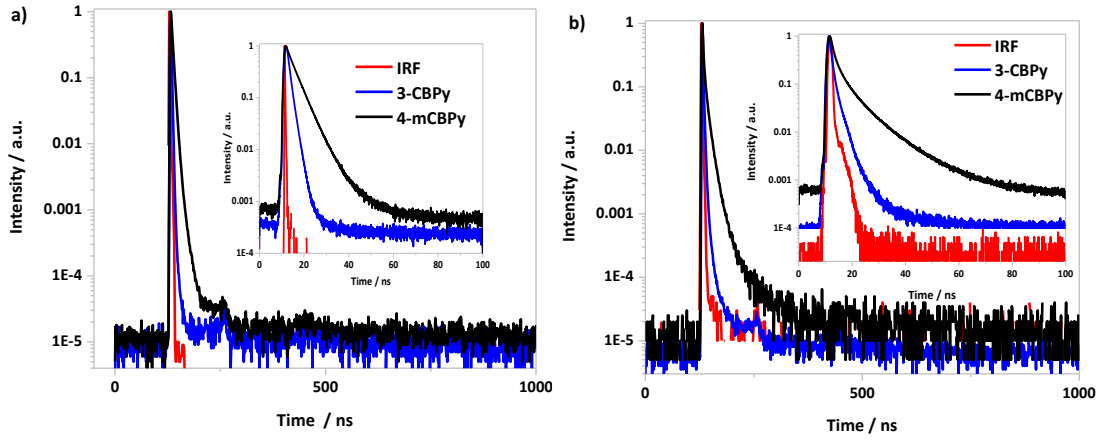

Figure **5.7**. Time-resolved PL spectra of **3-CBPy** and **4-mCBPy** (a) in toluene and (b) neat film (λ_{exc} = 379 nm).

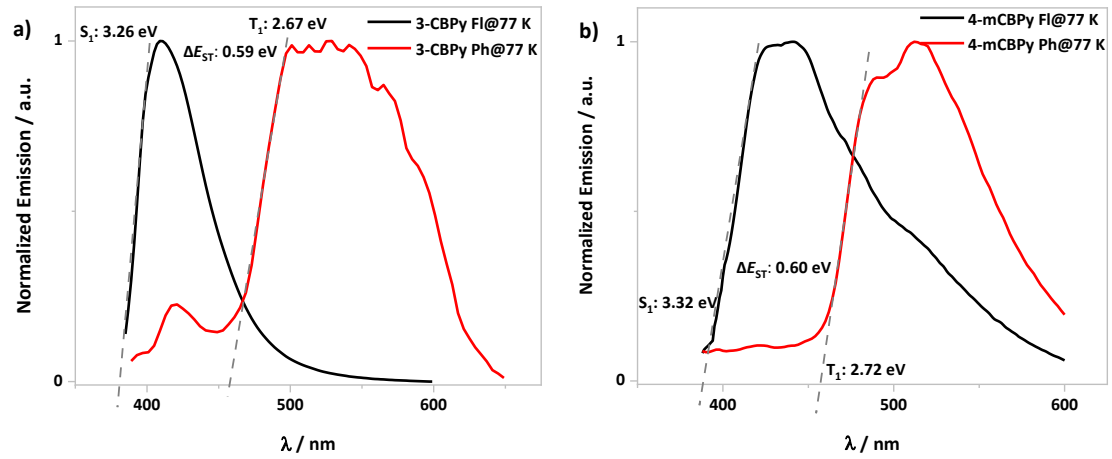

Figure **5.8**. Fluorescence and phosphorescence spectra (by 10 ns and 2 ms) of (a) **3-CBPy** and (b) **4-mCBPy** neat film, measured at 77 K (λ_{exc} = 379 nm).

Table **5.1**. Summary of key optoelectronic properties of **3-CBPy** and **4-mCBPy**

Host	λ_{abs} **(ε)[a] / nm (10^3 M^{-1} cm^{-1})**	E_{opt} **/ eV**	λ_{PL}[a] **/ nm**	$S_1/T_1/\Delta E_{ST}$ [b] **/ eV**	**HOMO/LUMO [c] / eV**	$\Delta E_{H\text{-}L}$[d] **/ eV**
3-CBPy	346 (46)/291 (26)	3.35	384	3.26/2.67/0.59	-5.75/-2.59	3.16
4-mCBPy	336 (21)/323 (17) 289 (34)	3.49	392	3.32/2.72/0.60	-5.80/-2.70	3.10

[a] Measured in PhMe. [b] S_1 energy determined from the onset of the prompt fluorescence spectra at 77 K and the T_1 determined from the onset of the phosphorescence spectra at 77 K (after 2 ms). [c] E_{HOMO} = -(E_{ox}^{onset} vs Fc/Fc^+ + 4.8) eV, E_{LUMO} = -(E_{red}^{onset} vs Fc/Fc^+ + 4.8) eV.[37] [d] $E_{H\text{-}L}$ = |E_{LUMO}-E_{HOMO}|.

To evaluate the energy transfer efficiency between each of the two hosts and the emitter, we measured the Φ_{PL} and time-resolved PL spectra of ca. 50 nm thick thermally evaporated films of 7 wt% **tri-PXZ-TRZ** doped in **3-CBPy** and **4-mCBPy**. For comparison, 7 wt% **tri-PXZ-TRZ** doped film in **CBP** and **mCBP** were also prepared as these hosts had been employed in the previously reported OLEDs. The Φ_{PL} of the **tri-PXZ-TRZ** in **4-mCBPy** film is 50% while in **3-CBPy** it was slightly lower at 45%. The corresponding Φ_{PL} values in **mCBP** and **CBP** are 47% and 40%, respectively. As shown in Figure **5.9a**, the emission of films of **tri-PXZ-TRZ** in both **3-CBPy** and **4-mCBPy** showed a single peak originating from the emitter, whereas the emission spectra of the **CBP** and **mCBP** films revealed emission from both the host (400 nm) and the emitter (420 nm). These results imply a much less efficient FRET process in **CBP** and **mCBP** compared to the bipyridine-based host films. As shown in Figure **5.9b**, the time-resolved PL decay

traces of the films measured under vacuum exhibited both a nanosecond τ_p and a microsecond τ_d at room temperature. The PL decays exhibited similar prompt lifetimes in all four hosts, which are ca. 25 ns. The τ_d is slightly shorter in **3-CBPy** (3.7 μs) and **4-mCBPy** (4.0 μs) than in **CBP** (3.9 μs) and **mCBP** (5.0 μs). The prompt component of the photoluminescence quantum yield (Φ_F) and delayed component of the photoluminescence quantum yield (Φ_d) efficiencies of **tri-PXZ-TRZ** in each of the hosts were calculated from the PL decays by integrating the transient PL signals from 0 to 0.5 μs as originating from the prompt fluorescence and integrating signals from 0.5 μs to 45 μs as delayed fluorescence. The kinetics parameters of **tri-PXZ-TRZ** in different hosts are summarized in Table **5.2**. The four films all exhibited a high k_{RISC} (~2 × 10^5 s^{-1}), and the **3-CBPy** and **4-mCBPy**-based films exhibited faster k_p, k_d and k_r^S than **CBP**- and **mCBP**-based films. These results imply that in **3-CBPy** and **4-mCBPy** the excitons on **tri-PXZ-TRZ** can radiatively decay more quickly thereby avoiding triplet exciton accumulation which can negatively impact both device stability and efficiency roll-off.

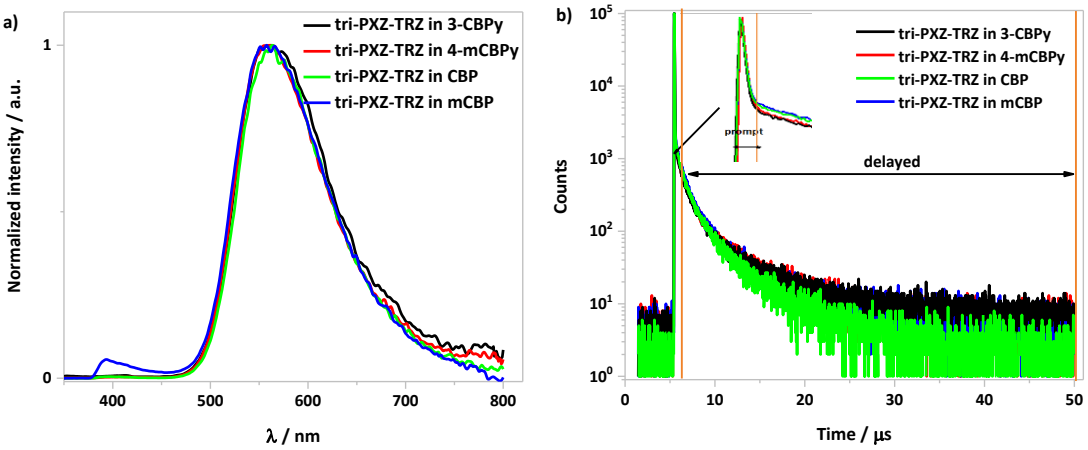

Figure **5.9**. (a) Photoluminescence spectra of 7 wt% doped **tri-PXZ-TRZ** in different hosts and (b) transit PL decay curves of 7 wt% doped **tri-PXZ-TRZ** in different hosts (λ_{exc} = 379 nm).

Table 5.2: Exciton lifetime and the kinetic constants of **tri-PXZ-TRZ** in different host materials

Host	τ_p [a] /ns	τ_d [b] /μs	Φ_{PL} [c] /%	Φ_p [d] /%	Φ_d [e] /%	k_p [f] / 10^{-7} s^{-1}	k_d [g] / 10^{-5} s^{-1}	k_r^{sh} / 10^{-7} s^{-1}	k_{ISC} [i] / 10^{-7} s^{-1}	k_{RISC} [j] / 10^{-5} s^{-1}	k_{nr}^{T} [k] / 10^{-5} s^{-1}
3-CBPy	19	3.7	45	22	23	5.26	2.70	1.16	4.10	3.62	1.20
4-mCBPy	20	4.0	50	28	22	5.10	2.50	1.43	3.67	2.72	1.73
CBP	26	3.9	40	20	20	3.85	2.56	0.77	3.08	3.20	1.92
mCBP	24	5.0	47	22	25	4.17	2.00	0.92	3.25	2.92	1.36

[a] Prompt emission lifetime. [b] Delayed emission lifetime. [c] Photoluminescence quantum yield. [d] Prompt component of Φ_{PL}. [e] Delayed component of Φ_{PL}. [f] Prompt fluorescence decay rate constant. [g] Delayed fluorescence decay rate constant. [h] Radiative decay rate constant from the singlet excited state. [i] Intersystem crossing rate constant. [j] Reverse intersystem crossing rate constant. [k] Non-radiative decay rate constant from the triplet excited state.

5.7 Electroluminescence characteristics

The suitably high T_1 energies **3-CBPy and 4-mCBPy** imply that the two hosts can confine the triplet excitons of the yellow emitter **tri-PXZ-TRZ**. We expected that the two bipyridine-containing hosts would also have ambipolar charge transport characteristics that would improve OLED performance. To test this, hole-only devices with the configuration of ITO/NPB (10 nm)/tris(4-carbazoyl-9-ylphenyl)amine (TCTA) (5 nm)/Host (30 nm)/NPB (15 nm)/Al (100 nm) and electron-only devices with the configuration of ITO/TmPyPB (15 nm)/ Host (30 nm)/TmPyPB (15 nm)/LiF (1 nm)/Al (100 nm) were fabricated. As shown in Figure **5.10**, the devices with **3-CBPy** and **4-mCBPy** exhibit suppressed hole transport and largely enhanced

electron transport compared to those with **CBP** and **mCBP**. These results point to an improved charge carrier balance in the **3-CBPy** and **4-mCBPy**-based devices.

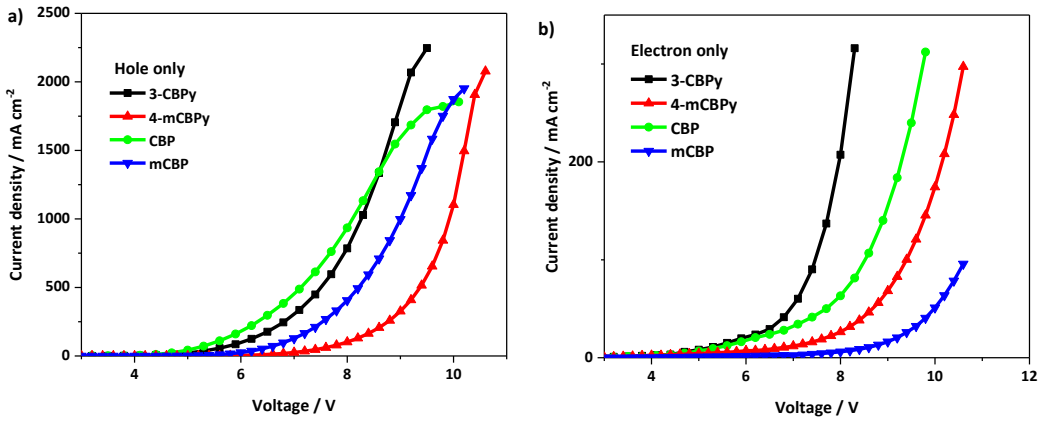

Figure **5.10**. Current density-voltage characteristics of (a) hole-only and (b) electron-only devices of the four hosts

Next, we fabricated yellow OLEDs with the following structure: ITO/NPB (30 nm)/TCTA (20 nm)/host (30 nm)/PPT (5 nm)/TmPyPB (60 nm)/LiF (1 nm)/Al (100 nm), where host is as follows: Device A: **tri-PXZ-TRZ**:**3-CBPy** (7 wt%), Device B: **tri-PXZ-TRZ**:**4-mCBPy** (7 wt%), Device C: **tri-PXZ-TRZ**:**CBP** (7 wt%), Device D: **tri-PXZ-TRZ**:m**CBP** (7 wt%). In the devices, NPB was used as the hole injection layer, TCTA) was used as the hole-transporting layer, PPT was use as a hole blocking layer, and TmPyPB was used as a combined electron-transporting and injection layer. Figure **5.11a** shows a proposed energy level diagram for our devices, indicating that the chosen stack architecture is likely to provide efficient injection and confinement of charge carriers to the emission layer (EML), and Figure **5.11e** shows the

molecular structures of materials used in devices. A doping concentration of 7 wt% was applied across all OLEDs in this study, which is similar to the concentration adopted in the original report (6 wt%).[13]

The *J*-V-L characteristics of the fabricated yellow OLEDs are shown in Figure **5.11b** and the performance of the four devices are summarized in Table **5.3.** The devices based on **3-CBPy** (Device A) and **4-mCBPy** (Device B) exhibited relatively lower turn-on voltages (~ 2.5 V) compared to Device D based on **mCBP** (~ 3 V). Device C using **CBP** also exhibited low turn-on voltage of 2.5 V; however, this device showed poor stability at high voltage as the luminance plateaued and the current density increased dramatically. Figure **5.11c** shows the EQE curves as a function of luminance. An EQE_{max} of 19.4% was obtained at a luminance of 3 cd m^{-2} for Device B based on **4-mCBPy** while the EQE_{max} for Device D based on **mCBP** was lower at 16.7% and occurred at a luminance of less than 1 cd m^{-2}. The EQE_{max} for Device A based on **3-CBPy** was 15.6% at a luminance 2 cd m^{-2} while the Device C based on **CBP** showed very low EQE at low brightness due to relatively large leakage current but an EQE_{max} of 14.8 % at a luminance 300 cd m^{-2}. The low EQE of Device C could be ascribed in part to the unbalanced charge transport in **CBP** which leads to poor exciton utilization. Impressively, at a brightness of 10,000 cd m^{-2}, the EQE for Device B remained high at 16.0%, showing very low roll-off of 18%, while for Devices A, C and D, the $EQE_{10,000}$ dropped to 9.9%, 11.0%, and 11.5%, respectively corresponding to 36%, 26%, and 31% roll-off, respectively. The **3-CBPy**-based Device A exhibited more severe efficiency roll-off, which could be attributed to the fast k_{ISC} of **tri-PXZ-TRZ** in **3-CBPy** that leads to increased triplet exciton accumulation. The maximum brightness for Devices A and B

both reached 86 000 cd m^{-2}, much higher than that achieved for Devices C and D, where maximum brightness reached only 38 000 cd m^{-2}. The electroluminescence (EL) spectrum of Device A (λ_{EL} = 561 nm) was slightly red-shifted relative to those of Devices B, C, and D (λ_{EL} – 555, 554, and 554 nm, respectively, Figure **5.11d**). The high EQE and small efficiency roll-off make the device based on **tri-PXZ-TRZ/4-mCBPy** among the best yellow OLEDs employing TADF emitters (Table **5.4**). We attribute the superior electroluminescence performance of the **4-mCBPy**-based Device B to a combination of improved electron transport, which results in better charge balance within the EML, and the highly efficient energy transfer from host to emitter. For the **3-CBPy**-based Device A, as the Φ_{PL} of the emitter in **3-CBPy** is lower than in **4-mCBPy** or **mCBP**, the EQE_{max} of Device A is also slightly lower than Devices B (**4-mCBPy**) and D (**mCBP**).

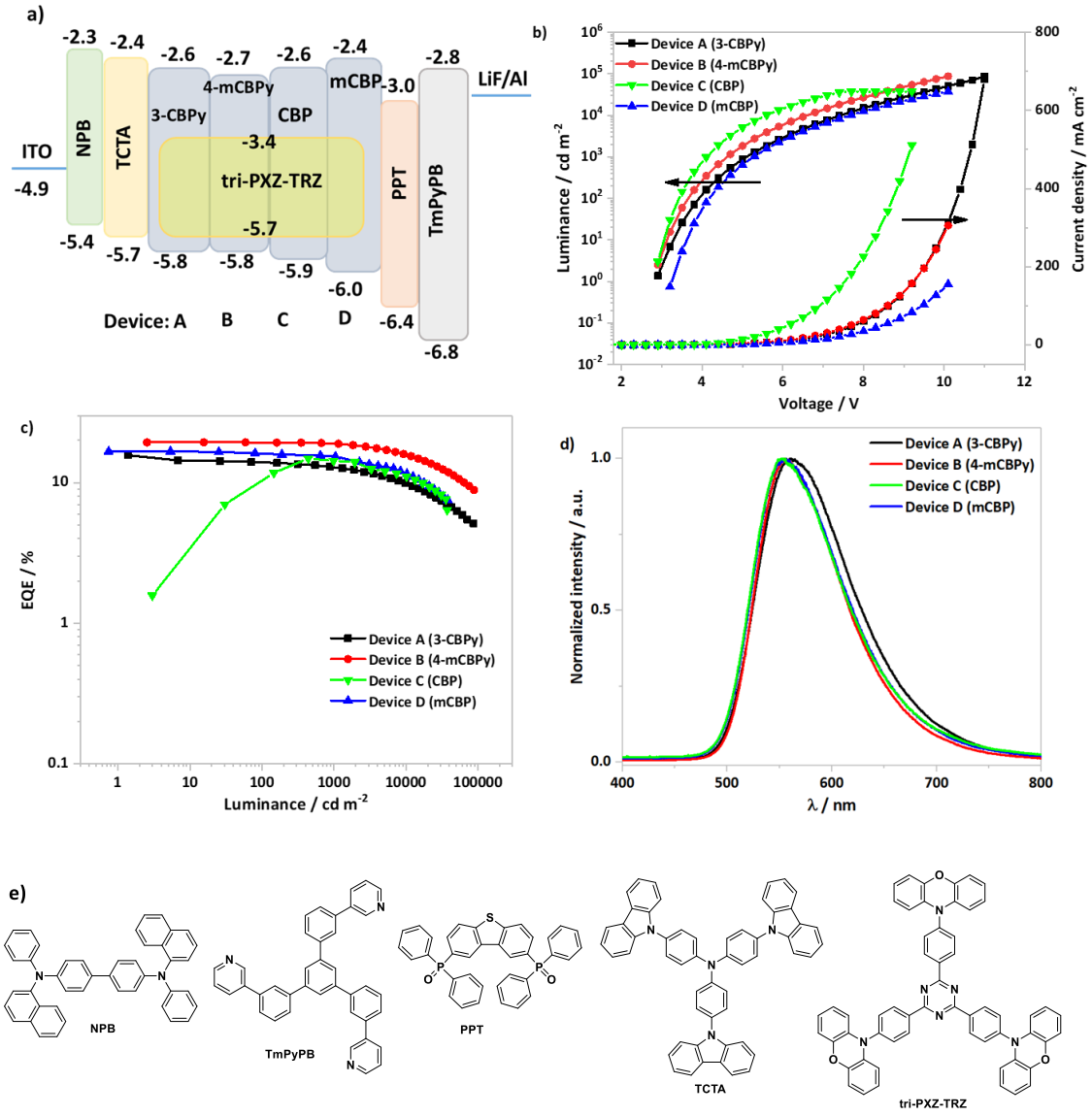

Figure **5.11**. Optimized OLEDs devices based on **3-CBPy** (Device A), **4-mCBPy** (Device B), **CBP** (Device C), and m**CBP** (Device D). (a) Energy level diagram of the device structure, (b) Current density-voltage-luminance characteristics, (c) EQE-luminance characteristics, (d) EL spectra, (e) molecular structure of materials used in devices.

Table **5.3**. Summary of OLEDs performance based on **3-CBPy** (Device A), **4-mCBPy** (Device B), **CBP** (Device C), and **mCBP** (Device D).

Devices	**V_{on} / V**	**λ_{EL} / nm**	**CIE @ 8V**	**EQE_{max}/EQE_{1000}/ EQE_{10000}/ %**	**Roll-off @ 1 000 /10 000 cd m^{-2} / %**	**CE_{max} / cd/A**	**Lum_{max}/ cd m^{-2}**
Device A	2.5	561	(0.46, 0.52)	15.6/12.7/9.9	19/36	48.2	86 796
Device B	2.5	555	(0.44, 0.53)	19.4/18.9/16.0	2/18	63.4	87 886
Device C	2.5	554	(0.44, 0.54)	14.8/13.9/11.0	6/26	43.0	37 288
Device D	3.0	554	(0.44, 0.53)	16.7/15.3/11.5	8/31	54.3	37 952

Table **5.4**. OLEDs device summary of representative yellow TADF emitters.

Emitters	**Hosts**	**CIE**	**EQE_{max}/ EQE_{1000}/ EQE_{10000}/ %**	**Roll-off @ $10^3/10^4$ cd m^{-2} / %**	**Lum_{max} / cd m^{-2}**	**Ref.**
tri-PXZ-TRZ	4-mCBPy	(0.44, 0.53)	19.4/18.9/16.0	2/18	88 000	This work
tri-PXZ-TRZ	CBP	N. A.	21.0/19.2/16.5	8/21	70 000	[15]
tri-PXZ-TRZ	mCBP	N. A.	13.4/N.A./N.A.	N.A./N.A.	N.A.	[16]
TBP-PXZ	CBP	(0.45, 0.53)	17.7/16.0/12.7	10/28	49 240	[17]
TXO-TPA	mCP	(0.45, 0.53)	18.5/6.0/N. A.	68/ N. A.	16 300	[18]
PXZDSO2	CBP	(0.44, 0.54)	16.7/13.7/N.A.	18/ N. A.	17 000	[19]
DBT-BZ-DMAC	CBP	(0.23, 0.51)	17.9/10.9/N.A.	39/N. A.	10 000	[20]
3,6-2TPA-TXO	CBP	(0.39, 0.54)	24.3/3.7/N. A.	85/ N. A.	1 600	[21]
Ac-CNP	mCBP	(0.47, 0.51)	13.3/9.1/6.0	32/55	70 630	[22]

5.8 Conclusion

This study demonstrates the potential of the bipyridine core as an effective acceptor an ambipolar host materials. Two bipolar host materials **3-CBPy** and **4-mCBPy** containing *n*-type carbazoles and *p*-type bipyridine moieties were synthesized and characterized in detail. Both materials possessed high singlet energy and triplet energies, and suitable HOMO and LUMO levels, that made them ideal hosts for yellow TADF-based OLEDs. Indeed, the materials enabled OLEDs with enhanced EQE and reduced efficiency roll-off when paired with a yellow TADF emitter. In particular, the device based on **4-mCBPy** exhibited a low turn-on voltage of 2.5 V along with an EQE_{max} of 19.4 %. This device also showed dramatically reduced efficiency roll-off; at a luminance of 10,000 cd m^{-2} its EQE remained at 16.0%.

5.9 Experimental section

General consideration

All experiments were carried out with commercial solvents from Fisher Scientific Ltd, except where specifically mentioned. Commercially obtained chemicals were used as received. All manipulations were carried out under an inert atmosphere using standard Schlenk line techniques. ^{1}H NMR, and ^{13}C NMR were recorded at room temperature on a Bruker Avance spectrometer at 400 MHz and 100 MHz, respectively. ^{1}H NMR and ^{13}C NMR spectra were referenced to the residual solvent peaks ($CDCl_3$ = 7.26 ppm for ^{1}H NMR and 77.16 ppm for ^{13}C NMR). The following abbreviations have been used for multiplicity assignments: “s” for singlet, “d” for doublet, “t” for triplet, “m” for multiplet and “br” for broad. Elemental analysis was measured by

London Metropolitan University. Samples for high resolution mass spectrum (HRMS) were sent to the National Mass Spectrometry Facility in Swansea (EPSRC) for analysis by nano-electrospray on an Orbitrap instrument.

Materials and synthesis

Synthesis of 9-(5-bromopyridin-2-yl)-9H-carbazole

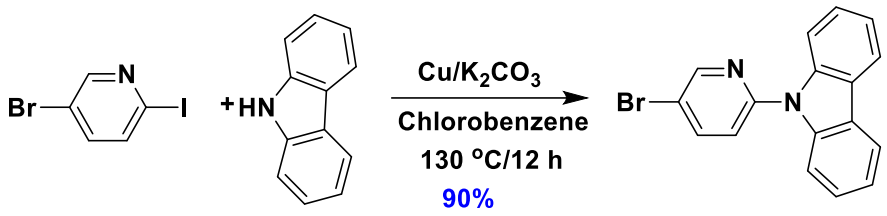

9-(5-bromopyridin-2-yl)-9H-carbazole was synthesized via a modified Ullman coupling reaction.[7] Carbazole (1.7 g, 10 mmol, 1 equiv.), 5-bromo-2-iodopyridine (3.1 g, 11 mmol, 1.1 equiv.), copper powder (640 mg, 10 mmol, 1 equiv.), and potassium carbonate (4.2 g, 30 mmol, 3 equiv.) were dissolved in 20 mL of chlorobenzene. The solution was degassed by three freeze-pump-thaw cycles and then stirred at 130 °C for 12 h. The mixture was washed with water and extracted with dichloromethane (DCM) (3×30 mL). The organic solvent was concentrated under reduced pressure. The crude product was purified by silica gel chromatography using DCM/hexanes = 1/1 as the eluent to obtain 9-(5-bromopyridin-2-yl)-9H-carbazole as a white powder.

9-(5-bromopyridin-2-yl)-9H-carbazole: $\mathbf{R_f}$ = 0.5 (50% DCM/Hexane). **Yield:** 90%. **Mp:** 113 - 115˚C (Lit Mp: 113.1 °C[6]). **^{1}H NMR (500 MHz, $CDCl_3$) δ (ppm):** 8.80 (d, *J* = 2.5 Hz, 1H), 8.15

(d, *J* = 7.7 Hz, 2H), 8.03 (dd, *J* = 8.5, 2.5 Hz, 1H), 7.85 (d, *J* = 8.3 Hz, 2H), 7.57 (d, *J* = 8.5 Hz, 1H), 7.49 (dd, *J* = 8.3, 7.1 Hz, 2H), 7.44 (dd, *J* = 6.1, 1.4 Hz, 1H), 7.41 – 7.35 (m, 2H). **^{13}C NMR (126 MHz, $CDCl_3$) δ (ppm):** 150.6, 141.0, 139.3, 136.2, 126.4, 124.5, 121.3, 120.3, 120.0, 116.9, 111.1. **HRMS** (LTQ Orbitrap XL) **$[M+H]^+$ Calculated: ($C_{17}H_{11}{}^{79}BrN_2$)** : 273.9849; found: 273.9841. The characterization matches that of the literature.[7]

Synthesis of 6,6'-di(9H-carbazol-9-yl)-3,3'-bipyridine (3-CBPy):

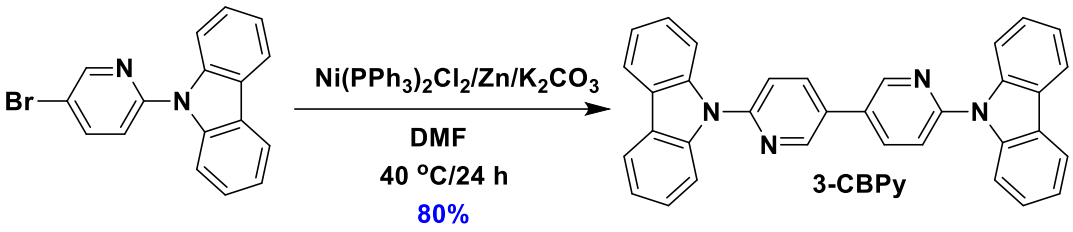

6,6'-di(9H-carbazol-9-yl)-3,3'-bipyridine (3-CBPy) was synthesized by a nickel(0)-catalyzed homo-coupling reaction.[8] 9-(5-bromopyridin-2-yl)-9H-carbazole (1.6 g, 5 mmol, 1 equiv.), bis(triphenylphosphine)nickel(II) chloride (330 mg, 0.5 mmol, 0.1 equiv.), zinc powder (100 mg, 1.5 mmol, 0.3 equiv.), and potassium carbonate (2.1 g, 15 mmol, 3 equiv.) were dissolved in 10 mL of DMF. The solution was degassed by three freeze-pump-thaw cycles and then stirred at 40 °C for 24 h. The mixture was washed with 100 mL of saturated saline solution and extracted with ethyl acetate (3×30 mL). The organic solvent was concentrated under reduced pressure. The crude product was purified by silica gel chromatography using DCM/hexanes = 1/1 as the eluent to obtain **3-CBPy** as a white powder.

6,6'-di(9H-carbazol-9-yl)-3,3'-bipyridine (3-CBPy): R_f = 0.4 (50% DCM/Hexane). **Yield:** 80%. **Mp:** 241-243˚C. **^{1}H NMR (500 MHz, $CDCl_3$) δ (ppm):** 9.08 (d, *J* = 2.3 Hz, 1H), 8.24 (dd, *J* = 8.1, 3.2 Hz, 1H), 8.20 – 8.15 (m, 2H), 7.99 (d, *J* = 8.2 Hz, 2H), 7.86 (dd, *J* = 8.3, 2.4 Hz, 1H), 7.53 (ddd, *J* = 8.3, 7.1, 1.3 Hz, 2H), 7.44 – 7.35 (m, 2H). **^{13}C NMR (126 MHz, $CDCl_3$) δ (ppm):** 151.7, 147.6, 139.4, 136.7, 130.2, 126.4, 124.6, 121.3, 120.3, 118.9, 111.3. **HRMS** (LTQ Orbitrap XL) **$[M+H]^+$ Calculated: ($C_{34}H_{23}N_4$)** : 487.1910, found 487.1917. **Elemental analysis: Calcd for $C_{34}H_{22}N_4$**: C, 83.93; H, 4.56; N, 11.51. Found: C, 84.02; H, 4.59; N, 11.48. **HPLC:** 10% H_2O/MeCN, 1.0 mL min^{-1}, 300 nm; tr (98.0 %) = 5.4 min.

Synthesis of 4,4'-di(9H-carbazol-9-yl)-4,4'-bipyridine (4-mCBPy):

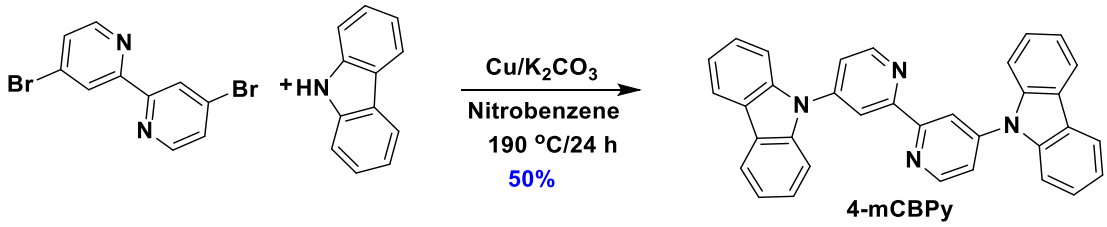

4-mCBPy was synthesized via a modified Ullman coupling reaction.[7] 4,4'-dibromo-2,2'-bipyridine (1.6 g, 5 mmol, 1 equiv.), carbazole (2.5 g, 15 mmol, 3 equiv.), copper powder (640 mg, 10 mmol, 2 equiv.) and potassium carbonate (4.2 g, 30 mmol, 6 equiv.) were dissolved in 20 mL of nitrobenzene. The solution was degassed by three freeze-pump-thaw cycles and then stirred at 190 °C for 24 h. The mixture was washed with water and extracted with dichloromethane (DCM) for three times (3×30 mL). The organic solvent was poured into 100 mL of methanol to crash out

the product and this was filtered to obtain a grey crude product. The crude product was purified by silica gel chromatography using DCM as the eluent to obtain **4-mCBPy** as a white powder.

4,4'-di(9H-carbazol-9-yl)-4,4'-bipyridine (4-mCBPy): R_f = 0.3 (DCM). **Yield:** 50%. **Mp:** 255-256˚C. **^{1}H NMR (500 MHz, $CDCl_3$) δ (ppm):** 9.11 (d, *J* = 2.1 Hz, 1H), 9.01 (d, *J* = 5.6 Hz, 1H), 8.19 (d, *J* = 7.8 Hz, 2H), 7.92 – 7.85 (m, 1H), 7.81 (d, *J* = 8.3 Hz, 2H), 7.61 – 7.51 (m, 2H), 7.43 (t, *J* = 7.5 Hz, 2H). **^{13}C NMR (126 MHz, $CDCl_3$) δ (ppm):** 151.8, 149.3, 139.1, 126.8, 126.6, 124.8, 122.1, 121.1, 120.7, 119.1, 110.3. **HRMS** (LTQ Orbitrap XL) **$[M+H]^+$ Calculated: ($C_{34}H_{23}N_4$)** : 487.1910, found 487.1917. **Elemental analysis: Calcd for $C_{34}H_{22}N_4$**: C, 83.93; H, 4.56; N, 11.51. Found: C, 83.86; H, 4.60; N, 11.43. **HPLC:** 10% H_2O/MeCN, 1.0 mL min^{-1}, 300 nm; tr (99.1 %) = 6.7 min.

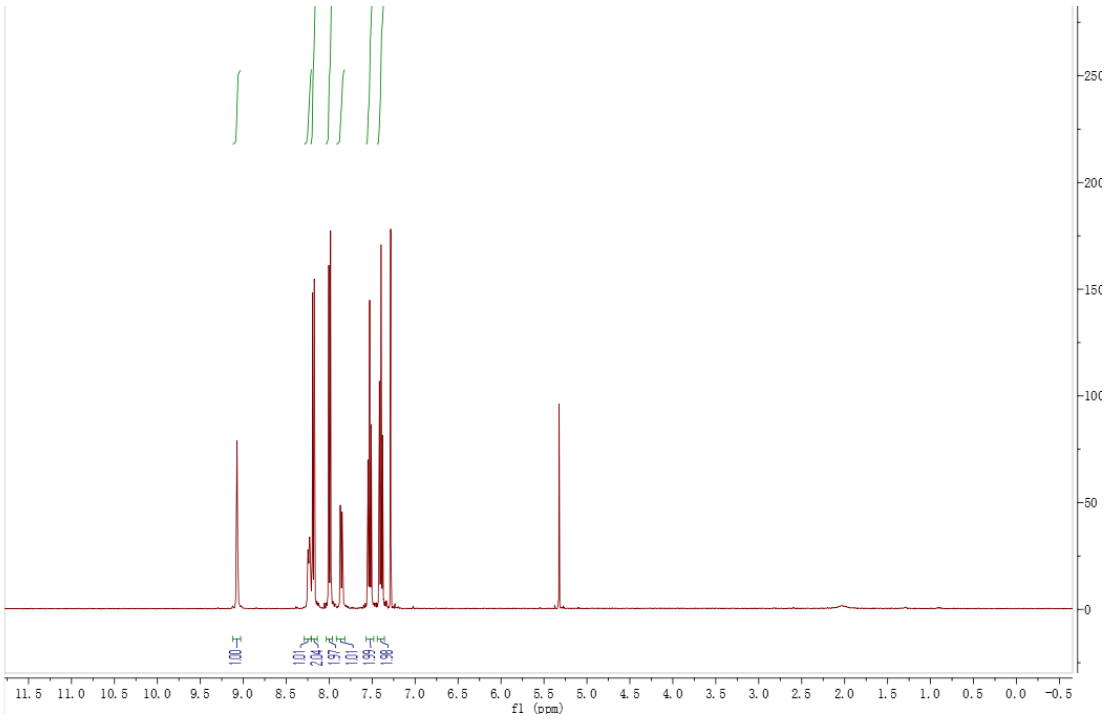

Figure **5.12**. ^{1}H NMR of **3-CBPy** in $CDCl_3$

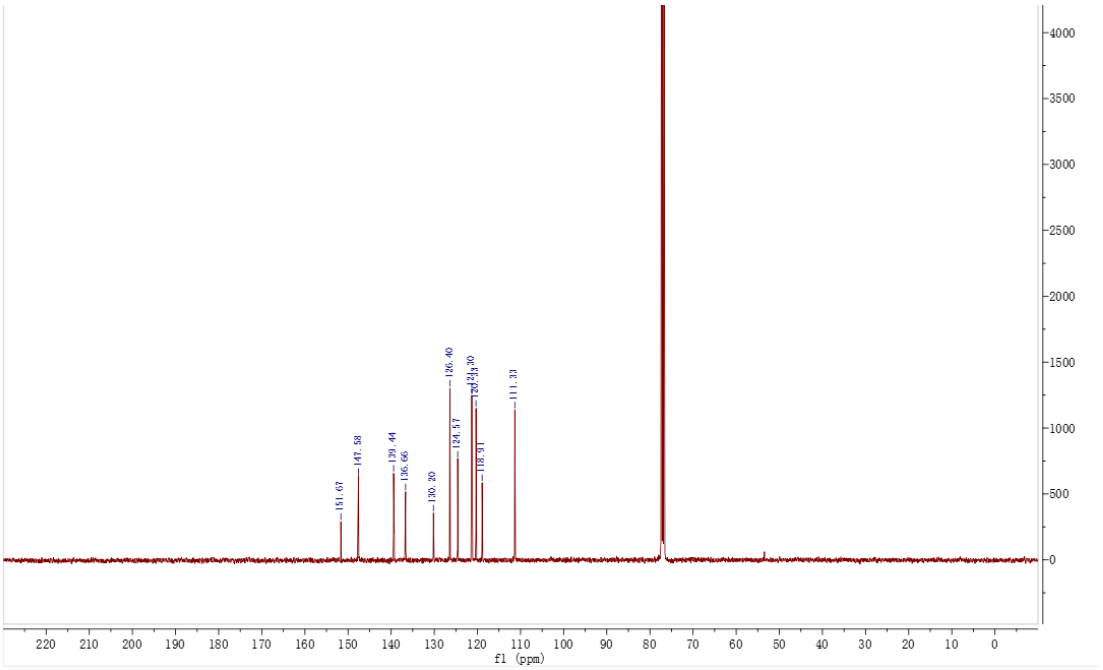

Figure **5.13**. ^{13}C NMR of **3-CBPy** in $CDCl_3$

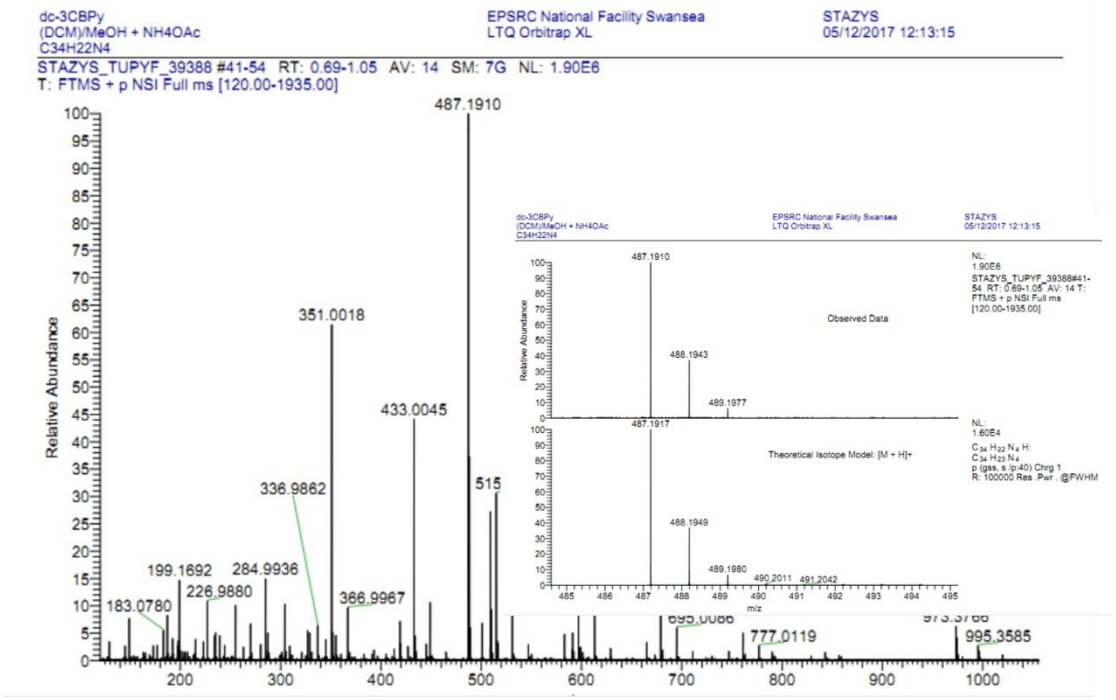

Figure **5.14**. HRMS of **3-CBPy**

LONDON metropolitan university

Elemental Analysis Service

Please send completed form and samples to:

Stephen Boyer
School of Human Sciences
Science Centre
London Metropolitan University
29 Hornsey Road
London N7 7DD

Telephone: 020 7133 3605
Fax: 020 7133 2577
Email: s.boyer@londonmet.ac.uk

Sample submitted by: Dongyang Chen
Address: **EZC group, School of Chemistry, University of St Andrews, North Haugh,St Andrews, Fife, KY16 9ST**
Telephone: 07743430420 Email: dc217@st-andrews.ac.uk
Date Submitted:25/04/2018

Please submit ca. 5 mg of sample.

Sample Reference No.: dc-3CBPy
Name of Compound: 3CBPy
Molecular Formula: C34H22N4
Stability: Air stable
Hazards: none
Other Remarks:

Element	Expected %	Found (1)	Found (2)	
Carbon	83.93	84.03	84.03	
Hydrogen	4.56	4.77	4.69	
Nitrogen	11.51	11.50	11.45	

Authorising Signature:

Date Completed: 27/5/18	Signature:
Comments:	

Figure **5.15**. Elemental analysis of **3-CBPy**

SHIMADZU LabSolutions **Analysis Report**

<Sample Information>

Sample Name	: 3-CBPy		
Sample ID	: 3-CBPy		
Data Filename	: 01102018_3-CBPy_3-CBPy_006.lcd		
Method Filename	: AcN (90).lcm		
Batch Filename	: 011018.lcb		
Vial #	: 1-39	Sample Type	: Unknown
Injection Volume	: 10 uL		
Date Acquired	: 01/10/2018 22:24:27	Acquired by	: ezc-7
Date Processed	: 01/10/2018 22:54:29	Processed by	: ezc-7

<Chromatogram>

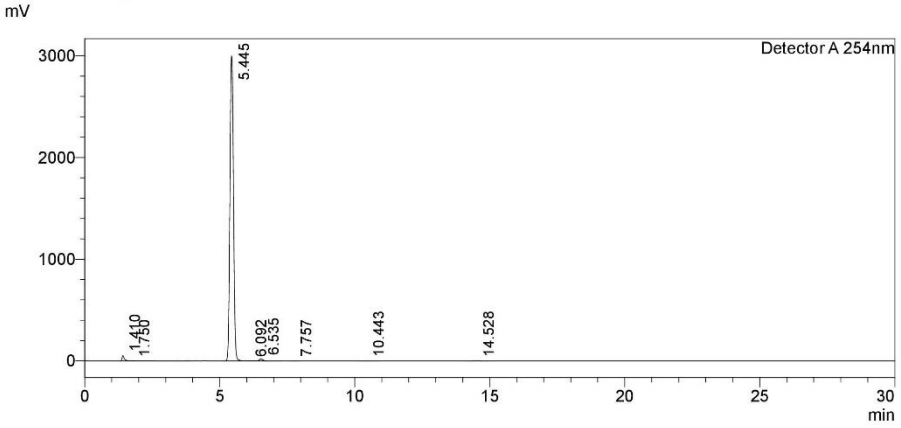

<Peak Table>

Detector A 254nm

Peak#	Ret. Time	Area	Height	Area%
1	1.410	338102	52940	1.262
2	1.750	2082	403	0.008
3	5.445	26250940	3000054	97.992
4	6.092	6040	784	0.023
5	6.535	170094	18635	0.635
6	7.757	2662	269	0.010
7	10.443	4582	352	0.017
8	14.528	14294	956	0.053
Total		26788796	3074393	100.000

Figure **5.16**. HPLC report of **3-CBPy**

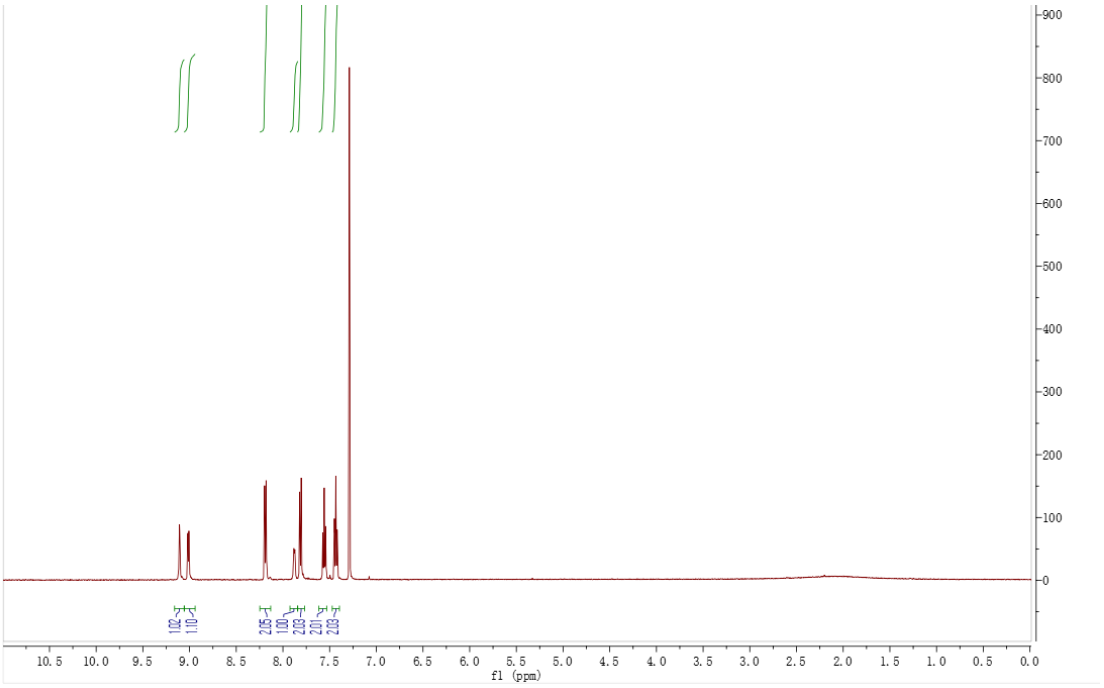

Figure **5.17**. ^{1}H NMR of **4-mCBPy** in $CDCl_3$

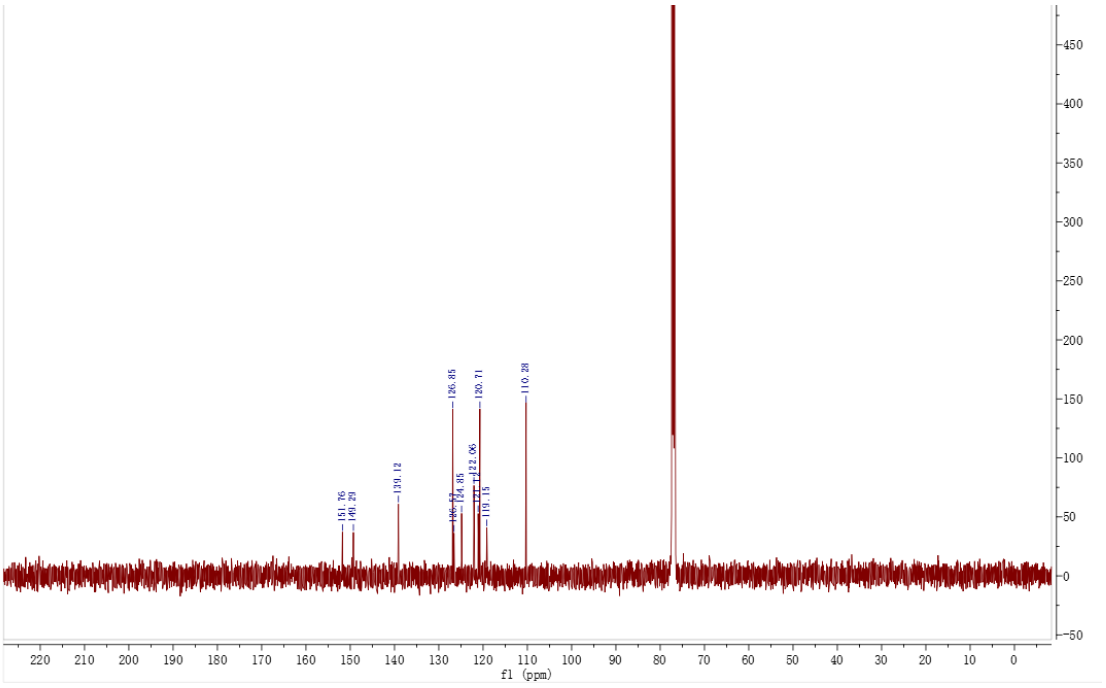

Figure **5.18**. ^{13}C NMR of **4-mCBPy** in $CDCl_3$

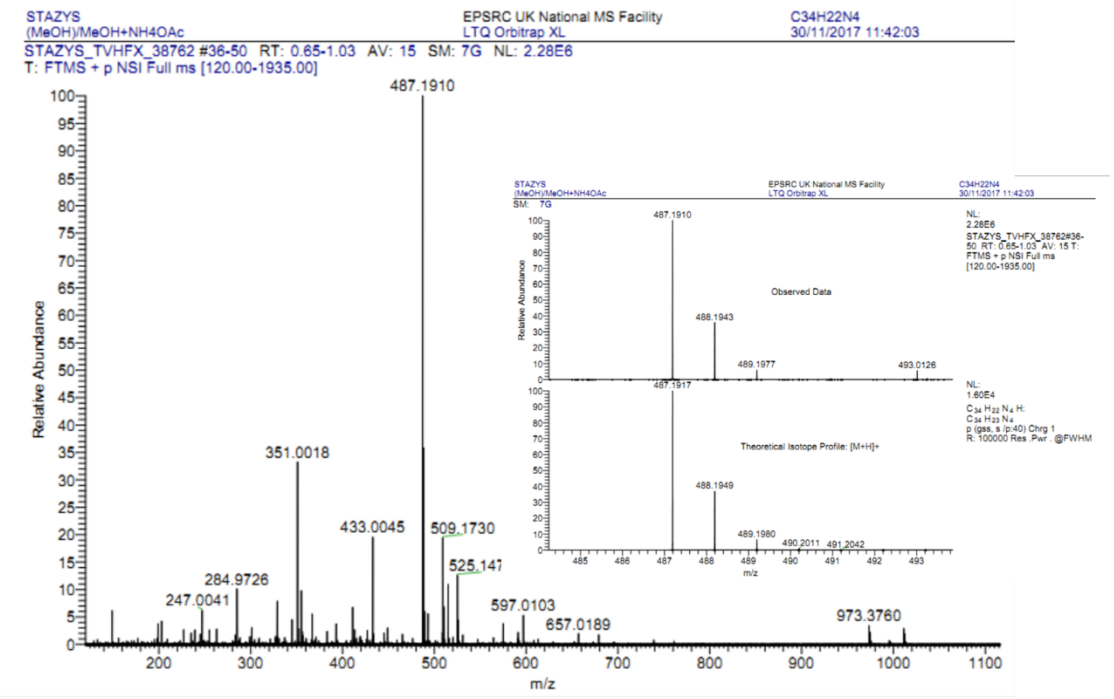

Figure **5.19**. HRMS of **4-mCBPy**

LONDON metropolitan university

Elemental Analysis Service

Please send completed form and samples to:

Stephen Boyer
School of Human Sciences
Science Centre
London Metropolitan University
29 Hornsey Road
London N7 7DD

Telephone: 020 7133 3605
Fax: 020 7133 2577
Email: s.boyer@londonmet.ac.uk

Sample submitted by: Dongyang Chen
Address: **EZC group, School of Chemistry, University of St Andrews, North Haugh,St Andrews, Fife, KY16 9ST**
Telephone: 07743430420 Email: dc217@st-andrews.ac.uk
Date Submitted:25/04/2018

Please submit ca. 5 mg of sample.

Sample Reference No.: dc-mCBPy-4
Name of Compound: 4-mCBPy
Molecular Formula: C34H22N4
Stability: Air stable
Hazards: none
Other Remarks:

Element	Expected %	Found (1)	Found (2)	
Carbon	83.93	83.86	83.86	
Hydrogen	4.56	4.60	4.67	
Nitrogen	11.51	11.38	11.43	

Authorising Signature:

Date Completed: 030618	Signature:
Comments:	

Figure **5.20**. Elemental analysis of **4-mCBPy**

SHIMADZU LabSolutions **Analysis Report**

<Sample Information>

Sample Name	: 4-mCBPy		
Sample ID	: MeCN(90) dc 4-mCBPy		
Data Filename	: 26082018_MeCN(90) dc 4-mCBPy_008.lcd		
Method Filename	: AcN (90).lcm		
Batch Filename	: ACN 90.lcb		
Vial #	: 1-47	Sample Type	: Unknown
Injection Volume	: 10 uL		
Date Acquired	: 26/08/2018 14:19:14	Acquired by	: ezc-7
Date Processed	: 26/08/2018 14:49:17	Processed by	: ezc-7

<Chromatogram>

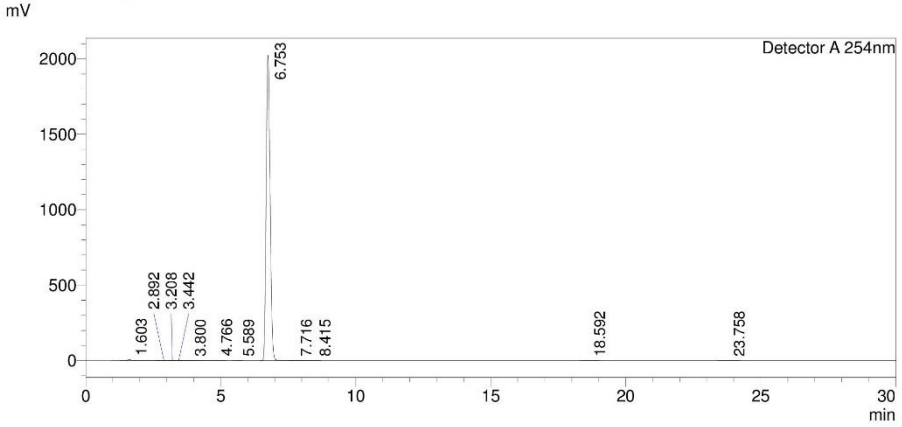

<Peak Table>

Detector A 254nm

Peak#	Ret. Time	Area	Height	Conc.	Unit	Area%
1	1.603	104626	6559	0.000		0.515
2	2.892	10550	484	0.000		0.052
3	3.208	3773	382	0.000		0.019
4	3.442	6602	340	0.000		0.033
5	3.800	4017	237	0.000		0.020
6	4.766	17555	1906	0.000		0.086
7	5.589	1625	181	0.000		0.008
8	6.753	20137458	2023869	0.000		99.146
9	7.716	17134	1088	0.000		0.084
10	8.415	1405	133	0.000		0.007
11	18.592	3256	170	0.000		0.016
12	23.758	2907	125	0.000		0.014
Total		20310910	2035475			100.000

Figure **5.21.** HPLC report of **4-mCBPy**

Reference

(1) Huang, H.; Wang, Y.; Wang, B.; Zhuang, S.; Pan, B.; Yang, X.; Wang, L.; Yang, C. Controllably Tunable Phenanthroimidazole-Carbazole Hybrid Bipolar Host Materials for Efficient Green Electrophosphorescent Devices. *J. Mater. Chem. C* **2013**, *1*, 5899–5908. https://doi.org/10.1039/c3tc30832d.

(2) Chou, H. H.; Cheng, C. H. A Highly Efficient Universal Bipolar Host for Blue, Green, and Red Phosphorescent OLEDs. *Adv. Mater.* **2010**, *22*, 2468–2471. https://doi.org/10.1002/adma.201000061.

(3) Li, J.; Ding, D.; Tao, Y.; Wei, Y.; Chen, R.; Xie, L.; Huang, W.; Xu, H. A Significantly Twisted Spirocyclic Phosphine Oxide as a Universal Host for High-Efficiency Full-Color Thermally Activated Delayed Fluorescence Diodes. *Adv. Mater.* **2016**, *28*, 3122–3130. https://doi.org/10.1002/adma.201506286.

(4) Lin, C. C.; Huang, M. J.; Chiu, M. J.; Huang, M. P.; Chang, C. C.; Liao, C. Y.; Chiang, K. M.; Shiau, Y. J.; Chou, T. Y.; Chu, L. K.; Lin, H. W.; Cheng, C. H. Molecular Design of Highly Efficient Thermally Activated Delayed Fluorescence Hosts for Blue Phosphorescent and Fluorescent Organic Light-Emitting Diodes. *Chem. Mater.* **2017**, *29*, 1527–1537. https://doi.org/10.1021/acs.chemmater.6b03979.

(5) Tao, Y.; Yang, C.; Qin, J. Organic Host Materials for Phosphorescent Organic Light-Emitting Diodes. *Chem. Soc. Rev.* **2011**, *40*, 2943–2970. https://doi.org/10.1039/c0cs00160k.

(6) Zhang, J.; Ding, D.; Wei, Y.; Xu, H. Extremely Condensing Triplet States of DPEPO-Type Hosts through Constitutional Isomerization for High-Efficiency Deep-Blue Thermally Activated Delayed Fluorescence Diodes. *Chem. Sci.* **2016**, *7*, 2870–2882. https://doi.org/10.1039/c5sc04848f.

(7) Wong, M. Y.; Zysman-Colman, E. Purely Organic Thermally Activated Delayed Fluorescence Materials for Organic Light-Emitting Diodes. *Adv. Mater.* **2017**, *29*, 1605444. https://doi.org/10.1002/adma.201605444.

(8) Chatterjee, T.; Wong, K. T. Perspective on Host Materials for Thermally Activated Delayed Fluorescence Organic Light Emitting Diodes. *Adv. Opt. Mater.* **2019**, *7*, 1800565. https://doi.org/10.1002/adom.201800565.

(9) Li, W.; Li, J.; Liu, D.; Wang, F.; Zhang, S. Bipolar Host Materials for High-Efficiency Blue Phosphorescent and Delayed-Fluorescence OLEDs. *J. Mater. Chem. C* **2015**, *3*, 12529–12538. https://doi.org/10.1039/c5tc02997j.

(10) Kang, J. S.; Hong, T. R.; Kim, H. J.; Son, Y. H.; Lampande, R.; Kang, B. Y.; Lee, C.; Bin, J. K.; Lee, B. S.; Yang, J. H.; Kim, J.; Park, S.; Cho, M. J.; Kwon, J. H.; Choi, D. H. High-Performance Bipolar Host Materials for Blue TADF Devices with Excellent External Quantum Efficiencies. *J. Mater. Chem. C* **2016**, *4*, 4512–4520. https://doi.org/10.1039/c6tc00385k.

(11) Gao, K.; Liu, K.; Li, X. L.; Cai, X.; Chen, D.; Xu, Z.; He, Z.; Li, B.; Qiao, Z.; Chen, D.; Cao, Y.; Su, S. J. An Ideal Universal Host for Highly Efficient Full-Color, White

Phosphorescent and TADF OLEDs with a Simple and Unified Structure. *J. Mater. Chem. C* **2017**, *5*, 10406–10416. https://doi.org/10.1039/c7tc04149g.

(12) Cui, L. S.; Ruan, S. Bin; Bencheikh, F.; Nagata, R.; Zhang, L.; Inada, K.; Nakanotani, H.; Liao, L. S.; Adachi, C. Long-Lived Efficient Delayed Fluorescence Organic Light-Emitting Diodes Using n-Type Hosts. *Nat. Commun.* **2017**, *8*, 2250. https://doi.org/10.1038/s41467-017-02419-x.

(13) Uoyama, H.; Goushi, K.; Shizu, K.; Nomura, H.; Adachi, C. Highly Efficient Organic Light-Emitting Diodes from Delayed Fluorescence. *Nature* **2012**, *492*, 234–238.

(14) Cui, L. S.; Kim, J. U.; Nomura, H.; Nakanotani, H.; Adachi, C. Corrigendum to: Benzimidazobenzothiazole-Based Bipolar Hosts to Harvest Nearly All of the Excitons from Blue Delayed Fluorescence and Phosphorescent Organic Light-Emitting Diodes. *Angew. Chemie - Int. Ed.* **2016**, *55* (40), 6864-6868. https://doi.org/10.1002/anie.201605553.

(15) Li, W.; Li, J.; Liu, D.; Li, D.; Wang, F. Cyanopyridine Based Bipolar Host Materials for Green Electrophosphorescence with Extremely Low Turn-On Voltages and High Power Efficiencies. *ACS Appl. Mater. Interfaces* **2016**, *8*, 21497–21504. https://doi.org/10.1021/acsami.6b04395.

(16) Lin, H. W.; Lu, C. W.; Lin, L. Y.; Chen, Y. H.; Lin, W. C.; Wong, K. T.; Lin, F. Pyridine-Based Electron Transporting Materials for Highly Efficient Organic Solar Cells. *J. Mater. Chem. A* **2013**, *1*, 1770–1777. https://doi.org/10.1039/c2ta00253a.

(17) Lee, J.; Lee, S.; Kim, J. H.; Kang, S. O.; Han, W. S. Triaryl Boron Derivatives of Pyridine as Electron Transporting Materials for Blue Phosphorescent Organic Light-Emitting Diodes. *Org. Electron.* **2018**, *62*, 5–11. https://doi.org/10.1016/j.orgel.2018.07.014.

(18) Tao, Y.; Wang, Q.; Yang, C.; Wang, Q.; Zhang, Z.; Zou, T.; Qin, J.; Ma, D. A Simple Carbazole/Oxadiazole Hybrid Molecule: An Excellent Bipolar Host for Green and Red Phosphorescent OLEDs. *Angew. Chemie - Int. Ed.* **2008**, *47*, 8104–8107. https://doi.org/10.1002/anie.200803396.

(19) Song, W.; Shi, L.; Gao, L.; Hu, P.; Mu, H.; Xia, Z.; Huang, J.; Su, J. [1,2,4]Triazolo[1,5- *a*]Pyridine as Building Blocks for Universal Host Materials for High-Performance Red, Green, Blue and White Phosphorescent Organic Light-Emitting Devices. *ACS Appl. Mater. Interfaces* **2018**, *10*, 5714–5722. https://doi.org/10.1021/acsami.7b18202.

(20) Lee, C. W.; Lee, J. Y. Benzo[4,5]Thieno[2,3-b]Pyridine Derivatives as Host Materials for High Efficiency Green and Blue Phosphorescent Organic Light-Emitting Diodes. *Chem. Commun.* **2013**, *49*, 1446–1448. https://doi.org/10.1039/c2cc38049h.

(21) Tanaka, H.; Shizu, K.; Nakanotani, H.; Adachi, C. Twisted Intramolecular Charge Transfer State for Long-Wavelength Thermally Activated Delayed Fluorescence. *Chem. Mater.* **2013**, *25*, 3766–3771. https://doi.org/10.1021/cm402428a.

(22) Tao, S.; Ji, E.; Shi, L.; Liu, N.; Xu, L.; Dai, B. Copper-Catalyzed C-N Bond Exchange of N-Heterocyclic Substituents around Pyridine and Pyrimidine Cores. *Synth.* **2017**, *49*, 5120–5130. https://doi.org/10.1055/s-0036-1590893.

(23) Nishio, M.; Umezawa, Y.; Honda, K.; Tsuboyama, S.; Suezawa, H. CH/π Hydrogen Bonds in Organic and Organometallic Chemistry. *CrystEngComm* **2009**, *11*, 1757–1788. https://doi.org/10.1039/b902318f.

(24) Nishio, M. CH/π Hydrogen Bonds in Crystals. *CrystEngComm* **2004**, *6*, 130–158. https://doi.org/10.1039/b313104a.

(25) Schrögel, P.; Langer, N.; Schildknecht, C.; Wagenblast, G.; Lennartz, C.; Strohriegl, P. Meta-Linked CBP-Derivatives as Host Materials for a Blue Iridium Carbene Complex. *Org. Electron.* **2011**, *12*, 2047–2055. https://doi.org/10.1016/j.orgel.2011.08.012.

(26) Adamo, C.; Barone, V. Toward Reliable Density Functional Methods without Adjustable Parameters: The PBE0 Model. *J. Chem. Phys.* **1999**, *110*, 6158–6170. https://doi.org/10.1063/1.478522.

(27) Pople, J. A.; Binkley, J. S.; Seeger, R. Theoretical Models Incorporating Electron Correlation. *Int. J. Quantum Chem.* **1976**, *10*, 1–19. https://doi.org/10.1002/qua.560100802.

(28) Gritzner, G.; Kuta, J. Recommendations on Reporting Electrode Potentials in Nonaqueous Solvents (Recommendations 1983). *Pure Appl. Chem.* **1984**, *56*, 461–466. https://doi.org/10.1351/pac198456040461.

(29) Bagnich, S. A.; Rudnick, A.; Schroegel, P.; Strohriegl, P.; Köhler, A. Triplet Energies and Excimer Formation in Meta - and Para -Linked Carbazolebiphenyl Matrix Materials. **2015**, *373*, 140446 https://doi.org/10.1098/rsta.2014.0446.

Chapter 6

Controlling the Emitter's Orientation in Solution-processed OLEDs using a Liquid Crystalline Multi-resonance TADF Emitter

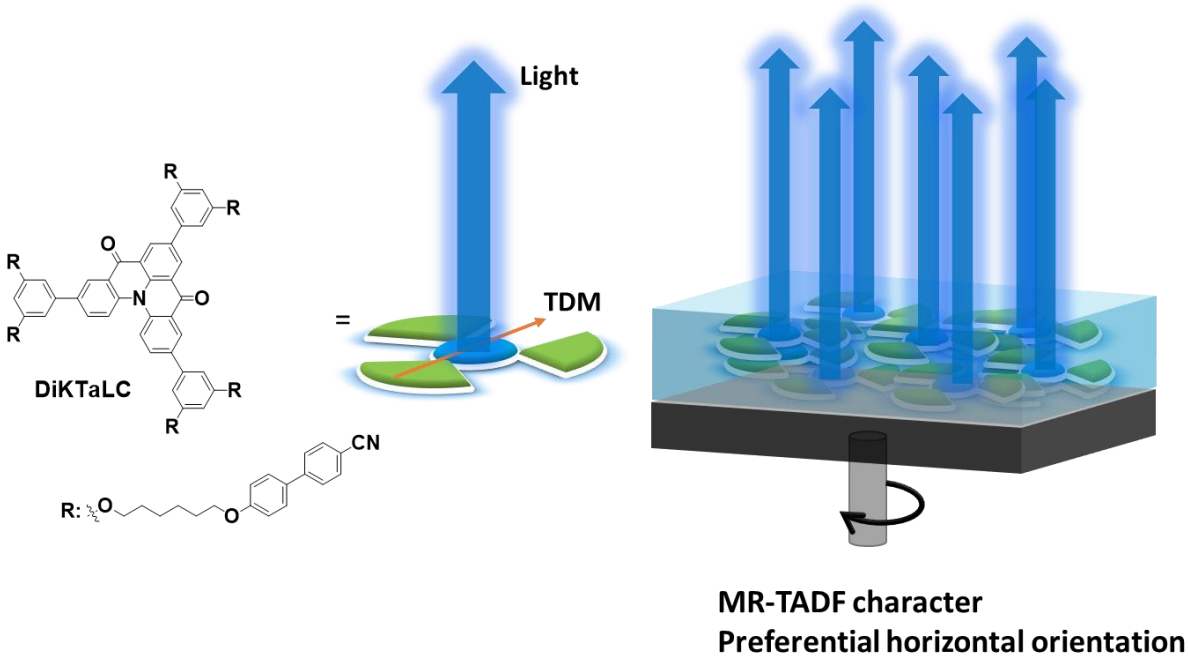

Manuscript of this project is under preparation as

Dongyang Chen,[a] Francisco Tenopala Carmona,[b] Julius A. Knöller,[c] Andreas Mischok,[b] David Hall,[a,d] Subeesh Madayanad Suresh,[a] Tomas Matulaitis,[a] Yoann Olivier,[d] Laschat Sabine,[c] Malte Gather,[b] Eli Zysman-Colman[a]*

Collaborators in this Chapter are from

[a] Organic Semiconductor Centre, EaStCHEM School of Chemistry, University of St Andrews, St Andrews, Fife, KY16 9ST, UK

[b] Organic Semiconductor Centre, SUPA School of Physics and Astronomy, University of St Andrews, St Andrews, Fife, KY16 9SS, UK

[c] Institut für Organische Chemie, Universität Stuttgart, Pfaffenwaldring 55, 70569 Stuttgart, Germany

[d] Laboratory for Chemistry of Novel Materials, University of Mons, Mons, Belgium

David Hall helped the SCS-CC2 calculation, Subeesh Madayanad Suresh provided the starting material of Br_3DiKTa, and Tomas Matulaitis carried out the iCCD measurement.

Julius A. Knöller carried out the liquid crystal property investigation, including DSC, POM, WAXS/SAXS measurements.

Francisco Tenopala Carmona and Andreas Mischok carried out the orientation study, including

VASE and angle-resolved PL spectroscopy measurements.

I designed the molecule **DiKTaLC** presented in this project and completed the synthesis and characterization, electrochemistry, photophysics in solutions and PMMA films, and I am the principal author of the manuscript.

6.1 Introduction

OLEDs can be categorized into vacuum-deposited OLEDs (VD-OLEDs), and solution-processed OLEDs (SP-OLEDs), depending on the technique used for their fabrication.[1] For VD-OLEDs, small molecule weight materials are sublimed into the vapor phase via heating in a high-vacuum environment (pressure < 10^{-6} Torr) to afford multilayer structures of very high purity.[1] With appropriate heating and choice of materials, the vacuum-deposited films can exhibit high densities, high thermal stability, and the emitter molecules can show a high degree of horizontal molecular orientation,[1] which are critical for device to be both stable and show a high EQE_{max}. These advantages make vacuum-deposition the preferred technique for OLEDs fabrication, and to date, commercial OLEDs are mainly produced by vacuum-deposited. However, the fabrication process is both energy intensive and materials wasteful, and a complex operation process is required to control for doping concentration and film thickness, which contribute to the relatively high fabrication cost associated with VD-OLEDs.[2] SP-OLEDs offer a number of potential advantages, such as low-cost manufacturing, high processing efficiency, compatibility with flexible substrates, a relatively small amount of wasted material, and a wider materials choice from small molecule[3,4] to polymer[5] and dendrimer.[2,6] However, the poor film quality and morphology fabricated by solution-processed methods lead to inferior device lifetime and severe efficiency roll-off of SP-OLEDs, which has in part retarded the commercialization of SP-OLEDs.[2]

The efficiency of the OLEDs is based in part by the capacity of the emitter material to harvest both the emissive singlet and triplet excitons generated within the emission layer to produce light, reflected in the IQE. There are two classes of materials that can attain up to 100%

IQE: phosphorescent emitters[7] and TADF emitters.[8–10] Organic TADF emitters harvest all excitons as a result to the small ΔE_{ST}, which permits the non-emissive triplets to be efficiently up-converted into emissive singlets by a RISC process.[11,12] As discussed in **Chapter 1**, The EQE of the OLED is not only depends on the IQE but also the η_{out}, as shown in equation (6.1):[13]

$$EQE = IQE \times \eta_{out} \quad (6.1)$$

The η_{out} is dependent on the orientation of the transition dipole momentum (TDM) of the emitter molecules. For the case where the TDMs are randomly oriented within the emissive layer, the η_{out} typically has a value of 20-30%, thus indicating that a small amount of the light produced within the emissive layer actually exists the device for productive use.[14,15] A general method to improve the η_{out} is to horizontally orient the TDM of the emitters, as the emission of light proceeds perpendicularly to the TDM.[16] It is possible to infer the average orientation of the TDMs within a film,[17] which is done typically by either angle-resolved photoluminescence or variable angle spectroscopic ellipsometry (VASE) studies.[16,18,19] Yokoyama's fundamental work on small molecule orientation behavior in vacuum-deposited films has demonstrated that to minimize the surface energy, the ''first'' layer of the molecules deposited on the interface adopt horizontal orientation, and the horizontal orientation is fixed by successively overlaying molecules.[1] Indeed, the orientation of the TDM in vacuum-deposited films is influenced by not only the intrinsic anisotropy of the emitter molecule,[20] but also molecular backbone length,[21] molecular weight, and molecular thickness on the *z* axis.[22,23] There are now a number of examples of VD-OLEDs that contain highly horizontally oriented TADF emitters.[17] For SP-OLEDs, however, the emitters are simultaneously condensed and solidified during the spin-coating, and their isotropic

behavior in solution is largely conserved within film. Moreover, the solvent volatilization leaves voids in the film, which provides sufficient space for the emitters to re-orient to a thermodynamically more stable configuration, resulting in a net isotropic orientation.[24] Thus, unlike emitters that can show preferential horizontal orientation in vacuum-deposited films, emitters in solution-processed films do not show any preferred orientation. This is exemplified for the TADF emitter **DACT-II**, which shows 86% of horizontally orientation in vacuum-deposited doped films in CBP, but the same molecule is isotropic in solution-processed films.[25,26] A strategy to obtain highly horizontally oriented TDMs in solution-processed films must exploit intermolecular interactions to drive the assembly of higher order films.

Liquid crystalline (LC) materials can form highly ordered microstructures via intermolecular interaction and give rise to anisotropic properties.[27,28] The alignment direction of LC materials can be controlled by simple thermal treatment, electrical field treatment, and mechanical force treatment.[29–31] Luminous LC materials have been used as emitter in OLEDs due to their controllable photophysical and thermal properties, and charge carrier mobility.[32,33] Pal *et al*. reported a fluorescent discotic liquid crystal **DLC1.1** incorporating a tetraphenylethylene as an emitting core.[34] The material exhibits columnar hexagonal mesophases at room temperature, which were confirmed by POM and SAXS/WAXS experiments. The compound exhibited a Φ_{PL} of 82% and λ_{PL} of 505 nm as a 3 wt% doped CBP film. Non-doped solution-processed OLEDs with **DLC1.1** achieved an EQE_{max} of 4.4%.[34] Murawski *et al*. investigated the TDM orientation of the LC emitter perylene-3,4,9,10-tetracarboxylic tetraethyl ester (PTCTE), when doped in different host materials.[19] The TDM of PTCTE shows preferential horizontal orientation (72%

horizontal) as a 2 wt% doped TCTA:TPBi film but with a low Φ_{PL} of 14%; however, the orientation is isotropic in a TCTA:B3PYMPM film (Φ_{PL} of 13%).[19] As a result, the OLEDs based on PTCTE/TCTA:B3PYMPM exhibits very low EQE_{max} below 0.3% at λ_{EL} of 550 nm, while for device based on PTCTE/TCTA:TPBi showed an improved EQE_{max} of 0.8% at λ_{EL} of 580 nm.[19] Mesogenic phosphorescent emitters based on iridium and platinum have also been employed in solution-processed OLEDs, and these devices have the potential to show higher EQE_{max} due to the ability of the emitter to convert both singlet and triplet excitons to light.[35,36] Wang *et al*. reported two chiral, LC cyclometalated platinum complexes ***R*-Pt** and ***S*-Pt** where mesogenic groups were added to the *β*-diketonato ligand to induce liquid crystallinity.[37] Nematic phases are found for both complexes at 141 °C by a combination of POM, differential scanning calorimetry, and small-angle X-ray scattering.[37] An increase of the dissymmetry factor (g_{PL}) from 0.004 to 0.06 was observed for the annealed neat film of ***R*-Pt**, which hints at an ordered orientation after annealing; however, the TDM of ***R*-Pt** was not investigated in this work.[37] The Φ_{PL} of ***R*-Pt** and ***S*-Pt** are 75 and 44%, respectively, in degassed DCM. The solution-processed OLEDs based on ***R*-Pt** and ***S*-Pt** exhibit λ_{EL} of 540 nm and EQE_{max} of 11.3% and 7.5%, respectively, which indicates over 80% of IQE presuming the η_{out} is 20%.[37] Although there are examples of the use of both organic fluorescent and metal-based phosphorescent liquid crystals, to date there is only one recent report of a liquid crystalline TADF emitter. Bruce *et al*. presented the first two examples of TADF emitters showing liquid crystalline character by connecting alkoxy chains to the TADF emitting core 2,5-di(N,N'-carbazolyl)terephthalonitrile (**3b**) or 2,3,5,6-tetra(N,N'-carbazolyl)terephthalonitrile (**4b**).[38] Columnar hexagonal mesophase are observed for **3b** and **4b**,

at 181 °C and 191 °C, and both compounds exhibit delayed emission in toluene solution with delayed lifetimes of 5.5 μs and 1.0 μs, respectively.[38] However, neither emitter orientation nor the use of these compounds in OLEDs were investigated. Janssen *et al*. tried to control the emitter orientation in solution-processed devices by doping emitters into a nematic LC host material poly(9,9-dioctylfluorene) (PFO), which can form horizontally aligned film after annealing.[39] However, this host/guest system is only effective for certain *p*-phenylenevinylene oligomers and did not improve the orientation of the TADF emitter ***t*Bu-DACT-II**, which shows the same vertical preferential (42% vertical) orientation in solution-processed PFO or TPBi films.[39] These studies opened a new horizon for the use of liquid crystalline materials in OLEDs, especially in terms of the tuning of the film morphology and molecular orientation.

In this Chapter, we represent the first example of a liquid crystalline MR-TADF emitter. The structure is based on our previously reported MR-TADF compound **DiKTa**, which was elaborated with mesogenic groups consisting of 1,6-dioxyhexyl-[1,1'-biphenyl]-4-carbonitrile chains. The compound **DiKTaLC** (Figure **6.1**) exhibits MR-TADF character with delayed lifetime of 70.2 μs, and narrow emission spectra with FWHM = 53 nm and λ_{PL} = 514 nm, as a neat thin film with a Φ_{PL} of 41%. The liquid crystalline character of **DiKTaLC** was confirmed by POM, as the material displays nematic liquid crystalline phase under 108 °C. The as-prepared spin-coated neat film of **DiKTaLC** shows preferential horizontal orientation with a = 0.26, which is preserved after annealing at 100 °C. The electroluminescence performance of **DiKTaLC** in OLEDs is presently being investigated.

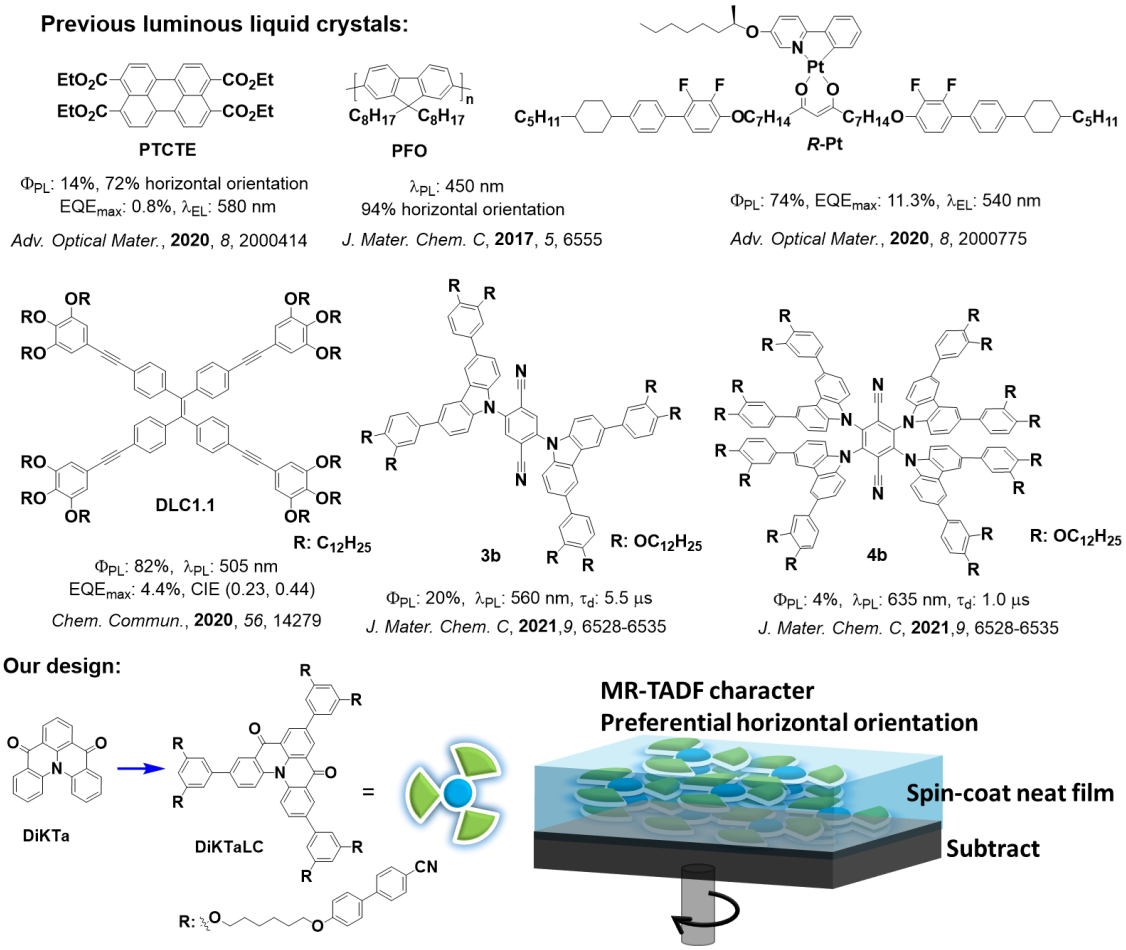

Figure **6.1**. Molecular structures of previously reported luminous liquid crystals and our MR-TADF liquid crystal, **DiKTaLC**.

6.2 Computational Studies

We first wished to establish the optoelectronic properties of the MR-TADF emitter core and how these differ from the reference compound, **DiKTa**. We thus modelled the optoelectronic properties of a model system, **DiKTaPh(OMe)$_2$**, by spin-Component Scaling Coupled-Cluster second-order approximate coupled-cluster (SCS-CC2) calculations, which we have previously shown to be more accurate than density functional theory.[40,41] We also modelled

at the PBE0/6-31G(d,p) level of theory both **DiKTaPh(OMe)$_2$** and **DiKTaLC**.[42,43] The electron density distribution of the HOMO and LUMO obtained by DFT of **DiKTaPh(OMe)$_2$** and **DiKTaLC** are similar while the difference density plots obtained by SCS-CC2 of **DiKTaPh(OMe)$_2$** show the characteristic alternating pattern associated with MR-TADF compounds; the S_2 state possesses strong n-π* character. The mesogen chains of **DiKTaLC** are not involved in the HOMO and LUMO distributions. The HOMO and LUMO energies of **DiKTaPh(OMe)$_2$** are -5.66 eV and -2.00 eV, respectively, while the HOMO energy of **DiKTaLC** is 0.17 eV destabilized (-5.83 eV) and LUMO energy is 0.17 eV stabilized (-2.17 eV). As a result, the HOMO/LUMO energy gap (ΔE_g) is the same for both compounds at 3.66 eV (Figure **6.2a**).

The energies of the S_1 and T_1 states of **DiKTaPh(OMe)$_2$** are calculated to be 3.28 eV and 3.03 eV, respectively, which are slightly stabilized compared to those of **DiKTa** (S_1 = 3.45 eV, T_1 = 3.18 eV) or **Mes$_3$DiKTa** (S_1 = 3.32 eV, T_1 = 3.06 eV), due to the similar inductive electron-accepting effect of the *meta*-disposed dimethoxyphenyl groups.[44] The corresponding ΔE_{ST} of **DiKTaPh(OMe)$_2$** is 0.25 eV, which is modestly decreased compared to that of **DiKTa** and **Mes$_3$DiKTa** (0.27 and 0.26 eV, respectively).[44] Like **DiKTa** and **Mes$_3$DiKTa**, high *f* from S_1 is predicted to be 0.22 for **DiKTaPh(OMe)$_2$**, which reflects the significant overlap of the electron density distributions of the HOMO and LUMO of the short-range charge transfer excited state. The S_1 state TDM vector of the **DiKTaPh(OMe)$_2$** is calculated to be (–0.45 D, –0.06 D, –0.65 D) with a small angle of 8.2^o to the plane of the molecule (X/Y plane in Figure **6.2b**). This result indicates that the TDM orientation of the **DiKTaLC** highly co-aligns with the molecular orientation.

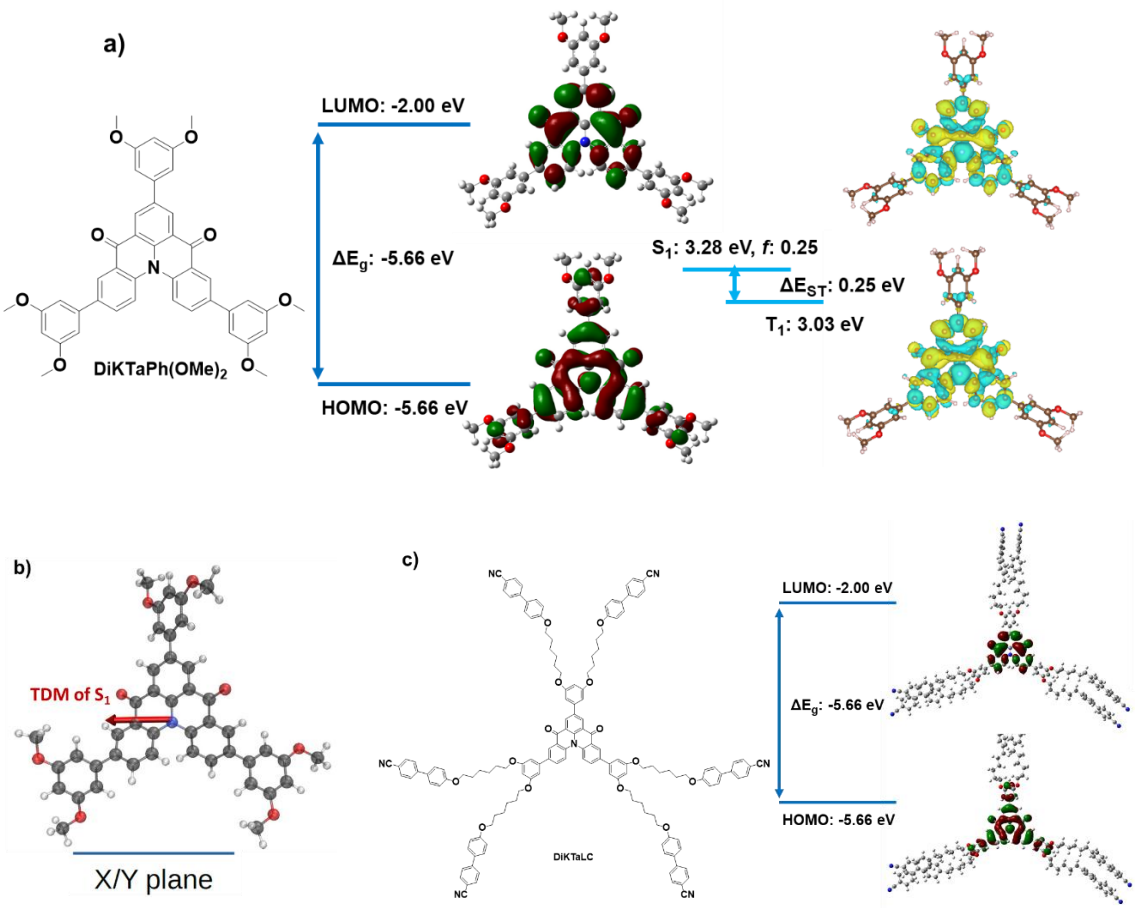

Figure **6.2**. a) Topology of HOMO and LUMO orbitals and difference density plots of lowest singlet and triplet excited states for **DiKTaPhOMe**. b) S_1 state TDM vector of **DiKTaPhOMe**. c) Topology of HOMO and LUMO orbitals for **DiKTaLC**.

6.3 Synthesis

The mesogenic **BrC6BPC** intermediate was obtained in two steps of S_N2 reactions between 1,6-dibromohexane and 4-Cyano-4'-hydroxybiphenyl and then 5-bromobenzene-1,3-diol with assistance of cesium carbonate in acetone as outlined in Scheme **6.1**. The **BrC6BPC** was then converted to **BPinC6BPC** under palladium-catalysed Miyaura borylation conditions.[49]

The intermediate **Br$_3$DiKTa** was synthesized following our previously developed protocol,[44] and this was coupled to the mesogenic group, **BPinC6BPC**, under Suzuki-Miyaura cross-coupling conditions in 68% yield to afford **DiKTaLC**.[50] The identity and purity of the title compound was determined by a combination of ^{1}H and ^{13}C NMR spectroscopy, high resolution mass spectrometry, melting point, elemental analysis, and high-performance liquid chromatography.

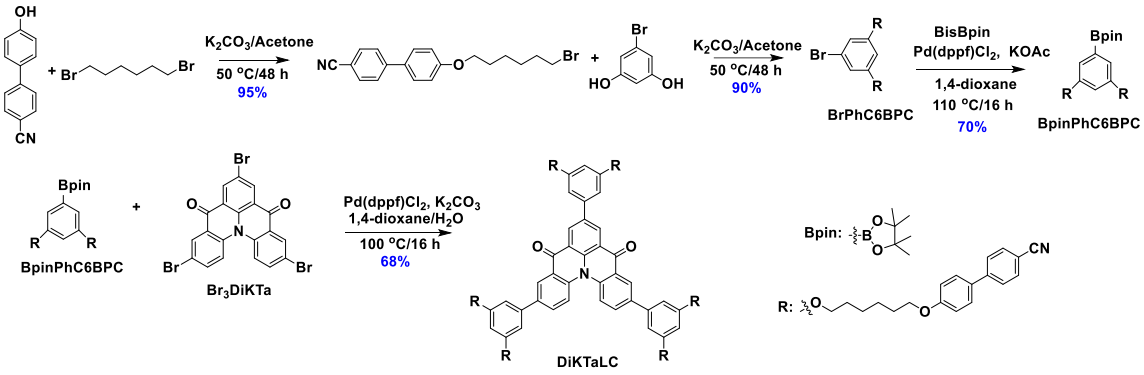

Scheme **6.1**. Synthesis of **DiKTaLC**.

6.4 Electrochemistry

The electrochemical properties of **DiKTaLC** were investigated by CV and DPV in DCM using (*n*-Bu$_4$N)PF$_6$ as the supporting electrolyte (Figure **6.3**). The CV trace of **DiKTaLC** exhibits irreversible reduction and oxidation waves with E^{red} of -1.49 V and E^{ox} at 1.34 V vs SCE, determined from the DPV. The corresponding HOMO and LUMO values for of **DiKTaLC** are -5.68 and -2.84 eV, respectively. Compared to the HOMO/LUMO values of -5.86/-3.26 for **Mes$_3$DiKTa**,[44] **DiKTaLC** shows more stabilized HOMO and destabilized LUMO values, which

is ascribe to the electron-accepting properties of the peripheral groups and also match our DFT calculation.

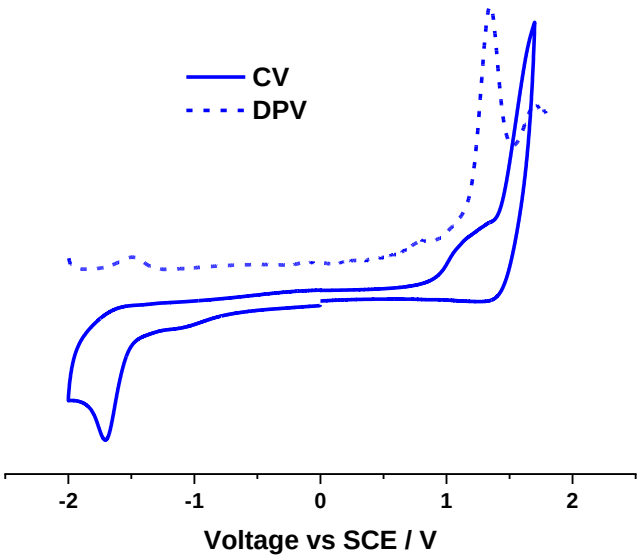

Figure **6.3**. CV and DPV traces of **DiKTaLC** in DCM with 0.1 M n-Bu_4NPF_6 as the supporting electrolyte. Measured condition: scan rate 100 mV/s, calibrated against a Fc/Fc^+ redox couple and referenced 0.46 V versus SCE.[45]

6.5 Photophysical Properties

The absorption spectrum in toluene of **DiKTaLC** (Figure **6.4a**) mirrors those of **DiKTa** and **Mes$_3$DiKTa** with a low-energy band at 464 nm at a molar extinction coefficient (ε) of around 20 $\times 10^3$ M^{-1} cm^{-1} associated with the SRCT state,[45] and a the high intensity absorption ($\varepsilon > 100 \times 10^3$ M^{-1} cm^{-1}) band at 305 nm attributed to a superposition of locally excited π-π*

transitions from the 4-cyanobiphenyl moieties and the **DiKTa** core.[46] The PL spectrum of **DiKTaLC** in toluene shows a narrow emission band (FWHM = 33 nm) with an emission maximum, λ_{PL}, of 487 nm, and a small Stokes shift of 24 nm. The Φ_{PL} of **DiKTaLC** is 39% in oxygen-free toluene, which is comparable to the 37% measured for **Mes$_3$DiKTa**.[45] **DiKTaLC** shows structured vibronic progression in nonpolar cyclohexane, which is resolved in higher polar solvents. The moderate positive solvatochromism is characteristic of MR-TADF compounds, which emit from a SRCT state (Figure **6.4b**). Compared to structureless fluorescence spectra at room temperature in 2-methyl-tetrahydrofuran, the prompt fluorescence and phosphorescence spectra at 77 K show a more pronounced structured emission (Figure **6.4c**). The S_1 (2.74 eV) and T_1 (2.55 eV) energies of **DiKTaLC** were determined from the onset of prompt fluorescence and phosphorescence spectra. The ΔE_{ST} of 0.19 eV is close to the SCS-CC2 calculated value of 0.25 eV, which is sufficiently small to enable RISC process. The time-resolved PL in degassed toluene (Figure **6.4d**) shows a prompt fluorescence lifetime (τ_p) of 7 ns and a delayed emission lifetime (τ_d) of 1.0 μs, which is only a very small contribution (0.5%) to the overall emission decay.

We next measured the photophysical properties of **DiKTaLC** in 10 wt% doped PMMA and neat films. The 10 wt% doped films and neat films of **DiKTaLC** show almost identical emission spectra (Figure **6.4a**) that are modestly red-shifted at 512 nm and 514 nm, and slightly broadened with FWHM of 50 nm and 53 nm, respectively, compared to the PL in toluene. The Φ_{PL} values of **DiKTaLC** in 10 wt% doped films and neat films are 52% and 41%, respectively. The high Φ_{PL} of **DiKTaLC** in the neat film indicates that the pendant mesogenic chains can readily suppress the concentration quenching of the planar emitting core, which has been observed

to varying degrees in both **DiKTa** and **Mes$_3$DiKTa**.[45] The time-resolved PL decays of **DiKTaLC** exhibits the same τ_p of 7 ns in both doped and neat films, while the average delayed emission lifetimes are 155.5 µs and 70.2 µs, respectively, significantly longer than that observed in toluene (Figure **6.5**). Temperature-dependent time-resolved PL decays reveal that the delayed emission is thermally activated in both doped and neat films (Figure **6.5**).

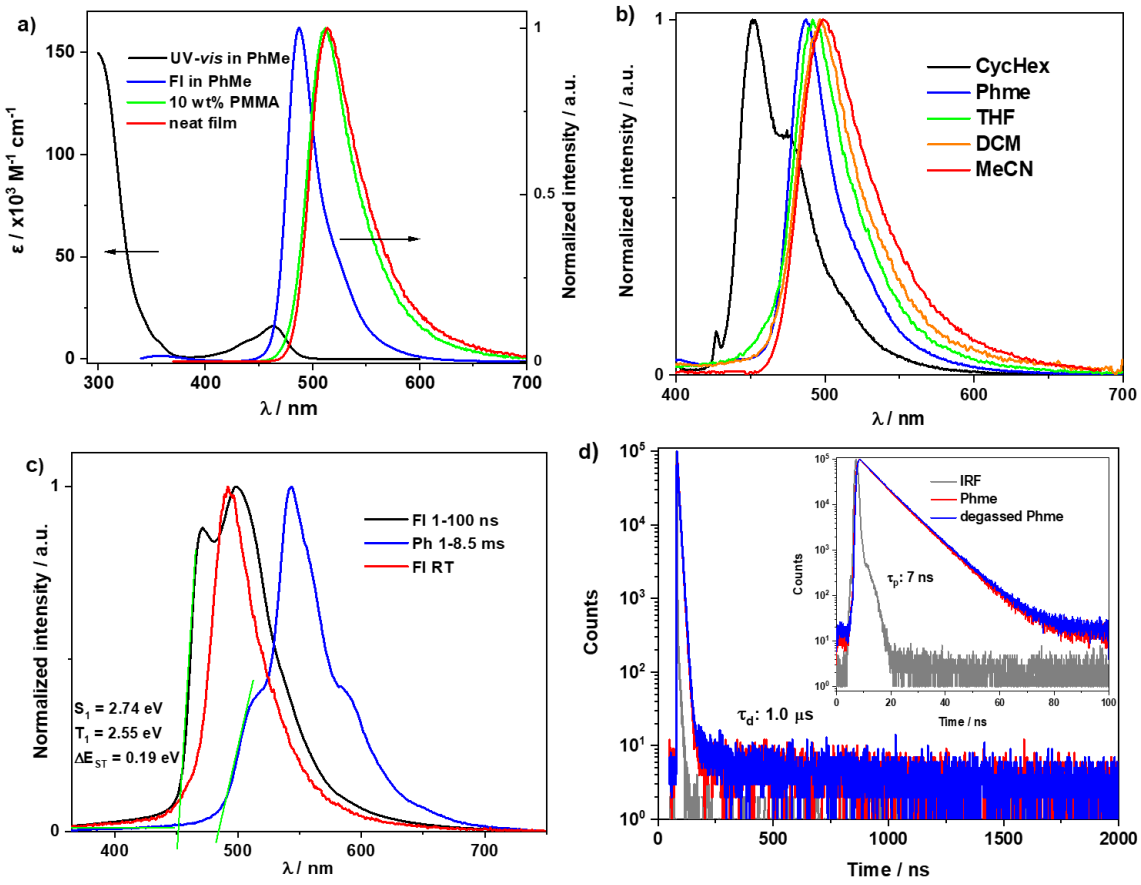

Figure **6.4**. Photophysics of **DiKTaLC** in solutions. a) UV-*vis* absorption and fluorescence in toluene. b) Solvatochromatic PL study of **DiKTaLC**, λ_{exc} = 340 nm. c) Steady-state PL in room temperature, prompt PL at 77 K (delay: 1 ns, gate: 100 ns), and phosphorescence spectra at 77 K (delay: 1 ms, gate: 8.5 ms) in 2-methyl-tetrahydrofuran, λ_{exc} = 343 nm. d) Time resolved PL **DiKTaLC** in aerate and degassed toluene, λ_{exc} = 379 nm.

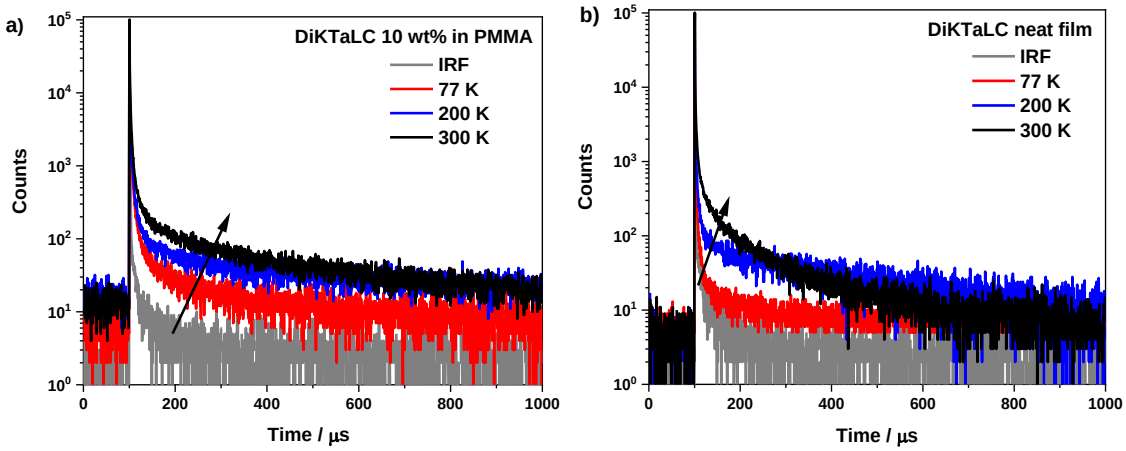

Figure **6.5**. Temperature-dependent time-resolved PL decay spectra of a) 10 wt% doped PMMA films and b) neat film of **DiKTaLC**.

6.6 Thermal properties

Liquid crystal materials usually show characteristic thermal behavior. Differential scanning calorimetry (DSC), polarising optical microscopy (POM), wide and small angle Xray scattering (WAXS and SAXS) measurements were conducted to gain insight into the thermal properties of **DiKTaLC** and to confirm the liquid crystalline behavior of the compound. The DSC trace of **DiKTaLC** exhibits a glass transition (T_g) at 82 °C during the first heating cycle and cleared into the isotropic phase at 110 °C (Figure **6.6**). During a further two heating / cooling cycles, only the clearing transition at 110 °C could be observed. The POM investigation of **DiKTaLC** reveals unfeatured textures (Figure **6.7a**) at 90 °C; further, the textures changed upon application of a shear force and exhibits a combination of birefringence and fluidity, which is characteristic for liquid crystals. Although no crystallization was observed via POM, the textures could not be sheared below 80 °C indicating the formation of a glass. The uniform textures with

Schlieren-like defects in Figures **6.7b** and **6.7c** and the thread-like texture in Figure **6.7d** hint at a nematic liquid crystalline phase. Homeotropic alignment (aromatic core lying parallel to substrate) was found around the clearing point where shearing resulted in characteristic "flashes" of uniform textures that quickly (1-5 s) realign in a homeotropic fashion. Further, the cooling process on glass slides, silylated glass slides, and polyimide coated slides led to reorientation of the mesogenic moiety and resulted in grainy or thread-like textures (Figure **6.7d**).

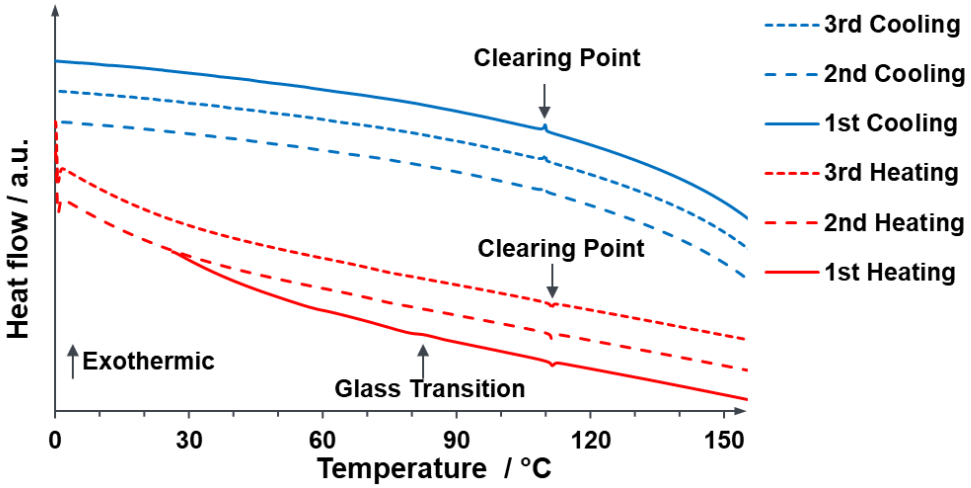

Figure **6.6**. DSC traces of **DiKTaLC** (range: 0 – 160 °C, rate: 5 K / min).

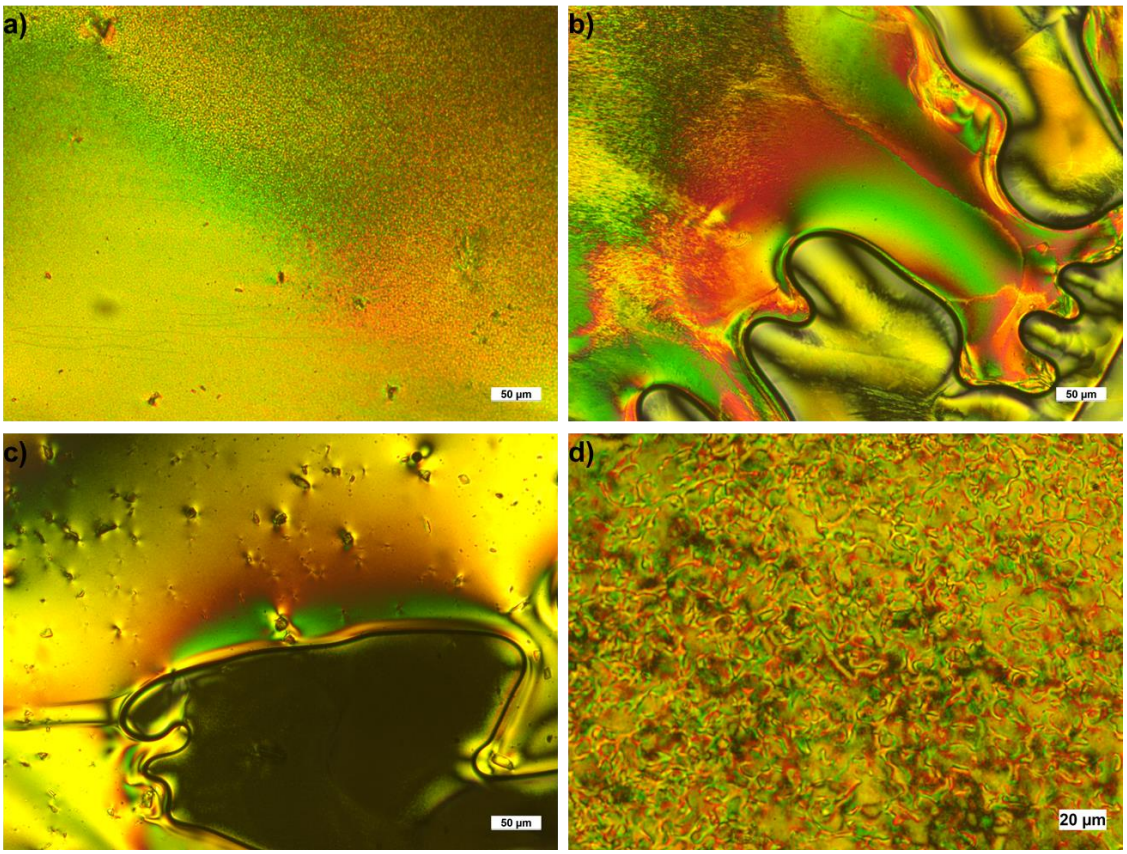

Figure **6.7**. POM textures of **DiKTaLC** between glass slides taken upon cooling from the isotropic phase at a) 90 °C, b) 105 °C, c) 108 °C and d) 108 °C between silylated glass slides (cooling rate: 1 K / min, 100 × magnification)

X-ray scattering profiles of **DiKTaLC** reveal three diffuse reflexes (2θ = 2.9°, 5.2° and 17.7°) at 100 °C. The wide-angle reflex (halo) at 2θ = 17.7° corresponds to a distance of 5 Å and results from the distance of the (molten) side chains. The small angle reflexes at 2θ = 2.9°, 5.2° correspond to distances of 16.9 Å and 31.0 Å, respectively. Typically, only one small angle reflex (resulting from the lateral molecule to molecule distance) would be expected for nematic discotic liquid crystals. This reflex correlates with the molecular size but is typically smaller due to overlap

of the molecules in the fluid nematic phase. Several calamitic mesogens (i.e., rod-shaped) based on cyanobiphenyls exhibit an equilibrium of monomeric and dimeric species in their nematic phase, resulting in two small angle reflexes.[47] Such an aggregation behavior could explain the occurrence of two reflexes in case of **DiKTaLC**. Thus, from the diffuse reflexes and the characteristic Schlieren and thread-like textures from the POM study, we can conclude **DiKTaLC** to be nematic discotic (N_D); however, we could not observe any π-π reflex in the wide angle regime typical for columnar nematic (N_{col}) mesogens.

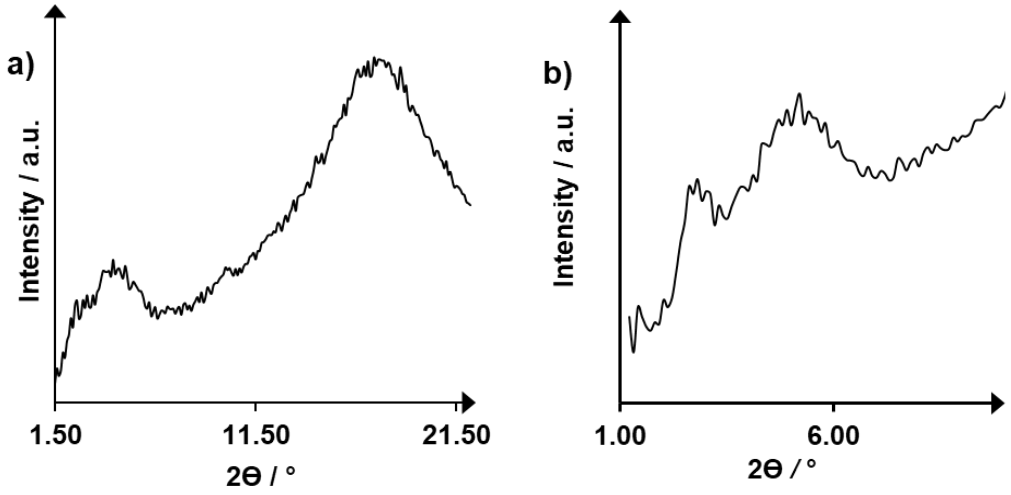

Figure **6.8**. a) WAXS profile of **DiKTaLC** recorded at 100 °C and b) SAXS profile of **DIKALC** recorded at 100 °C with diffuse reflexes at 2θ = 2.9, 5.2 and 17.7 °.

6.7 Orientation studies

To quantitatively estimate the degree of **DiKTaLC** orientation in amorphous organic films, variable angle spectroscopic ellipsometry (VASE) and angle-resolve PL measurements were applied to the neat film of **DiKTaLC**. The spin-coated neat films were

prepared on the hydrophilic glass substrate or silicon substrate using different concentrations of **DiKTaLC** in chloroform (10 or 20 mg/mL) at spin speeds of 4000 RPM, followed by 60 seconds of drying step under nitrogen flow. The VASE and angle-resolve PL measurements were taken both before and after 1 hour of annealing at 100 °C. The results of the VASE analysis are shown in Figure **6.9**, and the order parameter (*S*) of the TDM in the films can be calculated from the absorption extinction coefficients in the horizontal and vertical directions (k_o and k_e). The resulting anisotropy factor, *a*, was calculated from equation (6.2) :

$$S = \frac{k_e - k_o}{k_e + 2k_o} = \frac{3a-1}{2} \qquad (6.2)$$

For an amorphous film, $a = 0.33$ would correspond to perfectly isotropic orientation, while $a < 0.33$ indicates a preferentially horizontal orientation. The VASE analysis shows that for unannealed film, the values of *a* at 290 nm and 475 nm are 0.20 and 0.29, respectively, which indicate 80% and 71% of horizontally orientation, respectively. For the annealed film, the TDM at 293 nm shows 94% of horizontally orientation ($a = 0.06$), and at 474 nm the TDM remains orientation with 69% of horizontally orientation ($a = 0.31$). The orientation of the TDM of the emitters in the film were separately obtained by angle-resolved PL spectroscopy measurements. The PL spectra of the annealed film show a slight blue-shift in the peak wavelength and an increased PL intensity. The resulting anisotropy factor *a* was derived by fitting the angle-resolved PL spectra of the samples at the peak wavelength, and a birefringence constant was used for these fits. As shown in Figure **6.10**, both the unannealed and annealed films exhibit preferential horizontal orientation with $a = 0.26$, which matches the result from VASE at 475 nm. As the absorption at 290 nm mainly comes from the 4-cyanobiphenyl moieties of the mesogenic chains,

the changes in the anisotropy factor observed by VASE indicate that there is mesogenic chain reorganization during the annealing process, which is characteristic of discotic liquid crystals,[48] and is consistent with the POM measurements. While the absorption at 475 nm and the PL emission originates from the short-range charge-transfer of the discotic emitting core, the consistency between the anisotropy factor measured by both VASE and angle-resolved PL spectroscopy measurements indicate that the long-range alignment of the discotic cores is preserved during the annealing process.

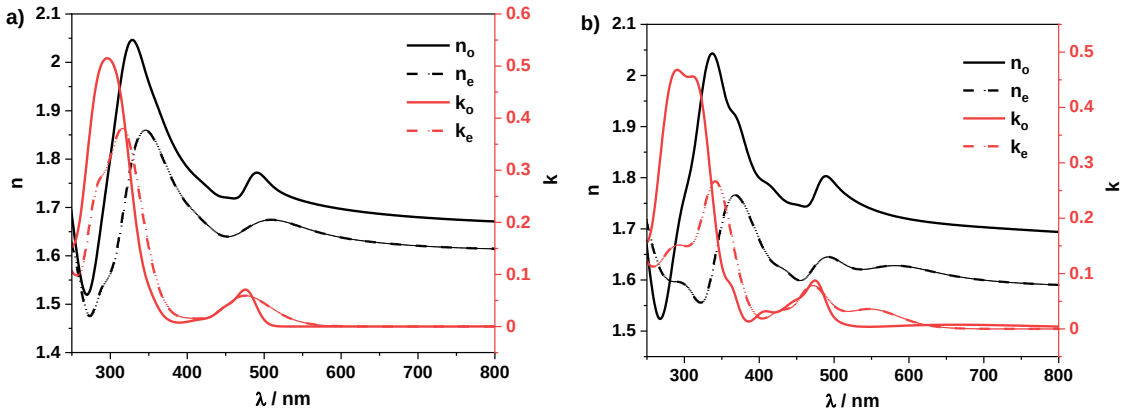

Figure **6.9**. Anisotropic refractive indices and extinction coefficients of **DiKTaLC** neat film a) before and b) after annealing. The black solid and dashed lines show the refractive indices in the horizontal and vertical directions (n_o and n_e), respectively. The red solid and dashed lines show the extinction coefficients in the horizontal and vertical directions (k_o and k_e), respectively.

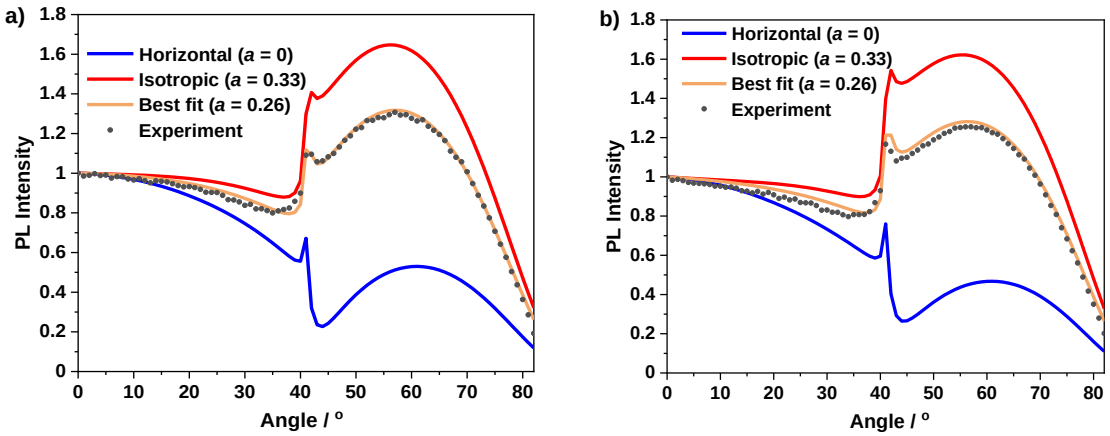

Figure **6.10**. Angular dependence of the PL intensity at the peak emission wavelength of **DiKTaLC** films a) before and b) after annealing. The black dots are the experimental data. The other curves represent the simulated intensity for a perfect horizontal alignment of emitters (blue line), for an isotropic orientation (red line), and for the best fit to the experimental data (grey line). The corresponding anisotropy factors *a* for each curve are indicated in the legend of each panel. All data sets were normalized to the intensity at 0° of the corresponding curves.

6.8 Conclusions and outlook

By connecting mesogenic chains onto a MR-TADF emitting core, **DiKTaLC**, an emitter exhibits MR-TADF and liquid crystal character in the solid state was synthesized and characterized. **DiKTaLC** exhibits a narrow emission spectrum (FWHM = 53 nm, λ_{PL} = 514 nm) and Φ_{PL} of 41% in neat film. The time-resolved PL decay of **DiKTaLC** exhibits τ_p of 7 ns and τ_d of 70.2 µs in neat film and the temperature-dependent time-resolved decays further reveal that the delayed emission is thermally activated in neat film. The liquid crystal character of **DiKTaLC** was confirmed by POM and DSC measurements, where the material displays nematic liquid

crystalline phase under 108 ºC. The as prepared spin-coated neat film of **DiKTaLC** shows preferential horizontal orientation of the TDM, which can improve the η_{out} in OLEDs. The electroluminescence properties of **DiKTaLC** in OLEDs are under investigation with collaborators.

6.9 Experimental section

General consideration

All experiments were carried out with commercial solvents from Fisher Scientific Ltd, except where specifically mentioned. Commercially obtained chemicals were used as received. All manipulations were carried out under an inert atmosphere using standard Schlenk line techniques. ^{1}H NMR, and ^{13}C NMR were recorded at room temperature on a Bruker Avance spectrometer at 400 MHz and 100 MHz, respectively. ^{1}H NMR and ^{13}C NMR spectra were referenced to the residual solvent peaks ($CDCl_3$ = 7.26 ppm for ^{1}H NMR and 77.16 ppm for ^{13}C NMR). The following abbreviations have been used for multiplicity assignments: “s” for singlet, “d” for doublet, “t” for triplet, “m” for multiplet and “br” for broad. Elemental analysis was measured by London Metropolitan University. Samples for high resolution mass spectrum (HRMS) were sent to the National Mass Spectrometry Facility in Swansea (EPSRC) for analysis by nano-electrospray on an Orbitrap instrument.

Materials and synthesis

N,N-bis(2-methoxycarbonylphenyl)aniline (**MeCA**)

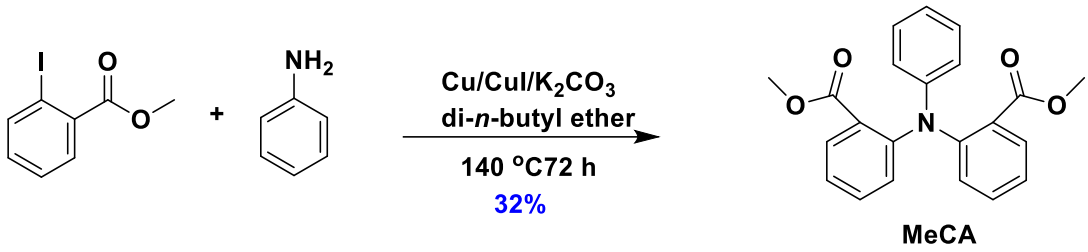

To a 2-neck flask held under nitrogen was charged with aniline (2.3 mL, 25 mmol, 1 equiv.), methyl 2-iodobenzoate (11.0 mL, 75 mmol, 3 equiv.), copper (0.47 g, 7.4 mmol, 0.3 equiv.), copper(I) iodide (0.32 g, 1.73 mmol. 0.07 equiv.), anhydrous potassium carbonate (10.5 g, 75 mmol, 3 equiv.), and 25 mL anhydrous di-*n*-butyl ether. The resulting reaction mixture was heated to reflux and stirred for 3 days. After cooling to room temperature, the reaction mixture was filtered through a pad of celite. The filtrate was then mixed with dichloromethane and washed with water (3 × 50 mL). The organic layer was then dried using anhydrous sodium sulfate and concentrated under reduced pressure. The resulting crude product was purified by column chromatography on silica gel (EtOAc : hexane = 20 : 80). The corresponding fractions were collected and evaporated under reduced pressure to afford the desired product as a white S8 crystalline solid, which was then filtered and washed with hexane.

Yield: 32% (2.9 g). **R_f**: 0.54 (EtOAc : hexane = 20 : 80 on silica gel). Mp: 145 °C. **^{1}H NMR (400 MHz, $CDCl_3$) δ (ppm)**: 7.65 (dd, *J* = 7.7, 1.6 Hz, 2H), 7.43-7.39 (m, 2 H), 7.20-7.11 (m, 6 H), 6.88-6.84 (m, 1 H), 6.77-6.75 (m, 2 H), 3.39 (s, 6 H). **^{13}C NMR (100 MHz, $CDCl_3$) δ (ppm)**: 168.0, 148.6, 146.6, 132.8, 131.1, 129.1, 128.8, 128.0, 124.1, 121.8, 120.8, 51.9. **HRMS (ESI-MS) $[M+H]^+$ Calculated**: ($C_{22}H_{19}NO_4$) 362.1387; **Found**: 362.1387.

Dimethyl 6,6'-((4-bromophenyl)azanediyl)bis(3-bromobenzoate) (**3Br-MeCA**)

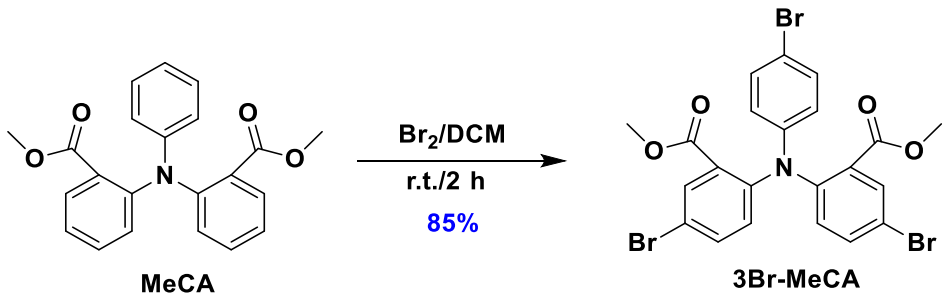

To **MeCA** (4 g, 11.10 mmol, 1 equiv.) in 100 mL dichloromethane, bromine (1.7 mL, 33.3 mmol, 3 equiv.) was added dropwise. After 1 h stirring at room temperature, further bromine (0.1 mL) was added dropwise, and stirring continued for 0.5 h. The reaction was quenched by the addition of a 10% solution of sodium hydroxide (50 mL). The organic layer was separated, washed with water (3 × 50 mL), dried with anhydrous sodium sulfate and concentrated under reduced pressure. The crude product was purified by flash chromatography on silica gel (10 : 90 EtOAc : hexanes) to afford the **3Br-MeCA** as a light yellow solid.

Yield: 85% (5.6 g). **R_f**: 0.45 (10 : 90 EtOAc : hexanes on silica gel). **Mp**: 134 - 136 °C. **^{1}H NMR (500 MHz, $CDCl_3$) δ (ppm)**: 7.81 (d, *J* = 2.4 Hz, 2H), 7.53 (dd, *J* = 8.6, 2.4 Hz, 2H), 7.26-7.22 (m, 2H), 7.05 (dd, *J* = 8.6, 2.4 Hz, 2H), 6.61-6.58 (m, 2H), 3.46 (s, 6 H). **^{13}C NMR (125 MHz, $CDCl_3$) δ (ppm)**: 166.0, 147.1, 144.7, 136.1, 134.1, 132.2, 130.6, 129.4, 122.1, 117.8, 114.8, 52.4. **HRMS (ESI-MS) $[M+H]^+$ Calculated**: ($C_{22}H_{16}{}^{79}Br_3NO_4$); 595.8702; **Found**: 595.8700.

3,7,11-tribromoquinolino[3,2,1-de]acridine-5,9-dione (Br_3DiKTa)

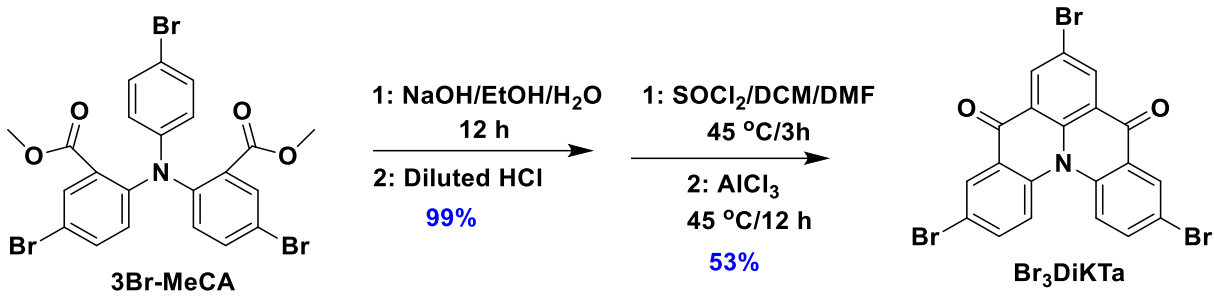

Compound **3Br-MeCA** (5 g, 8.4 mmol, 1 equiv.) was combined with sodium hydroxide (1.68 g, 42 mmol, 5 equiv.) in 40 mL of an ethanol/water (1/1) mixture. The reaction was heated to reflux for 12 h. After cooling to room temperature, the pH was adjusted to 2-3 by addition of dilute hydrochloric acid. The diacid precipitated as a light green solid and was collected by vacuum filtration, washed thoroughly with water, dried under vacuum (4.75, 99% yield) and used without further purification and characterization. The diacid (4 g, 7.1 mmol, 1 equiv.) was dispersed in 60 mL dichloromethane under a nitrogen atmosphere. To the reaction mixture were added sequentially thionyl chloride (1.03 mL, 14.2 mmol, 2 equiv.) and 7 drops of DMF. After 3 h under reflux, the reaction mixture was cooled to room temperature. Under a positive flow of nitrogen, aluminum chloride (9.46 g, 71 mmol, 10 equiv.) was added slowly (exothermic reaction). After refluxing for 12 h, the reaction mixture was cooled to room temperature and the reaction quenched by dropwise addition of water with vigorous stirring (exothermic reaction). The resulting mixture was combined with dichloromethane (150 mL), the organic layer was then separated. The remaining aqueous layer was washed with dichloromethane (3 × 50 mL) to completely remove the yellow insoluble product from water. The organic fractions were combined, and the solvent volume was concentrated under reduced pressure. The product was filtered and washed with methanol and hexane to afford the desired product as a yellow solid.

Yield: 53% (2.0 g). **M_p**: Decomposed at 364 °C. **^{1}H NMR (500 MHz, CDCl3) δ (ppm)**: 8.81 (s, 2H), 8.59 (d, *J* = 2.2 Hz, 2H), 7.95 (d, *J* = 8.9 Hz, 2H), 7.81 (dd, *J* = 8.9, 2.5 Hz, 2H). ^{13}C NMR was not recorded due to poor solubility of this compound. **HRMS (ESI-MS) $[M]^+$ Calculated**: 530.8100 ($C_{20}H_8{}^{79}Br_3NO_2$); Found: 530.8088.

4'-((6-bromohexyl)oxy)-[1,1'-biphenyl]-4-carbonitrile (BrC6CN)

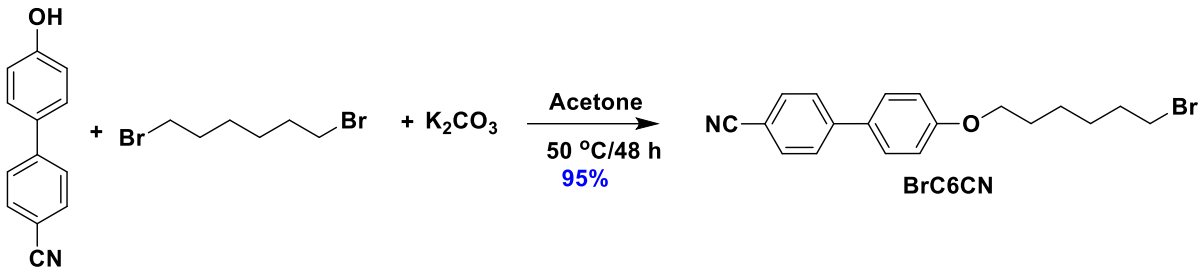

To a 250 mL flask were added 4'-hydroxy-[1,1'-biphenyl]-4-carbonitrile (2.0 g, 10 mmol, 1 equiv.), 1,6-dibromohexane (7.3 g 30 mmol, 3 equiv.), potassium carbonate (4.2, 30 mmol, 3 equiv.). The mixture was degassed by three cycles of vacuum-nitrogen purging and 50 mL of acetone was injected. The mixture was stirred at 50 °C for 24 h under nitrogen atmosphere. After completion of reaction, 50 mL of water was added to the reaction mixture and extracted with DCM (3 × 100 mL). The combined organic layers were dried with anhydrous magnesium sulfate. The organic solvent was removed under reduced pressure and the crude product was purified by silica gel column chromatography. DCM/Hexane=1/4 was used as eluent to afford **BrC6CN** as a white solid.

Yield: 95% (3.4 g). **R_f**: 0.45 (25% DCM/hexanes on silica gel). **Mp**: 56 °C. **^{1}H NMR (400 MHz, $CDCl_3$) δ (ppm)**: 7.75 – 7.62 (m, 4H), 7.55 (d, J = 8.8 Hz, 2H), 7.01 (d, *J* = 8.8 Hz, 2H), 4.04 (t, *J* = 6.4 Hz, 2H), 3.45 (dt, *J* = 7.9, 6.8 Hz, 2H), 2.03 – 1.79 (m, 4H), 1.69 – 1.38 (m, 4H).**^{13}C NMR (101 MHz, $CDCl_3$) δ (ppm)**: 160.8, 159.7, 145.3, 132.6, 131.4, 122.8, 115.1, 110.2, 100.6, 68.3, 31.6, 529.2, 25.8, 22.6, 14.0. **HRMS (ESI-MS) $[M+1]^+$ Calculated**: ($C_{19}H_{20}{}^{79}BrNO$); 358.0807; **Found**: 358.0804.

4',4'''-((((5-bromo-1,3-phenylene)bis(oxy))bis(hexane-6,1-diyl))bis(oxy))bis(([1,1'-biphenyl]-4-carbonitrile)) (BrPhC6BPC)

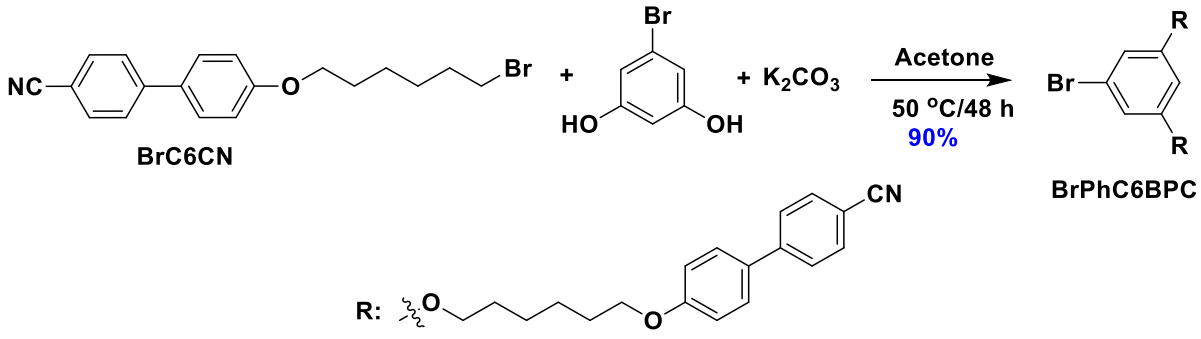

To a 100 mL flask were added **BrC6CN** (1.8 g, 5 mmol, 2.5 equiv.), 5-bromobenzene-1,3-diol (380 mg, 2 mmol, 1 equiv.), and potassium carbonate (840 mg, 6 mmol, 3 equiv.). The mixture was degassed by three cycles of vacuum-nitrogen purging and 50 mL of acetone was injected. The mixture was stirred at 50 °C for 24 h under nitrogen atmosphere. After completion of reaction, 20 mL of water was added to the reaction mixture and extracted with DCM (3 × 50 mL). The combined organic layers were dried with anhydrous magnesium sulfate. The organic solvent was

removed under reduced pressure and the crude product was purified by silica gel column chromatography. DCM/Hexane=1/2 was used as eluent to afford **BrPhC6BPC** as a white solid.

Yield: 90% (1.3 g). **R_f**: 0.45 (25% DCM/hexanes on silica gel). **Mp**: 133 °C. **^{1}H NMR (400 MHz, $CDCl_3$) δ (ppm)**: 7.76 – 7.63 (m, 8H), 7.58 – 7.53 (m, 4H), 7.02 (dd, *J* = 8.9, 2.5 Hz, 4H), 6.67 (d, *J* = 2.2 Hz, 2H), 6.39 (t, *J* = 2.2 Hz, 1H), 4.05 (q, *J* = 6.3 Hz, 8H), 3.95 (t, *J* = 6.3 Hz, 8H), 1.97 – 1.75 (m, 0H), 1.59 (dp, *J* = 16.1, 3.6, 3.0 Hz, 8H). **^{13}C NMR (101 MHz, $CDCl_3$) δ (ppm)**: 160.7, 159.7, 145.2, 132.6, 131.4, 128.3, 127.1, 122.9, 119.1, 115.1, 110.2, 110.1, 100.6, 68.1, 29.2, 25.9. **HRMS (ESI-MS) $[M+NH_4]^+$ Calculated**: ($C_{44}H_{47}{}^{79}BrN_3O_4$); 760.2744; **Found**: 760.2741.

4',4'''-((((5-(4,4,5,5-tetramethyl-1,3,2-dioxaborolan-2-yl)-1,3-phenylene)bis(oxy))bis(hexane-6,1-diyl))bis(oxy))bis([1,1'-biphenyl]-4-carbonitrile) (BpinPhC6BPC)

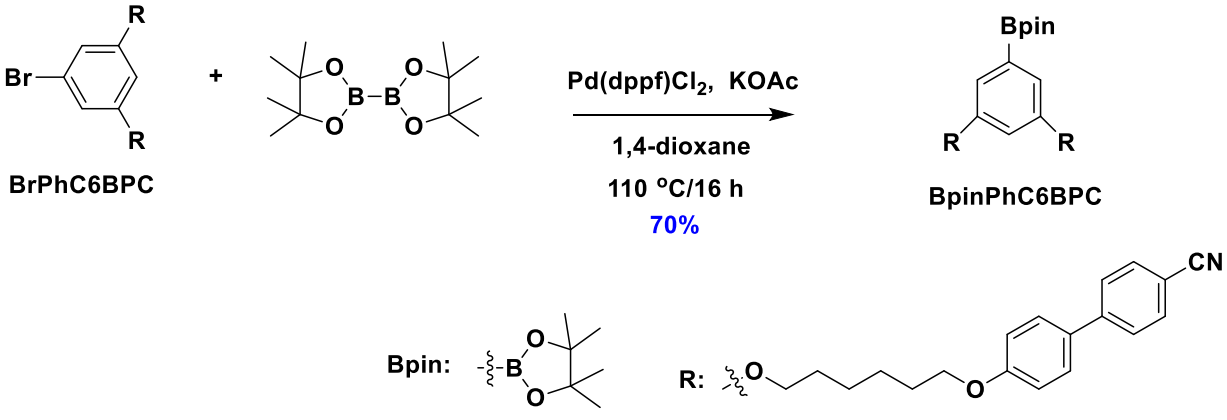

To a 100 mL flask were added **BrPhC6BPC** (1.5 g, 2 mmol, 1 equiv.), bis(pinacolato)diboron (750 mg, 3 mmol, 1.5 equiv.), Pd(dppf)Cl_2 (150 mg, 0.2 mmol, 0.1 equiv.) and potassium acetate (600 mg, 6 mmol, 3 equiv.). The mixture was degassed by three cycles of vacuum-nitrogen purging and 20 mL of 1,4-dioxane was injected. The mixture was stirred at 110 ºC for 16 h under nitrogen atmosphere. After completion of reaction, 20 mL of water was added to the reaction mixture and extracted with DCM (3 × 50 mL). The combined organic layers were dried with anhydrous magnesium sulfate. The organic solvent was removed under reduced pressure and the crude product was purified by silica gel column chromatography. DCM was used as eluent to afford **BpinPhC6BPC** as a white solid.

Yield: 70% (1.1 g). **R_f**: 0.55 (DCM on silica gel). **Mp**: 103 °C. **^{1}H NMR (400 MHz, $CDCl_3$) δ (ppm)**: 7.77 – 7.62 (m, 8H), 7.55 (d, J = 8.8 Hz, 4H), 7.02 (d, *J* = 8.8 Hz, 4H), 6.96 (d, *J* = 2.4 Hz, 2H), 6.59 (s, 1H), 4.03 (dt, *J* = 13.3, 6.4 Hz, 8H), 1.85 (dt, *J* = 13.9, 6.7 Hz, 8H), 1.57 (p, *J* = 3.6 Hz, 8H), 1.36 (s, 12H). **^{13}C NMR (101 MHz, $CDCl_3$) δ (ppm)**: 159.9, 159.7, 145.3, 132.6, 131.3, 128.3, 127.1, 119.1, 115.1, 112.3, 110.0, 110.0, 105.2, 83.9, 68.0, 67.8, 29.3, 29.2, 25.9, 25.8, 24.9. **HRMS (ESI-MS) $[M+H]^+$ Calculated**: ($C_{50}H_{56}BN_2O_6$); 791.4153; **Found**: 791.4234.

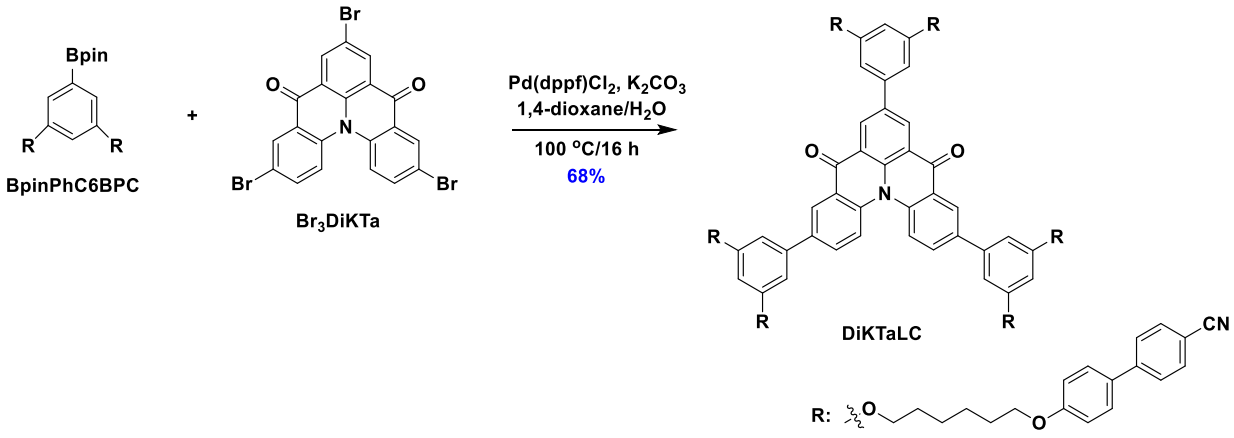

To a 250 mL flask were added **Br_3DiKTa** (270 mg, 0.5 mmol, 1 equiv.), **BpinPhC6BPC** (1.6 g, 2 mmol, 4 equiv.), Pd(dppf)Cl_2 (75 mg, 0.1 mmol, 0.2 equiv.), potassium carbonate (420 mg, 3 mmol, 6 equiv.), 20 mL of 1,4-dioxane and 4 mL of water. The mixture was degassed by three cycles of freeze-pump-thaw and stirred at 110 °C for 16 h under nitrogen atmosphere. After completion of reaction, 20 mL of water was added to the reaction mixture and extracted with DCM (3 × 50 mL). The combined organic layers were dried with anhydrous magnesium sulfate. The organic solvent was removed under reduced pressure and the crude product was purified by silica gel column chromatography, DCM/Hex = 1/3 was used as eluent to afford **DiKTaLC** as a yellow solid.

Yield: 68%. **R_f** = 0.52 (50% DCM/Hexane). **Mp:** 115 ˚C. **^{1}H NMR (400 MHz, $CDCl_3$) δ (ppm):** 9.02 (s, 2H), 8.75 (d, *J* = 2.3 Hz, 2H), 8.24 (d, *J* = 8.9 Hz, 2H), 7.97 (dd, J = 8.9, 2.3 Hz, 2H), 7.74 – 7.59 (m, 24H), 7.57 – 7.48 (m, 12H), 7.01 (dd, *J* = 8.9, 2.4 Hz, 12H), 6.96 (d, *J* = 2.2 Hz, 2H), 6.90 (d, *J* = 2.2 Hz, 4H), 6.57 (d, *J* = 2.0 Hz, 3H), 4.08 (dt, *J* = 13.0, 4.0 Hz, 24H), 1.95 – 1.88 (m, 24H), 1.63 (s, 24H). **^{13}C NMR δ (ppm):** 178.6, 160.9, 159.7, 145.2, 140.8, 138.8, 138.2, 132.6, 131.3, 128.3, 127.0, 126.5, 123.8, 119.1, 115.1, 110.1, 105.8, 100.9, 68.0, 29.2, 25.9.

HRMS (MALDI-TOF): [M+Na]$^+$ Calculated $[C_{152}H_{137}N_7O_{14}Na]^+$: 2308.0155, found 2308.0296. **Elemental analysis: Calcd for $C_{152}H_{137}N_7O_{14}$**: C, 79.87; H, 6.04; N, 4.29. **Found**: C, 79.45; H, 6.16; N, 4.34. **HPLC** 10% THF/MeCN, 1.0 mL min^{-1}, 300 nm; tr (96.8 %) = 16.4 min.

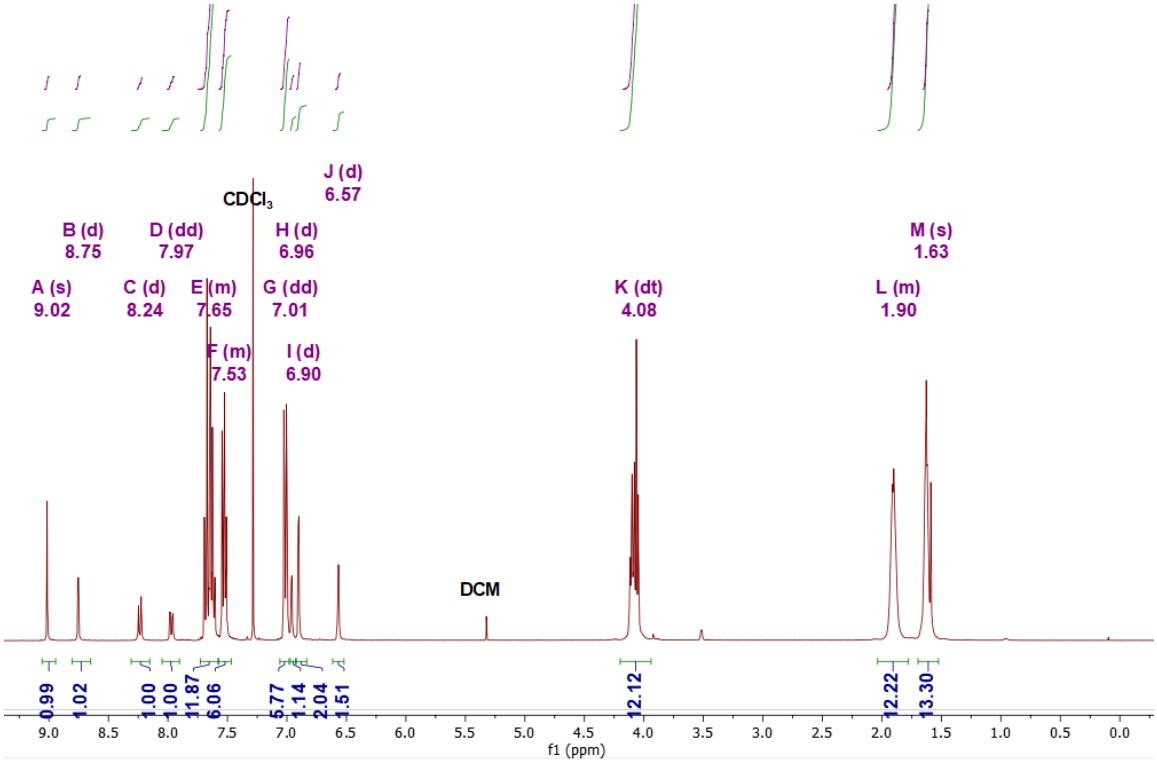

Figure **6.11**. ^{1}H NMR of **DiKTaLC** in $CDCl_3$

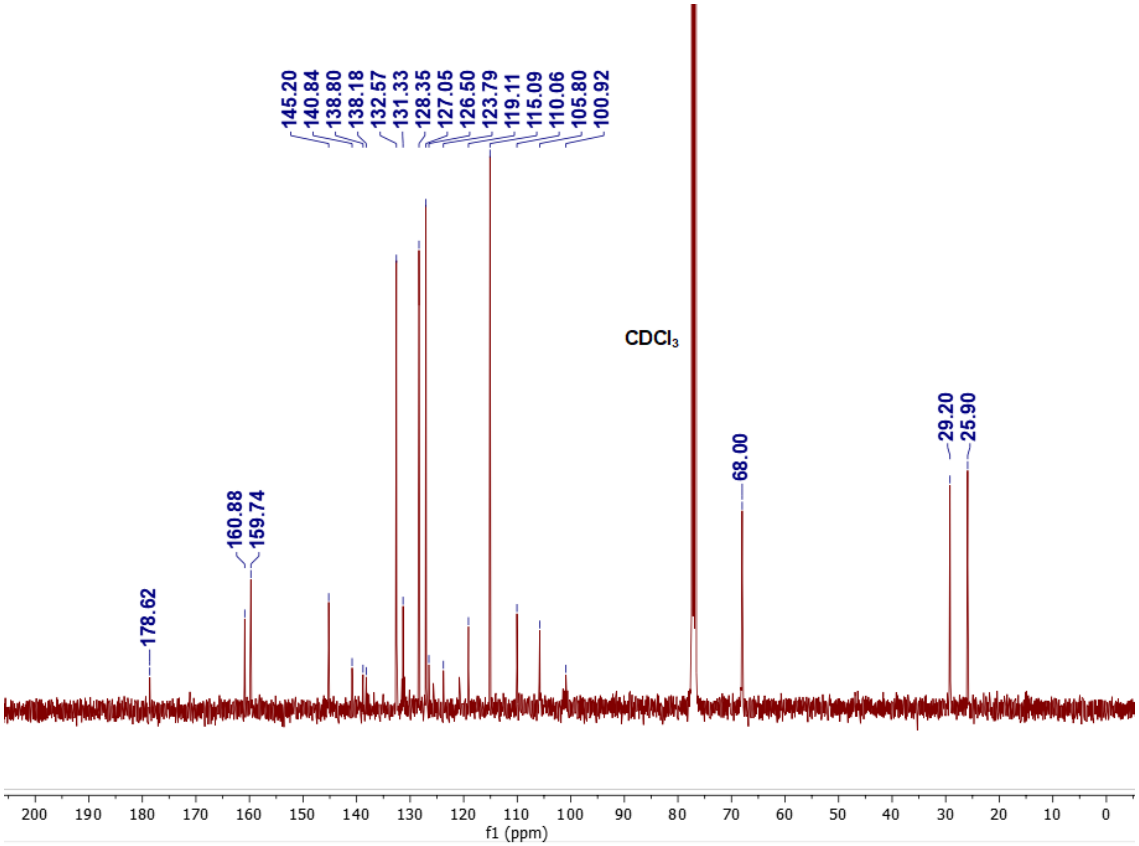

Figure **6.12.** ^{13}C NMR of **DiKTaLC** in $CDCl_3$

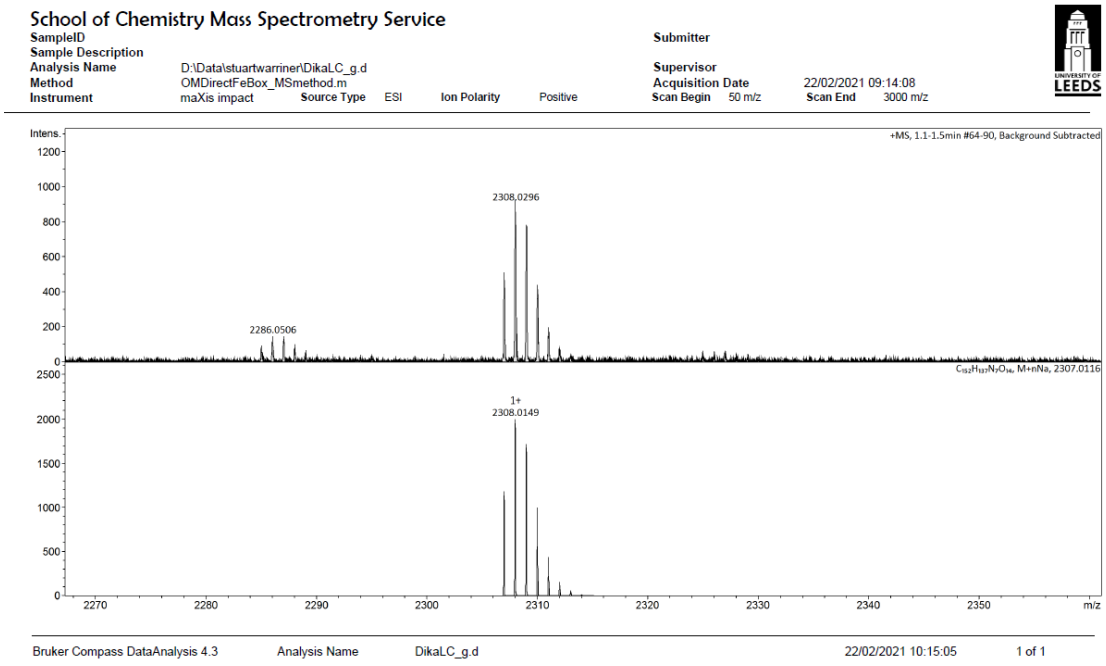

Figure **6.13**. HRMS of **DiKTaLC**

Elemental Analysis Service Request Form

Researcher name Dongyang Chen

Researcher email dc217@st-andrews.ac.uk

NOTE: Please submit ca. 10 mg of sample

Sample reference number	dc-III 18
Name of Compound	DiKTaLC
Molecular formula	$C_{152}H_{137}N_7O_{14}$
Stability	stable
Hazards	low hazard
Other Remarks	

Analysis type:

Single ☐ **Duplicate**√☐ **Triplicate**☐

Analysis Result:

Element	Expected %	Found (1)	Found (2)	Found (3)
Carbon	79.87	79.44	79.47	
Hydrogen	6.04	6.17	6.16	
Nitrogen	4.29	4.30	4.37	
Oxygen				

Authorising Signature:

Date completed	21.05.21
Signature	J-Pc
comments	

Figure **6.14**. Elemental analysis of **DiKTaLC**

SHIMADZU LabSolutions **Analysis Report**

<Sample Information>

Sample Name	: dc-C6CO		
Sample ID	: THF/AcN=10/90		
Data Filename	: 19042021-THF/AcN DCC6CNDiKTa		
Method Filename	: THF/AcN 10%		
Batch Filename	: DCC6CNDiKTa.lcb		
Vial #	: 1-19	Sample Type	: Unknown
Injection Volume	: 10 uL		
Date Acquired	: 19/04/2021 21:03:25 21:03:25	Acquired by	: ezc-7
Date Processed	: 19/04/2021 21:33:28 21:33:28	Processed by	: ezc-7

<Chromatogram>

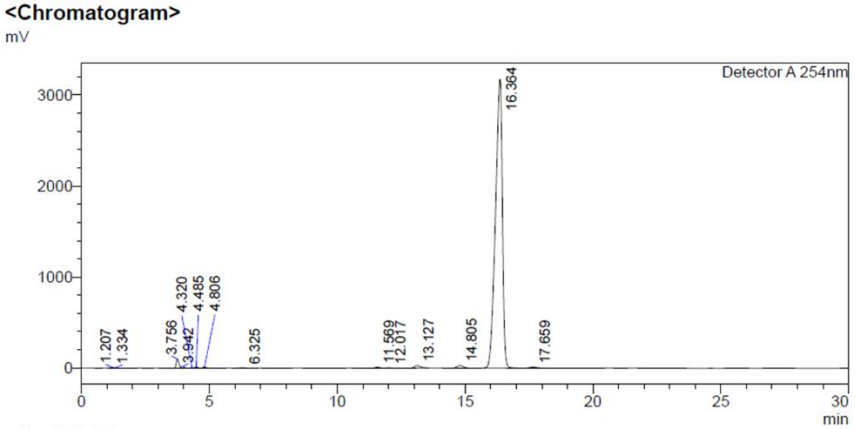

<Peak Table>

Detector A 254nm

Peak#	Ret. Time	Area	Height	Conc.	Unit	Mark	Name
1	1.207	58705	8199	0.097			
2	1.334	21706	4127	0.036		V	
3	3.756	738453	100717	1.219			
4	3.942	129583	16779	0.214		V	
5	4.320	37704	5264	0.062		V	
6	4.485	104153	12833	0.172		V	
7	4.806	103467	10696	0.171		V	
8	6.325	63977	4440	0.106			
9	11.569	128581	10054	0.212			
10	12.017	56687	4345	0.094		V	
11	13.127	412097	26334	0.680			
12	14.805	478776	28213	0.790			
13	16.364	58067721	3172628	96.832			
14	17.659	191785	9181	0.317			
Total		60593394	3413811				

Figure **6.15**. HPLC report of **DiKTaLC**

Reference

(1) Shibata, M.; Sakai, Y.; Yokoyama, D. Advantages and Disadvantages of Vacuum-Deposited and Spin-Coated Amorphous Organic Semiconductor Films for Organic Light-Emitting Diodes. *J. Mater. Chem. C* **2015**, *3*, 11178–11191. https://doi.org/10.1039/c5tc01911g.

(2) Huang, T.; Jiang, W.; Duan, L. Recent Progress in Solution Processable TADF Materials for Organic Light-Emitting Diodes. *J. Mater. Chem. C* **2018**, *6*, 5577–5596. https://doi.org/10.1039/c8tc01139g.

(3) Cho, Y. J.; Yook, K. S.; Lee, J. Y. High Efficiency in a Solution-Processed Thermally Activated Delayed-Fluorescence Device Using a Delayed-Fluorescence Emitting Material with Improved Solubility. *Adv. Mater.* **2014**, *26*, 6642–6646. https://doi.org/10.1002/adma.201402188.

(4) Wada, Y.; Kubo, S.; Kaji, H. Adamantyl Substitution Strategy for Realizing Solution-Processable Thermally Stable Deep-Blue Thermally Activated Delayed Fluorescence Materials. *Adv. Mater.* **2018**, *30*, 1705641. https://doi.org/10.1002/adma.201705641.

(5) Shao, S.; Hu, J.; Wang, X.; Wang, L.; Jing, X.; Wang, F. Blue Thermally Activated Delayed Fluorescence Polymers with Nonconjugated Backbone and Through-Space Charge Transfer Effect. *J. Am. Chem. Soc.* **2017**, *139*, 17739–17742. https://doi.org/10.1021/jacs.7b10257.

(6) Albrecht, K.; Matsuoka, K.; Fujita, K.; Yamamoto, K. Carbazole Dendrimers as Solution-Processable Thermally Activated Delayed-Fluorescence Materials. *Angew. Chemie - Int. Ed.* **2015**, *54*, 5677–5682. https://doi.org/10.1002/anie.201500203.

(7) Pal, A. K.; Krotkus, S.; Fontani, M.; Mackenzie, C. F. R.; Cordes, D. B.; Slawin, A. M. Z.; Samuel, I. D. W.; Zysman-Colman, E. High-Efficiency Deep-Blue-Emitting Organic Light-Emitting Diodes Based on Iridium(III) Carbene Complexes. *Adv. Mater.* **2018**, *30*, 1804231. https://doi.org/10.1002/adma.201804231.

(8) Song, J.; Lee, H.; Jeong, E. G.; Choi, K. C.; Yoo, S. Organic Light-Emitting Diodes: Pushing Toward the Limits and Beyond. *Adv. Mater.* **2020**, *32*, 1907539. https://doi.org/10.1002/adma.201907539.

(9) Hong, G.; Gan, X.; Leonhardt, C.; Zhang, Z.; Seibert, J.; Busch, J. M.; Bräse, S. A Brief History of OLEDs—Emitter Development and Industry Milestones. *Adv. Mater.* **2021**, *33*, 2005630. https://doi.org/10.1002/adma.202005630.

(10) Wong, M. Y.; Zysman-Colman, E. Purely Organic Thermally Activated Delayed Fluorescence Materials for Organic Light-Emitting Diodes. *Adv. Mater.* **2017**, *29*, 1605444. https://doi.org/10.1002/adma.201605444.

(11) Uoyama, H.; Goushi, K.; Shizu, K.; Nomura, H.; Adachi, C. Highly Efficient Organic Light-Emitting Diodes from Delayed Fluorescence. *Nature* **2012**, *492*, 234–238. https://doi.org/10.1038/nature11687.

(12) Cui, L.; Gillett, A. J.; Zhang, S.; Ye, H.; Liu, Y.; Chen, X.; Lin, Z.; Evans, E. W.; Myers, W. K.; Ronson, T. K.; Nakanotani, H.; Reineke, S.; Bredas, J.; Adachi, C.; Friend, R. H. Fast Spin-Flip Enables Efficient and Stable Organic Electroluminescence from Charge-Transfer States. *Nat. Photon.* **2020**, *14*, 636–642.

(13) Naqvi, B. A.; Schmid, M.; Crovini, E.; Sahay, P.; Naujoks, T.; Rodella, F.; Zhang, Z.; Strohriegl, P.; Bräse, S.; Zysman-Colman, E.; Brütting, W. What Controls the Orientation of TADF Emitters? *Front. Chem.* **2020**, *8*, 750. https://doi.org/10.3389/fchem.2020.00750.

(14) Meerheim, R.; Furno, M.; Hofmann, S.; Lüssem, B.; Leo, K. Quantification of Energy Loss Mechanisms in Organic Light-Emitting Diodes. *Appl. Phys. Lett.* **2010**, *97*, 253305. https://doi.org/10.1063/1.3527936.

(15) Yokoyama, D.; Adachi, C. In Situ Real-Time Spectroscopic Ellipsometry Measurement for the Investigation of Molecular Orientation in Organic Amorphous Multilayer Structures. *J. Appl. Phys.* **2010**, *107*, 123512. https://doi.org/10.1063/1.3432568.

(16) Yokoyama, D. Molecular Orientation in Small-Molecule Organic Light-Emitting Diodes. *J. Mater. Chem.* **2011**, *21*, 19187. https://doi.org/10.1039/c1jm13417e.

(17) Tenopala-Carmona, F.; Lee, O. S.; Crovini, E.; Neferu, A. M.; Murawski, C.; Olivier, Y.; Zysman-colman, E.; Gather, M. C. Identification of the Key Parameters for Horizontal Transition Dipole Orientation in Fluorescent and TADF Organic Light-Emitting Diodes. *Adv. Mater.* **2021**, *33*, 2100677. https://doi.org/10.1002/adma.202100677.

(18) Kim, K. H.; Lee, S.; Moon, C. K.; Kim, S. Y.; Park, Y. S.; Lee, J. H.; Lee, J. W.; Huh, J.; You, Y.; Kim, J. J. Phosphorescent Dye-Based Supramolecules for High-Efficiency Organic Light-Emitting Diodes. *Nat. Commun.* **2014**, *5*, 5769. https://doi.org/10.1038/ncomms5769.

(19) Keum, C.; Becker, D.; Archer, E.; Bock, H.; Kitzerow, H.; Gather, M. C.; Murawski, C. Organic Light-Emitting Diodes Based on a Columnar Liquid-Crystalline Perylene Emitter. *Adv. Opt. Mater.* **2020**, *8*, 2000414. https://doi.org/10.1002/adom.202000414.

(20) Yokoyama, D.; Sakaguchi, A.; Suzuki, M.; Adachi, C. Horizontal Orientation of Linear-Shaped Organic Molecules Having Bulky Substituents in Neat and Doped Vacuum-Deposited Amorphous Films. *Org. Electron.* **2009**, *10*, 127–137. https://doi.org/10.1016/j.orgel.2008.10.010.

(21) Yokohama, D.; Setoguchi, Y.; Sakaguchi, A.; Suzuki, M.; Adachi, C. Orientation Control of Linear-Shaped Molecules in Vacuum-Deposited Organic Amorphous Films and Its Effect on Carrier Mobilities. *Adv. Funct. Mater.* **2010**, *20*, 386–391. https://doi.org/10.1002/adfm.200901684.

(22) Yokoyama, D.; Sasabe, H.; Furukawa, Y.; Adachi, C.; Kido, J. Molecular Stacking Induced by Intermolecular C-H···N Hydrogen Bonds Leading to High Carrier Mobility in Vacuum-Deposited Organic Films. *Adv. Funct. Mater.* **2011**, *21*, 1375–1382. https://doi.org/10.1002/adfm.201001919.

(23) Watanabe, Y.; Yokoyama, D.; Koganezawa, T.; Katagiri, H.; Ito, T.; Ohisa, S.; Chiba, T.; Sasabe, H.; Kido, J. Control of Molecular Orientation in Organic Semiconductor Films

Using Weak Hydrogen Bonds. *Adv. Mater.* **2019**, *31*, 1808300. https://doi.org/10.1002/adma.201808300.

(24) Lampe, T.; Schmidt, T. D.; Jurow, M. J.; Djurovich, P. I.; Thompson, M. E.; Brütting, W. Dependence of Phosphorescent Emitter Orientation on Deposition Technique in Doped Organic Films. *Chem. Mater.* **2016**, *28*, 712–715. https://doi.org/10.1021/acs.chemmater.5b04607.

(25) Kaji, H.; Suzuki, H.; Fukushima, T.; Shizu, K.; Suzuki, K.; Kubo, S.; Komino, T.; Oiwa, H.; Suzuki, F.; Wakamiya, A.; Murata, Y.; Adachi, C. Purely Organic Electroluminescent Material Realizing 100% Conversion from Electricity to Light. *Nat. Commun.* **2015**, *6*, 8476. https://doi.org/10.1038/ncomms9476.

(26) Suzuki, K.; Adachi, C.; Kaji, H. Solution-Processable Thermally Activated Delayed Fluorescence Emitters for Application in Organic Light Emitting Diodes. *J. Soc. Inf. Disp.* **2017**, *25*, 480–485. https://doi.org/10.1002/jsid.598.

(27) Herbst, S.; Soberats, B.; Leowanawat, P.; Lehmann, M.; Würthner, F. A Columnar Liquid-Crystal Phase Formed by Hydrogen-Bonded Perylene Bisimide J-Aggregates. *Angew. Chemie - Int. Ed.* **2017**, *56*, 2162–2165. https://doi.org/10.1002/anie.201612047.

(28) Chen, Z.; Baumeister, U.; Tschierske, C.; Würthner, F. Effect of Core Twisting on Self-Assembly and Optical Properties of Perylene Bisimide Dyes in Solution and Columnar Liquid Crystalline Phases. *Chem. - A Eur. J.* **2007**, *13*, 450–465. https://doi.org/10.1002/chem.200600891.

(29) Eccher, J.; Faria, G. C.; Bock, H.; Von Seggern, H.; Bechtold, I. H. Order Induced Charge Carrier Mobility Enhancement in Columnar Liquid Crystal Diodes. *ACS Appl. Mater. Interfaces* **2013**, *5*, 11935–11943. https://doi.org/10.1021/am403681q.

(30) Keum, C. M.; Liu, S.; Al-Shadeedi, A.; Kaphle, V.; Callens, M. K.; Han, L.; Neyts, K.; Zhao, H.; Gather, M. C.; Bunge, S. D.; Twieg, R. J.; Jakli, A.; Lüssem, B. Tuning Charge Carrier Transport and Optical Birefringence in Liquid-Crystalline Thin Films: A New Design Space for Organic Light-Emitting Diodes. *Sci. Rep.* **2018**, *8*, 699. https://doi.org/10.1038/s41598-018-19157-9.

(31) Liao, X.; Kahle, F. J.; Liu, B.; Bässler, H.; Zhang, X.; Köhler, A.; Greiner, A. Polarized Blue Photoluminescence of Mesoscopically Ordered Electrospun Non-Conjugated Polyacrylonitrile Nanofibers. *Mater. Horizons* **2020**, *7*, 1605–1612. https://doi.org/10.1039/d0mh00002g.

(32) Bala, I.; Singh, N.; Yadav, R. A. K.; De, J.; Gupta, S. P.; Singh, D. P.; Dubey, D. K.; Jou, J. H.; Douali, R.; Pal, S. K. Room Temperature Perylene Based Columnar Liquid Crystals as Solid-State Fluorescent Emitters in Solution-Processable Organic Light-Emitting Diodes. *J. Mater. Chem. C* **2020**, *8*, 12485–12494. https://doi.org/10.1039/d0tc02754e.

(33) Bala, I.; Yang, W. Y.; Gupta, S. P.; De, J.; Yadav, R. A. K.; Singh, D. P.; Dubey, D. K.; Jou, J. H.; Douali, R.; Pal, S. K. Room Temperature Discotic Liquid Crystalline Triphenylene-Pentaalkynylbenzene Dyads as an Emitter in Blue OLEDs and Their Charge

Transfer Complexes with Ambipolar Charge Transport Behaviour. *J. Mater. Chem. C* **2019**, *7*, 5724–5738. https://doi.org/10.1039/c9tc01178a.

(34) De, J.; Abdul, A. H.; Yadav, R. A. K.; Gupta, S. P.; Bala, I.; Chawla, P.; Kesavan, K. K.; Jou, J. H.; Pal, S. K. AIE-Active Mechanoluminescent Discotic Liquid Crystals for Applications in OLEDs and Bio-Imaging. *Chem. Commun.* **2020**, *56*, 14279–14282. https://doi.org/10.1039/d0cc05813k.

(35) Liu, S. H.; Lin, M. S.; Chen, L. Y.; Hong, Y. H.; Tsai, C. H.; Wu, C. C.; Poloek, A.; Chi, Y.; Chen, C. A.; Chen, S. H.; Hsu, H. F. Polarized Phosphorescent Organic Light-Emitting Devices Adopting Mesogenic Host-Guest Systems. *Org. Electron.* **2011**, *12*, 15–21. https://doi.org/10.1016/j.orgel.2010.09.020.

(36) Wang, Y.; Fan, J.; Shi, J.; Qi, H.; Baranoff, E.; Xie, G.; Li, Q.; Tan, H.; Liu, Y.; Zhu, W. Influence of Integrated Alkyl-Chain Length on the Mesogenic and Photophysical Properties of Platinum-Based Metallomesogens and Their Application for Polarized White OLEDs. *Dye. Pigment.* **2016**, *133*, 238–247. https://doi.org/10.1016/j.dyepig.2016.05.024.

(37) Qian, G.; Yang, X.; Wang, X.; Herod, J. D.; Bruce, D. W.; Wang, S.; Zhu, W.; Duan, P.; Wang, Y. Chiral Platinum-Based Metallomesogens with Highly Efficient Circularly Polarized Electroluminescence in Solution-Processed Organic Light-Emitting Diodes. *Adv. Opt. Mater.* **2020**, *8*, 2000775. https://doi.org/10.1002/adom.202000775.

(38) Suleymanova, A. F.; Shafikov, M. Z.; Whitwood, A. C.; Czerwieniec, R.; Bruce, D. W. Liquid-Crystalline TADF Materials Based on Substituted Carbazoles and Terephthalonitrile. *J. Mater. Chem. C* **2021**, *9*, 6528–6535. https://doi.org/10.1039/d1tc00443c.

(39) Senes, A.; Meskers, S. C. J.; Greiner, H.; Suzuki, K.; Kaji, H.; Adachi, C.; Wilson, J. S.; Janssen, R. A. J. Increasing the Horizontal Orientation of Transition Dipole Moments in Solution Processed Small Molecular Emitters. *J. Mater. Chem. C* **2017**, *5*, 6555–6562. https://doi.org/10.1039/C7TC01568B.

(40) Pershin, A.; Hall, D.; Lemaur, V.; Sancho-Garcia, J. C.; Muccioli, L.; Zysman-Colman, E.; Beljonne, D.; Olivier, Y. Highly Emissive Excitons with Reduced Exchange Energy in Thermally Activated Delayed Fluorescent Molecules. *Nat. Commun.* **2019**, *10*, 597. https://doi.org/10.1038/s41467-019-08495-5.

(41) Suresh, S. M.; Duda, E.; Hall, D.; Yao, Z.; Bagnich, S.; Slawin, A. M. Z.; Bässler, H.; Beljonne, D.; Buck, M.; Olivier, Y.; Köhler, A.; Zysman-Colman, E. A Deep Blue B,N-Doped Heptacene Emitter That Shows Both Thermally Activated Delayed Fluorescence and Delayed Fluorescence by Triplet-Triplet Annihilation. *J. Am. Chem. Soc.* **2020**, *142*, 6588–6599. https://doi.org/10.1021/jacs.9b13704.

(42) Pople, J. A.; Binkley, J. S.; Seeger, R. Theoretical Models Incorporating Electron Correlation. *Int. J. Quantum Chem.* **1976**, *10*, 1–19. https://doi.org/10.1002/qua.560100802.

(43) Adamo, C. Toward Reliable Density Functional Methods without Adjustable Parameters : The PBE0 Model. *J. Chem. Phys.* **1999**, *110*, 6158–6170.

(44) Hall, D.; Suresh, S. M.; dos Santos, P. L.; Duda, E.; Bagnich, S.; Pershin, A.; Rajamalli, P.; Cordes, D. B.; Slawin, A. M. Z.; Beljonne, D.; Köhler, A.; Samuel, I. D. W.; Olivier, Y.; Zysman-Colman, E. Improving Processability and Efficiency of Resonant TADF Emitters: A Design Strategy. *Adv. Opt. Mater.* **2020**, *8*, 1901627. https://doi.org/10.1002/adom.201901627.

(45) Connelly, N. G.; Geiger, W. E. Chemical Redox Agents for Organometallic Chemistry. *Chem. Rev.* **1996**, *96*, 877–910. https://doi.org/10.1021/cr940053x.

(46) Mishra, M.; Dabrowski, R. S.; Vij, J. K.; Mishra, A.; Dhar, R. Electrical and Electro-Optical Parameters of 4′-Octyl-4-Cyanobiphenyl Nematic Liquid Crystal Dispersed with Gold and Silver Nanoparticles. *Liq. Cryst.* **2015**, *42*, 1580–1590. https://doi.org/10.1080/02678292.2015.1071438.

(47) Ramou, E.; Ahmed, Z.; Welch, C.; Karahaliou, P. K.; Mehl, G. H. The Stabilisation of the Nx Phase in Mixtures. *Soft Matter* **2016**, *12*, 888–899. https://doi.org/10.1039/c5sm01961c.

(48) Lee, J. S.; Prabu, A. A.; Kim, K. J. Annealing Effect upon Chain Orientation, Crystalline Morphology, and Polarizability of Ultra-Thin P(VDF-TrFE) Film for Nonvolatile Polymer Memory Device. *Polymer* **2010**, *51* (26), 6319–6333. https://doi.org/10.1016/j.polymer.2010.10.053.

(49) Ishiyama, T.; Murata, M.; Miyaura, N. Palladium(0)-Catalyzed Cross-Coupling Reaction of Alkoxydiboron with Haloarenes: A Direct Procedure for Arylboronic Esters. *J. Org. Chem.* **1995**, *60*, 7508–7510. https://doi.org/10.1021/jo00128a024.

Chapter 7

The Utilization of Cycloparaphenylene for Thermally Activated Delayed Fluorescence Emitters

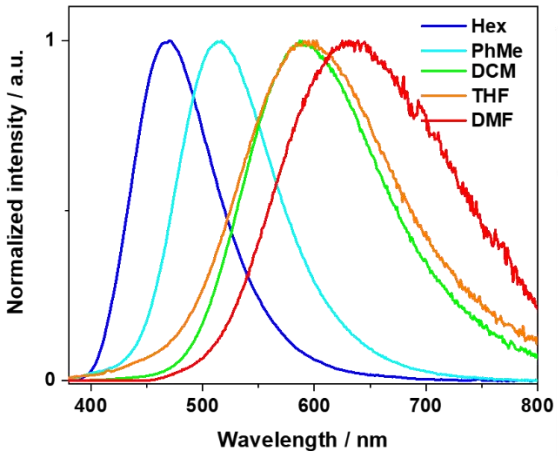

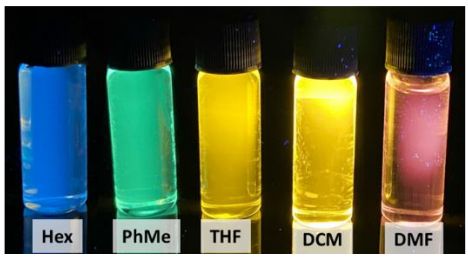

CPP with electron donors for TADF emitter design

Manuscript of this project is under preparation as

Dongyang Chen,[a] Yoshimasa Wada,[b] Changsheng Sun,[b] Eiichi Kayahara,[b] Katsuaki Suzuki,[b] Shigeru Yamago,[b] Hronori Kaji,[b] Eli Zysman-Colman[a]

Collaborators in this Chapter are from

[a] Organic Semiconductor Centre, EaStCHEM School of Chemistry, University of St. Andrews, St. Andrews, Fife, KY16 9ST, United Kingdom.

[b] Institute for Chemical Research, Kyoto University, Uji 611-0011, Japan

The syntheses of **4PXZPh-[10]CPP** was carried out in Institute for Chemical Research, Kyoto University under supervision of Prof. Eiichi Kayahara and Prof. Shigeru Yamago. The research in Kyoto is funded by ICR Young Researcher International Internship and International Visitors: Journals | Institute for Chemical Research, Kyoto University.

Dr. Yoshimasa Wada and Dr. Katsuaki Suzuki carried out the photophysics in solid state and the OLEDs device fabrication.

I designed the molecule **4PXZPh-[10]CPP** presented in this project and completed the synthesis and characterization, DFT and TD-DFT calculations, electrochemistry, photophysics in solutions, and I am the principal author of the manuscript.

7.1 Introduction

Cycloparaphenylenes (CPPs) are the smallest building blocks of "armchair" carbon nanotubes and have attracted increasing attention due to their naturally curved nanohoops structure, which make them ideal templates for the host-guest chemistry investigation and bottom-up synthesis of carbon nanotubes.[1–4] Moreover, their curved and radially oriented π-system has generated increasing interest from the organic semiconductor community.[5–7] A cycloparaphenylene consists of a number of *para*-connected benzene rings to form a loop-like structure. The aesthetically beautiful structure belies the significant embedded strain that results from the distorted benzene rings in the nanohoops, particularly the smaller analogs, that renders the synthesis challenging. The first cycloparaphenylenes (**[9]CPP**, **[12]CPP**, and **[18]CPP**) were synthesized using a strategy where cyclohexadienes were employed to afford intermediates that could more easily accommodate the curved structure prior to aromatization in the final step.[8] A complementary strategy involves the formation of platinium complexes precursors that then can be demetalated to stitch the CPP together under reducing conditions. Seminal contributions from Bertozzi *et al.*,[5,8] Jasti *et al.*, Itami *et al.*,[9] and Yamago *et al.*,[10] amongst others, have demonstrated how the synthesis of CPPs can be scaled and how these structures can be elaborated further to generate compounds with interesting optoelectronic properties.[11–17]

Tetsuro Majima *et al*. systematically investigated the size dependence of the absorption, fluorescence and phosphorescence spectra from **[8]CPP** to **[12]CPP** and found that although the absorption spectra were rather insensitive to the size of the CPPs, larger Stokes

shifts were observed for the smaller CPPs as the singlet and triplet state energies increased with the number of benzene units.[13,17,18] The size dependence can be explained by the stronger structural relaxation from the Franck-Condon state for smaller CPPs, which also leads to very low Φ_{PL} of [**8]CPP** (<10%) compared to 66% and 72% for **[12]CPP** and **[13]CPP** in THF, respectively.[17] The CPPs show reversible oxidation waves in the cyclic voltammograms, with smaller CPPs possessing anodically shifted oxidation potentials (i.e., stabilized HOMO levels), which match the DFT calculations.[13] The DFT calculations also predicted that the LUMO levels would stabilize with decreasing unit number; however, reduction waves could not be observed within the potential window of tetrachloroethane. The optoelectronic properties of CPPs can be tuned by decoration with electron-donating or withdrawing groups.[19] Itami *et al*. incorporated the electron acceptor benzothiadiazole (BT) into the ring to construct a macrocycles **BT[10]CPP**.[20] The DFT calculations reveals the LUMO of **BT[10]CPP** is localized on the acceptor moiety, with the LUMO level stabilized by 0.8 eV compared to the reference **[10]CPP**, while the HOMOs are located on the remaining benzene rings on the macrocycle and are slightly destabilized compared to that of **[10]CPP**.[20] The CT character of **BT[10]CPP** is evident in the absorption spectrum where a new band at 450 nm was observed, which correlates to the HOMO→LUMO transition as assigned by TD-DFT calculations. The emission spectrum of **BT[10]CPP** is red-shifted by over 100 nm with λ_{PL} of 571 nm and Φ_{PL} of 59% in DCM, compared to λ_{PL} of 466 nm and Φ_{PL} of 65% for **[10]CPP**; moreover, the emission spectrum red-shifts in with increasing solvent polarity, which is consistent with emission from a state of charge-transfer character.[20] Tan *et al*. reported the incorporation of four BT moieties within

[12]CPP and the molecule **TB[12]CPP** shows a similar absorption spectrum and similar positive solvatochromism behavior to those of **BT[10]CPP**.[21] The λ_{PL} of **TB[12]CPP** is 569 nm and the Φ_{PL} is 81% in chloroform while in 10 wt% doped PMMA film, the Φ_{PL} increases to 98% at λ_{PL} of 550 nm.[21] Shigeru *et al.* connected electron-donating alkoxy groups on **[10]CPP**, in chloroform the molecule **6C** emits at 477 nm with Φ_{PL} of 59% compared to 470 nm and 46% for the reference **[10]CPP**.[11] The electron-only device based on **6C** showed a space charge limited current (SCLC), with moderate electron mobility of 4.5×10^{-6} cm^2 V^{-1} s^{-1} at 0.7 MV cm^{-1}, which demonstrates the potential of this compound as an electron transport material.[11] Computational studies from Sancho-García *et al*. provided insight that incorporation of an electron-withdrawing group (pyridine, pyridinium, and methyl pyridinium) can not only affect the HOMO/LUMO distribution and energies but also tune the ΔE_{ST}.[22] For the proposed molecule ***N*-methylaza-[8]CPP$^+$**, where a methyl pyridinium unit is incorporated into the CPP skeleton and used as an electron-acceptor, the DFT calculations show that the LUMO of ***N*-methylaza-[8]CPP$^+$** is located on the methyl pyridinium unit as well as the adjacent benzene rings and the HOMO is located across the remaining benzene rings, while for the reference [**8]CPP**, the HOMO, and LUMO are delocalized over the whole molecule.[22] As a result, the ΔE_{ST} decreases from 0.50 eV for **[8]CPP** to 0.23 eV for ***N*-methylaza-[8]CPP$^+$**.[22] This is the first evidence for the potential of this class of compounds to exhibit TADF, where a small ΔE_{ST} is required to promote RISC at ambient temperatures, and also indicates that D-A structure is not necessary to induce CT character with HOMO/LUMO seperation.[22]

TADF compounds have generated much interest as these can be used as emitters in electroluminescent devices capable of harvesting both singlet and triplet excitons and efficient conversion to light.[23–25] The RISC rate (k_{RISC}) is proportional to $|V_{SOC}|^2 \times \exp[-(\Delta E_{ST}^2)]$ where $|V_{SOC}|^2$ is the spin-orbit coupling matrix element between S_1 and T_1, and ΔE_{ST} is the energy gap between S_1 and T_1.[26] A common strategy to enhance k_{RISC} and promote TADF is to minimize the ΔE_{ST}, which can be achieved by reducing the overlap of the HOMO and LUMO orbitals.[27–29] Previous work on CPPs has demonstrated that CPP derivatives can exhibit CT character in their excited states and the required HOMO/LUMO separation to show TADF by suitable decoration of the CPP core.[21,22] In this work, we employed DFT and TDA-DFT calculations to design the CPP-based TADF emitter **4PXZPh-[10]CPP**, where four bulky electron-donating moieties 10-phenyl-10H-phenoxazine are connected to **[10]CPP**. The calculations predict a ΔE_{ST} of 0.08 eV. **4PXZPh-[10]CPP** shows weak TADF CT emission in polar solvents. The photoluminescence quantum yield is improved in the thin 2,6-bis(9H-carbazol-9-yl)pyridine (PyD2) film to 25%, with delayed lifetime 0.1 μs. We demonstrated the first CPP—based solution-processed OLED , which shows sky-blue emission with an EQE_{max} of 0.04%.

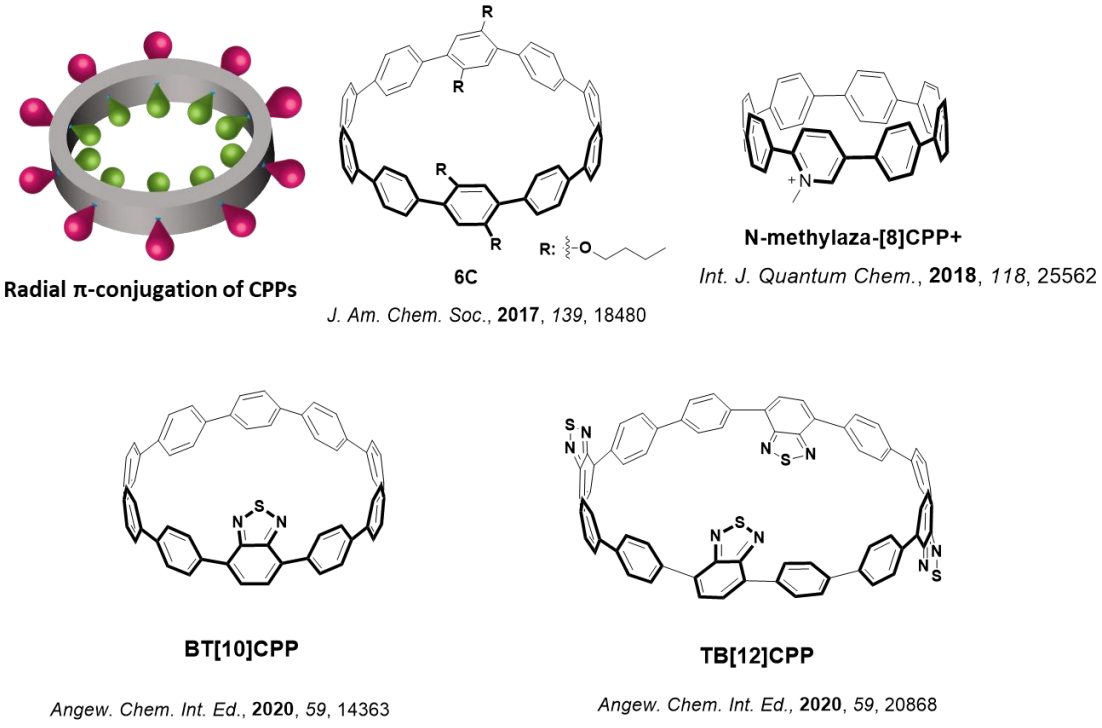

Figure **7.1**. Molecular structures of cycloparaphenylene based emitters

7.2 Synthesis

The synthesis of **4PXZPh-[10]CPP** is shown in Scheme **7.1**, and the synthesis of CPP intermediate **OH-[10]CPP** followed the 12-steps route firstly reported by Shigeru *et al* which is the first example of gram-scale synthesis of CPP and CPP derivatives.[11] The synthesis starts from the 2,5-di(3-butenyloxy)-1,4-benzoquinone (**dBuOBQ**), which was reacted with the *in situ* formed 4-bromo-4′-lithiobiphenyl to obtain **DPBuOBQ** in 65% yield. The **DPBuOBQ** was protected as its triethylsilyl (TES) diether, and **TesBuOBQ** was converted to **BpinBuOBQ** via a bromide-borane exchange reaction in modest yield. The boronic acid pinacol ester (Bpin) group allows **BpinBuOBQ** to coordinate with $Pt(COD)Cl_2$ to form the bisplatinum complex and

the cyclophane intermediate **TesBuO-8Ph2Ch** formed in 20% yield over two steps upon platinum extrusion during reflux with PPh_3. The TES groups of **TesBuO-8Ph2Ch** were removed using tetrabutylammonium fluoride (TBAF) and **BuO-[10]CPP** was formed upon reductive aromatization of **OHBu-8Ph2Ch** in a yield of 80% with H_2SnCl_4 prepared *in situ* from $SnCl_2$ and concentrated HCl. The BuO groups on **BuO-[10]CPP** were converted to triflate groups (**OTf-[10]CPP**) in a four-step (67% yield over the four steps) sequence consisting of an OsO_4-catalyzed dihydroxylation reaction followed by a $NaIO_4$-mediated oxidative cleavage of the resulting diol, and subsequent retro Michael reaction by employing *i*-$PrNH_2$/AcOH to offord **OH-[10]CPP**.

OH-[10]CPP can pleasantly converted to **OTf-[10]CPP** using trifluoromethane sulfonic anhydride (Tf_2O) in the presence of pyridine. Finally, the **OTf-[10]CPP** reacted with the electron-donor moiety **BpinPhPXZ** under Suzuki-Miyaura cross-coupling conditions to obtain **4PXZPh-[10]CPP** with a yield of 45%.[43] The identity and purity of **4PXZPh-[10]CPP** was verified by a combination of melting point, determination, ^{1}H NMR, ^{13}C NMR spectroscopy, high-resolution mass spectrometry, high performance liquid chromatography and elemental analyses.

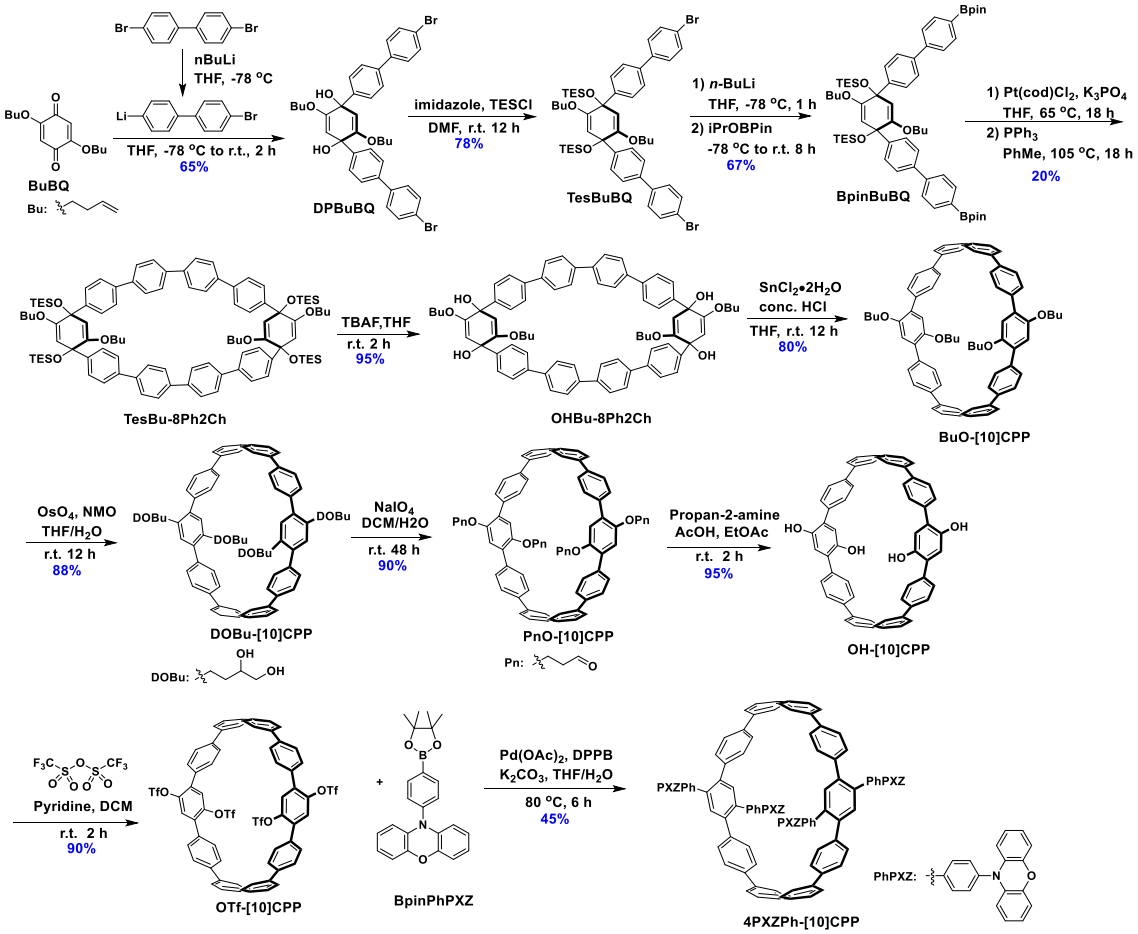

Scheme **7.1**. Synthesis of **4PXZPh-[10]CPP**.

7.3 Theoretical calculations

To gain insight into the electronic structure of **4PXZPh-[10]CPP**, DFT calculations, and time-dependent DFT calculations using the Tamm-Dancoff approximation (TDA-DFT) calculations were performed on **4PXZPh-[10]CPP** and the reference compound **[10]CPP**. The ground state, singlet, and triplet excited state geometries were calculated in the gas phase at the PBE0/6-31g(d, p) level of theory.[30,31] As shown in Figure **7.2a**, the HOMO of **4PXZPh-[10]CPP** is localized on two of the phenoxazine donors while the pseudo-degenerate

HOMO−1 is located on the other two phenoxazine. The LUMO of **4PXZPh-[10]CPP** is delocalized across the CPP moiety. For parent **[10]CPP**, the HOMO and LUMO are distributed across the whole molecule (Figure **7.2b**). The HOMO of **4PXZPh-[10]CPP** is stabilized to -5.49 eV compared to -5.66 eV for **[10]CPP**, while the LUMO of **4PXZPh-[10]CPP** is only slightly destabilized to -1.88 eV compared to -1.94 eV for **[10]CPP**, reflecting the small electronic coupling between the HOMO and the LUMO. As a result, the HOMO-LUMO gap (ΔE_g) of **4PXZPh-[10]CPP** is reduced to 3.07 eV compared to 3.72 eV in **[10]CPP**. The spatially separated HOMO and LUMO ensures **4PXZPh-[10]CPP** possesses a small ΔE_{ST}. TDA-DFT calculations indicate that the S_1 energy of **4PXZPh-[10]CPP** (2.65 eV) is stabilized by 0.47 eV compared to that **[10]CPP** while the T_1 energy (2.57 eV) is slightly destabilized by 0.01 eV compared to **[10]CPP**, thereby results a ΔE_{ST} of 0.08 eV for **4PXZPh-[10]CPP**. The natural transition orbital (NTO) analysis of **4PXZPh-[10]CPP** reveals a charge-transfer (CT) transition for S_1 from the PXZ donors to the CPP moiety, while the HONTO for T_1 is delocalized over the whole molecule and LUNTO is located on the CPP moiety, which suggest a state of LE and CT mixed character. Four near degenerate triplet states lie between S_1 and T_1 of **4PXZPh-[10]CPP**, and specifically, the transition for T_2 (2.60 eV) shows resemblance to T_1 with mixed LE-CT character, while the transitions for degenerate T_3 to T_5 (~2.64 eV) are similar to S_1 with CT character (Figure **7.3**). The degenerate intermediate triplets can lead to multiple RISC transition channels via HFC mechanism and spin-vibronic coupling mechanism to S_1,[32,33] resulting in a more efficient RISC process. For **[10]CPP**, both S_1 and T_1 transitions are π–π^* locally excited (LE) in nature over the whole molecule. The different orbital types involved in

S_1 and T_1 for **4PXZPh-[10]CPP** result in non-negligible spin-orbit coupling. Indeed, the spin-orbital outcoupling matrix elements (SOCME) between S_1 and T_1 of **4PXZPh-[10]CPP** are calculated to be 0.1523 cm^{-1} compared to 0.0217 cm^{-1} for **[10]CPP**. Thereby RISC in **4PXZPh-[10]CPP** can occur both via direct SOC between S_1 and T_1, and indirectly via intermediate triplet states involved HFC and spin-vibronic coupling mechanisms. The oscillator strength (*f*) for **4PXZPh-[10]CPP** is slightly reduced to 0.06, compared to 0.08 of **[10]CPP**, which is ascribed to the decreased HOMO/LUMO overlap.

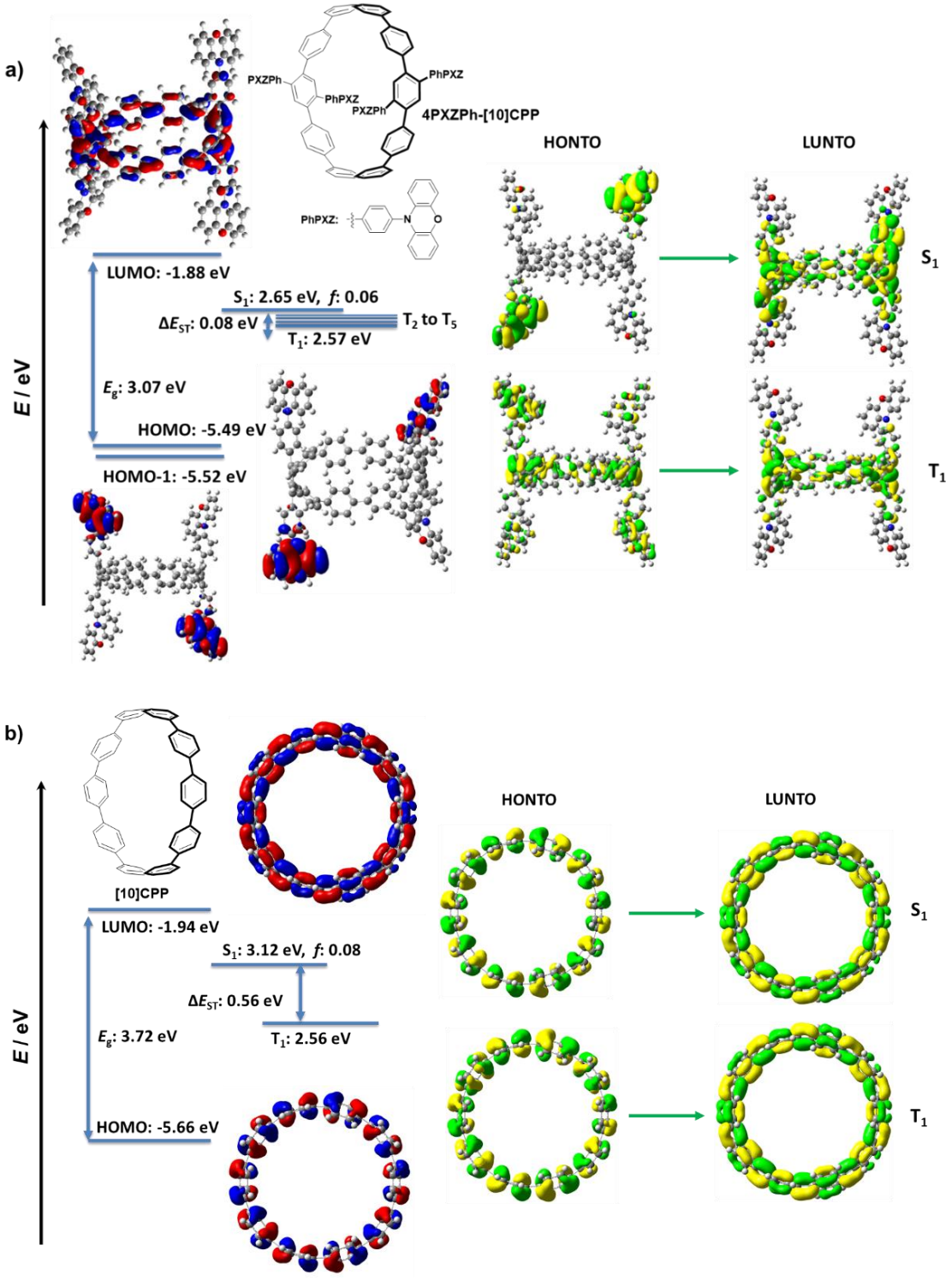

Figure **7.2**. Theoretical modelling of the energies of the HOMO/LUMO and the S_1 and T_1 states of **4PXZPh-[10]CPP**, and reference compound **[10]CPP** in the gas phase and the electron density distribution of the frontier molecular orbitals (isovalue = 0.02).

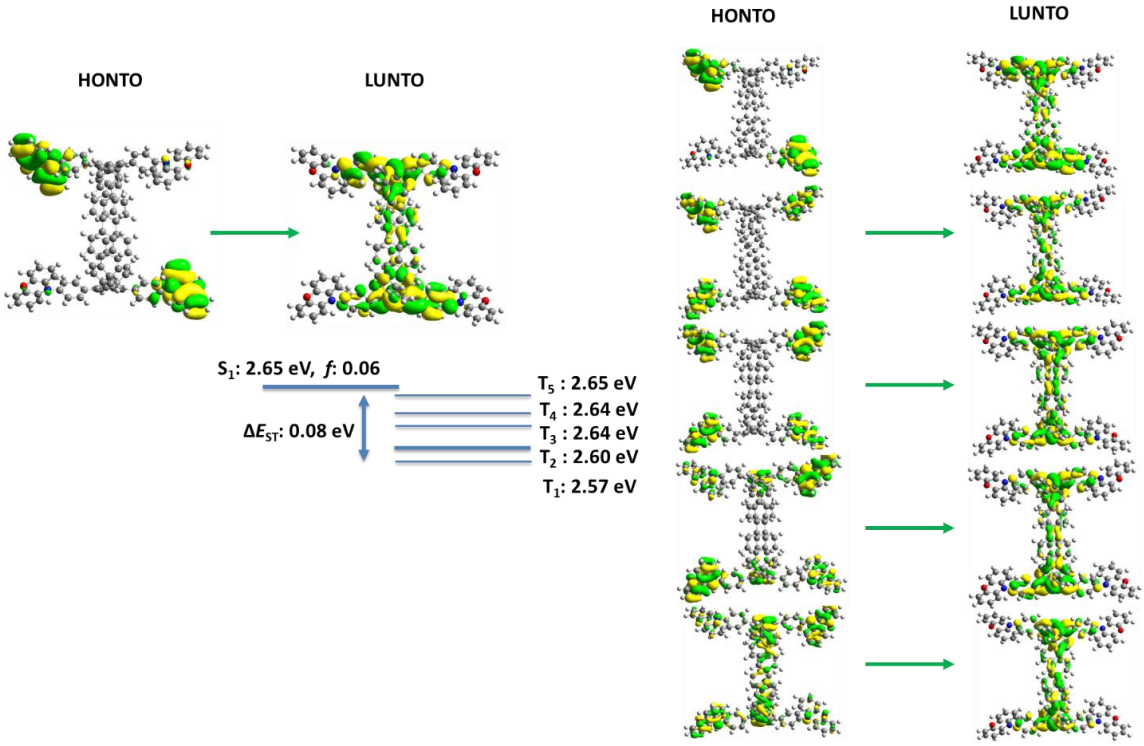

Figure **7.3**. Natural transition orbitals analysis of **4PXZPh-[10]CPP**

Table **7.1**. Exited states involved in the main UV-vis transitions of **4PXZPh-[10]CPP**

Compounds	**Excited State**	**Energy/ eV; nm**	***f***	**Nature**	**Character of the transition**
4PXZPh-[10]CPP	S_1	2.65; 468	0.0580	H→L (71%) (H−1)→(L+1) (15%)	CT
	S_6	2.93; 424	0.0127	H→L (18%) (H−1)→(L+1) (68%)	HLCT
	S_{10}	3.29; 377	0.0051	H→(L+1) (79%) H→(L+2) (14%)	HLCT

7.4 Electrochemistry

CV and DPV were measured in dichloromethane with *n*-Bu_4NPF_6 as the supporting electrolyte in order to experimentally ascertain HOMO and LUMO energy levels. A reversible oxidation wave ($E_{1/2}$ = 0.66 V vs SCE), ascribed to the oxidation of the PXZ groups,

was observed for **4PXZPh-[10]CPP** from CV, while the DPV shows a single oxidation peak at 0.67 V vs SCE. The HOMO of **4PXZPh-[10]CPP** is calculated to be −5.01 eV from the DPV result, which is more stabilized than that of **[10]CPP** (−5.54 eV) measured in $C_2H_2Cl_4$.[13] Similar to other CPPs,[13,16] no reduction wave was observed for **4PXZPh-[10]CPP** within the DCM solvent window. The LUMO level for **4PXZPh-[10]CPP** (−2.08 eV) was inferred from the HOMO energies and the optical gap (E_g), which itself was determined from the intersection of the normalized absorption and fluorescence spectra in toluene at 2.93 eV. The LUMO level of **4PXZPh-[10]CPP** is destabilized compared to that of **[10]CPP** (−2.54),[13] which matches the trend observed by DFT calculations.

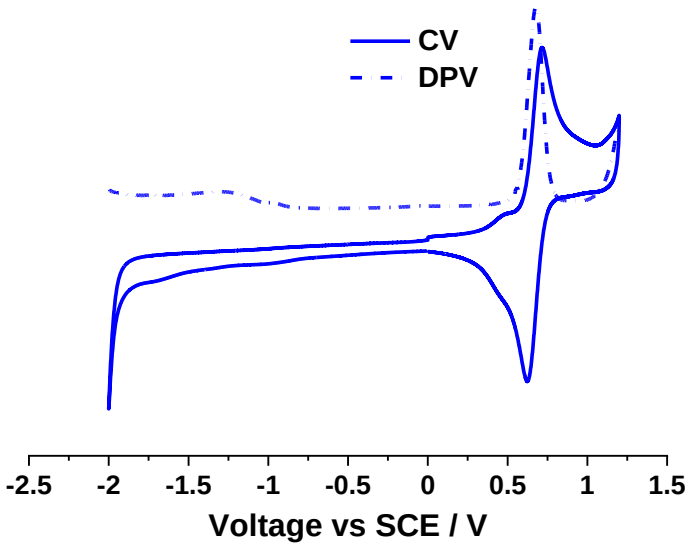

Figure **7.4**. CV and DPV curves of **4PXZPh-[10]CPP** in DCM with 0.1 M *n*-Bu_4NPF_6 as the supporting electrolyte. Measured condition: scan rate 0.1 V/s, calibrated using an external standard (Fc/Fc^+=0.46 eV versus SCE.[34]

7.5 Optoelectronic characterization

The photophysical properties of **4PXZPh-[10]CPP** were investigated in solution and films. Room-temperature UV-*vis* absorption and PL spectra **4PXZPh-[10]CPP** and the reference compound **[10]CPP** in dilute toluene solution are shown in Figure **7.5a**. The absorption profile of **4PXZPh-[10]CPP** is similar to that of **[10]CPP** with a slightly stronger absorption ($\varepsilon = 1.0 \times 10^3\ M^{-1}\ cm^{-1}$) at 400 nm, which is ascribed to a mixed LE and ICT transition according to the TDA-DFT calculations, and a moderately stronger absorption at 340 nm, which according to TDA-DFT calculation is ascribed to a LE transition distributed across the CPP skeleton and phenoxazine moieties. The photoluminescence spectrum of **4PXZPh-[10]CPP** is broad, unstructured and red-shifted at λ_{PL} = 508 nm compared to the vibrationally structured spectrum of **[10]CPP** at λ_{PL} = 470 nm. The profiles of the spectra suggest that the emissive state of **4PXZPh-[10]CPP** is CT in nature while that of **[10]CPP** is LE in nature. The optical gaps in toluene of **4PXZPh-[10]CPP** and **[10]CPP** are 2.93 and 3.01 eV (Figure **7.5b**), respectively, mirroring the trend in Φ_{PL}. The photoluminescence quantum yield, Φ_{PL}, of **4PXZPh-[10]CPP** is 34% compared to 77% of **[10]CPP**. The emission spectrum of **4PXZPh-[10]CPP** is bathochromically shifted and becomes broader with increasing solvent polarity, behavior that corroborates the CT nature of the emissive excited state (Figure **7.6b**).

We next measured the time-resolved PL decay of **4PXZPh-[10]CPP** in different polarity solvents (Figure **7.6c**). In non-polar solvent hexane, **4PXZPh-[10]CPP** exhibits a τ_p of 4.4 ns but no delayed emission within a time window of 2 μs; however, in PhMe, DCM, and THF, delayed emission was also observed with τ_p of, respectively, 11.0, 14.5, and 13.6 ns and

delayed lifetimes, τ_d, of 0.2, 0.4, and 0.5 µs, respectively. However, the delayed emission is weak and constitutes only about 4% of the total emission decay. These results indicate that the polar solvents stabilize the S_1 state to sufficiently decrease ΔE_{ST} to permit RISC at ambient temperatures. In DMF, the τ_p is 3.1 ns, and no delayed emission was detected. This divergence in behavior was ascribed to significantly enhanced non-radiative decay in the strongly polar medium that effectively quenches the emission.[35]

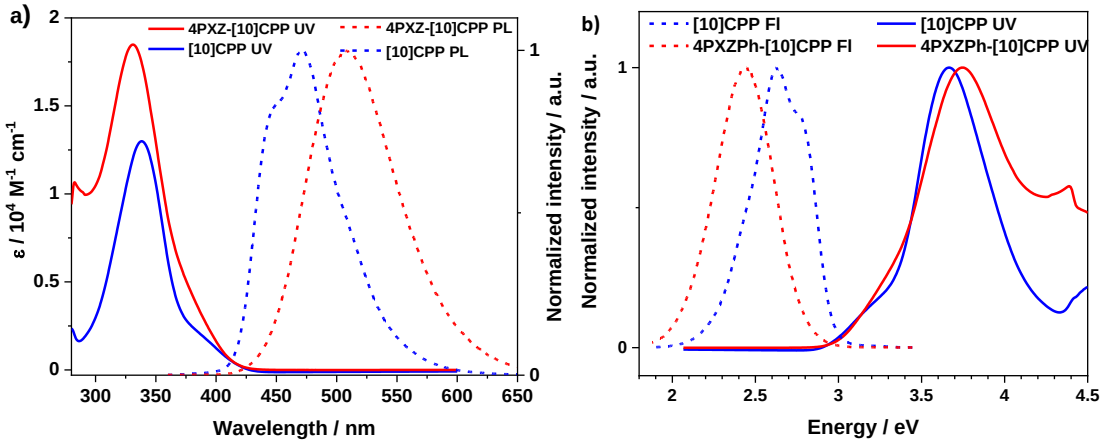

Figure **7.5**. a) Absorption and normalized emission spectra of **4PXZPh-[10]CPP** and **[10]CPP** in toluene solution (10^{-5} M), λ_{exc} = 340 nm, b) normalized UV-vis and fluorescence spectra of **4PXZPh-[10]CPP** and **[10]CPP** in toluene

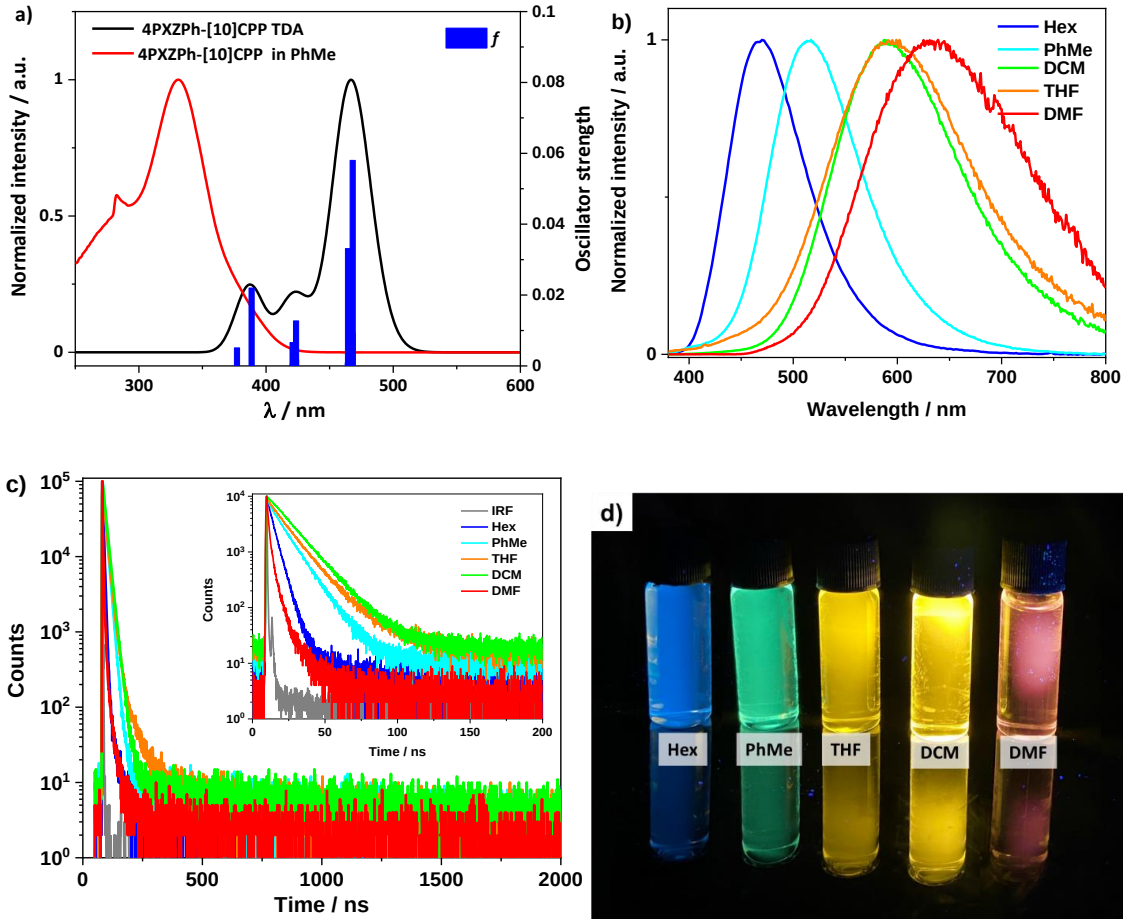

Figure **7.6**. a) Calculated and experimental (in toluene) UV-vis spectra and oscillator strength (*f*) for **4PXZPh-[10]CPP**, b) solvatochromic emission study of **4PXZPh-[10]CPP** (λ_{exc} = 375 nm), c) Transient PL decays of **4PXZPh-[10]CPP** in hexane, PhMe, THF, DCM and DMF (λ_{exc} = 375 nm) and d) Photos of photoexcited **4PXZPh-[10]CPP** in different solvents.

We next investigated the photophysics of **4PXZPh-[10]CPP** in doped film. Bipolar hosts PyD2 and PPF were chosen due to their suitable HOMO/LUMO levels and high triplet state energies. As shown in Figure **7.7a**, **4PXZPh-[10]CPP** shows sky-blue emission with λ_{PL} = 480 nm and Φ_{PL} = 25% in the 15 wt% doped PyD2 film. Triexponential decay was observed

with τ_1 (1.7 ns, 73%), τ_2 (8.9 ns, 26%) and τ_3 (51.3 ns, 1%), respectively (Figure **7.7b**). In 15 wt% doped PPF film, **4PXZPh-[10]CPP** shows sky-blue emission with λ_{PL} = 490 nm, Φ_{PL} = 29% (Figure **7.8a**), and triexponential decay with τ_1 (4.1 ns, 82%), τ_2 (17.2 ns, 17%) and τ_3 (103.3 ns, 1%), respectively, respectively (Figure **7.8b**). The temperature dependence of the transient PL decay in both doped PyD2 and PPF films were performed from 300 K to 200 K. However, the delayed emission component in both films exhibited only a very small increase with decreasing temperature, suggesting that the long-lived emission is phosphorescence.[36–38] The decay of **4PXZPh-[10]CPP** in PyD2 and PPF indicate that this material doesn't show TADF character in these host materials. In the future, the S_1 and T_1 energies of **4PXZPh-[10]CPP** in these hosts will be investigated to help understanding the characteristics of **4PXZPh-[10]CPP**.

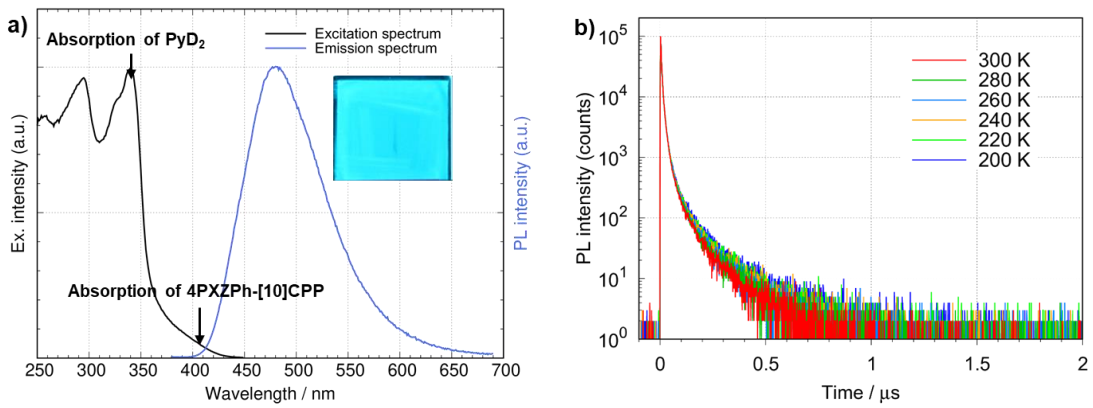

Figure **7.7** a) Absorption and emission spectra and b) Transient PL decay spectra of **4PXZPh-[10]CPP**/PyD_2 film (λ_{exc} = 365 nm).

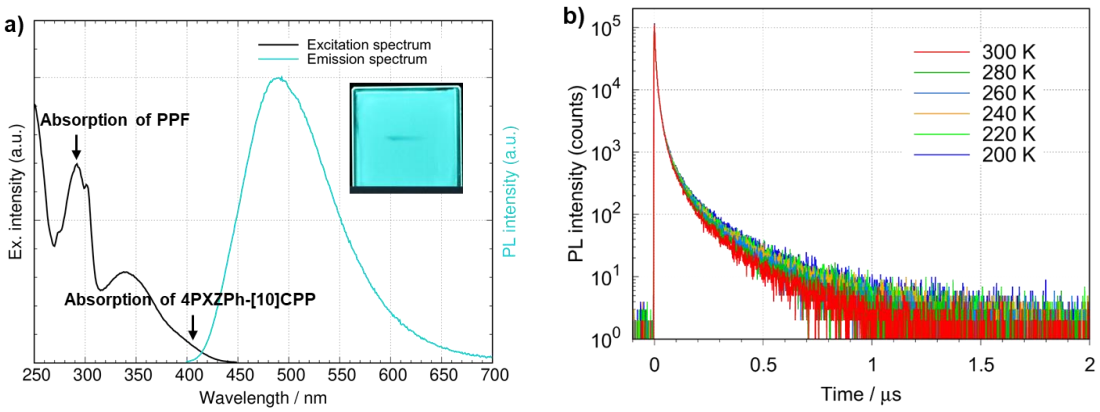

Figure **7.8** a) absorption and emission spectra and b) Transient PL decay spectra of **4PXZPh-[10]CPP**/PPF film (λ_{exc} = 365 nm).

7.6 Electroluminescence Properties

With a view to exploring the potential of **4PXZPh-[10]CPP** as an emitter in OLEDs, a solution-processed OLEDs was fabricated using the architecture: Indium tin oxide (ITO) (50 nm)/poly(3,4-ethylenedioxy thiophene) polystyrene sulfonate (PEDOT:PSS) (40 nm)/15 wt% **4PXZPh-[10]CPP**:PyD_2/PPF (5 nm)/1,3-bis[3,5-di(pyridin-3-yl)phenyl] benzene (BmPyPhB) (45 nm)/lithium quinolin-8-olate (Liq) (1 nm)/Al (80 nm). PEDOT:PSS layer and the emitting layer were deposited by spin-coating and the other layers were thermally vacuum-deposited. In the device, PEDOT:PSS was used as a hole injection and transporting layer, BmPyPhB was used as an electron-transporting and injection layer, and PPF was used as an exciton blocking layer. The **4PXZPh-[10]CPP** exhibits sky-blue emission with λ_{EL} = 490 nm, and EQE_{max} of 0.04 % at 1 mA cm^{-2}. The low EQE_{max} is due to the low Φ_{PL} of **4PXZPh-**

[10]CPP in PyD2 and suppressed RISC process in PyD2 host. This is the first report of an electroluminescent device employing a CPP-based emitter material.

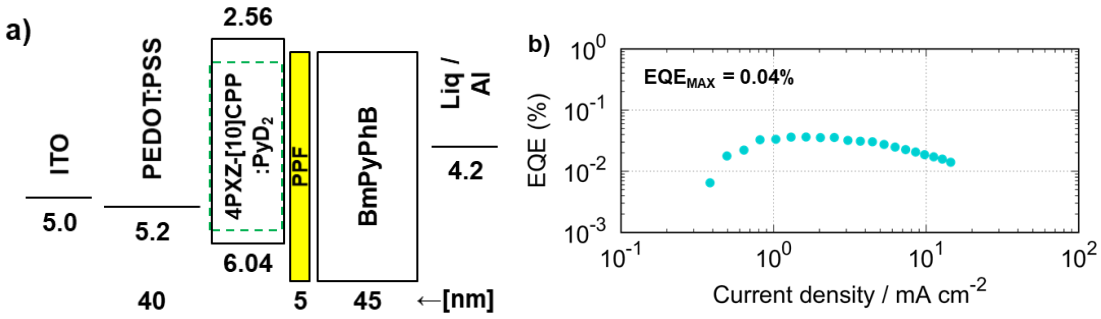

Figure **7.9** a) device stack of **4PXZPh-[10]CPP** based OLEDs, b) EQE-current density characteristics.

7.7 Conclusion and outlook

In this work, we explored the possibility of using CPP within a TADF emitter design. DFT and time-dependent DFT within the Tamm-Dancoff approximation calculations were employed to design the CPP-based TADF emitter, **4PXZPh-[10]CPP**. **4PXZPh-[10]CPP** contains four bulky electron-donating 10-phenyl-10H-phenoxazine (PXZPh) moieties connected to a **[10]CPP** core. This compound possesses suitable HOMO/LUMO separation and the TDA-DFT calculations predict a small ΔE_{ST} of 0.08 eV. **4PXZPh-[10]CPP** exhibited green emission in PhMe with λ_{PL} = 508 nm, and Φ_{PL} = 34% and biexponential emission decay kinetics in both DCM and THF with delayed lifetimes, τ_d of 0.4 and 0.5 µs, respectively. In the ambipolar host PyD2, **4PXZPh-[10]CPP** is moderately bright and showed sky-blue emission with λ_{PL} = 480 nm, Φ_{PL} = 25% in the 15 wt% doped film. We fabricated solution-processed OLEDs based on

4PXZPh-[10]CPP, and the device exhibits sky-blue emission with λ_{EL} of 490 nm and EQE_{max} of 0.04%. Detailed photophysics study of **4PXZPh-[10]CPP** in host materials and device optimization will be carried out in future.

7.8 Experimental section

General consideration

All experiments were carried out with commercial solvents from Fisher Scientific Ltd, except where specifically mentioned. Commercially obtained chemicals were used as received. All manipulations were carried out under an inert atmosphere using standard Schlenk line techniques.

^{1}H NMR, and ^{13}C NMR were recorded at room temperature on a Bruker Avance spectrometer at 400 MHz and 100 MHz, respectively. ^{1}H NMR and ^{13}C NMR spectra were referenced to the residual solvent peaks ($CDCl_3$ = 7.26 ppm for ^{1}H NMR and 77.16 ppm for ^{13}C NMR). The following abbreviations have been used for multiplicity assignments: “s” for singlet, “d” for doublet, “t” for triplet, “m” for multiplet and “br” for broad. Elemental analysis was measured by London Metropolitan University. Samples for high resolution mass spectrum (HRMS) were sent to the National Mass Spectrometry Facility in Swansea (EPSRC) for analysis by nano-electrospray on an Orbitrap instrument.

Materials and synthesis

Synthesis of BrPhPXZ (10-(4-bromophenyl)-10H-phenoxazine)

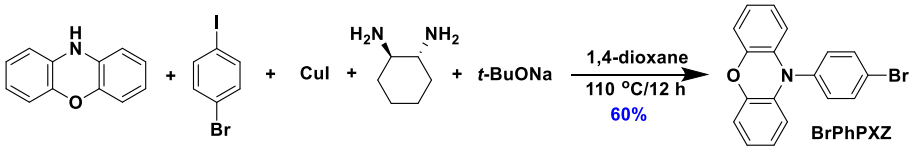

BrPhPXZ was synthesized as literature.[39] To a 250 mL three-neck flask were added phenoxazine (1.8 g, 10 mmol, 1 equiv.), 1-bromo-4-iodobenzene (4.2 g, 15 mmol, 1.5 equiv.), copper (I) iodide (190 mg, 1 mmol, 0.1 equiv.), (±)-*trans*-1,2-diaminocyclohexane (230 mg, 2 mmol, 0.2 equiv.), sodium *tert*-butoxide (3.0 g, 30 mmol, 3 equiv.) and 50 mL of 1,4-dioxane. Oxygen was excluded from the reaction by three freeze-pump-throw cycles. After warming to room temperature, the suspension was heated to 110 °C and stirred for 12 hours. After cooling, 100 mL of saturated ammonium chloride solution was poured into the reaction mixture and the organic phase was extracted with DCM (50 mL × 3). The combined organic layers were dried with anhydrous magnesium sulfate. The organic solvent was removed under reduced pressure and the crude product was purified by silica gel column chromatography. (DCM/Hexane=1/10) to afford **BrPhPXZ** as a white solid (1.3 g).

Yield: 60%. **R_f**: 0.67 (10% DCM/hexanes). **Mp**: 194-196 °C (Lit. Mp.[39] 196-198 °C). **^{1}H NMR (400 MHz, $CDCl_3$) δ (ppm)**: 7.76 (d, *J* = 8.6 Hz, 2H), 7.27 (d, *J* = 8.5 Hz, 2H), 6.88 – 6.66 (m, 4H), 6.63 (td, *J* = 7.6, 1.9 Hz, 2H), 5.94 (dd, *J* = 7.8, 1.5 Hz, 2H). **^{13}C NMR (100 MHz, CDCl3) δ (ppm)**: 143.9, 138.1, 134.4, 134.0, 132.8, 123.3, 122.4, 121.6, 115.6, 113.2. **HRMS** (LTQ Orbitrap XL) **$[M+H]^+$ Calculated: ($C_{18}H_{13}NO^{79}Br$)** 338.0102; **Found:** 338.0110. The characterization matches that previously reported.[39]

Synthesis of BpinPhPXZ (10-(4-(4,4,5,5-tetramethyl-1,3,2-dioxaborolan-2-yl) phenyl)-10*H*-

phenoxazine)

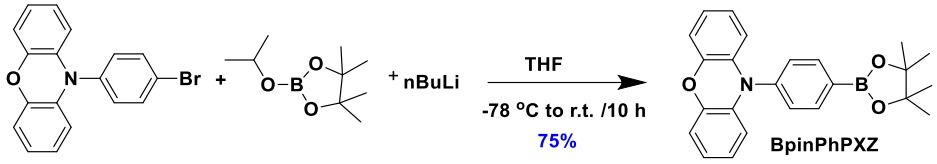

BpinPhPXZ was synthesized as literature.[40] To a 100 mL two-neck flask, 10-(4-bromophenyl)-10H-phenoxazine (1.7 g, 5 mmol, 1 equiv.) was added and degassed by three cycles of vacuum-nitrogen purging. 30 mL of dry THF was then injected into the flask. The solution was cooled to -78 ºC using a dry ice/acetone bath and *n*-butyllithium (1.6 M) (3.4 mL, 5.5 mmol, 1.1 equiv.) was added dropwise into the solution. The mixture was stirred at -78 ºC for 1 hour and 2-isopropoxy-4,4,5,5-tetramethyl-1,3,2-dioxaborolane (1.1 g, 6 mmol, 1.2 equiv.) was injected into the solution. The mixture was stirred at -78 ºC for 30 min before warming to room temperature. The reaction mixture was stirred overnight. The reaction was quenched with MeOH (1 mL) and the reaction was poured into icy water followed by extraction with DCM (50 mL × 3). The combined organic layers were dried with anhydrous magnesium sulfate. The organic solvent was removed under reduced pressure and the crude product was purified by silica gel column chromatography (DCM/Hexane=2/8) to afford **BpinPhPXZ** as a white solid (1.4 g).

Yield: 75%. **R_f**: 0.62 (20% DCM/hexanes). **Mp**: 155-157 °C (Lit. Mp.[40] 156-158 ºC). **^{1}H NMR (500 MHz, $CDCl_3$) δ (ppm)**: 8.05 (d, *J* = 8.2 Hz, 2H), 7.38 (d, *J* = 8.2 Hz, 2H), 6.70 (dd, *J* = 7.8, 1.6 Hz, 2H), 6.65 (td, *J* = 7.6, 1.5 Hz, 2H), 6.59 (td, *J* = 7.7, 1.7 Hz, 2H), 5.93 (dd, *J* = 7.9, 1.5 Hz, 2H), 1.41 (s, 12H). **^{13}C NMR (125 MHz, $CDCl_3$) δ (ppm)**: 143.9, 141.6, 137.5, 134.2, 130.1, 123.2, 121.3, 115.4, 113.3, 84.2, 24.9. **HRMS** (LTQ Orbitrap XL) **$[M+H]^+$ Calculated: ($C_{24}H_{25}NO_3B$)** 336.1849; **Found:** 336.1852. The characterization matches that previously

reported.[40]

Synthesis of BuBQ (2,5-bis(but-3-en-1-yloxy) cyclohexa-2,5-diene-1,4-dione)

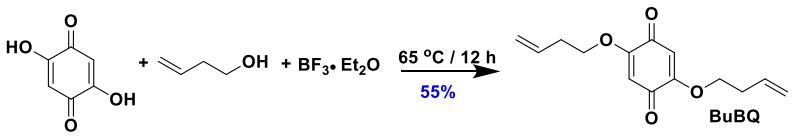

The synthesis of **BuBQ** follows the literature procedure.[11] To a 500 mL three-neck flask was added 2,5-dihydroxy-1,4-benzoquinone (14.0 g, 100 mmol, 1 equiv.) and the flask degassed by three cycles of vacuum-nitrogen purging. 3-buten-1-ol (37.1 g, 2 mol, 20 equiv.) and $BF_3{\cdot}OEt_2$ (30.0 mL, 220 mmol, 2.2 equiv.) were added and the mixture was stirred at 65 ºC for 12 h. After cooling, the resulting mixture was filtered and washed with methanol to afford a brown crude product. The crude product was purified by silica gel column chromatograph (DCM/Hexane=1/1) to afford **BuBQ** as a yellow solid (8.5 g).

Yield: 55%. **R_f**: 0.54 (50% DCM/hexanes). **Mp**: 181-183 °C (Lit. Mp.[41] 181 °C). **^{1}H NMR ($CDCl_3$, 400 MHz) δ (ppm)**: 5.83 ppm (s, 2H), 3.93 (t, *J* = 6.8 Hz, 4H), 1.83 (quin, *J* = 6.8 Hz, 4H), 1.48 (sext, *J* = 8.0 Hz, 4H), 0.97 (t, *J* = 7.6 Hz, 6H). **^{13}C NMR ($CDCl_3$, 100 MHz) δ (ppm)**: 181.9, 158.8, 105.8, 69.5, 30.2, 19.1, 13.6. **HRMS** (MALDI-TOF) **$[M+H]^+$ Calculated: ($C_{14}H_{17}O_4$)** 249.1121, **Found:** 249.1391. The characterization matches that previously reported.[11]

Synthesis of DPBuBQ ((1''R,4''R)-4,4''''-dibromo-2'',5''-bis(but-3-en-1-yloxy)-[1,1':4',1'':4'',1''':4''',1''''-quinquephenyl]-1'',4''-diol)

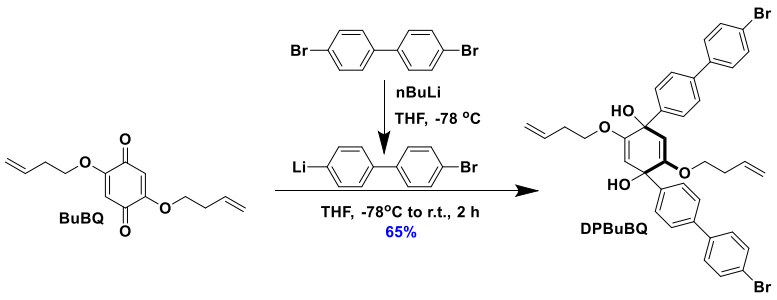

The synthesis of **DPBuBQ** follows the literature procedure.[11] To a 1 L three-neck flask was added 4,4'-dibromo-1,1'-biphenyl (31.1 g, 100 mmol, 4.0 equiv.) and the flask degassed by three cycles of vacuum-nitrogen purging before. THF (300 mL) was added to the flask. The solution was cooled down to -78 ºC using a dry ice/acetone bath and *n*-butyllithium (1.6 M) (3.4 mL, 5.5 mmol, 1.1 equiv.) was added dropwise into the solution. The mixture was stirred at -77 ºC for 1 hour and the solution was transferred via cannula to a -78 ºC solution of **BuBQ** (6.2 g, 25 mmol, 1 equiv.) in THF (200 mL). The mixture was stirred at -78 ºC for 1 h before warming to room temperature over 2 h. The reaction was quenched by saturated NH_4Cl solution (40 mL) and the mixture poured into icy water and then extracted with ethyl acetate (100 mL×3). The combined organic layers were dried with anhydrous sodium sulfate. The organic solvent was removed under reduced pressure and the crude product was purified by silica gel column chromatography (Ethyl actate/Hexane=1/9) to afford **DPBuBQ** as a white solid (48.8 g).

Yield: 65%. **R_f**: 0.44 (20% ethyl acetate/hexanes). **Mp**: 87 °C (Lit. Mp.[11] 88-89 °C). **^{1}H NMR ($CDCl_3$, 400 MHz) δ (ppm)**: 7.56 (d, *J* = 8.4 Hz, 8H), 7.50 (d, *J* = 8.4 Hz, 16 H), 7.46 (d, *J* = 8.4 Hz, 8H), 5.67 (ddt, *J* = 17.2, 10.4, 6.8 Hz, 2H), 5.10 (s, 2H), 5.00 (d, *J* = 18.8 Hz, 2H), 4.97 (d, *J* = 10.4 Hz, 2H), 3.83-3.92 (dt, *J* = 9.0, 7.0 Hz, 2H), 3.73-3.82 (dt, *J* = 9.0, 7.1 Hz, 2H), 3.03 (s, 4H), 2.35 (q, *J* = 6.8 Hz, 4H). **^{13}C NMR ($CDCl_3$, 100 MHz) δ (ppm)**: 154.2, 144.7, 138.9, 137.9,

134.1, 131.9, 128.6, 126.7, 126.2, 121.6, 117.1, 103.1, 73.9, 66.8, 32.9. **HRMS** (MALDI-TOF) **[M+Na]$^+$ Calculated: ($C_{38}H_{34}Br_2O_4Na$)** 735.0716, **Found:** 735.0724. The characterization matches that previously reported.[11]

Synthesis of TesBuBQ ((((1''R,4''R)-4,4''''-dibromo-2'',5''-bis(but-3-en-1-yloxy)-[1,1':4',1'':4'',1''':4''',1''''-quinquephenyl]-1'',4''-diyl)bis(oxy))bis(triethylsilane))

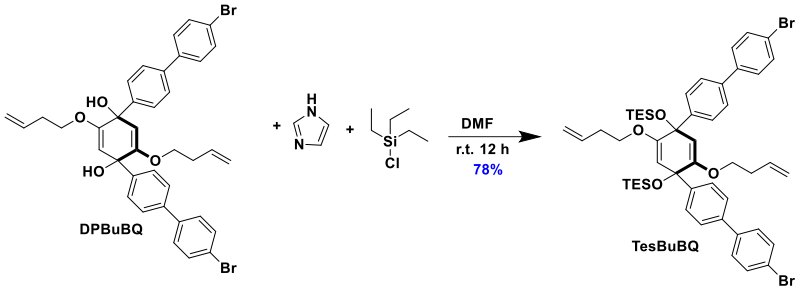

The synthesis of **TesBuBQ** follows the literature procedure.[11] To a 250 mL three-neck flask were added **DPBuBQ** (7.2 g, 10 mmol, 1 equiv.) and imidazole (3.4g, 50 mmol, 5 equiv.) and the flask degassed by three cycles of vacuum-nitrogen purging. DMF (50 mL) was then added followed by dropwise addition of triethylchlorosilane (5 mL, 30 mmol, 3 equiv.). The solution was stirred at room temperature for 12 h. The resulting mixture was poured into icy water and extracted by DCM (50 mL×3). The combined organic layers were dried with anhydrous sodium sulfate. The organic solvent was removed under reduced pressure and the crude product was purified by silica gel column chromatography (Ethyl actate/Hexane=0.2/9.8) to afford **TesBuBQ** as a white solid (7.1 g).

Yield: 78%. **R_f**: 0.54 (10% ethyl acetate/hexanes). **Mp**: 85-86 °C (Lit. Mp.[11] 86-88 °C). **^{1}H NMR ($CDCl_3$, 400 MHz) δ (ppm)**: 7.54 (d, *J* = 8.4 Hz, 4H), 7.46 (d, *J* = 8.8 Hz, 4H), 7.45 (s, 8H), 5.66-5.77 (m, 2H), 5.01 (d, *J* = 17.2 Hz, 2H), 4.97 (d, *J* = 10.1 Hz, 2H), 4.86 (s, 2H), 3.73-3.80 (dt, *J*

= 9.2, 6.4 Hz, 2H), 3.61-3.69 (dt, *J* = 9.0, 7.1 Hz, 2H), 2.38 (q, *J* = 6.8 Hz, 4H), 0.97 (t, *J* = 8.0 Hz, 18H), 0.55-0.74 (m, 12H). **^{13}C NMR ($CDCl_3$, 100 MHz) δ (ppm)**: 153.9, 146.1, 139.9, 137.8, 134.5, 131.8, 128.6, 127.0, 126.0, 121.3, 116.2, 104.0, 66.5, 33.3, 7.2, 6.4. **HRMS** (MALDI-TOF) **$[M]^+$ Calculated: ($C_{50}H_{62}Br_2O_4Si_2$)** 942.2533, **Found:** 942.2557. The characterization matches that previously reported.[11]

Synthesis of BpinBQ ((((1''R,4''R)-2'',5''-bis(but-3-en-1-yloxy)-4,4''''-bis(4,4,5,5-tetramethyl-1,3,2-dioxaborolan-2-yl)-[1,1':4',1'':4'',1''':4''',1''''-quinquephenyl]-1'',4''-diyl)bis(oxy))bis(triethylsilane))

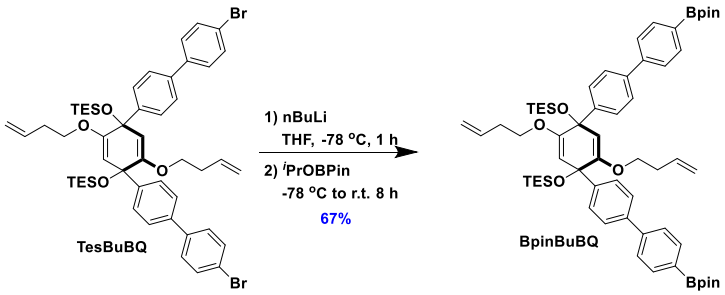

The synthesis of **BpinBuBQ** follows the literature procedure.[11] To a 250 mL three-neck was added **TesBuBQ** (4.7 g, 5 mmol, 1 equiv.) and the flask was degassed by three cycles of vacuum-nitrogen purging. Dry THF (30 mL) was then added. The solution was cooled to -78 °C using a dry ice/acetone bath and *n*-butyllithium (1.6 M) (8 mL, 12.5 mmol, 2.5 equiv.) was added dropwise into the solution. The mixture was stirred at -78 °C for 1 hour and tri*iso*propyl borate (3.1 mL, 15 mmol, 3 equiv.) was added dropwise. The mixture was stirred at -78 °C for 30 min before warming to room temperature and stirred overnight. The reaction was quenched with methanol (1 mL) and the reaction was poured into icy water followed by extraction with DCM (50 mL × 3). The

combined organic layers were dried with anhydrous sodium sulfate. The organic solvent was removed under reduced pressure and the crude product was washed with methanol and recrystallized from DCM/methanol = 1/10 to afford **BpinBuBQ** as white solid (3.2 g).

Yield: 67%. **R_f**: 0.44 (10% ethyl acetate/hexanes). **Mp**: 88-90 °C (Lit. Mp.[11] 88-89°C). **^{1}H NMR ($CDCl_3$, 400 MHz) δ (ppm)**: 7.86 (d, *J* = 8.4 Hz, 4H), 7.62 (d, *J* = 8.4 Hz, 4H), 7.52 (d, *J* = 8.4 Hz, 4H), 7.46 (d, *J* = 8.4 Hz, 4H), 5.66-5.78 (ddt, *J* = 17.2, 10.4, 6.8 Hz, 2H), 5.18 (dq, *J* = 17.2, 1.7 Hz, 2H), 4.99 (dq, *J* = 10.4, 1.6 Hz, 2H), 4.87 (s, 2H), 3.73-3.82 (dt, *J* = 9.0, 6.6 Hz, 2H), 3.59-3.70 (dt, *J* = 9.0, 7.1 Hz, 2H), 2.38 (q, *J* = 6.8 Hz, 4H), 1.36 (s, 24 H), 0.97 (t, *J* = 8.0 Hz, 18 H), 0.57-0.79 (m, 12H). **^{13}C NMR ($CDCl_3$, 100 MHz) δ (ppm)**: 153.9, 146.0, 143.7, 139.3, 135.2, 134.5, 127.0, 126.8, 126.4, 126.3, 116.7, 104.0, 83.8, 75.3, 66.4, 33.3, 24.9, 7.2, 6.4. **HRMS** (MALDI-TOF) **$[M]^+$ Calculated: ($C_{62}H_{86}Br_2O_8Si_2$)** 1035.6193, **Found:** 1035.6170. The characterization matches that previously reported.[11]

Synthesis of TesBu-8Ph2Ch ((5^1*R*, 5^4*R*, 10^1*S*, 10^4*S*)-5^2, 5^5, 10^2, 10^5-tetra(but-3-en-1-yloxy)-5^1, 5^4, 10^1, 10^4-tetra(oxytriethylsilane)-1, 2, 3, 4, 6, 7, 8, 9 (1, 4)-octabenzena-5, 10 (1, 4)-dicyclo hexane cyclodecaphane-5^2, 5^5, 10^2, 10^5-tetraene)

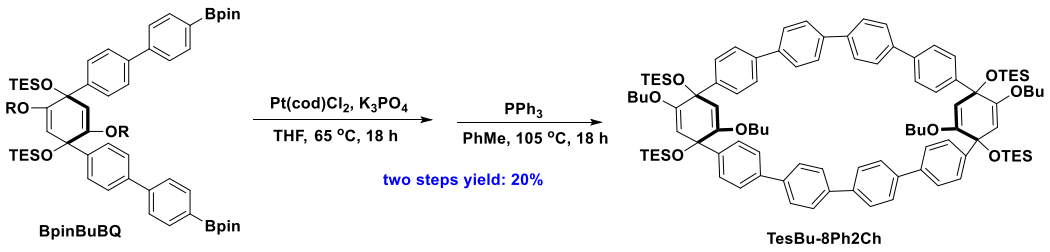

The synthesis of **TesBu-8Ph2Ch** follows the literature procedure.[11] To a 250 mL three-neck were added **BpinBuBQ** (2.1 g, 2 mmol, 1 equiv.), $Pt(cod)Cl_2$ (374 mg, 2 mmol, 1 equiv.), K_3PO_4 (2.2

g, 10 mmol, 5 equiv.) and the flask degassed by three cycles of vacuum-nitrogen purging. Dry THF (100 mL) was then added. The solution was stirred at 65 ºC overnight, cooled to room temperature and then poured into water. The mixture was extracted with DCM (50 mL×3) and the combined organic layers were dried with anhydrous sodium sulfate. The organic solvent was removed under reduced pressure to afford the crude Pt-complex product as white solid. The Pt-complex and triphenylphosphine (2.6 g, 10 mmol, 5 equiv.) were added to a 250 mL three-neck RBF, which was then degassed by three cycles of vacuum-nitrogen purging. Toluene (100 mL) was added, and the solution was stirred at 105 ºC overnight. The resulting mixture was washed with brine (20 mL) and extracted with DCM (50 mL×3). The organic phase was dried with by anhydrous sodium sulfate and removed under reduced pressure to afford the crude product as beige solid. The crude product was purified by silica gel column chromatography (DCM/hexane=1/5) and 2.5H polystyrene gel permeation chromatography (chloroform as eluent) to afford **TesBu-8Ph2Ch** as a white solid (400 mg).

Two steps yield: 20%. **R_f**: 0.54 (15% DCM/hexanes). **Mp**: 153 °C (Lit. Mp.[11] 150 °C). **^{1}H NMR ($CDCl_3$, 400 MHz) δ (ppm)**: 7.47 (d, *J* = 8.4 Hz, 8H), 7.33 (d, *J* = 8.4 Hz, 8H), 7.08 (d, *J* = 8.0 Hz, 8H), 6.99 (d, *J* = 8.8 Hz, 8H), 6.96 (d, *J* = 8.8 Hz, 8H), 5.87-6.00 (m, 4H). 5.17 (s, 4H), 5.14 (s, 4H), 5.10-5.24 (m, 8H), 3.85-3.69 (m, 8H), 2.52-2.69 (m, 8H), 1.00 (t, *J* = 8.0 Hz, 36H), 0.60-0.77 (m, 24H). **^{13}C NMR ($CDCl_3$, 100 MHz) δ (ppm)**: 156.0, 155.7, 140.0, 138.8, 134.5, 134.5, 127.6, 126.8, 126.8, 126.7, 126.1, 117.1, 104.2, 103.7, 75.1, 75.0, 66.8, 33.5, 7.2, 6.4. **HRMS** (MALDI-TOF) **$[M]^+$ Calculated: ($C_{100}H_{124}O_8Si_2$)** 1564.8368, **Found:** 1564.8319. The characterization matches that previously reported.[11]

Synthesis of OHBu-8Ph2Ch ((5^1*R*, 5^4*R*, 10^1*S*, 10^4*S*)-5^2, 5^5, 10^2, 10^5-tetra(but-3-en-1-yloxy)-1, 2, 3, 4, 6, 7, 8, 9 (1, 4)-octabenzena-5, 10(1, 4)-dicyclohexanacyclodecaphane-5^2, 5^5, 10^2, 10^5-tetraene-5^1, 5^4, 10^1, 10^4-tetraol)

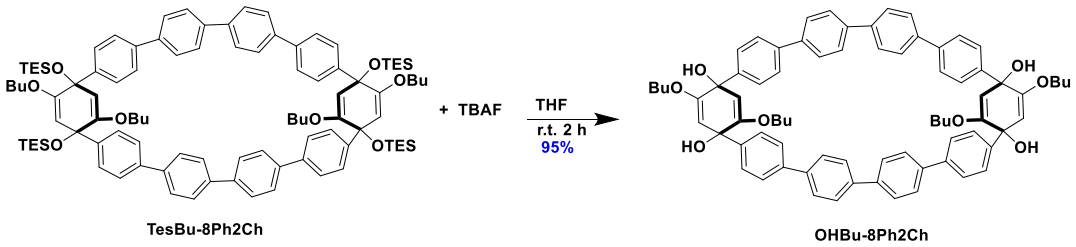

TesBu-8Ph2Ch OHBu-8Ph2Ch

The synthesis of **OHBu-8Ph2Ch** follows the literature procedure.[11] To a 100 mL flask were added **TesBu-8Ph2Ch** (1.6 g, 1 mmol, 1 equiv.) and TBAF (1.00 M) (5 mL, 5 mmol, 5 equiv) in THF (25 mL). The solution was stirred at room temperature for 2 hours and then poured into icy water. The precipitate was filtrated and washed with hexane to afford **OHBu-8Ph2Ch** as a white solid (1.2 g).

Yield: 67%. **R$_f$**: 0.30 (40% ethyl acetate/hexanes). **Mp**: 211-213 °C (Lit. Mp. 210 °C). **^{1}H NMR (CDCl$_3$, 400 MHz) δ (ppm)**: 7.56 (d, *J* = 8.4 Hz, 2H), 7.50 (d, *J* = 3.2 Hz, 16H), 7.46 (d, *J* = 8.4 Hz, 8H), 5.60-5.73 (ddt, *J* = 17.2, 104, 6.8 Hz, 2H), 5.10 (s, 4H), 5.00 (d, *J* = 17.2 Hz, 4H), 4.97 (d, *J* = 10.4 Hz, 4H), 3.83-3.92 (dt, *J* = 9.2, 6.4 Hz, 4H), 3.73-3.82 (dt, *J* = 9.2, 6.4 Hz, 4H), 3.02 (s, 4H), 2.38 (q, *J* = 6.8 Hz, 8H). **^{13}C NMR (CDCl$_3$, 100 MHz) δ (ppm)**: 155.6, 155.1, 142.3, 142.2, 139.5, 138.8, 134.1, 134.1, 127.6, 126.9, 126.6, 117.4, 117.4, 103.7, 102.9, 73.7, 73.6, 67.2, 67.2, 33.3, 33.2. **HRMS** (MALDI-TOF) **[M]$^+$ Calculated: (C$_{76}$H$_{68}$O$_8$)** 1108.4909, **Found:** 1108.4864. The characterization matches that previously reported.[11]

Synthesis of BuO-[10]CPP ((10^4*R*, *E*)-2^2, 2^5, 7^2, 7^5-tetra(but-3-en-1-yloxy)-1, 2, 3, 4, 6, 7, 8(1, 4)-heptabenzena-5, 9, 10(1, 4)-tricyclohexanacyclodecaphane-5^2, 5^4, 9^1, 9^5, 10^1, 10^5-hexaene)

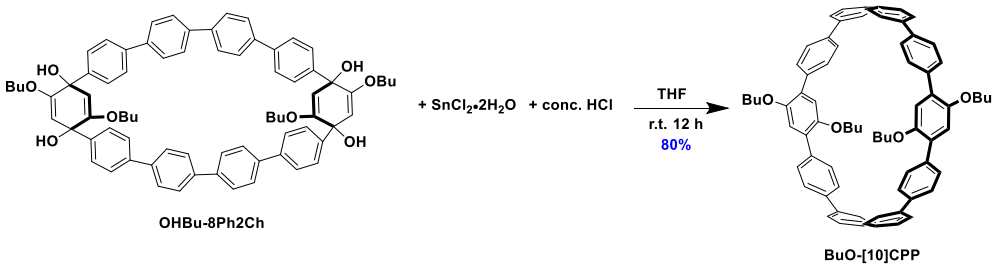

The synthesis of **BuO-[10]CPP** follows the literature procedure.[11] To a 250 mL flask containing a solution of $SnCl_2 \cdot H_2O$ (1.1 g, 5 mmol, 5 equiv) in THF (50 mL) was added concentrated HCl (12 N) (0.8 mL, 10 mmol, 10 equiv) and the reaction mixture stirred at room temperature for 1 hour. A solution of **OHBu-8Ph2Ch** (1.1 g, 1 mmol, 1 equiv) in THF (20 mL) was added and the mixture was stirred at room temperature overnight. The reaction was quenched with 10% aqueous NaOH solution and extracted with ethyl acetate (50 mL×3). The combined organic layers were dried with anhydrous sodium sulfate. The organic solvent was removed under reduced pressure and the crude product was purified by silica gel column chromatography (DCM) to afford **BuO-[10]CPP** as a white solid (780 mg).

Yield: 80%. **R$_f$**: 0.64 (50% DCM/hexanes). **Mp**: 255-256 °C (Lit. Mp.[11] 251 °C). **^{1}H NMR (CDCl$_3$, 400 MHz) δ (ppm)**: 7.62 (d, *J* = 8.4 Hz, 8H), 7.60 (d, *J* = 8.4 Hz, 8H), 7.54 (d, *J* = 8.4 Hz, 8H), 7.48 (d, *J* = 8.4 Hz, 8H), 6.86 (s, 4H), 5.76-5.88 (ddt, *J* = 17.2, 10.4, 6.8 Hz, 2H), 5.11 (d, *J* = 17.2 Hz, 4H), 5.05 (d, *J* = 10.4 Hz, 4H), 3.90 (s, *J* = 6.4 Hz, 8H), 2.46 (q, *J* = 6.2 Hz, 8H). **^{13}C NMR (CDCl$_3$, 100 MHz) δ (ppm)**: 151.3, 138.6, 136.6, 134.8, 129.6, 129.5, 127.5, 127.1, 126.6, 116.9, 116.6, 69.3, 34.0. **HRMS** (MALDI-TOF) **[M]$^+$ Calculated: (C$_{76}$H$_{68}$O$_8$)** 1040.4799, **Found:** 1040.4793. The characterization matches that previously reported.[11]

Synthesis of DOBu-[10]CPP ((10^4*R*, *E*)-2^2, 2^5, 7^2, 7^5-tetra(3,4-dihydroxybutoxy)-1, 2, 3, 4, 6, 7, 8(1, 4)-heptabenzena-5, 9, 10(1, 4)-tricyclohexanacyclodecaphane-5^2, 5^4, 9^1, 9^5, 10^1, 10^5-hexaene)

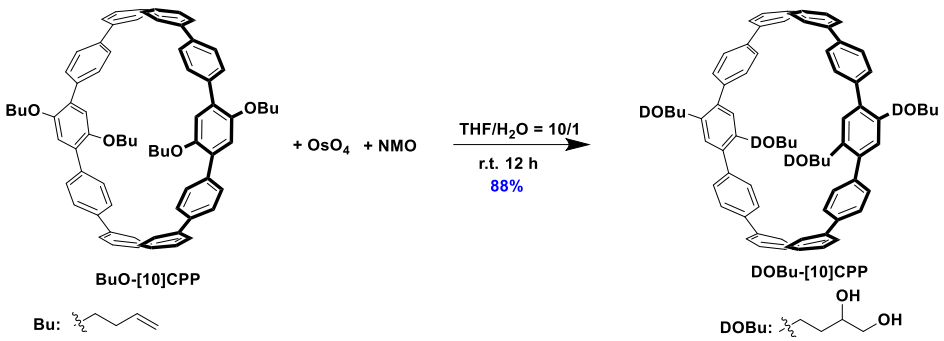

The synthesis of **DOBu-[10]CPP** follows the literature procedure.[42] To a 250 mL flask were added **BuO-[10]CPP** (1.0 g, 1 mmol, 1 equiv.), OsO_4 (0.1 mmol, 26 mg, 0.1 equiv), and *N*-methylmorpholine *N*-oxide (NMP) (515 mg, 4.4 mmol, 4.4 equiv.). THF (100 mL) and H_2O (10 mL) were added and the solution was stirred at room temperature for 12 hours. The resulting solution was washed with 10% aqueous Na_2SO_3 solution (20 mL) and brine (30 mL) before extracted with ethyl acetate (50 mL×3). The combined organic layers were dried with anhydrous sodium sulfate. The organic solvent was removed under reduced pressure to afford the crude product as brown solid, which was purified by recrystallization from DCM/hexane = 1/5 to afford the product as a yellow solid (900 mg).

Yield: 88%. **R$_f$**: 0.40 (50% DCM/hexanes). **Mp**: 354-355 °C (Lit. Mp.[42] 350 °C). **^{1}H NMR (DMSO-d$_6$, 400 MHz) δ (ppm)**: 7.73 (d, *J* = 8.4 Hz, 8H), 7.70 (d, *J* = 8.4 Hz, 8H), 7.66 (d, *J* = 8.4 Hz, 8H), 7.59 (d, *J* = 8.4 Hz, 8H), 6.99 (s, 4H), 4.53 (t, *J* = 6.4 Hz, 8H), 4.02 (t, *J* = 6.4 Hz, 8H), 3.53-3.65 (m, 4H), 3.30 (m, 8H), 1.85-1.97 (m, 4H), 1.54-1.65 (m, 4H). **^{13}C NMR (DMSO-**

d_6, 100 MHz) δ (ppm): 150.5, 137.7, 137.4, 136.8, 136.0, 129.2, 127.9, 127.2, 126.8, 126.3, 115.0, 68.0, 65.9, 33.3. **HRMS** (MALDI-TOF) **$[M]^+$ Calculated: ($C_{76}H_{72}O_{12}$)** 1176.4799, **Found:** 1176.5041. The characterization matches that previously reported.[42]

Synthesis of PnO-[10]CPP ((10⁴*R*, *E*)-2², 2⁵, 7², 7⁵-tetra(oxypropanal)-1, 2, 3, 4, 6, 7, 8(1, 4)-heptabenzena-5, 9, 10(1, 4)-tricyclohexanacyclodecaphane-5², 5⁴, 9¹, 9⁵, 10¹, 10⁵-hexaene)

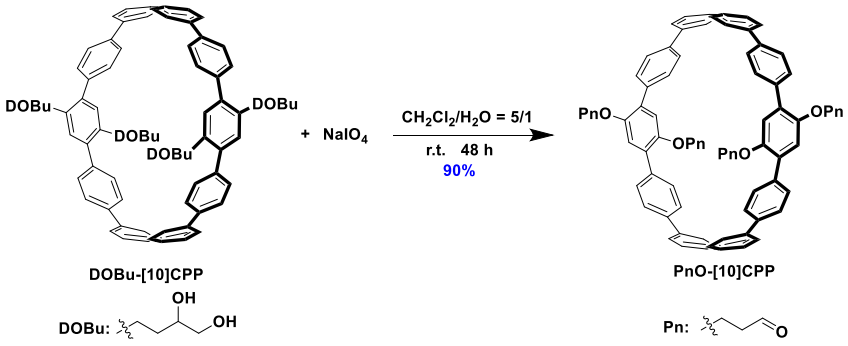

The synthesis of **PnO-[10]CPP** follows the literature procedure.[42] To a 500 mL flask were added **BhO-[10]CPP** (588 mg, 0.5 mmol, 1 equiv.), $NaIO_4$ (2.1 g, 10 mmol, 20 equiv.) in CH_2Cl_2 (200 mL), and H_2O (40 mL). The mixture was stirred at room temperature vigorously for 48 hours. The organic layer was washed with 10% aqueous Na_2SO_3 solution (10 mL) and brine (15 mL). The organic layers were dried with anhydrous sodium sulfate and the solvent removed under reduced pressure to afford the product **PnO-[10]CPP** as a yellow solid (540 mg).

Yield: 90%. **R_f**: 0.66 (50% DCM/hexanes). **Mp**: 280-281 °C (Lit. Mp.[42] 285 °C). **^{1}H NMR (DMSO-d_6, 400 MHz) δ (ppm)**: 9.66 (t, *J* = 5.6, 1.6 Hz, 4H), 7.75 (d, *J* = 8.8 Hz, 8H), 7.65 (d, *J* = 8.8 Hz, 8H), 7.63 (d, *J* = 8.8 Hz, 8H), 7.57 (d, *J* = 8.8 Hz, 8H), 7.03 (s, 4H), 4.25 (t, *J* = 5.6 Hz, 8H), 2.81 (td, *J* = 5.6, 1.6 Hz, 8H). **^{13}C NMR (DMSO-d_6, 100 MHz) δ (ppm)**: 201.8, 150.3, 137.6, 137.5, 136.8, 135.7, 129.3, 128.2, 127.2, 126.8, 126.2, 115.4, 63.1, 42.7. **HRMS** (MALDI-

TOF) **[M]$^+$ Calculated: ($C_{72}H_{56}O_8$)** 1048.3970, **Found:** 1048.4024. The characterization matches that previously reported.[42]

Synthesis of OH-[10]CPP ((10^4*R*, *E*)-1, 2, 3, 4, 6, 7, 8(1, 4)-heptabenzena-5, 9, 10(1, 4)-tricyclohexanacyclodecaphane-5^2, 5^4, 9^1, 9^5, 10^1, 10^5-hexaene-2^2, 2^5, 7^2, 7^5-tetraol)

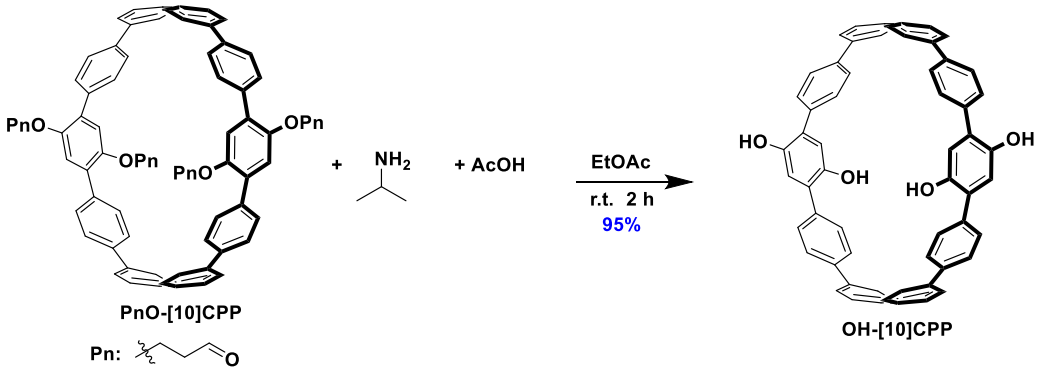

The synthesis of **OH-[10]CPP** follows the literature procedure.[42] To a 500 mL flask were added **PnO-[10]CPP** (524 mg, 0.5 mmol, 1 equiv.), isopropylamine (0.22 mL, 2.5 mmol, 5 equiv.), acetic acid (0.14 mL, 2.5 mmol, 5 equiv.), and ethyl acetate (200 mL). The mixture was bubbled with nitrogen for 30 min and stirred at room temperature for 2 hours. The reaction was quenched with 20 mL of water and extracted with ethyl acetate (50 mL×3). The combined organic layers were dried with anhydrous sodium sulfate. The organic solvent was removed under reduced pressure to afford the crude product as brown solid, which was purified by recrystallization from DCM/hexane = 1/20 to afford **OH-[10]CPP** as a yellow solid (400 mg).

Yield: 95%. **R_f**: 0.68 (50% ethyl acetate/hexanes). **Mp**: 209-211 °C (Lit. Mp.[42] 210 °C). **^{1}H NMR ($CDCl_3$, 400 MHz) δ (ppm)**: 7.62 (d, *J* = 8.8 Hz, 8H), 7.57 (d, *J* = 8.8 Hz, 8H), 7.52 (d, *J* = 8.8 Hz, 8H), 6.74 (s, 4H), 4.85 (s, 4H). **^{13}C NMR ($CDCl_3$, 100 MHz) δ (ppm)**: 147.1, 139.5, 138.4, 138.1, 135.6, 129.3, 129.1, 127.8, 127.7, 127.3, 118.1. **HRMS** (MALDI-TOF) **[M]$^+$ Calculated:**

($C_{60}H_{40}O_4$) 824.2921, **Found:** 824.2923. The characterization matches that previously reported.[42]

Synthesis of OTf-[10]CPP ((10⁴*R*, *E*)-1, 2, 3, 4, 6, 7, 8(1, 4)-heptabenzena-5, 9, 10(1, 4)-tricyclohexanacyclodecaphane-5², 5⁴, 9¹, 9⁵, 10¹, 10⁵-hexaene-2², 2⁵, 7², 7⁵-tetra (trifluoromethanesulfonate))

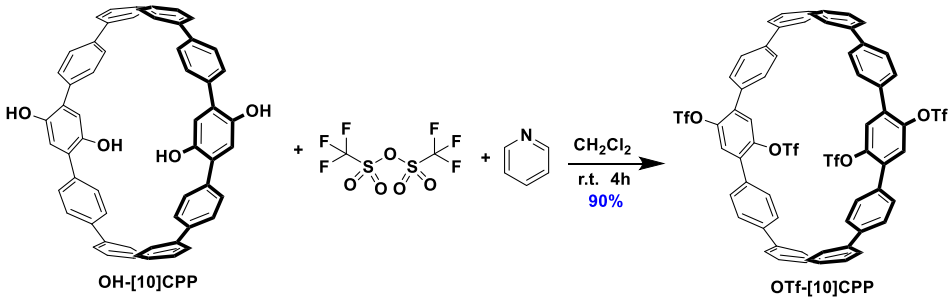

The synthesis of **OTf-[10]CPP** follows the literature procedure.[42] To a 200 mL flask were added **OH-[10]CPP** (412 mg, 0.5 mmol, 1 equiv.), triflic anhydride (1.6 mL, 10 mmol, 20 equiv.), pyridine (5 mL, 30 mmol, 60 equiv) and the solution degassed by three cycles of vacuum-nitrogen purging. Dry DCM (50 mL) was then added. The solution was stirred at room temperature for 4 hours and then quenched with 1mL water. The mixture was extracted with ethyl acetate (50 mL × 3) and the combined organic layers were dried with anhydrous sodium sulfate. The organic solvent was removed under reduced pressure to afford the crude product, which was purified by washing with 10 mL of hexane to give **OTf-[10]CPP** as a white solid (420 mg).

Yield: 90%. **R_f**: 0.60 (10% ethyl acetate/hexanes). **Mp**: 298-299 °C (Lit Mp.[42] 301 °C). **^{1}H NMR ($CDCl_3$, 400 MHz) δ (ppm)**: 7.62 (d, *J* = 8.8 Hz, 8H), 7.57 (d, *J* = 8.8 Hz, 8H), 7.52 (d, *J* = 8.8 Hz, 8H), 6.84 (s, 4H). **^{13}C NMR ($CDCl_3$, 100 MHz) δ (ppm)**: 147.1, 140.3, 138.4, 138.1, 135.6,

129.3, 129.1, 127.8, 127.7, 127.3, 118.1, 118.0. **HRMS** (MALDI-TOF) **$[M]^+$ Calculated: ($C_{64}H_{36}F_{12}O_{12}S_4$)** 1352.0898, **Found:** 1352.0901. The characterization matches that previously reported.[42]

Synthesis of 4PXZPh-[10]CPP ((10⁴*R*, *E*)-1, 2, 3, 4, 6, 7, 8(1, 4)-heptabenzena-5, 9, 10(1, 4)-tricyclohexanacyclodecaphane-5², 5⁴, 9¹, 9⁵, 10¹, 10⁵-hexaene-2², 2⁵, 7², 7⁵-tetra(4-phenyl-10*H*-phenoxazine))

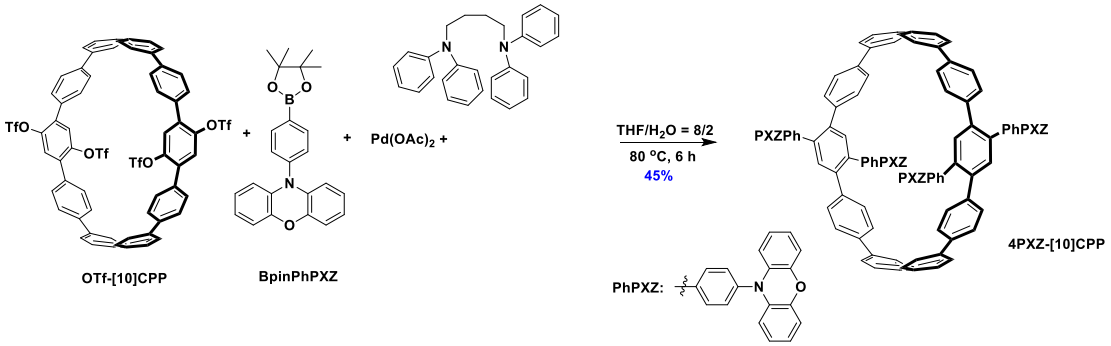

To a 50 mL Schlenk tube were added **OTf-[10]CPP** (68 mg, 0.05 mmol, 1 equiv.), BpinPhPXZ (192 mg, 0.5 mmol, 10 equiv.), palladium(II) acetate (3 mg, 0.01 mmol, 0.2 equiv), butane-1,4-diamine (2 mg, 0.02 mmol, 0.4 equiv), potassium carbonate (200 mg, 1.5 mol, 30 equiv), THF (8 mL), and water (2 mL). The tube as degassed by three cycles of freeze-pump-thaw. The suspension was heated to 80 °C and stirred for 6 hours. After cooling, saturated ammonium chloride solution (100 mL) was added followed by extraction with ethyl acetate (20 mL×3). The combined organic layers were dried with anhydrous magnesium sulfate. The organic solvent was removed under reduced pressure. The crude product was purified by silica gel column chromatography (ethyl acetae/hexane=1/9) and 2.5H polystyrene gel permeation chromatography (chloroform as eluent) to afford **4PXZ-[10]CPP** as a yellow solid (25 mg).

Yield: 45%. **R_f**: 0.44 (10% ethyl acetate/hexanes). **Mp**: 288-289 °C. **^{1}H NMR ($CDCl_3$, 400 MHz) δ (ppm)**: 7.52 (d, *J* = 8.6 Hz, 8H), 7.47 – 7.40 (m, 12H), 7.36 (t, *J* = 8.6 Hz, 16H), 7.19 (dd, *J* = 8.4, 6.3 Hz, 14H), 6.79 – 6.60 (m, 24H), 6.04 – 5.92 (dd, *J* = 7.8, 1.5 Hz, 8H).**^{13}C NMR ($CDCl_3$, 100 MHz) δ (ppm)**: 154.2, 144.6, 140.9, 140.2, 139.6, 138.9, 138.0, 137.9, 134.4, 134.1, 133.9, 132.8, 131.9, 128.9, 128.6, 126.8, 126.2, 123.3, 122.4, 121.6, 117.1, 115.6, 113.2, 103.2. **HRMS** (MALDI-TOF) **$[M]^+$ Calculated: ($C_{132}H_{84}N_4O_4$)** 1789.6526; **Found**: 1789.6573. **Elemental analysis: Calced for $C_{132}H_{84}N_4O_4$**: C, 88.57; H, 4.73; N, 3.13. Found: C, 87.08; H, 4.77; N, 3.42. **HPLC:** 50% MeOH/MeCN, 1.0 mL min^{-1}, 254 nm; tr (96.5 %) = 31.3 min.

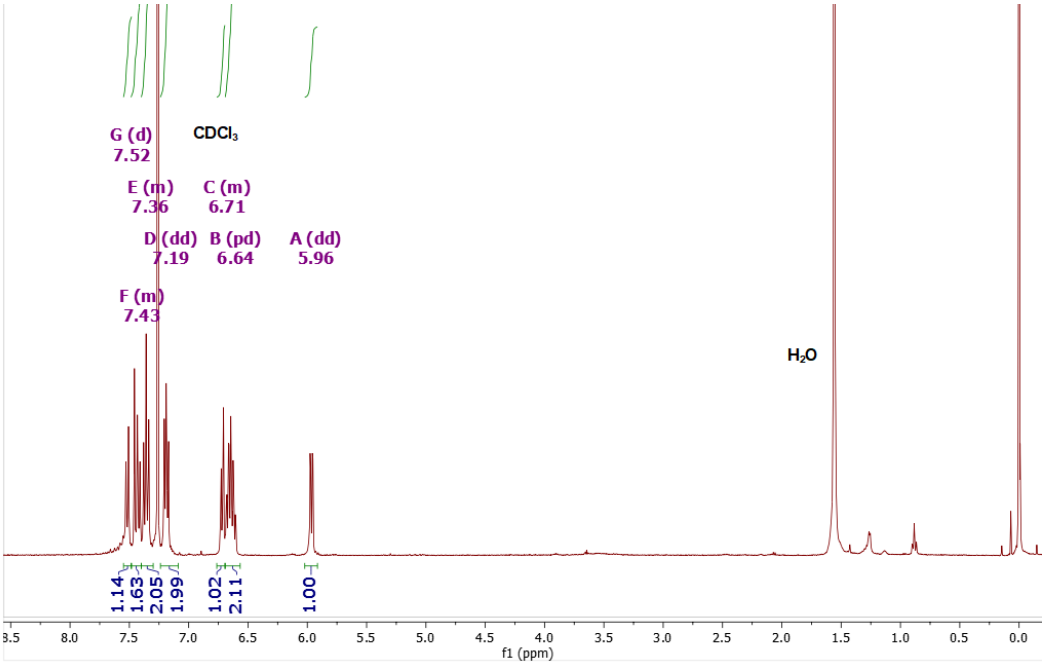

Figure **7.10**. ^{1}H NMR of **4PXZ-[10]CPP** in $CDCl_3$.

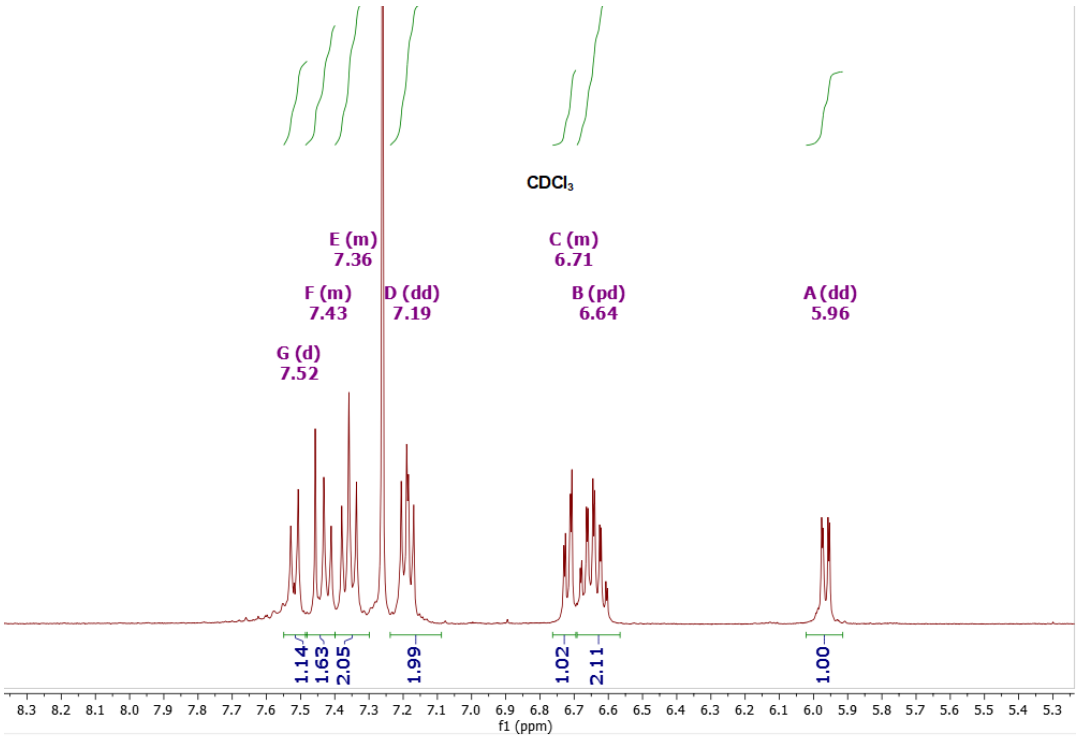

Figure **7.11**. Zoomed ^{1}H NMR of **4PXZ-[10]CPP** in $CDCl_3$.

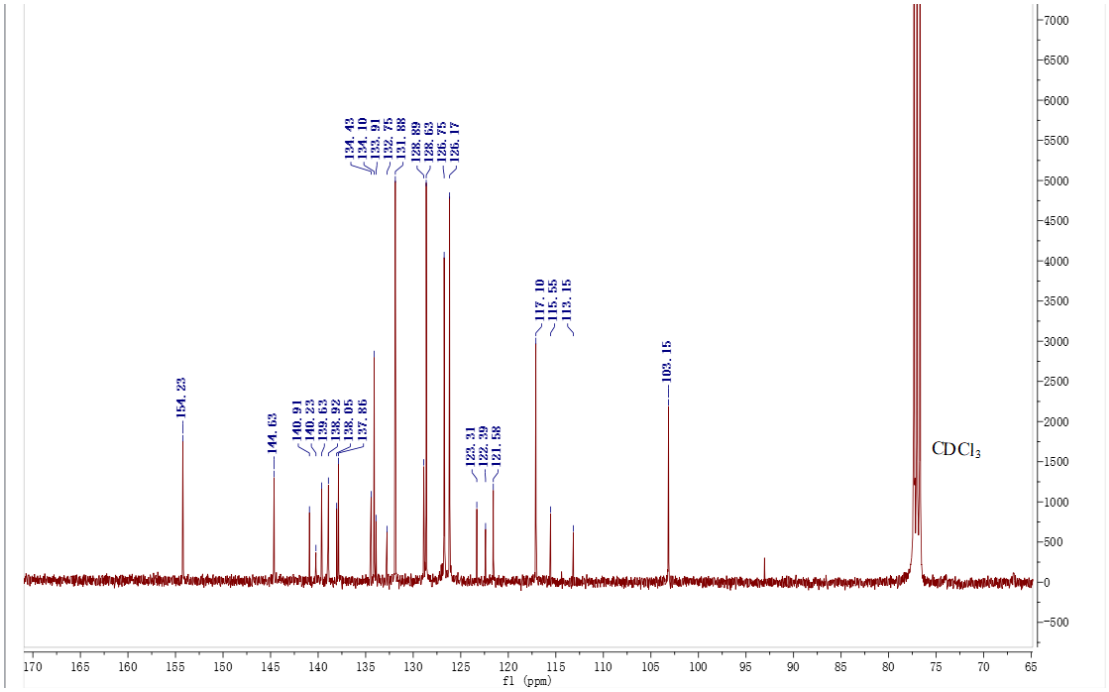

Figure **7.12**. ^{13}C NMR of **4PXZ-[10]CPP** in $CDCl_3$.

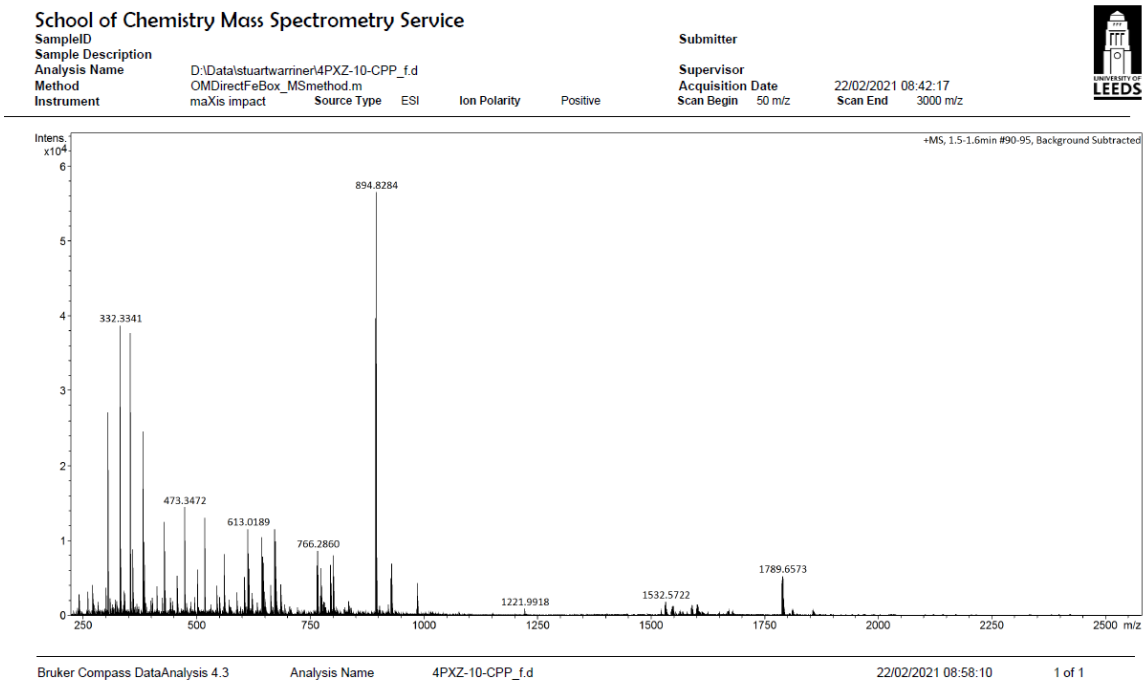

Figure **7.13**. HRMS of **4PXZ-[10]CPP**.

Elemental Analysis Service Request Form

Researcher name Dongyang Chen

Researcher email dc217@st-andrews.ac.uk

NOTE: Please submit ca. 10 mg of sample

Sample reference number	dc-III 09
Name of Compound	4PXZ-[10]CPP
Molecular formula	C132H84N4O4
Stability	stable
Hazards	low hazard
Other Remarks	

Analysis type:

Single ☐ **Duplicate**√☐ **Triplicate**☐

Analysis Result:

Element	Expected %	Found (1)	Found (2)	Found (3)
Carbon	88.57	87.15	87.01	
Hydrogen	4.73	4.66	4.89	
Nitrogen	3.13	3.58	3.27	
Oxygen				

Authorising Signature:

Date completed	21.05.21
Signature	J-P Li
comments	

Figure **7.14**. Elemental analysis of **4PXZ-[10]CPP**.

SHIMADZU LabSolutions **Analysis Report**

<Sample Information>

Sample Name	: dc-4PXZ10CPP		
Sample ID	: 4PXZ10CPP		
Data Filename	: 20042018_dc-C7CzMeOH50_dc-C7Cz_001.lcd		
Method Filename	: AcN (50) MeOH (50).lcm		
Batch Filename	: 4PXZ10CPP		
Vial #	: 1-31	Sample Type	: Unknown
Injection Volume	: 100 uL		
Date Acquired	: 19/04/2021 19:07:06	Acquired by	: ezc-7
Date Processed	: 19/04/2021 20:07:09	Processed by	: ezc-7

<Chromatogram>

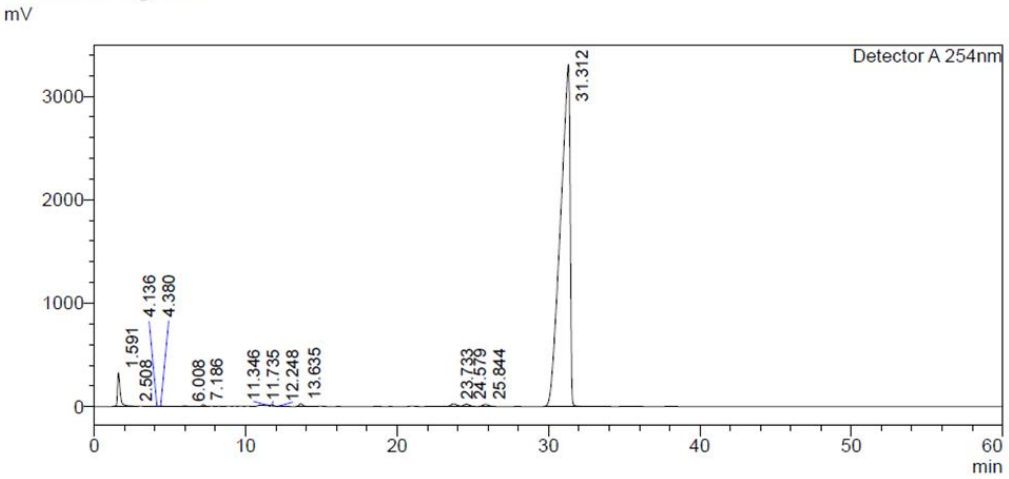

<Peak Table>

Detector A 254nm

Peak#	Ret. Time	Area	Height	Conc.	Unit	Mark	Name
1	1.591	3994745	326001	2.644		S	
2	2.508	5700	819	0.004		T	
3	4.136	25224	3011	0.017			
4	4.380	36000	4560	0.024		V	
5	6.008	69788	4763	0.046			
6	7.186	190533	17619	0.126			
7	11.346	111424	6706	0.074			
8	11.735	141195	10160	0.093		V	
9	12.248	62837	4701	0.042			
10	13.635	424742	27072	0.281			
11	23.733	627967	24711	0.416			
12	24.579	573290	22472	0.380		V	
13	25.844	526043	20035	0.348			
14	31.312	144274052	3307451	96.506			
Total		151063539	3780080				

Figure **7.15**. HPLC report of **4PXZ-[10]CPP**.

References

(1) Iwamoto, T.; Watanabe, Y.; Sadahiro, T.; Haino, T.; Yamago, S. Size-Selective Encapsulation of C60 by [10]Cycloparaphenylene: Formation of the Shortest Fullerene-Peapod. *Angew. Chemie - Int. Ed.* **2011**, *50*, 8342–8344. https://doi.org/10.1002/anie.201102302.

(2) Iwamoto, T.; Watanabe, Y.; Takaya, H.; Haino, T.; Yasuda, N.; Yamago, S. Size- and Orientation-Selective Encapsulation of C70 by Cycloparaphenylenes. *Chem. - A Eur. J.* **2013**, *19*, 14061–14068. https://doi.org/10.1002/chem.201302694.

(3) Xia, J.; Bacon, J. W.; Jasti, R. Gram-Scale Synthesis and Crystal Structures of [8]- and [10]CPP, and the Solid-State Structure of C 60[10]CPP. *Chem. Sci.* **2012**, *3*, 3018–3021. https://doi.org/10.1039/c2sc20719b.

(4) Li, K.; Xu, Z.; Deng, H.; Zhou, Z.; Dang, Y.; Sun, Z. Dimeric Cycloparaphenylenes with a Rigid Aromatic Linker. *Angew. Chemie - Int. Ed.* **2021**, *60*, 7649–7653. https://doi.org/10.1002/anie.202016995.

(5) Darzi, E. R.; Hirst, E. S.; Weber, C. D.; Zakharov, L. N.; Lonergan, M. C.; Jasti, R. Synthesis, Properties, and Design Principles of Donor-Acceptor Nanohoops. *ACS Cent. Sci.* **2015**, *1*, 335–342. https://doi.org/10.1021/acscentsci.5b00269.

(6) Tang, Y.; Li, J.; Du, P.; Zhang, H.; Zheng, C.; Lin, H.; Du, X.; Tao, S. Fullerene's Ring: A New Strategy to Improve the Performance of Fullerene Organic Solar Cells. *Org. Electron.* **2020**, *83*, 105747. https://doi.org/10.1016/j.orgel.2020.105747.

(7) Aydin, G.; Koçak, O.; Güleryüz, C.; Yavuz, I. Structural Order and Charge Transfer in Highly Strained Carbon Nanobelts. *New J. Chem.* **2020**, *44*, 15769–15775. https://doi.org/10.1039/d0nj03455j.

(8) Jasti, R.; Bhattacharjee, J.; Neaton, J. B.; Bertozzi, C. R. Carbon Nanohoop Structures. *J. Am. Chem. Soc.* **2008**, *130*, 17646–17647. https://doi.org/10.1021/ja807126u.

(9) Takaba, H.; Omachi, H.; Yamamoto, Y.; Bouffard, J.; Itami, K. Selective Synthesis of [12]Cyeloparaphenylene. *Angew. Chemie - Int. Ed.* **2009**, *48*, 6112–6116. https://doi.org/10.1002/anie.200902617.

(10) Yamago, S.; Watanabe, Y.; Iwamoto, T. Synthesis of [8]Cycloparaphenylene from a Square-Shaped Tetranuclear Platinum Complex. *Angew. Chemie - Int. Ed.* **2010**, *49*, 757–759. https://doi.org/10.1002/anie.200905659.

(11) Kayahara, E.; Sun, L.; Onishi, H.; Suzuki, K.; Fukushima, T.; Sawada, A.; Kaji, H.; Yamago, S. Gram-Scale Syntheses and Conductivities of [10]Cycloparaphenylene and Its Tetraalkoxy Derivatives. *J. Am. Chem. Soc.* **2017**, *139*, 18480–18483. https://doi.org/10.1021/jacs.7b11526.

(12) Kayahara, E.; Patel, V. K.; Xia, J.; Jasti, R.; Yamago, S. Selective and Gram-Scale Synthesis of [6]Cycloparaphenylene. *Synlett* **2015**, *26*, 1615–1619. https://doi.org/10.1055/s-0034-1380714.

(13) Iwamoto, T.; Watanabe, Y.; Sakamoto, Y.; Suzuki, T.; Yamago, S. Selective and Random Syntheses of [n]Cycloparaphenylenes (n = 8-13) and Size Dependence of Their

Electronic Properties. *J. Am. Chem. Soc.* **2011**, *133*, 8354–8361. https://doi.org/10.1021/ja2020668.

(14) Segawa, Y.; Fukazawa, A.; Matsuura, S.; Omachi, H.; Yamaguchi, S.; Irle, S.; Itami, K. Combined Experimental and Theoretical Studies on the Photophysical Properties of Cycloparaphenylenes. *Org. Biomol. Chem.* **2012**, *10*, 5979–5984. https://doi.org/10.1039/c2ob25199j.

(15) Kawanishi, T.; Ishida, K.; Kayahara, E.; Yamago, S. Selective and Gram-Scale Synthesis of [8]Cycloparaphenylene. *J. Org. Chem.* **2020**, *85*, 2082–2091. https://doi.org/10.1021/acs.joc.9b02844.

(16) Kayahara, E.; Kouyama, T.; Kato, T.; Yamago, S. Synthesis and Characterization of [n]CPP (n = 5, 6, 8, 10, and 12) Radical Cation and Dications: Size-Dependent Absorption, Spin, and Charge Delocalization. *J. Am. Chem. Soc.* **2016**, *138*, 338–344. https://doi.org/10.1021/jacs.5b10855.

(17) Fujitsuka, M.; Cho, D. W.; Iwamoto, T.; Yamago, S.; Majima, T. Size-Dependent Fluorescence Properties of [n]Cycloparaphenylenes (n = 8-13), Hoop-Shaped π-Conjugated Molecules. *Phys. Chem. Chem. Phys.* **2012**, *14*, 14585–14588. https://doi.org/10.1039/c2cp42712e.

(18) Fujitsuka, M.; Lu, C.; Iwamoto, T.; Kayahara, E.; Yamago, S.; Majima, T. Properties of Triplet-Excited [n]Cycloparaphenylenes (n = 8-12): Excitation Energies Lower than Those

of Linear Oligomers and Polymers. *J. Phys. Chem. A* **2014**, *118*, 4527–4532. https://doi.org/10.1021/jp504689q.

(19) Lovell, T. C.; Fosnacht, K. G.; Colwell, C. E.; Jasti, R. Effect of Curvature and Placement of Donor and Acceptor Units in Cycloparaphenylenes: A Computational Study. *Chem. Sci.* **2020**, *11*, 12029–12035. https://doi.org/10.1039/d0sc03923c.

(20) Lovell, T. C.; Garrison, Z. R.; Jasti, R. Synthesis, Characterization, and Computational Investigation of Bright Orange-Emitting Benzothiadiazole [10]Cycloparaphenylene. *Angew. Chemie - Int. Ed.* **2020**, *59*, 14363–14367. https://doi.org/10.1002/anie.202006350.

(21) Qiu, Z. L.; Tang, C.; Wang, X. R.; Ju, Y. Y.; Chu, K. S.; Deng, Z. Y.; Hou, H.; Liu, Y. M.; Tan, Y. Z. Tetra-Benzothiadiazole-Based [12]Cycloparaphenylene with Bright Emission and Its Supramolecular Assembly. *Angew. Chemie - Int. Ed.* **2020**, *59*, 20868–20872. https://doi.org/10.1002/anie.202008505.

(22) Graham, C.; Moral, M.; Muccioli, L.; Olivier, Y.; Pérez-Jiménez, Á. J.; Sancho-García, J. C. N-Doped Cycloparaphenylenes: Tuning Electronic Properties for Applications in Thermally Activated Delayed Fluorescence. *Int. J. Quantum Chem.* **2018**, *118*, 1–13. https://doi.org/10.1002/qua.25562.

(23) Hong, G.; Gan, X.; Leonhardt, C.; Zhang, Z.; Seibert, J.; Busch, J. M.; Bräse, S. A Brief History of OLEDs—Emitter Development and Industry Milestones. *Adv. Mater.* **2021**, *33*, 2005630. https://doi.org/10.1002/adma.202005630.

(24) Uoyama, H.; Goushi, K.; Shizu, K.; Nomura, H.; Adachi, C. Highly Efficient Organic Light-Emitting Diodes from Delayed Fluorescence. *Nature* **2012**, *492*, 234–238. https://doi.org/10.1038/nature11687.

(25) Etherington, M. K.; Gibson, J.; Higginbotham, H. F.; Penfold, T. J.; Monkman, A. P. Revealing the Spin-Vibronic Coupling Mechanism of Thermally Activated Delayed Fluorescence. *Nat. Commun.* **2016**, *7*, 13680. https://doi.org/10.1038/ncomms13680.

(26) Penfold, T. J.; Gindensperger, E.; Daniel, C.; Marian, C. M. Spin-Vibronic Mechanism for Intersystem Crossing. *Chem. Rev.* **2018**, *118*, 6975−7025. https://doi.org/10.1021/acs.chemrev.7b00617.

(27) Dos Santos, P. L.; Chen, D.; Rajamalli, P.; Matulaitis, T.; Cordes, D. B.; Slawin, A. M. Z.; Jacquemin, D.; Zysman-Colman, E.; Samuel, I. D. W. Use of Pyrimidine and Pyrazine Bridges as a Design Strategy to Improve the Performance of Thermally Activated Delayed Fluorescence Organic Light Emitting Diodes. *ACS Appl. Mater. Interfaces* **2019**, *11*, 45171–45179. https://doi.org/10.1021/acsami.9b16952.

(28) Rajamalli, P.; Chen, D.; Li, W.; Samuel, I. D. W.; Cordes, D. B.; Slawin, A. M. Z.; Zysman-Colman, E. Enhanced Thermally Activated Delayed Fluorescence through Bridge Modification in Sulfone-Based Emitters Employed in Deep Blue Organic Light-Emitting Diodes. *J. Mater. Chem. C* **2019**, *7*, 6664–6671. https://doi.org/10.1039/c9tc01498e.

(29) Kaji, H.; Suzuki, H.; Fukushima, T.; Shizu, K.; Suzuki, K.; Kubo, S.; Komino, T.; Oiwa, H.; Suzuki, F.; Wakamiya, A.; Murata, Y.; Adachi, C. Purely Organic Electroluminescent

Material Realizing 100% Conversion from Electricity to Light. *Nat. Commun.* **2015**, *6*, 8476. https://doi.org/10.1038/ncomms9476.

(30) Adamo, C.; Barone, V. Toward Reliable Density Functional Methods without Adjustable Parameters: The PBE0 Model. *J. Chem. Phys.* **1999**, *110* (13), 6158–6170. https://doi.org/10.1063/1.478522.

(31) Moral, M.; Muccioli, L.; Son, W. J.; Olivier, Y.; Sancho-Garcia, J. C. Theoretical Rationalization of the Singlet-Triplet Gap in Oleds Materials: Impact of Charge-Transfer Character. *J. Chem. Theory Comput.* **2015**, *11*, 168–177. https://doi.org/10.1021/ct500957s.

(32) Ogiwara, T.; Wakikawa, Y.; Ikoma, T. Mechanism of Intersystem Crossing of Thermally Activated Delayed Fluorescence Molecules. *J. Phys. Chem. A* **2015**, *119*, 3415–3418. https://doi.org/10.1021/acs.jpca.5b02253.

(33) Hosokai, T.; Matsuzaki, H.; Nakanotani, H.; Tokumaru, K.; Tsutsui, T.; Furube, A.; Nasu, K.; Nomura, H.; Yahiro, M.; Adachi, C. Evidence and Mechanism of Efficient Thermally Activated Delayed Fluorescence Promoted By Delocalized Excited States. *Sci. Adv.* **2017**, *3*, 1603282, https://doi.org/10.1126/sciadv.1603282.

(34) Gritzner, G.; Kuta, J. Recommendations on Reporting Electrode Potentials in Nonaqueous Solvents (Recommendations 1983). *Pure Appl. Chem.* **1984**, *56*, 461–466. https://doi.org/10.1351/pac198456040461.

(35) Stsiapura, V. I.; Kurhuzenkau, S. A.; Kuzmitsky, V. A.; Bouganov, O. V.; Tikhomirov, S. A. Solvent Polarity Effect on Nonradiative Decay Rate of Thioflavin T. *J. Phys. Chem. A* **2016**, *120*, 5481–5496. https://doi.org/10.1021/acs.jpca.6b02577.

(36) Goushi, K.; Yoshida, K.; Sato, K.; Adachi, C. Organic Light-Emitting Diodes Employing Efficient Reverse Intersystem Crossing for Triplet-to-Singlet State Conversion. *Nat. Photonics* **2012**, *6*, 253–258. https://doi.org/10.1038/nphoton.2012.31.

(37) Rajamalli, P.; Senthilkumar, N.; Gandeepan, P.; Huang, P.-Y.; Huang, M.-J.; Ren-Wu, C.-Z.; Yang, C.-Y.; Chiu, M.-J.; Chu, L.-K.; Lin, H.-W.; Cheng, C.-H. A New Molecular Design Based on Thermally Activated Delayed Fluorescence for Highly Efficient Organic Light Emitting Diodes. *J. Am. Chem. Soc.* **2016**, *138*, 628–634. https://doi.org/10.1021/jacs.5b10950.

(38) Wang, Y.; Yi, Y.; Wang, P.; Chen, Y.; Wei, X.; Wang, R.; Li, Z.; Liu, Y.; Duan, R.; Liu, J.; Yamada-Takamura, Y. Triplet Decay-Induced Negative Temperature Dependence of the Transient Photoluminescence Decay of Thermally Activated Delayed Fluorescence Emitter. *J. Mater. Chem. C* **2017**, *5*, 12077–12084. https://doi.org/10.1039/C7TC04025C.

(39) Kitamoto, Y.; Namikawa, T.; Ikemizu, D.; Miyata, Y.; Suzuki, T.; Kita, H.; Sato, T.; Oi, S. Light Blue and Green Thermally Activated Delayed Fluorescence from 10H-Phenoxaborin-Derivatives and Their Application to Organic Light-Emitting Diodes. *J. Mater. Chem. C* **2015**, *3*, 9122–9130. https://doi.org/10.1039/C5TC01380A.

(40) Park, I. S.; Lee, S. Y.; Adachi, C.; Yasuda, T. Full-Color Delayed Fluorescence Materials Based on Wedge-Shaped Phthalonitriles and Dicyanopyrazines: Systematic Design,

Tunable Photophysical Properties, and OLED Performance. *Adv. Funct. Mater.* **2016**, *26*, 1813–1821. https://doi.org/10.1002/adfm.201505106.

(41) Kitagawa, H.; Kobori, Y.; Yamanaka, M.; Yoza, K.; Kobayashi, K. Encapsulated-Guest Rotation in a Self-Assembled Heterocapsule Directed toward a Supramolecular Gyroscope. *Proc. Natl. Acad. Sci. U. S. A.* **2009**, *106*, 10444–10448. https://doi.org/10.1073/pnas.0812660106.

(42) Kayahara, E.; Nakano, M.; Sun, L.; Ishida, K.; Yamago, S. Syntheses of Tetrasubstituted [10]Cycloparaphenylenes by a Pd-Catalyzed Coupling Reaction. Remarkable Effect of Strain on the Oxidative Addition and Reductive Elimination. *Chem. - An Asian J.* **2020**, *15*, 2451–2455. https://doi.org/10.1002/asia.202000711.

(43) Ishiyama, T.; Murata, M.; Miyaura, N. Palladium(0)-Catalyzed Cross-Coupling Reaction of Alkoxydiboron with Haloarenes: A Direct Procedure for Arylboronic Esters. *J. Org. Chem.* **1995**, *60*, 7508–7510. https://doi.org/10.1021/jo00128a024.

Chapter 8

Experimental methods

8.1 Thermal analysis

Thermogravimetric analysis (TGA) was conducted on a Mettler TGA/DSC3 with a heating rate of 10 K/min under nitrogen flow. The samples were heated from 25 °C to 700 °C and the thermal decomposition (Td) was determined at a 5% weight loss. Differential scanning calorimetry was performed with a Mettler DSC3+ in pierced Al pans at 10 K/min under nitrogen flow. For each sample were carried out 4 cycles. 1st cycle : Heating at 10 K/mins, cooling at 100 K/min; 2nd cycle : Heating at 10 K/min, cooling at 100 K/min; 3rd cycle : Heating at 20 K/min, cooling at 100 K/min; 4th cycle : Heating at 40 K/min, cooling at 10 K/min. The glass transition *T*g was determined as the midpoint temperature of the step and the melting temperature (*T*m) was determined as the maximum value of the peak. These calculations were performed by Mettler STARe 15.00a software.

8.2 Electrochemistry measurements

Cyclic Voltammetry (CV) and Differential pulse voltammetry (DPV) analysis was performed on an Electrochemical Analyzer potentiostat model 620D from CH Instruments. Samples were prepared in acetonitrile (MeCN) or Dichloromethane (DCM) or Dimethlformamide (DMF) solutions, which were degassed by sparging MeCN or DCM or DMF with saturated nitrogen gas for 5 minutes prior to measurements. All measurements were performed using 0.1 M tetra-*n*-

butylammonium hexafluorophosphate, [nBu$_4$N]PF$_6$, in MeCN or DCM or DMF. An Ag/Ag$^+$ electrode was used as the reference electrode; a glassy carbon electrode was used as the working electrode; and a platinum electrode was used as the counter electrode. The redox potentials are reported relative to a saturated calomel electrode (SCE) with a ferrocene/ferrocenium (Fc/Fc$^+$) redox couple as the internal standard (0.38 V vs SCE).[1] The HOMO and LUMO energies were determined using the relation $E_{HOMO/LUMO} = -(E_{ox} / E_{red} + 4.8)$ eV, where E_{ox} and E_{red} are the maxima of anodic and cathodic peak potentials, respectively calculated from DPV relative to Fc/Fc$^+$.[2]

8.3 Photophysical measurements

Solutions and Spin-coated film using PMMA host

Optically dilute solutions of concentrations on the order of 10^{-5} or 10^{-6} M were prepared in HPLC grade *n*-hexane (Hex), toluene (PhMe), tetrahydrofuran (THF), ethyl acetate (EA), dichloromethane (DCM), and acetonitrile (MeCN); ii) Spin-coated films were produced from chloroform solutions of blends (10 wt% guest to host) at 2000 rpm for 60 seconds. Absorption spectra of solutions were recorded at room temperature on a Shimadzu UV-1800 double beam spectrophotometer using a 1 cm quartz cuvette. Molar absorptivity values were determined from at least five independent solutions at varying concentrations with absorbance ranging from 1.26 $\times 10^{-4}$ to 3.43 $\times 10^{-5}$ M. For emission studies, aerated solutions were bubbled with compressed air for 5 min prior to spectra acquisition. Degassed solutions were prepared via three freeze-pump-thaw cycles and spectra were taken using home-made Schlenk quartz cuvette. Steady-state

emission spectra and time-resolved decay curves were measured using an Edinburgh Instruments F980 spectrofluorimeter. The steady-state spectra were measured using excitation at 340 nm (Xenon lamp) while the time-resolved decay curves were recorded at room temperatures with excitation at 378 nm (PDL 800-D pulsed diode laser). Photoluminescence quantum yields for solutions were determined using the optically dilute method[3] in which four sample solutions with absorbances of ca. 0.10, 0.075, 0.050 and 0.025 at 360 nm were used. The Beer-Lambert law was found to remain linear at the concentrations of the solutions. For each sample, linearity between absorption and emission intensity was verified through linear regression analysis with the Pearson regression factor (R^2) for the linear fit of the data set surpassing 0.9. Individual relative quantum yield values were calculated for each solution and the values reported represent the slope obtained from the linear fit of these results. The quantum yield of the sample, Φ_{PL}, can be determined by the equation $\Phi_{PL} = (\Phi_r * \frac{A_r}{A_s} * \frac{I_s}{I_r} * \frac{n_s^2}{n_r^2})$,[3] where A stands for the absorbance at the excitation wavelength (λ_{exc}: 360 nm), I is the integrated area under the corrected emission curve and n is the refractive index of the solvent with the subscripts "s" and "r" representing sample and reference respectively. Φ_r is the absolute quantum yield of the external reference quinine sulfate (Φ_r = 54.6% in 1 *N* H_2SO_4).[4] The experimental uncertainty in the emission quantum yields is conservatively estimated to be 10%, though we have found that statistically we can reproduce Φ_{PL}s to 3% relative error.

To prepare the 10 wt% doped films of emitters in a host matrix, 90% w/w (90 mg) of host was dissolved in 1 mL of solvent and to this, 10% w/w (10 mg) of emitter was added. Thin films were

then spin-coated on a quartz substrate using a spin speed of 1500 rpm for 60 s to give a thickness of ~80 nm. Time-resolved decay curves for prompt fluorescence (100 ns and 10 μs time window) were measured using time correlated single photon counting (TCSPC) while time-resolved delayed fluorescence decays were measured using multi-channel scaling (MCS). The singlet-triplet splitting energy, ΔE_{ST}, was estimated by recording the prompt fluorescence spectra and phosphorescence emission at 77 K. The films were excited by a Q-switched Nd:YAG laser emitting at 343 nm (Laser-export). Emission from the samples was focused onto a spectrograph (Chromex imaging, 250is spectrograph) and detected on a sensitive gated iCCD camera (Stanford Computer Optics, 4Picos) having subnanosecond resolution. Phosphorescence spectra were measured 1 ms after the excitation of the Nd:YAG laser with iCCD exposure time of 10 ms. Prompt fluorescence spectra were measured 4 ns after the excitation of the femtosecond laser with iCCD exposure time of 100 ns. Photoluminescence quantum yield, Φ_{PL}, for solid films were measured using an integrating sphere in a Hamamatsu C9920-02 system with excitation at 330 nm under air and constant nitrogen gas flow.

Spin-Coated film using DPEPO, PPF or CBP host

Spin-coated films were produced from chloroform solutions of blends (for example: 10 wt% guest to host for DPEPO) at 1000 rpm for 30 seconds. The steady-state spectra were recorded at room temperature on a HORIBA FluoroMax Plus. Transient PL measurements were performed at room temperature filled with He gas using Hamamatsu Quantaurus-Tau C11367-01. Φ_{PL}s were measured under nitrogen gas flow employing an integrating sphere in a Hamamatsu C9920-02.

Fitting of time-resolved luminescence measurements

Time-resolved PL measurements were fitted to a sum of exponentials decay model, with chi-squared (χ^2) values between 1 and 2, using the EI FLS980 software. Each component of the decay is assigned a weight, (w_i), which is the contribution of the emission from each component to the total emission.

The average lifetime was then calculated using the following:

- Two exponential decay model:

$$\tau_{AVG} = \tau_1 w_1 + \tau_2 w_2$$

with weights defined as $w_1 = \frac{A1\tau_1}{A1\tau_1 + A2\tau_2}$ and $w_2 = \frac{A2\tau_2}{A1\tau_1 + A2\tau_2}$ where A1 and A2 are the preexponential-factors of each component.

- Three exponential decay model:

$$\tau_{AVG} = \tau_1 w_1 + \tau_2 w_2 + \tau_3 w_3$$

with weights defined as $w_1 = \frac{A1\tau_1}{A1\tau_1 + A2\tau_2 + A3\tau_3}$, $w_2 = \frac{A2\tau_2}{A1\tau_1 + A2\tau_2 + A3\tau_3}$ and $w_3 = \frac{A3\tau_3}{A1\tau_1 + A2\tau_2 + A3\tau_3}$ where A1, A2 and A3 are the preexponential-factors of each component.

Analysis of rate constants

As deduced and listed in the literature,[5] k_{RISC}, k_{ISC}, k_r^S and k_{nr}^S are analysed based on following equations:

$$k_{\mathrm{RISC}} \approx \frac{k_{\mathrm{p}} + k_{\mathrm{d}}}{2} - \sqrt{\left(\frac{k_{\mathrm{p}} + k_{\mathrm{d}}}{2}\right)^2 - k_{\mathrm{p}} k_{\mathrm{d}} \left(1 + \frac{\Phi_{\mathrm{PL}}^{\mathrm{d}}}{\Phi_{\mathrm{PL}}^{\mathrm{p}}}\right)} \qquad (9.1)$$

$$k_{\mathrm{ISC}} = \frac{k_{\mathrm{p}} k_{\mathrm{d}}}{k_{\mathrm{RISC}}} \frac{\Phi_{\mathrm{PL}}^{\mathrm{d}}}{\Phi_{\mathrm{PL}}^{\mathrm{p}}} \quad (9.2)$$

$$k_{\mathrm{r}}^{\mathrm{S}} \approx (k_{\mathrm{r}}^{\mathrm{S}} + k_{\mathrm{nr}}^{\mathrm{S}}) \Phi_{\mathrm{PL}}/100 \quad (9.3)$$

$$k_{\mathrm{nr}}^{\mathrm{S}} \approx (k_{\mathrm{r}}^{\mathrm{S}} + k_{\mathrm{nr}}^{\mathrm{S}})(100 - \Phi_{\mathrm{PL}})/100 \quad (9.4)$$

where k_{p} and k_{d} are the rate constants of the prompt and delayed fluorescence components, respectively; k_{ISC} and k_{RISC} are rate constants of intersystem crossing and reverse intersystem crossing, respectively; Φ_{PL}, Φ_{PL}^{d} and Φ_{PL}^{p} were the photoluminescence (PL) quantum yields of total, delayed and prompt components, respectively; k_r^S and k_{nr}^S are the radiative and non-radiative rate constants of the lowest excited singlet state, respectively. Here, k_{p}, k_{d}, Φ_{PL}, Φ_{PL}^{d} and Φ_{PL}^{p} are obtained from the transient PL experiments and PL quantum efficiency measurements.

8.4 Theoretical calculations

The calculations were performed with the Gaussian 09 revision D.018 suite for the density functional theory (DFT).[6] Ground state optimized structures were obtained using PBE0 functionals[7] each employing the 6-31G(d,p) basis set with dispersion effects included.[8] Excited state calculations were performed for each within the Tamn-Dancoff approximation (TDA).[9] The results of spin-orbit coupling matrix element (SOCME) calculation were extracted by PySOC program after TDA calculation.[10] Molecular orbitals were visualized using GaussView 6.0 software.[11] Bond lengths and torsions were measured using Gaussview 6.0 package.[11]

8.5 Molecular orientation measurements

Films of ~50 nm thickness of **tri-PXZ-TRZ**:host (7% wt) in Chapter **5** were deposited on 1 mm glass substrates via thermal evaporation. While the spin-coated neat films of **DiKTALC** in Chapter **6** were prepared on the hydrophilic glass substrate or silicon substrate using different concentrations of **DiKTaLC** in chloroform (10 or 20 mg/mL) at spin speeds of 4000 RPM, followed by 60 seconds of drying step under nitrogen flow. All the substrates were previously cleaned by ultrasound bath in acetone (15 min) and *iso*propanol (15 min), followed by 3 min etching with oxygen plasma. All films were encapsulated in a nitrogen-filled glovebox immediately after evaporation.

Angle-resolved photoluminescence spectra of each sample were acquired using a setup similar to the literature.[12] The samples were coupled to a cylindrical glass lens using immersion oil and excited with a high-power LED with peak emission at 365 nm. The long-wavelength tail of the LED was cut using a short-pass filter with cut-off wavelength at 425 nm. Spectra were acquired from 0° to 90° using a home-built automated scanning setup. The transverse electric (TE) component of the emission was blocked by a polariser. The measured spectral radiant intensity emitted by these films was fitted to the following equation using a least-squares method:[12]

$$I(\theta, \lambda, a) = aI_{TM,v} + (\frac{1-a}{2})I_{TM,h}, \quad (9.5)$$

where a is the free fitting parameter called anisotropy factor and $I_{TM,v}$ and $I_{TM,h}$ are the vertical and horizontal transverse magnetic components of the spectral radiant intensity, respectively. The latter quantities were calculated from a transfer-matrix method combined with an electromagnetic dipole model, as reported in the literature.[13]

8.6 OLEDs fabrication and testing

Vacuum-deposited OLEDs

OLED devices were fabricated using pre-cleaned indium-tin-oxide (ITO) coated glass substrates with ITO thickness of 90 nm. The OLED devices had a pixel size of 2 mm × 1 mm. The small molecules and cathode layers were thermally evaporated using an angstrom deposition chamber at 10^{-7} mbar at 0.3 A/s or 0.6 A/s for organic layers and 3 A/s for cathode. OLED testing was performed using a Keithey 2400 sourcemeter and photodiode, assuming that the OLEDs show Lambertian emission. Eletroluminescence spectra were collected using an Oriel MS125 spectrograph coupled to an Andor DV420-BU CCD camera.

Solution-processed OLEDs

PEDOT:PSS (Heraeus, AI 4083) was spin-coated onto pre-cleaned ITO substrate at 500 rpm for 1 s then at 4000 rpm for 12 s, and at 500 rpm for 1 s. The film was dried at 120 ℃ under air condition for 30 min followed by N_2 flow for 10 min. The 10 mg mL^{-1} emitter in chloroform solution was stirred at 1000 rpm at 30 ℃ for 1 h before spin-coated onto the PEDOT:PSS layer at 1000 rpm for 30 s. The device was dried at 30 ℃ under vacuum for 30 min and cooled down under N_2 flow for 5 min. The BmPyPhB (30 nm), Liq (1 nm), and Al (80 nm) layers were vacuum deposited at ~10^{-4} Pa using a deposition apparatus (SE-4260, ALS Technology, Japan), resulting in active areas of 4 mm^2 for each pixel. Performance of OLEDs were characterized using an integrating sphere integrated with an absolute EQE measurement system (C9920-12, Hamamatsu

Photonics, Japan) equipped with a source meter (2400, Keithley, Japan). The device performances were measured in the forward direction in 200-meV steps.

References

(1) Connelly, N. G.; Geiger, W. E. Chemical Redox Agents for Organometallic Chemistry. *Chem. Rev.* **1996**, *96* , 877–910.

(2) Cardona, C. M.; Li, W.; Kaifer, A. E.; Stockdale, D.; Bazan, G. C. Electrochemical Considerations for Determining Absolute Frontier Orbital Energy Levels of Conjugated Polymers for Solar Cell Applications. *Adv. Mater.* **2011**, *23* (20), 2367–2371. https://doi.org/10.1002/adma.201004554.

(3) Demas, J. N.; Crosby, G. A. The Measurement of Photolumineseence Quantum Yields. A Review. *J. Phys. Chem.* **1971**, *75* (8), 991–1024. https://doi.org/10.1021/j100678a001.

(4) Melhuish, W. H. Quantum Efficiencies of Fluorescence of Organic Substan Ces: Effect of Solvent and Concentration of the Fluorescent Solute. *J. Phys. Chem.* **1961**, *65* (2), 229–235. https://doi.org/10.1021/j100820a009.

(5) Wada, Y.; Nakagawa, H.; Matsumoto, S.; Wakisaka, Y.; Kaji, H. Organic Light Emitters Exhibiting Very Fast Reverse Intersystem Crossing. *Nat. Photonics* **2020**, *14* (10), 643–649. https://doi.org/10.1038/s41566-020-0667-0.

(6) Frisch, M. J.; Trucks, G. W.; Schlegel, H. B.; Scuseria, G. E.; Robb, M. A.; Cheeseman, J. R.; Scalmani, G.; Barone, V.; Mennucci, B.; Petersson, G. A.; Nakatsuji, H.; Caricato, M.; Li, X.; Hratchian, H. P.; Izmaylov, A. F.; Bloino, J.; Zheng, G.; Sonnenberg, J. L.; Had, M.; Fox, D. J. Gaussian 09, Revis. D.01. Wallingford, CT. 2009.

(7) Adamo, C. Toward Reliable Density Functional Methods without Adjustable Parameters : The PBE0 Model. *J. Chem. Phys.* **1999**, *110*, 6158–6170.

(8) Pople, J. A.; Binkley, J. S.; Seeger, R. Theoretical Models Incorporating Electron Correlation. *Int. J. Quantum Chem.* **1976**, *10*, 1–19. https://doi.org/10.1002/qua.560100802.

(9) Hirata, S.; Head-Gordon, M. Time-Dependent Density Functional Theory within the Tamm–Dancoff Approximation. *Chem. Phys. Lett.* **1999**, *314*, 291–299. https://doi.org/10.1016/S0009-2614(99)01149-5.

(10) Gao, X.; Bai, S.; Fazzi, D.; Niehaus, T.; Barbatti, M.; Thiel, W. Evaluation of Spin-Orbit Couplings with Linear-Response Time-Dependent Density Functional Methods. *J. Chem. Theory Comput.* **2017**, *13*, 515–524. https://doi.org/10.1021/acs.jctc.6b00915.

(11) Dennington, R.; Keith, T. A.; Millam, J. M. GaussView, Version 6.1. Semichem Inc.: Shawnee Mission, KS, 2019.

(12) Graf, A.; Liehm, P.; Murawski, C.; Hofmann, S.; Leo, K.; Gather, M. C. Correlating the Transition Dipole Moment Orientation of Phosphorescent Emitter Molecules in OLEDs with Basic Material Properties. *J. Mater. Chem. C* **2014**, *2*, 10298–10304. https://doi.org/10.1039/c4tc00997e.

(13) Furno, M.; Meerheim, R.; Hofmann, S.; Lüssem, B.; Leo, K. Efficiency and Rate of Spontaneous Emission in Organic Electroluminescent Devices. *Phys. Rev. B* **2012**, *85*, 115205. https://doi.org/10.1103/PhysRevB.85.115205.

Chapter 9

Appendix

9.1 Characterization Data

Relevant characterization data is provided in electronic form in a CD at the end of this thesis.

9.2 Publications arising from my work

9.2.1 Published Manuscripts

(1) **Chen, D.**; Kusakabe, Y.; Ren, Y.; Sun, D.; Rajamalli, P.; Wada, Y.; Suzuki, K.; Kaji, H.; Zysman-Colman, E. Multichromophore Molecular Design for Efficient Thermally Activated Delayed Fluorescence Emitters with Near-Unity Photoluminescence Quantum Yields. *J. Org. Chem.*, **2021**. https://doi.org/https://doi.org/10.26434/chemrvix.14560860.v1.

(2) **Chen, D.**; Zysman-Colman, E. Exploring the Possibility of Using Fluorine-Involved Non-Conjugated Electron-Withdrawing Groups for Thermally Activated Delayed Fluorescence Emitters by TD-DFT Calculation. *Beilstein J. Org. Chem.* **2021**, *17*, 210–223. https://doi.org/10.3762/BJOC.17.21.

(3) Rajamalli, P.; **Chen, D.**; Suresh, S. M.; Tsuchiya, Y.; Adachi, C.; Zysman-Colman, E. Planar and Rigid Pyrazine-Based TADF Emitter for Deep Blue Bright Organic Light-Emitting Diodes. *European J. Org. Chem.* **2021**, *2021* (16), 2285–2293.

https://doi.org/10.1002/ejoc.202100086.

(4) **Chen, D.**; Rajamalli, P.; Tenopala-Carmona, F.; Carpenter-Warren, C. L.; Cordes, D. B.; Keum, C. M.; Slawin, A. M. Z.; Gather, M. C.; Zysman-Colman, E. Bipyridine-Containing Host Materials for High Performance Yellow Thermally Activated Delayed Fluorescence-Based Organic Light Emitting Diodes with Very Low Efficiency Roll-Off. *Adv. Opt. Mater.* **2020**, *8* (1), 1–10. https://doi.org/10.1002/adom.201901283.

(5) Dos Santos, P. L.; **Chen, D.**; Rajamalli, P.; Matulaitis, T.; Cordes, D. B.; Slawin, A. M. Z.; Jacquemin, D.; Zysman-Colman, E.; Samuel, I. D. W. Use of Pyrimidine and Pyrazine Bridges as a Design Strategy to Improve the Performance of Thermally Activated Delayed Fluorescence Organic Light Emitting Diodes. *ACS Appl. Mater. Interfaces* **2019**, *11* (48), 45171–45179. https://doi.org/10.1021/acsami.9b16952.

(6) Rajamalli, P.; **Chen, D.**; Li, W.; Samuel, I. D. W.; Cordes, D. B.; Slawin, A. M. Z.; Zysman-Colman, E. Enhanced Thermally Activated Delayed Fluorescence through Bridge Modification in Sulfone-Based Emitters Employed in Deep Blue Organic Light-Emitting Diodes. *J. Mater. Chem. C* **2019**, *7* (22), 6664–6671. https://doi.org/10.1039/c9tc01498e.

(7) Weidlich, F.; Esumi, N.; **Chen, D.**; Mück-Lichtenfeld, C.; Zysman-Colman, E.; Studer, A. Mild C−F Activation in Perfluorinated Arenes through Photosensitized Insertion of Isonitriles at 350 Nm. *Adv. Synth. Catal.* **2020**, *362* (2), 376–383. https://doi.org/10.1002/adsc.201901126.

9.2.2 Unpublished Manuscripts

(1) **Chen, D.**; Tenopala-Carmona, F.; Knöller, J. A.; Mischok, A.; Hall, D.; Suresh, S. M.; Matulaitis, T.; Olivier, Y.; Laschat, S.; Gather, M.; Zysman-Colman, E. Controlling the Emitter's Orientation in Solution-processed OLEDs using a Liquid Crystalline Multi-resonance TADF Emitter.

(2) **Chen, D.**; Wada, Y.; Sun, L.; Kayahara, E.; Suzuki, K.; Yamago, S.; Kaji, H.; Zysman-Colman, E. The Utilization of Cycloparaphenylene for Thermally Activated Delayed Fluorescence Emitters.

9.3 Conference Contributions

9.3.1 Oral Presentations

1. Synthesis symposium, University St Andrews, May 2017.
2. Synthesis symposium, University St Andrews, March 2018.
3. Synthesis symposium, University St Andrews, December 2019.

9.3.2 Poster Presentations

1. TADF symposium, Frankfurt, Germany, September 2017.
2. Postgraduate Symposium, University of St Andrews, December 2019.
3. TADF conference online December 2021.